UNIVERSITÉ DE STRASBOURG

ÉCOLE DOCTORALE DES SCIENCES CHIMIQUES

Institut de Science et d'Ingénierie Supramoléculaires

THÈSE présentée par :

Mariel RUIZ KUBLI

soutenue le : **30 Octobre 2020**

pour obtenir le grade de : **Docteur de l'université de Strasbourg**

Discipline/ Spécialité : Chimie

Design and synthesis of hybrid particles

for drug delivery

THÈSE dirigée par :
Mme DE COLA Luisa   Professeur, Université de Strasbourg

RAPPORTEURS :
M. MARTÍNEZ MAÑEZ Ramón   Professeur, Universitat Politècnica de València (Espagne)
M. LODEIRO ESPIÑO Carlos   Professeur, Universidade NOVA de Lisboa (Portugal)

AUTRES MEMBRES DU JURY :
M. MERTZ Damien   Docteur et directeur de recherche, Université de Strasbourg
M. BONNEVIOT Laurent   Professeur, ENS de Lyon

Acknowledgments

I would like to thank to many people who made this thesis possible.

My gratitude to Prof. Luisa De Cola for giving me the opportunity to work with her, to let me perform my PhD studies aboard in her multicultural honorable group at ISIS. For the guidance through this thesis, the suggestions, discussions, and time despite her always very busy schedule.

I would like to express my gratitude to the jury members who kindly accepted to judge this thesis: Prof. Ramón Martínez Mañez, Prof. Carlos Lodeiro Espiño and Dr. Damien Mertz.

I want to express my deep gratitude to our direct collaborators, Prof. Jaume Veciana, and Prof. Nora Ventosa, a great honor to work under your direction. For the meetings, questions and advices, all this made me become a more ordered designer scientist. Special thanks to Dr. Mariana Köber, to listen me with enthusiasm, for the collaboration, suggestions, and guidance.

The realization of this thesis has only been possible due to the numerous and fruitful collaborations all along this work. It is a great pleasure to thank Prof. Didier Pascal from University of Strasbourg for the STORM experiments. Prof. Jesús Santamaria and Dr. Víctor Sebastián from the University of Zaragoza for the Cryo-STEM accoupled by EDX. From our group, thank you very much to Laura Talamini for the cell viability tests, to Etienne Piantanida and Pierre Picchetti for the SAXS and XPS measurements. My sincere gratitude to Charles Lochenie for his support and guidance, suggestions and advises. Thank you to Guillem Vargas Nadal for the creation of some QS pictures presented in this thesis.

I express my gratitude to the Mexican National Council for Science and Technology (CONACYT) for financing my PhD (Scholarship 440357). Thanks to the RISE Nano-oligomed Project to give me the opportunity to work in Nanomol Technologies ICMAB by the European Union's Horizon 2020

I would like to thank also to all my ISIS group. For me, my second family: I had the honor to work with a lot of smart and strong nice people. All of you have marked a sign in my heart and I am deeply grateful to life because I had the opportunity to meet you. For the time in the lab, for make me grow in the scientific area, and general in life, for all the support and love. Thank you.

I would have to express my gratitude to Dr. Brian Di Marco, Dr. Luis Guillermo Moreno Alcantar, Dr. Mike Dentinger, Dr. Ricardo Totovao, Dr. Judit Morla, Lidia Ballell and Adrian Tamayo Serra for the hard work reading this thesis for its improvement. Thank you for the interest, help and motivation.

To all already mentioned including Dr. Matteo Bessi, Dr. John Ddungu, and Dr. Giuseppe Alonci, I would never forget all the adventures we lived together. So many good moments. My home is my heart, and you will be always my guests.

Dr. María Elena Valle Medina and Dr. Joel Montalvo Acosta, gracias por abrirme sus corazones y hacerme sentir siempre con amor y compañía, los quiero muchísimo.

Per descomptat, m'agradaria agrair de nou a l'Adrian per tot el seu suport i paciència. Per estar al meu costat durant l'elaboració d'aquesta tesis, per tot el seu temps, dedicació i la seva ajuda. Perquè la teva ajuda ho ha fet tot més fàcil. De tot cor, gracies. A la seva família gràcies per adoptar-me en temps de covid amb els braços oberts.

Lastly and most importantly I would like to thank my family that supports me with my dream to carry my PhD abroad even when this meant to be far from each other. To my mother: Patricia Elena Kubli Hernandez por alentarme a cumplir mis sueños, por darme fuerza, compañía inclusive a distancia, por estar siempre ahí, siempre en nuestros corazones. Por todo tu infinito amor, gracias. To my father: Juan Jose Ruiz Bohorquez soy la mujer que quise ser y estoy agradecida por toda su educación, sus cuidados, sus consejos, sus consentideras, su apoyo y amor. Gracias por todo.

2HEO	*N*-(2-hydroxy ethyl) oleamide
AEA	Anandamide
APTES	(3-aminopropyl)triethoxysilane
B-SQS	Breakable silica coated Quatsomes
BTSPD	Bis(triethoxysilylpropyl)tetrasulfide
CBDs	Cannabinoids
CF	Compressed fluid
Chol	Cholesterol
CLSM	Confocal Laser Scanning Microscopy
Cryo-STEM	Cryo-scanning transmission electron microscopy
CryO-TEM	Cryogenic Transmission electron microscopy
CTAB	Cetrimonium bromide
Cyan5	Cyanine5 NHS ester
DCM	dichloromethane
DDS	Drug delivery systems
DELOS-SUSP	Depressurization of an Expanded Organic Solution
Dh	Hydrodynamic diameter
DiI	1,1'-dioctadecyl-3,3,3'3'-tetramethylindocarbocyanine perchlorate
DMF	Dimethylformamide
DIPEA	*N,N*-Diisopropylethylamine
DiR	1,1'-Dioctadecyl-3,3,3',3'-Tetramethylindotricarbocyanine Iodide
DLS	Dynamic light scattering
Dodecyl	Dodecyltriethoxysilane
EDX	Energy-dispersive X-ray spectroscopy
EPA	Environmental Protection Agency

FDA	Food and Drug Administration
FITC	Fluorescein isothiocyanate
FONS	Fluorescent organic nanoparticles
GSH	Glutathione
HBTU	N,N,N',N'-Tetramethyl-O-(1H-benzotriazol-1-yl)uronium Hexafluorophosphate
HR ESI-TOF-MSC	High Resolution Electrospray Ionization Time of flight-mass spectrometry chromatography
IR	Infrared
L-NVs	Lipid-based nanovesicles
MBds	microbeads
MS	Microspheres
MSNPs	Mesoporous Silica Nanoparticles
NaOH	Sodium Hydroxide
NB-SQS	Non- breakable silica Quatsomes
NMs	Nanomaterials
NPs	Nanoparticles
NR	Nile Red
Orange 2	4-[(2-Hydroxy-1-naphthalenyl)azo]benzenesulfonic acid monosodium salt
PBS	Phosphate Buffer Saline
PC	phosphatidylcholine
PEG	Poly(ethylene glycol)
PFOTS	1H,1H,2H,2H-Perfluoro-Octyltriethoxysilane
PVA	Poly(vinyl alcohol)
QACs	Quaternary ammonium compounds
QS	Quatsomes

REV	reverse-phase evaporation
RT	Room temperature
SAXS	Small angle X-ray scattering
scRPE	supercritical reverse phase evaporation,
SEM	Scanning electron microscope
SORP	Self-organized precipitation
SQS	Silica Coated Quatsomes
STEM	Scanning transmission electron microscopy
SUVs	Small unilamellar vesicles
TEA	Triethanolamine
TEM	Transmission electron microscopy
TEMOS	Tetramethyl orthosilicate
TEOS	Tetraethyl orthosilicate
TGA	Thermogravimetric analysis
THC	Tetrahydrocannabinol
TMB	Trimethylbenzene
UV-Vis	Ultraviolet-Visible
XPS	X-ray photoelectron spectroscopy
ZP	Zeta Potential

TABLE OF CONTENTS

Les nanomatériaux (NM) ont été explorés au cours des dernières décennies et ont gagné en importance dans les avancées technologiques en raison de leurs propriétés physiques, chimiques et biologiques accordables.[1] Les nanomatériaux sont classés en fonction de leur taille, de leur composition, de leur forme et de leur origine. En raison de la croissance accrue de la recherche, les industries sont devenues particulièrement intéressées par l'exploration et le développement de nouvelles technologies pour produire des nanomatériaux. L'un des grands domaines d'intérêt de la recherche est celui des applications nanomédicales dans lesquelles le défi consiste à produire des matériaux non toxiques pour l'imagerie biomédicale, la biodétection, le diagnostic et la thérapie.

Pour l'industrie pharmaceutique, l'administration et le ciblage des médicaments ont constitué des approches intéressantes pour créer une "balle magique", un matériau capable d'administrer des médicaments au bon endroit, à la bonne concentration et pendant la bonne période, sans modification chimique du matériau, réalisant ainsi la biodégradabilité et la biocompatibilité du nanoporteur.[2-4] Différents exemples de nanoplateformes d'administration de médicaments existent aujourd'hui. Elles sont essentiellement divisées en trois groupes principaux : matrices organiques, matériaux inorganiques et nanoparticules hybrides.[5] Des systèmes comme les dendrimères,[6–9] liposomes,[10,11] « quantum dots »,[12] nanoparticules polymères,[13,14] matériaux à base de silice,[15–17] nanotubes de carbone,[18,19] nanoparticules métalliques,[20] etc. révolutionnent le domaine de la médecine pour la détection précoce, le diagnostic et le traitement de diverses maladies comme le cancer, le VIH, la maladie d'Alzheimer, le glaucome, la dépression, pour n'en citer que quelques-unes.[3,21–23]

Les nanoparticules hybrides, composées de composants inorganiques et organiques, peuvent être préparées selon plusieurs stratégies ; leur production est basée sur l'optimisation de leurs effets thérapeutiques synergiques. Ensuite, la combinaison des vecteurs de médicaments doit être conçue de manière rationnelle pour s'adapter à de multiples médicaments ou modalités thérapeutiques avec une libération contrôlée dans le temps des cargaisons individuelles.[24] Cette thèse, intitulée "Conception et synthèse de particules hybrides pour la libération de médicaments", repose sur la combinaison de plusieurs systèmes d'administration pour former de nouveaux matériaux hybrides destinés à des applications biomédicales. Des systèmes hybrides principalement constitués de structures de silice et combinés à de l'acide polylactique-glycolique (PLGA), un matériau polymère, ou à des vésicules non lipidiques appelées quatsomes (QS) sont présentés dans cette thèse. Pour une compréhension approfondie des chapitres, voici un bref résumé des nanoparticules de silice, des supports polymères PLGA et des QS.

Parmi tous les matériaux inorganiques, les nanoparticules de silice mésoporeuses sont devenues un support prédominant pour les applications d'administration de médicaments en raison de leur taille, de leur morphologie et de leur porosité réglable. Le piégeage efficace des médicaments dans leur structure poreuse, suivi d'une libération contrôlée en réponse à des stimuli endogènes ou exogènes tels que la lumière, la température, les ultrasons ou le pH, a fait des nanostructures de silice mésoporeuse des vecteurs d'administration très prometteurs.[25] Les systèmes de silice à réponse aux stimuli redox, dont la structure comporte des liaisons S-S clivables, sont une bonne stratégie pour l'administration de médicaments dans les cellules, car ils répondent par un comportement autodestructeur aux stimuli présents dans l'environnement intracellulaire une fois que la cible est atteinte.[26–28]

Les polymères ont été largement explorés dans le domaine de l'administration de médicaments en raison de leurs propriétés uniques de biocompatibilité et de biodégradation.[29] Des nanoparticules polymères biodégradables ont été utilisées dans de larges applications dans les domaines de l'administration et de la libération de médicaments, de la vaccination, du ciblage, de la thérapie des tumeurs et des systèmes de diagnostic.[30–34] Parmi tous les polymères, le PLGA est considéré comme un bon candidat pour les applications d'administration de médicaments en raison de leur biocompatibilité et de leur biodégradabilité. Le PLGA peut être métaboliquement hydrolysé en monomères, l'acide lactique et l'acide glycolique. Il a été

démontré que les particules de PLGA, sous forme de microparticules ou de nanoparticules,[35] sont capables de transporter et d'administrer diverses classes de médicaments creusés comme les vaccins,[36] peptides,[37] protéines,[38,39] et les médicaments hydrophobes.[40] Les avantages de l'utilisation de ces particules de PLGA sont la réduction de la fréquence des injections, des niveaux thérapeutiques soutenus de médicaments, l'administration de médicaments spécifiques à un site et des formulations qui peuvent être modifiées pour un nombre quelconque de profils de libération souhaités.[41,42]

Au cours des 50 dernières années, de nombreux nanomédicaments ont été mis au point et approuvés pour l'administration à l'homme sur la base de nanovésicules lipidiques. Les liposomes sont le plus célèbre système d'administration de médicaments basé sur les phospholipides.[43] Leur potentialité dans l'administration de médicaments est due à leur biocompatibilité.[43] Cependant, ils présentent de faibles stabilités colloïdales et chimiques.[44,45] C'est pourquoi une autre classe de vésicules, appelées "nanovésicules à base de lipides non liposomiques", a suscité beaucoup d'attention. À partir de ces matériaux, les Quatsomes, bicouche unilamellaire nanovésicules constituées de tensioactifs à base d'ammonium quaternaire et de stérols, ont été utilisées comme modèle pour l'administration de médicaments. Leur stabilité en termes de morphologie, de taille, de lamellarité et d'organisation supramoléculaire de la membrane les rend intéressantes pour les applications d'administration de médicaments dans le cadre du développement de nouveaux nanomédicaments.[46–49]

OBJECTIF : L'objectif de cette thèse est ensuite de développer différentes classes de matériaux hybrides nanostructurées afin d'assurer l'interface entre les systèmes inorganiques et organiques. En particulier, utiliser des matériaux souples et durs combinés dans un seul système pour développer des systèmes dégradables pour des applications de délivrance de médicaments.

C'est pourquoi il est d'abord présenté ici l'utilisation d'un nouveau système hybride consistant en une combinaison d'un matériau polymère avec l'inclusion de nanoparticules de silice mésoporeuse pour l'encapsulation et la délivrance de cannabinoïdes (CBDs) et de médicaments chimiothérapeutiques pour le traitement du cancer. Des exemples dans la littérature ont montré que la combinaison de CBDs avec des agents chimiothérapeutiques renforce l'action antitumorale.[50] Différentes sortes de nanoparticules de silice mésoporeuse (MSNP) ont été

synthétisées comme modèles des systèmes inorganiques qui peuvent encapsuler un médicament anticancéreux pour la libération du médicament chimiothérapeutique.[51] Ces NP de silice chargées d'un médicament chimiothérapeutique sont à leur tour chargées dans des transporteurs PLGA[36] qui contiennent également un endocannabinoïde actif ou son analogue (CBD), ce qui donne un système hybride de livraison en tandem sans précédent (CBDs-MSNPs@PLGA-MBds) (**Figure 0.1**).
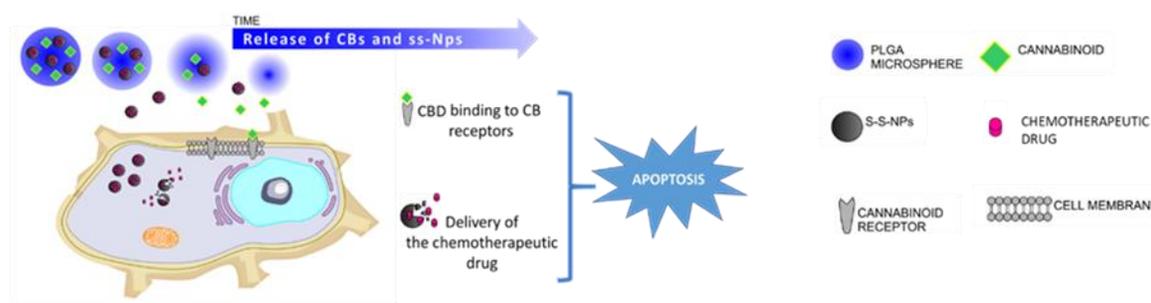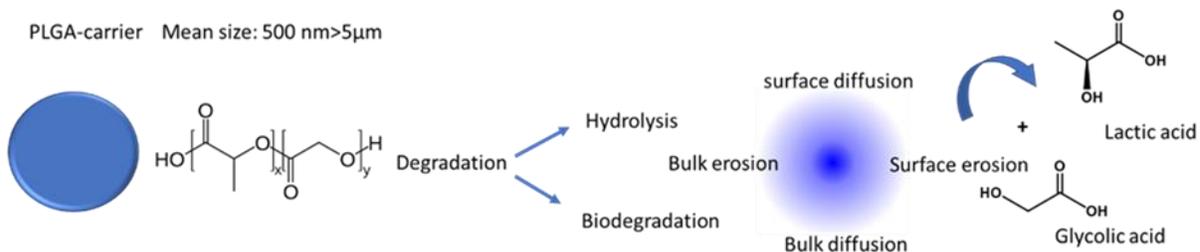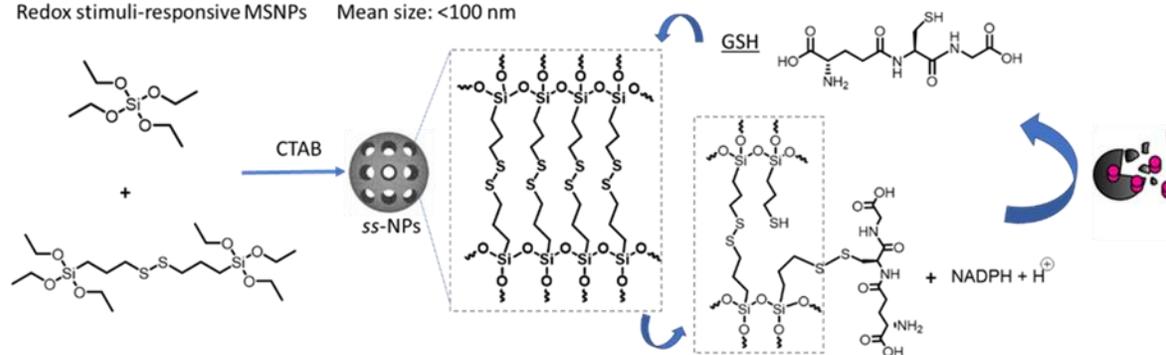
Figure 0.1. A) Système hybride et mécanisme d'action en tant que stratégie de traitement du cancer consistant en la combinaison de deux matériaux : le PLGA et la silice mésoporeuse comme vecteurs pour le chargement des cannabinoïdes et un médicament chimiothérapeutique pour augmenter l'apoptose des cellules cancéreuses. **B)** des porteurs de PLGA et une représentation schématique de son processus de dégradation et **C)** des MSNP réagissant aux stimuli redox pour la libération du médicament chimiothérapeutique.

Pour la préparation des supports PLGA, trois méthodologies ont été testées pour produire des particules dans la gamme de taille de 500 nm > 5 μm, par la méthode d'évaporation du solvant,[52–54] la méthode SORP, qui consiste en une procédure sans surfactant par une voie de précipitation auto-organisée[55,56] et la méthode du gabarit hydrogel.[57] Une taille spécifique est nécessaire pour garantir que le médicament cannabinoïde sera libéré à l'extérieur de la cellule car les récepteurs cannabinoïdes sont des protéines intramembranaires (IMP) situées dans la bicouche lipidique de la membrane cellulaire.[58] De plus, non seulement la taille joue un rôle important, mais l'homogénéité de l'échantillon est nécessaire car le comportement des nanoparticules en tant que systèmes de libération de médicaments est fortement affecté par cette propriété.[59]

Par la méthode d'évaporation du solvant, les PLGA@MS ont été obtenus avec deux distributions principales de taille de diamètre d'environ 1.47±0.37 μm et 14.9±3.7 μm. L'inclusion des MSNP peut être faite mais la polydispersité du système a donné l'information que cette méthodologie n'était pas la meilleure pour poursuivre les études. En utilisant la méthodologie SORP, des sphères PLGA d'environ 600 nm et 1 μm peuvent être réalisées avec un tensioactif libre. L'incorporation de MSNP donne des agglomérations de PLGA@MS avec 20 et 5 % p/p. D'autre part, l'incorporation d'un endocannabinoïde perturbe la formation des sphères même à faible charge (5 % p/p).

Par conséquent, pour toutes les procédures essayées, la méthode du gabarit d'hydrogel a été la seule dans laquelle l'homogénéité concernant la taille et la morphologie est préservée même avec l'inclusion de cannabinoïdes et de nanoparticules de silice mésoporeuse (**Figure 0.2**). Les porteurs, appelés perles en raison de leur forme, avaient un diamètre de 20 μm. Des images confocales ont été prises des différents PLGA@systems chargés de rouge du Nil, de N-(2-hydroxy éthyl) oléamide (2HEO) et d'Anandamide (AEA) dans le PLGA@porteur (**Figure 0.2 A-C**). Le 2HEO et l'AEA ont été synthétisés et caractérisés par RMN, IR, HR ESI-TOF-MS ; ces composés représentent l'analogue et la molécule active d'un groupe de cannabinoïdes appelé endocannabinoïde.[60] Le 2HEO ou l'AEA peuvent être chargés en pourcentage élevé (20 % p/p) dans les PLGA@MBds donnant des systèmes CBDs-PLGA@MBds. La **figure 0.2D** montre le système MSNPs@PLGA@carrier system, où les MSNPs ont été chargées avec de l'orange 2 pour imiter le chargement d'un médicament chimiothérapeutique. À leur tour, ces MSPN ont été

insérées dans le PLGA@porteur. Les images confocales présentes ici ont été prises à l'aide d'un laser d'une longueur d'onde de 488 nm.

Ensuite, voici un nouveau système hybride de livraison en tandem sans précédent (MNPs@PLGA-MBds) basé sur des systèmes cassables et dégradables, un support polymère biodégradable poly(acide lactique-co-glycolique) approuvé par la FDA[61] qui peut transporter efficacement les CBDs et les nanoparticules de silice mésoporeuse (*ss*-NPs), préparé avec un disulfure de liaison sensible à l'oxydoréduction[51] et chargé de médicaments chimiothérapeutiques. Cette conception couvre l'exigence de délivrer deux types de médicaments différents dans deux parties différentes de la cellule (intra et extra-membranaire), ce qui ouvre une nouvelle barrière pour le développement de systèmes de délivrance de médicaments.
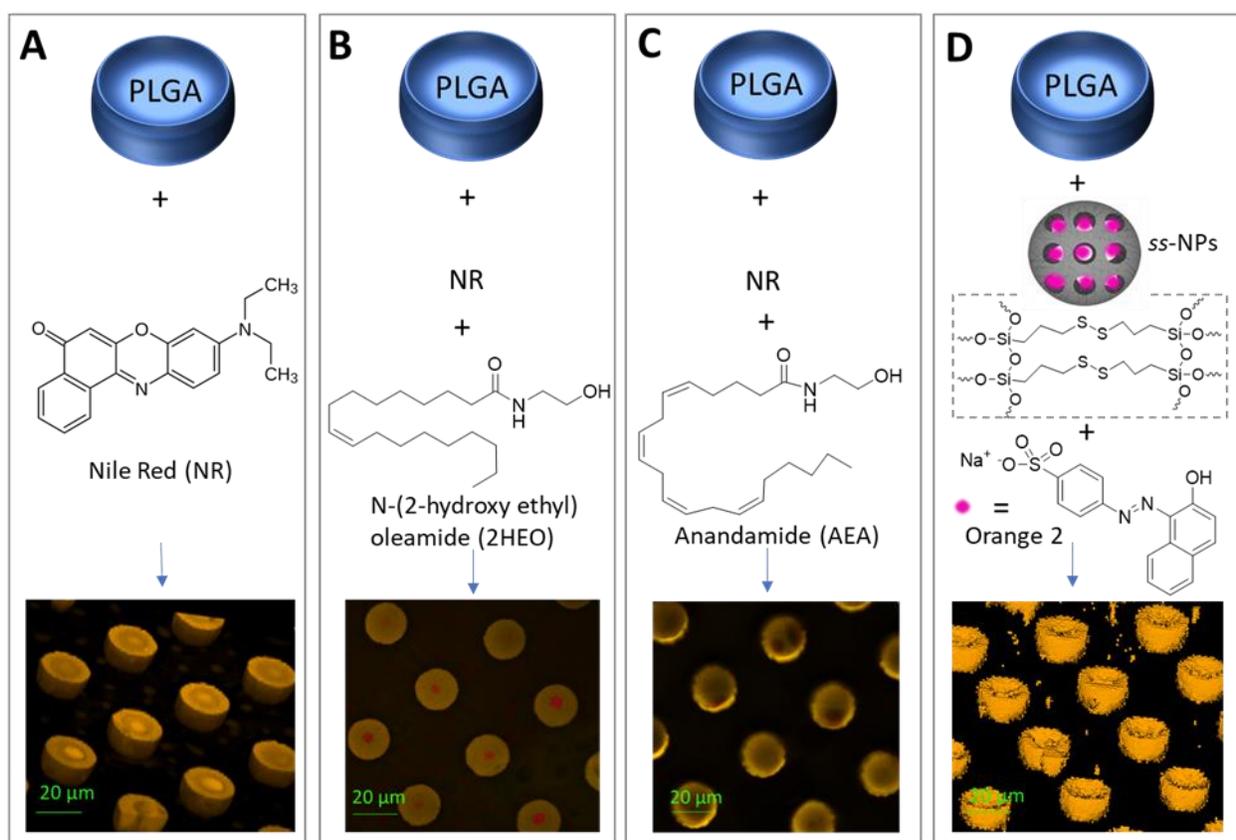
Figure 0.2. Représentation schématique des différents systèmes hybrides synthétisés pour la charge de molécules hydrophobes, en particulier **A)** Rouge du Nil, **B)** N-(2-hydroxy éthyl) oleamide (2HEO) et **C)** Anandamide (AEA) dans le PLGA@carrier. Le 2HEO et l'AEA représentent l'analogue et l'endocannabinoïde actif. **D)** Montre la représentation du système MSNPs@PLGA@porteur. L'orange 2 a été chargé dans les MSNPs redox-stimuli-MSNPs pour imiter le médicament chimiothérapeutique. Les images confocales ont été prises en utilisant une longueur d'onde laser de 488 nm.

Ensuite, il est présenté un autre matériau hybride réalisé en combinaison avec des vésicules de base non lipidiques, appelées Quatsomes et de la silice. Les quatsomes (QS) sont des structures vésiculaires thermodynamiquement stables, composées de tensioactifs quaternaires et de stérols (**Figure 0.3A**). Leur stabilité concerne leur morphologie, leur taille, leur lamellarité et leur organisation supramoléculaire membranaire.[62,63] Ces vésicules peuvent charger des médicaments hydrophobes ou hydrophiles et peuvent donc servir à plusieurs applications, y compris l'administration de médicaments. L'idée est de combiner les Quatsomes avec une enveloppe de silice pour protéger la vésicule, ce qui donne plus de stabilité structurelle et mécanique au QS, contre l'agglomération et les fuites internes pendant le stockage, le transport et l'application. De plus, cette enveloppe pourrait empêcher la perte de la cargaison pour les applications de livraison de médicaments, garantissant que tous les médicaments chargés arriveront au point de destination. En outre, nous présentons ici la formation d'une enveloppe de silice sensible au stimulus, qui, en présence d'un agent réducteur (existant en forte concentration dans les cellules cancérigènes), se brise en petits morceaux libérant la cargaison et empêchant ainsi l'accumulation de la matière dans le corps.

Pour la synthèse de la coquille de silice, différents silanes ont été testés ; TEMOS, TEOS et APTES pour produire la coquille de silice non cassable enrobée de QS (NB-SQS) et la combinaison de ceux-ci avec le BTSPD pour produire la coquille sensible au stimuli (stimuli redox) pour former une coquille de silice cassable sur QS (B-SQS) (**Figure 0.3B**).
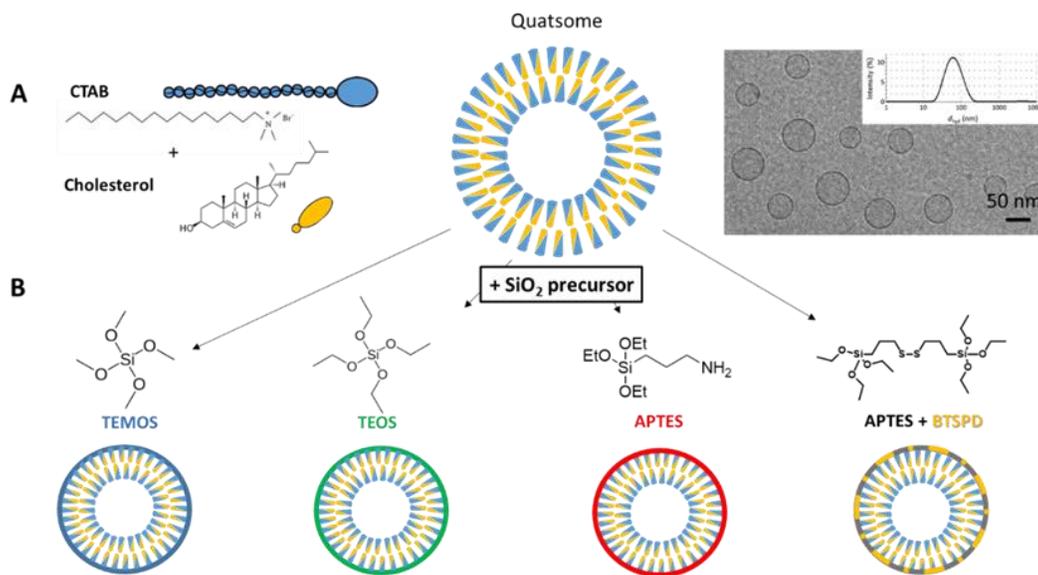
Figure 0.3. **A)** Composition du SQ. **B)** Différents SQ revêtus de silice synthétisés.

7

De tous les silanes essayés, ce sont les TEOS et TEMOS qui ont permis d'observer un dépôt de silice dans le QS. La **Figure 0.4** montre les images au Cryo-MET et la distribution des tailles de diamètre du NB-SQS en utilisant des TEMOS et TEOS comme précurseurs de silice, après 4 et 2 jours de réaction, respectivement. La taille des DLS et le potentiel zêta au cours du temps pendant leur préparation révèlent un changement de taille et de ZP de 85±2 nm et 94±15 mV à 116±3 nm et 36±3 mV pour le système utilisant TEMOS (**Figure 0.4A**), et à 159±3 nm et 29±1 mV pour le système utilisant TEMOS (**Figure 0.4B**).
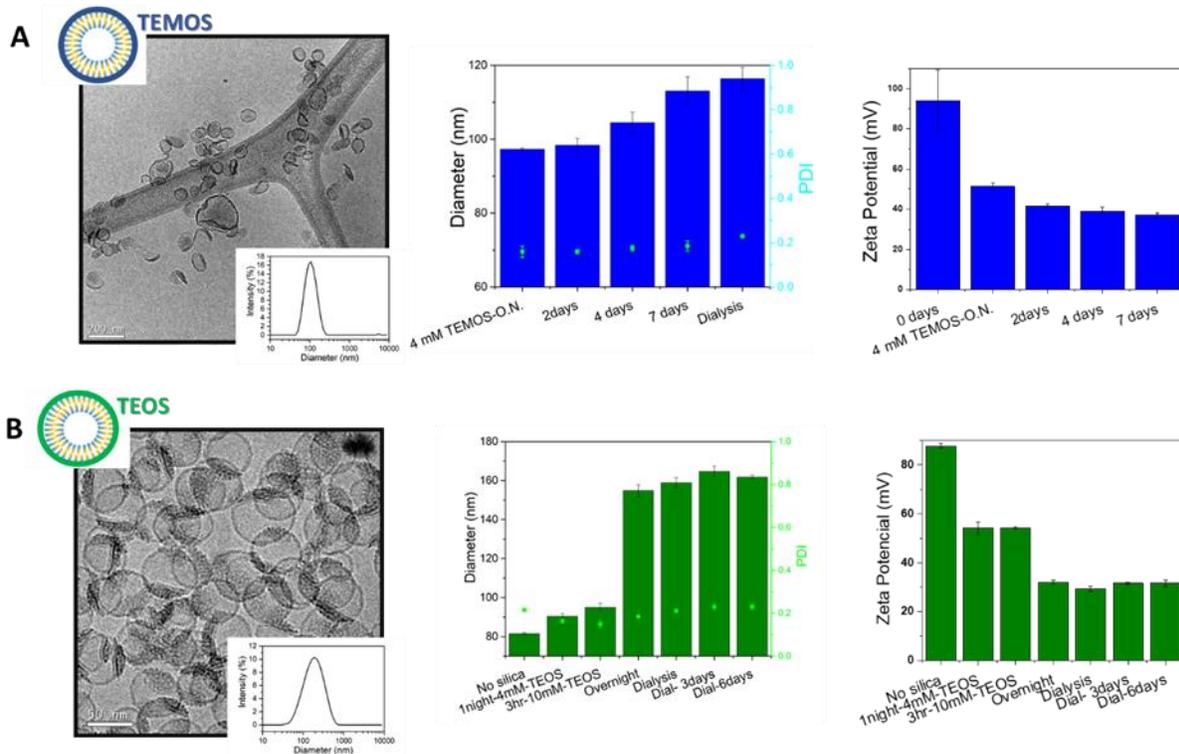
Figure 0.4. SQ à revêtement incassable utilisant **A)** TEMOS et **B)** TEOS. Cryo-MET et distribution de la taille du diamètre (après 4 et 2 jours de réaction, respectivement). Taille des DLS et potentiel zêta dans le temps pendant leur préparation.

Pour le QS à revêtement de silice cassable réagissant au stimulus Redox (B-S-QS), un mélange d'APTES et de BTSPD a été utilisé (**Figure 0.5A**). La **Figure 0.5B** montre l'image au MEB de l'échantillon après une nuit d'agitation (diamètre initial de QS = 114±26 nm). La distribution de taille du MEB, comptage effectué sur 300 nanoparticules, a donné un diamètre moyen de 143±19 nm de particules BS-QS. On a essayé la synthèse avec des QS d'une taille de 50 nm (diamètre initial de QS = 58±1 nm et ZP = 84±2) pour travailler avec des particules qui sont mieux absorbées par les cellules.[64] Les images au MET (**Figure 0.5C**) montrent la présence de silice autour du QS

et ce qui pourrait être des particules de silice. Les données de DLS (**Figure 0.5D**) montrent deux populations différentes de taille 58±12 nm et 185±42 nm, la seconde population pourrait être attribuée à l'agglomération du BS-QS. L'analyse des images de Cryo-MEB donne un diamètre de 32±6 nm (moyenne de plus de 200 particules), et une épaisseur de coquille de 9±2 nm ; valeur supérieure aux 4-5 nm de la membrane QS (**Figures 0.5E** et **0.5F**).
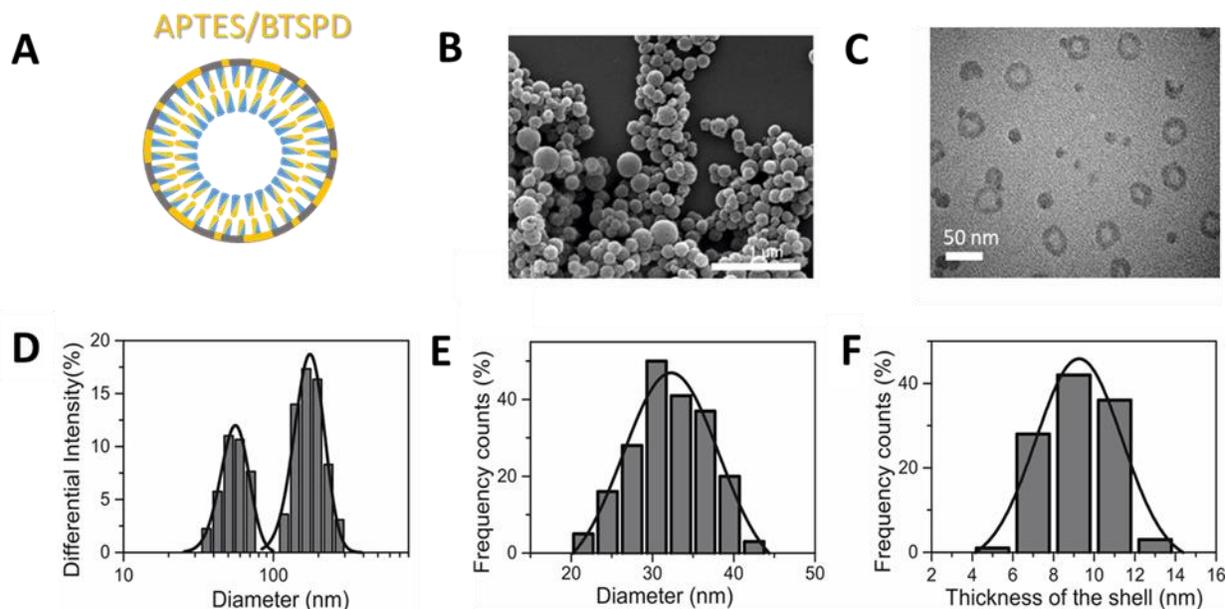
Figure 0.5. A) Schéma représentatif **B)** Images MEB et **C)** MET pour les QS recouverts de silice (APTES/BTSPD). Barre d'échelle 1µm et 50 nm, respectivement. **D)** Distribution de taille des B-SQS mesurée par DLS donnant deux populations de taille de 58±12 nm et 185±42 nm. **E)** Distribution des diamètres de taille du TEM (comptage effectué sur 200 particules de silice QS ; diamètre moyen 32±6 nm) et **F)** Distribution de l'épaisseur de la taille de la coquille du MET (comptage effectué sur 100 particules de silice QS ; épaisseur moyenne de la coquille 9±2nm).

D'autre part, le SQ et la silice ont été étiquetés avec un fluorophore donneur (DiI) et accepteur (Cyan5), respectivement (**Figure 0.6A**), pour obtenir un transfert d'énergie de résonance (FRET)[65] dans le cas où la silice est attachée au SQ. Ces systèmes agissent comme des biosondes luminescentes et leur étude vise à déterminer le potentiel de ces matériaux en tant que systèmes d'administration de médicaments. Pour cela, le DiI a été chargé dans la membrane hydrophobe du QS,[66] et l'ester de cyanine 5 NHS a été fixé de manière covalente à la silice par les groupes amino de l'APTES, produisant le système Cyan5-BS-QS-DiI (**Figure 0.6B**). Contrôles avec un seul colorant (Cyan5-BS-QS et BS-QS-DiI), les spectres d'émission et d'excitation (**Figure 0.6C**) de BS-QS-DiI cassable (lignes roses ; avec des longueurs d'onde d'excitation et d'émission de λ_{exc} = 525

nm et λ_{exc} = 625 nm, respectivement) et Cyan5-BS-QS (lignes bleues ; λ_{exc} = 600 nm et λ_{exc} = 750 nm) montrent un chevauchement de l'émission du donneur (BS-QS-DiI) et de l'excitation de l'accepteur (Cyan5-BS-QS), confirmant la possibilité d'observer le FRET dans le système Cyan5-BS-QS-DiI. En effet, une efficacité élevée du FRET est observée dans les spectres d'émission et d'excitation du système Cyan5-BS-QS-DiI (**Figure 0.6D**; λ_{exc} = 500 nm et λ_{exc} = 750 nm), avec une efficacité de 94 % du FRET (valeur obtenue à partir du rendement quantique QY (E=1-(QYDA(D)/QYD(D)), indiquant que les deux colorants sont largement proches (à une distance inférieure à 10 nm) en raison de la formation de silice autour du QS.
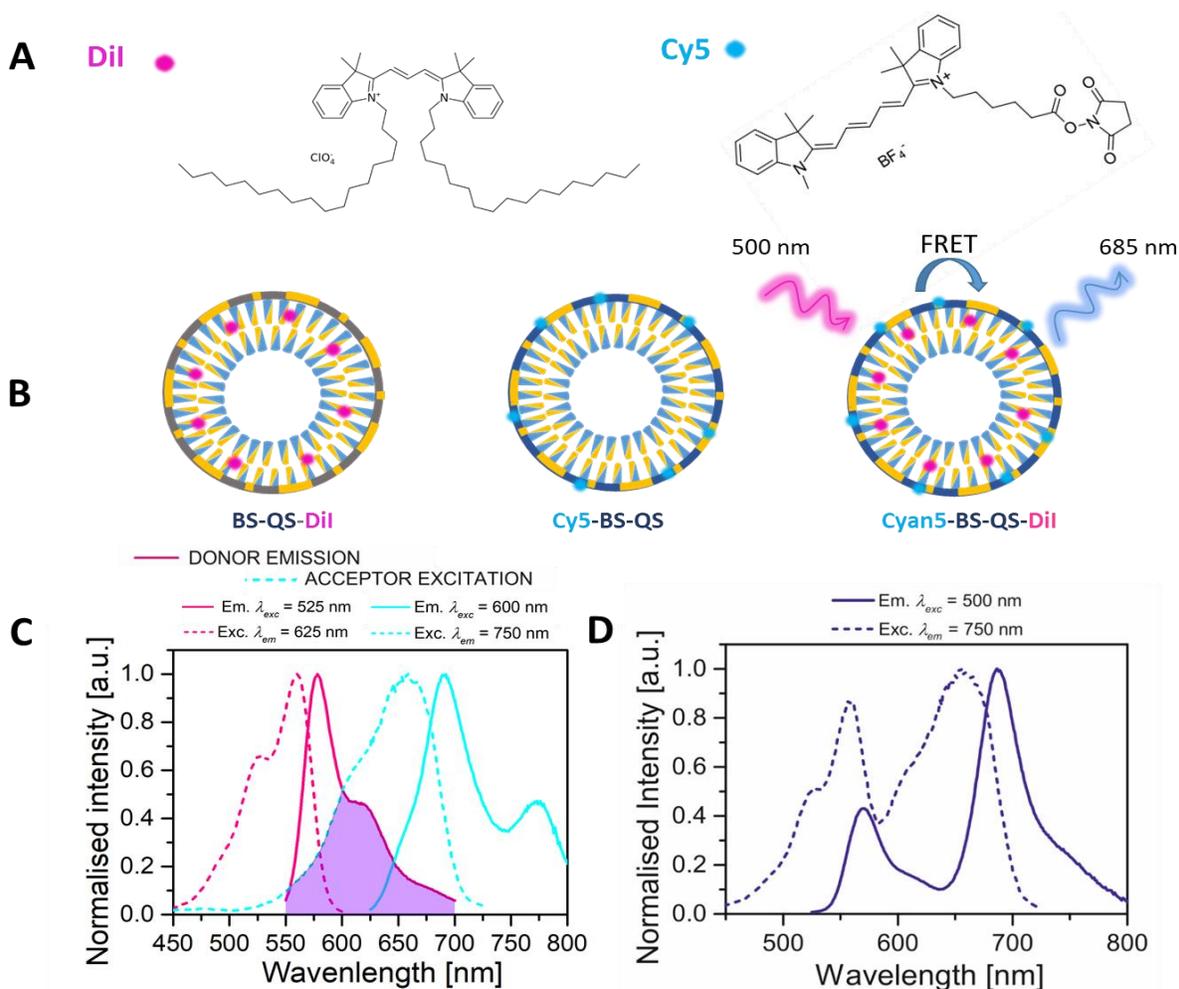
Figure 0.6. A) Colorants utilisés pour l'étiquette silice QS. **B)** Schéma représentatif de l'étiquette silice QS. **C)** Spectres d'émission et d'excitation de la silice cassable QS chargée en DiI (BS-QS-DiI) (lignes roses); les longueurs d'onde d'excitation et d'émission étaient respectivement de 525 et 625 nm. Et sa translation avec les spectres d'émission et d'excitation de la silice cassable QS chargée de Cyan5 (Cyan5-BS-Qs) (lignes bleues); longueur d'onde d'excitation et d'émission à 600 et 750 nm, respectivement. **D)** Spectres d'émission et d'excitation du DiI-QS (Cyan5-BS-Qs-DiI) revêtu de silice cassable Cyan5 (Cyan5-BS-Qs-DiI) ; excitation à 500 nm et émission à 750 nm.

Les images de Cyan5-BS-QS (λ_{exc} = 642 nm) obtenues par microscopie à reconstruction optique stochastique (STORM) (**Figure 0.7**) montrent des taches de taille comprise entre 300 nm, ce qui suggère que le Cyan5-APTES forme effectivement la coquille de silice sur le QS.
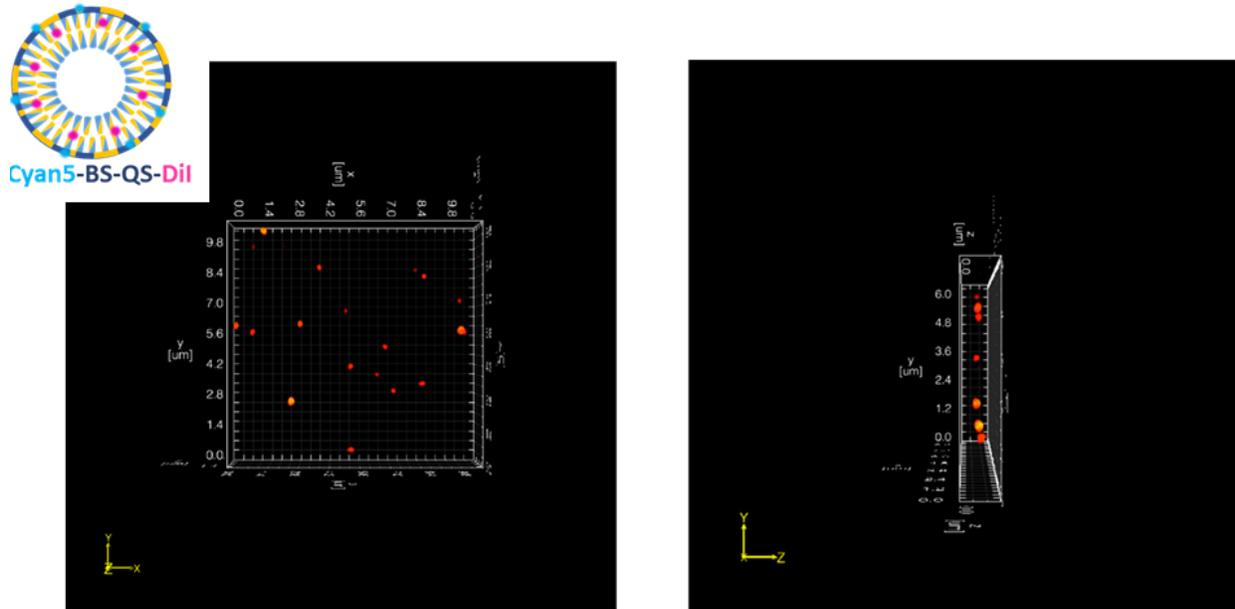
Figure 0.7. Schéma du QS cassable utilisé pour l'analyse STORM (Cyan5-BS-QS-DiI) et les images STORM du QS cassable de Cyan5 (micromètre u.m.).

Afin de savoir s'il y a une possibilité de rupture dans le BS-QS en présence d'un agent réducteur, des tests de rupture ont été effectués pour dégrader l'enveloppe de silice. La cassabilité du BS-QS a été étudiée en présence de glutathion (GSH) (**Figure 0.8A**). En présence de 10 mM de GSH, l'absorbance du Cyan5-BS-QS, placé dans un tube à membrane semi-perméable (taille de coupure des pores de 14 kDa), appelant ici cette méthode un système ouvert, montre une diminution progressive dans le temps (**Figure 0.8B**), atteignant pratiquement zéro après 12 jours (**Figure 0.8C** et **D**). Ces résultats suggèrent que le lien disulfure du BTSPD commence à se rompre en présence de l'agent réducteur, produisant de petits morceaux de silice marquée au Cyan5 qui finissent par quitter le tube de la membrane.
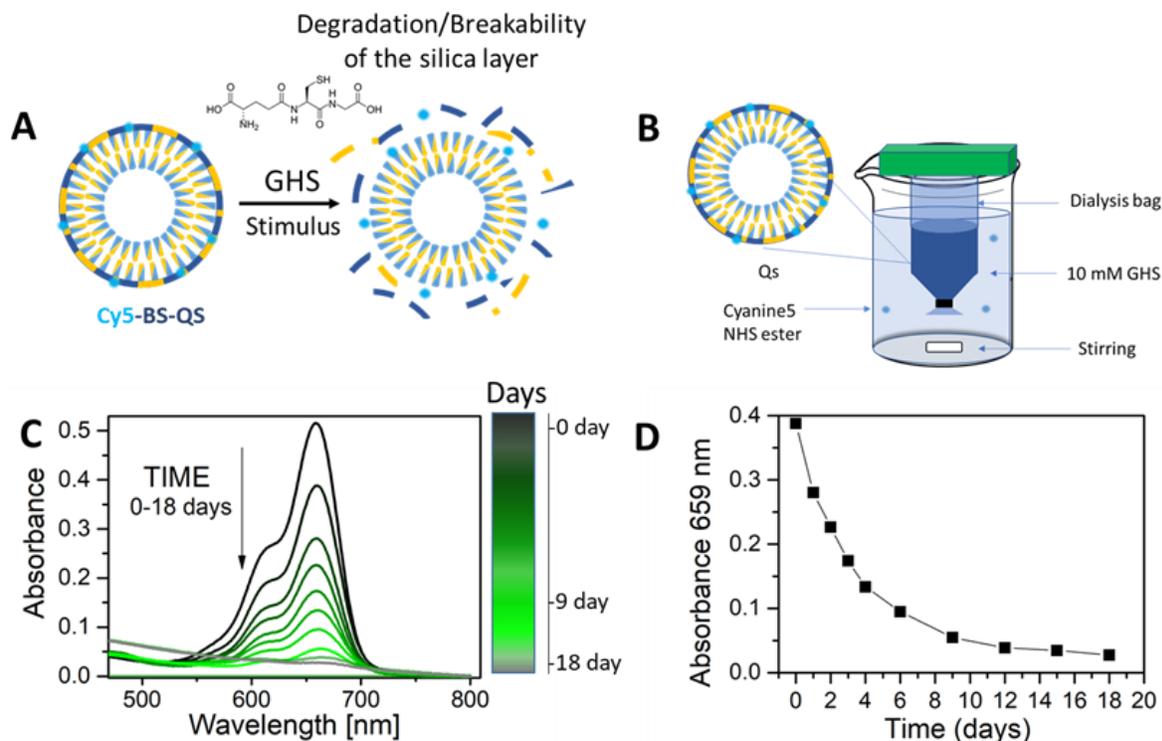
Figure 0.8. A) Schéma du Cyn5-BS-Qs et de sa dégradation en présence du GSH. **B)** Schéma d'expérience pour le test de cassabilité (méthode de dialyse). **C)** Spectres d'absorption du Cyn5-BS-Qs après le temps en présence de 10 mM de glutathion. **D)** Spectres d'absorption à 659 nm à travers le temps du QS de Cyan5-Breakable.

Une autre méthodologie a été utilisée pour étudier la cassabilité du Cyan5-BS-QS-DiI, appelée ici système proche, dans laquelle la solution QS est confinée dans une cuvette en quartz avec 10 mM de GSH. Le changement d'émission a été étudié à des intervalles de temps définis (**Figure 0.9A**). L'intensité normalisée de l'émission à 562 et 659 nm, représentant le DiI et la Cyanine5 dans le Cyan5-BS-QS-DiI dans le temps en présence de 10 mM de GSH, est indiquée dans les **Figures 0.9B** et **C** (après 24 et 44 jours, respectivement). Le rapport Accepteur/Donneur de l'échantillon après ces périodes est présenté dans les **Figures 0.9D** et **E**. Au cours de cette période, la longueur d'onde d'émission maximale du donneur (DiI) diminue alors que celle de l'accepteur (Cyanine5) augmente. Le rapport entre l'accepteur et le donneur augmente, ce qui signifie que le FRET dans le système augmente également. Cette observation peut s'expliquer par le fait que, au moment où la coquille de silice se brise en présence du GSH, le colorant Cyanine5 s'internalise dans la partie hydrophobe du QS où le DiI est chargé (car ce colorant a davantage un caractère

hydrophobe), rapprochant ainsi les deux colorants l'un de l'autre, ce qui augmente alors le transfert d'énergie entre le donneur et l'accepteur.
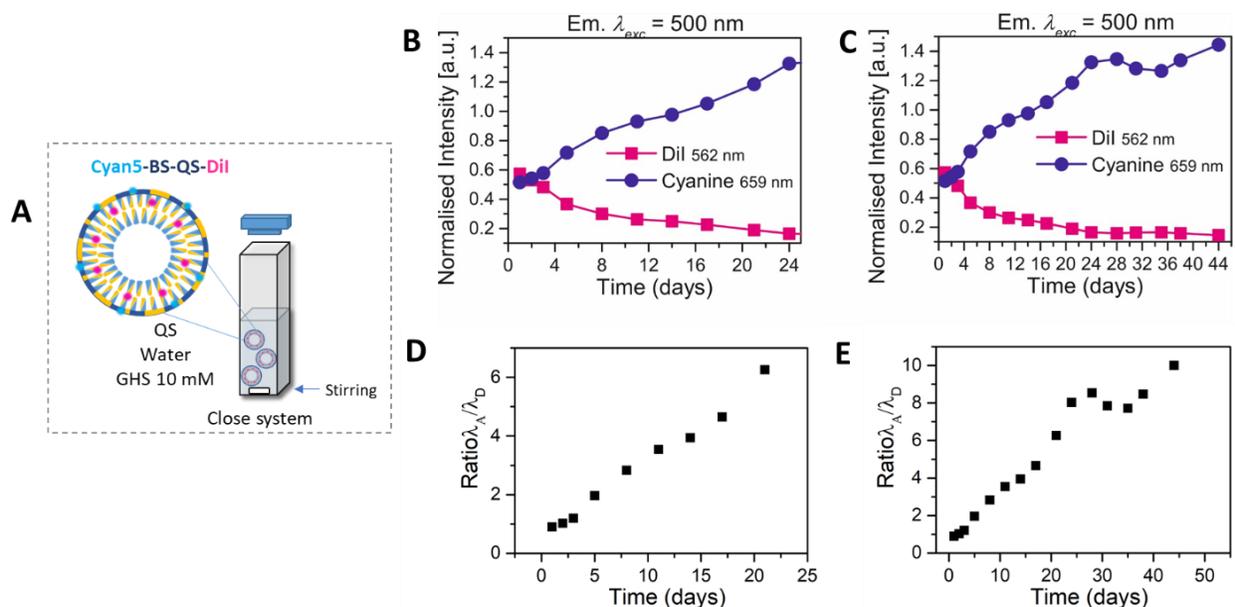
Figure 0.9. A) Schéma du test de cassabilité utilisant une méthodologie proche. **B)** et **C)** Intensité normalisée de l'émission à 562 et 659 nm représentant le DiI et le Cyanine5 dans le QS cassable du Cyan5 chargé de DiI après le temps en présence de 10 mM de Glutathion après 24 et 44 jours, respectivement. **D)** et **E)** Ratio Accepteur/Donneur de l'échantillon après 24 et 44 jours.

L'impact d'une enveloppe de silice cassable et non cassable sur les quatsomes de protection pour la libération d'une molécule hydrophobe chargée dans la membrane a été étudié. En particulier, la libération de DiI a été suivie dans le temps dans trois systèmes différents : 1) le QS chargé de DiI (QS+DiI), 2) le QS chargé de DiI et revêtu d'une coquille cassable (QS+DiI+ss-coquille de silice) et 3) le QS chargé de DiI et revêtu d'une coquille de silice non cassable (QS+DiI+coquille de silice) (**Figure 0.10A**). Les deux derniers systèmes étaient recouverts de TEMOS comme précurseur pour former la couche de silice. Pour réaliser l'expérience de libération, des QS chargés de DiI (avec ou sans coquille de silice) ont été placés dans un tube à membrane semi-perméable (avec une taille de coupure des pores de 3,5 kDa),[67–69] et l'émission de DiI a été filtrée (λ_{exc} = 500 nm) dans le réservoir extérieur pendant une période de 400h (**Figure 0.10B**). Alors qu'au départ, l'émission était pratiquement nulle, en raison de l'absence de molécules de DiI, l'émission a augmenté en cinq heures pour les QS avec et sans revêtement (**Figure 0.10C**) par rapport aux QS sans revêtement (QS-DiI). Cependant, les QS revêtus de silice avec coque cassable et non cassable (BS-

QS-DiI et NB-QS-DiI) ont montré une réduction de l'intensité lumineuse émise de 63 %. Par conséquent, la libération de DiI est entravée par l'enveloppe de silice et, dans les premières heures, le blindage fonctionne aussi bien pour l'enveloppe cassable que pour l'enveloppe incassable. Cependant, après des périodes plus longues (> 124h), la coque de silice cassable commence à libérer plus de DiI que la coque incassable (**Figure 0.10D**), ce qui montre une émission trois fois plus élevée après 16 jours.
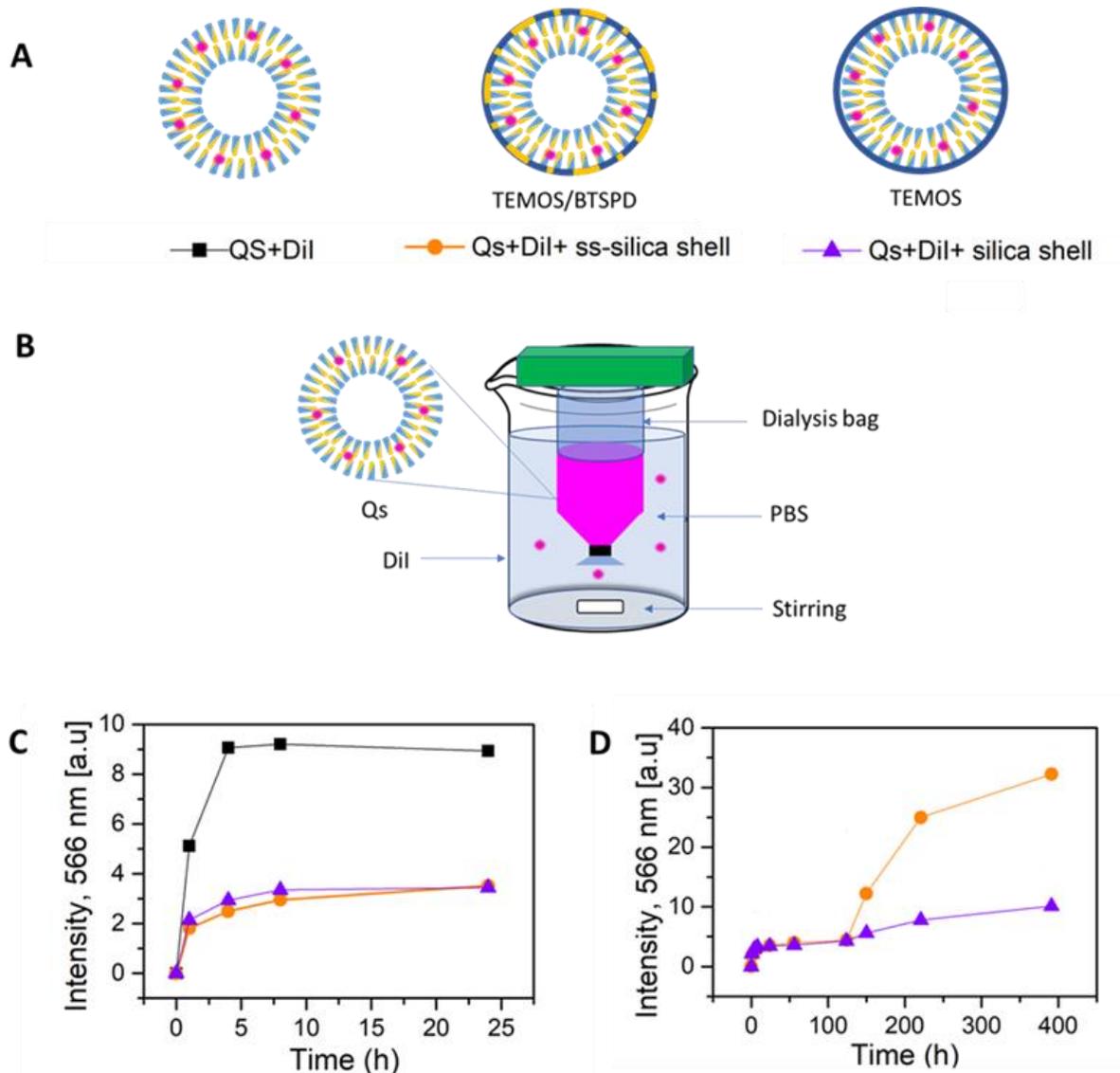
Figure 0.10. A) Représentation schématique du SQ chargé avec DiI, B-S-QS et NB-S-QS chargé avec DiI. Étude de libération in vitro des QS-DiI (noir), BS-QS-DiI (rouge) et NB-QS-DiI (bleu). **B)** Intensité d'émission à 566 nm dans le temps (λexc= 500 nm) **C)** après 25 et **D)** 400 h.

En conclusion de cette partie : Les QS de silice enduite d'étiquettes ont été synthétisées afin de disposer d'une autre sonde de caractérisation de la formation de la coquille de silice. Des études de cassabilité, de perméabilité, de confocalisation, de tempête et de libération ont été réalisées avec ces systèmes. Des études de caractérisation par FRET (transfert d'énergie) ont été réalisées pour le QS chargé, révélant que le colorant à l'intérieur du QS et le colorant dans la coquille de silice sont à une distance approximative de < 10 nm. Des analyses confocales et STORM ont été effectuées pour sonder la présence de la silice de l'étiquette et la caractérisation de celle-ci. Des tests ont été effectués pour étudier la cassabilité de l'échantillon en présence d'un agent réducteur (GSH). En utilisant plusieurs méthodologies (système ouvert et système fermé), il a été révélé que la cassabilité de l'enveloppe de silice modifie le FRET dans le système au cours du temps. Les études de libération montrent une protection de 62 % du médicament chargé en utilisant un colorant hydrophobe comme médicament modèle pendant les 25 premières heures de libération. D'autres études devraient être menées pour tester la libération de médicaments hydrophiles dans ces systèmes.

Dans d'autres études, on a étudié la formation d'une enveloppe de silice cassable dans un autre type de Quatsomes, constitué de cholestérol et de chlorure de Myristalkonium (MKC) pour utiliser un système moins toxique pour les applications d'administration de médicaments.[70] La valeur initiale de la taille du diamètre hydrodynamique de l'échantillon MKC-QS était de 26±19 nm et 81±19 nm (**Figure 0.11A**). Après l'ajout du mélange de silanes (TEMOS et BTSPD), la taille du diamètre est passée à 64±14 nm et 221±57 nm pour les deux tailles de distribution (**Figure 0.11B**). **Figure 0.11C** représente des images au Cryo-MEB de l'échantillon final après nettoyage par dialyse.
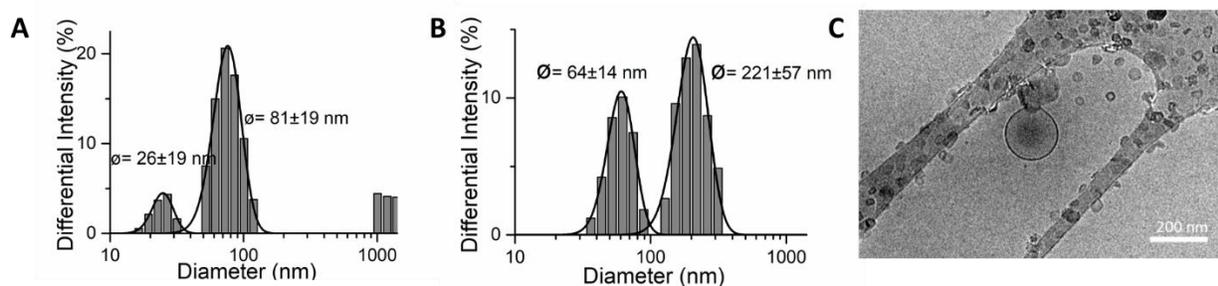
Figure 0.11. Mesures DLS pour le MKC-QS revêtu de silice cassable. En utilisant TEMOS et BTSPD. **A)** MKC-QS initial, **B)** après addition de silane et réaction de 4 h et **C)** images Cryo-MET de l'échantillon final.

Dans un autre projet, il est proposé d'inclure l'utilisation du tensioactif MKC dans la synthèse des nanoparticules de silice mésoporeuse comme modèle pour leur formation. Des nanoparticules de silice non cassables et des nanoparticules de silice cassables ont été préparées (NB-MSNPs). Les particules à réponse redox sont fabriquées en utilisant un lien disulfure comme groupe organique (ss-MSNPs). De plus, de gros pores ont été créés sur les nanoparticules mésoporeuses cassables en utilisant ce tensioactif MKC comme modèle (Big pores-ss-MSNPs). La **Figure 0.12** montre ces 3 systèmes avec un résumé de leur caractérisation; la caractérisation morphologique, les distributions de taille de diamètre hydrodynamique et la distribution de taille de pore ont été prises par des mesures MEB, DLS et d'adsorption N_2, respectivement. Pour les 3 systèmes, la forme de ces particules est sphérique avec des distributions hydrodynamiques des diamètres de 115±40, 119±28 et 137±34 nm pour les NB-MSNPs, ss-MSNPs et les big pores-ss-MSNPs, respectivement. La distribution de la taille des pores pour les NB-MSNPs montre une taille de diamètre de 3,2 nm, alors que, pour les non cassables, il a été montré une taille de diamètre de 2,3 nm ; d'autre part, en faisant les grands pores avec les nanoparticules cassables, une longue distribution de taille est observable jusqu'à 30 nm, montrant que ces matériaux appartiennent à des systèmes mésoporeux.

Pour tester les nanoparticules de silice non cassables (NB-MSNPs) et les particules cassables sensibles à l'oxydoréduction (ss-MSNPs) fabriquées par MKC comme modèle, un test de viabilité cellulaire a été effectué en utilisant 3 lignées cellulaires différentes. Les cellules HeLa (cellules cancéreuses du col de l'utérus) et C6 (cellules de gliome) ont été étudiées en tant que lignées tumorigènes, et les MCF10 en tant que non tumorigènes à 3 concentrations différentes de NP, 10,50 et 100 µg/mL. Les nanoparticules sans tensioactif (après son retrait) ont été testées dans cette expérience (**Figure 0.13**).

Les NP cassables et non cassables fabriquées par le tensioactif MKC et après son élimination (MKC), ont une bonne viabilité cellulaire ; aucune toxicité n'a été détectée à 10, 50 et 100 µg/ml (100 % de la viabilité cellulaire) avec les lignées cellulaires MCF10, C6 et HeLa. Ces observations suggèrent que la MKC peut être une bonne option pour préparer les MSNP à faire de meilleurs systèmes pour les applications biologiques.
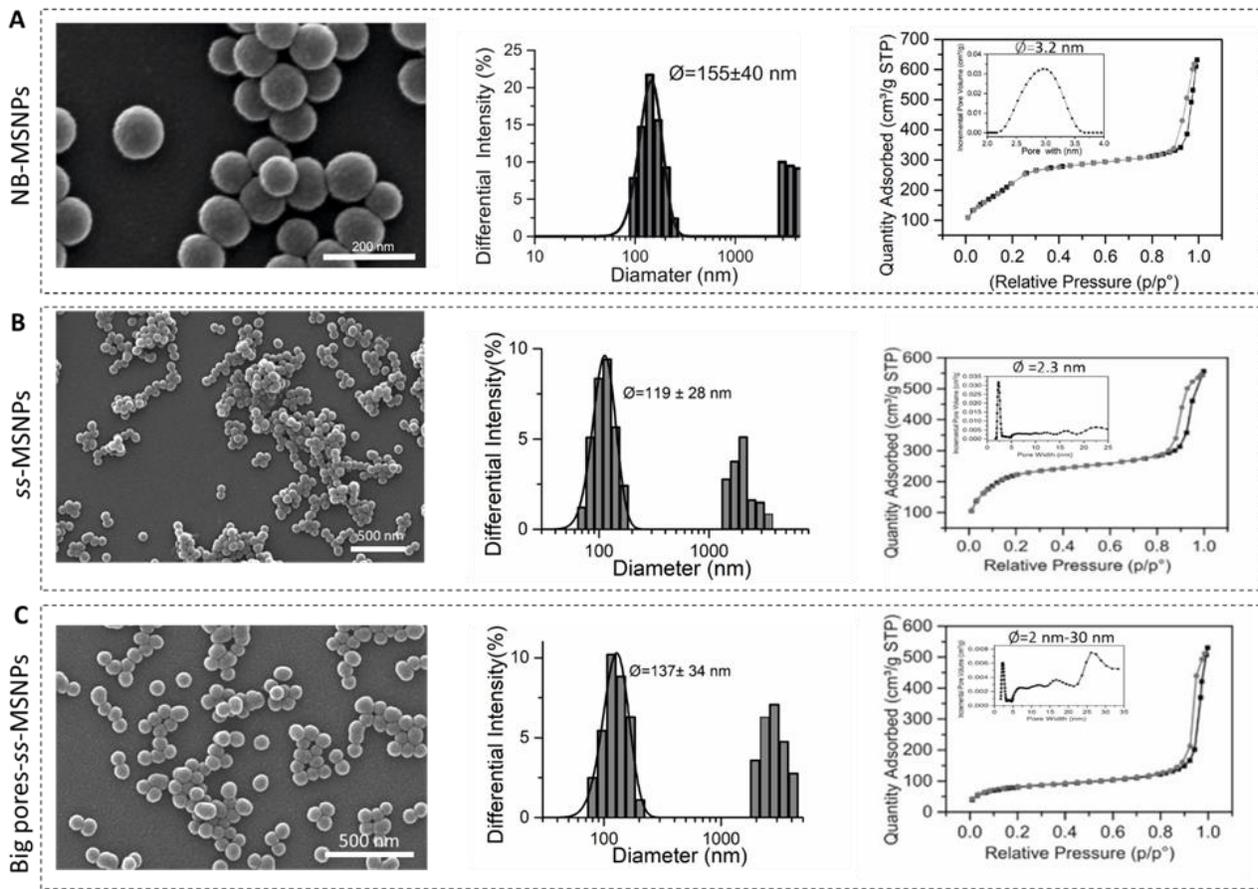
Figure 0.12. Caractérisation des **A)** Nanoparticules de silice non cassables (NB-MSNP). **B)** des particules sensibles à l'oxydoréduction (ss-MSNPs) et **C)** des nanoparticules mésoporeuses cassables à gros pores (Big pores-ss-MSNPs) en utilisant un agent tensioactif MKC comme modèle. Les mesures d'adsorption de SEM, DLS et N2, montrent respectivement leur morphologie, la taille de leur diamètre et leur distribution poreuse.
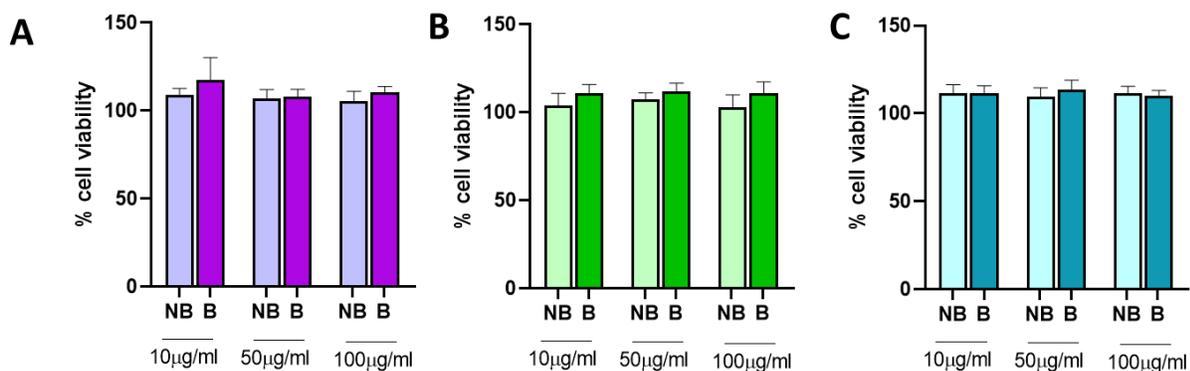
Figure 0.13. Essai de viabilité de **A)** MCF10, **B)** C6 et **C)** cellules Hela exposées à différentes concentrations de NP ; non cassables, et cassables (NB et B, respectivement), avec MKC et sans MKC pendant 24 heures. Les valeurs sont normalisées par rapport aux cellules non traitées et exprimées en % de cellules viables. Toutes les données sont représentées sous forme de moyenne ± S.D., l'analyse statistique a été effectuée par ANOVA à sens unique et par le test post hoc de la Turquie.

En conclusion de tous ces travaux : un nouveau matériau hybride réalisé par PLGA et des nanoparticules de silice mésoporeuse a été réalisé sous forme de système multi-délivrance. Il a été construit pour délivrer des cannabinoïdes et des médicaments chimiothérapeutiques afin de produire une activité synergétique contre le cancer (*chapitre 2*). Le système est conçu de manière à ce que les deux médicaments soient administrés dans deux parties différentes de la cellule (intra et extra-membranaire). Cela ouvre une nouvelle barrière au développement des systèmes d'administration de médicaments. Dans ce projet, deux cannabinoïdes différents ont été synthétisés et caractérisés par RMN, IR, HR ESI-TOF-MS comme exemples d'un analogue et d'un endocannabinoïde actif. Différents types de MSNP ont été synthétisés comme exemple de toutes les variétés de matériaux qui peuvent être inclus dans les véhicules PLGA@. Différentes techniques ont été utilisées pour synthétiser les véhicules PLGA : la méthode d'évaporation des solvants, la méthode de précipitation auto-organisée (SORP) et la méthode des modèles d'hydrogel. Cette dernière méthode est la seule qui préserve l'homogénéité de taille et de morphologie, même avec l'inclusion de cannabinoïdes et de nanoparticules de silice mésoporeuse.

Un deuxième matériau hybride basé sur une vésicule de base non lipidique, appelé Quatsomes et silice, a été fabriqué (*chapitre 3*). La construction est conçue pour condenser la silice autour des vésicules en formant une coquille autour d'elles, pour donner plus de stabilité structurelle et mécanique au QS ; principalement pour empêcher la perte de cargaison avant qu'elle n'arrive au point de destination. Ce matériau contribue au développement d'applications pour l'administration de médicaments. De plus, des systèmes d'enveloppe de silice réactifs ont été synthétisés pour fabriquer des matériaux de réponse organique redox, qui se brisent spécifiquement en présence d'un agent réducteur, à l'intérieur des cellules cancéreuses, libérant la cargaison et se brisant en petits morceaux pour empêcher l'accumulation dans le corps. Ces matériaux pourraient avoir un intérêt potentiel pour des applications biomédicales.

Des molécules fluorescentes ont été mises dans le système QS recouvert de silice pour produire des coquilles de silice Label QS pour différents objectifs (*chapitre 4*). Ces systèmes pourraient agir comme des bio-sondes luminescentes et leur étude porte sur la recherche de leur potentiel en tant que système d'administration de médicaments. De plus, des systèmes de réponse aux stimuli redox- label ont été synthétisés pour réaliser différentes études. Des études de caractérisation

par transfert d'énergie (FRET) ont été réalisées pour les QS chargés, révélant que le colorant à l'intérieur des Q et le colorant dans la coquille de silice sont à une distance approximative de < 10 nm. Des analyses confocales et de tempête ont été effectuées pour vérifier la présence de la silice de l'étiquette et la caractérisation de celle-ci. Des tests de cassabilité ont été effectués en présence d'un agent réducteur (GSH) ; il a été révélé que la cassabilité de la coquille de silice modifie le FRET dans le système au cours du temps. Le test de perméabilité a montré la protection du QS lorsque la coquille de silice est présente. Les études de libération montrent une protection des 62 % du médicament chargé en utilisant un colorant hydrophobe comme médicament modèle dans les 25 premières heures de libération. D'autres études devraient être menées pour tester la libération de médicaments hydrophiles sous ces systèmes.

La coquille de silice cassable par réaction d'oxydoréduction a été fabriquée dans un nouveau type de Quatsome fabriqué par le chlorure de Myristalkonium (MKC). Ces matériaux sont synthétisés en faveur de la formation d'un système plus biocompatible pour l'administration ultérieure de médicaments proposée (*chapitre 5*). Dans ce chapitre, il est également proposé d'inclure l'utilisation de l'agent de surface MKC dans la synthèse de nanoparticules de silice mésoporeuse comme modèle pour leur formation. Des nanoparticules de silice non cassables et des nanoparticules de silice cassables ont été préparées. Les particules à réponse d'oxydoréduction sont fabriquées en utilisant un lien disulfure comme groupe organique. De plus, de gros pores ont été créés à partir de nanoparticules mésoporeuses cassables en utilisant ce tensioactif MKC comme modèle. Des systèmes plus biocompatibles pourraient découler de ces travaux afin d'améliorer les matériaux d'administration des médicaments pour les applications biomédicales. En conclusion générale, cette thèse explore la combinaison de différents systèmes pour former des matériaux hybrides afin de réaliser leurs propriétés uniques attribuées à un seul matériau. Les conceptions sont censées développer de nouvelles alternatives dans le domaine des nanomatériaux pour les applications d'administration de médicaments.

REFERENCES

(1)   Jeevanandam, J.; Barhoum, A.; Chan, Y. S.; Dufresne, A.; Danquah, M. K. Review on Nanoparticles and Nanostructured Materials: History, Sources, Toxicity and Regulations. *Beilstein Journal of Nanotechnology* **2018**, *9* (1), 1050–1074.

(2)   Kim, K.-M.; Kang, J.-H.; Vinu, A.; Choy, J.-H.; Oh, J.-M. Inorganic Nanomedicines and Their Labeling for Biological Imaging. *Current Topics in Medicinal Chemistry* **2013**, *13* (4), 488–503.

(3)   Arias, J. L. *Nanotechnology and Drug Delivery, Volume One: Nanoplatforms in Drug Delivery*; Arias, J. L., Ed.; CRC Press, 2014.

(4)   *Applications of Targeted Nano Drugs and Delivery Systems: Nanoscience and Nanotechnology in Drug Delivery*; Mohapatra, S., Ranjan, S., Dasgupta, N., Kumar, R., Thomas, S., Eds.; Elsevier, 2018.

(5)   Gessner, I.; Neundorf, I. Nanoparticles Modified with Cell-Penetrating Peptides: Conjugation Mechanisms, Physicochemical Properties, and Application in Cancer Diagnosis and Therapy. *International Journal of Molecular Sciences* **2020**, *21* (7), 2536.

(6)   Tomalia, D. A.; Baker, H.; Dewald, J.; Hall, M.; Kallos, G.; Martin, S.; Roeck, J.; Ryder, J.; Smith, P. A New Class of Polymers: Starburst-Dendritic Macromolecules. *Polymer Journal* **1985**, *17* (1), 117–132.

(7)   Bharali, D. J.; Khalil, M.; Gurbuz, M.; Simone, T. M.; Mousa, S. A. Nanoparticles and Cancer Therapy: A Concise Review with Emphasis on Dendrimers. *International Journal of Nanomedicine* **2009**, *4* (1), 1–7.

(8)   Gillies, E. R.; Fréchet, J. M. J. Dendrimers and Dendritic Polymers in Drug Delivery. *Drug Discovery Today* **2005**, *10* (1), 35–43.

(9)   Sandoval-Yañez, C.; Castro Rodriguez, C. Dendrimers: Amazing Platforms for Bioactive Molecule Delivery Systems. *Materials* **2020**, *13* (3), 570.

(10)   Allen, T. M.; Cullis, P. R. Liposomal Drug Delivery Systems: From Concept to Clinical Applications. *Advanced Drug Delivery Reviews* **2013**, *65* (1), 36–48.

(11)   Grimaldi, N.; Andrade, F.; Segovia, N.; Ferrer-Tasies, L.; Sala, S.; Veciana, J.; Ventosa, N. Lipid-Based Nanovesicles for Nanomedicine. *Chemical Society Reviews* **2016**, *45* (23), 6520–6545.

(12) Alivisatos, A. P.; Gu, W.; Larabell, C. Quantum Dots as Cellular Probes. *Annual Review of Biomedical Engineering* **2005**, *7* (1), 55–76.

(13) Tang, Z.; He, C.; Tian, H.; Ding, J.; Hsiao, B. S.; Chu, B.; Chen, X. Polymeric Nanostructured Materials for Biomedical Applications. *Progress in Polymer Science* **2016**, *60*, 86–128.

(14) De Souza, R.; Zahedi, P.; Allen, C. J.; Piquette-Miller, M. Polymeric Drug Delivery Systems for Localized Cancer Chemotherapy. *Drug Delivery* **2010**, *17* (6), 365–375.

(15) Huo, Q.; Liu, J.; Wang, L. Q.; Jiang, Y.; Lambert, T. N.; Fang, E. A New Class of Silica Cross-Linked Micellar Core-Shell Nanoparticles. *Journal of the American Chemical Society* **2006**, *128* (19), 6447–6453.

(16) Hoffmann, F.; Cornelius, M.; Morell, J.; Fröba, M. Silica-Based Mesoporous Organic-Inorganic Hybrid Materials. *Angewandte Chemie International Edition* **2006**, *45* (20), 3216–3251.

(17) Argyo, C.; Weiss, V.; Bräuchle, C.; Bein, T. Multifunctional Mesoporous Silica Nanoparticles as a Universal Platform for Drug Delivery. *Chemistry of Materials* **2014**, *26* (1), 435–451.

(18) Dresselhaus, M. S.; Dresselhaus, G.; Eklund, P. C.; Rao, A. M. Carbon Nanotubes. In *The physics of fullerene-based and fullerene-related materials*; Andreoni, W., Ed.; Kluwer Academic Publishers, 2000; pp 331–379.

(19) Popov, V. N. Carbon Nanotubes: Properties and Application. *Materials Science and Engineering R: Reports* **2004**, *43* (3), 61–102.

(20) Toshima, N.; Yonezawa, T. Bimetallic Nanoparticles - Novel Materials for Chemical and Physical Applications. *New Journal of Chemistry* **1998**, *22* (11), 1179–1201.

(21) Kumar Teli, M.; Mutalik, S.; Rajanikant, G. K. Nanotechnology and Nanomedicine: Going Small Means Aiming Big. *Current Pharmaceutical Design* **2010**, *16* (16), 1882–1892.

(22) Etheridge, M. L.; Campbell, S. A.; Erdman, A. G.; Haynes, C. L.; Wolf, S. M.; McCullough, J. The Big Picture on Nanomedicine: The State of Investigational and Approved Nanomedicine Products. *Nanomedicine: Nanotechnology, Biology, and Medicine* **2013**, *9* (1), 1–14.

(23) Bamrungsap, S.; Zhao, Z.; Chen, T.; Wang, L.; Li, C.; Fu, T.; Tan, W. Nanotechnology in Therapeutics: A Focus on Nanoparticles as a Drug Delivery System. *Nanomedicine* **2012**, *7* (8), 1253–1271.

(24)   He, C.; Lu, J.; Lin, W. Hybrid Nanoparticles for Combination Therapy of Cancer. *Journal of Controlled Release* **2015**, *219*, 224–236.

(25)   Guha, A.; Shaharyar, M. A.; Ali, K. A.; Roy, S. K.; Kuotsu, K. Smart and Intelligent Stimuli Responsive Materials: An Innovative Step in Drug Delivery System. *Current Biochemical Engineering* **2019**, *6* (1), 41–52.

(26)   Gao, W.; Chan, J. M.; Farokhzad, O. C. PH-Responsive Nanoparticles for Drug Delivery. *Molecular Pharmaceutics* **2010**, *7* (6), 1913–1920.

(27)   Strong, L. E.; West, J. L. Thermally Responsive Polymer–Nanoparticle Composites for Biomedical Applications. *Wiley Interdisciplinary Reviews: Nanomedicine and Nanobiotechnology* **2011**, *3* (3), 307–317.

(28)   Ganta, S.; Devalapally, H.; Shahiwala, A.; Amiji, M. A Review of Stimuli-Responsive Nanocarriers for Drug and Gene Delivery. *Journal of Controlled Release* **2008**, *126* (3), 187–204.

(29)   Anderson, J. M.; Shive, M. S. Biodegradation and Biocompatibility of PLA and PLGA Microspheres. *Advanced Drug Delivery Reviews* **2012**, *64*, 72–82.

(30)   Allen, T. M.; Cullis, P. R. Drug Delivery Systems: Entering the Mainstream. *Science* **2004**, *303* (5665), 1818–1822.

(31)   des Rieux, A.; Fievez, V.; Garinot, M.; Schneider, Y. J.; Préat, V. Nanoparticles as Potential Oral Delivery Systems of Proteins and Vaccines: A Mechanistic Approach. *Journal of Controlled Release* **2006**, *116* (1), 1–27.

(32)   Kamaly, N.; Xiao, Z.; Valencia, P. M.; Radovic-Moreno, A. F.; Farokhzad, O. C. Targeted Polymeric Therapeutic Nanoparticles: Design, Development and Clinical Translation. *Chemical Society Reviews* **2012**, *41* (7), 2971–3010.

(33)   Janib, S. M.; Moses, A. S.; MacKay, J. A. Imaging and Drug Delivery Using Theranostic Nanoparticles. *Advanced Drug Delivery Reviews* **2010**, *62* (11), 1052–1063.

(34)   Liang, R.; Dong, L.; Deng, R.; Wang, J.; Wang, K.; Sullivan, M.; Liu, S.; Wang, J.; Zhu, J.; Tao, J. Surfactant-Free Biodegradable Polymeric Nanoparticles Generated from Self-Organized Precipitation Route: Cellular Uptake and Cytotoxicity. *European Polymer Journal* **2014**, *57*, 187–201.

(35)   Kang, J.; Schwendeman, S. P. Comparison of the Effects of Mg(OH)2 and Sucrose on the Stability of Bovine Serum Albumin Encapsulated in Injectable Poly(D,L-Lactide-Co-Glycolide) Implants. *Biomaterials* **2002**, *23* (1), 239–245.

(36)   Jiang, W.; Gupta, R. K.; Deshpande, M. C.; Schwendeman, S. P. Biodegradable Poly(Lactic-Co-Glycolic Acid) Microparticles for Injectable Delivery of Vaccine Antigens. *Advanced Drug Delivery Reviews* **2005**, *57* (3), 391–410.

(37)   Wang, J.; Wang, B. M.; Schwendeman, S. P. Mechanistic Evaluation of the Glucose-Induced Reduction in Initial Burst Release of Octreotide Acetate from Poly(D,L-Lactide-Co-Glycolide) Microspheres. *Biomaterials* **2004**, *25* (10), 1919–1927.

(38)   Schwendeman, S. P.; Langer, R.; Tracy, M. Recent Advances in the Stabilization of Proteins Encapsulated in Injectable PLGA Delivery Systems. *Critical Reviews^TM in Therapeutic Drug Carrier Systems* **2002**, *19* (1), 73–98.

(39)   Zhu, G.; Mallery, S. R.; Schwendeman, S. P. Stabilization of Proteins Encapsulated in Injectable Poly (Lactide-Co- Glycolide). *Nature Biotechnology* **2000**, *18* (1), 52–57.

(40)   Wischke, C.; Schwendeman, S. P. Principles of Encapsulating Hydrophobic Drugs in PLA/PLGA Microparticles. *International Journal of Pharmaceutics* **2008**, *364* (2), 298–327.

(41)   Freiberg, S.; Zhu, X. X. Polymer Microspheres for Controlled Drug Release. *International Journal of Pharmaceutics* **2004**, *282* (1–2), 1–18.

(42)   Zhang, Y.; Wischke, C.; Mittal, S.; Mitra, A.; Schwendeman, S. P. Design of Controlled Release PLGA Microspheres for Hydrophobic Fenretinide. *Molecular Pharmaceutics* **2016**, *13* (8), 2622–2630.

(43)   Bangham, A. D.; De Gier, J.; Greville, G. D. Osmotic Properties and Water Permeability of Phospholipid Liquid Crystals. *Chemistry and Physics of Lipids* **1967**, *1* (3), 225–246.

(44)   Dubois, M.; Zemb, T. Phase Behavior and Scattering of Double-Chain Surfactants in Diluted Aqueous Solutions. *Langmuir* **1991**, *7* (7), 1352–1360.

(45)   Caboi, F.; Monduzzi, M. Didodecyldimethylammonium Bromide Vesicles and Lamellar Liquid Crystals. A Multinuclear NMR and Optical Microscopy Study. *Langmuir* **1996**, *12* (15), 3548–3556.

(46)   Elizondo, E.; Veciana, J.; Ventosa, N. Nanostructuring Molecular Materials as Particles and

Vesicles for Drug Delivery, Using Compressed and Supercritical Fluids. *Nanomedicine* **2012**, *7* (9), 1391–1408.

(47)   Yoon, H. J., & Jang, W. D. Polymeric Supramolecular Systems for Drug Delivery. *Journal of Materials Chemistry* **2010**, *20* (2), 211–222.

(48)   Kubo, T.; Sugita, T.; Shimose, S.; Nitta, Y.; Ikuta, Y.; Murakami, T. Targeted Delivery of Anticancer Drugs with Intravenously Administered Magnetic Liposomes in Osteosarcoma-Bearing Hamsters. *International journal of oncology* **2000**, *17* (2), 309–315.

(49)   Sawant, R. R.; Torchilin, V. P. Challenges in Development of Targeted Liposomal Therapeutics. *AAPS Journal* **2012**, *14* (2), 303–315.

(50)   Torres, S.; Lorente, M.; Rodríguez-Fornés, F.; Hernández-Tiedra, S.; Salazar, M.; García-Taboada, E.; Barcia, J.; Guzmán, M.; Velasco, G. A Combined Preclinical Therapy of Cannabinoids and Temozolomide against Glioma. *Molecular Cancer Therapeutics* **2011**, *10* (1), 90–103.

(51)   Maggini, L.; Cabrera, I.; Ruiz-Carretero, A.; Prasetyanto, E. A.; Robinet, E.; De Cola, L. Breakable Mesoporous Silica Nanoparticles for Targeted Drug Delivery. *Nanoscale* **2016**, *8* (13), 7240–7247.

(52)   Minardi, S.; Fernandez-Moure, J. S.; Fan, D.; Murphy, M. B.; Yazdi, I. K.; Liu, X.; Weiner, B. K.; Tasciotti, E. Biocompatible PLGA-Mesoporous Silicon Microspheres for the Controlled Release of Bmp-2 for Bone Augmentation. *Pharmaceutics* **2020**, *12* (2), 118.

(53)   Minardi, S.; Pandolfi, L.; Taraballi, F.; Wang, X.; De Rosa, E.; Mills, Z. D.; Liu, X.; Ferrari, M.; Tasciotti, E. Enhancing Vascularization through the Controlled Release of Platelet-Derived Growth Factor-BB. *ACS Applied Materials and Interfaces* **2017**, *9* (17), 14566–14575.

(54)   Minardi, S.; Corradetti, B.; Taraballi, F.; Sandri, M.; Van Eps, J.; Cabrera, F. J.; Weiner, B. K.; Tampieri, A.; Tasciotti, E. Evaluation of the Osteoinductive Potential of a Bio-Inspired Scaffold Mimicking the Osteogenic Niche for Bone Augmentation. *Biomaterials* **2015**, *62*, 128–137.

(55)   Liang, R.; Dong, L.; Deng, R.; Wang, J.; Wang, K.; Sullivan, M.; Liu, S.; Wang, J.; Zhu, J.; Tao, J. Surfactant-Free Biodegradable Polymeric Nanoparticles Generated from Self-Organized Precipitation Route: Cellular Uptake and Cytotoxicity. *European Polymer Journal* **2014**, *57*, 187–201.

(56)   Liang, R.; Zhu, J. Monodisperse PLA/PLGA Nanoparticle Fabrication through a Surfactant-Free Route. *Journal of controlled release* **2011**, *152*, e129–e131.

(57)   Acharya, Ghanashyam, C. S. S.; McDermott, Matthew, Himanshu Mishra, Haesun Park, I. C. K.; Park, K. The Hydrogel Template Method for Fabrication of Homogeneous Nano/Microparticles. *Journal of Controlled Release* **2010**, *141* (3), 314–319.

(58)   Pertwee, R. G. The Pharmacology of Cannabinoid Receptors and Their Ligands: An Overview. *International Journal of Obesity* **2006**, *30* (1), S13–S18.

(59)   Elizondo, E.; Moreno, E.; Cabrera, I.; Córdoba, A.; Sala, S.; Veciana, J.; Ventosa, N. Liposomes and Other Vesicular Systems: Structural Characteristics, Methods of Preparation, and Use in Nanomedicine. *Progress in Molecular Biology and Translational Science* **2011**, *104*, 1–52.

(60)   De Petrocellis, L.; Melck, D.; Bisogno, T.; Di Marzo, V. Endocannabinoids and Fatty Acid Amides in Cancer, Inflammation and Related Disorders. *Chemistry and Physics of Lipids* **2000**, *108* (1–2), 191–209.

(61)   Kumari, A.; Yadav, S. K.; Yadav, S. C. Biodegradable Polymeric Nanoparticles Based Drug Delivery Systems. *Colloids and Surfaces B: Biointerfaces* **2010**, *75* (1), 1–18.

(62)   Ferrer-Tasies, L.; Moreno-Calvo, E.; Cano-Sarabia, M.; Aguilella-Arzo, M.; Angelova, A.; Lesieur, S.; Ricart, S.; Faraudo, J.; Ventosa, N.; Veciana, J. Quatsomes: Vesicles Formed by Self-Assembly of Sterols and Quaternary Ammonium Surfactants. *Langmuir* **2013**, *29* (22), 6519–6528.

(63)   Elizondo, E.; Larsen, J.; Hatzakis, N. S.; Cabrera, I.; Bjørnholm, T.; Veciana, J.; Stamou, D.; Ventosa, N. Influence of the Preparation Route on the Supramolecular Organization of Lipids in a Vesicular System. *Journal of the American Chemical Society* **2012**, *134* (4), 1918–1921.

(64)   Lu, F.; Wu, S. H.; Hung, Y.; Mou, C. Y. Size Effect on Cell Uptake in Well-Suspended, Uniform Mesoporous Silica Nanoparticles. *Small* **2009**, *5* (12), 1408–1413.

(65)   Morla-Folch, J.; Vargas-Nadal, G.; Zhao, T.; Sissa, C.; Ardizzone, A.; Kurhuzenkau, S.; Köber, M.; Uddin, M.; Painelli, A.; Veciana, J.; Belfield, K. D.; Ventosa, N. Dye-Loaded Quatsomes Exhibiting FRET as Nanoprobes for Bioimaging. *ACS Applied Materials & Interfaces* **2020**, *12* (18), 20253–20262.

(66)   Ardizzone, A.; Kurhuzenkau, S.; Illa-Tuset, S.; Faraudo, J.; Bondar, M.; Hagan, D.; Van Stryland, E. W.; Painelli, A.; Sissa, C.; Feiner, N.; Albertazzi, L.; Veciana, J.; Ventosa, N. Nanostructuring Lipophilic Dyes in Water Using Stable Vesicles, Quatsomes, as Scaffolds and Their Use as Probes for Bioimaging. *Small* **2018**, *14* (16), 1703851.

(67)   Hamedinasab, H.; Rezayan, A. H.; Mellat, M.; Mashreghi, M.; Jaafari, M. R. Development of Chitosan-Coated Liposome for Pulmonary Delivery of N-Acetylcysteine. *International Journal of Biological Macromolecules* **2020**, *156*, 1455–1463.

(68)   Hu, K.; Cao, S.; Hu, F.; Feng, J. Enhanced Oral Bioavailability of Docetaxel by Lecithin Nanoparticles: Preparation, in Vitro, and in Vivo Evaluation. *International Journal of Nanomedicine* **2012**, *7*, 3537–3545.

(69)   Yoon, H. Y.; Kwak, S. S.; Jang, M. H.; Kang, M. H.; Sung, S. W.; Kim, C. H.; Kim, S. R.; Yeom, D. W.; Kang, M. J.; Choi, Y. W. Docetaxel-Loaded RIPL Peptide (IPLVVPLRRRRRRRRC)-Conjugated Liposomes: Drug Release, Cytotoxicity, and Antitumor Efficacy. *International Journal of Pharmaceutics* **2017**, *523* (1), 229–237.

(70)   Liu, X.; Ardizzone, A.; Sui, B.; Anzola, M.; Ventosa, N.; Liu, T.; Veciana, J.; Belfield, K. D. Fluorenyl-Loaded Quatsome Nanostructured Fluorescent Probes. *ACS Omega* **2017**, *2* (8), 4112–4122.

Nanomaterials (NMs) have been explored in the last decades gained prominence in technological advancements due to their tuneable physical chemical and biological properties.[1] Nanomaterials are categorized depending on their size, composition, shape and origin. Due to their increased growth in some research fields, industries have developed a special interest to explore and develop new technologies to produce nanomaterials. One of the big research areas of interest is for nanomedicine applications which the challenge is producing non-toxic nanomaterials for biomedical imaging, biosensing, diagnostics and therapy.

For the pharmaceutical industry, drug delivery and targeting have been attractive approaches to create a "magic bullet", a material capable of delivering drugs in the right place, at the right concentration and for the right period of time, without chemical changes in the material, accomplishing the biodegradability and biocompatibility of the nano carrier.[2–4] Different examples of drug delivery nanoplatforms exist nowadays; basically, divided in three main groups: organic matrices, inorganic materials and hybrid nanoparticles.[5] Systems as dendrimers,[6–9] liposomes,[10,11] quantum dots,[12] polymeric nanoparticles,[13,14] silica-based materials,[15–17] carbon nanotubes,[18,19] metallic nanoparticles,[20] etc. are revolutionizing the field of medicine for the early detection, diagnosis, and treatment of various diseases as cancer, VIH, Alzheimer, glaucoma, depression, to mention some.[3,21–23]

Hybrid nanoparticles, composed by inorganic and organic components, can be prepared using several strategies; their production is based on the optimization of their synergistic therapeutic effects. Then, the combination of drug carriers need to be rationally designed to accommodate multiple therapeutic drugs or modalities with temporally controlled release of individual

cargos.[24] This thesis titled "Design and synthesis of hybrid particles for drug release" is based in the combination of several delivery systems to form new hybrid materials for biomedical applications. Hybrid systems mainly conformed by silica structures and combined with Poly Lactic-co-Glycolic Acid (PLGA), a polymeric material, or with non-lipidic vesicles called Quatsomes (QS) are presented in this thesis. For a deep understanding of the chapters, here is presented a brief resume of the silica nanoparticles, PLGA polymer carriers and QS.

Among all the inorganic materials, mesoporous silica nanoparticles have become a predominant carrier for drug delivery applications due to their tunable size, morphology, and porosity. The efficient entrapment of drugs within their porous structure followed by a controlled release upon endogenous or exogenous stimuli such as light, temperature, ultrasound, or pH, has made mesoporous silica nanostructures highly promising delivery vehicles.[25] Those versatilities upon stimuli response is due to their facility to incorporate functionality groups in the silica. Redox-stimuli response silica systems, reported presenting S-S cleavable bonds in their structure, which are a good strategy for drug delivery within cells, responding with self-destructive behaviour to stimuli present in the intracellular environment once the target is reached.[26–28]

Polymers have been widely explored in the area of drug delivery due to their unique biocompatibility and biodegradation properties,[29] biodegradable polymeric nanoparticles have been used in broad applications in the fields of drug delivery and release, vaccination, targeting, tumor therapy and diagnostic systems.[30–34] From all the polymers, PLGA is consider a good candidate for drug delivery applications due to their biocompatibility and biodegradability that can be metabolically hydrolysed into the monomers lactic acid and glycolic acid. PLGA particles, as microparticles or nanoparticles systems,[35] have been shown to be capable of carrying and delivering a variety of drug classes as vaccines,[36] peptides,[37] proteins,[38,39] and hydrophobic drugs.[40] The advantages of using these PLGA particles are the reduction of injection frequency, sustained therapeutic drug levels, site-specific drug delivery and formulations that can be changed for any number of desired release profiles.[41,42]

In the last 50 years, many nanodrugs have been developed and approved for human administration based on lipid nanovesicles. Liposomes are the most famous drug delivery systems based on phospholipids.[43] Their potentiality in drug delivery comes due to their biocompatibility.[43] Moreover, they present poor colloidal and chemical stabilities.[44,45] Because of

that reason, another class of vesicles, called "non-liposomal lipid-based nanovesicles", has been attracting a lot of attention. One of this non-liposomal lipid-based nanovesicles are the Quatsomes (QS), unilamellar bilayer nanovesicles constituted by quaternary ammonium surfactants and sterols have been used as a model for drug delivery. Their stability regarding their morphology, size, lamellarity, and membrane supramolecular organization make them interesting for drug delivery applications in the development of new nanomedicines.[46–49]

OBJECTIVE: The purpose of this thesis is then to develop different classes of hybrid nanostructured materials to interface inorganic/organic systems. In particular, the use of soft and hard materials combined in a single system to develop degradable systems for drug delivery applications.

Therefore, here it is presented the use of a new hybrid system consisting in a combination of a polymeric material with the inclusion of mesoporous silica nanoparticles for the encapsulation and delivery of cannabinoids (CBDs) and chemotherapeutic drugs for the treatment of cancer.

There are some examples in literature which have been shown that the combination of CBDs with chemotherapeutic agents enhances the antitumoral action.[50] Different kinds of mesoporous silica nanoparticles (MSNPs) were synthetized as models of the inorganic systems that can encapsulate an anti-cancer drug for the release of the chemotherapeutic drug. Moreover, breakable particles (redox stimuli response) were also produced as a degradable system, that will be included in this hybrid platform.[51] These silica NPs loaded with a chemotherapeutic drugs, in turn, are loaded in PLGA carriers[36] which also contains an active endocannabinoid or its analog (CBDs), resulting in an unprecedent hybrid tandem-delivery system (CBDs-MSNPs@PLGA-MBds) (**Figure 0.1**).
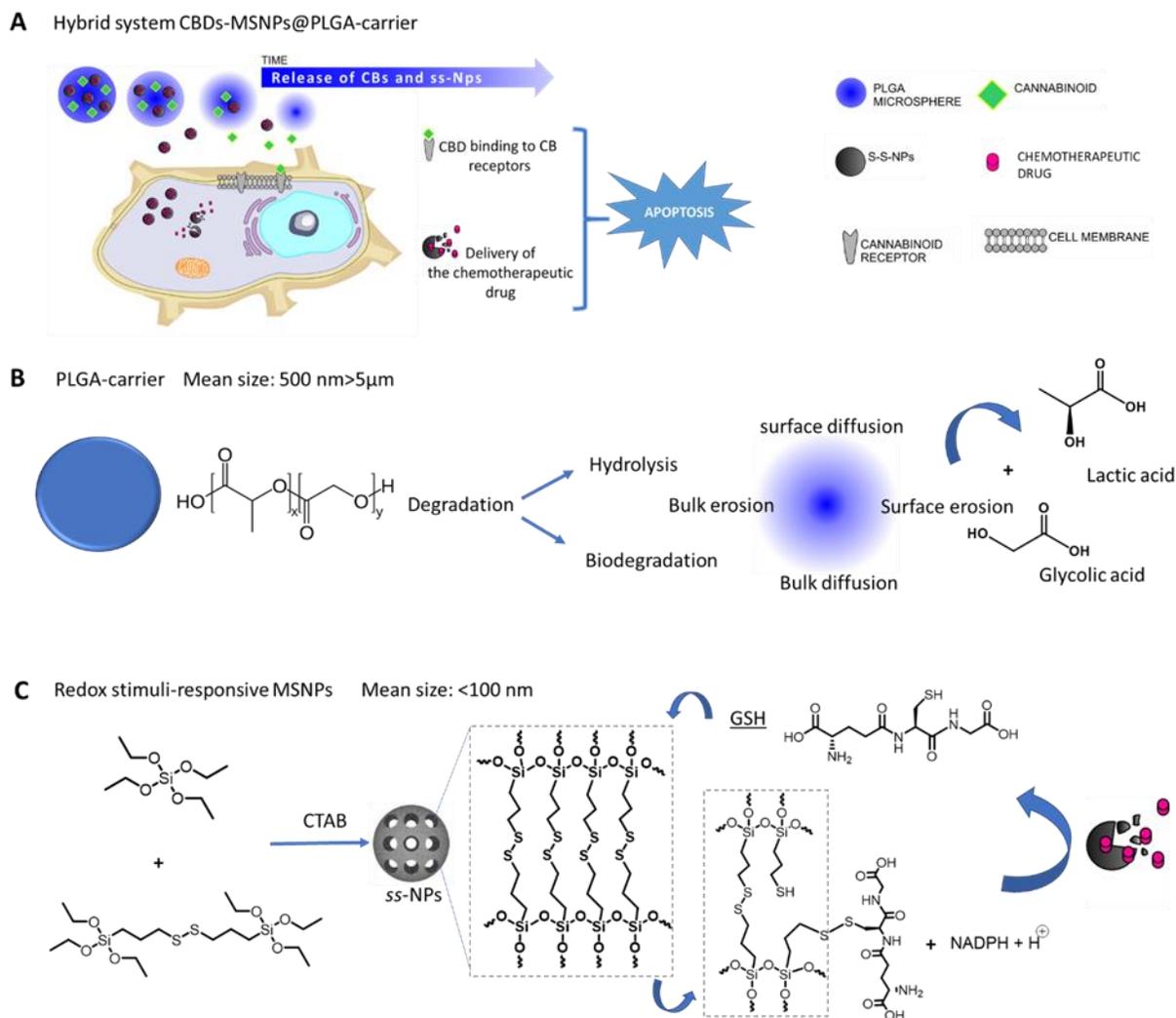
Figure 0.1. A) Hybrid system and mechanism of action as a cancer treatment strategy consisting in the combination of two materials PLGA and mesoporous silica carriers for the loading of cannabinoid and a chemotherapeutic drug to increase the apoptosis of cancer cells. **B)** PLGA- carriers and a schematic representation of its degradation process and **C)** Redox stimuli-responsive MSNPs for the release of the chemotherapeutic drug.

For the preparation of the PLGA carriers, three methodologies were tasted to produce particles in the range size of 500 nm>5 μm, by solvent evaporation method,[52–54] self-organized precipitation (SORP) method, which consist in a procedure that is without surfactant through a self-organized precipitation route[55,56] and the hydrogel template method.[57] A specific size is required to ensure than the cannabinoid drug will be released outside the cell as the cannabinoid receptors are intramembrane proteins (IMP) located in the lipid bilayer of the cell membrane.[58]

Moreover, not only the size plays an important role, homogeneity in the sample is required since the behaviour of nanoparticles as drug delivery systems is highly affected by this property.[59]

By the solvent evaporation method, PLGA@MS were obtained with two main diameter size distributions of around 1.47±0.37 μm and 14.9± 3.7 μm. The inclusion of MSNPs can be carried out but the polydispersity of the system provided the information that this methodology was not the best one to continue the studies. Using the SORP methodology, PLGA spheres of around 600 nm and 1 μm could be synthesized with a free surfactant. The incorporation of MSNPs gives agglomerations of the PLGA@MS with 20 and 5% w/w. On the other hand, the incorporation of an endocannabinoid perturbs the formation of the spheres even at low loading (5 % w/w).

Therefore, for all the procedures tried, the hydrogel template method was the only one in which the homogeneity regarding size and morphology is preserved even with the inclusion of cannabinoids and mesoporous silica nanoparticles (**Figure 0.2**). The carriers, called beads due to its shape, were of 20 μm diameter size. Confocal images were taken of the different PLGA@systems loaded with Nile Red, N-(2-hydroxy ethyl) oleamide (2HEO) and Anandamide (AEA) in the PLGA@carrier (**Figure 0.2A** and **0.2C**). 2HEO and AEA were synthetized and characterized by NMR, IR, HR ESI-TOF-MS. Those compounds represent the analogue and the active molecule of a group of cannabinoids called endocannabinoid.[60] 2HEO or AEA can be loaded in high percentage (20 % w/w) in the PLGA@MBds giving CBDds-PLGA@MBds systems. **Figure 0.2D** shows the MSNPs@PLGA@carrier system, where MSNPs were loaded with the dye orange 2 (4-[(2-Hydroxy-1-naphthalenyl)azo]benzenesulfonic acid monosodium salt) to mimic the loading of a chemotherapeutic drug. In turn, these MSPNs were inserted in the PLGA@carrier. The confocal images (**Figure 0.2**) were taken using a laser wavelength of 488 nm.

Then, here is presented a new unprecedent hybrid tandem-delivery system (MNPs@PLGA-MBds) based on breakable and degradable systems. A Food and Drug Administration (FDA)-approved poly(lactic-co-glycolic acid) biodegradable polymer carrier[61] can effectively transport CBDs and mesoporous silica nanoparticles (*ss*-NPs),it was prepared with a redox-responsive linker disulfide[51] and loaded with chemotherapeutic drugs. This design covers the requirement to deliver two different type of drugs in two different parts of the cell (intra and extra membranal) which opens a new barrier for the development of drug delivery systems.
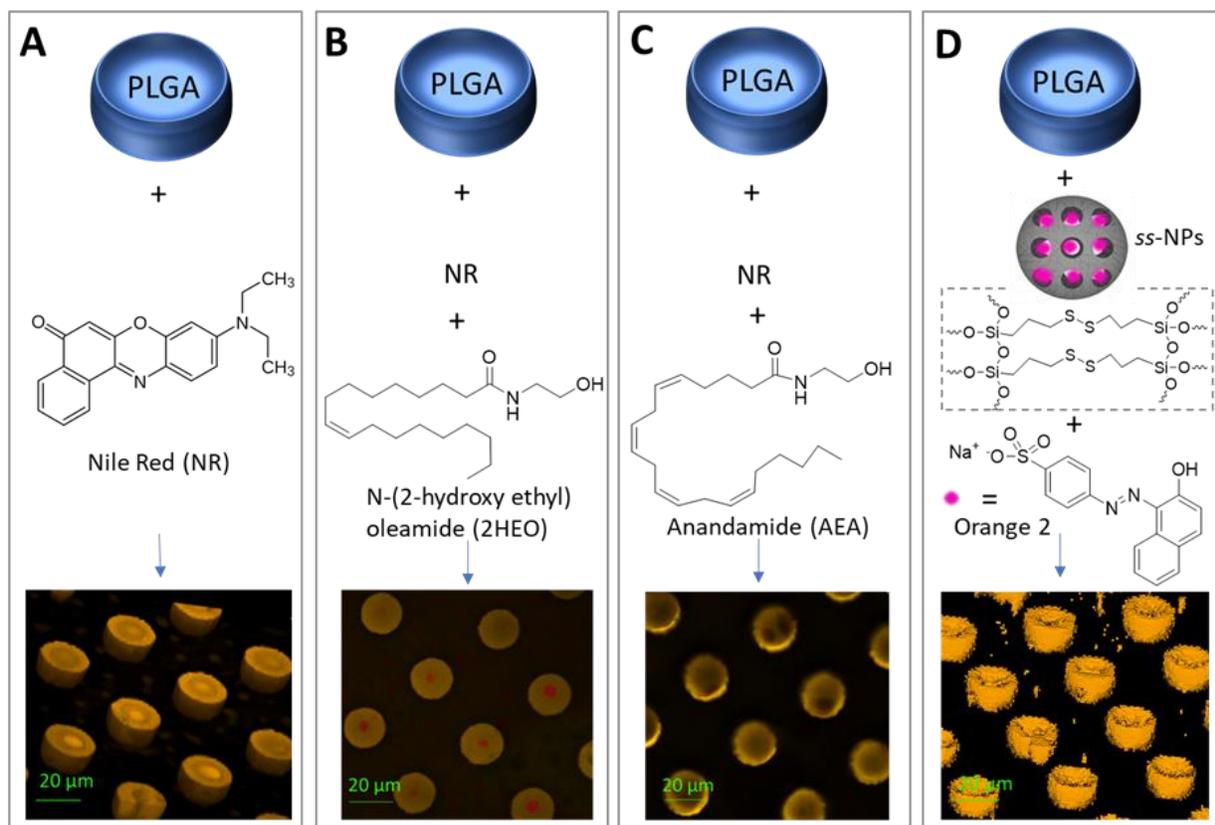
Figure 0.2. Schematic representation of the different hybrid systems synthetized for the loading of hydrophobic molecules, in particular **A)** Nile Red, **B)** N-(2-hydroxy ethyl) oleamide (2HEO) and **C)** Anandamide (AEA) in the PLGA@carrier. 2HEO and AEA represents the analog and the active endocannabinoid. **D)** Shows the representation of the MSNPs@PLGA@carrier system. Orange 2 was loaded in the redox-stimuli-MSNPs to mimic the chemotherapeutic drug. The confocal images were taken using a laser wavelength of 488 nm.

After that, it is presented another hybrid material done in combination of non-lipid-based vesicles, called QS and silica. QS are thermodynamically stable vesicular structures, composed of quaternary surfactants and sterols (**Figure 0.3A**). Their stability regards their morphology, size, lamellarity, and membrane supramolecular organization.[62,63] These vesicles can load hydrophobic or hydrophilic drugs working therefore for several applications, including drug delivery. The idea is to combine QS with a silica shell to protect the vesicle, giving more structural and mechanical stability to the QS, against agglomeration and internal leakage during storage, transporting and application. Moreover, this shell could prevent the loss of cargo for drug delivery applications, making sure that all the drug loaded will arrive to the targeted point.

Furthermore, here is presented the formation of a stimulus responsive silica shell, which, in presence of a reducing agent (existing in high concentrations in carcinogenic cells), breaks in small pieces releasing the cargo and preventing then the accumulation of the material in the body.

For the synthesis of the silica shell, different silanes were tested: TEMOS, TEOS and APTES to produce the non-breakable silica coated QS (NB-SQS) and the combination of these with BTSPD to produce the stimulus responsive shell (redox stimuli) to form a breakable silica shell on QS (B-SQS) (**Figure 0.3B**).
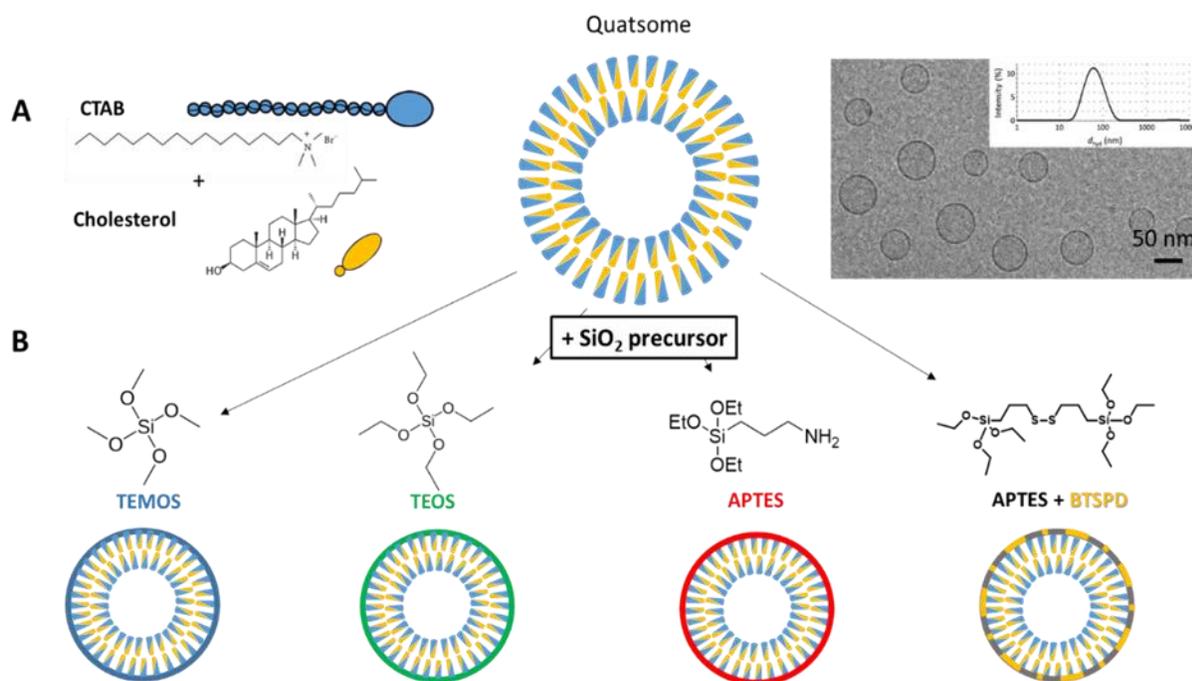
Figure 0.3. A) Composition of the QS. **B)** Different silica-coated QS synthetized.

From all the silanes tested, TEOS and TEMOS were the ones which a deposition of silica in the QS was observable. **Figure 0.4** shows the Cryo-TEM images and diameter size distribution of the NB-SQS using TEMOS and TEOS as silica precursors, after 4 and 2 days of reaction, respectively. DLS-Size and Zeta Potential measurement were carried out over time during their preparation, which reveal a change in size distribution and Zeta Potential from 85±2 nm and 94±15 mV (QS) to 116±3 nm and 36±3 mV for the system using TEMOS to cover the QS (**Figure 0.4A**), and from 159±3 nm and 29±1 mV for the system using TEMOS to cover the QS (Figure **0.4B**).
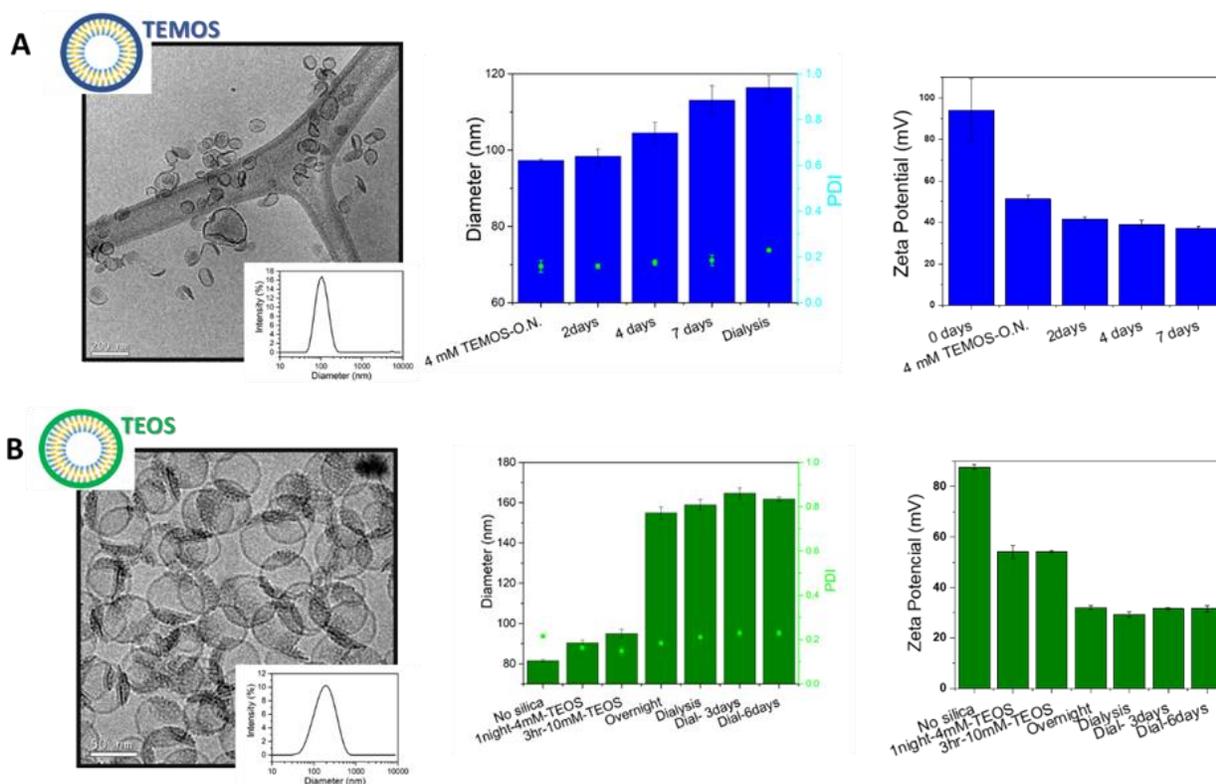
Figure 0.4. Non-breakable coated QS using **A)** TEMOS and **B)** TEOS. Cryo-TEM and diameter size distribution (after 4 and 2 days of reaction, respectively). DLS-Size and Zeta Potential over time during their preparation.

For the redox stimulus-responsive Breakable silica-coated QS (B-S-QS), a mixture of APTES and BTSPD was used (**Figure 0.5A**). **Figure 0.5B** shows the SEM picture of the sample after stirring overnight (initial diameter size distribution of QS was 114±26 nm). SEM size distribution, count performed on 300 nanoparticles, gave an average diameter of 143±19 nm BS-QS particles.

The second assay was tried with QS of a size of 50 nm, (initial diameter size of QS was 58±1 nm and Zeta Potential of 84±2 mV) which have a better uptake by the cells.[64] TEM images (**Figure 0.5C**) shows the presence of silica around the QS, however it could be particles of silica. DLS measurement (**Figure 0.5D**) show two different populations of size of 58±12 nm and 185±42 nm, the second population could be attributed to the agglomeration of the BS-QS. From Cryo-TEM image analysis yields a diameter size distribution of 32±6 nm (average over 200 particles). In this case, the silica shell thickness was 9±2 nm; which was larger than the 4-5 nm of the QS membrane (**Figure 0.5E** and **0.5F**).
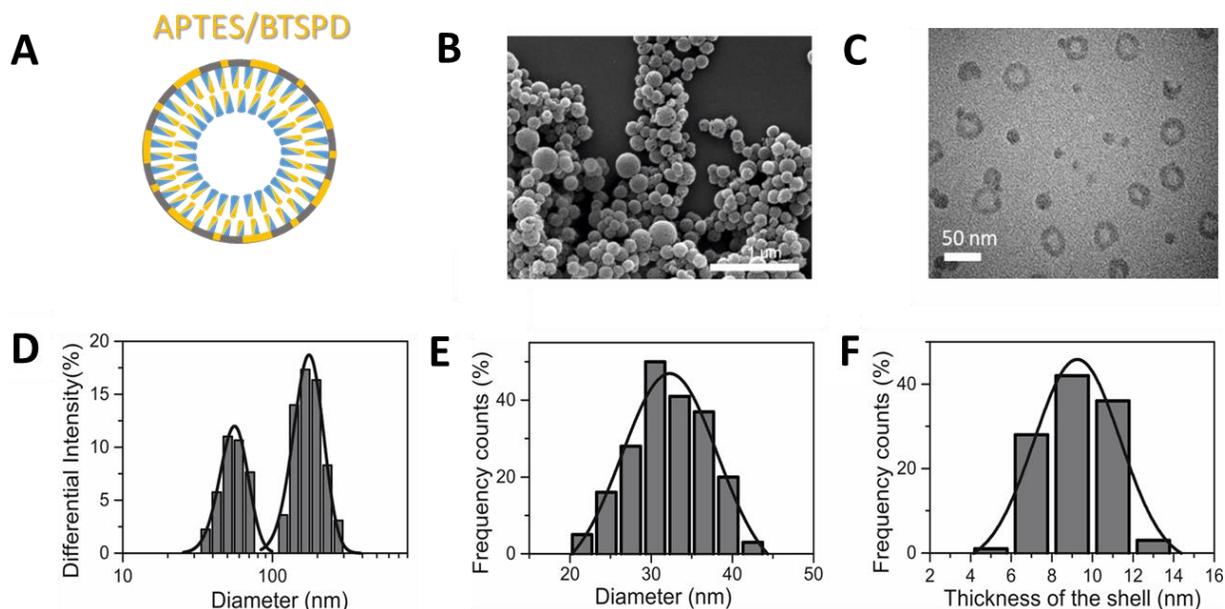
Figure 0.5. **A)** Representative scheme **B)** SEM and **C)** TEM images for the silica coated Qs (APTES/BTSPD). Scale bar 1μm and 50 nm, respectively. **D)** Size distribution of the B-SQS measured by DLS giving two populations of size of 58±12 nm and 185±42 nm. **E)** TEM size diameter distribution (count performed 200 silica-QS particles; average diameter 32±6 nm) and **F)** TEM size thickness of the shell distribution (count performed in 100 silica-QS particles; average thickness of the shell 9±2nm).

In the other hand, QS and silica were labelled with a donor (DiI) and acceptor (Cyan5) fluorophore (**Figure 0.6A**), respectively. These systems were employed to characterise the hybrid system by Förster Resonance Energy Transfer (FRET), which is a powerful tool to study nanosystems.[65] In case, the silica is attached to the QS FRET could be employed to understand the organization of the hybrid system. These systems act as luminescent bioprobes and their study focuses on the potentiality of these materials as drug delivery systems. For this, DiI was loaded into the hydrophobic QS membrane,[66] and cyanine 5 NHS ester was covalently attached to the silica through the amino groups of the APTES, producing the system Cyan5-BS-QS-DiI (**Figure 0.6B**). The control systems used were those synthetized only with one dye (Cyan5-BS-QS and BS-QS-DiI). The emission and excitation spectra (**Figure 0.6C**) of breakable BS-QS-DiI (pink lines; with excitation and emission wavelengths of λ_{exc} = 525 nm and λ_{em} = 625 nm, respectively) and Cyan5-BS-QS (blue lines; λ_{exc} = 600 nm and λ_{em} = 750 nm) show an overlap of the donor emission (BS-QS-DiI) and the acceptor excitation (Cyan5-BS-QS), which confirm the possibility to observe FRET in the Cyan5-BS-QS-DiI system. Indeed, a high FRET efficiency is observed in both emission and

excitation spectra of the Cyan5-BS-QS-DiI (**Figure 0.6D**; λ_{exc} = 500 nm and λ_{exc} = 750 nm). The 94 % of FRET efficiency was extracted from the experiments (value obtained from the Quantum yield QY (E=1-(QY$_{DA}$(D)/QY$_D$(D))), indicating that the two dyes are largely in close proximity (at a distance of less than 10 nm) due to the formation of silica around the QS.
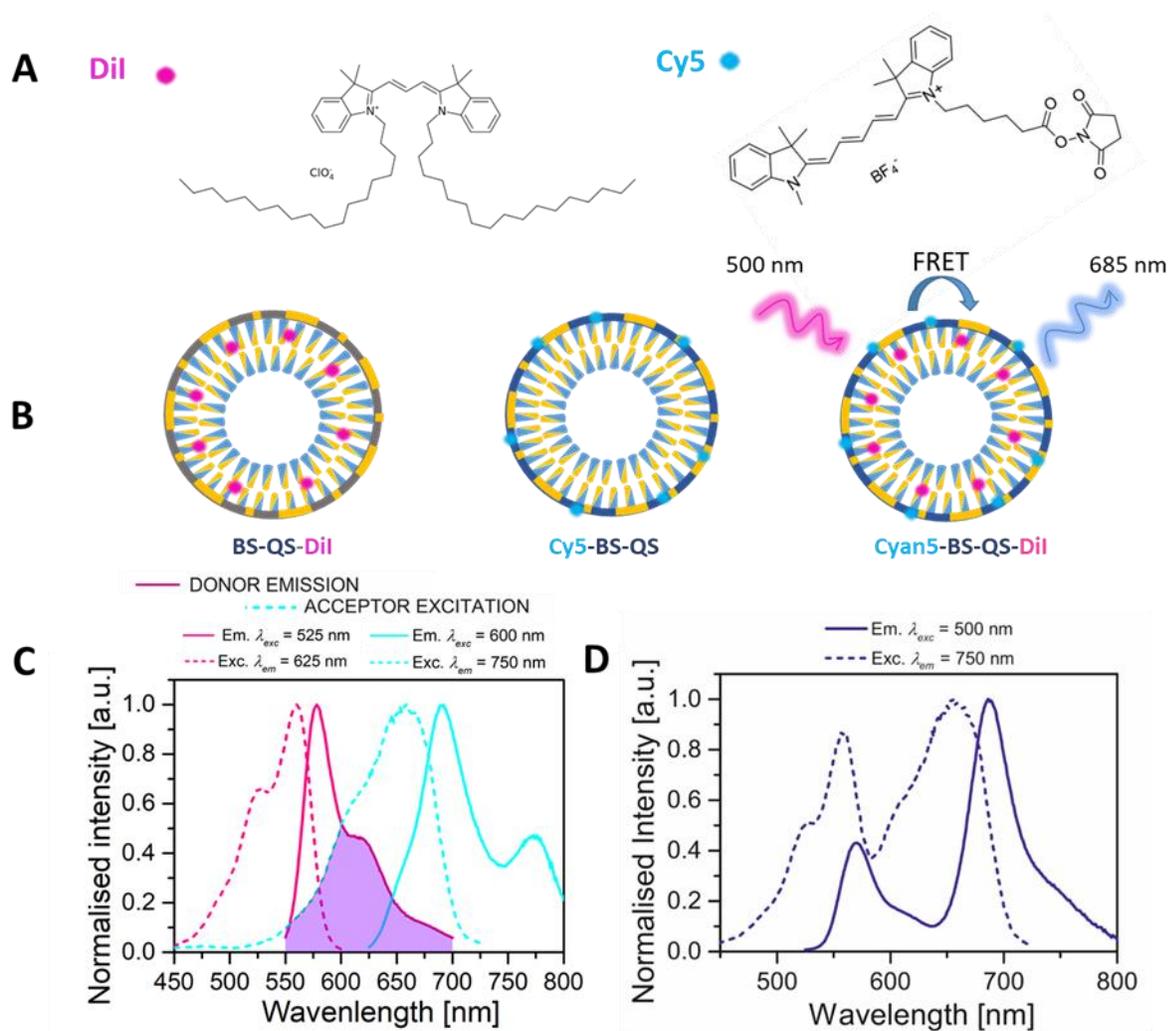
Figure 0.6. A) Dyes using for the label silica QS. **B)** Representative scheme of the label silica QS. **C)** Emission and excitation spectra of Breakable Silica QS loaded with DiI (BS-QS-DiI) (pink lines); Wavelength of excitation and emission were 525 and 625 nm, respectively. And its overlap with the Emission and excitation spectra of Cyan5 Breakable Silica QS (Cyan5-BS-Qs) (blue lines); excitation and emission wavelength at 600 and 750 nm, respectively. **D)** Emission and Excitation spectra of the Cyan5-Breakable Silica coated DiI-QS (Cyan5-BS-Qs-DiI) exciting at 500 nm and emitting at 750 nm.

Stochastic optical reconstruction microscopy (STORM) images of Cyan5-BS-QS (λ_{exc} = 642 nm) (**Figure 0.7**) show spots of sizes between 300 nm, suggesting that the Cyan5-APTES is indeed is forming the silica shell on the QS.
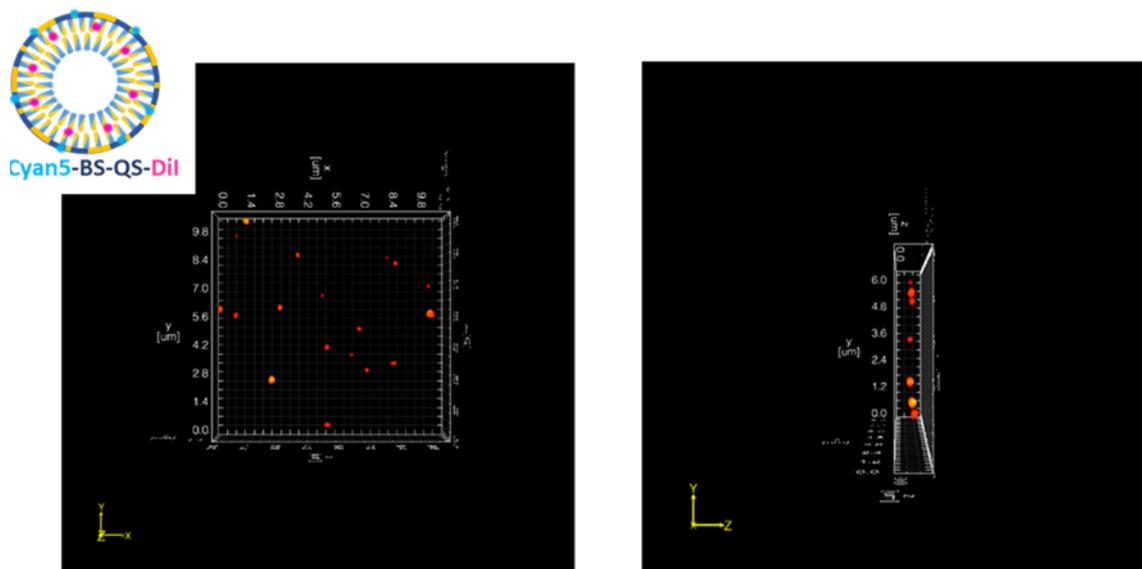
Figure 0.7. Scheme of the Breakable QS used for STORM analysis (Cyan5-BS-QS-DiI) and the STORM images of the of Cyan5-Breakable QS (u.m.micrometer).

In order to know if there is a breakability property in the BS-QS in presence of a reducing agent, breakability tests were performed to degrade the silica shell. The breakability of BS-QS was studied in presence of Glutathione (GSH) (**Figure 0.8A**). In the presence of 10 mM of GSH, the absorbance of Cyan5-BS-QS, which took place in a semi-permeable membrane tubing (pore cut-off size of 14 kDa), calling here this method as an open system: In this experiments, we observed a gradual decrease over time of the FRET signal (**Figure 0.8B**), reaching practically zero signal after 12 days (**Figure 0.8C** and **D**). These results suggest that the disulfide linker in the BTSPD starts to break in presence of the reducing agent (GSH), producing small pieces of Cyan5-labelled silica that eventually leave the membrane tubing.
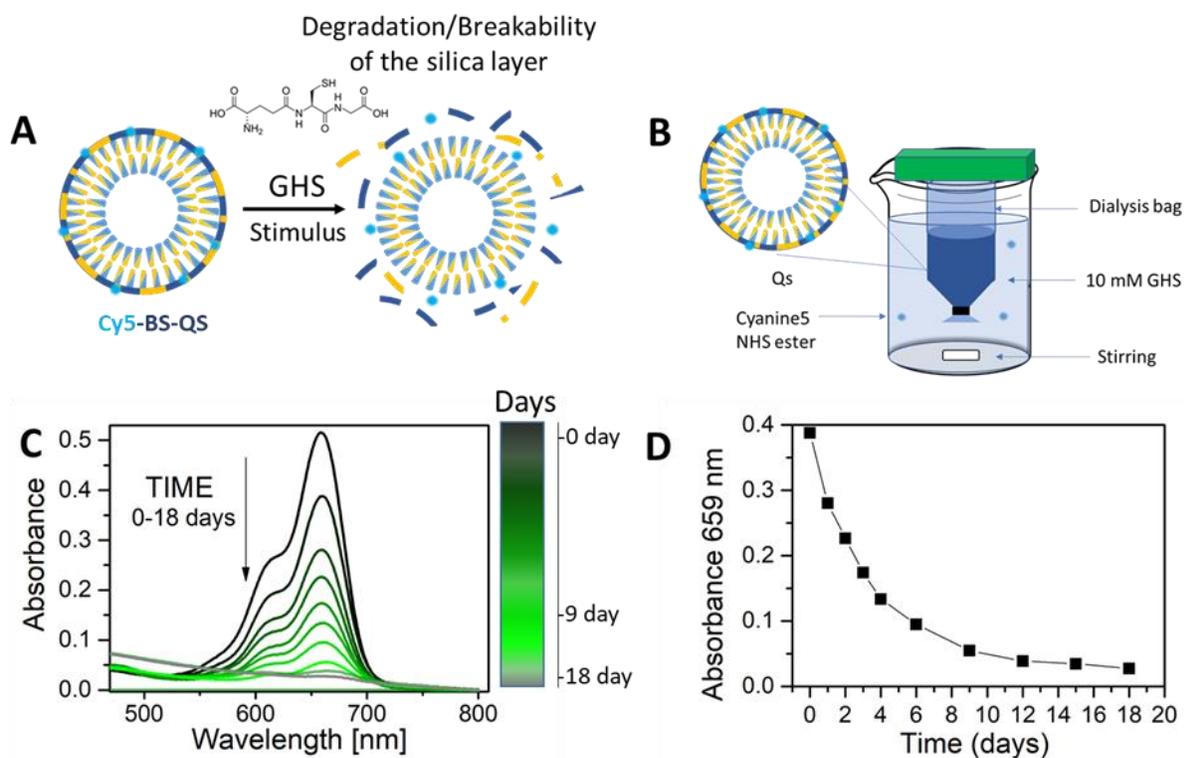
Figure 0.8. A) Scheme of the Cyn5-BS-Qs and its degradation in presence of GSH. **B)** Experiment diagram for the breakability test (dialysis methodology). **C)** Absorbance spectra of the Cyan5-Breakable QS after the time in the presence of 10 mM Glutathione. **D)** Absorbance spectra at 659nm through the time of the Cyan5-Breakable QS.

Another methodology was used to study the Cyan5-BS-QS-DiI breakability, called here closed system; in which the QS solution is confined in a Quartz cuvette with 10 mM of GSH and the emission was studied at defined time-intervals (**Figure 0.9A**). The normalized intensity of the emission at 562 and 659 nm, representing the DiI and the Cyanine5 in the Cyan5-BS-QS-DiI during the time in presence of 10 mM GSH, is shown in **Figure 0.9B** and **C** (after 24 and 44 days, respectively). The ratio Acceptor/Donor of the sample after these times are presented in **figure 0.9D** and **E**. Along the time the maximum emission wavelength of the donor (DiI) is decreasing while that of the acceptor (Cyanine5) is increasing. The ratio between the acceptor and the donor increases over the time which means that the FRET in the system is increasing too. This observation can be explained as, by the time silica shell is breaking in presence of GSH, and then the Cyan5 dye is internalizing into the hydrophobic part of the QS where the DiI is loaded (as this dye has more an hydrophobic character), bringing both dyes closer to each other, increasing then the energy transfer between the donor and the acceptor.
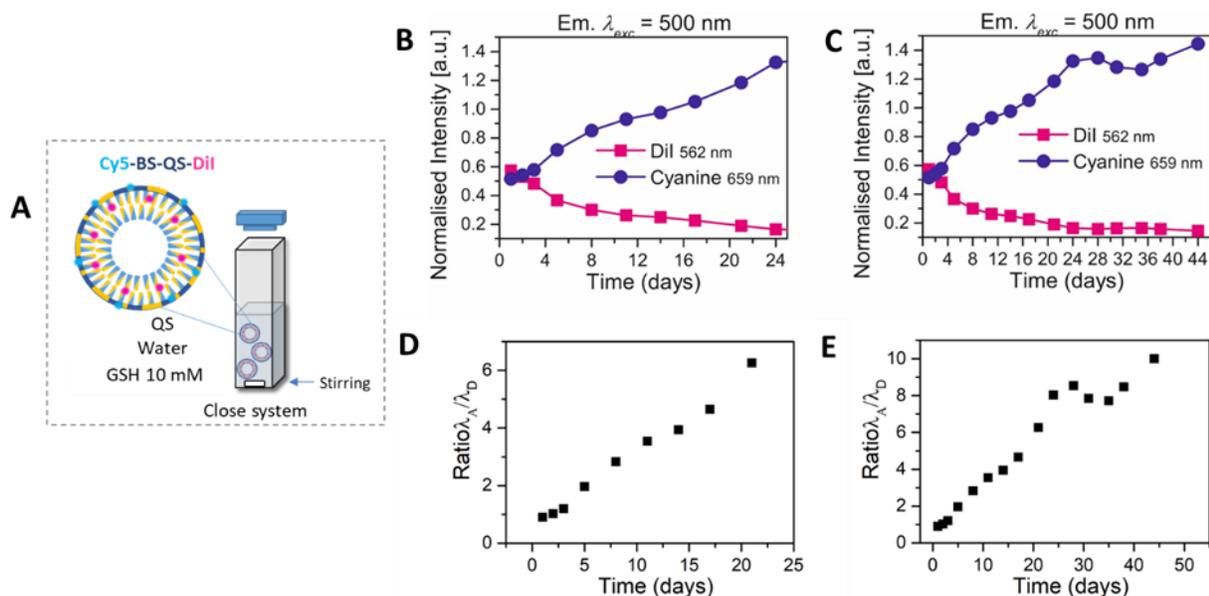
Figure 0.9. A) Scheme of the breakability test using a close methodology. **B)** and **C)** Normalized intensity of the emission at 562 and 659 nm representing the DiI and the Cyanine5 in the Cyan5-Breakable QS loaded with DiI after the time in the presence of 10 mM Glutathione after 24 and 44 days, respectively. **D)** and **E)** Ratio Acceptor/Donor of the sample after 24 and 44 days.

The impact of a breakable and non-breakable silica shell on the stability of the QS (silica shell protection effect) for the release of a hydrophobic molecule loaded in the membrane was studied. In particular the release of DiI have been monitored during time in three different systems: 1) The QS loaded with DiI (QS+DiI), 2) QS loaded with DiI and coated with a breakable shell (QS+DiI+ss-silica shell) and 3) QS loaded with DiI and coated with non-breakable silica shell (QS+DiI+silica shell) (**Figure 0.10 A**). The last two systems (2 and 3) were coated with TEMOS as the precursor to form the silica layer. The release experiment, DiI-loaded QS (with or without silica-shell), were placed in a semi-permeable membrane tubing (with a pore cut-off size of 3.5 kDa),[67–69] and the emission of DiI was screened (λ_{exc} = 500 nm) in the exterior reservoir for a time period of 400 h (**Figure 0.10B**). While that initially the emission was practically zero, due to the absence of DiI molecules, the emission increased in the time course of 5 hours for both coated QS (**Figure 0.10C**), lower in comparison with the non-coated QS (QS-DiI). Silica-coated QS with breakable and non-breakable shell (BS-QS-DiI and NB-QS-DiI) showed a reduction in the emitted light intensity of 63 %. Therefore, the release of DiI is hindered by the silica shell, and in the first hours the shielding effect works equally well for both systems (the breakable and non-breakable

shell). After longer times (> 124h), however, the breakable silica shell starts to release more DiI than the non-breakable (**Figure 0.10D**), showing a 3 times higher emission after 16 days.
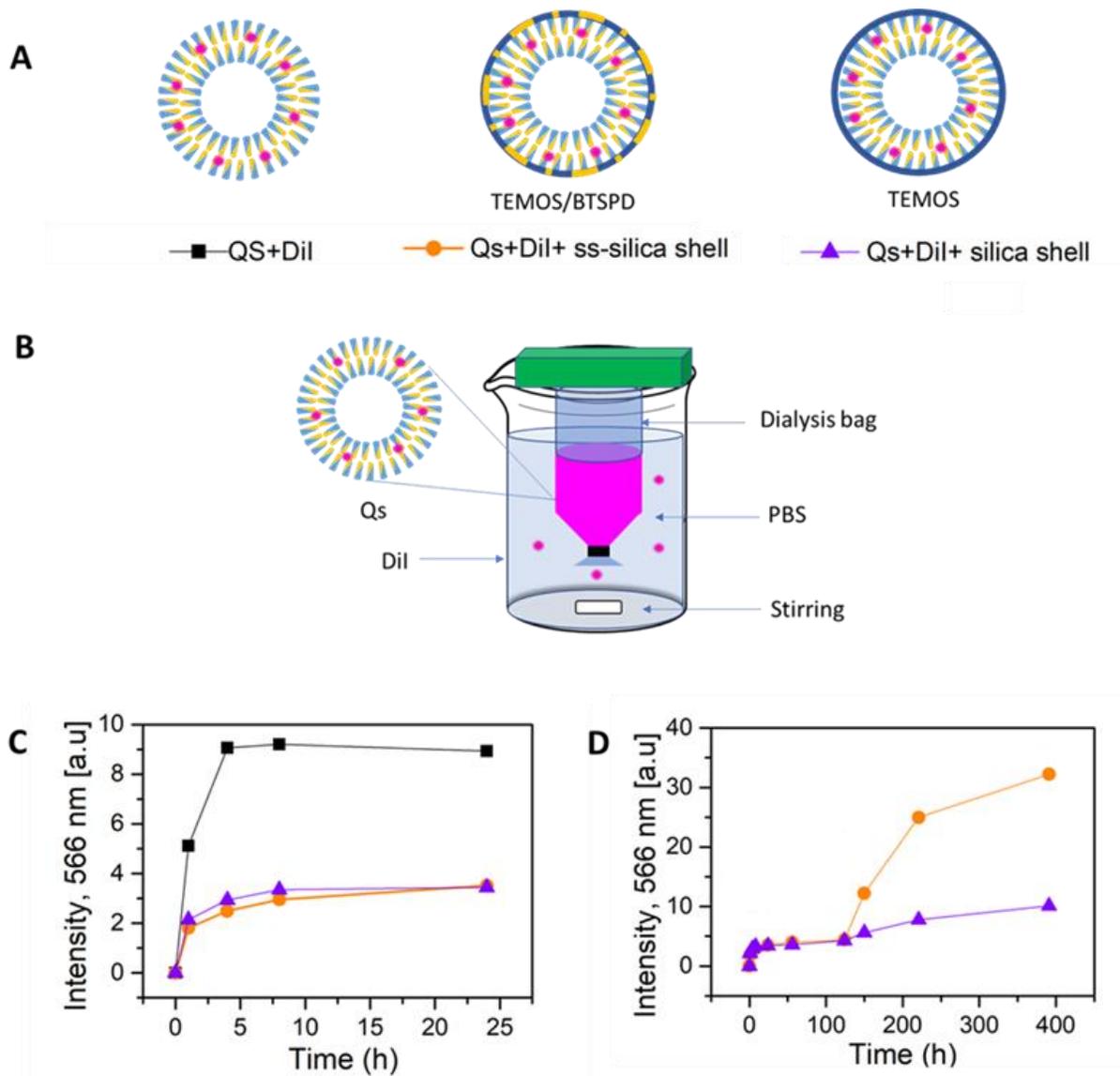
Figure 0.10. A) Schematic representation of the QS loaded with DiI, B-S-QS and NB-S-QS loaded with DiI. In vitro release study of the QS-DiI (black), BS-QS-DiI (red) and NB-QS-DiI (blue). **B)** Intensity Emission at 566 nm over the time (λ_{exc}= 500 nm) **C)** after 25 and **D)** 400 h.

Label Coated silica QS were synthetized in order to have another characterization proof of the silica shell formation. Breakability, permeability, confocal, STORM and release studies were carried out with these systems. Characterization using FRET (Energy transfer) studies were carried out for the loaded QS, revealing that the dye inside the QS and the dye in the silica shell are approximated in a distance < 10nm. Confocal and STORM analysis were done as a proof of

the presence of the labelled silica and its characterization. Breakability tests were carried out to study the breakability of the sample in presence of a reducing agent (GSH). Using several methodologies (open system and closed system), that revealed that the breakability of the silica shell modifies the FRET signal in the system during time. From the release studies is shown a protection of the 62 % of the drug loaded using a hydrophobic dye as a proof of concept of the drug delivery under the first 25h of release. Further investigations should be carried out on the release of hydrophilic drugs under these systems.

In other studies, the formation of breakable silica shell in another type of QS was investigated. In this case, the formulation of the QS was modified by Cholesterol and Myristalkonium chloride (MKC) to reduce the toxicity of the system for drug delivery applications.[70] The initial hydrodynamic diameter size distribution value of the MKC-QS sample was 26±19 nm and 81±19 nm (**Figure 0.11A**), after the addition of the mixture of silanes (TEMOS and BTSPD), the diameter size distribution increased to 64±4 nm and 221±57 nm for both groups of size distributions (**Figure 0.11B**). **Figure 0.11C** represents Cryo-TEM images of the final sample after cleaning by dialysis.
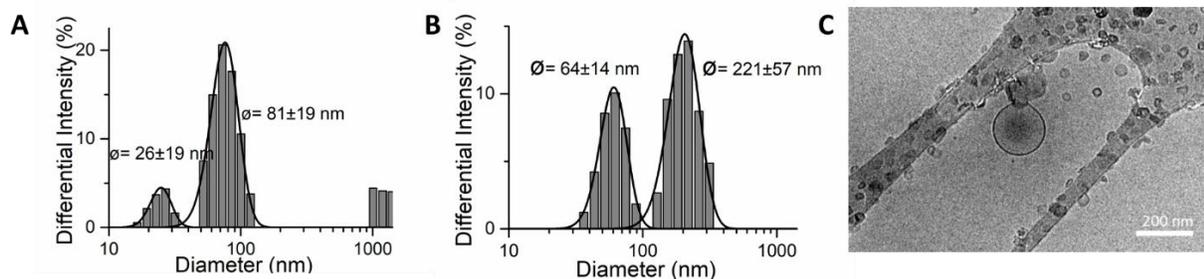
Figure 0.11. DLS meassurements for the Breakable silica coated MKC-QS. Using TEMOS and BTSPD. **A)** Initial MKC-QS, **B)** after the addition of silane and 4 h reaction and **C)** Cryo-TEM images of the final sample.

In another project, the use of the MKC surfactant was proposed to be included in the synthesis of mesoporous silica nanoparticles as a template for their formation. Non-breakable silica nanoparticles and breakable silica nanoparticles were prepared (NB-MSNPs). Stimulus redox-response particles are synthetized using a disulfide linker as an organic group (*ss*-MSNPs). Moreover, big pores were created on the breakable mesoporous nanoparticles using MKC surfactant as a template (Big pores-*ss*-MSNPs). **Figure 0.12** shows a schema of these 3 systems with a resume of their characterization: morphological characterization, hydrodynamic diameter

size distributions, and pore size distribution were taken by SEM, DLS and N_2 adsorption measurements, respectively. For all the systems, the shape of these particles is spherical with hydrodynamic diameter size distributions of 115±40, 119±28 and 137±34 nm for the NB-MSNPs, *ss*-MSNPs and the big pores-*ss*-MSNPs, respectively. The pore size distribution for the NB-MSNPs showed a diameter size distribution of 3.2 nm, while for the non-breakable the diameter pore size was 2.3 nm. Finally, the big pores with breakable nanoparticles was obtained, a long size distribution was achieved, of values until 30 nm, showing these materials as a mesoporous system.
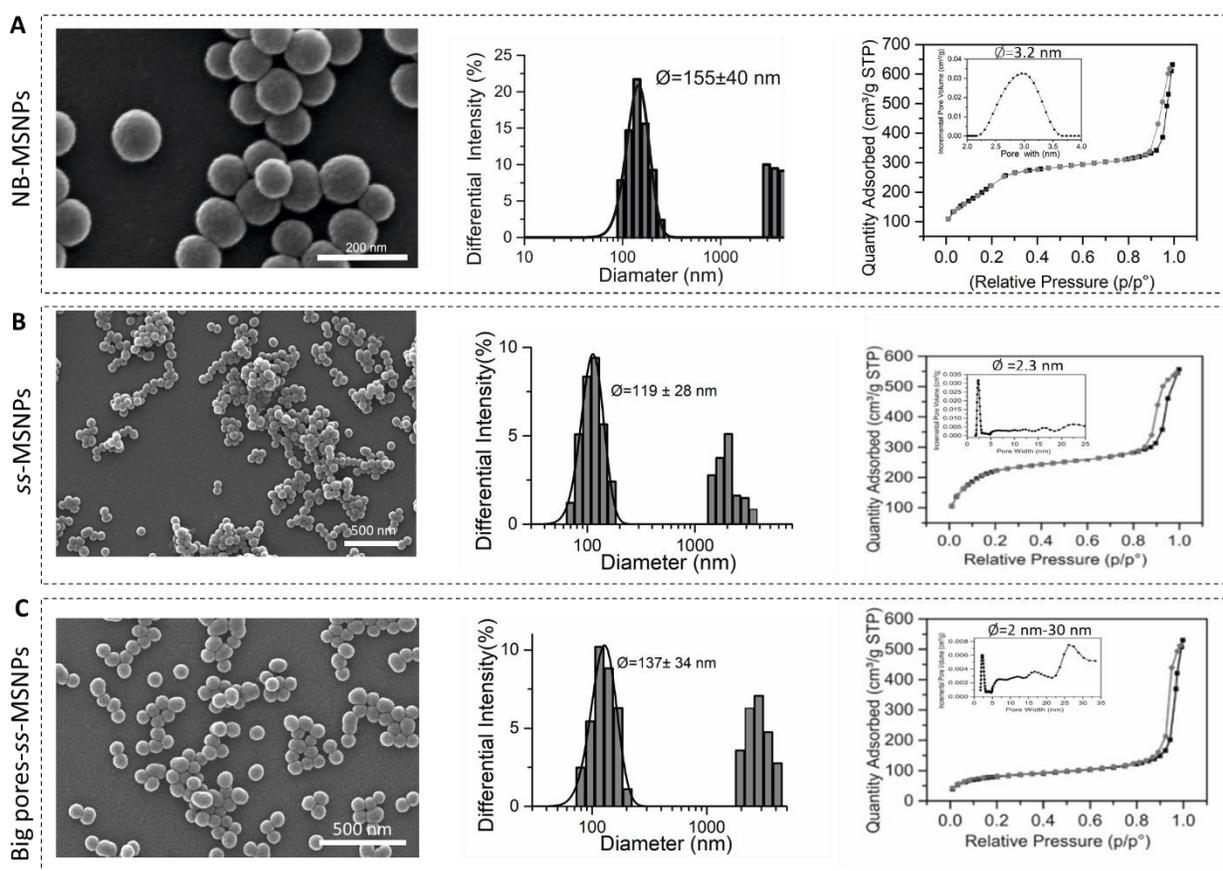
Figure 0.12. Characterization of the **A)** Non-breakable silica nanoparticles (NB-MSNPs). **B)** redox-responsive particles (*ss*-MSNPs) and **C)** big pores breakable mesoporous nanoparticles (Big pores-*ss*-MSNPs) using MKC surfactant as a template. SEM, DLS and N_2 adsorption measurements, shows their morphology, diameter size and porous distribution, respectively.

Different tests were realized with different kinds of silica nanoparticles as hybrids materials to study their biocompatibility. Non-breakable silica nanoparticles (NB-MSNPs) and breakable

redox-responsive particles (ss-MSNPs) synthetized by MKC as a template were studied. A cell viability test was performed using 3 different cell lines: HeLa (cervical cancer cells) and C6 (glioma cells) cells were studied as tumorigenic lines, and MCF10 as a non-tumorigenic. Additionally, the influence of the concentrations of NPs was studied, 10, 50 and 100 µg/mL were the selected concentrations. The nanoparticles without surfactant (after its removal) were tested in this experiment (**Figure 0.13**).

Breakable and non-breakable NPs were synthetized by MKC surfactant and after its removal (MKC), have a good cell viability and not toxicity was detected at 10, 50 and 100 µg/ml (100 % of cell viability) with MCF10, C6 and HeLa cell lines. These observations suggest that MKC could be a good option to prepare MSNPs to make better systems for biological applications.
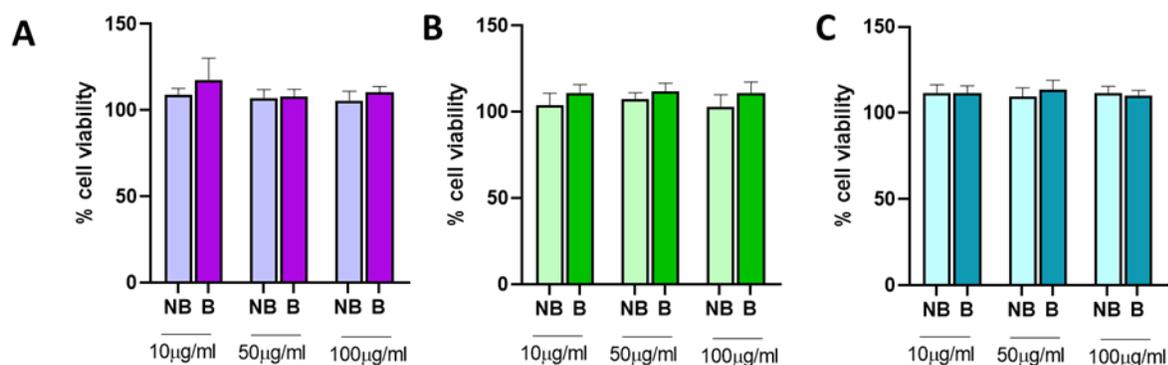
Figure 0.13. Viability assay of **A)** MCF10, **B)** C6 and **C)** Hela cells exposed to different concentrations of NPs; non-breakable, and breakable (NB and B, respectively), with MKC and w/o MKC for 24 hours. Values are normalized to untreated cells and expressed in % of viable cells. All data are represented as mean ± S.D., statistical analysis was performed by One-way ANOVA and Turkey's post hoc test.

A new hybrid material done by PLGA and mesoporous silica nanoparticles was done as a multi-delivering system. It was built in order to deliver cannabinoids and chemotherapeutic drugs to produce a synergetic activity against cancer (*Chapter 2*). The system is designed in the way that the two drugs are delivered in two different parts of the cell (intra and extra membranal). This opens a new barrier for the development of drug delivery systems. In this project, two different cannabinoids were synthetized and characterized by NMR, IR, HR ESI-TOF-MS as examples of an analogue and active endocannabinoids. Different kinds of MSNPs were synthetized as an example of all the varieties of materials that can be included in the PLGA@vehicles. Different techniques were used to synthetize the PLGA@vehicles as: solvent evaporation method, self-

organized precipitation route (SORP) and hydrogel template method. This last one methodology was the only one in which the homogeneity regarding size and morphology was preserved even with the inclusion of cannabinoids and mesoporous silica nanoparticles

A second hybrid material based on QS and silica was fabricated (*Chapter 3*). The construction is designed to condensate silica around the QS forming a shell around them. The formation of the silica shell provides an excellent structural and mechanical stability to the QS, mainly the shell prevents the loss of cargo before the nanocarrier arrives to the targeting point. This material contributes for the development of new generation of drug delivery applications. Moreover, responsive silica shell systems were synthetized to make redox-organic response materials, which specifically breaks in presence of a reducing agent, inside cancer cells, releasing the cargo and breaking in small pieces to prevent accumulation in the body. These materials could have a potential interest for biomedical applications.

Fluorescent molecules have been introduced in the silica coated QS system to produce *Label silica shell QS* for different objectives (*Chapter 4*). These systems could act as luminescent bio probes and their study focuses on their potentiality as a drug delivery system. Moreover, stimuli redox- label response systems were synthetized to make different studies. Characterization using FRET (Energy transfer) were carried out for the loaded QS, revealing that the dye inside the QS and the dye in the silica shell are approximated in a distance < 10nm. Confocal and STORM analyses were carried out as a proof of the presence of the label silica and its characterization. Breakability tests were done in presence of a reducing agent (GSH) and it revealed that the breakability of the silica shell could modifies the FRET signal in the system during time. Permeability tests showed the protection of the QS when the silica shell is present. Release studies showed a protection of the 62 % of the drug loaded using a hydrophobic dye as a model drug under the first 25h of release. Further investigations should be carried out on the release of hydrophilic drugs under these systems.

Stimulus redox-response breakable silica shell was fabricated in a new kind of QS synthetized by Myristalkonium chloride (MKC) and Cholesterol. These materials are synthetized in favour of the formation for more biocompatible systems for further drug delivery proposes (*Chapter 5*). In this chapter also the use of the MKC surfactant is proposed to be included in the synthesis of mesoporous silica nanoparticles as a template for their formation. Non-breakable silica

nanoparticles and Breakable silica nanoparticles were prepared. Stimulus redox-response particles are carried out using a disulfide linker as an organic group. Moreover, big pores were created on the breakable mesoporous nanoparticles using this MKC surfactant as a template. These new systems provide a more biocompatible systems which could help to obtain better drug delivery materials for biomedical applications.

As a general conclusion, in this thesis it is explored the combination of different systems to form hybrid materials to perform their singular properties attributed to one material. The designs are thought to develop new alternatives in the field of nanomaterials for drug delivery applications.

REFERENCES

(1)   Jeevanandam, J.; Barhoum, A.; Chan, Y. S.; Dufresne, A.; Danquah, M. K. Review on Nanoparticles and Nanostructured Materials: History, Sources, Toxicity and Regulations. *Beilstein Journal of Nanotechnology* **2018**, *9* (1), 1050–1074.

(2)   Kim, K.-M.; Kang, J.-H.; Vinu, A.; Choy, J.-H.; Oh, J.-M. Inorganic Nanomedicines and Their Labeling for Biological Imaging. *Current Topics in Medicinal Chemistry* **2013**, *13* (4), 488–503.

(3)   Arias, J. L. *Nanotechnology and Drug Delivery, Volume One: Nanoplatforms in Drug Delivery*; Arias, J. L., Ed.; CRC Press, 2014.

(4)   *Applications of Targeted Nano Drugs and Delivery Systems: Nanoscience and Nanotechnology in Drug Delivery*; Mohapatra, S., Ranjan, S., Dasgupta, N., Kumar, R., Thomas, S., Eds.; Elsevier, 2018.

(5)   Gessner, I.; Neundorf, I. Nanoparticles Modified with Cell-Penetrating Peptides: Conjugation Mechanisms, Physicochemical Properties, and Application in Cancer Diagnosis and Therapy. *International Journal of Molecular Sciences* **2020**, *21* (7), 2536.

(6)   Tomalia, D. A.; Baker, H.; Dewald, J.; Hall, M.; Kallos, G.; Martin, S.; Roeck, J.; Ryder, J.; Smith, P. A New Class of Polymers: Starburst-Dendritic Macromolecules. *Polymer Journal* **1985**, *17* (1), 117–132.

(7)   Bharali, D. J.; Khalil, M.; Gurbuz, M.; Simone, T. M.; Mousa, S. A. Nanoparticles and Cancer Therapy: A Concise Review with Emphasis on Dendrimers. *International Journal of Nanomedicine* **2009**, *4* (1), 1–7.

(8)   Gillies, E. R.; Fréchet, J. M. J. Dendrimers and Dendritic Polymers in Drug Delivery. *Drug Discovery Today* **2005**, *10* (1), 35–43.

(9)   Sandoval-Yañez, C.; Castro Rodriguez, C. Dendrimers: Amazing Platforms for Bioactive Molecule Delivery Systems. *Materials* **2020**, *13* (3), 570.

(10)   Allen, T. M.; Cullis, P. R. Liposomal Drug Delivery Systems: From Concept to Clinical Applications. *Advanced Drug Delivery Reviews* **2013**, *65* (1), 36–48.

(11)   Grimaldi, N.; Andrade, F.; Segovia, N.; Ferrer-Tasies, L.; Sala, S.; Veciana, J.; Ventosa, N. Lipid-Based Nanovesicles for Nanomedicine. *Chemical Society Reviews* **2016**, *45* (23), 6520–6545.

(12)   Alivisatos, A. P.; Gu, W.; Larabell, C. Quantum Dots as Cellular Probes. *Annual Review of Biomedical Engineering* **2005**, *7* (1), 55–76.

(13)   Tang, Z.; He, C.; Tian, H.; Ding, J.; Hsiao, B. S.; Chu, B.; Chen, X. Polymeric Nanostructured Materials for Biomedical Applications. *Progress in Polymer Science* **2016**, *60*, 86–128.

(14)   De Souza, R.; Zahedi, P.; Allen, C. J.; Piquette-Miller, M. Polymeric Drug Delivery Systems for Localized Cancer Chemotherapy. *Drug Delivery* **2010**, *17* (6), 365–375.

(15)   Huo, Q.; Liu, J.; Wang, L. Q.; Jiang, Y.; Lambert, T. N.; Fang, E. A New Class of Silica Cross-Linked Micellar Core-Shell Nanoparticles. *Journal of the American Chemical Society* **2006**, *128* (19), 6447–6453.

(16)   Hoffmann, F.; Cornelius, M.; Morell, J.; Fröba, M. Silica-Based Mesoporous Organic-Inorganic Hybrid Materials. *Angewandte Chemie International Edition* **2006**, *45* (20), 3216–3251.

(17)   Argyo, C.; Weiss, V.; Bräuchle, C.; Bein, T. Multifunctional Mesoporous Silica Nanoparticles as a Universal Platform for Drug Delivery. *Chemistry of Materials* **2014**, *26* (1), 435–451.

(18)   Dresselhaus, M. S.; Dresselhaus, G.; Eklund, P. C.; Rao, A. M. Carbon Nanotubes. In *The physics of fullerene-based and fullerene-related materials*; Andreoni, W., Ed.; Kluwer Academic Publishers, 2000; pp 331–379.

(19)   Popov, V. N. Carbon Nanotubes: Properties and Application. *Materials Science and Engineering R: Reports* **2004**, *43* (3), 61–102.

(20)   Toshima, N.; Yonezawa, T. Bimetallic Nanoparticles - Novel Materials for Chemical and Physical Applications. *New Journal of Chemistry* **1998**, *22* (11), 1179–1201.

(21)   Kumar Teli, M.; Mutalik, S.; Rajanikant, G. K. Nanotechnology and Nanomedicine: Going Small Means Aiming Big. *Current Pharmaceutical Design* **2010**, *16* (16), 1882–1892.

(22)   Etheridge, M. L.; Campbell, S. A.; Erdman, A. G.; Haynes, C. L.; Wolf, S. M.; McCullough, J. The Big Picture on Nanomedicine: The State of Investigational and Approved Nanomedicine Products. *Nanomedicine: Nanotechnology, Biology, and Medicine* **2013**, *9* (1), 1–14.

(23)   Bamrungsap, S.; Zhao, Z.; Chen, T.; Wang, L.; Li, C.; Fu, T.; Tan, W. Nanotechnology in Therapeutics: A Focus on Nanoparticles as a Drug Delivery System. *Nanomedicine* **2012**, *7* (8), 1253–1271.

(24)   He, C.; Lu, J.; Lin, W. Hybrid Nanoparticles for Combination Therapy of Cancer. *Journal of Controlled Release* **2015**, *219*, 224–236.

(25)   Guha, A.; Shaharyar, M. A.; Ali, K. A.; Roy, S. K.; Kuotsu, K. Smart and Intelligent Stimuli Responsive Materials: An Innovative Step in Drug Delivery System. *Current Biochemical Engineering* **2019**, *6* (1), 41–52.

(26)   Gao, W.; Chan, J. M.; Farokhzad, O. C. PH-Responsive Nanoparticles for Drug Delivery. *Molecular Pharmaceutics* **2010**, *7* (6), 1913–1920.

(27)   Strong, L. E.; West, J. L. Thermally Responsive Polymer–Nanoparticle Composites for Biomedical Applications. *Wiley Interdisciplinary Reviews: Nanomedicine and Nanobiotechnology* **2011**, *3* (3), 307–317.

(28)   Ganta, S.; Devalapally, H.; Shahiwala, A.; Amiji, M. A Review of Stimuli-Responsive Nanocarriers for Drug and Gene Delivery. *Journal of Controlled Release* **2008**, *126* (3), 187–204.

(29)   Anderson, J. M.; Shive, M. S. Biodegradation and Biocompatibility of PLA and PLGA Microspheres. *Advanced Drug Delivery Reviews* **2012**, *64*, 72–82.

(30)   Allen, T. M.; Cullis, P. R. Drug Delivery Systems: Entering the Mainstream. *Science* **2004**, *303* (5665), 1818–1822.

(31)   des Rieux, A.; Fievez, V.; Garinot, M.; Schneider, Y. J.; Préat, V. Nanoparticles as Potential Oral Delivery Systems of Proteins and Vaccines: A Mechanistic Approach. *Journal of Controlled Release* **2006**, *116* (1), 1–27.

(32)   Kamaly, N.; Xiao, Z.; Valencia, P. M.; Radovic-Moreno, A. F.; Farokhzad, O. C. Targeted Polymeric Therapeutic Nanoparticles: Design, Development and Clinical Translation. *Chemical Society Reviews* **2012**, *41* (7), 2971–3010.

(33)   Janib, S. M.; Moses, A. S.; MacKay, J. A. Imaging and Drug Delivery Using Theranostic Nanoparticles. *Advanced Drug Delivery Reviews* **2010**, *62* (11), 1052–1063.

(34)   Liang, R.; Dong, L.; Deng, R.; Wang, J.; Wang, K.; Sullivan, M.; Liu, S.; Wang, J.; Zhu, J.; Tao, J. Surfactant-Free Biodegradable Polymeric Nanoparticles Generated from Self-Organized Precipitation Route: Cellular Uptake and Cytotoxicity. *European Polymer Journal* **2014**, *57*, 187–201.

(35)   Kang, J.; Schwendeman, S. P. Comparison of the Effects of Mg(OH)2 and Sucrose on the Stability of Bovine Serum Albumin Encapsulated in Injectable Poly(D,L-Lactide-Co-Glycolide) Implants. *Biomaterials* **2002**, *23* (1), 239–245.

(36)   Jiang, W.; Gupta, R. K.; Deshpande, M. C.; Schwendeman, S. P. Biodegradable Poly(Lactic-Co-Glycolic Acid) Microparticles for Injectable Delivery of Vaccine Antigens. *Advanced Drug Delivery Reviews* **2005**, *57* (3), 391–410.

(37)   Wang, J.; Wang, B. M.; Schwendeman, S. P. Mechanistic Evaluation of the Glucose-Induced Reduction in Initial Burst Release of Octreotide Acetate from Poly(D,L-Lactide-Co-Glycolide) Microspheres. *Biomaterials* **2004**, *25* (10), 1919–1927.

(38)   Schwendeman, S. P.; Langer, R.; Tracy, M. Recent Advances in the Stabilization of Proteins Encapsulated in Injectable PLGA Delivery Systems. *Critical Reviews^{TM} in Therapeutic Drug Carrier Systems* **2002**, *19* (1), 73–98.

(39)   Zhu, G.; Mallery, S. R.; Schwendeman, S. P. Stabilization of Proteins Encapsulated in Injectable Poly (Lactide-Co- Glycolide). *Nature Biotechnology* **2000**, *18* (1), 52–57.

(40)   Wischke, C.; Schwendeman, S. P. Principles of Encapsulating Hydrophobic Drugs in PLA/PLGA Microparticles. *International Journal of Pharmaceutics* **2008**, *364* (2), 298–327.

(41)   Freiberg, S.; Zhu, X. X. Polymer Microspheres for Controlled Drug Release. *International Journal of Pharmaceutics* **2004**, *282* (1–2), 1–18.

(42)   Zhang, Y.; Wischke, C.; Mittal, S.; Mitra, A.; Schwendeman, S. P. Design of Controlled Release PLGA Microspheres for Hydrophobic Fenretinide. *Molecular Pharmaceutics* **2016**, *13* (8), 2622–2630.

(43)   Bangham, A. D.; De Gier, J.; Greville, G. D. Osmotic Properties and Water Permeability of Phospholipid Liquid Crystals. *Chemistry and Physics of Lipids* **1967**, *1* (3), 225–246.

(44)   Dubois, M.; Zemb, T. Phase Behavior and Scattering of Double-Chain Surfactants in Diluted Aqueous Solutions. *Langmuir* **1991**, *7* (7), 1352–1360.

(45)   Caboi, F.; Monduzzi, M. Didodecyldimethylammonium Bromide Vesicles and Lamellar Liquid Crystals. A Multinuclear NMR and Optical Microscopy Study. *Langmuir* **1996**, *12* (15), 3548–3556.

(46)   Elizondo, E.; Veciana, J.; Ventosa, N. Nanostructuring Molecular Materials as Particles and

Vesicles for Drug Delivery, Using Compressed and Supercritical Fluids. *Nanomedicine* **2012**, *7* (9), 1391–1408.

(47)   Yoon, H. J., & Jang, W. D. Polymeric Supramolecular Systems for Drug Delivery. *Journal of Materials Chemistry* **2010**, *20* (2), 211–222.

(48)   Kubo, T.; Sugita, T.; Shimose, S.; Nitta, Y.; Ikuta, Y.; Murakami, T. Targeted Delivery of Anticancer Drugs with Intravenously Administered Magnetic Liposomes in Osteosarcoma-Bearing Hamsters. *International journal of oncology* **2000**, *17* (2), 309–315.

(49)   Sawant, R. R.; Torchilin, V. P. Challenges in Development of Targeted Liposomal Therapeutics. *AAPS Journal* **2012**, *14* (2), 303–315.

(50)   Torres, S.; Lorente, M.; Rodríguez-Fornés, F.; Hernández-Tiedra, S.; Salazar, M.; García-Taboada, E.; Barcia, J.; Guzmán, M.; Velasco, G. A Combined Preclinical Therapy of Cannabinoids and Temozolomide against Glioma. *Molecular Cancer Therapeutics* **2011**, *10* (1), 90–103.

(51)   Maggini, L.; Cabrera, I.; Ruiz-Carretero, A.; Prasetyanto, E. A.; Robinet, E.; De Cola, L. Breakable Mesoporous Silica Nanoparticles for Targeted Drug Delivery. *Nanoscale* **2016**, *8* (13), 7240–7247.

(52)   Minardi, S.; Fernandez-Moure, J. S.; Fan, D.; Murphy, M. B.; Yazdi, I. K.; Liu, X.; Weiner, B. K.; Tasciotti, E. Biocompatible PLGA-Mesoporous Silicon Microspheres for the Controlled Release of Bmp-2 for Bone Augmentation. *Pharmaceutics* **2020**, *12* (2), 118.

(53)   Minardi, S.; Pandolfi, L.; Taraballi, F.; Wang, X.; De Rosa, E.; Mills, Z. D.; Liu, X.; Ferrari, M.; Tasciotti, E. Enhancing Vascularization through the Controlled Release of Platelet-Derived Growth Factor-BB. *ACS Applied Materials and Interfaces* **2017**, *9* (17), 14566–14575.

(54)   Minardi, S.; Corradetti, B.; Taraballi, F.; Sandri, M.; Van Eps, J.; Cabrera, F. J.; Weiner, B. K.; Tampieri, A.; Tasciotti, E. Evaluation of the Osteoinductive Potential of a Bio-Inspired Scaffold Mimicking the Osteogenic Niche for Bone Augmentation. *Biomaterials* **2015**, *62*, 128–137.

(55)   Liang, R.; Dong, L.; Deng, R.; Wang, J.; Wang, K.; Sullivan, M.; Liu, S.; Wang, J.; Zhu, J.; Tao, J. Surfactant-Free Biodegradable Polymeric Nanoparticles Generated from Self-Organized Precipitation Route: Cellular Uptake and Cytotoxicity. *European Polymer Journal* **2014**, *57*, 187–201.

(56)   Liang, R.; Zhu, J. Monodisperse PLA/PLGA Nanoparticle Fabrication through a Surfactant-Free Route. *Journal of controlled release* **2011**, *152*, e129–e131.

(57)   Acharya, Ghanashyam, C. S. S.; McDermott, Matthew, Himanshu Mishra, Haesun Park, I. C. K.;
         Park, K. The Hydrogel Template Method for Fabrication of Homogeneous Nano/Microparticles.
         Journal of Controlled Release **2010**, *141* (3), 314–319.

(58)   Pertwee, R. G. The Pharmacology of Cannabinoid Receptors and Their Ligands: An Overview.
         International Journal of Obesity **2006**, *30* (1), S13–S18.

(59)   Elizondo, E.; Moreno, E.; Cabrera, I.; Córdoba, A.; Sala, S.; Veciana, J.; Ventosa, N. Liposomes and
         Other Vesicular Systems: Structural Characteristics, Methods of Preparation, and Use in
         Nanomedicine. *Progress in Molecular Biology and Translational Science* **2011**, *104*, 1–52.

(60)   De Petrocellis, L.; Melck, D.; Bisogno, T.; Di Marzo, V. Endocannabinoids and Fatty Acid Amides in
         Cancer, Inflammation and Related Disorders. *Chemistry and Physics of Lipids* **2000**, *108* (1–2),
         191–209.

(61)   Kumari, A.; Yadav, S. K.; Yadav, S. C. Biodegradable Polymeric Nanoparticles Based Drug Delivery
         Systems. *Colloids and Surfaces B: Biointerfaces* **2010**, *75* (1), 1–18.

(62)   Ferrer-Tasies, L.; Moreno-Calvo, E.; Cano-Sarabia, M.; Aguilella-Arzo, M.; Angelova, A.; Lesieur, S.;
         Ricart, S.; Faraudo, J.; Ventosa, N.; Veciana, J. Quatsomes: Vesicles Formed by Self-Assembly of
         Sterols and Quaternary Ammonium Surfactants. *Langmuir* **2013**, *29* (22), 6519–6528.

(63)   Elizondo, E.; Larsen, J.; Hatzakis, N. S.; Cabrera, I.; Bjørnholm, T.; Veciana, J.; Stamou, D.; Ventosa,
         N. Influence of the Preparation Route on the Supramolecular Organization of Lipids in a Vesicular
         System. *Journal of the American Chemical Society* **2012**, *134* (4), 1918–1921.

(64)   Lu, F.; Wu, S. H.; Hung, Y.; Mou, C. Y. Size Effect on Cell Uptake in Well-Suspended, Uniform
         Mesoporous Silica Nanoparticles. *Small* **2009**, *5* (12), 1408–1413.

(65)   Morla-Folch, J.; Vargas-Nadal, G.; Zhao, T.; Sissa, C.; Ardizzone, A.; Kurhuzenkau, S.; Köber, M.;
         Uddin, M.; Painelli, A.; Veciana, J.; Belfield, K. D.; Ventosa, N. Dye-Loaded Quatsomes Exhibiting
         FRET as Nanoprobes for Bioimaging. *ACS Applied Materials & Interfaces* **2020**, *12* (18), 20253–
         20262.

(66)   Ardizzone, A.; Kurhuzenkau, S.; Illa-Tuset, S.; Faraudo, J.; Bondar, M.; Hagan, D.; Van Stryland, E.
         W.; Painelli, A.; Sissa, C.; Feiner, N.; Albertazzi, L.; Veciana, J.; Ventosa, N. Nanostructuring
         Lipophilic Dyes in Water Using Stable Vesicles, Quatsomes, as Scaffolds and Their Use as Probes
         for Bioimaging. *Small* **2018**, *14* (16), 1703851.

(67)   Hamedinasab, H.; Rezayan, A. H.; Mellat, M.; Mashreghi, M.; Jaafari, M. R. Development of Chitosan-Coated Liposome for Pulmonary Delivery of N-Acetylcysteine. *International Journal of Biological Macromolecules* **2020**, *156*, 1455–1463.

(68)   Hu, K.; Cao, S.; Hu, F.; Feng, J. Enhanced Oral Bioavailability of Docetaxel by Lecithin Nanoparticles: Preparation, in Vitro, and in Vivo Evaluation. *International Journal of Nanomedicine* **2012**, *7*, 3537–3545.

(69)   Yoon, H. Y.; Kwak, S. S.; Jang, M. H.; Kang, M. H.; Sung, S. W.; Kim, C. H.; Kim, S. R.; Yeom, D. W.; Kang, M. J.; Choi, Y. W. Docetaxel-Loaded RIPL Peptide (IPLVVPLRRRRRRRRC)-Conjugated Liposomes: Drug Release, Cytotoxicity, and Antitumor Efficacy. *International Journal of Pharmaceutics* **2017**, *523* (1), 229–237.

(70)   Liu, X.; Ardizzone, A.; Sui, B.; Anzola, M.; Ventosa, N.; Liu, T.; Veciana, J.; Belfield, K. D. Fluorenyl-Loaded Quatsome Nanostructured Fluorescent Probes. *ACS Omega* **2017**, *2* (8), 4112–4122.

CHAPTER 1

General Introduction

ABSTRACT

This chapter provides a general background for the understanding of the work presented along this thesis. The first part gives a general definition of nanotechnology and a short description of the different nanoparticles used in the field of nanomedicine. Organic, Inorganic and hybrid materials are described in the second part. The third part presents information about silica nanoparticles, as an example of promising inorganic systems for nanomedicine applications. Their versatility in the synthesis makes possible the formation of silica-based mesoporous organic-inorganic hybrid materials which are also described here. In the fourth part, several examples of organic systems as lipid and non-lipid-base nanovesicles for nanomedicine are described.

1.1. Nanotechnology for nanomedicine for drug delivery

As a technology of the 21st century, nanotechnology, involves the manipulation of physical-chemical, biological and optical properties at the nanoscale, for the design of functional materials with dimensions that ranges from 1-100 nm.[1] The concept of employing nanotechnology in biomedical research and clinical practice is best known as nanomedicine. According to the European Science Foundation, "*Nanomedicine is the science and technology of diagnosing, treating and preventing disease and traumatic injury, of relieving pain, and of preserving and improving human health, using molecular tools and molecular knowledge of the human body*".[2] Its study involves the development of diverse kinds of materials for the specific delivery of therapeutic agents to treat different diseases. Systems as dendrimers,[3–6] liposomes,[7,8] quantum dots,[9] polymeric nanoparticles,[10,11] silica-based materials,[12–14] carbon nanotubes,[15,16] metallic nanoparticles,[17] etc. are revolutionizing the field of medicine for the early detection, diagnosis, and treatment of various diseases as cancer, human immunodeficiency viruses (HIV), Alzheimer, glaucoma, depression, to mention some.[18–21]

From all the different medical applications that these nanostructured materials can present, biomedical imaging, biosensing, diagnostics and therapy are included. Drug delivery and targeting are attractive approaches for the pharmaceutical industry to explore therapeutic agents capable of selective delivery to specific areas in the body, ensuring high efficiency of the drug, and reducing side effects. The intention is to create a "magic bullet" (a concept first introduced by Paul Ehrlich in 1891),[22] for delivering drugs to the right place, at the right concentration, for the right period of time, without chemical changes in the material before delivering, accomplishing the biodegradability and biocompatibility of the nanocarrier.[19,23,24] However, drug delivery systems (DDS) nowadays have many limitations as poor bioavailability, undesirable side effects, low-drug-loading capabilities, low therapeutic effectiveness, lack of the target delivery, among others. Therefore, a lot of effort has been made in this research investigation field for biomedical applications.[24]

1.2. Nanoparticles for biomedical applications

Drug-loaded nanoparticulate systems, also called nanomedicines or nanodrugs, are potential carriers of active drugs. These systems are based on nanoparticles (NPs), which are defined as

particulate dispersions of solid particles in the range of 10-100 nm that can load a drug, which can be dissolved, entrapped, encapsulated, or attached to the nanoparticle matrix.[24] NPs have been interesting platforms to improve some results in drug efficacy as they can optimize the drug concentration into the site of action, enhancing the pharmacokinetic and pharmacodynamic profiles and having minimal toxicity in healthy tissues.[25,26] Some of the advantages are due to the fact that carriers can increase the solubility and enhance the stability of hydrophobic materials and drugs during their transportation until they reach the point of interest. Additionally, NPs could be taken by the mononuclear phagocyte system, thereof their circulation in the system is prolonged, enhancing then a successful targeting.[24]

The NPs fate and therapeutic outcome is strongly affected by their particular chemical composition and other specific structural features, including surface properties (e.g., charge and hydrophilic to hydrophobic ratio), general physical characteristics (e.g., size, shape, and stiffness) and functionalization (**Figure 1.1**).[27] There are NPs based on inorganic materials,[23,28] organic matrices,[29] or hybrid (inorganic/organic core/shell) structures.[19,30] Through the specific design of the synthetic methodology, the shape, size and surface characteristics can be controlled.[31–33]
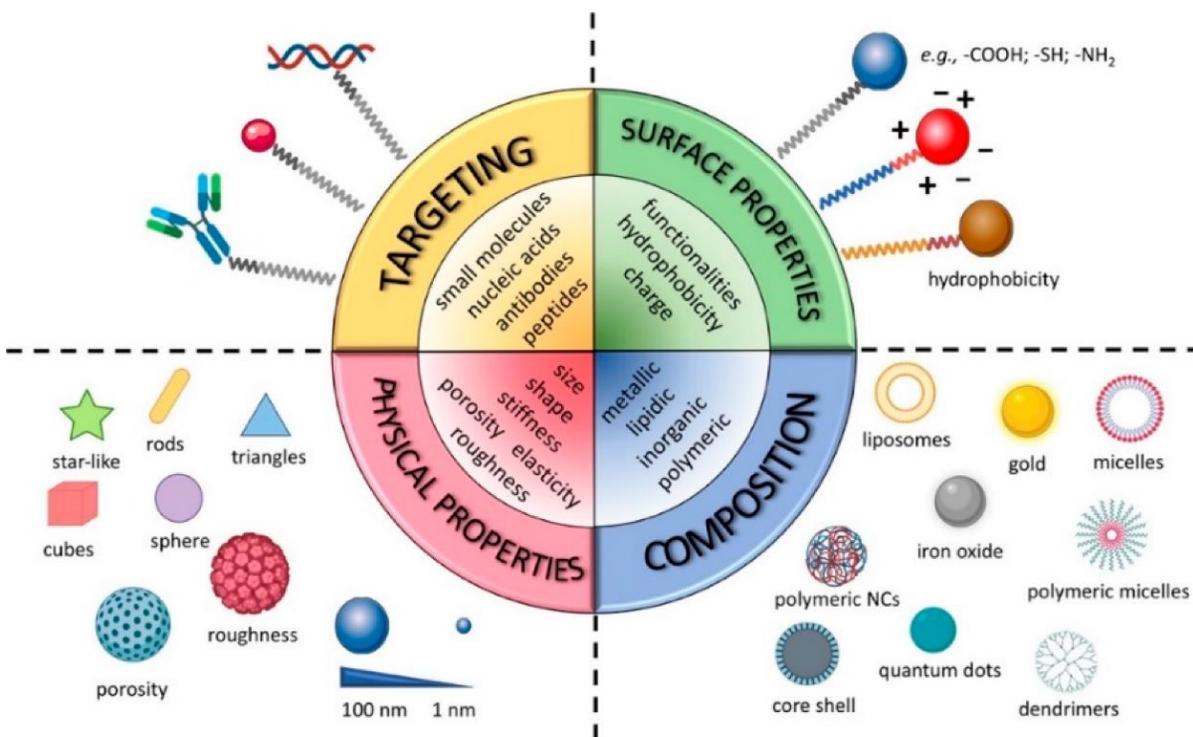

Figure 1.1. Tunable physical and chemical properties of nanocarriers (NCs). Reprinted with permission from ref 27. (Copyright 2019, MDPI).

As a resume, the advantages of using NPs as drug delivery systems include that: **1)** there is a huge versatility in its composition. **2)** The particle size and surface properties can be easily manipulated to achieve passive and active drug targeting. The site-specific targeting can be achieved by attaching targeting ligands to their surface. **3)** Carriers can protect drugs from being dissolved in the bloodstream, making then a sustain of the drug during transportation until their delivery to the specific target tissue-cell. **4)** The controllable drug release at the target organ increases the drug therapeutic efficacy, reducing the side effects of drugs, as their accumulation in kidneys liver, spleen, and other non-targeted organs. **5)** Control in the particle biocompatibility and degradability by modulating the matrix of the NPs. **6)** Multi-deliver of drugs; delivering a combination of imaging and therapeutic agents for real-time monitoring of therapeutic efficacy. **7)** The versatility in the route of administration in the system e.g. oral, nasal, parenteral, intra-ocular etc.[34–37]

1.3. Organic, inorganic and composite nanoparticles (Hybrid nanoparticles)

Different examples of drug delivery nanoplatforms exist nowadays (**Figure 1.2**). They can be divided into three main groups: organic matrices, inorganic materials and composite nanoparticles.[38]

From the organic platform, lipid-based NPs involve micelles,[39] dendrimers,[5] liposomes,[7] niosomes[40] and solid lipids.[41] Among the vast variety of polymer-based NPs, nonbiodegradable polymers, as polystyrene or poly(methyl methacrylate) (PMMA), have shown to cause inflammatory reactions and to have a high toxicity.[42] Therefore, new more compatible and biodegradable polymers have been used, as those based on poly(lactic acid) (PLA), poly(D-lactic-co-glycolic acid) (PLGA), and polysaccharides like chitosan or dextran.[10,19,38,43]

To promote specific interaction with cells, organic NPs are often functionalized with biomolecules. Alternatively, self-assembly of natural biomolecular building blocks has been used for the formation of organic NPs that are made up of proteins, oligonucleotides, and peptides.[44] In general, these organic particles could be employed for drug delivery applications.[45]

Compared to their organic counterparts, inorganic-based NPs offer high mechanical strength and chemical stability, resistance to enzymatic degradation and disintegration through biological fluids. Some examples are the carbon nanotubes,[15,16] quantum dots,[46] metallic- or bimetallic-

based NPs[17] and mesoporous silica NPs.[47] Their easy modulation in size, morphology and composition makes them optimal for sensitive nanoplatforms with desired electrical, optical, and magnetic properties for biomedical applications.[38,48]

Mostly, organic and inorganic materials have been synthesized not only for the early detection of dysfunctional cellular pathways but also for therapeutic purposes. For detection, as contrast agents for near-infrared tomography, photoacoustic tomography and fluorescence imaging.[19] For therapeutics, the controlled killing of diseased cells is commonly performed through the application of heat (photothermal therapy, hyperthermia), ultrasound, radiation, activation of reactive oxygen species (photodynamic therapy), gene and immune-modulation, the delivery of high payloads of molecular drugs or combinations thereof.[49]

On the other hand, composite nanoparticles as hybrids particles, comprising the inorganic/organic (core/shell) nanoparticles and the 2D hybrids, combine different materials in one multi-component particle. These systems aim to overcome the limitations of the single-component structures. Hybrid particles can offer superior solubility and biocompatibility compared to individual materials; shells can prevent the contact of toxic core materials, providing a proper functionalized surface with biomolecules or biocompatible polymers. [50] For example, the combination of silicon nanostructures modified with metal or metal oxide NPs has interesting applications in biosensing.[51] Moreover, inorganic-organic composites, as the combination of polymers encapsulating magnetic particles, or metallic NPs with biodegradable polysugar-shells, have antimicrobial activity properties.[52] Besides, organic-organic composites, as lipids chromophores and polymers conjugated to DNA, have been used to enhance the reactivity of a range of hydrophobic molecules and polymers with DNA.[39] 2D hybrid materials, as graphene oxide in combination with inorganic and organic NPs are interesting platforms for theragnostic applications.[38,53]
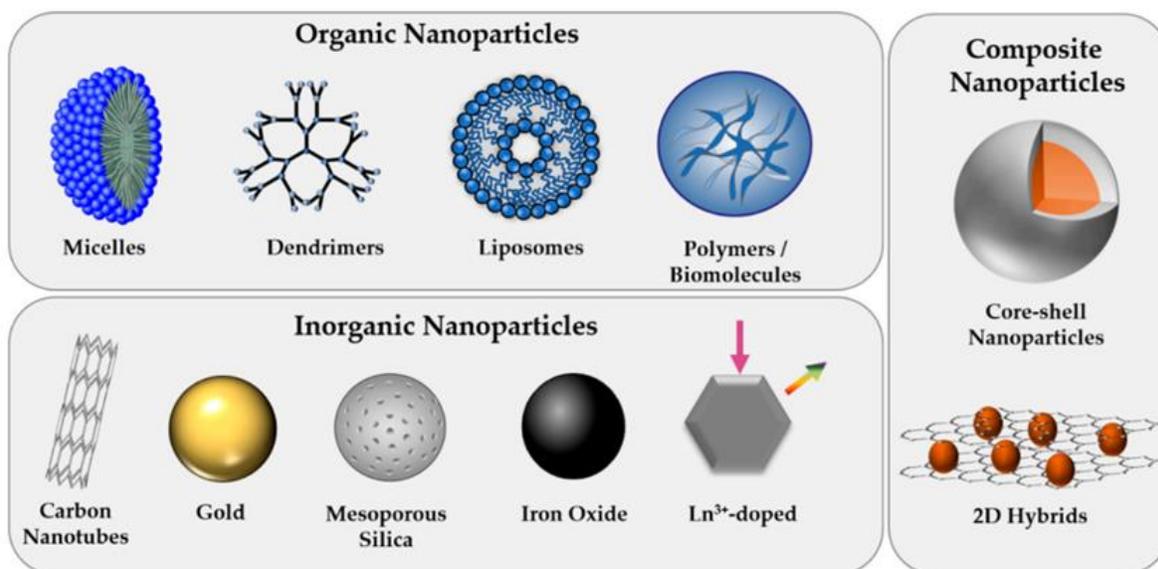
Figure 1.2. Representative organic, inorganic, and composite nanocarriers for drug delivery applications. Reprinted with permission from ref 38. (Copyright 2020, MDPI)

Using all these nanoplatforms, the advance of nanomedicine has been increased exponentially, with a high number of preclinical and clinical investigations.[39] In the last 50 years, many nanodrugs have been developed and approved for human administration. Several liposome-based formulations examples in the market are: Doxil®, a formulation of doxorubicin, approved in 1995 by the US Food and Drug Administration (FDA) for treating AIDS-related Kaposi sarcoma.[54] Myocet®, a formulation of Doxorubicin, approved by the FDA to be used in a combination therapy for metastatic breast cancerger.[55] Lipoplatin®, liposomal cisplatin, in Phase III for the treatment of pancreatic, head and neck, breast, gastric, and non- squamous non-small cell lung cancers, mesothelioma.[56] DaunoXome®, liposomal encapsulation of Daunorubicin, approved by the FDA for Kaposi sarcoma.[57] Depocyte®, liposomal cytarabine formulation, for use against lymphomatous meningitis.[58] For drug-loaded polymer formulations: Abraxane®, an albumin-based nanoparticle, protein-bound paclitaxel, approved by the FDA for clinical use for the treatment of breast cancer, non-small cell lung cancer, and pancreatic cancer.[59] Regarding polymeric nanoparticles, Genexol-PM® is a mPEG-PLA platform encapsulating Paclitaxel ® for breast cancer applications.[60]

Besides all the kind of nanoplatforms under investigation, there remains a gap between technological advances and clinical applications. NPs have limitations associated basically to their

engineering; their small size and large surface area can lead to particle aggregation, making the *in vivo* activity of this nanoplatforms limited to be introduced as nanodrugs into the clinic.[37]

Hybrid nanoparticles composed of inorganic and organic components can be prepared using many strategies; their production is based on the optimization of their synergistic therapeutic effects. Then, the combination of drug carriers needs to be rationally designed to accommodate multiple therapeutic drugs or modalities with temporally controlled release of individual cargos.[61] This thesis entitled "Design and synthesis of hybrid particles for drug delivery" is based on the combination of several delivery systems to form new hybrid materials for biomedical applications. Hybrid systems mainly formed by silica NPs combined with PLGA, or with non-lipidic vesicles called Quatsomes (QS) are presented in this thesis.

1.4. Silica NPs for drug delivery

Given their tunable size, morphology and porosity, silica NPs have become predominant among all inorganic carrier materials for drug delivery applications. The efficient entrapment of high payloads of cargo molecules within their porous structure, followed by the controlled and sustained release of loaded molecules upon endogenous or exogenous stimuli, such as light,[62,63] temperature,[64,65] ultrasound,[66,67] or pH,[68,69] has made mesoporous silica nanostructures highly promising delivery vehicles.[70–72] Moreover, silica NPs have been considered a potential carrier for several biomedical applications due to their biocompatibility, low toxicity, and scalable synthetic availability.[47,73] Their multiple and diverse surface modifications allow then precise control of the surface chemistry to modulate drug or chemical loading, nanoparticle dispersion, blood circulation, and site-specific targeting.[74] The ability to combine these properties produces multimodal nanoparticles for theragnostic applications, such as biomedical imaging, assaying, therapeutic delivery, monitoring, etc.[74]

Several synthetic techniques have been developed to produce silica particles with a narrow range of sizes and nearly uniform composition. The Stöber method, developed in 1968, continues to be a widely employed method for synthesizing silica nanoparticles. It involves sol-gel processing,[75] in which tetraethyl orthosilicate (TEOS) or other organosilanes precursors are mixed with water and alcohol in a base-catalyzed reaction.[76] The size of the obtained particles depends on the solvent and the starting silicate derivatives concentration. Additionally, the Stöber method can

be employed without templates to form solid particles. This reaction involves hydrolysis and condensation reactions of the inorganic alkoxide monomers in order to develop colloidal particles (sol) and consequently convert them into a network (gel) (**Figure 1.3**). The hydrolysis step takes place by the addition of water to the TEOS solution under neutral, acidic, or basic conditions, and it leads the formation of silanol groups (Si-OH). The mechanism of hydrolysis is catalyst-dependent, and its reaction rate depends on the pH and the water or ethanol content. The latter is the most common organic co-solvent, it dissolves the alkoxysilanes, which are not water-soluble, facilitating the hydrolysis step by mixing the alkoxysilane with the water in the reaction.[77]

In the second step, the silanol group condensates with another silanol group (by water condensation reaction) or with an alkoxysilane (by alcohol condensation) to build a strong siloxane linkage (Si-O-Si) with a loss of water or alcohol. While the number of Si-O-Si bridges increases, the siloxane matrix can aggregate into a sol, which disperses in the solution into small silicate clusters. Condensation of the latter silicate clusters leads to the formation of a network (a gel), trapping the water and the alcohol.[78]
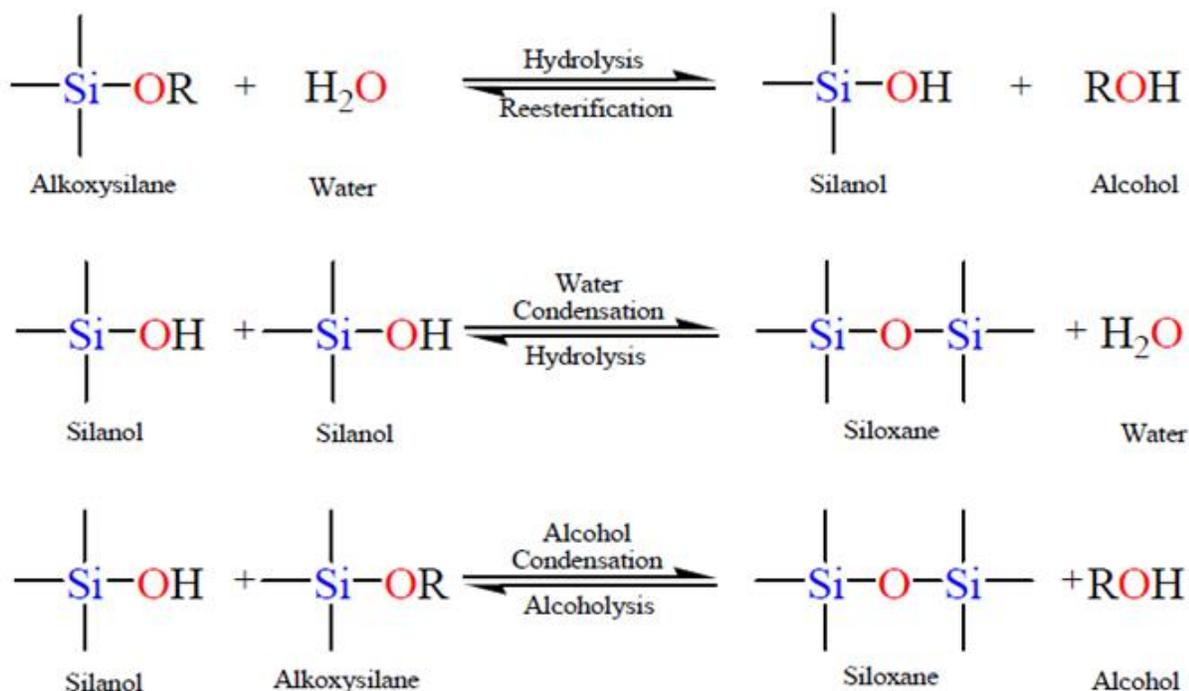

Figure 1.3. Sol-gel general reaction scheme, involving the hydrolysis and two kind of condensation processes: water condensations or alcohol condensation. Reprinted with permission from ref 78. (Copyright 2012, MDPI)

As explained previously, the rates and mechanisms of hydrolysis and condensation reactions are strongly affected by the 1) types of precursors, 2) kind of catalyst (acid or base), 3) alkoxy- group to water ratio (Rw) for alkoxide precursors, 4) solvent, 5) temperature, 6) presence of electrolytes and 7) concentration of the components in the precursors mixtures etc.

For the precursors, Si-OR groups of silicon alkoxides must first be hydrolyzed before condensation reactions can take place. The hydrolysis rates of alkoxysilanes are influenced by steric factors: the more steric the R group, the lower the rates of hydrolysis; this means that the reactions rates follow the order $Si(OMe)_4 > Si(OEt)_4 > Si(OnPr)_4 > Si(OiPr)_4$.[79]

Additionally, the rates and mechanisms of hydrolysis and condensation reactions are strongly affected by the identity of the catalyst. From a mechanistic point of view, reactions under acidic or basic conditions must be considered separately. Under acidic conditions (see **Figure 1.4**), the deprotonated silanol ($\equiv$Si-O$^-$), the silanol ($\equiv$Si-OH), or the alkoxysilane ($\equiv$Si-OR) groups are electrophilically attacked by a proton in a rapid first step. Then, a good leaving group is originated, alcohol or water, in the hydrolysis and condensation part. With the protonation, the electron density is withdrawn from the central silicon atom (giving a positive charge molecule), rendering the species more electrophilic and thus, more susceptible to be attacked by water (in hydrolysis reactions) or silanol/alkoxysilane groups (in condensation reactions).[78,79]

Under basic conditions (see **Figure 1.4**), the reaction proceeds by a nucleophilic attack of either an OH$^-$ (in hydrolysis reactions) or a $\equiv$Si-O$^-$ ion (in condensation reactions) to the silicon atom with an SN_2 type mechanism. The OH$^-$ or $\equiv$Si-O$^-$ groups are formed by the deprotonation of water or silanol ($\equiv$Si-OH) groups.[78,79]

It should be mentioned that under strong alkaline conditions, the Si-O-Si bonds can be cleaved again by the OH$^-$. The inductive effects of the substituents attached in the silicon atom can stabilize or not the transitions states of the intermediates during the hydrolysis and condensation processes. Moreover, it should be taken into account that the electron density at the silicon atom decreases as $\equiv$Si-R´ > $\equiv$Si-OR > $\equiv$Si-OH > $\equiv$Si-O-Si, and the reaction rates for hydrolysis and condensation under acidic conditions increase in the same order as the electron density. For base catalysis, a negatively charged intermediate must be stabilized. Therefore, the reaction rates for hydrolysis and condensation increase in the reverse order of the electron density, what explains the pH dependence of the hydrolysis and condensation of silicon alkoxides. In this case, the

minimal reaction rate for hydrolysis is at pH 7, and for condensation around pH acid. At pH values lower than 3, hydrolysis is favored, and then, condensation is the rate-determining step. In contrast, at higher pH values, the condensation rate is faster, being the hydrolysis the rate-determining step (meaning that the hydrolyzed species are immediately consumed by the condensation) (**Figure 1.5**). Catalysis by fluoride ions is similar to that of hydroxide ions (basic conditions).[78,79]
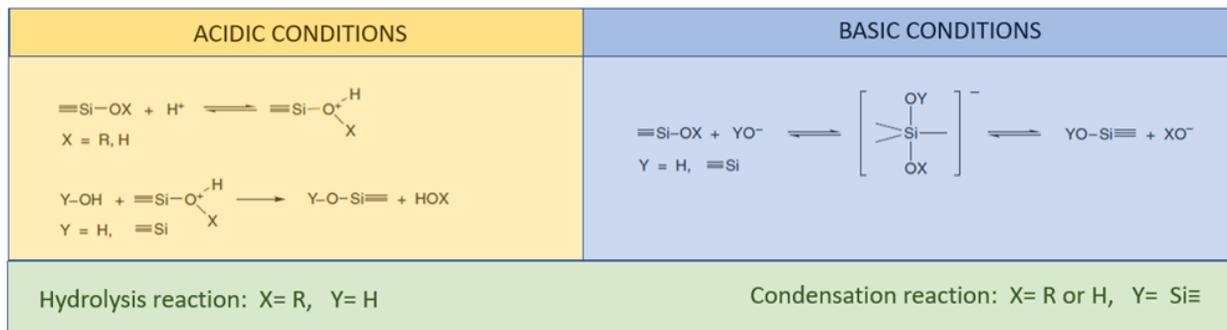

Figure 1.4. Schematic representation of the different mechanism given by acidic and basic conditions in the hydrolysis and condensation of silica. Reprinted with permission from ref 12. (Copyright 2006, American Chemistry Society)
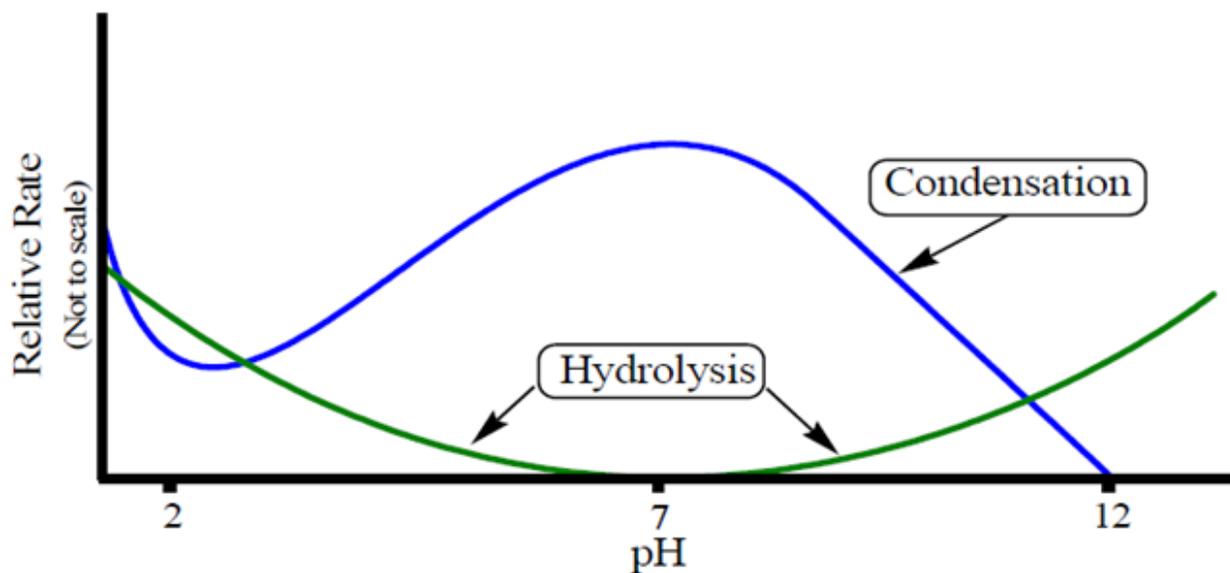

Figure 1.5. pH dependence for the hydrolysis and condensation rates of the silica polymerization. Reprinted with permission from ref 11. (Copyright 2010, Taylor & Francis Group)

1.4.1. Silica-Based Mesoporous Organic-Inorganic hybrid materials

Mesoporous silica NPs (MSNPs) are hybrid materials of organic-inorganic systems. There are characterized for having large surface areas and a pore size between 2 and 15 nm. The organic phase is composited from supramolecular aggregates of ionic surfactants (most common: long-chain alkyl-trimethylammonium halides) that work as a template of an ordered mesostructured composite in which the silica precursors condensate under basic conditions. To obtain the mesoporous material, the removal of the surfactant by extraction or calcination must be done (**Figure 1.6**).
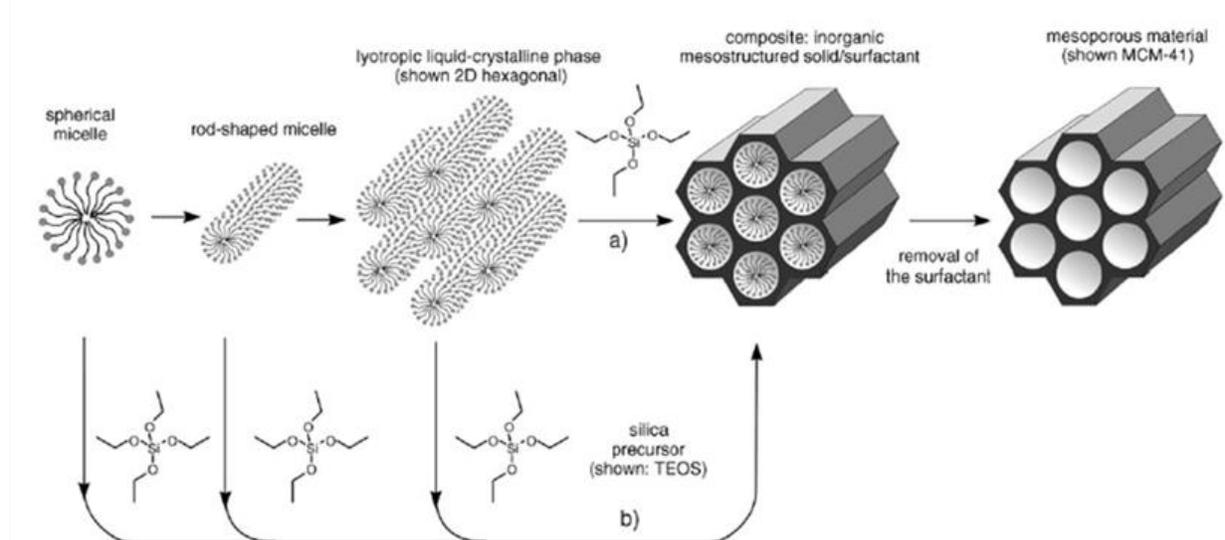

Figure 1.6. Representation of the templated synthesis of MSNPs (Stöber process), following a) true liquid crystal template and b) cooperative liquid-crystal template mechanism. Reprinted with permission from ref 80. (Copyright 1992, Macmillan Publishers Limited)

To produce these hybrid organic-inorganic materials, an attractive interaction between the template and the silica precursor is needed to ensure the inclusion of the template without phase separation taking place. The different interactions are shown in **Figure 1.7**:[13,81] 1) in basic conditions: where the silica species are anions and quaternary ammonium surfactants (S^+I^-, S: surfactant; I: inorganic species). 2) In acidic conditions (below the isoelectric point of the Si-OH; pH~2), the silica species are positively charged, to produce an interaction with the cationic surfactant, it is necessary to add a mediator X^- (usually a halide) ($S^+X^-I^+$). 3) With negatively charged surfactants as long-chain alkyl phosphates, the reaction with the silica species can be done in basic media with a mediator ion M^+ ($S^-M^+I^-$). 4) The interaction between a negatively

charged surfactant and the silica species in acidic media (S⁻I⁺). 5) Interaction through hydrogen bonds happens when a nonionic surfactant is used S^0, as long-chained amine or polyethylene oxide with uncharged silica species (S^0I^0). 6) Or hydrogen bonds interactions through ion pairs pathway ($S^0(XI)^0$).[13]
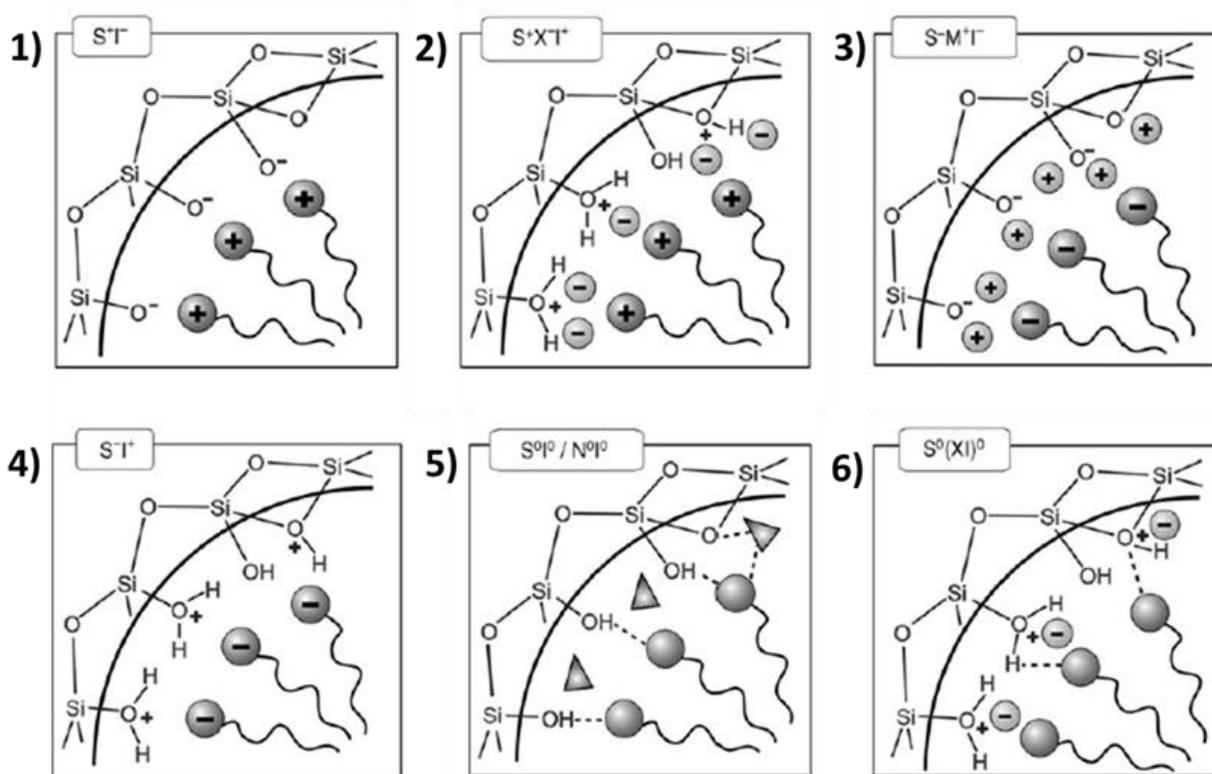

Figure 1.7. Interactions between the inorganic species and the head group of the surfactant with consideration of the possible synthetic pathway in acidic, basic, or neutral media. Electrostatic: **1)** S^+I^-, **2)** $S^+X^-I^+$, **3)** $S^-M^+I^-$, **4)** S^-I^+ and through hydrogen bonds: 5) S^0I^0, and 6) $S^0(XI)^0$. Where S=surfactant, M= mediator and I= inorganic species. Reprinted with permission from ref 13. (Copyright 2006, Wiley-VCH Verlag GmbH & Co. KGaA, Weinheim)

The incorporation of functionalities can be achieved by A) *Grafting:* a subsequent attachment of organic components in a pure silica matrix; the process is carried by the reaction of organosilanes type (R'O)₃SiR and ClSiR₃, or silazanes HN(SiR₃)₃ with silanol groups of the surface of the pores. Depending on the size of the organic residue, the pore size can be diminished or completely blocked if it is a bulky specie (**Figure 1.8A**).[82,83] B) *Co-condensation one-pot synthesis:* a simultaneous reaction of condensable inorganic silica species and silylated organic compounds. TEOS or TEMOS are used in a combination with terminal trialkoxyorganosilanes of the type

(R'O)$_3$SiR in the presence of structural-directing agents (surfactants) leading the materials with organic residues attached covalently (**Figure 1.8B**).[84,85] C) *Periodic Mesoporous Organosilicas*: The use of bisilylated organic precursors of the type (R'O)$_3$Si-R-Si(OR')$_3$ leads to periodic mesoporous organosilica. In this case, the organic units are incorporated in the 3-D network structure through two covalent bonds, which are distributed homogeneously in the silica matrix. [86,87] These materials have potential applications in catalysis, adsorption, chromatography, nanoelectronics, or as active compounds for release (**Figure 1.8C**).[13]
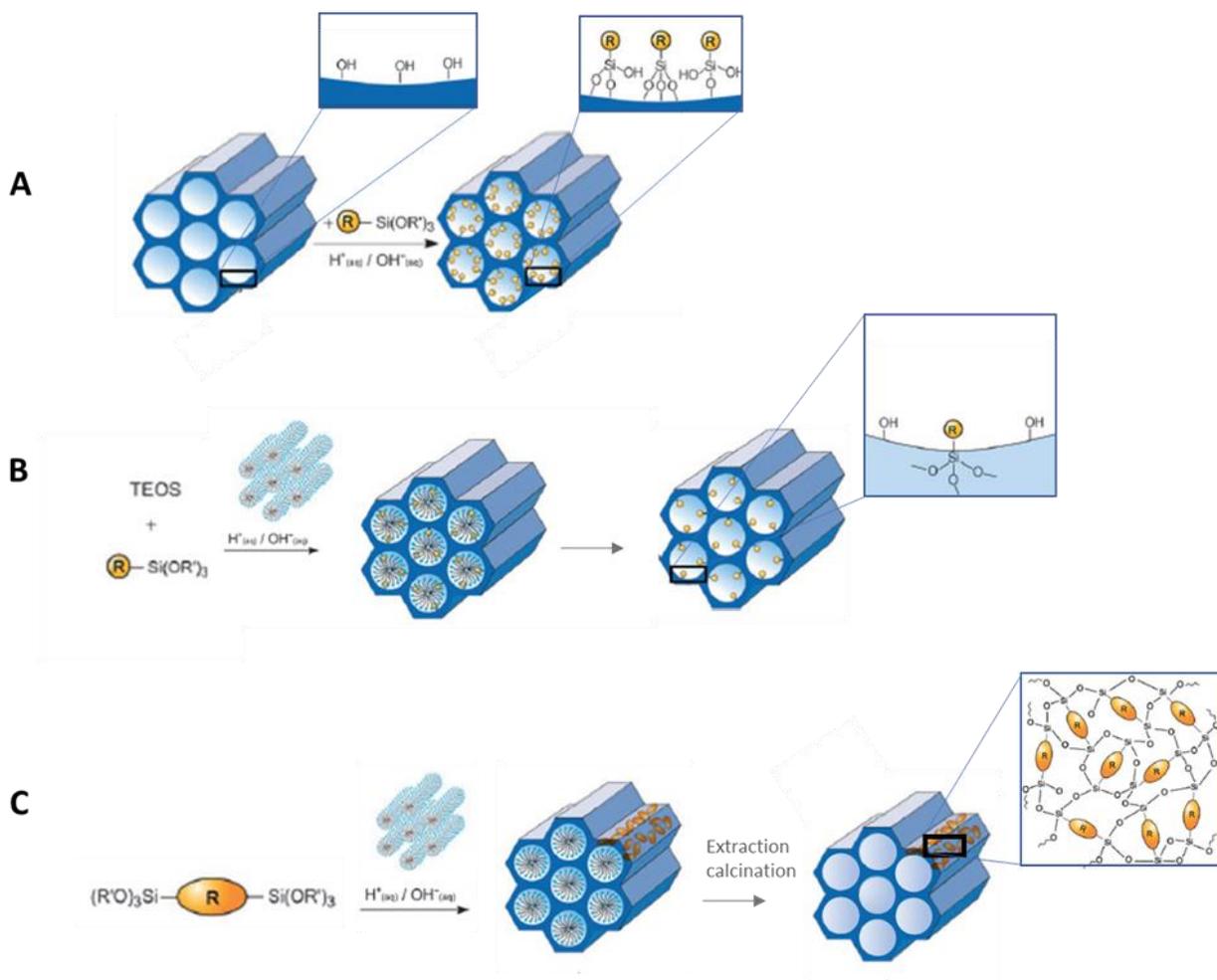

Figure 1.8. Representation of the three different ways of the incorporation of functional moieties by **A)** Grafting, **B)** Co-condensation one-pot synthesis and **C)** by the production of Periodic Mesoporous Organosilicas. Adapted with permission from ref 13. (Copyright 2006, Wiley-VCH Verlag GmbH & Co. KGaA, Weinheim)

1.4.2. Mesoporous Silica Nanoparticles (MSNPs) as stimuli-responsive systems for drug delivery

MSNPs have been interesting for diagnostic and therapeutic applications [14,88,89] including cancer treatment,[90] infectious diseases treatment,[91] and different bone illnesses.[92] In general, any drug delivery system goal is to load the maximum amount of cargo molecules, releasing the cargo on a specific targeting point avoiding premature and unspecific release; in the case of cancer treatment, deep penetration in the tumor zone is required.[93] Then, MSNPs can be worthy platforms to achieve these requirements.

To load drugs in this type of system, there exist two different ways: 1) *in situ*, during the synthetic path or 2) *post-sorption*, by physisorption or chemosorption.[94] These approaches involve physical adsorption from solution into the pores, physical adsorption from solution onto the outer surface and covalent grafting. Then, the high surface of MSNPs ensures higher drug loadings that other type of NPs.[95]

Furthermore, the functionalization of mesoporous silica nanoparticles with stimuli-responsive moieties as gatekeepers can prevent early leakage of the payload and consequently, offer better control of the delivery.[96] Exogenous and endogenous stimuli-responsive silica nanocarriers have been already developed, which present interesting release properties. Here, we describe some different stimulus which could be used to release a drug:

- The use of alternated magnetic fields taking advantage of the magnetocaloric effect. The release of the cargo can be induced by the rise of temperature of the magnetic NPs that contained the drug.[97]

- By using light drug delivery systems responsive to a specific wavelength irradiation is also possible.[98,99] For this, photo-responsive molecules can offer a spatiotemporal control on the drug release providing a deep and precise tissue penetration and minimal harm to tissues.[100] One interesting example is the release of paclitaxel by light radiation of the MSNPs linked with o-nitrobenzyl and capped with gold nanoparticles.[101]

- pH-sensitive systems (e.g. supramolecular interaction between aromatic amines and β-cyclodextrin were used as nanovalves able to respond to acidic pH to clog MCM-41 pores for specific cellular compartment delivery.[102]

Moreover, along the redox stimuli-response systems those based on disulfide bonds, there exist some examples of successful drug delivery in the intracellular environment once the target is reached, for example in response to the presence of glutathione (GSH).[103–106] GSH is a redox agent present in the cellular environment inside (2-10 mM) and outside (2-10 µM) the cells.[107–110] Then, this molecule can play an important role in breaking these responsive materials. Taking this into account, in our group it has been reported a redox responsive mesoporous-silica nanoparticle containing disulfide bridges (ss-NPS) (30% of the organic group). This system degrades inside glioma C6 cancer cells as a response to the reducing stimuli. Additionally, these particles were also externally functionalized (arginylglycylaspartic acid), which increased the uptake of the particles, without affecting the redox-triggered structural breakdown and consequently, they could act as drug delivery carriers (**Figure 1.9**).[111]
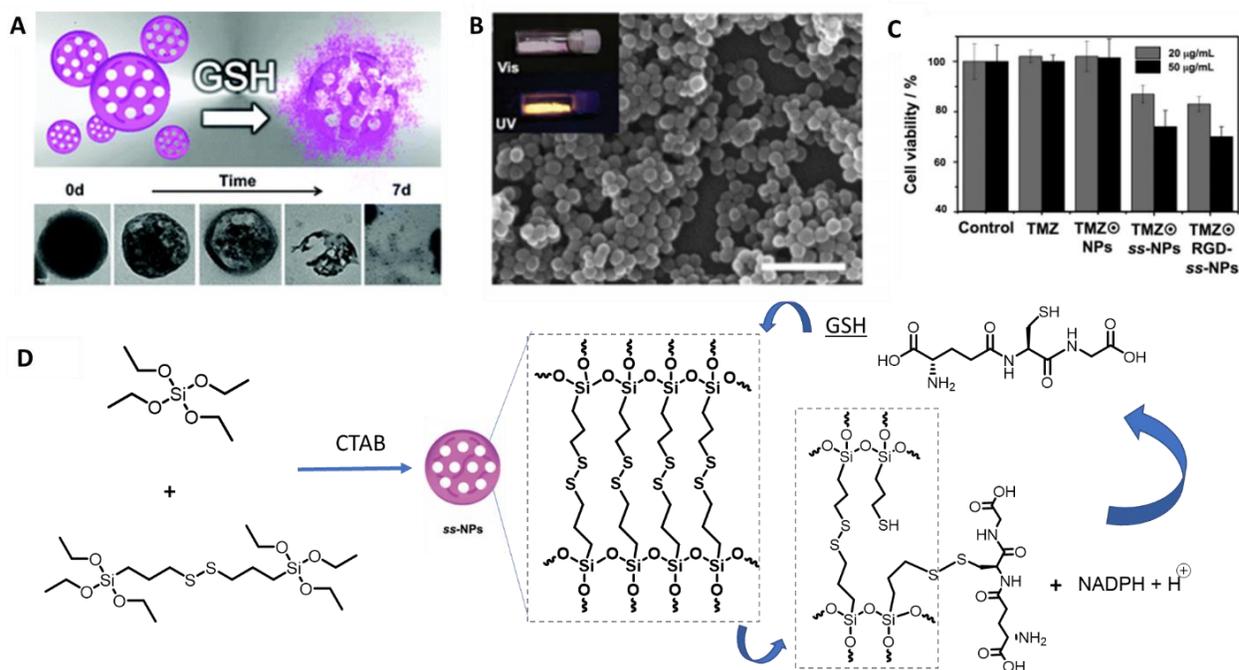

Figure 1.9. **A)** Schematic representation of the redox-stimulus-responsive nanoparticle and their breakability test followed by TEM analysis of a suspension of ss-NPs undergoing GSH reduction (0–7 d). **B)** SEM image of ss-NPs. Scale bar = 500 nm. Inset: image of the ss-NPs under Vis and UV illumination. **C)** Cell viability of glioma C6 cells measured after incubation for 3 h the NPs loaded with temozolomide (TMZ). **D)** Representation of the fabrication of *ss*-NPs and its breakability under Glutathione (GSH). Adapted with permission from ref 111. (Copyright 2016, Royal Society of Chemistry)

1.4.3. Biocompatibility of MSNPs

Even if MSNPs have been intensively investigated for different biological or medical applications, they have not been approved by the FDA for their use yet, since several conditions must be accomplished.[112–114] Among these conditions, it is determinant to know its biodistribution, the clearance routes and the final fate in the body; the uptake, biodistribution, and elimination pathways.[115] On the other hand, the administration of NPs to the body can be done through not only intravenous but also through subcutaneous or intratumoral injections. It should be mentioned that pre-clinical studies have shown that MSNPs are, in general, nontoxic in many biological systems if they are prepared with certain optimized structural features and applied at the right dosages.[116–119] However, the huge variability of the MSNPs properties in terms of particle size, shape, pore structure, composition, or type of synthetic method, makes complex to give a universal description of the biocompatibility of this kind of material. Nowadays, there is some interest in studying the impact of size, shape, among other parameters in the metabolism of the materials, such as their endocytosis through cell membranes, interferences within cellular signaling and the interaction with cellular organelles.[120]

The effect of the particle size is one of the most important factors affecting biocompatibility. The size influences on how the nanomaterial interacts with cells or some cellular processes. The effect of the MSNPs size and cellular uptake and function was first studied by Vallhov *et al*.[121] and it was concluded that the dosage of the nanoparticles was an additional important parameter to consider for biocompatibility studies. Moreover, Mau and co-workers studied the internalization of MSNPs of different sizes in the range of 30 to 280 nm (most of them with hexagonal structure) in HeLa cells.[122] The cell proliferation and viability were found to be unaffected at a dosage of 100 µg/mL for all the different MSNPs sizes. Their cellular uptake varied in the order 50>30>110>170 nm, indicating that endocytosis is a complicated process dependent on many factors (**Figure 1.10**).[122] On the other hand, the effect of the size of MSNPs has been also investigated in mouse models by Shi et al. After injecting MSNPs of 80, 120, 200 and 360 nm intravenously, NPs showed non-toxic and non-inflammatory effects in all the tissues. Additionally, they also described different NPs accumulation in the organs following the order:

liver > spleen > lung > kidney/heart. Furthermore, the accumulation of MSNPs in each organ continuously increased but significantly decreased after 1 month.[123]
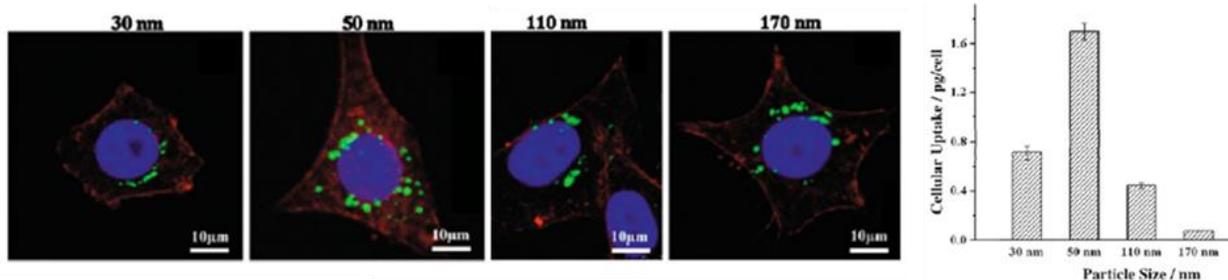

Figure 1.10. *In vitro* studies. Cellular uptake of differently sized MSNPS (containing fluorescent tags-green) in HeLa cells with treated of 100 µg/mL of 30, 50, 110, or 170 nm in size diameter. NPs, Cell skeleton and nucleus are in green, red and blue, respectively. The amount of silicon per cell was calculated and plotted as a function of size of MSNs. Reprinted with permission from ref 62. (Copyright 2019, American Chemistry Society). Reprinted with permission from ref 122. (Copyright 2009, Wiley-VCH Verlag GmbH & Co. KGaA, Weinheim)

1.5. Lipid-based nanovesicles for nanomedicine

Lipid-based nanovesicles (L-NVs) are small sphere-shaped bilayer vesicles formed by lipids. Briefly, vesicles are nano/microparticulate colloidal carriers, of usually 0.05– 5.00 µm in diameter, which are formed spontaneously when certain lipids are suspended in aqueous media. They consist of a small enclosed liquid compartments separated from its surroundings by one or more lipidic bilayers.[124] To form these bilayers, supramolecular entities are formed by self-assembly (**Figure 1.11**).[125]
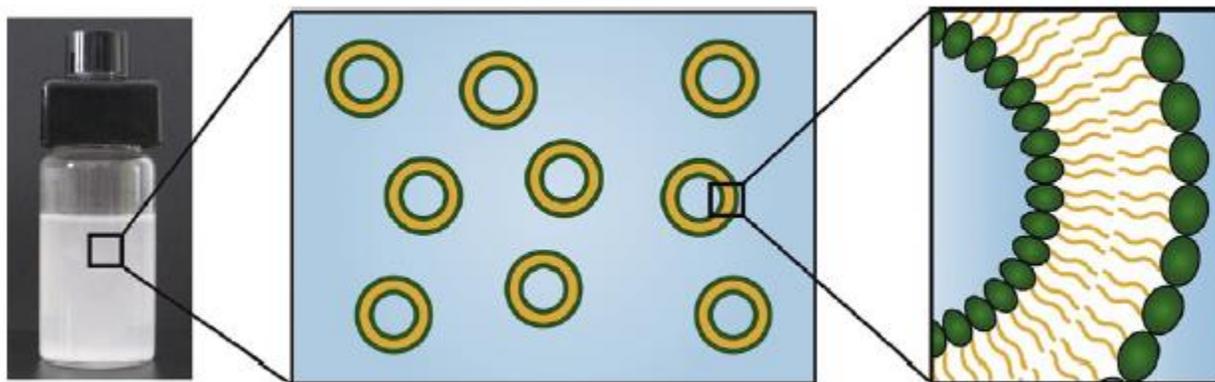

Figure 1.11. Representation of a vesicle structure and the lipidic bilayer formed. Reprinted with permission from ref 126. (Copyright 2011, Elsevier)

This molecular-self-assembly can be defined as spontaneous and reversible association and their success in molecular systems is determined by some characteristics of the system, such as, the components, interactions, adjustability, environment, mass transport and agitation.[125,127] Most of the self-assembling molecules possess an amphiphilic character, which means they contain hydrophilic and hydrophobic domains in their structure. This hydrophobic–hydrophilic character promotes their association through weak, noncovalent interactions to form ordered assemblies with different morphologies as spherical or rod-like micelles and amphiphilic bilayers (vesicles).[128–130] The thermodynamic driving force of this molecular self-assembly is provided by the desolvation, collapse, and intermolecular association of the hydrophobic part of the monomers. The tendency of the hydrophobic tails to minimize the contact with water is called hydrophobic effect. The geometry of the final assembly is determined by its packing parameter (p), defined as the ratio of the hydrophobic volume (v) to the product of the head group area (a) and the chain length (l). The structures formed according to the p value are: p<0.33, spherical micelles; 0.33<p<0.50 cylindrical micelles; 0.5<p<1 vesicles; p=1 planar bilayers; p>1 reverse micelles (**Figure 1.12**).[131]
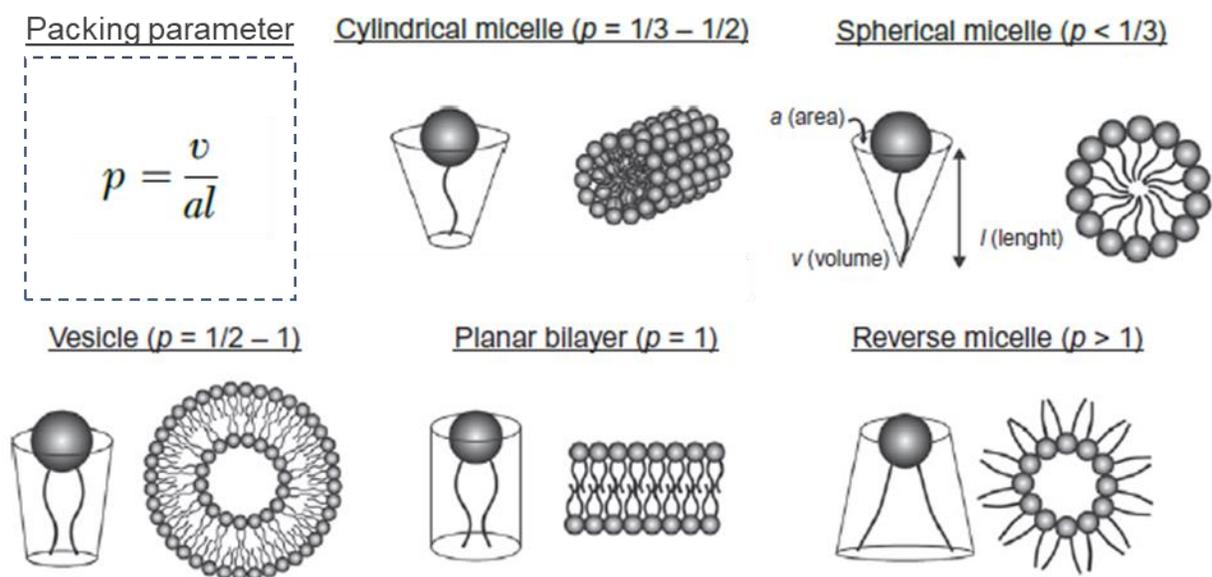

Figure 1.12. The packing parameter (p) and the relationship with the aggregates self-assembly morphologies of amphiphilic molecules under aqueous conditions. Adapted with permission from ref 131. (Copyright 1976, Royal Society of Chemistry)

L-NVs can be classified in 1) *Small unilamellar vesicles (SUVs)* also called nanovesicles, with sizes <200 nm and a single bilayer, 2) *Large unilamellar vesicles*, sizing from 200-1000 nm, 3) *Giant unilamellar vesciles*, >1000 nm, 4) *Multilamellar vesicles*, formed by concentric bilayers and 5) *Multivesicular vesicles*, composed by several small vesicles entrapped into larger ones (**Figure 1.13A**). This kind of particles can be functionalized with different ligands producing then smart and multifunctional nanoplataforms systems. [8]

Among the L-NVs, small unilamellar vesicles (SUVs) are the most frequently applied in nanomedicine due to their high homogeneity in size and structure. Their size can avoid the rapid clearance through the kidneys and also they have shown long circulation lifetime in the body avoiding the macrophagocytes.[132] Zangemeister-Wittke *et al.* reported that these systems can present proper accumulation in the tumors; having an enhanced permeability and retention effect in cancer cells.[133,134]

The most famous class of L-NVs, were discovered by Bangham *et al.* and subsequently called liposomes. They are constituted by natural phospholipids[135] that confer high biocompatibility.[136] Moreover, the presence of an aqueous core and lipid bilayers allows entrapping either hydrophilic or hydrophobic drugs, respectively.[137] However, liposomes usually present poor colloidal and chemical stability, as their membrane component are mostly insoluble and they tend to aggregate.[138,139] At the same time, some liposome *in vivo* studies reported a rapid clearance from blood after intravenous administration of these nanosystems.[140]

For these reasons, lots of efforts have been done to improve this kind of systems. Successful examples like the modification of the liposomes surface with polyethylene glycol (PEG), a hydrophilic synthetic polymer, has been done to improve their circulation time,[141] addition of Cholesterol (Chol) in the membrane, or the self-assembling with other components as surfactants,[142–144] polymers,[145,146] polypeptides,[147,148] fullerenes[149,150] have been incorporated in the liposomes to give rigidity to the system for an improvement of the *in vitro* and *in vivo* stability.[151,152]

Another class of vesicles, called "non-liposomal lipid-based nanovesicles" have been attracting attention nowadays as they have demonstrated a huge potential in pre-clinical stages,[69–74] and a good scalability for industrial purposes, also, they have been recognized as green technologies, and their lower costs comparing with the liposomal based vesicles are promising descriptions for

these systems. This category includes: niosomes,[40,142] transfersomes,[143,144] ethosomes,[153] sphingosomes,[154] virosomes [155] and Quatsomes, [156] to mention some (**Figure 1.13B**).
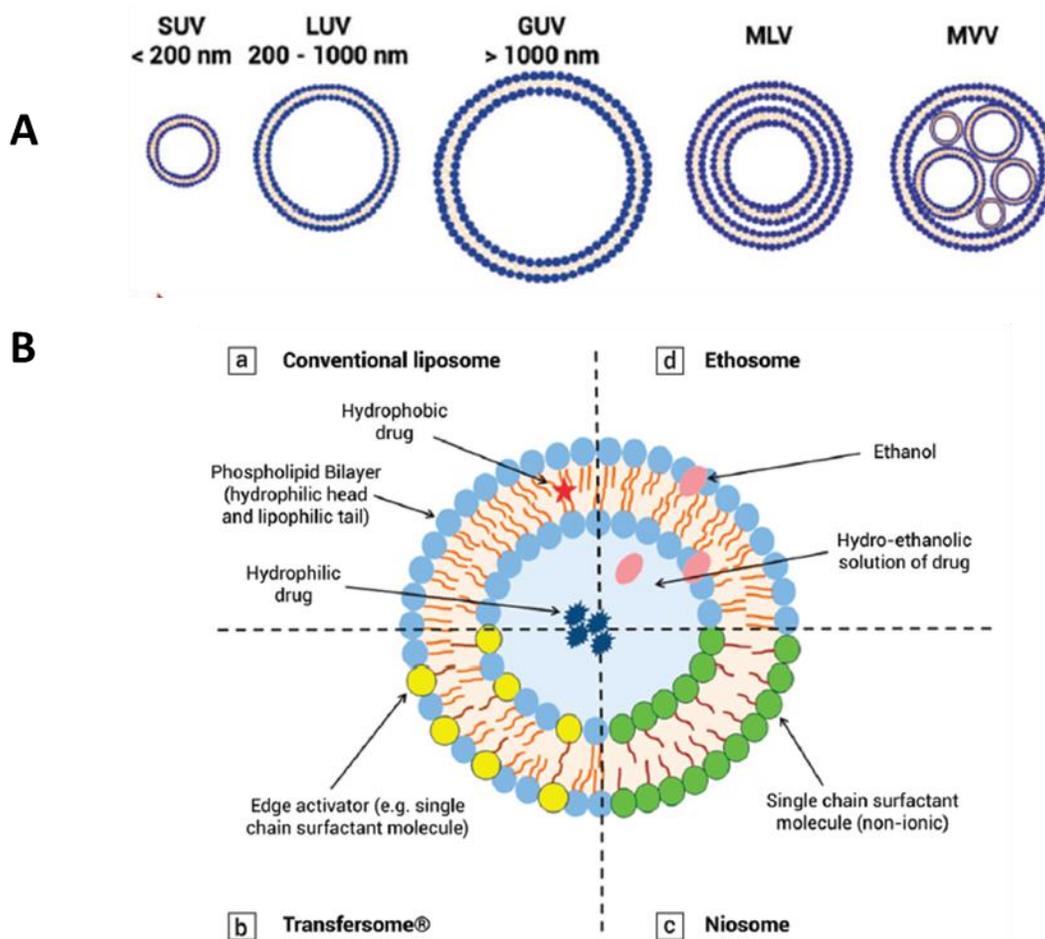

Figure 1.13. A) Representation of lipid-based vesicles and their classification regarding their size and lamellarity. E.g. small, large, and giant unilamellar vesicles (SUV, LUV, and GUV) and multi-lamellar and multi-vesicular vesicles (MLV and MVV). **B)** Schematic representation of various types of L-NVs. **(a)** Conventional liposomes; **(b)** transfersomes; **(c)** niosomes; and **(d)** ethosomes. Reprinted with permission from ref 8. (Copyright 2016, Royal Society of Chemistry)

Non-liposomal lipid-based nanovesicles differ in their composition: i) niosomes are made by Cholesterol (Chol) and non-ionic surfactants as alkyl ether, alkyl esters or alkyl amides, fatty acids, and amino acid compounds; [40,142,157] ii) transfersomes are composed by phospholipids (such as soya phosphatidylcholine (PC), egg PC, dipalmityl PC, among others) and surfactants (such as Spans 80, Tweens 80, sodium cholate etc.);[143,144] iii) ethosomes are based on phospholipids and alcohols (as ethanol or isopropanol),[153] iv) sphingosomes are built with Chol and sphingolipids; v) virosomes which include phospholipids together with viral envelope-proteins and vi) Quatsomes

that are formed by Chol and cationic surfactants (as quaternary ammonium salts).[156,158] Among these, sphingosomes and Quatsomes present better stability over time. They can stand for several months or years, respectively. In this work, Quatsomes have been used for construct hybrid nanostructures for drug delivery applications.

1.6. Quatsomes (QS)

Quatsomes are longstanding unilamellar bilayer nanovesicles constituted by the mixture of quaternary ammonium surfactants and sterols in defined molar ratios.[156,158,159] Their stability, in terms of morphology, size, lamellarity, and membrane supramolecular organization, is not dependent on temperature or dilution. [156,158]

The most used surfactants to form the Quatsomes membrane are widely used as disinfectants, algaecides, preservatives, detergents and antistatic components. This confers to Quatsomes an additional antibacterial feature.[160] The most common used quaternary ammonium surfactants are cetrimonium bromide (CTAB) (**Figure 1.14**), Myristalkonium chloride (MKC)[161] and cetylpyridinium chloride (CPC). While for the sterols, Chol and β-sitosterol can be also used. Indeed, Quatsomes prepared using antiseptic quaternary ammonium compounds (QACs) and Chol have shown good anti-biofilm capacity without adverse effect on the cells.[160]
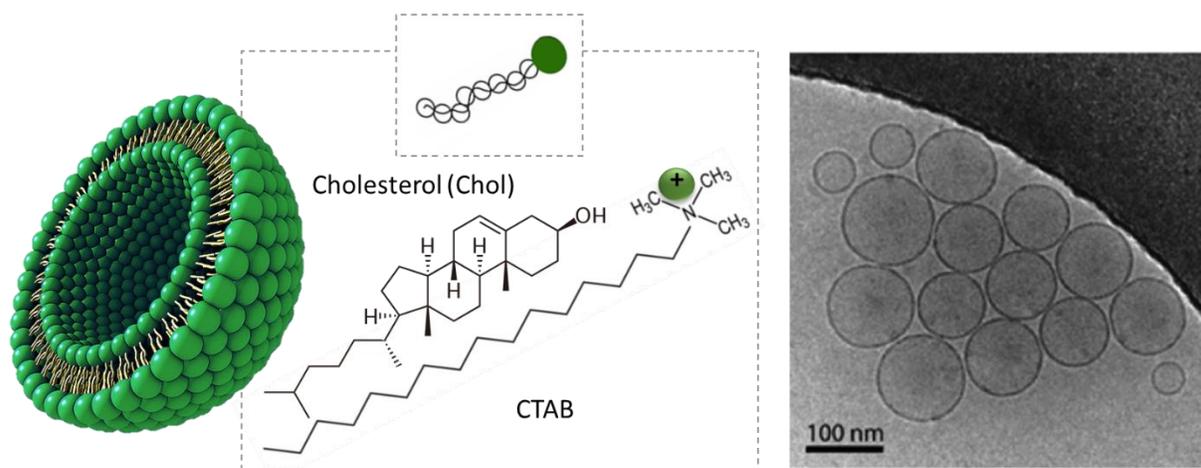

Figure 1.14. Cryo-TEM image of Quatsomes formed by the self-assembling of cholesterol and CTAB molecules. Adapted with permission from ref 156. (Copyright 2013, American Chemical Society)

Due to their structural and physicochemical properties, QS can be a feasible platform for loading, both hydrophilic and hydrophobic molecules. Moreover, they have shown to be effective in

enhancing specific bioactivity of proteins and to protect them against premature degradation in topical pharmaceutical formulations.[162] Overall, these properties make these vesicles interesting as drug delivery systems in the development of new nanomedicines.[163–166] The compression of the stratification in the QS is an important area of knowledge to develop future applications. Some examples of QS loaded were studied as a proof of concept to understand the dispersion of the dye (1,1'-dioctadecyl-3,3,3',3'-tetramethyl-indocarbocyanine perchlorate (DiI) and 1,1'-dioctadecyl-3,3,3',3'-tetramethyl-indodicarbocyanine perchlorate (DiD)) in the membrane.[167] QS-dye nano-formulations have been used as fluorescent organic nanoparticles (FONS).[167] They were prepared by CO_2-based DELOS technology (*vide infra*) and they showed excellent colloidal and photostability, outperforming compared to other nano-formulations. Additionally, these systems improved the optical properties of the fluorophores in water increasing their solubility in the media. FONS represent an interesting strategy for bioimaging applications as they present good brightness, photostability and biocompatibility.[168,169] Ventosa and coworkers showed the potential application in super-resolution microscopy of QS loaded with 1,1'-dioctadecyl-3,3,3',3'-tetramethyl-indocarbocyanine perchlorate (DiI) in vitro (**Figure 1.15**).[167]
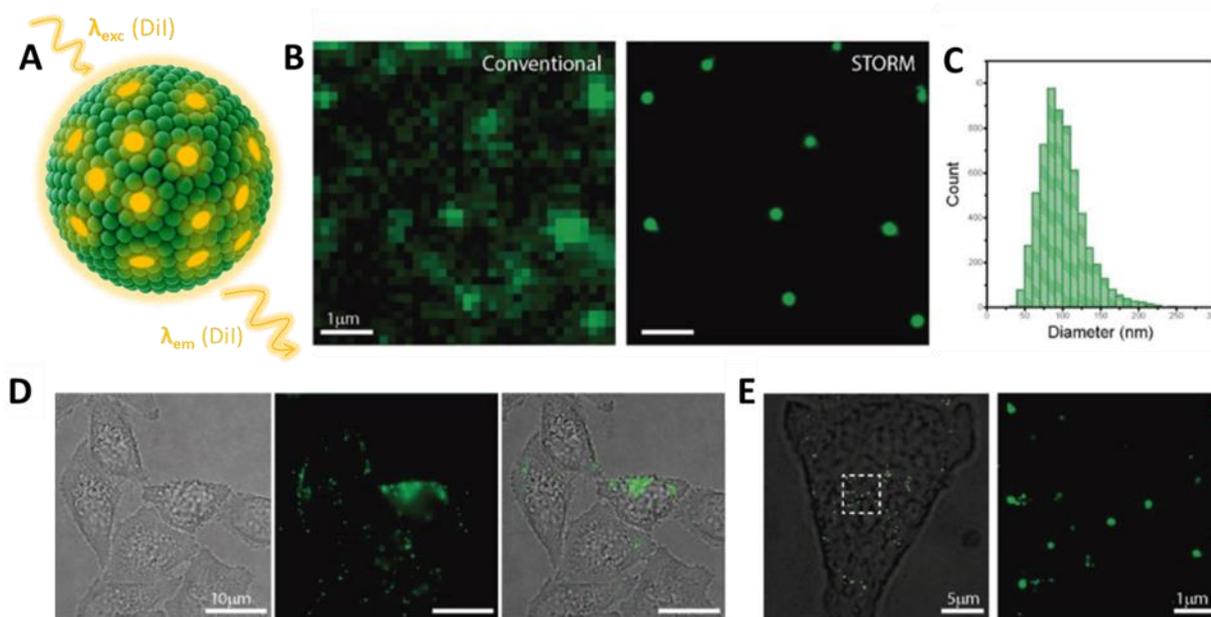

Figure 1.15. A) Scheme of the DiI-loaded in the QS. **B)** Conventional wide-field microscopy and STORM Images of DiI-loaded QS obtained (λ_{exc} = 561 nm), **C)** Distribution of the diameter size and **D)** Images by fluorescence microscopy of the internalization of DiI-loaded QS in HeLa cells. Adapted with permission from ref 167. (Copyright 2018, Wiley-VCH Verlag GmbH & Co. KGaA, Weinheim)

Recently, Ventosa *et al*. have also reported FONS based on QS nanovesicles containing a pair of carbocyanine fluorophores that display Förster resonance energy transfer (FRET) (**Figure 1.16**). FRET occurs when a donor fluorophore in the excited state non-radiatively transfers energy to a nearby acceptor fluorophore (typically within a distance of 1–10 nm).[170,171] Having QS loaded with a donor-acceptor pair rather than a single fluorophore gives the possibility to monitor the integrity of the nanostructure in cell media, body fluids and organs through FRET emission (which only occurs if the structure is preserved). It also gives a wider spectral gap between the excitation and emission wavelengths causing a reduction of the self-absorption and, hence, reducing the background noise.[172,173]
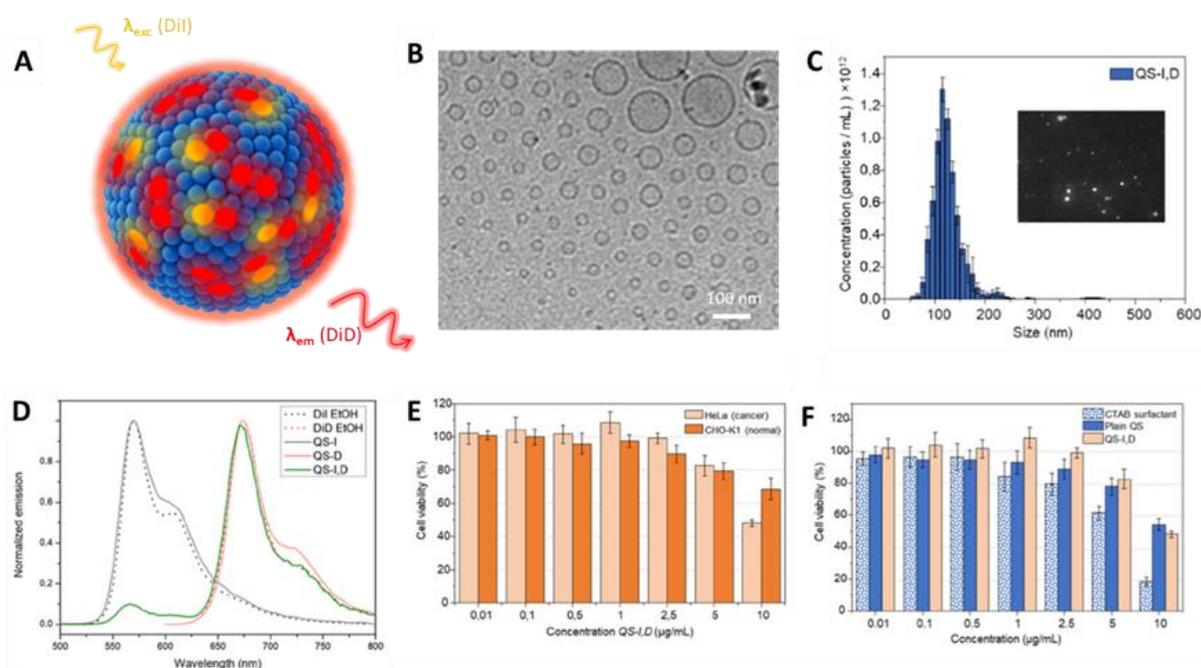

Figure 1.16. A) Scheme of the DiI-DID-loaded in the QS (loaded FRET pair), **B)** Cryo-TEM image of the FRET system and their **C)** diameter size distribution by tracking analysis (NTA). **D)** Normalized emission spectra of DiI and DiD in ethanol, QS-I,QS-D, and QS-I,D in water (λ_{ex}= 490 nm for DiI, QS-I, and QS-I,D; and λ_{ex}=590 nm for DiD and QS-D). **E)** and **F)** Cell viability assay of HeLa and CHO-K1 cells with different QS systems at various concentrations in HeLa and CHO-K1 cells. Adapted with permission from ref 173. (Copyright 2020, American Chemical Society)

Additionally, FONs are promising optical bioprobes due to their structural homogeneity stability inside the cells, high brightness, photostability and high FRET efficiency. There, the FONS were mainly localized in lysosomes. Biocompatibility test in cancer and normal cell lines (HeLa and

CHO-K1) showed high cell viability after 24 h of incubation with several concentrations of these QS, demonstrating low cytotoxicity for both cell lines up to a 5 µg/mL concentration. This cytotoxicity is due to the quaternary ammonium surfactant.[173,174]

1.6.1. Preparation of Quatsomes nanostructures

QS are self-assembled supramolecular architectures; they are formed spontaneously by hydrophobic interactions as a product of the recognition of their components triggered in aqueous media. The self-assembly construction is influenced by the environmental conditions, as temperature, pH, ionic strength, type, and concentration of components. The methods to prepare these systems are focused in obtain homogeneous vesicular organizations with controlled size, morphology, and supramolecular organization. This structural homogeneity is required since it affects the behavior of vesicles as drug delivery systems. For instance, in contrast with the uncontrolled behavior of an heterogeneous system, an homogeneous sample would behave as a controlled release system (having an homogeneous release of the drug, at the site of action in a determined time) (**Figure 1.17**).[126] Trying to reach these properties and moreover, to scale-up the synthesis from laboratory to the industry level several synthetical methods have been applied. [8]
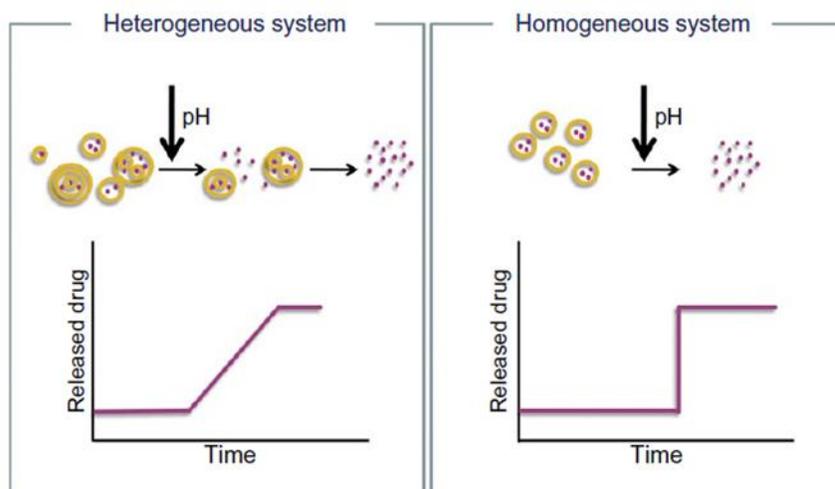

Figure 1.17. Illustration of the response of an external stimulus in a vesicular drug delivery system with and homogeneous (right) and heterogeneous (left) vesicles in terms of size and lamellarity. Reprinted with permission from ref 126. (Copyright 2011, Elsevier)

Conventional methods for vesicle production involve the dispersion of the self-assembled structures in an aqueous phase, being the thin film hydration or Bangham method the most used.[175] This technique provides large and heterogeneous MLVs with low encapsulation efficiencies. For their improvement, *reverse-phase methodologies* have emerged as the *reverse-phase evaporation (REV)* and the *solvent injection method.* The *reverse-phase evaporation (REV) method*[176] is based on the formation of inverted micelles upon addition of a small volume of aqueous phase to an organic solution of the lipids, followed by the removal of the organic solvent to finally obtain the MLVs. On the other hand, the *solvent injection method,*[177,178] produces unilamellar vesicles achieved by injecting a solution of lipids in ethanol or ether into an aqueous phase. With these two conventional techniques, usually big LUVS, MLVs and GUVs are obtained; therefore post-formation processing is required as, *sonication,*[179] *extrusion,*[180,181] and *high-pressure homogenization*[182] to achieve a desired size, lamellarity and homogeneity (**Figure 1.18**). However, despite the efforts to obtain homogeneous vesicles, the efficiency of encapsulation is another parameter that must be optimized in these systems.
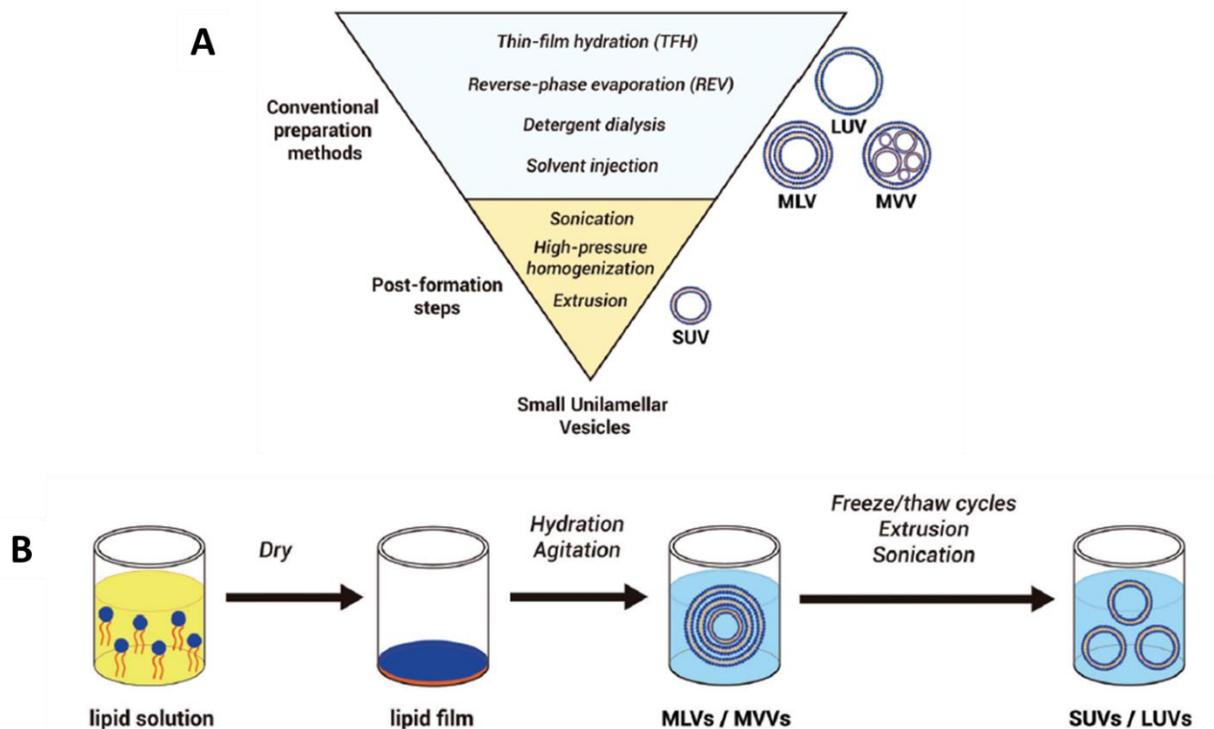

Figure 1.18. A) Conventional and post-formation steps to prepare vesicles. **B)** Schematic representation of the thin film hydration method. Adapted with permission from ref 126 (Copyright 2011, Elsevier) and 8 (Copyright 2016, Royal Society of Chemistry).

Because of this, new preparation methods are emerging to produce small unilamellar vesicles in order to increase the trapping efficiency and produce homogeneous materials for drug delivery purposes. Compressed fluid (CF) based technologies also named dense gas technologies, have gained importance in the last years for the production of high-quality homogeneous L-NVs. A CF is defined as a substance that in normal conditions of pressure and temperature exists as a gas while it is transformed in a liquid or supercritical fluid by increasing the pressure. The supercritical region is achieved when the substance is exposed to conditions above its critical pressure and temperature. The most common dense gas is carbon dioxide (CO_2), its critical pressure and temperature are 73 bar and 31 °C. Using this green substitute, several methodologies have emerged, reducing the amount of organic solvent in comparation with that used by conventional methods.[126,183]. Most of the methods using compressed CO_2 for L-NV production involve the formation of a mixture of this dense gas, the vesicle membrane constituents, and an organic solvent at a certain pressure and temperature; thereafter, vesicles are usually produced upon contact between this organic phase and an aqueous phase.[163,184]

The major techniques described using CF technology for the formation of vesicles include the methods of *injection*, *decompression*, *supercritical liposome*, *supercritical reverse phase evaporation* (scRPE), and more recently the *Depressurization of an Expanded Organic Solution (DELOS-SUSP) method*.[185] The DELOS-SUSP technique will be fully described as this methodology has been used to produce the QS used to produce hybrid systems in this work.

1.6.2. DELOS-SUSP Methodology for the preparation of QS

The DELOS-SUSP is a CF-based approach for the production of multifunctional small unilamellar vesicles. This process involves the depressurization of the CO_2 expanded liquid solution into an aqueous phase using conditions of pressure of 10 MPa and temperature 308K. **Figure 1.19** illustrates the procedure: in a first step, the hydrophobic components (Chol and cargo molecules) are dissolved in an organic solvent (most commonly EtOH) at atmospheric pressure (P) and working temperature (T_W). Then, the CO_2 is added to obtain the expanded solution of the components at a T_W and high pressure (P_W). Finally, the CO_2-expanded solution is depressurized, from P_W to P over a continuous aqueous flow, containing a surfactant (commonly CTAB), to give uniform unilamellar lipid nanovesicles.[126]
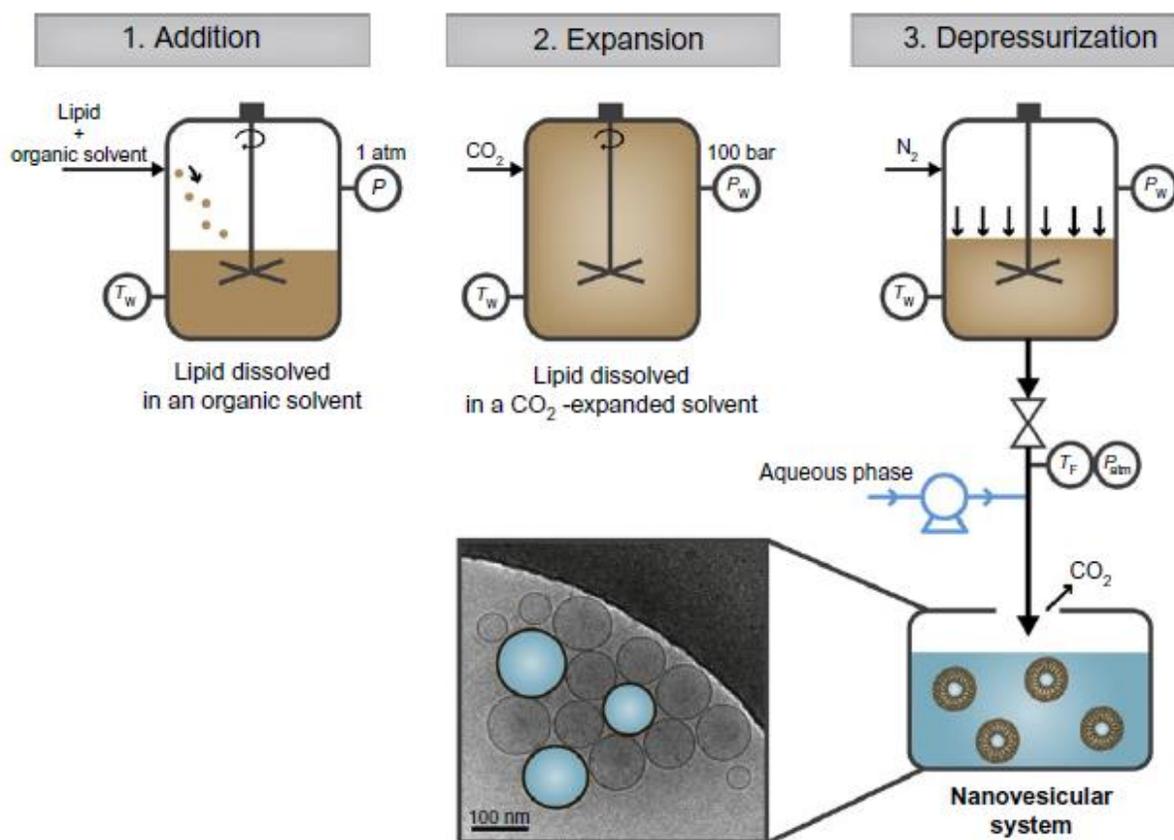
Figure 1.19. Schematic representation of the DELOS-SUSP method for the efficient preparation of multifunctional nanovesicle–bio-active hybrids. Reprinted with permission from ref 126. (Copyright 2011, Elsevier)

The large, abrupt and homogeneous temperature decrease caused by the depressurization provides more homogeneous vesicles in terms of size, morphology, and supramolecular organization, compared to conventional procedures (**Figure 1.20**).[185]

The incorporation of Chol in the lipid membrane vesicles sometimes requires to reduce their permeability and avoid leakage of the encapsulated molecule. Due to the poor solubility of Chol, the preparation of QS is problematic by conventional hydration procedures. By DELOS-susp, vesicles made by Chol and CTAB (1:1 molar ratio) can be prepared. The resulting formulation brings homogeneous, stable in time vesicles with diameters between 100-200 nm. To entrap active substances by DELOS-susp, the drug can be dissolved either in the expanded mixture or in the aqueous phase, depending in its hydrophobicity. As examples, the gentamicin sulphate

(hydrophilic antibiotic),[186] DiI or DID (hydrophobic dyes)[167,173], the growth factor (EGF protein)[187] have been incorporated into cholesterol-rich vesicles using this method.[185,188]
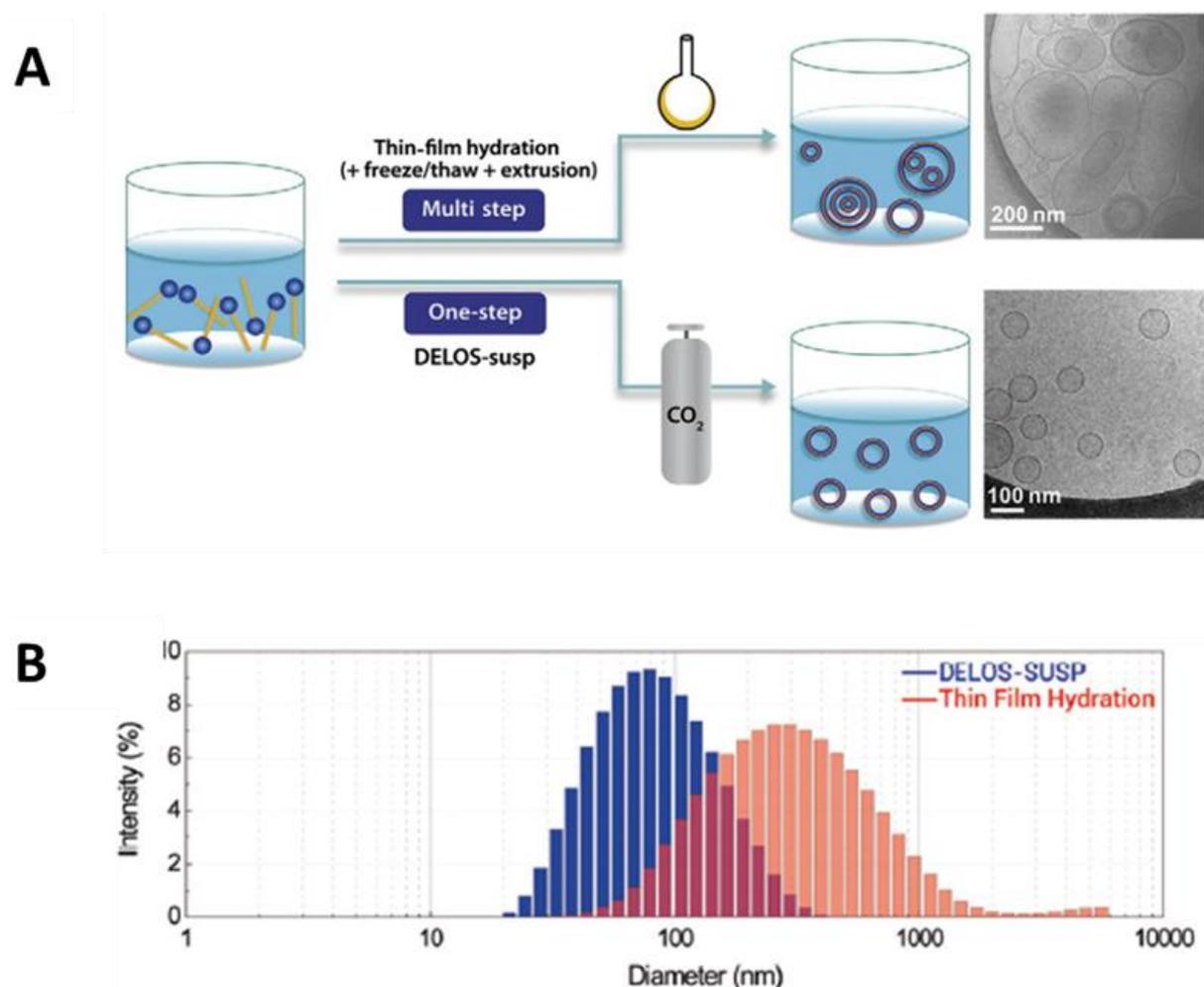

Figure 1.20. A) Schematic representation of the impact of the preparation procedure on the homogeneity and structural organization using a film hydration methodology, followed by multiple steps and DELOS-SUSP method for the preparation of nanovesicles. Cryo-TEM images correspond to antibiotic-loaded vesicular systems obtained with both methodologies. **B)** Particle size distribution curves measured by dynamic light scattering of disperse systems. Adapted with permission from ref 8. (Copyright 2016, Royal Society of Chemistry).

1.7. Aim of the thesis

The purpose of this thesis is to develop different classes of hybrid organic/inorganic nanostructured materials. In particular, to use soft and hard materials combined in a single

system, silica-coated shell-QS and MSNPs-PLGA@MBds hybrid systems. Besides this introductory part (*Chapter 1*), the results are organized in 4 experimental chapters as follows is described:

Chapter 2 presents the preparation of a new hybrid system consisting of PLGA (a polymeric material) with the inclusion of mesoporous silica nanoparticles in the matrix. In this system, the encapsulation of cannabinoids and chemotherapeutic drugs for the treatment of cancer has been proposed to create new delivery platforms for the release of two molecules in two different parts of the cell (intracellular and extracellular).

Chapter 3 includes the synthesis of a hybrid system based on a non-lipid-based vesicle (CTAB-based QS) and silica. This platform (Silica-Shielded Quatsomes, SQS) displays a silica shell around the vesicles to protect them from the environment giving more structural and mechanical stability. Also, it improves other functions (as avoiding aggregation or introducing new functional groups) by decreasing internal leakage during storage, transporting and application. Furthermore, the methodology was extended to integrate, as well, a stimulus redox-response silica shell in the synthesis of the hybrid material.

Chapter 4 explores the use of fluorescent molecules to produce labelled Silica Shell-QS, providing new luminescent bioprobes, capable of loading different molecules for drug delivery applications. Furthermore, label redox-organic responsive silica shell-QS breakability tests were shown in terms of FRET experiments.

Chapter 5 investigates the formation of a redox-organic responsive Silica Shell-QS synthesized with an alternative non-toxic surfactant (MKC). Additionally, the MKC was used as a non-toxic surfactant template for the synthesis of mesoporous silica NPs, to be used as a more biocompatible drug delivery system.

Altogether, this work shows the combination of different hybrid systems to develop a new promising generation of drug delivery silica-based nanoparticles which contribute to stabilize and introduce new functionalities to basic organic systems. So, the designs are thought to develop new alternatives in the field of nanomaterials for drug delivery applications.

The present study is intrinsically interdisciplinary, it involves not only material sciences but also organic chemistry, physical chemistry and biology. This work was carried out with the support of colleagues and collaborators, experts in different fields whose apports are deeply acknowledged.

1.8. REFERENCES

(1)   Tekade, R. K.; Maheshwari, R.; Soni, N.; Tekade, M.; Chougule, M. B. Nanotechnology for the Development of Nanomedicine. In *Nanotechnology-Based Approaches for Targeting and Delivery of Drugs and Genes*; Mishra, V., Kesharwani, P., Amin, M. C. I. M., Iyer, A., Eds.; Academic Press, **2017**; pp 3–61.

(2)   ESF, E. Nanomedicine: An ESF- European Medical Research Councils (EMRC) Forward Look Report. Strasbourg cedex, France **2004**.

(3)   Tomalia, D. A.; Baker, H.; Dewald, J.; Hall, M.; Kallos, G.; Martin, S.; Roeck, J.; Ryder, J.; Smith, P. A New Class of Polymers: Starburst-Dendritic Macromolecules. *Polymer Journal* **1985**, *17* (1), 117–132.

(4)   Bharali, D. J.; Khalil, M.; Gurbuz, M.; Simone, T. M.; Mousa, S. A. Nanoparticles and Cancer Therapy: A Concise Review with Emphasis on Dendrimers. *International Journal of Nanomedicine* **2009**, *4* (1), 1–7.

(5)   Gillies, E. R.; Fréchet, J. M. J. Dendrimers and Dendritic Polymers in Drug Delivery. *Drug Discovery Today* **2005**, *10* (1), 35–43.

(6)   Sandoval-Yañez, C.; Castro Rodriguez, C. Dendrimers: Amazing Platforms for Bioactive Molecule Delivery Systems. *Materials* **2020**, *13* (3), 570.

(7)   Allen, T. M.; Cullis, P. R. Liposomal Drug Delivery Systems: From Concept to Clinical Applications. *Advanced Drug Delivery Reviews* **2013**, *65* (1), 36–48.

(8)   Grimaldi, N.; Andrade, F.; Segovia, N.; Ferrer-Tasies, L.; Sala, S.; Veciana, J.; Ventosa, N. Lipid-Based Nanovesicles for Nanomedicine. *Chemical Society Reviews* **2016**, *45* (23), 6520–6545.

(9)   Alivisatos, A. P.; Gu, W.; Larabell, C. Quantum Dots as Cellular Probes. *Annual Review of Biomedical Engineering* **2005**, *7* (1), 55–76.

(10)   Tang, Z.; He, C.; Tian, H.; Ding, J.; Hsiao, B. S.; Chu, B.; Chen, X. Polymeric Nanostructured Materials for Biomedical Applications. *Progress in Polymer Science* **2016**, *60*, 86–128.

(11)   De Souza, R.; Zahedi, P.; Allen, C. J.; Piquette-Miller, M. Polymeric Drug Delivery Systems for Localized Cancer Chemotherapy. *Drug Delivery* **2010**, *17* (6), 365–375.

(12)   Huo, Q.; Liu, J.; Wang, L. Q.; Jiang, Y.; Lambert, T. N.; Fang, E. A New Class of Silica Cross-Linked Micellar Core-Shell Nanoparticles. *Journal of the American Chemical Society* **2006**, *128* (19), 6447–6453.

(13)   Hoffmann, F.; Cornelius, M.; Morell, J.; Fröba, M. Silica-Based Mesoporous Organic-Inorganic Hybrid Materials. *Angewandte Chemie International Edition* **2006**, *45* (20), 3216–3251.

(14)   Argyo, C.; Weiss, V.; Bräuchle, C.; Bein, T. Multifunctional Mesoporous Silica Nanoparticles as a Universal Platform for Drug Delivery. *Chemistry of Materials* **2014**, *26* (1), 435–451.

(15)   Dresselhaus, M. S.; Dresselhaus, G.; Eklund, P. C.; Rao, A. M. Carbon Nanotubes. In *The physics of fullerene-based and fullerene-related materials*; Andreoni, W., Ed.; Kluwer Academic Publishers, **2000**; pp 331–379.

(16)   Popov, V. N. Carbon Nanotubes: Properties and Application. *Materials Science and Engineering R: Reports* **2004**, *43* (3), 61–102.

(17)   Toshima, N.; Yonezawa, T. Bimetallic Nanoparticles - Novel Materials for Chemical and Physical Applications. *New Journal of Chemistry* **1998**, *22* (11), 1179–1201.

(18)   Kumar Teli, M.; Mutalik, S.; Rajanikant, G. K. Nanotechnology and Nanomedicine: Going Small Means Aiming Big. *Current Pharmaceutical Design* **2010**, *16* (16), 1882–1892.

(19)   *Nanotechnology and Drug Delivery, Volume One: Nanoplatforms in Drug Delivery*; Arias, J. L., Ed.; CRC Press, **2014**.

(20)   Etheridge, M. L.; Campbell, S. A.; Erdman, A. G.; Haynes, C. L.; Wolf, S. M.; McCullough, J. The Big Picture on Nanomedicine: The State of Investigational and Approved Nanomedicine Products. *Nanomedicine: Nanotechnology, Biology, and Medicine* **2013**, *9* (1), 1–14.

(21)   Bamrungsap, S.; Zhao, Z.; Chen, T.; Wang, L.; Li, C.; Fu, T.; Tan, W. Nanotechnology in

Therapeutics: A Focus on Nanoparticles as a Drug Delivery System. *Nanomedicine* **2012**, *7* (8), 1253–1271.

(22) Strebhardt, K.; Ullrich, A. Paul Ehrlich's Magic Bullet Concept: 100 Years of Progress. *Nature Reviews Cancer* **2008**, *8* (6), 473–480.

(23) Kim, K.-M.; Kang, J.-H.; Vinu, A.; Choy, J.-H.; Oh, J.-M. Inorganic Nanomedicines and Their Labeling for Biological Imaging. *Current Topics in Medicinal Chemistry* **2013**, *13* (4), 488–503.

(24) *Applications of Targeted Nano Drugs and Delivery Systems: Nanoscience and Nanotechnology in Drug Delivery*; Mohapatra, S., Ranjan, S., Dasgupta, N., Kumar, R., Thomas, S., Eds.; Elsevier, **2018**.

(25) Ehmann, F.; Sakai-Kato, K.; Duncan, R.; Pérez De La Ossa, D. H.; Pita, R.; Vidal, J. M.; Kohli, A.; Tothfalusi, L.; Sanh, A.; Tinton, S.; Robert, J. L.; Silva Lima, B.; Amati, M. P. Next-Generation Nanomedicines and Nanosimilars: EU Regulators' Initiatives Relating to the Development and Evaluation of Nanomedicines. *Nanomedicine* **2013**, *8* (5), 849–856.

(26) van der Meel, R.; Vehmeijer, L. J. C.; Kok, R. J.; Storm, G.; van Gaal, E. V. B. Ligand-Targeted Particulate Nanomedicines Undergoing Clinical Evaluation: Current Status. *Advanced Drug Delivery Reviews* **2013**, *65* (10), 1284–1298.

(27) Salvioni, L.; Rizzuto, M. A.; Bertolini, J. A.; Pandolfi, L.; Colombo, M.; Prosperi, D. Thirty Years of Cancer Nanomedicine: Success, Frustration, and Hope. *Cancers* **2019**, *11* (12), 1855.

(28) Kim, H. G.; Choi, J. H.; Kim, G. M.; Kim, K. M.; Lee, S. H.; Kim, Y. H. Controlled Drug Release Analysis of Monosized Drugloaded Plga Microparticles by Ligand-Sensitized Fluorescence. In *Proceedings of the 16th International Conference on Miniaturized Systems for Chemistry and Life Sciences, MicroTAS 2012*; **2012**; pp 1534–1536.

(29) Vauthier, C.; Bouchemal, K. Methods for the Preparation and Manufacture of Polymeric Nanoparticles. *Pharmaceutical Research* **2009**, *26* (5), 1025–1058.

(30) Feng, L.; Zhu, C.; Yuan, H.; Liu, L.; Lv, F.; Wang, S. Conjugated Polymer Nanoparticles:

Preparation, Properties, Functionalization and Biological Applications. *Chemical Society Reviews* **2013**, *42* (16), 6620–6633.

(31)   Trzciński, J. W.; Panariello, L.; Besenhard, M. O.; Yang, Y.; Gavriilidis, A.; Guldin, S. Synthetic Guidelines for the Precision Engineering of Gold Nanoparticles. *Current Opinion in Chemical Engineering* **2020**, *29*, 59–66.

(32)   Ali, S.; Perveen, S.; Ali, M.; Jiao, T.; Sharma, A. S.; Hassan, H.; Devaraj, S.; Li, H.; Chen, Q. Bioinspired Morphology-Controlled Silver Nanoparticles for Antimicrobial Application. *Materials Science and Engineering C* **2020**, *108*, 110421.

(33)   Travaglini, L.; De Cola, L. Morphology Control of Mesoporous Silica Particles Using Bile Acids as Cosurfactants. *Chemistry of Materials* **2018**, *30* (12), 4168–4175.

(34)   Mohanraj, V. J.; Chen, Y. Nanoparticles-A Review. *Tropical Journal of Pharmaceutical Research* **2006**, *5* (1), 561–573.

(35)   Burgess, P.; Hutt, P. B.; Farokhzad, O. C.; Langer, R.; Minick, S.; Zale, S. On Firm Ground: IP Protection of Therapeutic Nanoparticles. *Nature Biotechnology* **2010**, *28* (12), 1267–1270.

(36)   Farokhzad, O. C.; Langer, R. Impact of Nanotechnology on Drug Delivery. *ACS Nano* **2009**, *3* (1), 16–20.

(37)   Li, Z.; Tan, S.; Li, S.; Shen, Q.; Wang, K. Cancer Drug Delivery in the Nano Era: An Overview and Perspectives (Review). *Oncology Reports* **2017**, *38* (2), 611–624.

(38)   Gessner, I.; Neundorf, I. Nanoparticles Modified with Cell-Penetrating Peptides: Conjugation Mechanisms, Physicochemical Properties, and Application in Cancer Diagnosis and Therapy. *International Journal of Molecular Sciences* **2020**, *21* (7), 2536.

(39)   Trinh, T.; Chidchob, P.; Bazzi, H. S.; Sleiman, H. F. DNA Micelles as Nanoreactors: Efficient DNA Functionalization with Hydrophobic Organic Molecules. *Chemical Communications* **2016**, *52* (72), 10914–10917.

(40)   Rajera, R.; Nagpal, K.; Singh, S. K.; Mishra, D. N. Niosomes: A Controlled and Novel Drug Delivery System. *Biological & Pharmaceutical Bulletin* **2011**, *34* (7), 945–953.

(41)   Paliwal, R.; Paliwal, S. R.; Kenwat, R.; Kurmi, B. Das; Sahu, M. K. Solid Lipid Nanoparticles: A Review on Recent Perspectives and Patents. *Expert Opinion on Therapeutic Patents* **2020**, *30* (3), 179–194.

(42)   Banik, B. L.; Fattahi, P.; Brown, J. L. Polymeric Nanoparticles: The Future of Nanomedicine. *Wiley Interdisciplinary Reviews: Nanomedicine and Nanobiotechnology* **2016**, *8* (2), 271–299.

(43)   Bajpai, A. K.; Shukla, S. K.; Bhanu, S.; Kankane, S. Responsive Polymers in Controlled Drug Delivery. *Progress in Polymer Science (Oxford)* **2008**, *33* (11), 1088–1118.

(44)   Habibi, N.; Kamaly, N.; Memic, A.; Shafiee, H. Self-Assembled Peptide-Based Nanostructures: Smart Nanomaterials toward Targeted Drug Delivery. *Nano Today* **2016**, *11* (1), 41–60.

(45)   Mitragotri, S.; Stayton, P. Organic Nanoparticles for Drug Delivery and Imaging. *MRS Bulletin* **2014**, *39* (3), 219–223.

(46)   Probst, C. E.; Zrazhevskiy, P.; Bagalkot, V.; Gao, X. Quantum Dots as a Platform for Nanoparticle Drug Delivery Vehicle Design. *Advanced Drug Delivery Reviews* **2013**, *65* (5), 703–718.

(47)   Tang, F.; Li, L.; Chen, D. Mesoporous Silica Nanoparticles: Synthesis, Biocompatibility and Drug Delivery. *Advanced Materials* **2012**, *24* (12), 1504–1534.

(48)   Jiao, M.; Zhang, P.; Meng, J.; Li, Y.; Liu, C.; Luo, X.; Gao, M. Recent Advancements in Biocompatible Inorganic Nanoparticles towards Biomedical Applications. *Biomaterials Science* **2018**, *6* (4), 726–745.

(49)   Fan, W.; Yung, B.; Huang, P.; Chen, X. Nanotechnology for Multimodal Synergistic Cancer Therapy. *Chemical Reviews* **2017**, *117* (22), 13566–13638.

(50)   Janczak, C. M.; Aspinwall, C. A. Composite Nanoparticles: The Best of Two Worlds. *Analytical and Bioanalytical Chemistry* **2012**, *402* (1), 83–89.

(51)   Myndrul, V.; Iatsunskyi, I. Nanosilicon-Based Composites for (Bio)Sensing Applications:

Current Status, Advantages, and Perspectives. *Materials* **2019**, *12* (18), 2880.

(52) Garza-Cervantes, J. A.; Mendiola-Garza, G.; de Melo, E. M.; Dugmore, T. I. J.; Matharu, A. S.; Morones-Ramirez, J. R. Antimicrobial Activity of a Silver-Microfibrillated Cellulose Biocomposite against Susceptible and Resistant Bacteria. *Scientific Reports* **2020**, *10* (1), 1–7.

(53) Zhou, Y.; Jing, X.; Chen, Y. Material Chemistry of Graphene Oxide-Based Nanocomposites for Theranostic Nanomedicine. *Journal of Materials Chemistry B* **2017**, *5* (32), 6451–6470.

(54) James, N. D.; Coker, R. J.; Tomlinson, D.; Harris, J. R. W.; Gompels, M.; Pinching, A. J.; Stewart, J. S. W. Liposomal Doxorubicin (Doxil): An Effective New Treatment for Kaposi's Sarcoma in AIDS. *Clinical Oncology* **1994**, *6* (5), 294–296.

(55) Batist, G.; Ramakrishnan, G.; Rao, C. S.; Chandrasekharan, A.; Gutheil, J.; Guthrie, T.; Shah, P.; Khojasteh, A.; Nair, M. K.; Hoelzer, K.; Tkaczuk, K.; Park, Y. C.; Lee, L. W. Reduced Cardiotoxicity and Preserved Antitumor Efficacy of Liposome-Encapsulated Doxorubicin and Cyclophosphamide Compared with Conventional Doxorubicin and Cyclophosphamide in a Randomized, Multicenter Trial of Metastatic Breast Cancer. *Journal of clinical oncology* **2001**, *19* (5), 1444–1454.

(56) Stathopoulos, G. P.; Boulikas, T. Lipoplatin Formulation Review Article. *Journal of Drug Delivery* **2012**, *2012*, 581363.

(57) Kaposi's Sarcoma: DaunoXome Approved. *AIDS Treat News* **1996**, No. 79, 3–4.

(58) Salehi, B.; Selamoglu, Z.; Mileski, K. S.; Pezzani, R.; Redaelli, M.; Cho, W. C.; Kobarfard, F.; Rajabi, S.; Martorell, M.; Kumar, P.; Martins, N.; Santra, T. S.; Sharifi-Rad, J. Liposomal Cytarabine as Cancer Therapy: From Chemistry to Medicine. *Biomolecules* **2019**, *9* (12), 773.

(59) Green, M. R.; Manikhas, G. M.; Orlov, S.; Afanasyev, B.; Makhson, A. M.; Bhar, P. .; Hawkins, M. J. Abraxane, a Novel Cremophor-Free, Albumin-Bound Particle Form of Paclitaxel for the Treatment of Advanced Non-Small-Cell Lung Cancer. *Ann Oncol* **2006**, *17* (8), 1263–1268.

(60) Ahn, H. K.; Jung, M.; Sym, S. J.; Shin, D. B.; Kang, S. M.; Kyung, S. Y.; Park, J. W.; Jeong, S. H.; Cho, E. K. A Phase II Trial of Cremorphor EL-Free Paclitaxel (Genexol-PM) and Gemcitabine in Patients with Advanced Non-Small Cell Lung Cancer. *Cancer Chemotherapy and Pharmacology* **2014**, *74* (2), 277–282.

(61) He, C.; Lu, J.; Lin, W. Hybrid Nanoparticles for Combination Therapy of Cancer. *Journal of Controlled Release* **2015**, *219*, 224–236.

(62) Picchetti, P.; Dimarco, B. N.; Travaglini, L.; Zhang, Y.; Ortega-Liebana, M. C.; De Cola, L. Breaking with Light: Stimuli-Responsive Mesoporous Organosilica Particles. *Chemistry of Materials* **2020**, *32* (1), 392–399.

(63) Shi, C. E.; You, C. Q.; Pan, L. Facile Formulation of Near-Infrared Light-Triggered Hollow Mesoporous Silica Nanoparticles Based on Mitochondria Targeting for on-Demand Chemo/Photothermal/Photodynamic Therapy. *Nanotechnology* **2019**, *30* (32), 325102.

(64) Choi, Y.; Kim, J.; Yu, S.; Hong, S. PH-and Temperature-Responsive Radially Porous Silica Nanoparticles with High-Capacity Drug Loading for Controlled Drug Delivery. *Nanotechnology* **2020**, *31* (33), 335103.

(65) Guo, F.; Li, G.; Zhou, H.; Ma, S.; Guo, L.; Liu, X. Temperature and H2O2-Operated Nano-Valves on Mesoporous Silica Nanoparticles for Controlled Drug Release and Kinetics. *Colloids and Surfaces B: Biointerfaces* **2020**, *187*, 110643.

(66) Du, M.; Chen, Y.; Tu, J.; Liufu, C.; Yu, J.; Yuan, Z.; Gong, X.; Chen, Z. Ultrasound Responsive Magnetic Mesoporous Silica Nanoparticle-Loaded Microbubbles for Efficient Gene Delivery. *ACS Biomaterials Science & Engineering* **2020**, *6* (5), 2904–2912.

(67) Manzano, M.; Vallet-Regí, M. Ultrasound Responsive Mesoporous Silica Nanoparticles for Biomedical Applications. *Chemical Communications* **2019**, *55* (19), 2731–2740.

(68) Lin, J.; Peng, C.; Ravi, S.; Nur Alam Siddiki, A. K. M.; Zheng, J.; Balkus, K. J. Biphenyl Wrinkled Mesoporous Silica Nanoparticles for PH-Responsive Doxorubicin Drug Delivery. *Materials* **2020**, *13* (8), 1998.

(69) Wei, T.; Sheng, M.; Liu, C.; Sun, J.; Wu, X.; Bai, S. Fluorescent PH-Responsive Mesoporous

Silica Nanoparticles with Core-Shell Feature as a Traceable Delivery Carrier for Ibuprofen. *ChemistrySelect* **2020**, *5* (20), 6123–6130.

(70)   Abdo, G. G.; Zagho, M. M.; Khalil, A. Recent Advances in Stimuli-Responsive Drug Release and Targeting Concepts Using Mesoporous Silica Nanoparticles. *Emergent Materials* **2020**, *3* (3), 407–425.

(71)   García-Fernández, A.; Aznar, E.; Martínez-Máñez, R.; Sancenón, F. New Advances in In Vivo Applications of Gated Mesoporous Silica as Drug Delivery Nanocarriers. *Small* **2020**, *16* (3), 1902242.

(72)   Castillo, R. R.; Lozano, D.; González, B.; Manzano, M.; Izquierdo-Barba, I.; Vallet-Regí, M. Advances in Mesoporous Silica Nanoparticles for Targeted Stimuli-Responsive Drug Delivery: An Update. *Expert Opinion on Drug Delivery* **2019**, *16* (4), 415–439.

(73)   Watermann, A.; Brieger, J. Mesoporous Silica Nanoparticles as Drug Delivery Vehicles in Cancer. *Nanomaterials* **2017**, *7* (7), 189.

(74)   Liberman, A.; Mendez, N.; Trogler, W. C.; Kummel, A. C. Synthesis and Surface Functionalization of Silica Nanoparticles for Nanomedicine. *Surface Science Reports* **2014**, *69* (2–3), 132–158.

(75)   Yoldas, B. E. Modification of Polymer-Gel Structures. *Journal of Non-Crystalline Solids* **1984**, *63* (1–2), 145–154.

(76)   Stober, W.; Fink, A.; Ernst Bohn, D. Controlled Growth of Monodisperse Silica Spheres in the Micron Size Range 1. *Journal of colloid and interface science* **1968**, *26* (1), 62–69.

(77)   Wen, J.; Wilkes, G. L. Organic/Inorganic Hybrid Network Materials by the Sol-Gel Approach. *Chemistry of Materials* **1996**, *8* (8), 1667–1681.

(78)   ALOthman, Z. A. A Review: Fundamental Aspects of Silicate Mesoporous Materials. *Materials* **2012**, *5* (12), 2874–2902.

(79)   Schubert, U. Chemistry and Fundamentals of the Sol-Gel Process. In *The Sol-Gel Handbook*; Levy, D., Zayat, M., Eds.; **2015**; Vol. 1–3, pp 1–28.

(80)   Kresge, C. T.; Leonowicz, M. E.; Roth, W. J.; Vartuli, J. C.; Beck, J. S. Ordered Mesoporous Molecular Sieves Synthesized by a Liquid-Crystal Template Mechanism. *Nature* **1992**, *359* (6397), 710–712.

(81)   Huo, Q.; Margolese, D. I.; Ciesla, U.; Demuth, D. G.; Feng, P.; Gier, T. E.; Sieger, P.; Firouzi, A.; Chmelka, B. F.; Schüth, F.; Stucky, G. D. Organization of Organic Molecules with Inorganic Molecular Species into Nanocomposite Biphase Arrays. *Chemistry of Materials* **1994**, *6* (8), 1176–1191.

(82)   Walcarius, A.; Etienne, M.; Lebeau, B. Rate of Access to the Binding Sites in Organically Modified Silicates. 2. Ordered Mesoporous Silicas Grafted with Amine or Thiol Groups. *Chemistry of Materials* **2003**, *15* (11), 2161–2173.

(83)   Venkatesan, K. A.; Srinivasan, T. G.; Vasudeva Rao, P. R. Removal of Complexed Mercury by Dithiocarbamate Grafted on Mesoporous Silica. *Journal of Radioanalytical and Nuclear Chemistry* **2003**, *256* (2), 213–218.

(84)   Walcarius, A.; Delacôte, C. Rate of Access to the Binding Sites in Organically Modified Silicates. 3. Effect of Structure and Density of Functional Groups in Mesoporous Solids Obtained by the Co-Condensation Route. *Chemistry of Materials* **2003**, *15* (22), 4181–4192.

(85)   Cagnol, F.; Grosso, D.; Sanchez, C. A General One-Pot Process Leading to Highly Functionalised Ordered Mesoporous Silica Films. *Chemical Communications* **2004**, *4* (15), 1742–1743.

(86)   Loy, D. A.; Shea, K. J. Bridged Polysilsesquioxanes. Highly Porous Hybrid Organic-Inorganic Materials. *Chemical Reviews* **1995**, *95* (5), 1431–1442.

(87)   Shea, K. J.; Loy, D. A. Bridged Polysilsesquioxanes. Molecular-Engineered Hybrid Organic-Inorganic Materials. *Chemistry of Materials* **2001**, *13* (10), 3306–3319.

(88)   Lu, J.; Liong, M.; Zink, J. I.; Tamanoi, F. Mesoporous Silica Nanoparticles as a Delivery System for Hydrophobic Anticancer Drugs. *Small* **2007**, *3* (8), 1341–1346.

(89)   Vallet-Regí, M.; Colilla, M.; Izquierdo-Barba, I.; Manzano, M. Mesoporous Silica

Nanoparticles for Drug Delivery: Current Insights. *Molecules* **2018**, *23* (1), 47.

(90) Dilnawaz, F. Multifunctional Mesoporous Silica Nanoparticles for Cancer Therapy and Imaging. *Current Medicinal Chemistry* **2018**, *26* (31), 5745–5763.

(91) González, B.; Colilla, M.; Díez, J.; Pedraza, D.; Guembe, M.; Izquierdo-Barba, I.; Vallet-Regí, M. Mesoporous Silica Nanoparticles Decorated with Polycationic Dendrimers for Infection Treatment. *Acta Biomaterialia* **2018**, *68*, 261–271.

(92) Mora-Raimundo, P.; Lozano, D.; Manzano, M.; Vallet-Regí, M. Nanoparticles to Knockdown Osteoporosis-Related Gene and Promote Osteogenic Marker Expression for Osteoporosis Treatment. *ACS Nano* **2019**, *13* (5), 5451–5464.

(93) Manzano, M.; Vallet-Regí, M. Mesoporous Silica Nanoparticles for Drug Delivery. *Advanced Functional Materials* **2020**, *30* (2), 1902634.

(94) M. Rosenholm, J.; Sahlgren, C.; Linden, M. Multifunctional Mesoporous Silica Nanoparticles for Combined Therapeutic, Diagnostic and Targeted Action in Cancer Treatment. *Current Drug Targets* **2011**, *12* (8), 1166–1186.

(95) Li, Z.; Barnes, J. C.; Bosoy, A.; Stoddart, J. F.; Zink, J. I. Mesoporous Silica Nanoparticles in Biomedical Applications. *Chemical Society Reviews* **2012**, *41* (7), 2590–2605.

(96) Thomas, C. R.; Ferris, D. P.; Lee, J. H.; Choi, E.; Cho, M. H.; Kim, E. S.; Stoddart, J. F.; Shin, J. S.; Cheon, J.; Zink, J. I. Noninvasive Remote-Controlled Release of Drug Molecules in Vitro Using Magnetic Actuation of Mechanized Nanoparticles. *Journal of the American Chemical Society* **2010**, *132* (31), 10623–10625.

(97) Ruiz-Hernández, E.; Baeza, A.; Vallet-Regí, M. Smart Drug Delivery through DNA/Magnetic Nanoparticle Gates. *ACS Nano* **2011**, *5* (2), 1259–1266.

(98) Ding, X.; Liow, C. H.; Zhang, M.; Huang, R.; Li, C.; Shen, H.; Liu, M.; Zou, Y.; Gao, N.; Zhang, Z.; Li, Y.; Wang, Q.; Li, S.; Jiang, J. Surface Plasmon Resonance Enhanced Light Absorption and Photothermal Therapy in the Second Near-Infrared Window. *Journal of the American Chemical Society* **2014**, *136* (44), 15684–15693.

(99) Yang, X.; Liu, X.; Liu, Z.; Pu, F.; Ren, J.; Qu, X. Near-Infrared Light-Triggered, Targeted Drug Delivery to Cancer Cells by Aptamer Gated Nanovehicles. *Advanced Materials* **2012**, *24* (21), 2890–2895.

(100) Yang, J.; Lee, J.; Kang, J.; Oh, S. J.; Ko, H. J.; Son, J. H.; Lee, K.; Suh, J. S.; Huh, Y. M.; Haam, S. Smart Drug-Loaded Polymer Gold Nanoshells for Systemic and Localized Therapy of Human Epithelial Cancer. *Advanced Materials* **2009**, *21* (43), 4339–4342.

(101) Vivero-Escoto, J. L.; Slowing, I. I.; Wu, C. W.; Lin, V. S. Y. Photoinduced Intracellular Controlled Release Drug Delivery in Human Cells by Gold-Capped Mesoporous Silica Nanosphere. *Journal of the American Chemical Society* **2009**, *131* (10), 3462–3463.

(102) Meng, H.; Xue, M.; Xia, T.; Zhao, Y. L.; Tamanoi, F.; Stoddart, J. F.; Zink, J. I.; Nel, A. E. Autonomous in Vitro Anticancer Drug Release from Mesoporous Silica Nanoparticles by PH-Sensitive Nanovalves. *Journal of the American Chemical Society* **2010**, *132* (36), 12690–12697.

(103) Gao, W.; Chan, J. M.; Farokhzad, O. C. PH-Responsive Nanoparticles for Drug Delivery. *Molecular Pharmaceutics* **2010**, *7* (6), 1913–1920.

(104) Strong, L. E.; West, J. L. Thermally Responsive Polymer–Nanoparticle Composites for Biomedical Applications. *Wiley Interdisciplinary Reviews: Nanomedicine and Nanobiotechnology* **2011**, *3* (3), 307–317.

(105) Ganta, S.; Devalapally, H.; Shahiwala, A.; Amiji, M. A Review of Stimuli-Responsive Nanocarriers for Drug and Gene Delivery. *Journal of Controlled Release* **2008**, *126* (3), 187–204.

(106) Chen, Y.; Meng, Q.; Wu, M.; Wang, S.; Xu, P.; Chen, H.; Li, Y.; Zhang, L.; Wang, L.; Shi, J. Hollow Mesoporous Organosilica Nanoparticles: A Generic Intelligent Framework-Hybridization Approach for Biomedicine. *Journal of the American Chemical Society* **2014**, *136* (46), 16326–16334.

(107) Forman, H. J.; Zhang, H.; Rinna, A. Glutathione: Overview of Its Protective Roles, Measurement, and Biosynthesis. *Molecular Aspects of Medicine* **2009**, *30* (1–2), 1–12.

(108) Balendiran, G. K.; Dabur, R.; Fraser, D. The Role of Glutathione in Cancer. *Cell Biochemistry and Function* **2004**, *22* (6), 343–352.

(109) Schafer, F. Q.; Buettner, G. R. Redox Environment of the Cell as Viewed through the Redox State of the Glutathione Disulfide/Glutathione Couple. *Free Radical Biology and Medicine* **2001**, *30* (11), 1191–1212.

(110) Dentinger, M. Breakable Silica Nanoparticles for the in Vitro and in Vivo Delivery of Biomolecules, Doctoral dissertation, Université de Strasbourg, **2018**.

(111) Maggini, L.; Cabrera, I.; Ruiz-Carretero, A.; Prasetyanto, E. A.; Robinet, E.; De Cola, L. Breakable Mesoporous Silica Nanoparticles for Targeted Drug Delivery. *Nanoscale* **2016**, *8* (13), 7240–7247.

(112) Rosenholm, J. M.; Mamaeva, V.; Sahlgren, C.; Lindén, M. Nanoparticles in Targeted Cancer Therapy: Mesoporous Silica Nanoparticles Entering Preclinical Development Stage. *Nanomedicine* **2012**, *7* (1), 111–120.

(113) Narayan, R.; Nayak, U.; Raichur, A.; Garg, S. Mesoporous Silica Nanoparticles: A Comprehensive Review on Synthesis and Recent Advances. *Pharmaceutics* **2018**, *10* (3), 118.

(114) Bukara, K.; Schueller, L.; Rosier, J.; Martens, M. A.; Daems, T.; Verheyden, L.; Eelen, S.; Van Speybroeck, M.; Libanati, C.; Martens, J. A.; Van Den Mooter, G.; Frérart, F.; Jolling, K.; De Gieter, M.; Bugarski, B.; Kiekens, F. Ordered Mesoporous Silica to Enhance the Bioavailability of Poorly Water-Soluble Drugs: Proof of Concept in Man. *European Journal of Pharmaceutics and Biopharmaceutics* **2016**, *108*, 220–225.

(115) Bourquin, J.; Milosevic, A.; Hauser, D.; Lehner, R.; Blank, F.; Petri-Fink, A.; Rothen-Rutishauser, B. Biodistribution, Clearance, and Long-Term Fate of Clinically Relevant Nanomaterials. *Advanced Materials* **2018**, *30* (19), 1704307.

(116) Trewyn, B. G.; Giri, S.; Slowing, I. I.; Lin, V. S. Y. Mesoporous Silica Nanoparticle Based Controlled Release, Drug Delivery, and Biosensor Systems. *Chemical Communications* **2007**, No. 31, 3236–3245.

(117) Slowing, I. I.; Vivero-Escoto, J. L.; Wu, C. W.; Lin, V. S. Y. Mesoporous Silica Nanoparticles as Controlled Release Drug Delivery and Gene Transfection Carriers. *Advanced Drug Delivery Reviews* **2008**, *60* (11), 1278–1288.

(118) Manzano, M.; Colilla, M.; Vallet-Reg, M. Drug Delivery from Ordered Mesoporous Matrices. *Expert Opinion on Drug Delivery* **2009**, *6* (12), 1383–1400.

(119) Vivero-Escoto, J. L.; Slowing, I. I.; Lin, V. S. Y.; Trewyn, B. G. Mesoporous Silica Nanoparticles for Intracellular Controlled Drug Delivery. *Small* **2010**, *6* (18), 1952–1967.

(120) Asefa, T.; Tao, Z. Biocompatibility of Mesoporous Silica Nanoparticles. *Chemical Research in Toxicology* **2012**, *25* (11), 2265–2284.

(121) Vallhov, H.; Gabrielsson, S.; Strømme, M.; Scheynius, A.; Garcia-Bennett, A. E. Mesoporous Silica Particles Induce Size Dependent Effects on Human Dendritic Cells. *Nano Letters* **2007**, *7* (12), 3576–3582.

(122) Lu, F.; Wu, S. H.; Hung, Y.; Mou, C. Y. Size Effect on Cell Uptake in Well-Suspended, Uniform Mesoporous Silica Nanoparticles. *Small* **2009**, *5* (12), 1408–1413.

(123) He, Q.; Zhang, Z.; Gao, F.; Li, Y.; Shi, J. In Vivo Biodistribution and Urinary Excretion of Mesoporous Silica Nanoparticles: Effects of Particle Size and PEGylation. *Small* **2011**, *7* (2), 271–280.

(124) Bangham, A. D.; Standish, M. M.; Watkins, J. C. Diffusion of Univalent Ions across the Lamellae of Swollen Phospholipids. *Journal of Molecular Biology* **1965**, *13* (1), 238–252.

(125) Steed JW, Turner DR, W. K. *Core Concepts in Supramolecular Chemistry and Nanochemistry*, John Wiley.; John Wiley & Sons: Chichester (England), **2007**.

(126) Elizondo, E.; Moreno, E.; Cabrera, I.; Córdoba, A.; Sala, S.; Veciana, J.; Ventosa, N. Liposomes and Other Vesicular Systems: Structural Characteristics, Methods of Preparation, and Use in Nanomedicine. In *Progress in Molecular Biology and Translational Science*; Academic Press, **2011**; Vol. 104, pp 1–52.

(127) Rajagopal K, S. J. Self-Assembling Peptides and Proteins for Nanotechnological

Applications. *Current opinion in structural biology* **2004**, *14* (4), 480–486.

(128) Tu, R. S.; Tirrell, M. Bottom-up Design of Biomimetic Assemblies. *Advanced Drug Delivery Reviews* **2004**, *56* (11), 1537–1563.

(129) Wennerström, H.; Lindman, B. Micelles. Physical Chemistry of Surfactant Association. *Physics Reports* **1979**, *52* (1), 1–86.

(130) Lee, J. H.; Choi, Y. J.; Lim, Y. B. Self-Assembled Filamentous Nanostructures for Drug/Gene Delivery Applications. *Expert Opinion on Drug Delivery* **2010**, *7* (3), 341–351.

(131) Israelachvili, J. N.; Mitchell, D. J.; Ninham, B. W. Theory of Self-Assembly of Hydrocarbon Amphiphiles into Micelles and Bilayers. *Journal of the Chemical Society, Faraday Transactions 2: Molecular and Chemical Physics* **1976**, *72*, 1525–1568.

(132) Petros, R. A.; Desimone, J. M. Strategies in the Design of Nanoparticles for Therapeutic Applications. *Nature Reviews Drug Discovery* **2010**, *9* (8), 615–627.

(133) Hussain, S.; Plückthun, A.; Allen, T. M.; Zangemeister-Wittke, U. Antitumor Activity of an Epithelial Cell Adhesion Molecule-Targeted Nanovesicular Drug Delivery System. *Molecular Cancer Therapeutics* **2007**, *6* (11), 3019–3027.

(134) Swaminathan, J.; Ehrhardt, C. Liposomal Delivery of Proteins and Peptides. *Expert Opinion on Drug Delivery* **2012**, *9* (12), 1489–1503.

(135) Bangham, A. D.; De Gier, J.; Greville, G. D. Osmotic Properties and Water Permeability of Phospholipid Liquid Crystals. *Chemistry and Physics of Lipids* **1967**, *1* (3), 225–246.

(136) Mallick, S.; Choi, J. S. Liposomes: Versatile and Biocompatible Nanovesicles for Efficient Biomolecules Delivery. *Journal of Nanoscience and Nanotechnology* **2014**, *14* (1), 755–765.

(137) Pantos, A.; Tsiourvas, D.; Paleos, C. M.; Nounesis, G. Enhanced Drug Transport from Unilamellar to Multilamellar Liposomes Induced by Molecular Recognition of Their Lipid Membranes. *Langmuir* **2005**, *21* (15), 6696–6702.

(138) Dubois, M.; Zemb, T. Phase Behavior and Scattering of Double-Chain Surfactants in Diluted Aqueous Solutions. *Langmuir* **1991**, *7* (7), 1352–1360.

(139) Caboi, F.; Monduzzi, M. Didodecyldimethylammonium Bromide Vesicles and Lamellar Liquid Crystals. A Multinuclear NMR and Optical Microscopy Study. *Langmuir* **1996**, *12* (15), 3548–3556.

(140) Liu, D.; Liu, F.; Song, Y. K. Recognition and Clearance of Liposomes Containing Phosphatidylserine Are Mediated by Serum Opsonin. *BBA - Biomembranes* **1995**, *1235* (1), 140–146.

(141) Immordino, M. L.; Dosio, F.; Cattel, L. Stealth Liposomes: Review of the Basic Science, Rationale, and Clinical Applications, Existing and Potential. *International Journal of Nanomedicine* **2006**, *1* (3), 297–315.

(142) Marianecci, C.; Di Marzio, L.; Rinaldi, F.; Celia, C.; Paolino, D.; Alhaique, F.; Esposito, S.; Carafa, M. Niosomes from 80s to Present: The State of the Art. *Advances in Colloid and Interface Science* **2014**, *205*, 187–206.

(143) Cevc, G.; Blume, G. New, Highly Efficient Formulation of Diclofenac for the Topical, Transdermal Administration in Ultradeformable Drug Carriers, Transfersomes. *Biochimica et Biophysica Acta - Biomembranes* **2001**, *1514* (2), 191–205.

(144) Paul, A.; Cevc, G.; Bachhawat, B. K. Transdermal Immunisation with an Integral Membrane Component, Gap Junction Protein, by Means of Ultradeformable Drug Carriers, Transfersomes. *Vaccine* **1998**, *16* (2–3), 188–195.

(145) Discher, B. M.; Won, Y. Y.; Ege, D. S.; Lee, J. C. M.; Bates, F. S.; Discher, D. E.; Hammer, D. A. Polymersomes: Tough Vesicles Made from Diblock Copolymers. *Science* **1999**, *284* (5417), 1143–1146.

(146) Fan, Y.; Liu, Y.; Xi, J.; Guo, R. Vesicle Formation with Amphiphilic Chitosan Derivatives and a Conventional Cationic Surfactant in Mixed Systems. *Journal of Colloid and Interface Science* **2011**, *360* (1), 148–153.

(147) Kukula, H.; Schlaad, H.; Antonietti, M.; Förster, S. The Formation of Polymer Vesicles or "Peptosomes" by Polybutadiene-Block-Poly(L-Glutamate)s in Dilute Aqueous Solution. *Journal of the American Chemical Society* **2002**, *124* (8), 1658–1663.

(148) Gudlur, S.; Sukthankar, P.; Gao, J.; Avila, L. A.; Hiromasa, Y.; Chen, J.; Iwamoto, T.; Tomich, J. M. Peptide Nanovesicles Formed by the Self-Assembly of Branched Amphiphilic Peptides. *PLoS ONE* **2012**, *7* (9), e45374.

(149) Burger, C.; Hao, J.; Ying, Q.; Isobe, H.; Sawamura, M.; Nakamura, E.; Chu, B. Multilayer Vesicles and Vesicle Clusters Formed by the Fullerene-Based Surfactant C60(CH3)5K. *Journal of Colloid and Interface Science* **2004**, *275* (2), 632–641.

(150) Mohanta, V.; Dey, D.; Ramakumar, S.; Patil, S. Vesicular Nanostructure Formation by Self-Assembly of Anisotropic Penta-Phenol-Substituted Fullerene in Water. *Langmuir* **2015**, *31* (50), 13600–13608.

(151) Drummond, D. C.; Hong, K.; Park, J. W.; Benz, C. C.; Kirpgtin, D. B. Liposome Targeting to Tumors Using Vitamin and Growth Factor Receptors. *Vitamins and Hormones* **2000**, *60*, 285–332.

(152) Geng, S.; Yang, B.; Wang, G.; Qin, G.; Wada, S.; Wang, J.-Y. Two Cholesterol Derivative-Based PEGylated Liposomes as Drug Delivery System, Study on Pharmacokinetics and Drug Delivery to Retina. *Nanotechnology* **2014**, *25* (27), 275103.

(153) Touitou, E.; Dayan, N.; Bergelson, L.; Godin, B.; Eliaz, M. Ethosomes - Novel Vesicular Carriers for Enhanced Delivery: Characterization and Skin Penetration Properties. *Journal of Controlled Release* **2000**, *65* (3), 403–418.

(154) Saraf, S.; Gupta, D.; Kaur, C. D.; Saraf, S. Sphingosomes a Novel Approach to Vesicular Drug Delivery. *Int J Cur Sci Res* **2011**, *1* (2), 63–68.

(155) Felnerova, D.; Viret, J. F.; Glück, R.; Moser, C. Liposomes and Virosomes as Delivery Systems for Antigens, Nucleic Acids and Drugs. *Current Opinion in Biotechnology* **2004**, *15* (6), 518–529.

(156) Ferrer-Tasies, L.; Moreno-Calvo, E.; Cano-Sarabia, M.; Aguilella-Arzo, M.; Angelova, A.; Lesieur, S.; Ricart, S.; Faraudo, J.; Ventosa, N.; Veciana, J. Quatsomes: Vesicles Formed by Self-Assembly of Sterols and Quaternary Ammonium Surfactants. *Langmuir* **2013**, *29* (22), 6519–6528.

(157) Handjani-Vila, R. M.; Ribier, A.; Rondot, B.; Vanlerberghie, G. Dispersions of Lamellar Phases of Non-ionic Lipids in Cosmetic Products. *International Journal of Cosmetic Science* **1979**, *1* (5), 303–314.

(158) Elizondo, E.; Larsen, J.; Hatzakis, N. S.; Cabrera, I.; Bjørnholm, T.; Veciana, J.; Stamou, D.; Ventosa, N. Influence of the Preparation Route on the Supramolecular Organization of Lipids in a Vesicular System. *Journal of the American Chemical Society* **2012**, *134* (4), 1918–1921.

(159) Cano-Sarabia, M.; Angelova, A.; Ventosa, N.; Lesieur, S.; Veciana, J. Cholesterol Induced CTAB Micelle-to-Vesicle Phase Transitions. *Journal of Colloid and Interface Science* **2010**, *350* (1), 10–15.

(160) Thomas, N.; Dong, D.; Richter, K.; Ramezanpour, M.; Vreugde, S.; Thierry, B.; Wormald, P. J.; Prestidge, C. A. Quatsomes for the Treatment of Staphylococcus Aureus Biofilm. *Journal of Materials Chemistry B* **2015**, *3* (14), 2770–2777.

(161) Vargas-Nadal, G.; Muñoz-Ubeda, M.; Alamo, P.; Arnal, M. M.; Céspedes, V.; Köber, M.; Gonzalez, E.; Ferrer-Tasies, L.; Vinardell, M. P.; Mangues, R.; Veciana, J.; Ventosa, N. MKC-Quatsomes: A Stable Nanovesicle Platform for Bio-Imaging and Drug-Delivery Applications. *Nanomedicine: Nanotechnology, Biology, and Medicine* **2020**, *24*, 102136.

(162) Milián Héctor, J. S.; Ventosa, N.; Martínez Diáz, E.; Berlanga-Acosta, J.; Cabrera Puig, I.; Veciana, J. Vesicles Comprising Epidermal Growth Factor and Compositions Containing, **2012**.

(163) Elizondo, E.; Veciana, J.; Ventosa, N. Nanostructuring Molecular Materials as Particles and Vesicles for Drug Delivery, Using Compressed and Supercritical Fluids. *Nanomedicine* **2012**, *7* (9), 1391–1408.

(164) Yoon, H. J., & Jang, W. D. Polymeric Supramolecular Systems for Drug Delivery. *Journal of Materials Chemistry* **2010**, *20* (2), 211–222.

(165) Kubo, T.; Sugita, T.; Shimose, S.; Nitta, Y.; Ikuta, Y.; Murakami, T. Targeted Delivery of Anticancer Drugs with Intravenously Administered Magnetic Liposomes in Osteosarcoma-

Bearing Hamsters. *International journal of oncology* **2000**, *17* (2), 309–315.

(166) Sawant, R. R.; Torchilin, V. P. Challenges in Development of Targeted Liposomal Therapeutics. *AAPS Journal* **2012**, *14* (2), 303–315.

(167) Ardizzone, A.; Kurhuzenkau, S.; Illa-Tuset, S.; Faraudo, J.; Bondar, M.; Hagan, D.; Van Stryland, E. W.; Painelli, A.; Sissa, C.; Feiner, N.; Albertazzi, L.; Veciana, J.; Ventosa, N. Nanostructuring Lipophilic Dyes in Water Using Stable Vesicles, Quatsomes, as Scaffolds and Their Use as Probes for Bioimaging. *Small* **2018**, *14* (16), 1703851.

(168) Zhang, J.; Chen, R.; Zhu, Z.; Adachi, C.; Zhang, X.; Lee, C. S. Highly Stable Near-Infrared Fluorescent Organic Nanoparticles with a Large Stokes Shift for Noninvasive Long-Term Cellular Imaging. *ACS Applied Materials and Interfaces* **2015**, *7* (47), 26266–26274.

(169) Reisch, A.; Klymchenko, A. S. Fluorescent Polymer Nanoparticles Based on Dyes: Seeking Brighter Tools for Bioimaging. *Small* **2016**, *12* (15), 1968–1992.

(170) Förster, T. Delocalized Excitation and Excitation Transfer. Bulletin No. 18 (No. FSU-2690-18), Florida State University, Tallahassee. Dept. of Chemistry, **1965**.

(171) Lakowicz, J. R. Introduction to Fluorescence. In *Principles of Fluorescence Spectroscopy*; Springer US: Boston, MA, **2006**; pp 1–26.

(172) Sun, X.; Wang, G.; Zhang, H.; Hu, S.; Liu, X.; Tang, J.; Shen, Y. The Blood Clearance Kinetics and Pathway of Polymeric Micelles in Cancer Drug Delivery. *ACS Nano* **2018**, *12* (6), 6179–6192.

(173) Morla-Folch, J.; Vargas-Nadal, G.; Zhao, T.; Sissa, C.; Ardizzone, A.; Kurhuzenkau, S.; Köber, M.; Uddin, M.; Painelli, A.; Veciana, J.; Belfield, K. D.; Ventosa, N. Dye-Loaded Quatsomes Exhibiting FRET as Nanoprobes for Bioimaging. *ACS Applied Materials & Interfaces* **2020**, *12* (18), 20253–20262.

(174) Liu, X.; Ardizzone, A.; Sui, B.; Anzola, M.; Ventosa, N.; Liu, T.; Veciana, J.; Belfield, K. D. Fluorenyl-Loaded Quatsome Nanostructured Fluorescent Probes. *ACS Omega* **2017**, *2* (8), 4112–4122.

(175) Bangham, A. D.; Standish, M. M.; Weissmann, G. The Action of Steroids and Streptolysin S on the Permeability of Phospholipid Structures to Cations. *Journal of Molecular Biology* **1965**, *13* (1), 253–259.

(176) Szoka, F.; Papahadjopoulos, D. Procedure for Preparation of Liposomes with Large Internal Aqueous Space and High Capture by Reverse-Phase Evaporation. *Proceedings of the National Academy of Sciences of the United States of America* **1978**, *75* (9), 4194–4198.

(177) Batzri, S.; Korn, E. D. Single Bilayer Liposomes Prepared without Sonication. *BBA - Biomembranes* **1973**, *298* (4), 1015–1019.

(178) Deamer, D.; Bangham, A. D. Large Volume Liposomes by an Ether Vaporization Method. *Biochimica et Biophysica Acta (BBA)-Biomembranes* **1976**, *443* (3), 629–634.

(179) Woodbury, D. J.; Richardson, E. S.; Grigg, A. W.; Welling, R. D.; Knudson, B. H. Reducing Liposome Size with Ultrasound: Bimodal Size Distributions. *Journal of Liposome Research* **2006**, *16* (1), 57–80.

(180) Hope, M. J.; Bally, M. B.; Webb, G.; Cullis, P. R. Production of Large Unilamellar Vesicles by a Rapid Extrusion Procedure. Characterization of Size Distribution, Trapped Volume and Ability to Maintain a Membrane Potential. *BBA - Biomembranes* **1985**, *812* (1), 55–65.

(181) MacDonald, R. C.; MacDonald, R. I.; Menco, B. P. M.; Takeshita, K.; Subbarao, N. K.; Hu, L. rong. Small-Volume Extrusion Apparatus for Preparation of Large, Unilamellar Vesicles. *Biochimica et Biophysica Acta (BBA)-Biomembranes* **1991**, *1061* (2), 297–303.

(182) Bachmann, D.; Brandl, M.; Gregoriadis, G. Preparation of Liposomes Using a Mini-Lab 8.30 H High-Pressure Homogenizer. *International Journal of Pharmaceutics* **1993**, *91* (1), 69–74.

(183) Sun, Y.-P. *Supercritical Fluid Technology in Materials Science and Engineering: Syntheses: Properties, and Applications*; CRC Press, Taylor & Francis, **2002**.

(184) Otake, K.; Imura, T.; Sakai, H.; Abe, M. Development of a New Preparation Method of Liposomes Using Supercritical Carbon Dioxide. *Langmuir* **2001**, *17* (13), 3898–3901.

(185) Cano-Sarabia, M.; Ventosa, N.; Sala, S.; Patiño, C.; Arranz, R.; Veciana, J. Preparation of

Uniform Rich Cholesterol Unilamellar Nanovesicles Using CO 2-Expanded Solvents. *Langmuir* **2008**, *24* (6), 2433–2437.

(186) De Vicuñaç, E. E. S. New Molecule-Based Nanostructured Drug Carriers Prepared Using Compressed Fluids, Doctoral dissertation, Universitat Autònoma de Barcelona, Bellaterra, **2010**.

(187) Santana, H; Ventosa, N. Vesicles Which Include Epidermal Growth Factor and Compositions That Contain Same, February 6, **2014**.

(188) Ventosa, N.; Veciana, J.; Sala, S.; Cano-Sarabia, M. Method for Obtaining Micro- and Nano-Disperse Systems. US Patent 7,754,777, **2010**.

Design and synthesis of hybrid particles for tandem release of cannabinoids and chemotherapeutic drugs for the treatment of cancer tumors

ABSTRACT

Cancer has become one of the most difficult challenges of our time, accounting for millions of deaths each year. Cannabinoids (CBDs) have been extensively studied as chemotherapeutic drugs since they can inhibit tumor cell growth and induce apoptosis upon binding to the cannabinoid receptors that are overexpressed in cancer cells. Furthermore, examples in literature have shown that the combination of CBDs with chemotherapeutic agents enhances the antitumoral action. However, due to the poor solubility of CBDs and chemotherapeutic drugs, a new therapeutic strategy to deliver both agents into cancer tissues must be improved.

This chapter presents the design and synthesis of hybrid particles for the tandem release of cannabinoids and chemotherapeutic drugs for cancer treatments, based in the assemble of two main delivery systems PLGA@vehicles and MSNPs, for loading CBDs and chemotherapeutic drugs, respectively, in one system, resulting in an unprecedented hybrid tandem-delivery system (MSNPs@PLGA@vehicles) for the tandem release of two different drugs in two different parts of the target cells. Additionally, redox-organic stimulus MSNPs were synthesized to produce a material in which degradation induces silica debris to be easily removed from the body.

2.1. Introduction

Cancer has remained one of the largest medical challenges facing humanity, being the second leading cause globally accounted for 8.8 million deaths in 2015 according to the World Health Organization. The disease is characterized by the uncontrolled division of cells and their ability to spread.[1] This unregulated growth is caused by the damage to DNA, resulting in mutations, defects in cell cycles, and apoptotic machinery. Thus, agents that can modulate apoptosis can be useful for targeted therapy of cancer.[1]

Cannabinoids (CBDs) have been shown to inhibit tumor cell growth and induce apoptosis upon binding to the cannabinoid receptors that are overexpressed in cancer cells.[2] Moreover, several examples in the literature have shown that the combination of CBDs with chemotherapeutic agents enhances the antitumoral action.[3]

However, a major drawback of CBDs is their hydrophobicity, which limits their solubility in biologically relevant media. Therefore, improving their solubility remains an important challenge in CBDs research for cancer treatments.[2] For this, the main goal of this project is to implement a new strategy to entrap and deliver these drugs in targeting systems to enhance their activity. This means to build a new therapeutic platform capable to deliver both agents, CBDs and chemotherapeutic drugs, into cancer tissues. Their incorporation into polymeric carriers, implementing mesoporous silica nanoparticles (MSNPs) to load the chemotherapeutic drug, could be a feasible strategy. Once this system is administered to the body, CBDs should be released outside the cancerogenic membrane cells, where they will interact with the cannabinoid receptors that are present. Furthermore, the MSNPs will be internalized inside of these cells to then release the chemotherapeutic drug to enhance together the apoptosis of the cancerogenic cells. Although one of the main objectives is to treat cancerogenic cells, achieving a biocompatible and biodegradable system has been a crucial factor to consider in this thesis.

Therefore, here it is presented the use of a new hybrid system consisting of a combination of a polymeric material with the inclusion of mesoporous silica nanoparticles for the encapsulation and delivery of cannabinoids (CBDs) and chemotherapeutic drugs for the treatment of cancer.

Different kinds of mesoporous silica nanoparticles (MSNPs) were synthesized as models of the inorganic systems that can encapsulate an anti-cancer drug for the release of the chemotherapeutic drug. Moreover, breakable particles (redox stimuli response) were also produced as a degradable system, that will be included in this hybrid platform.[4] These silica NPs loaded with chemotherapeutic drugs, in turn, are loaded in poly(lactic-co-glycolic acid) (PLGA) carriers[5] which also contains an active endocannabinoid or its analog (CBDs), resulting in an unprecedented hybrid tandem-delivery system (CBDs-MSNPs@PLGA-MBds) (**Figure 2.1**).
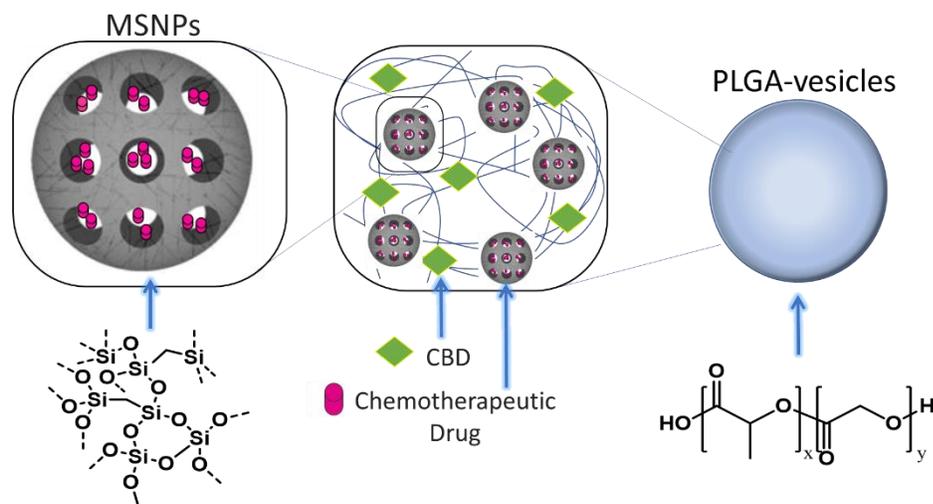
Figure 2.1. New hybrid system MSNPs@PLGA-vesicles for the tandem release of CBDs and chemoterapeutic drug.

The size of PLGA-vesicles and MSNPs had vital importance to the design of the new hybrid system (**Figure 2.2**). Monodisperse PLGA-vesicles with a diameter size in the range of 500 nm to 5 µm was required to have a carrier capable of releasing CBDS and MSNPs outside the cell, where the CBDs could be recognized by the CBs receptors present in the membrane of the cell[6] and the MSNPs could be taken by endocytosis inside the cell.[7] Studies in this field have demonstrated that the internalization of silica NPs is size-dependent, where MSNPs less than 100 nm in diameter show improved internalization and 50 nm particles show to have a maximum uptake.[8] Because of this, it was important to synthesize NPs with sizes between 30-50 nm that could have better cell internalization. It must be said that besides the size control in the synthesis of these materials, homogeneous PLGA vesicles and MSPNs had to be produced.

In the hybrid system, the MSNPs were not covalently linked but homogeneously dispersed in the PLGA. In the end, the main objective was to load two molecules, the CBDs and the chemotherapeutic drug to be after released in two different parts of the cell, to make them work in a synergetic way to induce the apoptosis of the cancer cell (**Figure 2.3**).
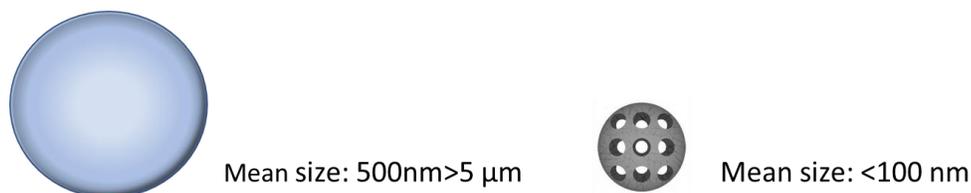
Figure 2.2. Size of the PLGA-vesicle and ss-NPs for the new hybrid system.
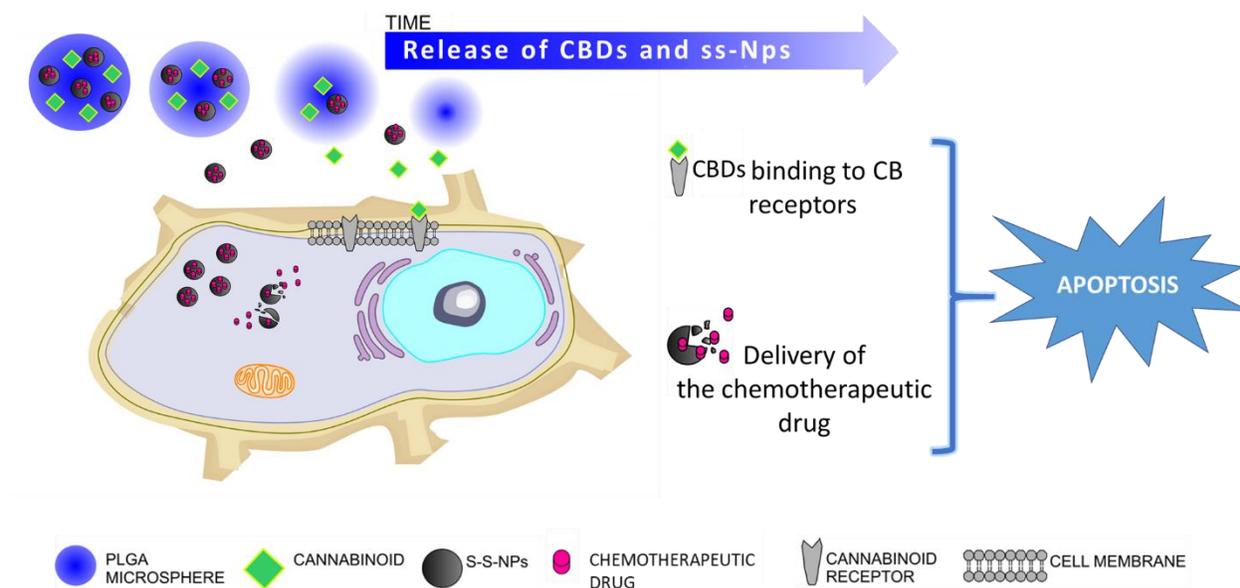
Figure 2.3. Hybrid mechanism system of the *ss*-NPs@PLGA-vesicles for the tandem release of CBDs and chemotherapeutic drugs.

These particles hold promise to deliver large drug concentration at the tumor sites while minimizing toxicity in healthy tissues. Systemic chemotherapy has been the most common therapeutic strategy methodology used and involves the intravenous administration of anti-cancer drugs at maximum tolerable doses with the undesirable side effect of collateral cell death.[9,10] The high dose administration is required because the chemotherapeutic drug has to cross several barriers before it is delivered in solid tumors (the transportation through the blood

circulatory system, across vasculature walls until it reaches the distant tumor sites).[11] These barriers result in a low therapeutic efficacy, as only a small portion of the administered drug reaches the tumor cells leading to ancillary toxicity to healthy tissues. Because of this, increased attention has been paid to localized delivery administration; where intratumoral injections or implantations are used to ensure a maximal therapeutic efficacy, with high doses in the targeting tumoral tissue and with minimal toxicity. Among all the materials, polymers have been extensively explored as a targeted drug delivery system,[12] been the PLGA a good candidate due to its biocompatibility and biodegradability.[13] Having said the above, the hybrid system described herein was designed to be used by intratumoral injections to ensure high drug localization in the tumor tissue for the main objective to improve the efficacy of the chemotherapeutic drug and the CBDs for the treatment of the cancer tumors (**Figure 2.4**).[12]
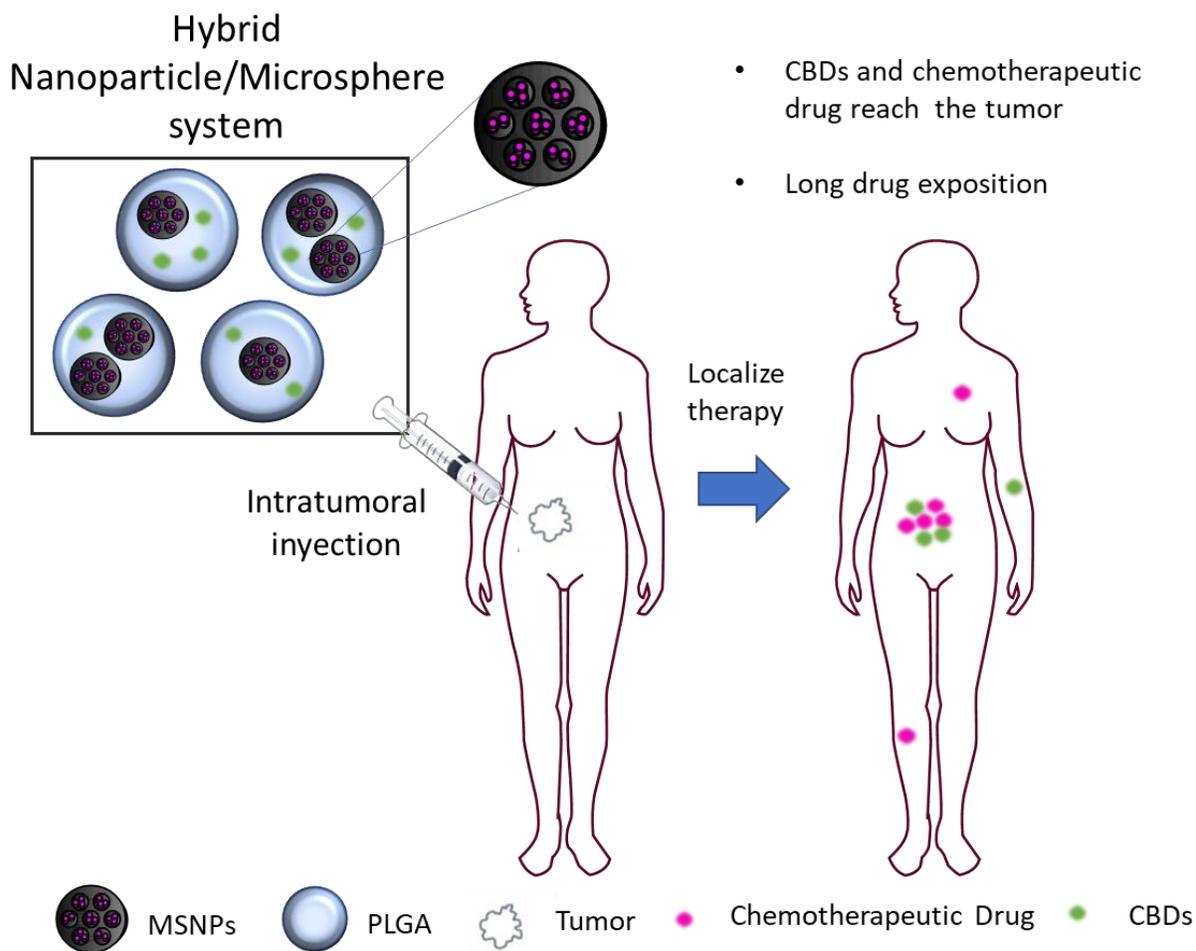
Figure 2.4. Administration approach for the Hybrid material to be used *in vivo* as a drug release cargo via Intratumoral injection.

2.2. Synthesis
2.2.1. Endocannabinoid and its analogs

Endocannabinoids are bioactive lipids that have a range of interesting activities mediated by two G-protein-coupled receptors (CB1 and CB2).[6,14] These molecules are increasingly appreciated for their role in inflammation and cancer.[15] The role of endocannabinoids in cancer has been implied by studies of the effects of exogenous cannabinoids, many derived from the plant *Cannabis sativa*, and synthetic compounds with activity at the CB1 and CB2 receptors.[16] The two primary endocannabinoids are anandamide (AEA) and 2-arachidonoylglycerol (2-AG). Studies have shown that endocannabinoids inhibit proliferation of cancer cells in culture and *in vivo*.[17,18]

Additionally, fatty acid amides are considered a new family of biologically important lipids as shown in different biochemical and pharmacological studies,[19,20] and they form part of the endocannabinoid family.[21] Studies with synthetic fatty acid amides show antiproliferative and anti-inflammatory activity against several tumor cell lines.[22–24] The effect of the endocannabinoid and fatty acid amides in cancer cell proliferation is reported to be by the binding to cannabinoids and vanilloids receptors.[2,15,25–29]

2.2.1.1. Synthesis of N-(2-fluoroethyl) oleamide (2FEO) and N-(2-hydroxy ethyl) oleamide (2HEO) as analogs of endocannabinoids, and anandamide (AEA) an active endocannabinoid.

N-(2-fluoroethyl)oleamide (2FEO)[30] and N-(2-hydroxy ethyl) oleamide (2HEO)[29] were synthesized as analogs of endocannabinoids, while anandamide (AEA)[31] was synthesized as an active specie. These compounds have pharmacologic activity similar to THC;[32] as they can bind to the cannabinoid receptors, inhibiting tumor cell growth and inducing apoptosis by modulating different cell signaling pathways in cancer cells.[24]

For the synthesis of 2HEO, a peptide coupling reaction was performed using oleic acid, HBTU as a coupling agent, and the 2-(fluoroethyl)amine (Scheme 2.1A). To produce 2HEO and AEA, the reactions were performed in two steps from their respective carboxylic acids (oleic and arachidonic acid). 1) A Fischer Esterification with H_2SO_4 and MeOH followed by a 2) Reaction with ethanolamine in presence of sodium methoxide in acetonitrile to produce the corresponding amides (Scheme 2.1B).
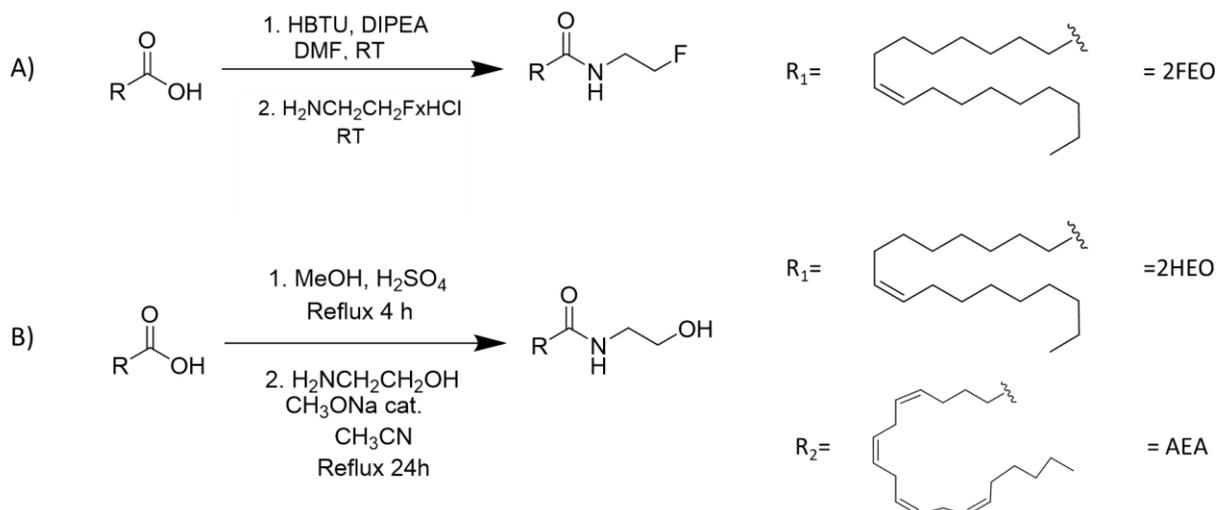
Scheme 2.1. A) Synthesis of 2FEO from oleic acid (R1) and **B)** Synthesis route of 2HEO and AEA from oleic acid (R1) and arachidonic acid (R2), respectively.

Synthesis of 2FEO

The synthesis of 2FEO was achieved through a peptide coupling reaction using HBTU as the coupling reagent with a combination of oleic acid and N,N-Diisopropylethylamine (DIPEA) in N,N-Dimethylformamide (DMF) under N_2 atmosphere for 5 minutes. 2-(fluoroethyl)amine hydrochloride was subsequently added and the mixture was stirred for 2 days at RT. The final product was a white waxy solid with a 69% of yield. ^{1}H NMR (δ 5.8 ppm, N–*H*) and ^{19}F NMR (δ −224.3 ppm, F-H) confirms the formation of the amide. ^{13}C NMR, IR and HR ESI-TOF-MS (327.3 g/mol) were done to complete its characterization (see experimental part 2.5.2.1).

Synthesis of 2HEO

Methyl oleate was prepared through a Fischer esterification of the corresponding carboxylic acid in methanol, generating a yellow oil/solid with a yield of 99.7% after 4h. The confirmation of the compound was characterized by ^{1}H NMR (δ 3.65 ppm, O-CH₃) and IR. The methyl oleate was reacted with ethanolamine in acetonitrile at reflux for 24h to obtain 2HEO with 86.5% of yield. The confirmation of the amide was obtained by ^{1}H NMR (δ 5.87 ppm, N–*H*). Further characterization was done with ^{13}C NMR, IR and HR ESI-TOF-MS (325.5g/mol) (see experimental part 2.5.2.2).

<u>Synthesis of AEA</u>

To synthesize AEA, arachidonic acid was esterified in methanol, obtaining a yellow oil in a 77% yield after 6h of reaction. The confirmation of the compound was obtained by ^{1}H NMR (δ 3.67 ppm, O-CH$_3$), ^{13}C NMR, IR and HR ESI-TOF-MS (318.26 g/mol) (see experimental part/synthesis of the Methyl arachidonate). Anandamide was finally obtained putting the Methyl arachidonate in presence of ethanolamine in Acetonitrile and refluxing for 24h, obtaining a brown oil in a 52% yield. ^{1}H NMR (δ 5.37 ppm, N–H) confirms the formation of the amide. ^{13}C NMR, IR and HR ESI-TOF-MS (347.28 g/mol) were done to complete its characterization (see experimental part 2.5.2.3).

2.2.2. Synthesis of MSNPs

<u>Synthesis and characterization of MSNPs</u>

To load the PLGA@carrier with MSNPs, several NPs were synthesized. The NPs that were synthesized as a potential carrier of the chemotherapeutic drug are illustrated in **Figure 2.5**. The particles synthesized are divided into two main groups, (1) non-breakable and (2) breakable NPs. For the first group (1): non-breakable NPs (NB-NPs), NPs with Dodecyltriethoxysilane groups (Dodecyl-NPs), and NPs with 1H,1H,2H,2H-Perfluoro-Octyltriethoxysilane (PFTOS) groups (PFOTS-NPs), were synthesized. The last two particles were synthesized as a new type of silica NPs modified with hydrophobic groups to increase hydrophobic interaction between the NPs and the hydrophobic loaded drugs (endocannabinoids). Also, Non-breakable NPs modified with APTES and Fluorescein isothiocyanate (FITC) were prepared (FTIC-NB-NPs).

For the second group (2): Breakable NPs with bis(triethoxysilyl-propyl)disulfide (BTSPD) linker (*ss*-NPs) (*ss*-NPs of ~100 nm), breakable NPs modified with APTES and Fluorescein isothiocyanate (FITC) to produce the FTIC-ss-NPs (*ss*-NPs of ~50 nm).
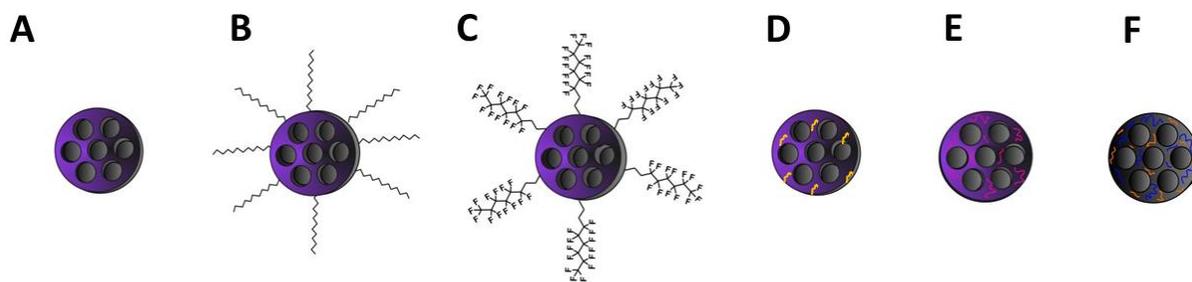
Figure 2.5. Potential MSNPs synthetized as carriers of the chemotherapeutic drug. **A)** NB-NPs, **B)** Dodecyl-NPs, **C)** PFOTS-NPs, **D)** FITC-NB-NPs, **E)** Breakable ss-NPs, and **F)** FITC-ss-NPs.

To produce MSNPs, a surfactant is used as a template for the silica. The most common surfactant is Cetrimonium bromide (CTAB). In 2001, CTAB-templated silica NPs were starting to be used as drug delivery systems,[33] and since then, it has been increased the attention in the field of nanomedicine.[34–38]. Two different methodologies were used in this thesis to synthetized the MSNPs: A) a modified Stöber process[39] and B) micelle templating method (**Figure 2.6A** and **B,** respectively).[40] The Stöber has been one of the most used methodologies for the synthesis of silica nanoparticles. It is a sol-gel process, that requires two steps: the hydrolysis and condensation of a molecular building block silane (*e.g.* tetraethyl orthosilicate (TEOS)) in presence of water in an alcoholic solution in basic or acidic conditions. While in the micelle templating method (another modification of the Stöber process), cationic micelles are formed (*e.g.* with CTAB) followed by the formation of oil drops of the silane (*e.g.* TEOS). The hydrolysis only occurs at the water-oil interface (thus allowed by electrostatic interactions between the micelle and the oil drop surface).[40] This condensation is carried out by triethanolamine (TEA), acting as a catalysis base for the hydrolysis of the silane, which also controls the reaction, acting as a complexing agent affecting the nucleation of MSNPs and avoiding agglomerations.[41] With these approaches MSNPs can be synthesized in a range of size from 20 to 110 nm.[40]
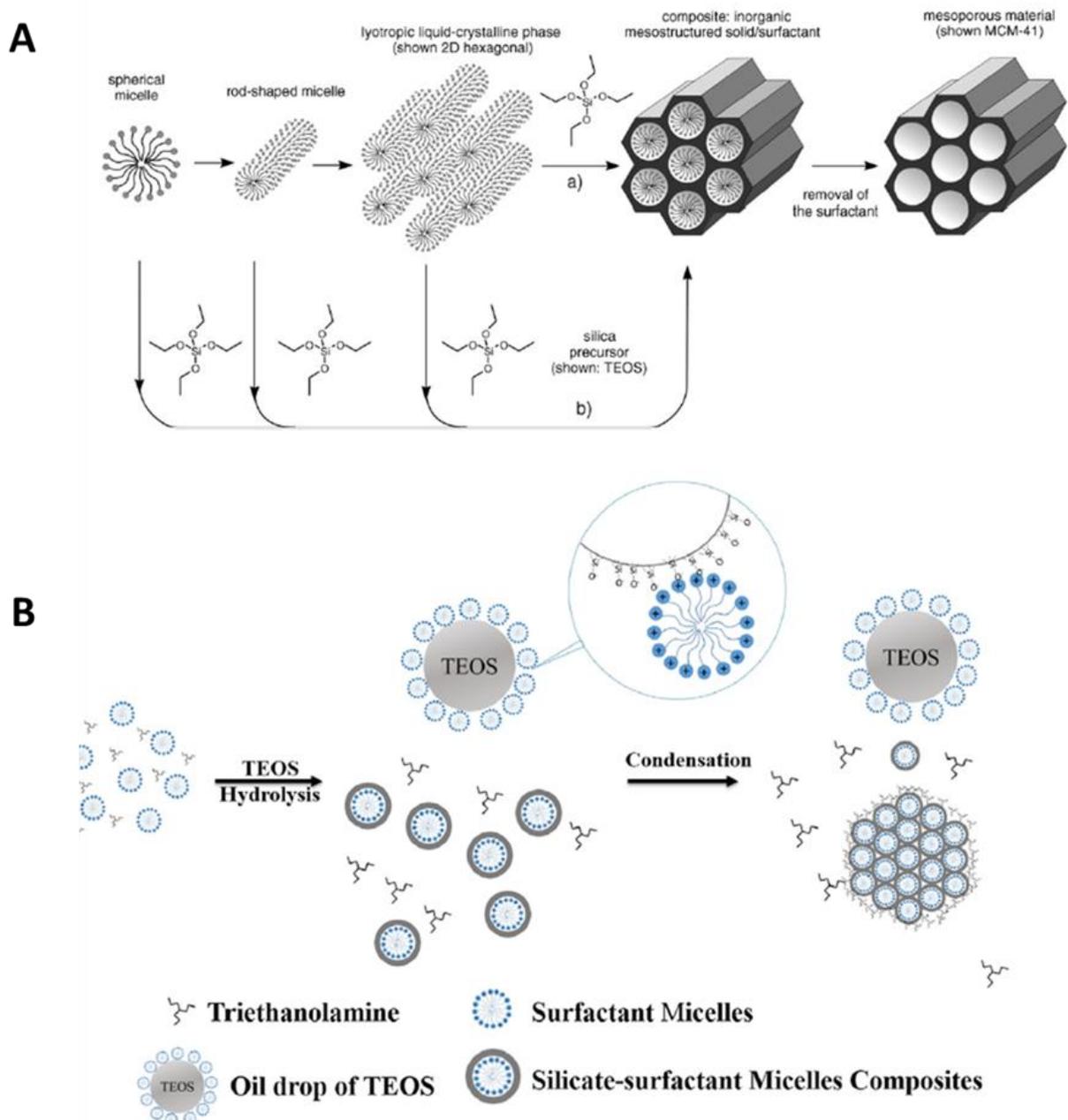
Figure 2.6. A) Representation of the templated synthesis of MSNPs (Stöber process), following a) true liquid crystal template and b) cooperative liquid-crystal template mechanism. **B)** Mechanism of the formation of MSNPs through micelle templating. Adapted with permission from ref 40 (Copyright 2016, Elsevier) and 42 (Copyright 1992, Macmillan Publishers Limited).

As it was said, the MSNPs prepared throughout this work utilize either method, where the selection of a methodology depended on the observed dispersity for the NPs prepared. In general, all the syntheses presented here were focused in obtain particles with diameter sizes

below 100 nm. The particles were characterized by different techniques such as SEM, STEM, DLS, EDX, XPS, IR, TGA, N_2 adsorption measurements and SAXS.

2.2.2.1. Synthesis of Non-Breakable MSNPs

Synthesis and characterization of NB-NPS

NB-NPs nanoparticles were synthesized using the micelle template method.[40] CTAB is used as a template for the formation of the pores and TEA as a catalyst for the reaction. TEOS is added as a silane for its condensation and after 1h at 95 °C under stirring, the particles are formed (see **Scheme 2.2**). After cleaning them from the reaction components and the CTAB, the particles were then characterized by SEM, EDX, IR, TGA, and N_2 adsorption.
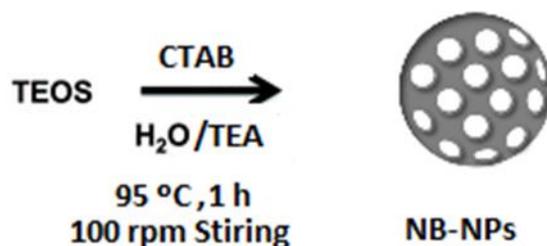
Scheme 2.2. Synthesis of NB-NPs particles using a micelle templating methodology.

Morphological characterization was performed using scanning electron microscopy (SEM) (**Figure 2.7A**). The NB-NPs display a monodisperse and homogeneous spherical morphology, with a particle size average diameter of 82±6 nm. The monodispersity of these particles was analyzed by measuring the diameter size of 100 particles and fitting the results to a gaussian plot. **Figure 2.7B** shows the Energy-dispersive X-ray spectroscopy analysis (EDX), where silicon and oxygen are observed at the surface of the material. **Figure 2.7C** present the IR spectrum of the NB-NPs where is shown the characteristic peak attributed to the presence of the Si-O bond at 1050 cm^{-1}. Thermogravimetric analysis (TGA) (**Figure 2.7D**) reveals the presence of 4.4% of organic material. To see the porosity of the system, N_2 adsorption measurements analysis were done (**Figures 2.7E** and **F**). These analyses show the NPs have a total pore volume of 1.09 $cm^3\,g^{-1}$ and a surface area of 789 $m^2\,g^{-1}$ with an average pore size of 2.8 nm.
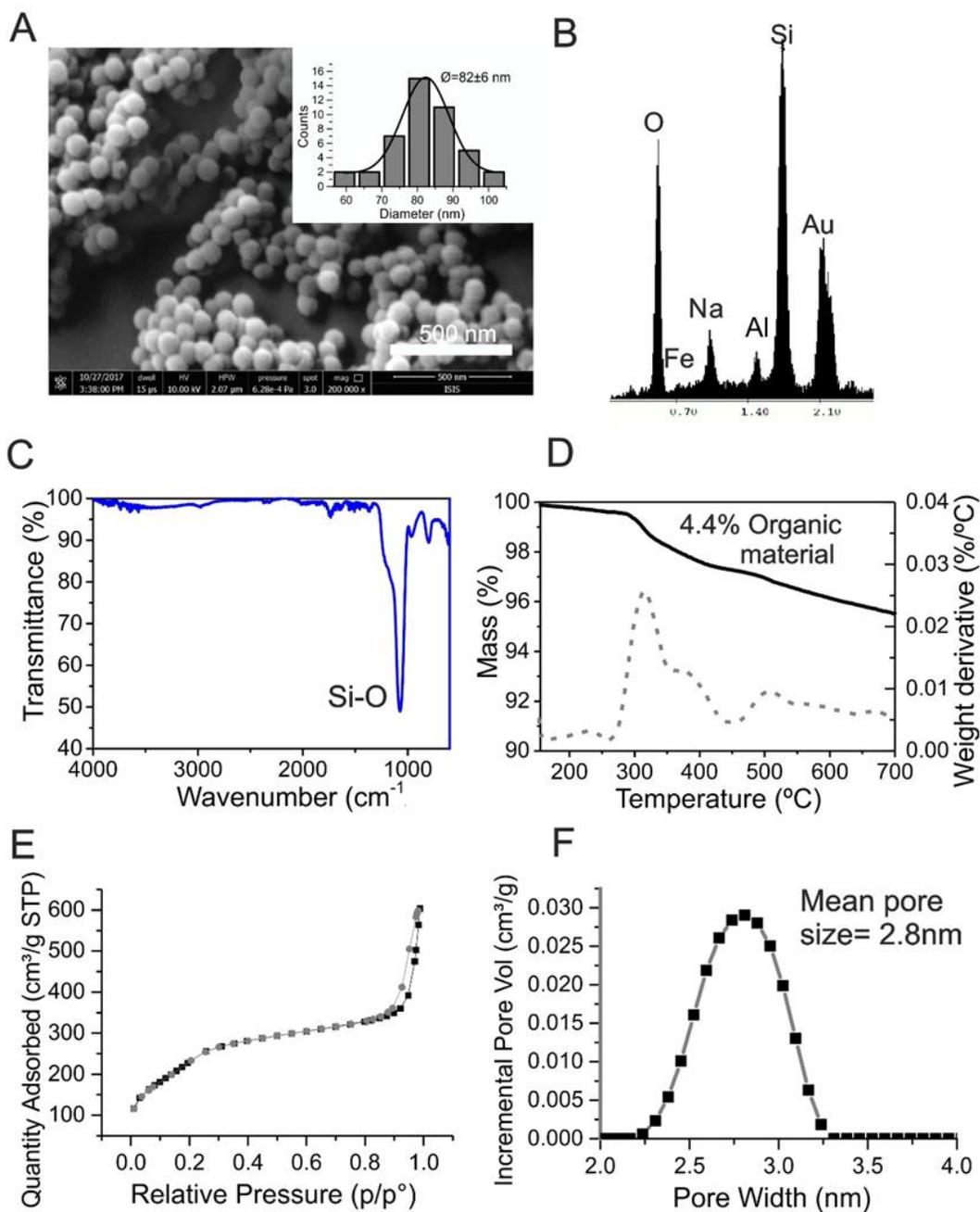
Figure 2.7. A) SEM and size distributions (count performed on 100 nanoparticles; average diameter 82±6 nm), **B)** EDX analysis and **C)** IR spectrum, **D)** TGA curve (the dashed line represents the derivative curve of the wt% loss; 4.4% Organic material), **E)** N_2 Adsorption/desorption curve, **F)** Pore size distribution obtained from N_2 adsorption analysis (average pore size 2.8 nm) of the Non-breakable particles.

Synthesis and characterization of Dodecyl-NPs

The synthesis of dodecyl-NPs was achieved through the micelle templating methodology (**Scheme 2.3**), where CTAB was the surfactant used to produce the pores and TEA acted as the

114

base catalysis of the reaction. The organic moiety dodecyltriethoxysilane (dodecyl) was inserted in the TEOS framework in a molar ratio 95:5 TEOS: Dodecyl and the reaction was run for 1 h at 95 °C and 100 rpm. After, the particles were washed with water and EtOH and a reflux with HCl was put to remove the surfactant from the NPs, making then porous. After a second post-treatment of washings, Dodecyl-NPs were characterized SEM, EDX, XPS, IR, TGA, N$_2$ adsorption techniques and SAXS.
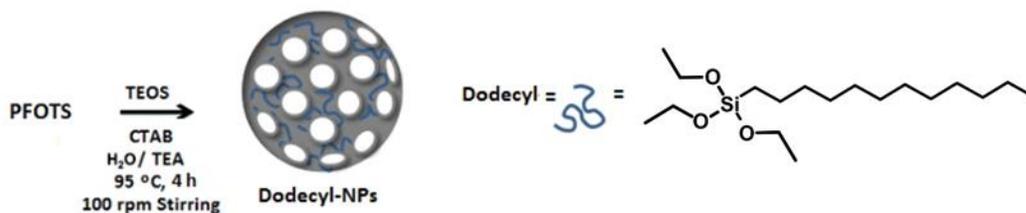
Scheme 2.3. Synthesis of dodecyl-NPs particles through the micelle templating method.

From SEM images, the morphologic characterization of dodecyl-NPs was started, showing a monodisperse homogeneous spherical morphology (**Figure 2.8A**). The monodispersity of these particles was analyzed by measuring the diameter size of 300 particles (counted from the SEM pictures) and fitting the results to a gaussian plot. The size average diameter of these particles was 137±9nm (**Figure 2.8A top**).

IR spectra showed the characteristic Si-O stretch at 1064 cm^{-1} (**Figure 2.8B**). The ratio between organic/inorganic moieties was characterized by TGA (**Figure 2.8C**), revealing a weight loss of 7% of organic material, which corresponds to the dodecyl silane moiety present in the framework of the NPs. This information tells than the efficiency of the incorporation of the silane is 44% (%Organic material expected = 16%).

EDX experiments show the presence of silicon, carbon and oxygen in the particles (**Figure 2.8D).** These results were corroborated with XPS experiments, exposing the presence of Oxygen (O1s), Carbon (C1s), and Silicium (Si2p) (**Figure 2.8E**), which confirms the presence of the dodecyl silane constructed by the alkyl chain. **Figure 2.8F** shows the deconvolution of the C1s peak, showing two characteristic bands of the presence of C-O and C-C bonds. This information says that there are dodecyl moieties inserted in the framework but there are some ethoxy groups that have not been reacted.
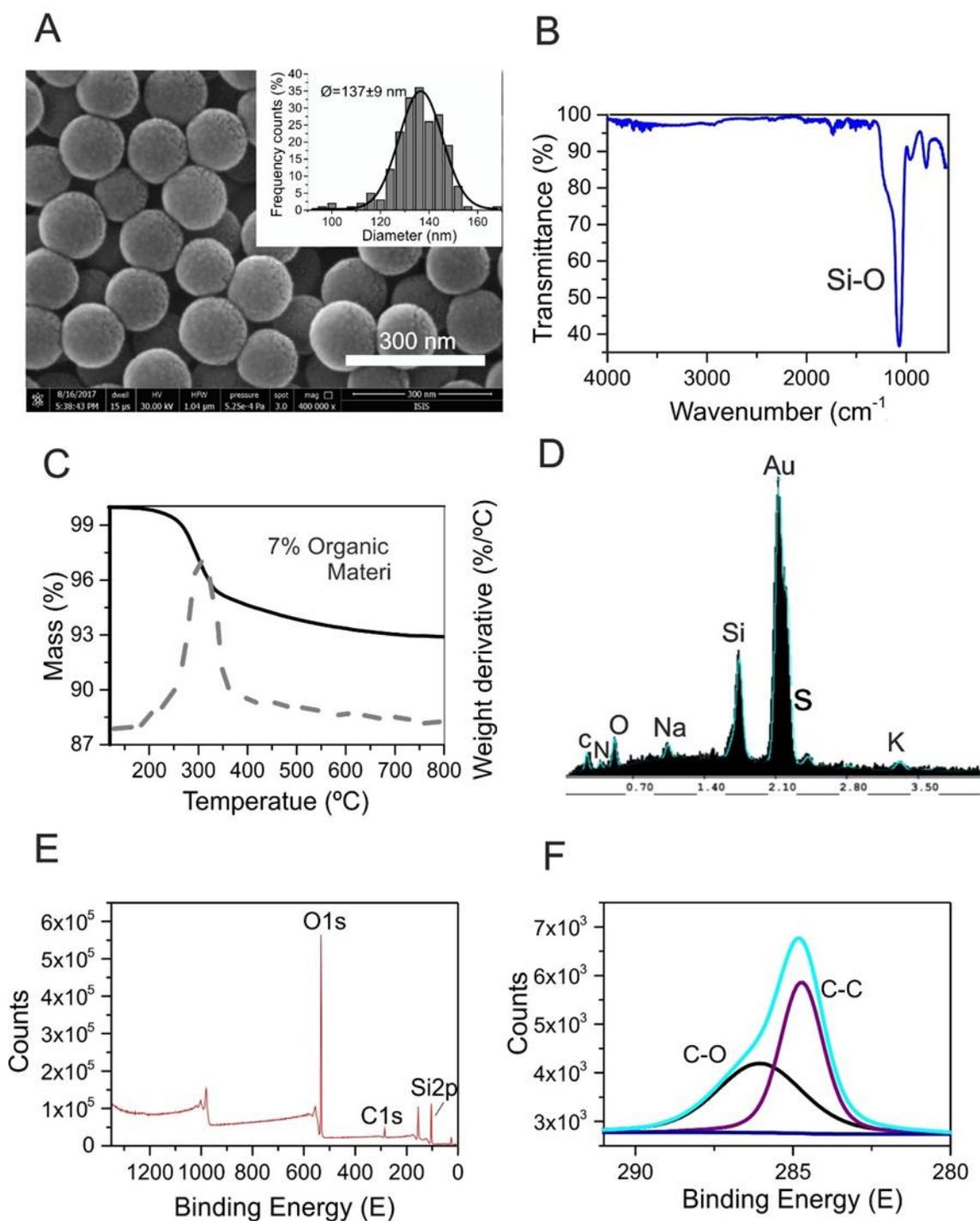
Figure 2.8. A) SEM and size distributions (count performed on 300 nanoparticles; average diameter 137±9 nm), **B)** IR analysis, **C)** TGA curve (the dashed line represents the derivative curve of the wt% loss; 7% Organic material) **D)** EDX, **E)** and **F)** XPS survey spectra of Dodecyl NPs.

To study the porosity in the system, N$_2$ adsorption measurements were performed. The N$_2$ adsorption/desorption curves show that the particles have a total pore volume of 1.14 cm^3 g^{-1}

and a BET surface area of 474 m^2g^{-1}, while the pore size distribution shown an average pore size of 3.5 nm (**Figure 2.9A** and **B**). To analyze the organization of their porosity, SAXS analysis was done. Showing a mesoporous NPs, with the characteristic (100) Bragg peak. Nevertheless, it is not observed the (110) and (200) peaks, showing that it is a certain relative order microphase of the porous, but also a disorder pore arrangement due to the presence of the Dodecyl moiety in the framework.
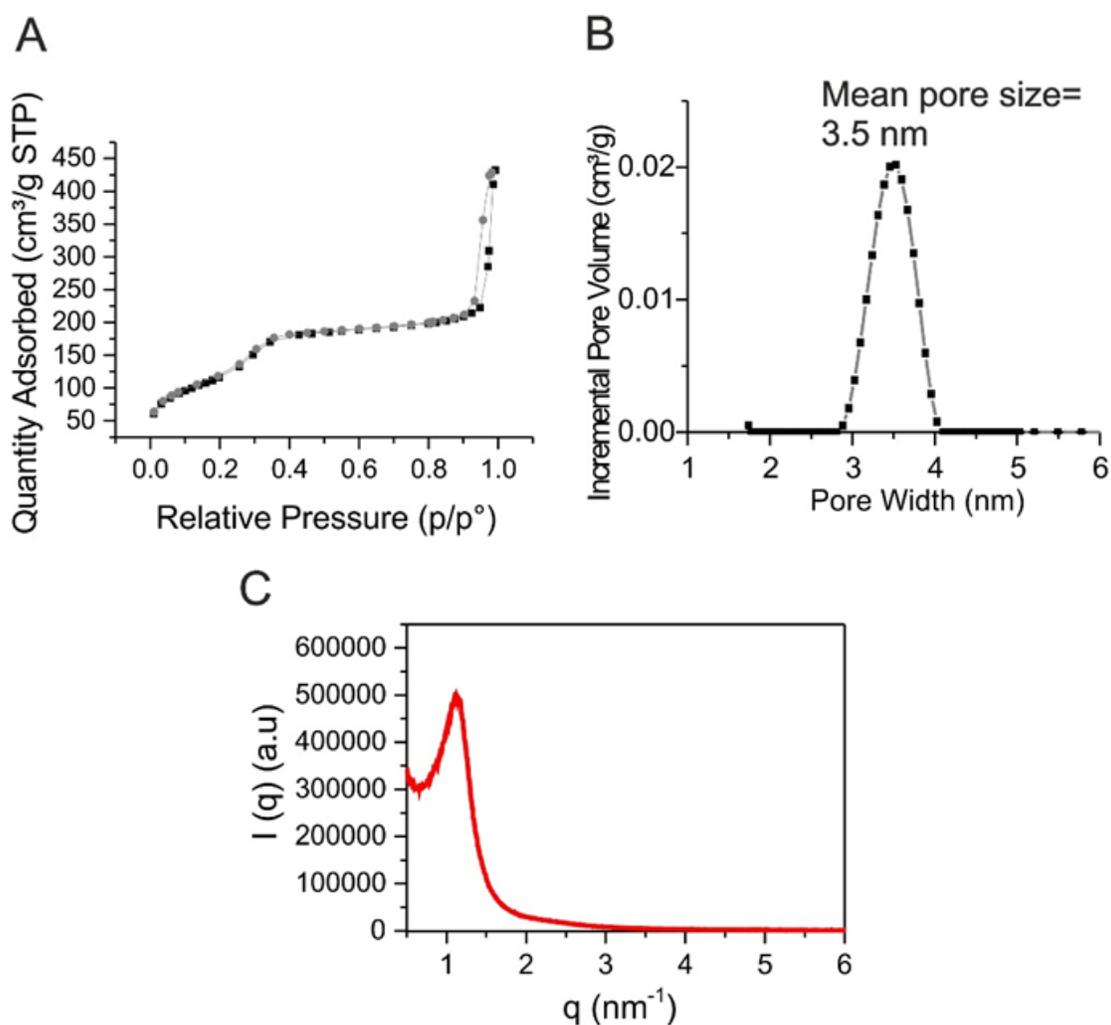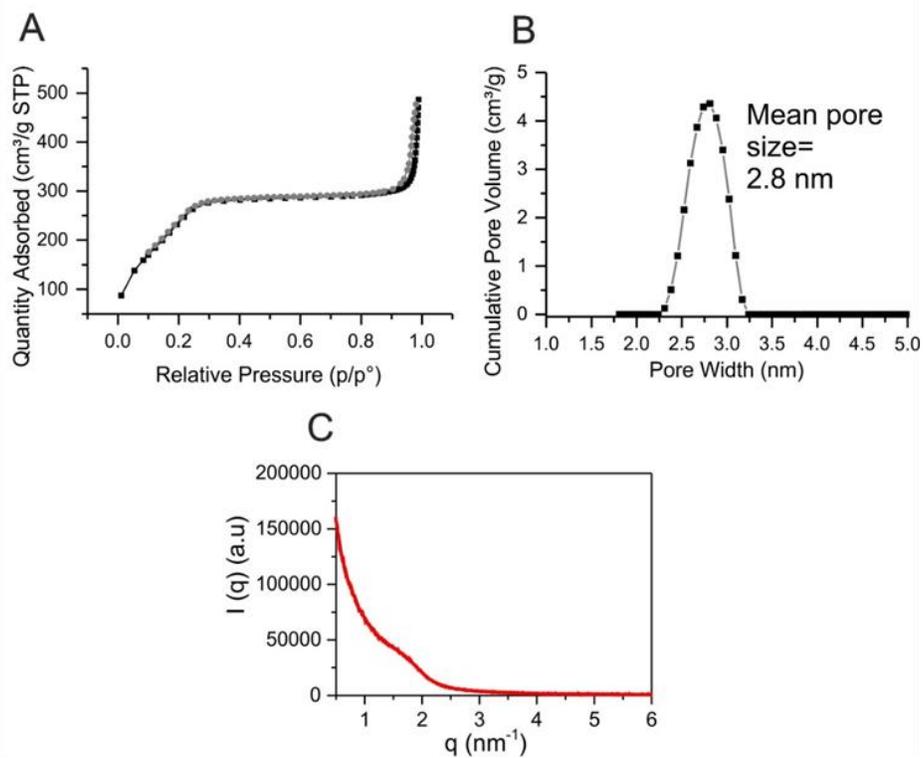

Figure 2.9. A) N_2 Adsorption/desorption curve, **B)** Pore size distribution obtained from N_2 adsorption analysis (Average pore size 3.5 nm) and **C)** SAXS analysis of the Dodecyl NPs.

Synthesis and characterization of PFOTS-NPs

PFOTS-NPs were prepared through a modified Stöber process (**Scheme 2.4**). CTAB was the surfactant and NaOH the base catalysis of the reaction. The organic moiety 1H,1H,2H,2H-

Perfluoro-Octyltriethoxysilane (PFOTS) was inserted in the TEOS framework in a molar ratio 95:5 TEOS:PFOTS. The reaction was run for 6h at 80 °C. Afterwards, the particles were treated as before described; washing, reflux with HCl and more washings to remove the surfactant from the NPs. PFOTS-NPs were characterized by SEM, EDX, XPS, IR, TGA, N_2 adsorption techniques and SAXS.

Scheme 2.4. Synthesis of the PFOTS particles using a micelle templating methodology.

Morphological characterization of the PFOTS-NPs was performed through SEM and scanning transmission electron microscopy (STEM) (**Figure 2.10A** and **B**). The PFOTS display a homogeneous spherical morphology with a particle size average diameter of 100±15 nm (counting of 100 particles from STEM images (**Figure 2.10B** top)). To corroborate this size and dispersity, DLS measurements were performed and showed one distribution of particles around 165±35nm (**Figure 2.10C**), which roughly coincides with the value calculated by the counting of NPs. IR spectra shows the presence of the characteristic pick Si-O bond at 1070 cm^{-1} (**Figure 2.10D**).

The incorporation of the PFOTS moieties was demonstrated by TGA, EDX and XPS analyses. TGA analysis show that 22% of the weight of the particle is organic material (**Figure 2.10E**); demonstrating than the efficiency of the incorporation of the silane is 22% (%Organic material expected = 25%). EDX analyses show the presence of F and C in the nanoparticles demonstrating the presence of perfluoro-octyl-silane in the NPs (**Figure 2.10F**). XPS analyses confirm these observations showing the presence also of the F and C elements (**Figure 2.11**). Moreover, **Figure 2.11B** shows the presence of two different fluorides CF_2 and CF_3 bonding to the carbon atoms in the chain of PFTOS molecule (CF3 and CF2) and the confirmation of C-C bonds. In **Figure 2.11C** is shown the presence of fluorine in the NPs.

The porosity of the PFOTS particles was studied using N_2 adsorption analysis, showing a total pore volume of 0.7528 $cm^3\,g^{-1}$ and a surface area of 917±29$m^2\,g^{-1}$ with an average pore size of 2.8 nm (**Figure 2.12A** and **B**). SAXS studies were done to see the porosity order and it is observed a single broad Bragg peak (100) (**Figure 2.12C**), suggesting a disorder in the porosity of the NPs after the incorporation of PFOTS.
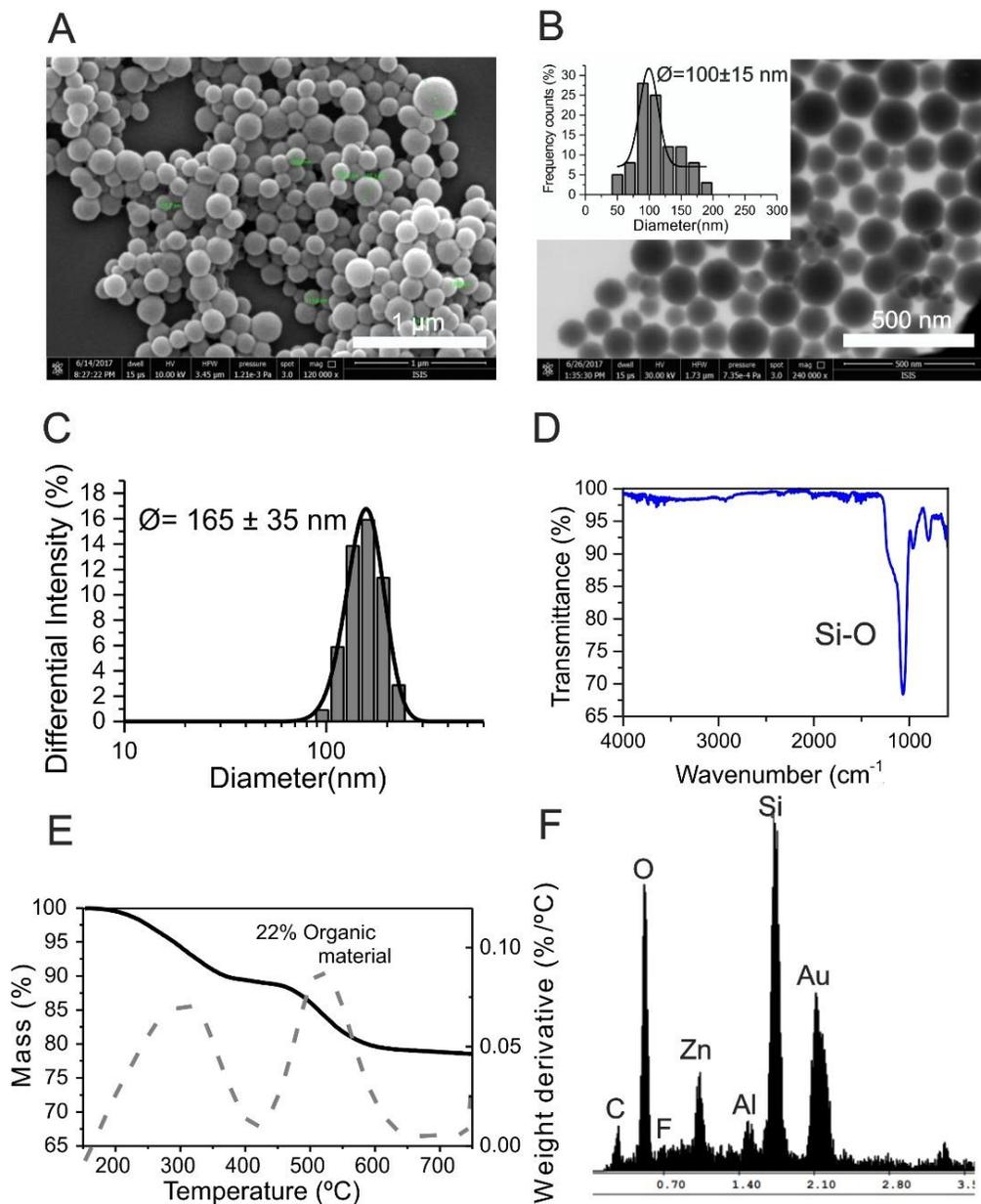
Figure 2.10. **A)** SEM and **B)** STEM size distributions (count performed on 300 nanoparticles; average diameter 100±15 nm).**C)** DLS analysis (average size diameter = 165±35 nm. **D)** IR analysis. **E)** TGA curve (the dashed line represents the derivative curve of the wt% loss; 22% Organic material) and **F)** EDX survey spectra of the PFOTS- NPs.
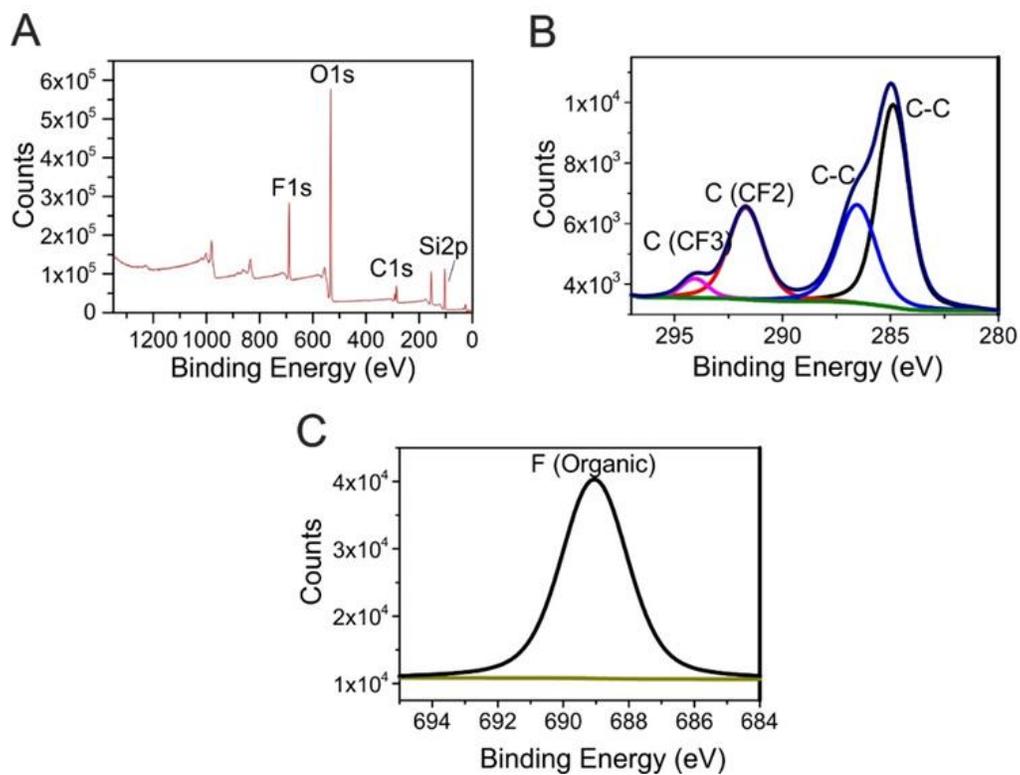
Figure 2.11. XPS survey spectra of the of PFOTS nanoparticles.

Figure 2.12. A) N_2 Adsorption/desorption curve, **B)** Pore size distribution obtained from N_2 adsorption analysis (Average pore size 2.8 nm) and **C)** SAXS analysis of the PFOTS nanoparticles.

Synthesis and characterization of FITC-NB-NPs

FITC-NB-NPs were prepared through a modified micellar templating process (**Scheme 2.5**). CTAB was the surfactant to produce the pores and TEA the base catalysis of the reaction. The organic moiety (3-aminopropyl)triethoxysilane (APTES) was reacted with FITC and inserted in the TEOS framework by mixing this solution with this silane before their addition to the CTAB solution. After 1h of reaction at 95 °C and under stirring 400 rpm, the particles were washed with EtOH and refluxed with HCl to remove the surfactant from the NPs. After a second post-treatment of washings, FITC-NB-NPs were dried and characterized by SEM, EDX, XPS, IR, TGA, N_2 adsorption techniques, SAXS and by photophysical studies.

Scheme 2.5. Synthesis of the FITC-NB-NPs particles using a micelle templating methodology.

The morphological characterization of these NPs was performed using SEM (**Figure 2.13A**). The FITC-NB-NPs display a monodisperse homogeneous spherical morphology with a particle size average diameter of 59±6nm (determined from 300 nanoparticles counting). DLS measurements determined an average size diameter of 82±17 nm (**Figure 2.13B**), in reasonable agreement with the counting method.

N_2 adsorption found a total pore volume of 1.06 $cm^3 \, g^{-1}$ and a BET surface area of 612 m^2/g, while from the pore size distribution is shown the average pore size of 3.7 nm (**Figure 2.13C** and **D**).

Photophysical studies were performed (**Figure 2.13E** and **F**). **Figure 2.13E** shows the absorption, emission, and excitation peaks of the FITC in the NPs, with a maximum excitation band at 478 nm and maximum emission at 516 nm that reveals the presence of the dye in the silica framework structure (in literature the maximum excitation band of the free dye is at 493 nm with maximum

emission at 519 nm). **Figure 2.13F** shows the lifetime of the dye in NPs τ_1=2.89 ns and τ_2=0.6 ns, 65 and 33%, respectively.
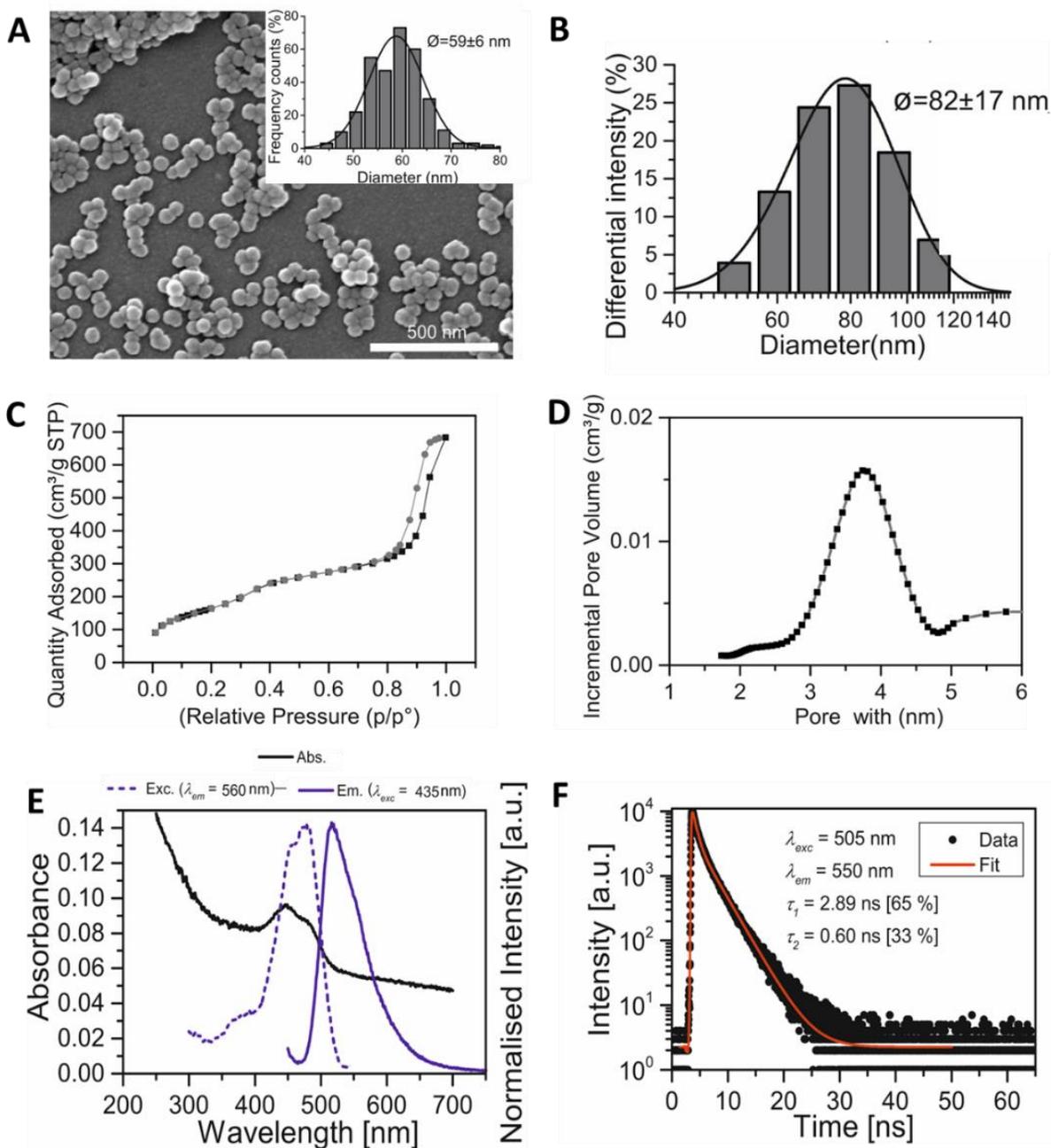
Figure 2.13. **A)** SEM and SEM distribution diameter size (counting performed on 300 nanoparticles FITC-NB-NPs; average diameter 59±6 nm). **B)** DLS analysis (average size diameter = 82±17 nm. **C)** N_2 Adsorption/desorption curve. **D)** Pore size distribution obtained from N_2 adsorption analysis (Average pore size 3.9 nm). **E)** Photophysical characterization of the FITC-NB-NPs. Absorption, emission, and excitation spectra (black line, blue full line, and blue dashed line, respectively). Wavelength of excitation and emission were 435 and 560 nm, respectively. **F)** Lifetime of the FITC-NB-NPs.

2.2.2.2. Synthesis of Breakable MSNPs

Synthesis and characterization of Breakable *ss*-NPS

ss-NPs nanoparticles were prepared through a modification of Stöber process.[4] Maggini L. synthetized in 2016 an organic modified MSNPs using Bis(triethoxysilylpropyl)tetrasulfide (BTSPD) and TEOS, 30:70 molar ratio. The redox-organic responsive NPs breaks in presence of glutathione (GSH), a reducing agent present in higher concentrations in cancer cells.[43–46] Those NPs could then breakdown releasing the cargo and cleaving in small pieces, preventing then the accumulation of the silica NPs in the body.[4]

The reaction was performed using CTAB as a template surfactant, while BTSPD:TEOS was added into a basic ethanol-water mixture, where the base causes hydrolysis of the silane. The synthesis was carried out for 6h at 80 °C and the reaction was stopped by washing the NPs with several cycles of centrifugation (**Scheme 2.6**). The surfactant is removed with HCl reflux and dried under vacuum. Finally, the NPs were characterized by SEM, DLS, EDX, XPS, IR, TGA, N_2 adsorption techniques and SAXS.
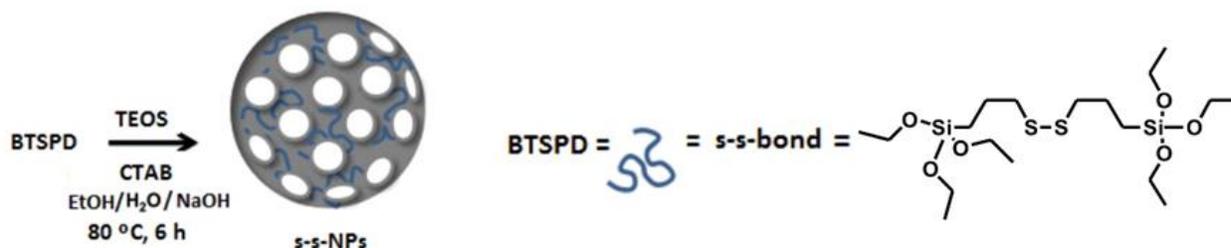
Scheme 2.6. Synthesis of *ss*-NPs particles prepared through a modification of Stöber process.

The morphology of these NPs was characterized by SEM that showed a homogeneous spherical morphology. The monodispersity of these particles was analyzed by measuring the diameter size of 300 particles and using a gaussian fit to determine the particle diameter and standard deviation. The size average diameter of these particles was 112±16 nm (**Figure 2.14A**). Dynamic light scattering analysis (DLS), the average size diameter of the *ss*-NPs was 195±47 nm (**Figure 2.14B**). This value suggests that some of the NPs were not totally dispersed at the time that the DLS was done, so agglomerations were observed.

EDX analysis was performed and with this data, it was observed the presence of silicon, sulfur and oxygen in the particles (**Figure 2.14C**). IR spectra shows the presence of the characteristic

pick Si-O bond at 1050 cm^{-1} (**Figure 2.14D**). The presence of the cleavable moiety within the NPs also is confirmed by elemental analysis of the material through an X-ray photoelectron spectroscopy analysis (XPS). **Figure 2.14E** shows the presence of oxygen (O1s), carbon (C1s), sulfur (S2p) and silicon (Si2p). Being the oxygen and silicon part of the silica framework and the carbon and sulfur part of the silica framework due to the presence of the organic linker. Furthermore, **Figure 2.14F** shows the deconvolution of the sulfur pick, where is visible the 3 characteristic bands for the S2p level.

Additionally, the ratio between organic/inorganic moieties was characterized by TGA (**Figure 2.14G**), revealing a weight loss of 28.8% due to the organic material which corresponds to the organic disulfide linker present in the framework of the NPs. The efficiency of the incorporation of the linker BTSPD silane is calculated giving a value of 65% (%Organic material expected = 44%). To study the porosity in the system, N$_2$ adsorption measurements were done. From the N$_2$ adsorption/desorption curves obtained, it can be observed that these particles have a total pore volume of 0.93 cm^3 g^{-1} and a BET surface area of 779 m^{2}g^{-1}, while from the pore size distribution is shown the average pore size of 1.9 nm (**Figure 2.15A** and **B**). To confirm the mesoporosity of the *ss*-NP, Small-angle X-ray scattering (SAXS) studies were performed (**Figure 2.15C**). These NPs show the characteristic (100) Bragg peak, but not the (110) and (200) peaks, saying that there is a certain relative order microphase of the porous and also a disorder pore arrangement due to the presence of the organic linker. Furthermore, SAXS experiments were used to calculate the average pore size, giving a value of 1.93 nm; a value that coincides with the one obtained using N$_2$ Adsorption measurements.
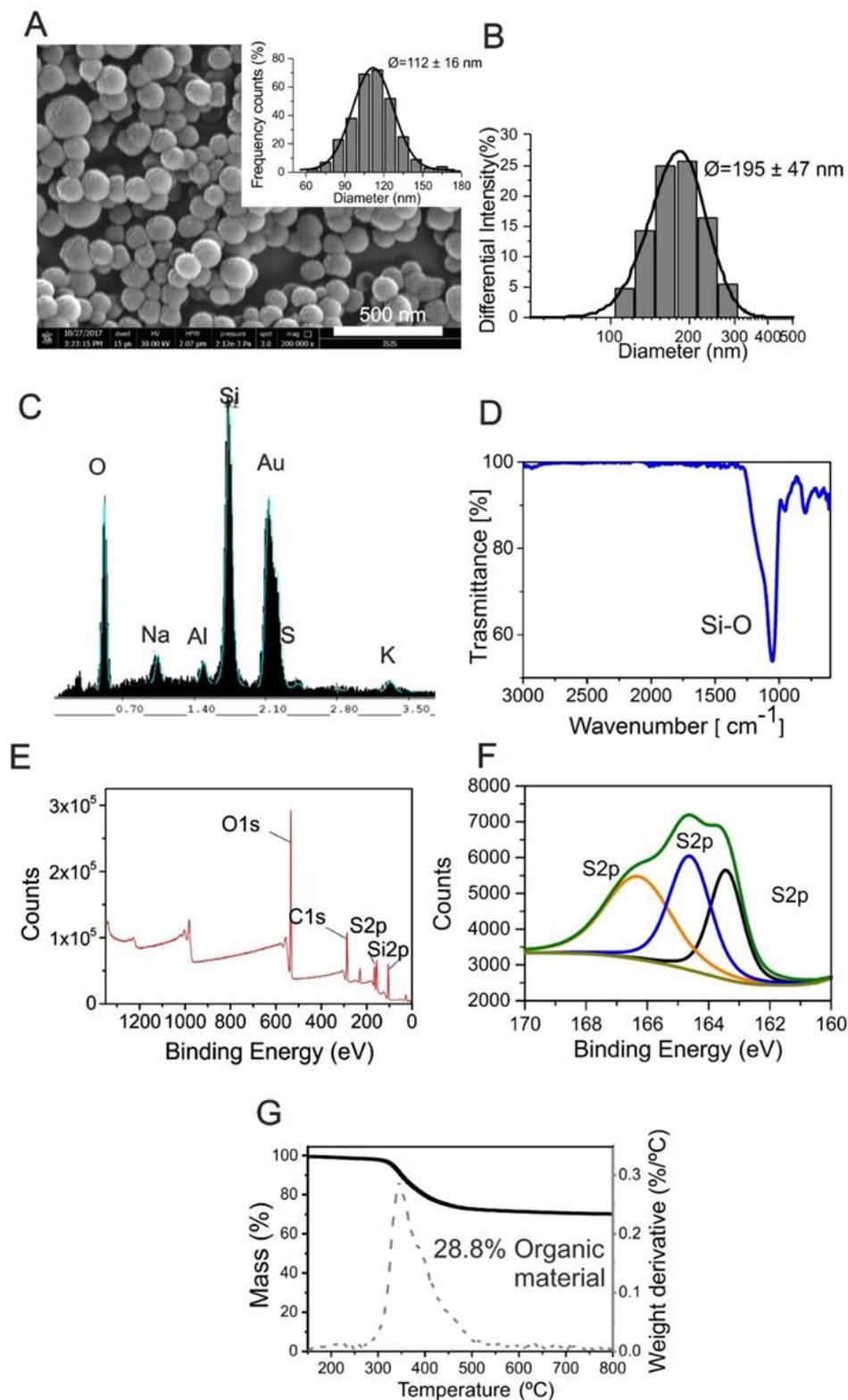
Figure 2.14. A) SEM and size distributions (count performed on 300 nanoparticles; average diameter 112±16 nm). **B)** DLS analysis (average size diameter =195±47 nm. **C)** EDX and **D)** IR analysis, **E)** and **F)** *XPS* survey spectra and *G)* TGA curve (the dashed line represents the derivative curve of the wt% loss; 28.8% Organic material) of the ss-NPs.
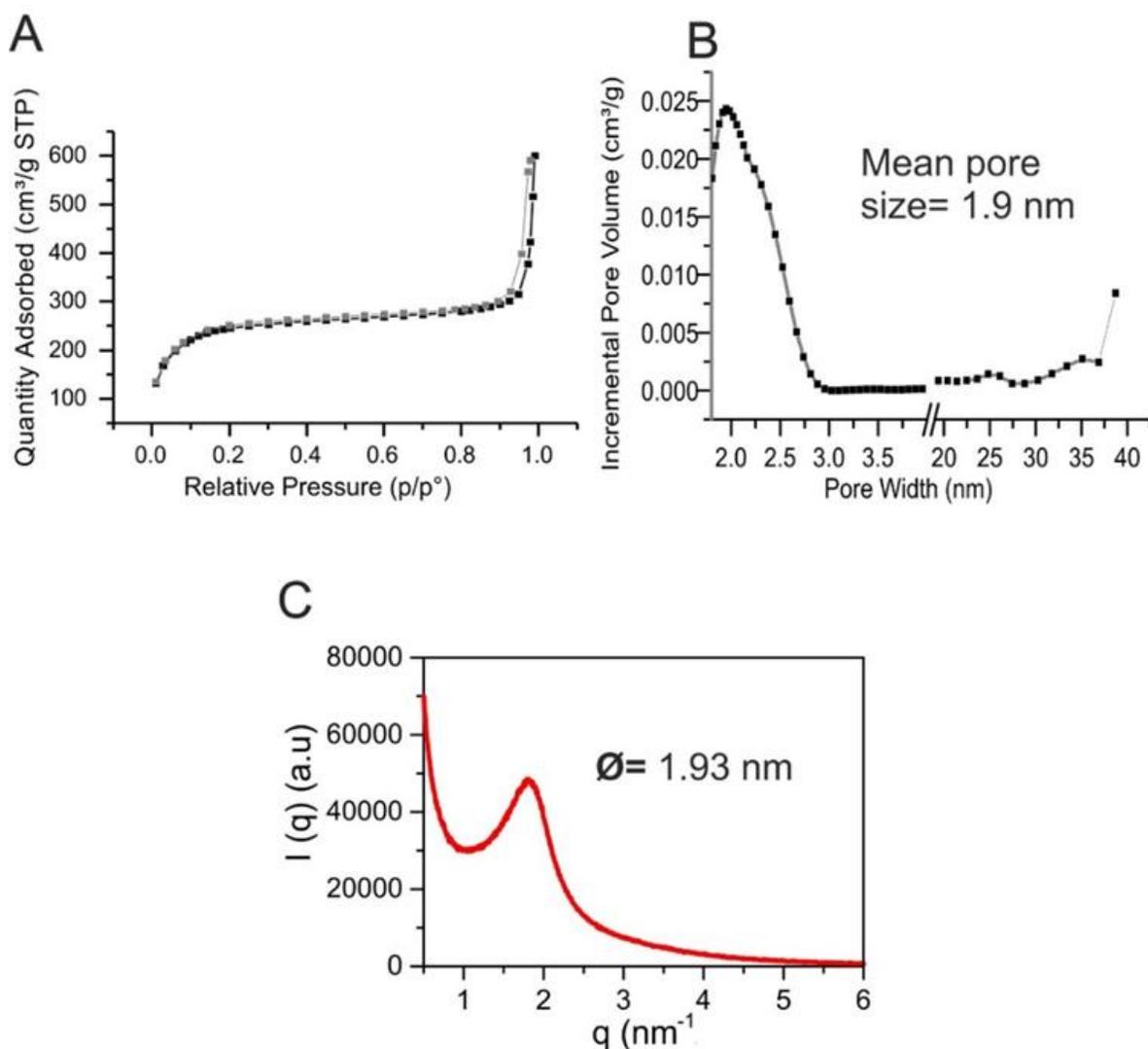
Figure 2.15. A) N_2 Adsorption/desorption curve, **B)** Pore size distribution obtained from N_2 adsorption analysis (Average pore size 1.9 nm) and **C)** SAXS analysis of the s-s NPs (Porous diameter = 1.9 nm).

Synthesis and characterization of FITC-*ss*-NPs

FITC-ss-NPs were prepared with a modified micelle templating method (**Scheme 2.7**). CTAB was the surfactant to produce the pores and TEA the base which catalyzed the reaction. The organic moiety (3-aminopropyl)triethoxysilane (APTES) was reacted with FITC and inserted in the TEOS:BTSPD framework (molar ratio 95:5 TEOS: BTSPD). After 1h of reaction at 95 °C and 400 rpm, the particles were washed with EtOH and refluxed with HCl to remove the surfactant from the NPs. After a second post-treatment of washings, FITC-ss-NPs were dried and characterized by SEM, TEM, TGA, N_2 adsorption techniques and photophysical studies were also carried on.
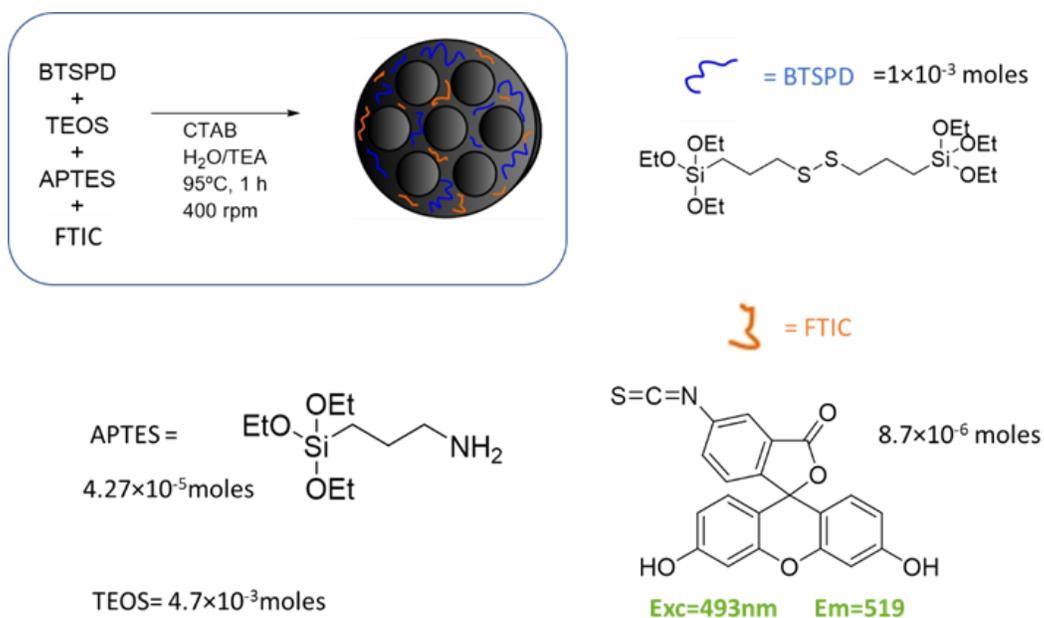
Scheme 2.7. Synthesis of FITC *ss*-NPs through the modified micelle templating method.

Morphological characterization of this NPs was performed using SEM and TEM (**Figure 2.16**). The FITC *ss*-NPs display a monodisperse spherical-oval morphology with a particle size average diameter of 48±6nm (counted performed in 300 nanoparticles from SEM images).
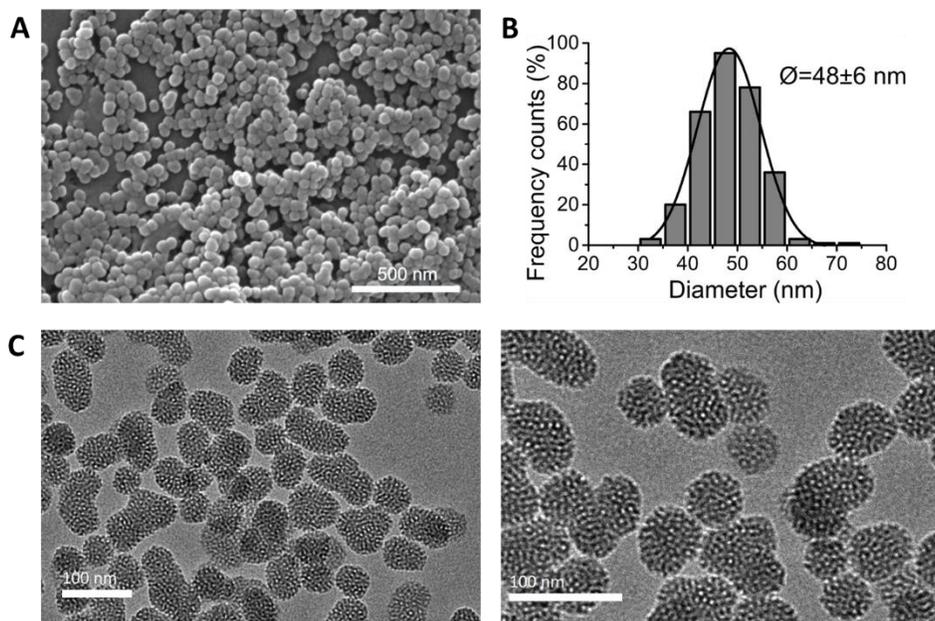
Figure 2.16. **A)** SEM image, **B)** SEM size distribution (count performed on 300 particles) and **C)** TEM pictures of the FTIC doped disulfide nanoparticles *ss*-NPs.

The ratio between organic/inorganic moieties was characterized by TGA (**Figure 2.17**). Revealing a weight loss of 7.6% of organic material (**Figure 2.71A**), which corresponds to the APTES, the BTSPD linker silanes and the FITC dye presents in the framework of the NPs. **Figure 2.17B** shows also the TGA of the FTIC compound, which indicates a ~90% weight loss between 300-600 °C.
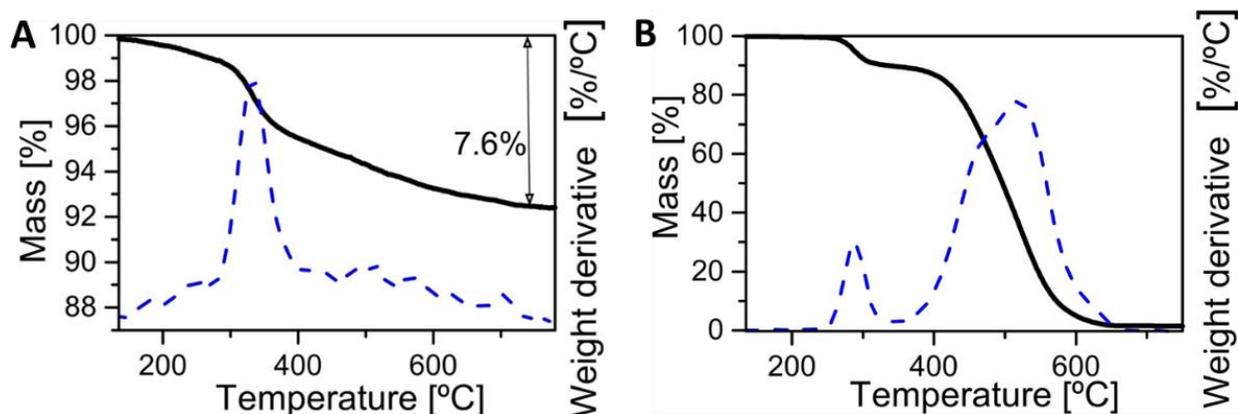
Figure 2.17. A) TGA of the FITC *ss*-NPs and **B)** the FITC dye.

In **Figure 2.16C** is observable the presence of porous in the NPs. To characterize them, N_2 adsorption analysis were performed. From the adsorption/desorption curves is obtained that these particles have a total pore volume of 1.05 cm^3 g^{-1} and a BET surface area of 739.58 m^2/g, while from the pore size distribution is shown the average pore size of 3.9 nm (**Figure 2.18A**). Breakable *ss*-NPs produced with this methodology were compared with these FITC-ss-NPs (**Figure 2.18B**). ss-NPs of around 56±8nm have a BET surface area of 718,68 m^2/g and average pore size of 3 nm.

To continue the characterization, photophysical studies were performed (**Figure 2.19**). **Figure 2.19A** shows the absorption, emission and excitation peaks of the FITC in the NPs, with a maximum excitation band at 486 nm and maximum emission at 519 nm revealing the presence of the dye in the silica framework structure (in literature, the maximum excitation band of the free dye is at 493 nm with maximum emission at 519 nm). Moreover, **Figure 2.19B** shows the lifetime of the dye in NPs τ_1=1.86 ns and τ_2=3.51 ns, 67 and 33%, respectively.
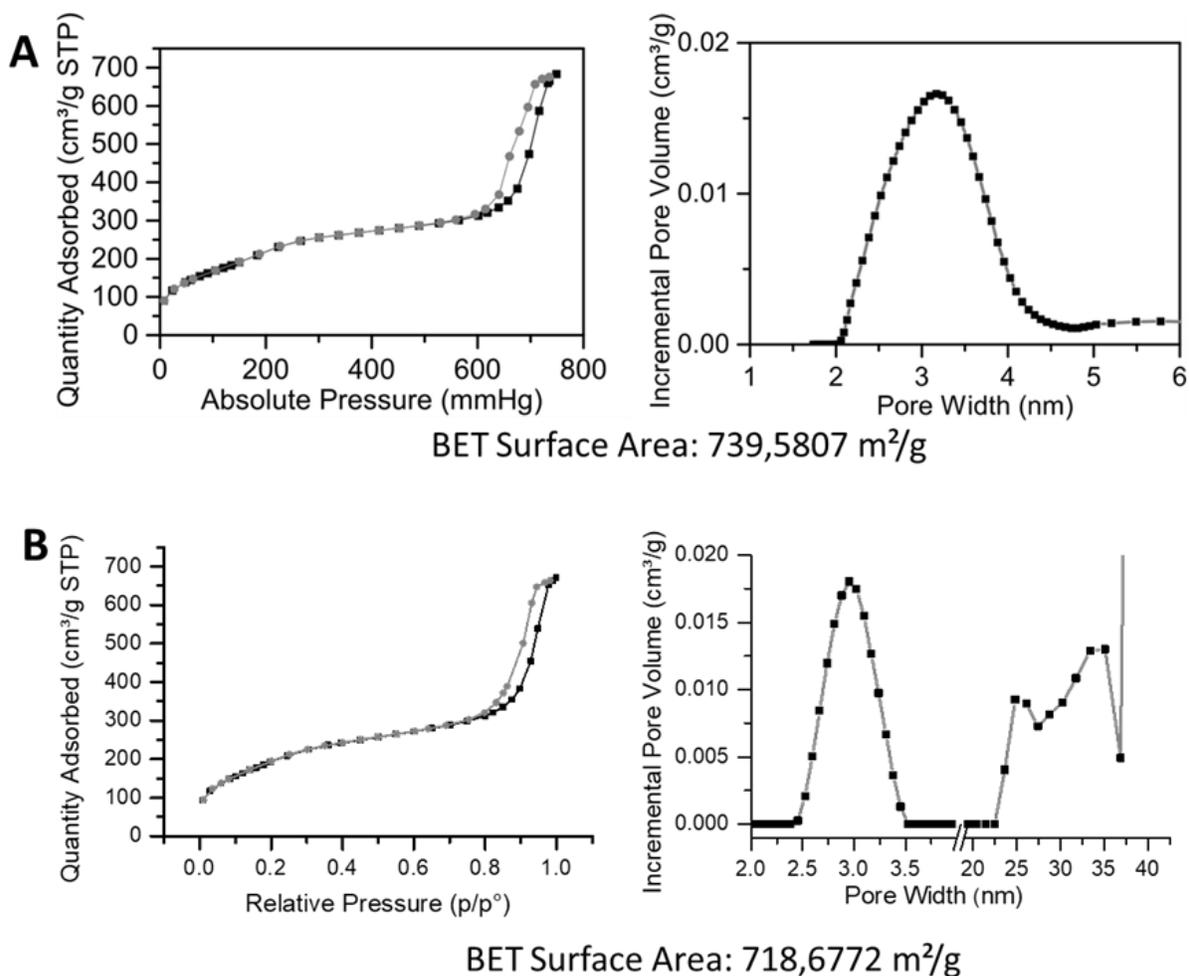
Figure 2.18. N$_2$ adsorption-desorption isotherm of **A)** FITC *ss*-NPs and **B)** *ss*-NPs done with the same methodology (micellar templating method).
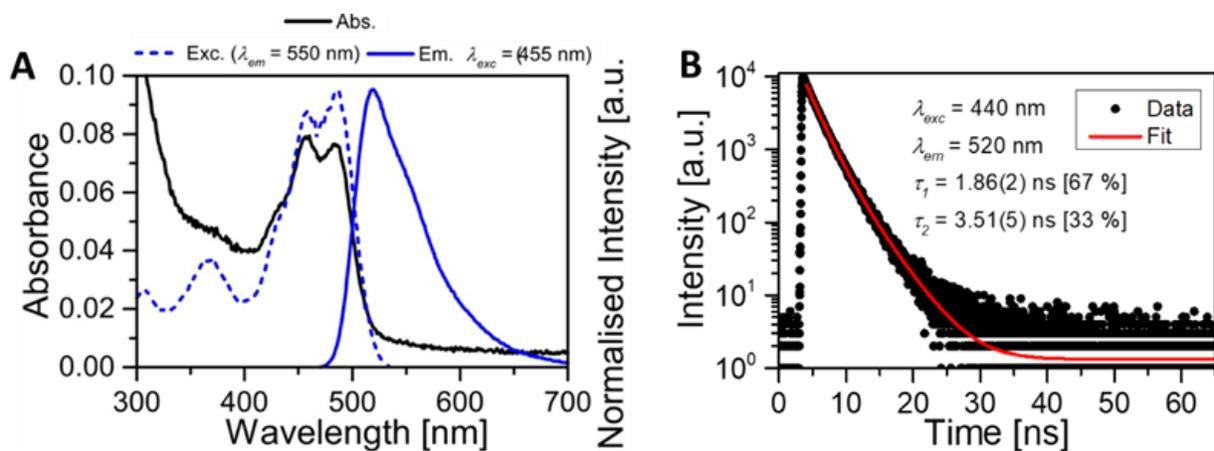
Figure 2.19. Photophysical characterization of the FITC *ss*-NPs. **A)** Absorption, emission, and excitation spectra (black line, blue full line, and blue dashed line, respectively). Wavelength of excitation and emission were 455 and 550 nm, respectively. **B)** Life time of the FITC *ss*-NPs.

129

2.2.2.2.1. Breakability test of the FITC *ss*-NPs

The breakability of the FITC *ss*-NPs was tested in the presence of GSH in PBS buffer at pH 7.4 and 37 °C to mimic the physiological conditions. **Figure 2.20** shows STEM images of the experiments run for 7 days and monitored at 1, 5 and 7 days. **Figure 2.20A** shows the NPs in the presence of GSH and while **Figure 2.20B** shows the same NPs in the absence of the reducing agent. These figures demonstrate the degradation of the NP through the first three days, while after 7 days few NPs are visible. With this, we can conclude that at these *in vitro* physiological conditions, the NPs breaks in small pieces, making therefore a stimulus breakable nanomaterial.

Besides that, the breakability of the FTIC-ss-NPs was tested in acidic conditions in acetate buffered aqueous solution at pH 5.2 and 37 °C in presence of GSH (**Figure 2.21**) over the same time duration as the last experiment (7 days), showing any breakage of these NPs over this time. With this data, it can be concluded that inside of the cancerogenic cells, where the pH is more acidic, these NPs will not break as easily as the ones that would be at higher pH. However, more experiments a longer time should be done to detect if these particles can break at this acidic condition after a longer period.
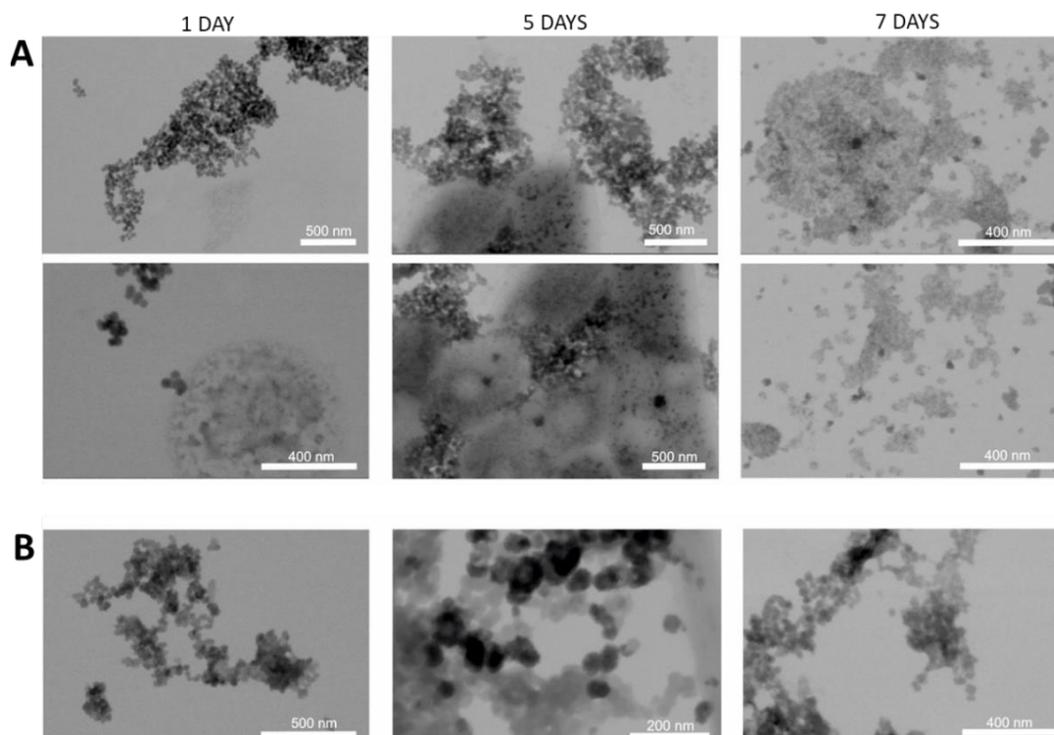
Figure 2.20. Breakability test of the FITC ss-NPs in PBS buffer pH 7.4 and 37 °C in **A)** presence of GHS 10 Mm and **B)** without GSH (Control experiment) during 1, 5 and 7 days.
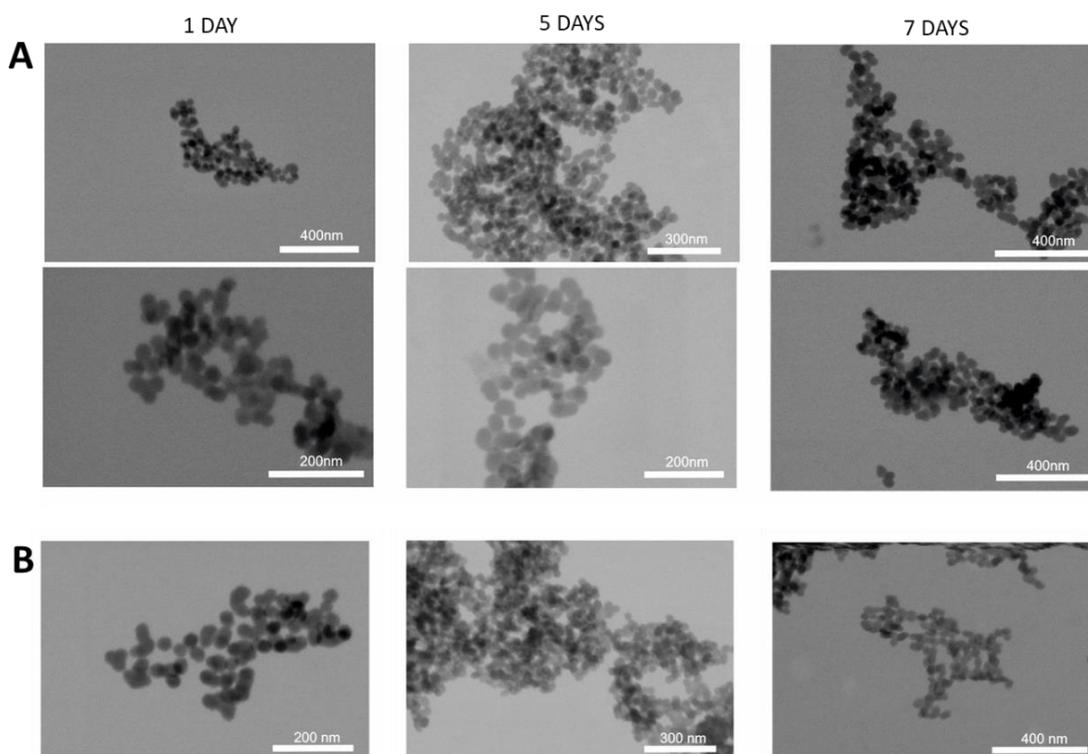
Figure 2.21. Breakability test of the FITC ss-NPs in Acetate buffer pH 5.2 and 37 °C in **A)** presence of GHS 10 Mm and **B)** without GHS (Control experiment) during 1, 5 and 7 days.

2.2.3. Synthesis and characterization of the PLGA@carriers

Due to their unique biocompatibility and biodegradation properties, [13] biodegradable polymeric nanoparticles have been used in broad applications in the fields of drug delivery and release, vaccination, targeting, tumor therapy and diagnostic systems.[47–51]

The proposed work herein requires a biocompatible[52] and biodegradable polymer. It has to be remarked that the factors influencing biodegradation of polymers include chemical structure (composition), physicochemical factors (ion exchange, ionic strength and pH), physical factors (shape, size, and porosity), morphology or microstructure and whether degradation occurs (through enzymatic or hydrolysis routes).[12,53]

Although localized chemotherapy is proposed to be promising to treat solid tumors, which account for more than 85% of all human cancers, few polymer-based formulations have reached clinical testing. One example is poly(lactic-co-glycolic acid) (PLGA), which has been associated with more than 500 patents[13,53] The majority of approved pharmaceutical implants or localized injectable delivery systems as OncoGel[TM 54] are based on PLGA.[12]

PLGA is considered as a biocompatible and biodegradable copolymer, and as such lean itself for use as a drug delivery carrier. PLGA can be metabolically hydrolyzed into lactic acid and glycolic acid monomers. These monomers are endogenous and are easily metabolized via the citric acid cycle. What is more, PLGA particles, as microparticles or nanoparticles systems,[55] are capable of carrying and delivering a variety of drug classes as vaccines, [5] peptides, [56]proteins, [57,58] and hydrophobic drugs.[59] The advantages of using these PLGA particles is the reduction of injection frequency, the sustained therapeutic drug levels, the site-specific drug delivery and that formulations can be changed for any number of desired release profiles.[60,61] For the preparation of PLGA vehicles, several methods have been developed as nanoprecipitation,[62] emulsion-solvent evaporation,[63] emulsion-diffusion,[64] self-organized precipitation (SORP),[51] salting out,[65] dialysis,[66] and supercritical fluid technology.[51,67]

To fabricate the PLGA polymer particles capable of loading CBDs and loaded *ss*-NPs solvent evaporation method, [68,69] SORP method,[51] and the hydrogel template method[70] were studied and compared in this thesis. The objective was to find a methodology in which the systems could have narrow size distribution yields, which leads to having high drug encapsulation efficiencies, better control over the dose and release behavior of the encapsulated drugs and better biocompatibility with cells and tissues.[51,71–74]

2.2.3.1. Synthesis of the PLGA@carriers by the solvent evaporation method

Solvent evaporation involves the emulsification of polymer in an aqueous phase and the dispersion in a volatile solvent like dichloromethane, chloroform, and ethyl acetate. Then, the solvent is evaporated using high temperature, vacuum or by continuous stirring. The size of particles can be controlled by adjusting parameters like manipulating the evaporation temperature, rate of evaporation, stirring rate, etc. This method has been practiced for the production of nanoparticles made by polymers such as, PLA, PLGA, PCL, polyhydroxybutyrate, etc.[75] and loaded with various drugs like tetanus toxoid, testosterone, loperamide, cyclosporin A, and indomethacin, to name a few.[76] As examples, Song *et al*.[77] used this method to prepare PLGA nanoparticles for various drug loading and Quellec *et al*.[78] to develop PEG-coated, PEG-PLAcopolymer nanospheres to load model proteins.[75,79] Furthermore, with this methodology, it

can be loaded hydrophobic species, as semiconductor nanocrystals (e.g., quantum dots, QDs), and magnetic NPs (MNPs).[51,80–82]

The fabrication of PLGA@carriers was first tried via a modified double-emulsion method, described by Minardi *et.al.* in several papers to produce PLGA microspheres (PLGA@MS) of around 1 µm and to load them with multiple payloads.[69,83,84] This consists of a double emulsion, where first, PLGA is dissolved in dichloromethane (DCM) at a concentration of 10% w/v. After, this solution is dropped in a solution of poly(vinyl alcohol (PVA) 2.5% w/v, and subsequently emulsified with a homogenization for 3 min at 10,000 rpm. The resulting emulsion is dropped into PVA 1% w/v and stirred overnight to allow DCM evaporation (**Scheme 2.8**). The resulting microspheres (MS) are washed with distilled water and recollected by centrifugation.
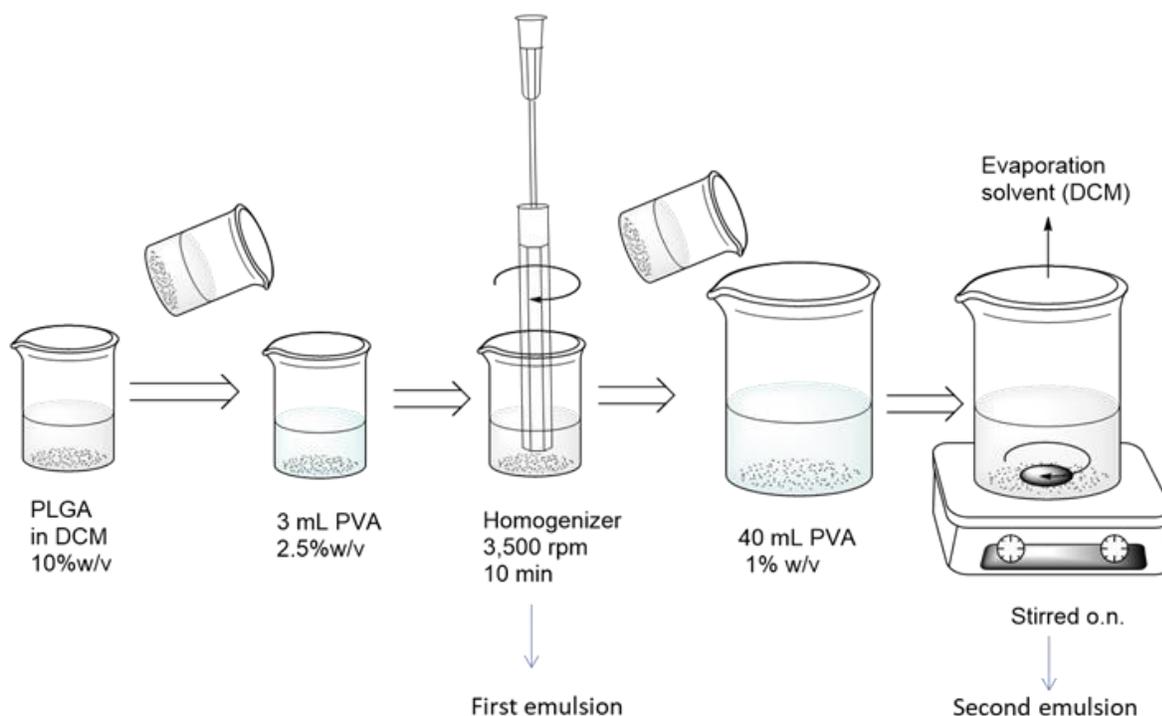
Scheme 2.8. Description of the preparation of PLGA@MS by the solvent evaporation "double-emulsion" method.

The morphology of the PLGA@MS was studied through SEM, which showed MS with spherical morphology with a particle size average diameter of 1.44±0.63 µm (counted performed in 300 nanoparticles from SEM images) (**Figure 2.22A** and **B**). By DLS, two size distributions were observed, where the average size diameter of the MS was 1.47±0.37 µm and 14.9±3.7 µm (**Figure 2.22C**). These values suggest that some of the MS were not well dispersed at the time that the

DLS was done, measuring the agglomeration of some PLGA@MS. **Figure 2.22D** shows the autocorrelation function of the sample, where the distribution size was obtained from the fitting range of 2-5000.
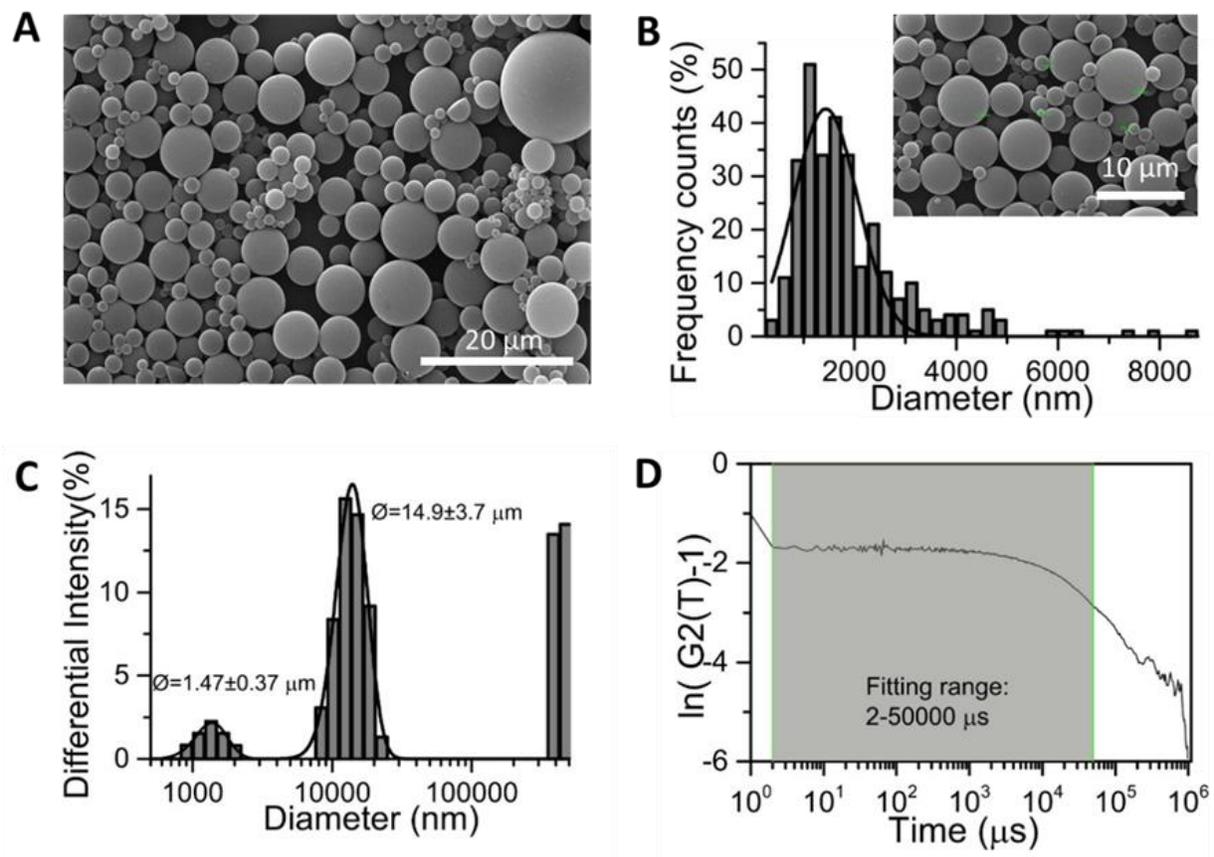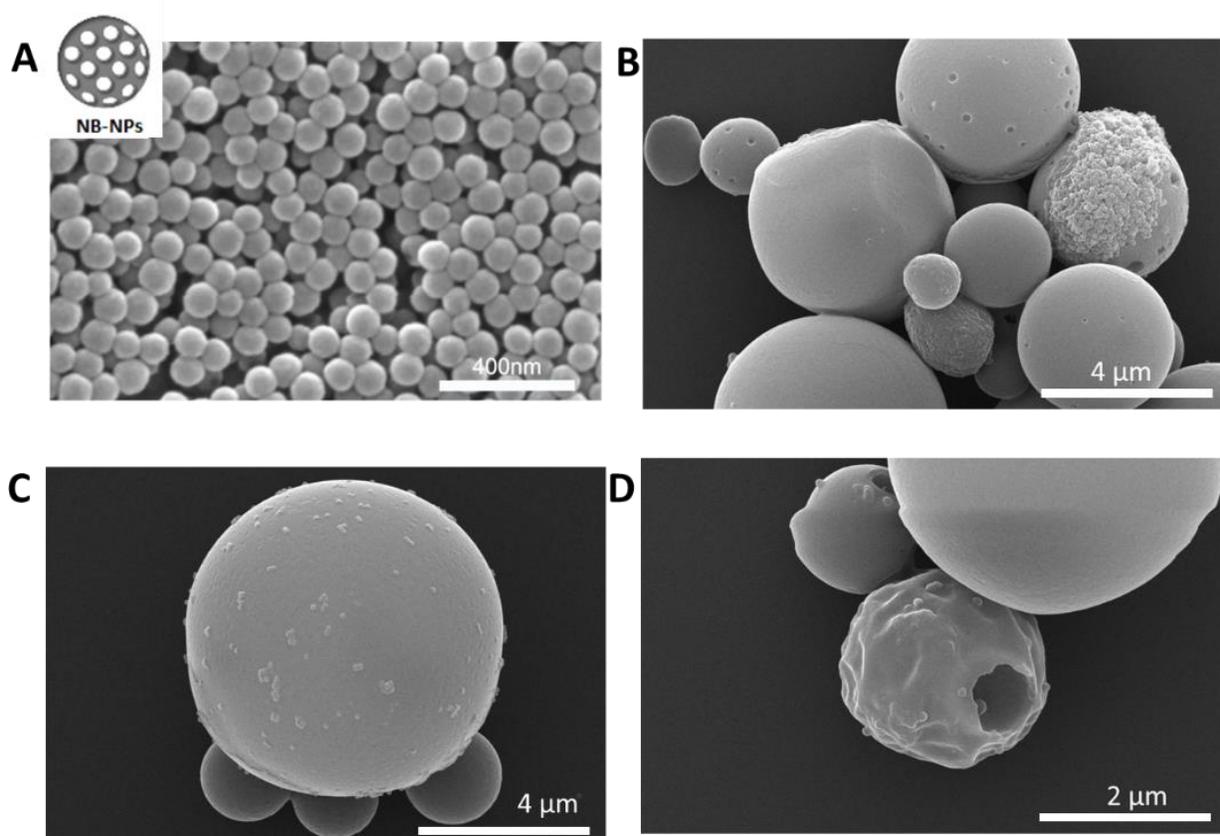

Figure 2.22. A) SEM image of the PLGA@MS using the solvent evaporation "double-emulsion" method (Scale bare 20 μm). **B)** SEM size distribution (count performed on 300 particles: average diameter 1.44±0.63 μm and SEM picture with a scale bare 5 μm. **C)** DLS result average diameter of 1.47±0.37 μm and 14.9±3.7 μm. Data obtained from the fitting range of 2-5000 of the **D)** autocorrelation function of the sample.

Synthesis of the NPs@PLGA@carriers by the solvent evaporation method

Non-breakable silica NPs were incorporated into the PLGA@MS using the modified double-emulsion method. Non-breakable NPs and Nile Red were dispersed in a solution of 10% w/v of PLGA in DCM. After this, the first and second emulsion were carrying out as previously described. **Figure 2.23A** shows the NB-NPs used, with a diameter size of around 97± 10 nm and with a mean pore size of 3.6 nm (done by the micellar templating method and characterized by SEM size diameter distribution and N_2-adsorption measurements). **Figure 2.23B** to **D** shows the result of

the incorporation of the NPS into the PLGA@MS. Additionally, in **Figure 2.23B** is visible how the NPs were covering the surface of the MS, but it has to be noticed that they were not dispersed in a homogeneous way along the MS. Moreover, it is shown how the surface of some MS had changed from a smooth surface to a bumpy one due to the incorporation of the NPs. In **Figure 2.23C** is shown how the NPs can be also dispersed in the MS and in **Figure 2.23D** is visible that some could incorporate the NPs in their interior. However, the study using this methodology was stopped because the formation of PLGA@MS was very polydisperse and the inclusion of the NPs was not in a homogeneous way.

Figure 2.24 shows the SEM pictures of the PLGA@MS during the incidence of the electron beam during the time (10 KV and spot 2 for few seconds of exposition). It is visible how the PLGA@MS are deforming due to the incidence of the beam, giving us information that indeed soft materials, are more delicate systems and must be treated differently, contrary to the silica NPS, that are hard materials and longer times are required before the sample is burned with the beam.

Figure 2.23. A) SEM image of the PLGA@MS using the solvent evaporation "double-emulsion" method (Scale bare 20 μm). **B)** to **C)** NPs@PLGA@MS (Scale bar 4 and 2μm).
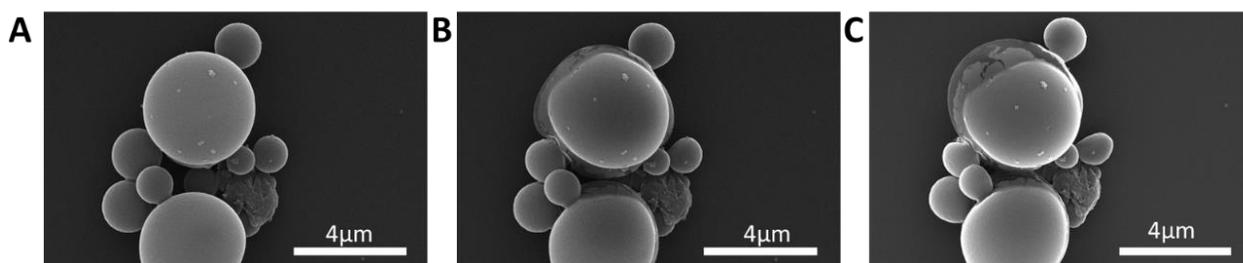
Figure 2.24. Images of the deformation of PLGA@MS loaded with NB-Silica by the incidence of the electron beam from the SEM equipment **A)**, before **B)** and **C)** and after the exposition of the beam for few seconds at 10 KV and spot 2.0 (Scale bare 4 μm).

The PLGA@vehicles loaded with MNPs generated a very polydispersed system. Moreover, this technique includes the use of surfactants during the preparation process via the emulsification approach (as PVA, Tween 80 or Triton X-100), where numerous purification stages are required. However, a residual surfactant can remind in the surface or encapsulated in the NPs, which can affect the drug delivery, biological activities, and cause cytotoxicity.[74,85–87] Residual PVA (non-ionic surfactant) can influence the pharmaceutical properties of NPs, presenting relatively lower cellular uptake compared to the surfactant-free NPs from the nanoprecipitation method.[86,87] To increase the biocompatibility and targeting capacity, some strategies like surface modification or functionalization were employed,[85,88] which certainly increases the complexity of the preparation process and the cost. Therefore, another synthesis route of PLGA@vehicles was studied.

2.2.3.2. SORP method

Liang *et al.* demonstrated the preparation of uniform biodegradable PLA and PLGA NPs without surfactant through self-organized precipitation (SORP) route.[51,89] The methodology was before used to prepare polymeric NPs with polystyrene (PS), poly(methyl methacrylate) (PMMA), polystyrenepolyisoprene (PS-PI) and PLA.[89,90] Then, NPs are formed based on a non-equilibrium process during slow evaporation of polymer solution.[91] NPs done by Liang *et.al.* demonstrated to be more promptly and effectively phagocytized by cells *in vitro*, compared to residual surfactant-coated NPs prepared from the emulsion–solvent evaporation method, providing a proof that the surfactant-free NPs have more advantages in cellular uptake and more safety in drug delivery and bio-imaging.[51]

The methodology consisted of dissolving the polymer (in this case PLGA) in a good solvent (THF) under stirring at room temperature. The addition was carried out by a syringe pump to have a controllable system (10 mL/h). After this, the THF is let it evaporate to finally produce the MS (**Scheme 2.9A**). The size and size distribution of the MS depends on the polymer concentration, the ratio of water to organic solvent, mixing rate and polymer molecular weight. [51]

In the **Scheme 2.9B** is shown the possible mechanism for the formation of uniform polymeric NPs during the organic solvent evaporation, which is described as following: when water is added gradually, the solubility of the polymer in the mixing solvent decreases and the polymer chain gradually folds compactly and become the small nuclei (known as the nucleation process). Then, as the good solvent evaporates, the nuclei adsorbs the free polymer chains and then, it develops to form the NPs (called the adsorption and growth process). Finally, the NPs are dispersed in the poor solvent when the good solvent was completely removed (called the precipitation process).
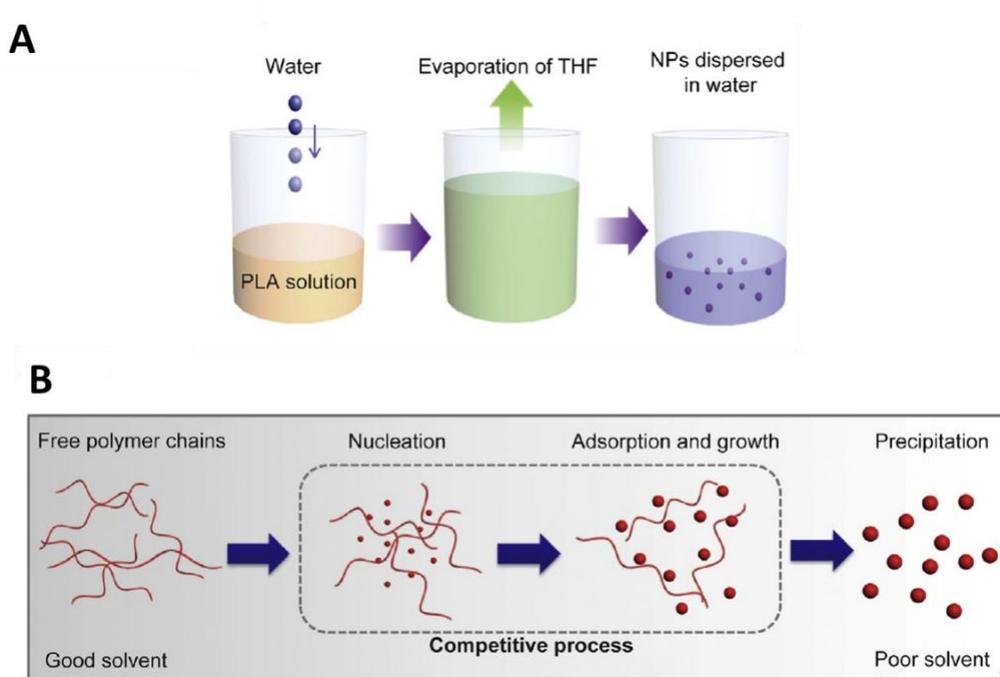
Scheme 2.9. A) Schematic illustration of experimental procedure for preparing the PLGA NPs with uniform size by SORP and **B)** Illustration showing the possible formation mechanism of polymeric NPs during the SORP preparation. Adapted with permission from ref 51. (Copyright 2014, Elsevier)

2.2.3.2.1. Preparation of the PLGA-MS by the SORP method

PLGA-MS were synthesized by the SORP method as is described by Liang *et al*. [51] To load them with a dye, Nile Red was put it in the THF solution (Table 1 in material and methods shows the

different trials prepared before achieving the optimized procedure). Using this methodology, it was observed that not only the polymer concentration but also the ratio of water to organic solvent, the mixing rate and the polymer molecular weight played a role in the production of these systems. Indeed, it is a very delicate synthesis in which any variation, inclusive the use of a different stirring bar or surface material of the flask reaction can make a difference in the result of the homogeneity of these particles.

In **Figure 2.25** is shown the results of the homogeneous monodisperse Nile Red-PLGA spheres. The diameter size of the particles taken by the counting of 300 particles from SEM pictures was 639±119 nm (**Figure 2.25A** and **B**). By DLS, the particles were given a value diameter size of 676±141 nm; this value is taken from the autocorrelation function of the sample using a fitting range of 4-3000 (**Figure 2.25C** and **D**), which agrees with the SEM size distribution.

Figure 2.26 shows the confocal images taken of the Nile Red-PLGA nanoparticles using a 63x objective. The fluorescent, PMT, the superimposition of these and the lambda mode is shown. These results give proof that indeed the dye is encapsulated in the PLGA matrix.
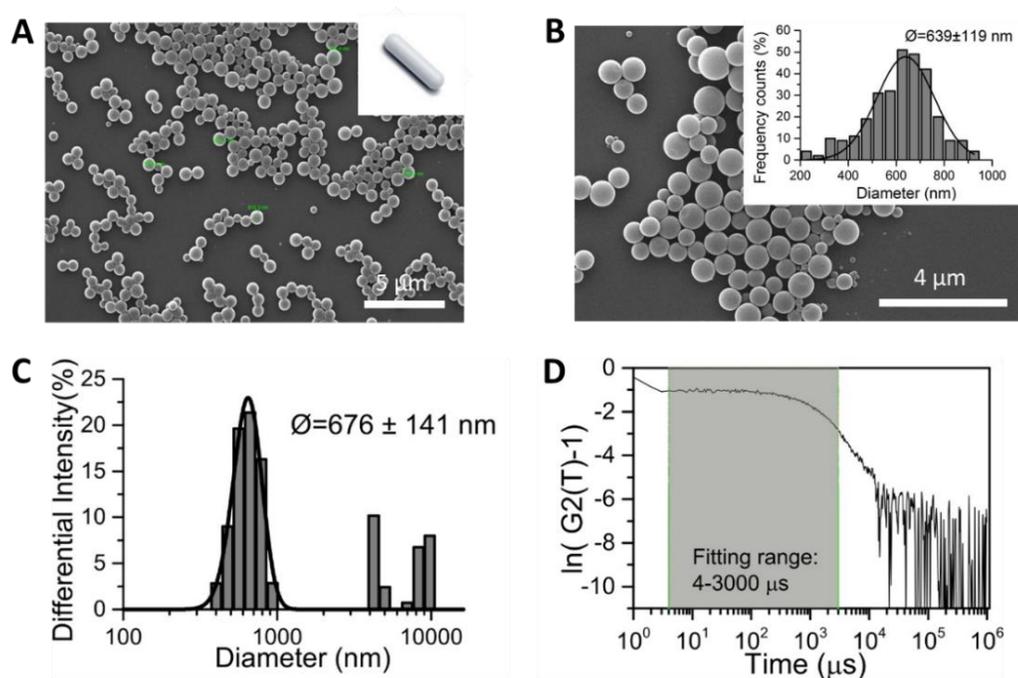
Figure 2.25. A) SEM image of the PLGA nanospheres using the SOAP methodology (scale bare 5 µm). **B)** SEM size distribution (count performed on 300 particles: average diameter 639±119 nm). **C)** DLS result average diameter of 676±141 nm. Data obtained from the fitting range of 4-3000 of the **D)** autocorrelation function of the sample.
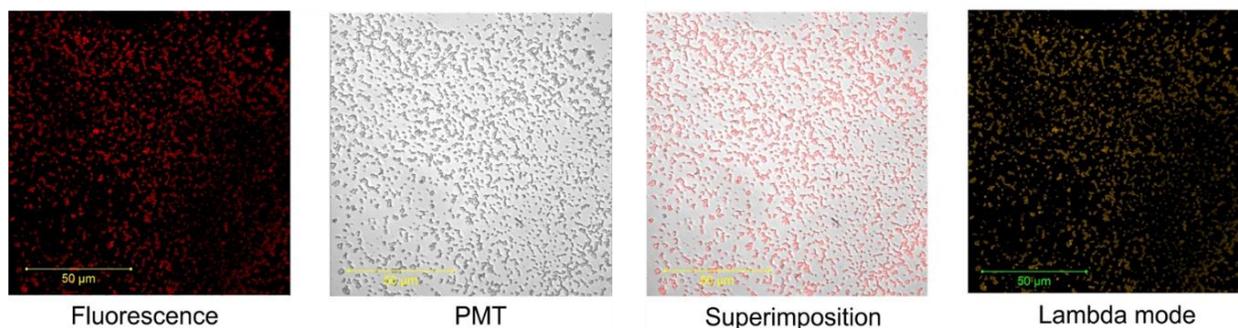
Figure 2.26. Confocal microscope images of the PLGA microspheres loaded with Nile Red using 63x objective.

After all the parameters were optimized to make these spheres, the reproducibility was checked. Spherical and monodisperse PLGA-NPs were reproduced. DLS results gave an average diameter of 604±135 nm and 710±141 nm, for the second and third try, respectively. With a yield of these reactions of 90 and 86.5%, for each one, respectively. It has to be said, that a flat small stirring bar, a flat surface of the reaction flask and a proper stirring rate are the keys to synthesize these particles (**Figure 2.27**).
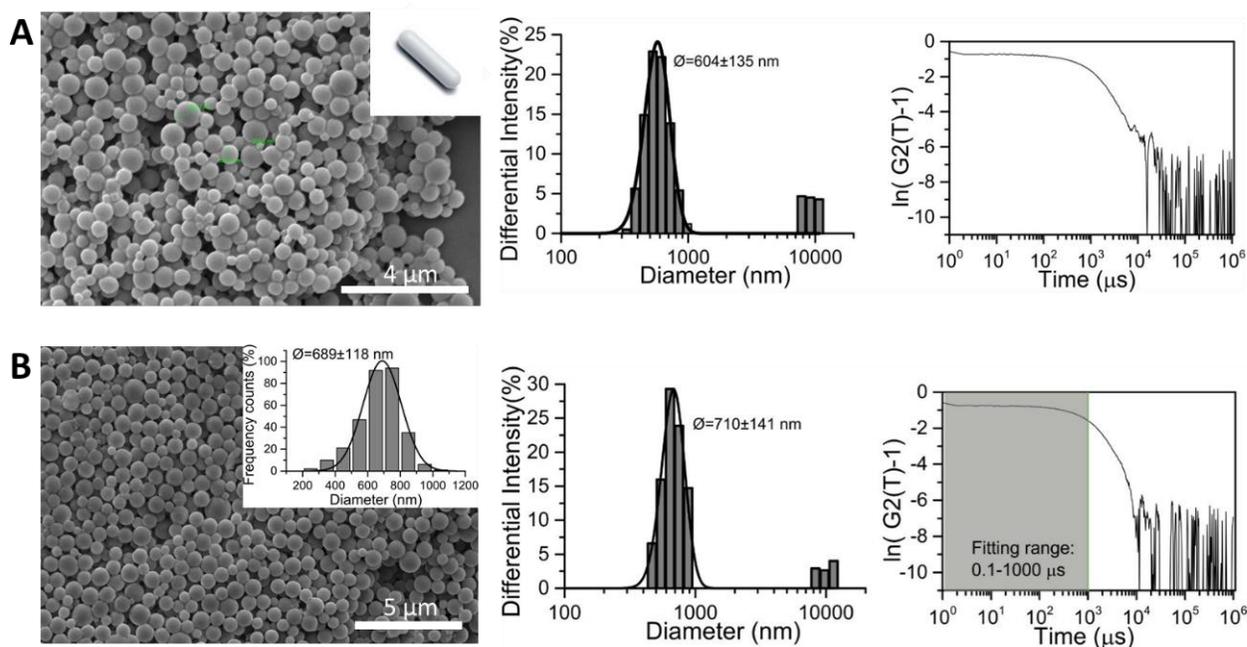
Figure 2.27. A) Second and **B)** Third repetition of the PLGA- spheres done by the SORP methodology. SEM and DLS result average diameter of 604±135 nm and 710±141 nm, respectively.

139

Figure 2.28 shows the results of the synthesis using the same methodology used before and reported by Liang *et al.*, but using a different stirring bar (the synthesis was repeated twice to see the reproducibility, **Figure 2.28A** and **B**, respectively). The stirring bar used this time was one with a pivot ring. SEM images show in both synthesis the presence of spherical polydisperse particles. The counting of 300 NPS, and DLS data shows two population distributions diameter sizes. For the first reaction (**Figure 2.28A**), DLS data shows size diameters of 233±55 nm and 650±111 nm; which agrees with the second synthesis done to confirm results, which shows distribution diameter sizes of 236±46 nm and 1312±265 nm (**Figure 2.28B**).
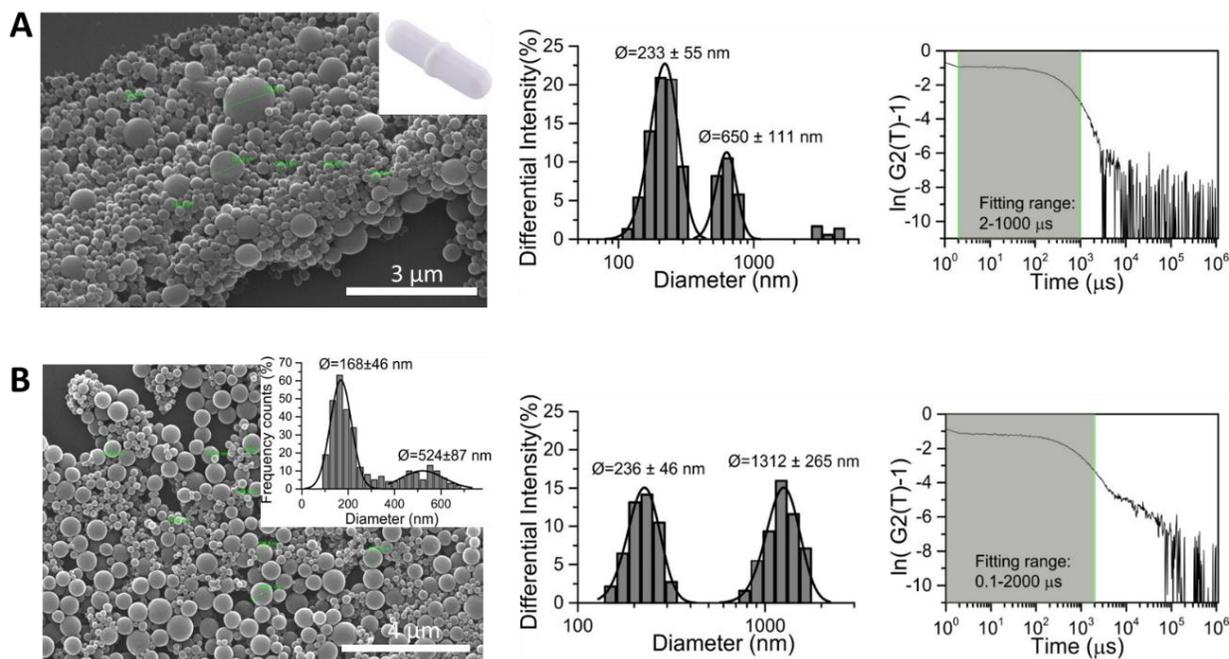
Figure 2.28. Experiments to produce the PLGA- spheres by the SORP methodology changing the stirring bar for one with a pivot ring . SEM and DLS results average diameter show two different populations: first synthesis **A)** size diameter of 233±55 nm and 650±111 nm; second synthesis B) size diameter of 236±46 nm and 1312±265 nm.

In **Figure 2.29** is shown how the synthesis depends on many factors. Another kind of polymorphisms was obtained with a change in the stirring velocity; instead of using 100 rpm, higher speed was applied by using 1200 rpm. In this case, the spheres obtained were not homogeneous, instead, steaks and spheres are presented in the sample (see SEM pictures in **Figure 2.29A**). Another contribution of this could be the stirring bar used (with the pivot ring). On

the other hand, in a first try to upscale the reaction 10 times more, it is observed the presence of rods-nanospheres (SEM pictures in **Figure 2.29B,** where an oval stirring bar was used for this synthesis). It has to be said that at that point it was not detected the importance of the stirring bar form.
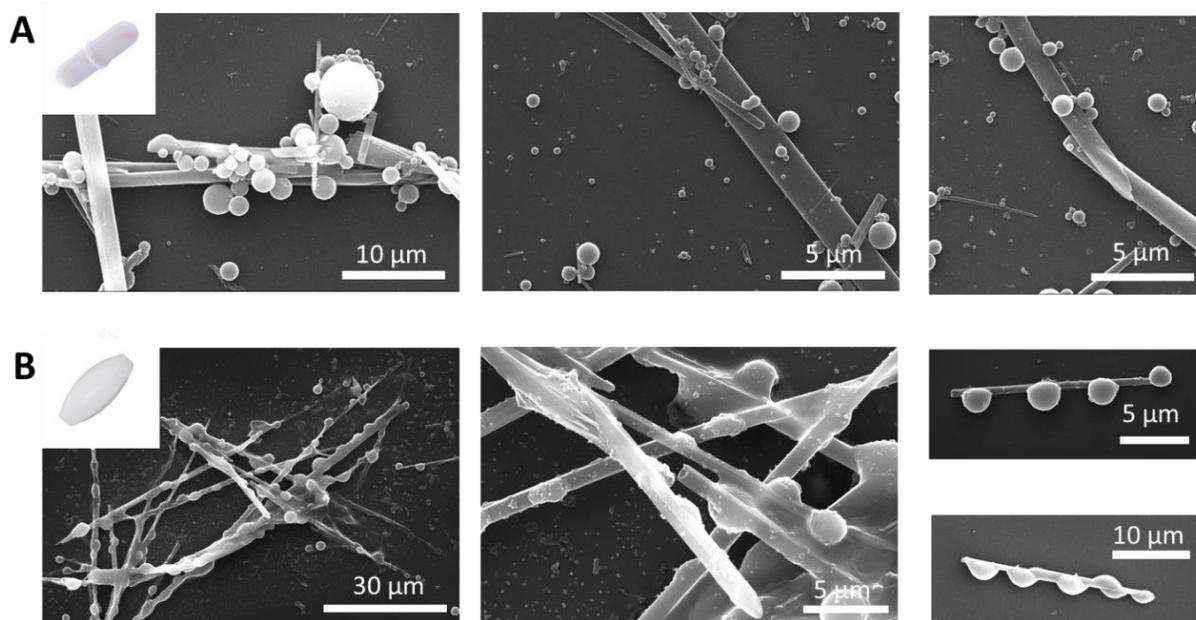
Figure 2.29. A) SEM image of the PLGA nanospheres using the SOAP methodology and high speed of stirring (scale bare 10 and 5 μm). B) SEM image of the PLGA rods-nanospheres using the SOAP methodology big-scale 10x (scale bare 30, 10 and 5 μm).

To optimize the upscale the reaction, the procedure was repeated twice at five-time scale. Microspheres with an average diameter of 1.1±0.2 μm were formed according to SEM size distribution counting on 300 particles (**Figure 2.30 A** and **B** shows the first and second try with a yield of 70 and 40%, respectively). DLS data corroborates with the data given for the SEM counting, reported an average size distribution diameter of 1.2±0.3 μm (**Figure 2.31**). With these results, we can say that the reaction was successfully scalable five times conserving the homogeneity of the particles.
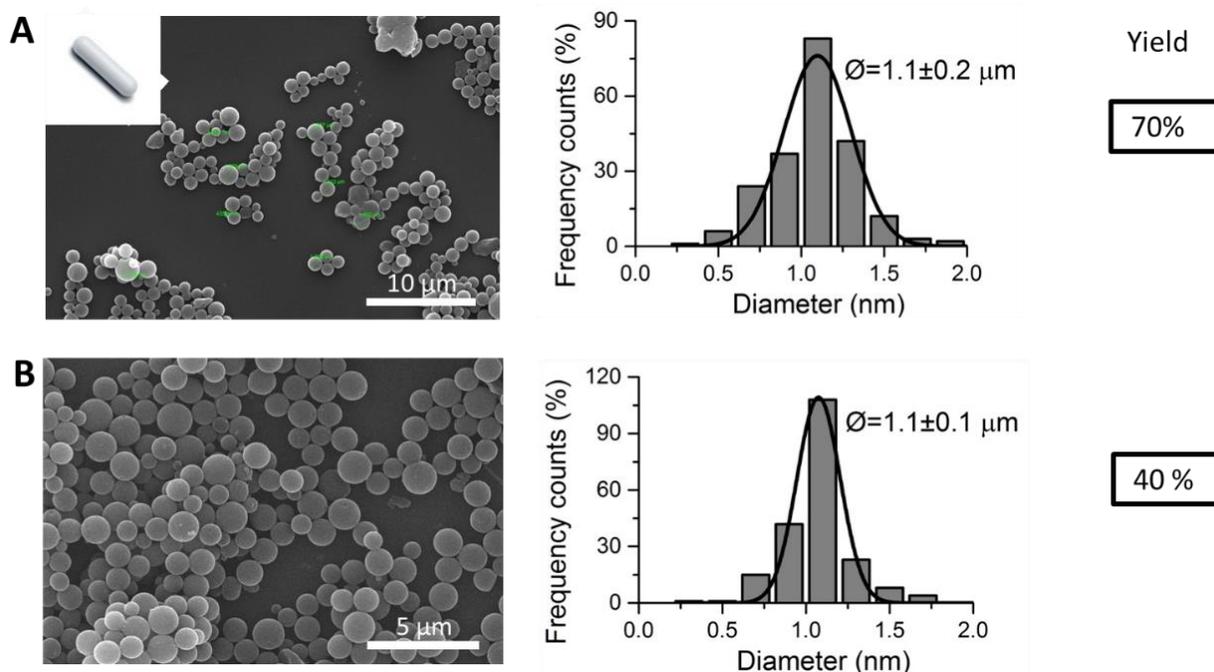
Figure 2.30. 5x Upscale reaction of the PLGA- spheres by the SORP methodology using a flat stirring bar and do it twice. SEM and their frequency counts reveal of 300 particles. First synthesis **A)** size diameter of 1.1±0.2 μm and 70% of yield. Second synthesis **B)** size diameter of 1.1±0.1 nm with 40% of yield.
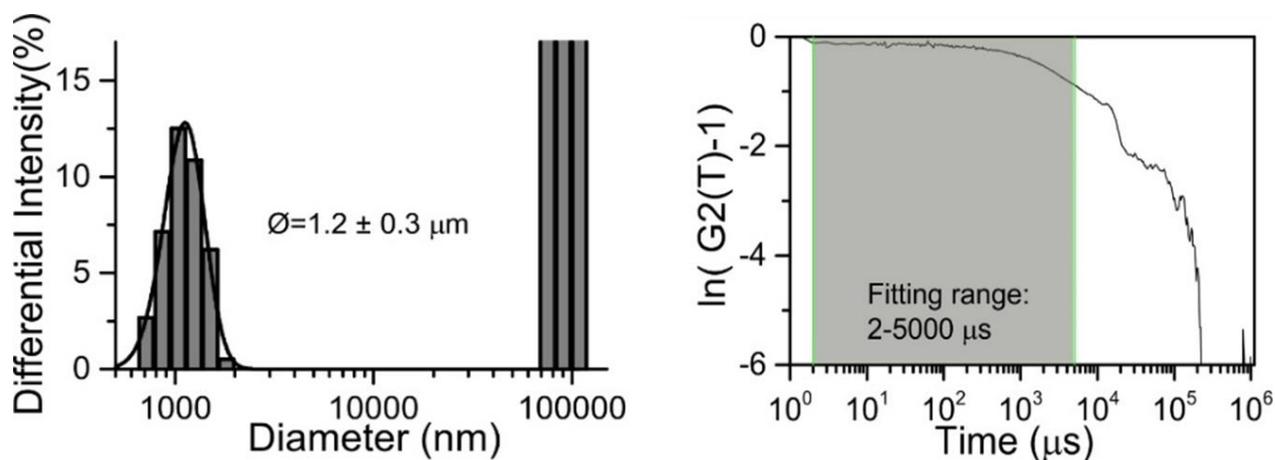
Figure 2.31. DLS result of size distribution of PLGA nanospheres produced from the SOAP methodology experiment with an average diameter of 1.2±0.3 μm, data obtained from the fitting range of 2-5000 of the autocorrelation function of the sample.

As a conclusion, using the free surfactant methodology SORP methodology, PLGA spheres loaded with Nile Red were successfully produced achieving monodisperse particles. It should be pointed out that the stirring bar is an important parameter to take into consideration for producing

monodisperse systems. A stirring bar with a pivot makes the formation of polydisperse particles with mainly two different size populations. Therefore, a flat stirring bar and a flat surface is necessarily for the control of the dispersity in the system. Additionally, scaling the reaction five times was possible following this observation. The next step was then to study the possibility to load these systems with MSNPs and with the cannabinoids.

2.2.3.2.2. Incorporation of MSNP in the PLGA-MS by the SORP method

Breakable MSNPs were included in the PLGA spheres. 20% and 5% w/w of FITC-*ss*-NPs with respect of the PLGA were dispersed in the THF solution (**Figure 2.32**). The production of PLGA spheres loaded with MSNPs was achieved in both cases. At higher percentages of MSNPs, the spheres become visible on the outside of the PLGA vehicle with a heterogeneous deposition. It is visible also how the PLGA spheres start to be connected between each other probably due to the interaction between the silica of the MSNPs (**Figure 2.32A**). When the percentage of silica NPs decreases to 5%, it is less visible the deposition of those nanoparticles outside the PLGA spheres, but it has to be denoted that it still exist a connection between the spheres (**Figure 2.32B**).
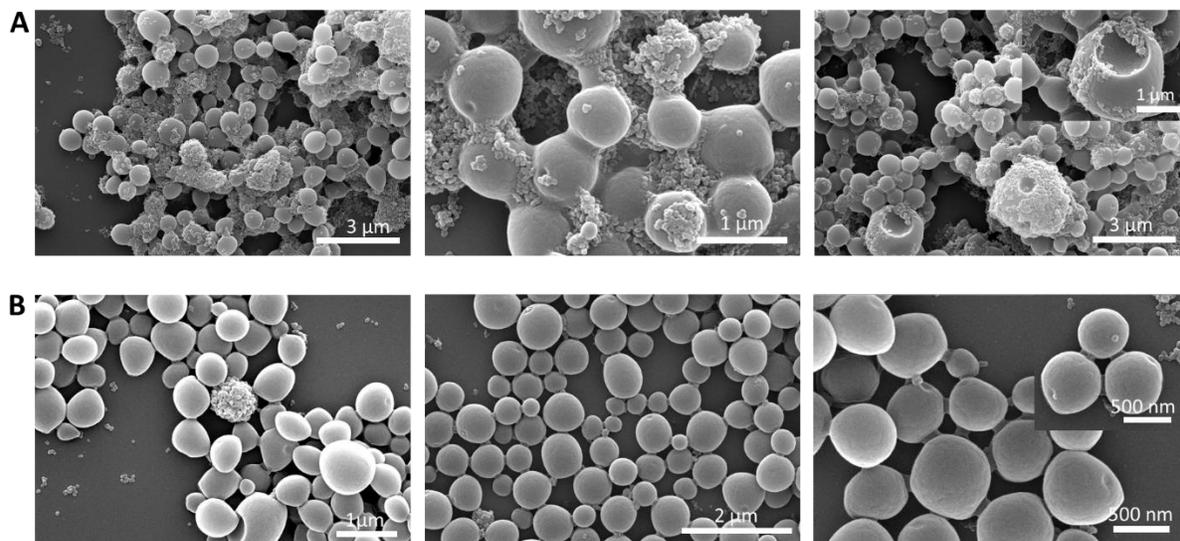
Figure 2.32. SEM image of the incorporation of **A)** 20% w/w and **B)** 5% MSNPs in the PLGA nanospheres using the SOAP methodology (scale bare 3, 2, 1 μm and 500 nm).

2.2.3.2.3. Incorporation of a cannabinoid analog in the PLGA-MS by the SORP method

Different percentages of the N-(2-hydroxy ethyl) oleamide synthetized as an analog of the endocannabinoid (2HEO) was incorporated in the synthesis by its dilution in the organic phase (THF) (**Figure 2.33**). It has to be said that high concentration of this molecule in the synthesis, breaks the formation the PLGA vesicles (**Figure 2.33 A** and **B** with 50% and 30% w/w of 2HEO). At 10% of 2HEO, the formation of some spheres was possible, but also bigger particles were formed (**Figure 2.33C** and **D**). At the same time, 5% w/w of 2HEO was not given better results for the formation of the spheres although small quantity of spheres was produced. (**Figure 2.33E**). The reaction without oleamide was run as a control of the formation of the PLGA spheres (**Figure 2.33F**), showing a good control of monodisperse particles.
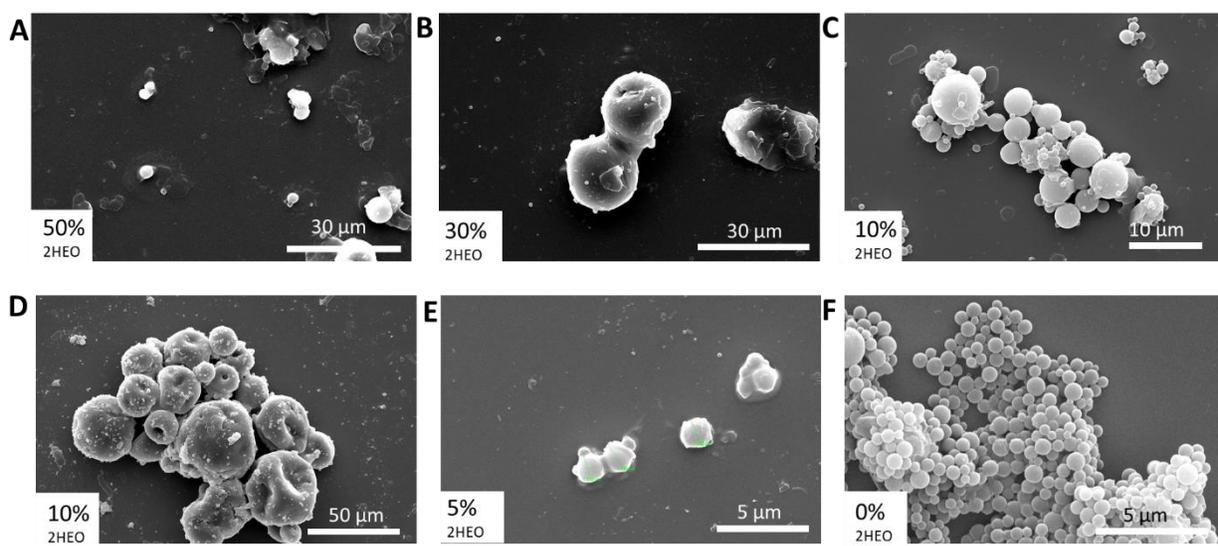
Figure 2.33. SEM images of the incorporation of **A)** 50%, **B)** 30%, **C)** and **D)** 10%, **E)** 5% and **F)** 0% w/w of 2HEO in the PLGA nanospheres using the SOAP methodology.

As a general conclusion, with the SORP methodology, PLGA spheres of around 600 nm and 1 µm can be done with a free surfactant. However, it is not a good way to make the incorporation of MSNPs as they start to make agglomerations or connections between the spheres with 20% and 5% w/w. Also, the loading of the analog of the endocannabinoid perturbs the formation of the spheres even by trying to incorporate 5% w/w. Because of these results, another additional methodology to produce vehicles with homogeneous size distribution and capable to load both systems was also tried.

2.2.3.3. Hydrogel template method

The hydrogel template method is part of a microfabrication process, which produces nano/microparticles for drug delivery with homogeneous particle size distributions, with optimal drug loading and release properties. Moreover, the nanoparticles can be produced homogeneously with any geometry and size desired while incorporating a diverse array of drugs with various hydrophilic characters and molecular weights. Other advantages are that with this approach, very high loading can be achieved and controllable drug release kinetic can be produced. This methodology is based on the unique properties of physical gels that can undergo sol-gel phase transition. To obtain particles, the method involves a simply dissolving of the template in aqueous solution.[70]

Scheme 2.10 shows the main concepts of the hydrogel template approach used to produce PLGA vehicles. The first step is to form a pattern on a silicon wafer master template, which is usually done by lithography. From it, a PDMS template is constructed to provide a positive mold of columns (A) in which a hydrogel solution is poured (B) and removed to form the negative mold with wells (C). This hydrogel mold is then filled with an organic solvent containing the polymer and drug substance (D). Finally, the particles are recollected by dissolving this template in water followed by centrifugation or filtration (E and F).
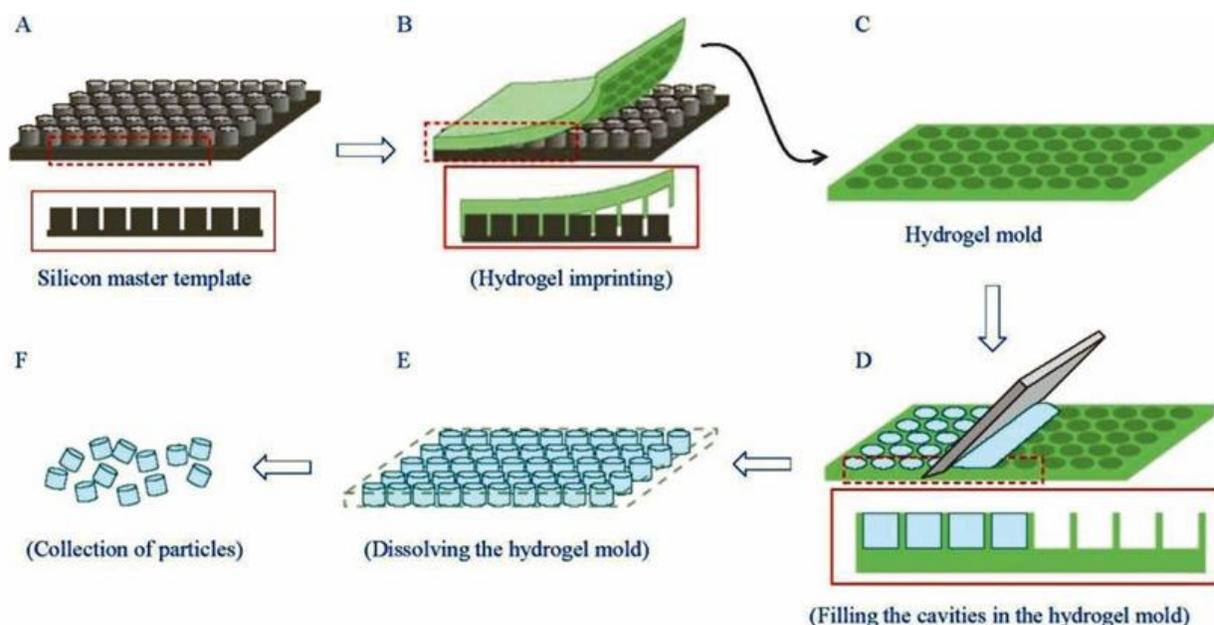
Scheme 2.10. Mold method of microparticle fabrication through the hydrogel template method. Reprinted with permission from AKINA, INC (Copyright 2015).

Using this technique, PLGA vehicles loaded with a fluorescent probe (Nile Red) were then produced. A solution of 20% and 30% of PLGA in DCM and Nile Red was spread it in the PVA template using two different tools to do it. It has been observed that using the razor as a tool to spread the polymer, does not give the formation of complete MBds (**Figure 2.34A**). Trying to optimize the methodology, 30% of PLGA solution was deposited observing the same results. To increase the material deposited in the holes, the PLGA solution was deposited 3 times in the PVA template (**Figure 2.34B**) were the MBds were better form. Changing the tool of deposition like by a slide glass or by putting just one layer of material, 20% and 30% of PLGA was enough to produce PLGA-vehicles with a cylindrical-concave shape (**Figure 2.34C-D**). **Table 2** in the material and methods part summarizes the experiments done to achieve the good technique to produce them.
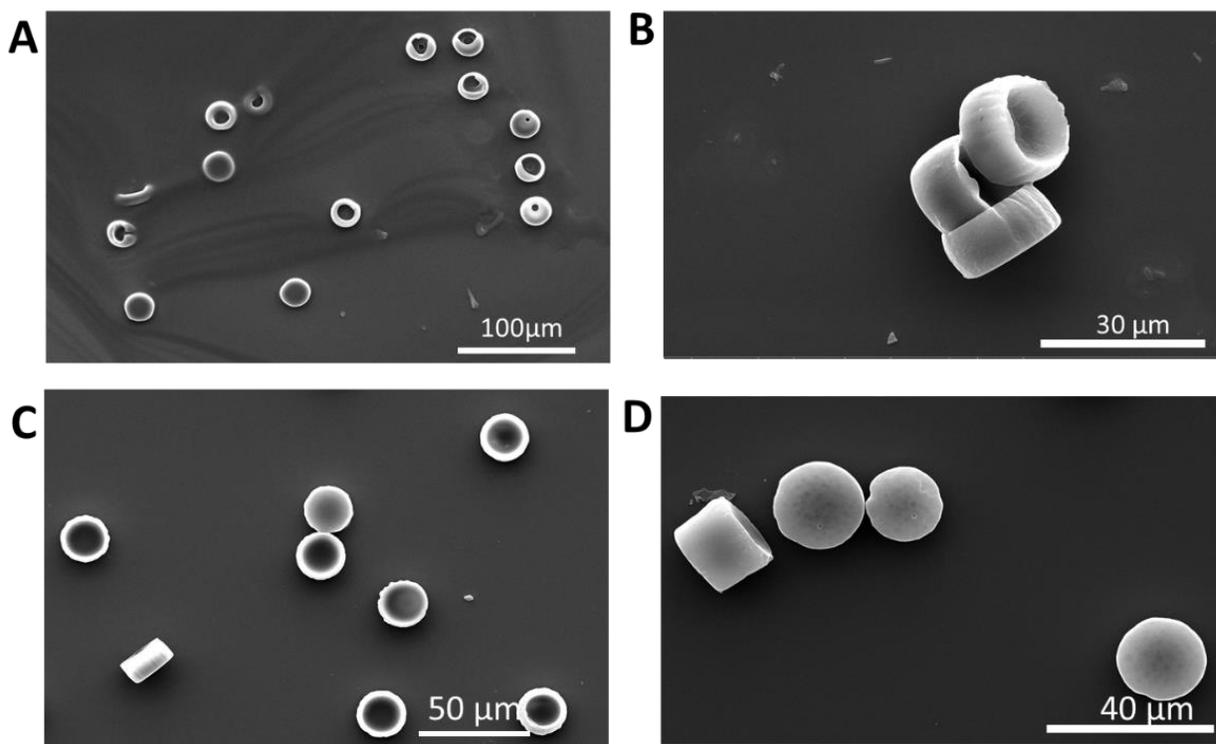
Figure 2.34. SEM pictures of the optimization of the production of PLGA-MBds using the hydrogel template technique. **A)** 20% PLGA MBds formed with the deposition of the solution using a razor, **B)** 30% PLGA MBds formed with the deposition of the solution using a razor putting 3 times layers of material. **C)** and **D)** 20% and 30% PLGA MBds formed with the deposition of the solution using a glass slide.

After the optimization of the procedure, in **Figure 2.35** is presented the morphological characterization of the PLGA-MBds done with PLGA at 20% loaded with Nile Red. SEM pictures

were taken to observe the particles after dissolving the PVA template. Which present a concave morphology with a very homogeneous size of 20 μm (**Figure 2.35A**). Confocal images were also taken of the material when they were in the hydrogel template (63x objective); homogeneous shape and size is observed. Here is appreciable how the patter of the template was filled with the polymer, the stability of the PVA material with the PLGA, how the beads do not present any kind of diffusion inside the matrix (**Figure 2.35B**). Finally, with the optical microscope, more images were collected using the light and a filter (**Figure 2.35 C** and **D**).
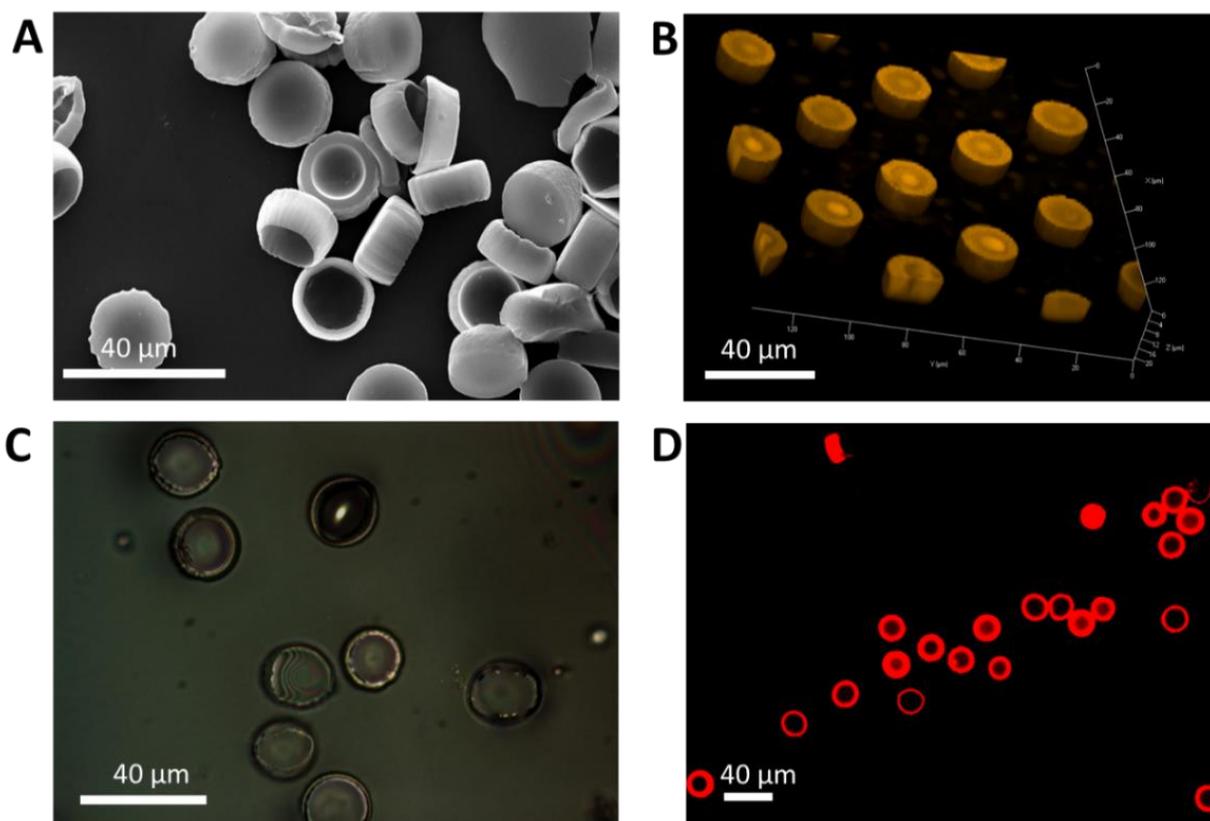
Figure 2.35. A) SEM image, **B)** Z-Stack confocal microscope image of the PLGA microspheres loaded with Nile Red using 63x objective **C)** and **D)** Light microscopy images.

2.2.3.3.1. Incorporation of cannabinoids in the PLGA-MBds by the hydrogel template method

Using the hydrogel template method,[70] the fabrication of 2HEO-PLGA@MBds was first done using Nile Red (NR) as a dye and the *N*-(2-hydroxy ethyl) oleamide (2HEO),where 20%w/w was loaded as a cannabinoid analog (see material and methods part) (**Scheme 11**). Confocal images were taken to see if the beads were formed with the inclusion of 2HEO; **Figures 2.36** and **2.37**

shows pictures using the 10x and 63x objective, respectively. We can see the fluorescence, PMT, superimposition and the lambda mode of the material, observing particles with a very monodisperse size and shape (20 µm diameter size particles are created which corresponds to the diameter size of the master template in which the PVA mold was done). In **Figure 2.37**, is clearer the morphology of the material, presenting a bead shape; in the lambda mode of the confocal image (real color of the material) is shown two different areas of emission, giving a yellow color and a red color in the center of it; with a λ_{max} at 592 and 611 nm. To understand this, fluorescence emission spectra were taken of a solution containing a mixture of Nile Red and PLGA, versus, Nile Red and 2HEO (in the same ratio as it was used to construct the PLGA-MBds) (**Figure 2.38**). In this case, it is observed to different emission bands with a λ_{max} at 636 and 648 nm, respectively. This shifting in the emission bands agrees with the ones observed by the confocal images (**Figure 2.37B**), where it can be then deduced that the red area is due to the accumulation of the 2HEO in the center of the beads.
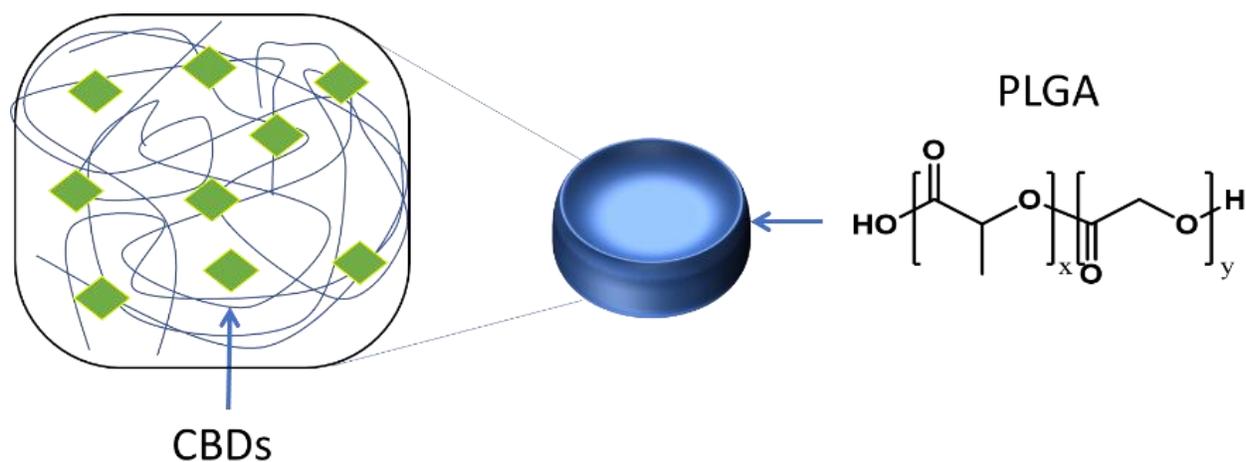
Scheme 2.11. Incorporation of the cannabinoid in the PLGA-MBds.
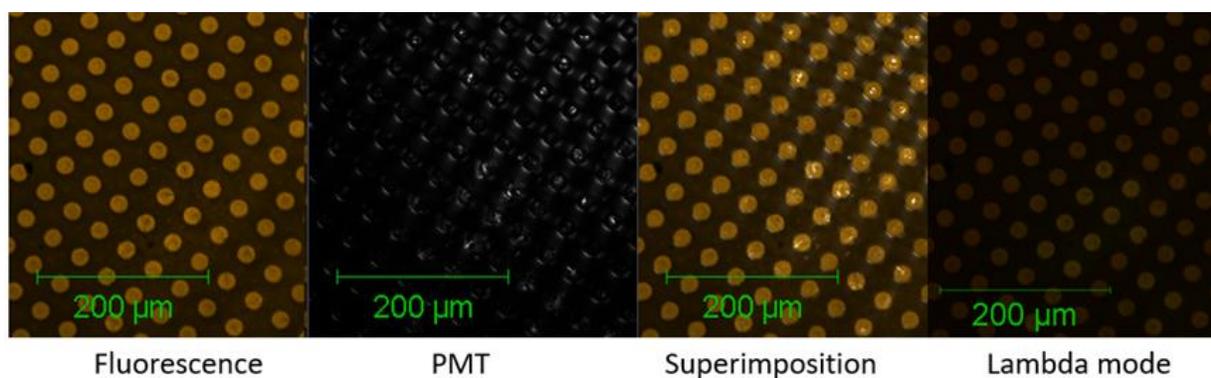
Figure 2.36. Confocal microscope images of the hydrogel filled by 2HEO-PLGA@MBds using 10x objective (scale bar 200µm).
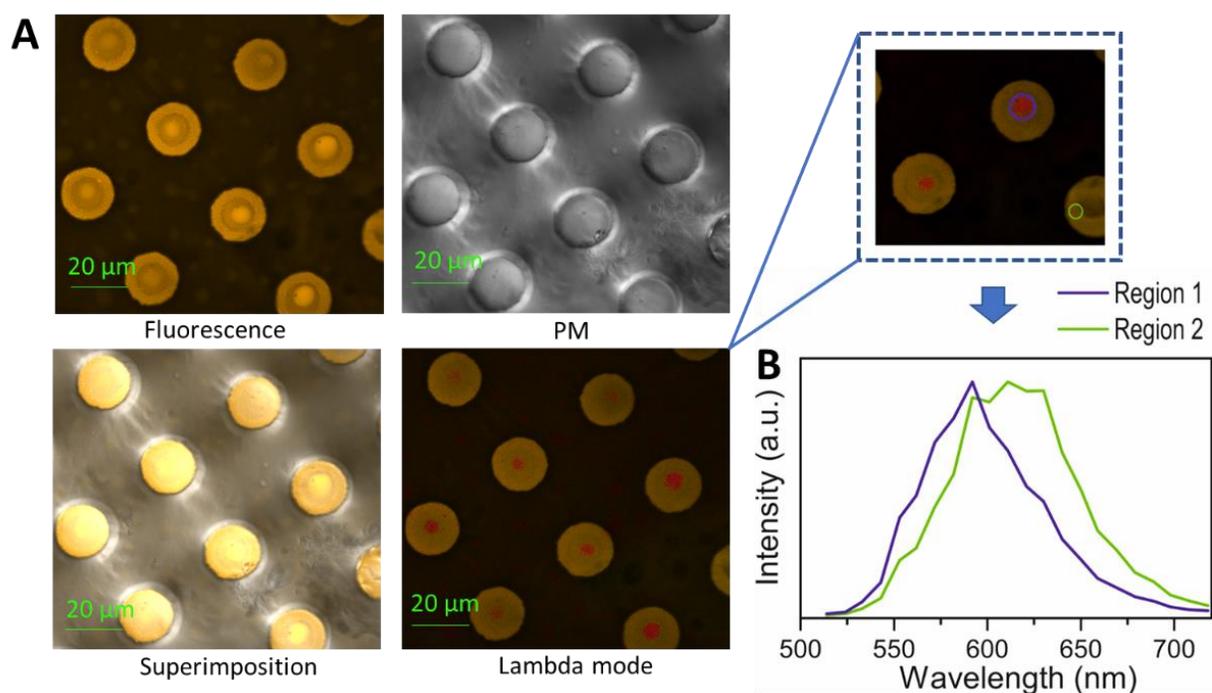
Figure 2.37. A) Confocal microscope images of 2HEO–PLGA@MBds loaded with Nile Red using 63x objective (scale bar 20µm). **B)** Emission spectra of the lambda mode of 2HEO taken from two different areas of the 2HEO-PLGA@MBds confocal images.
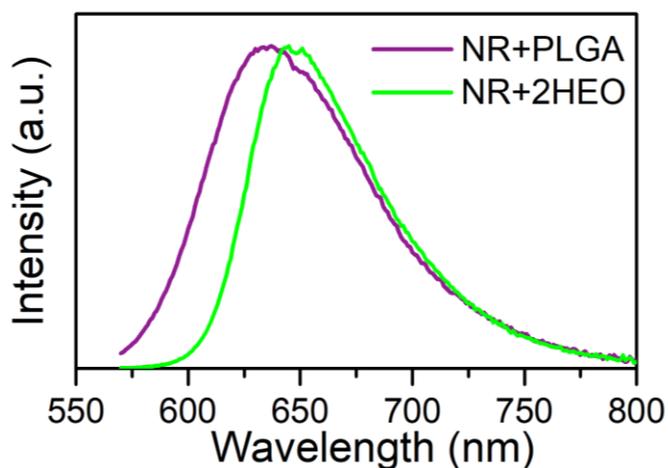
Figure 2.38. Emission spectra of NR in PLGA and NR with 2HEO using a fluorimeter.

On the other hand, using the same methodology,[70] the incorporation of 20% w/w of Anandamide (AEA) was tried as an endocannabinoid in the PLGA@MBds. Confocal images were taken to see if the beads were formed with the inclusion of AEA; **Figures 2.39** and **2.40** shows pictures using the 10x and 63x objective, respectively. The fluorescence, PMT, superimposition and the lambda mode of the material are showed. Monodisperse material with a diameter size of 20 µm and a concave shape is formed. The Lambda mode in these studies reveals also a material that inside has two compositions (**Figure 2.40A**-lambda mode); red and yellow colors represent different sections in the material; in contrast of the 2HEO-PLGA@MBd where the red color was in the center, in the AEA-PLGA@MBs the red color is localized in a disperse way through the material and sometimes it is localized in spots in a random position inside the MBds (**Figure 2.40A** lambda mode). These two regions correspond to different emission spectra with λ_{max} at 592 and 611 nm (**Figure 2.40B**).

In order to know to what corresponds the two different regions, emission spectra were performed of the Nile Red with PLGA and Nile Red with AEA at the same concentration in which they were designed to be inside of the MBds (see material and methods/ fluorescence emission spectra of PLGA-Nile Red and PLGA-AEA). In **Figure 2.41** is represented the emission of the two samples with λ_{max} at 637 and 644 nm, giving the information that the Nile Red in combination with the AEA has another emission profile than the Nile Red with PLGA. With this information, it

can be said that the areas represented in red in the lambda mode on the confocal images correspond to a higher concentration of AEA in the MBds.

As a conclusion on this part, *N*-(2-hydroxy ethyl) oleamide (2HEO) or Anandamide (2HEA), (an analog and active endocannabinoid) can be loaded to the PLGA@MBds in very weight percentage preserving the morphology of the beads.
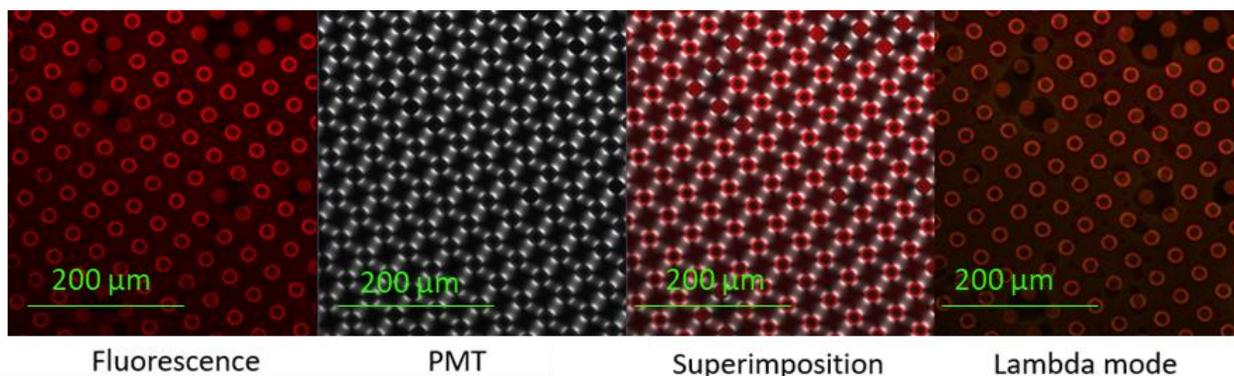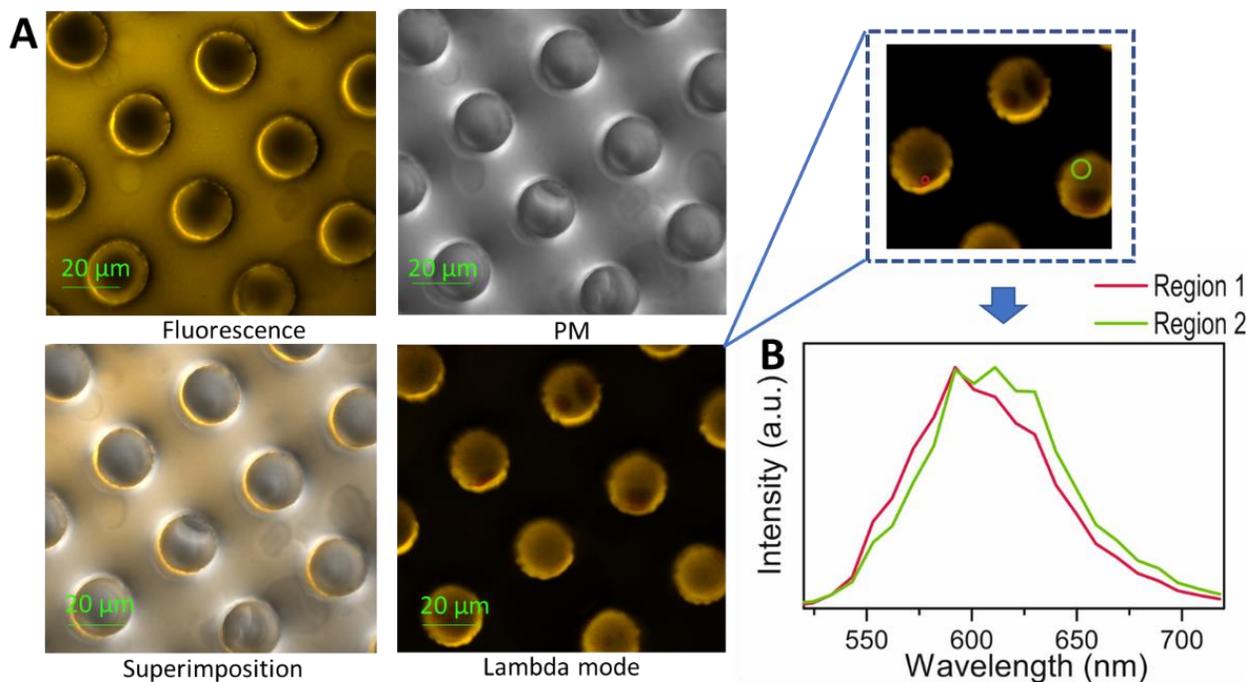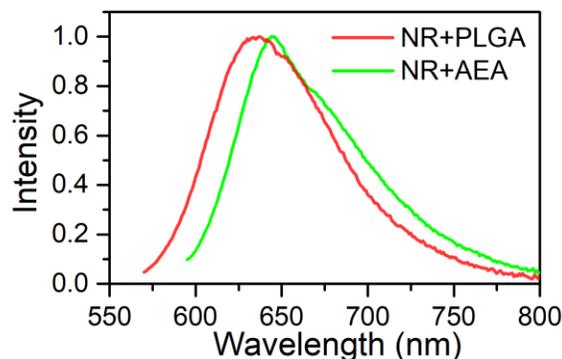

Figure 2.39. Confocal microscope images of the hydrogel filled by AEA-PLGA@MBds using 10x objective (scale bar 200µm).

Figure 2.40. A) Confocal microscope images of AEA–PLGA@MBds loaded with Nile Red using 63x objective (scale bar 20µm). **B)** Emission spectra of the lambda mode of AEA taken from two different areas of the AEA-PLGA@MBds confocal images.

Figure 2.41. Emission spectra of NR in PLGA and NR with AEA using a fluorimeter.

2.2.3.3.2. Incorporation of MSNP in the PLGA@MBds by the hydrogel template method

To study the incorporation of MSNPs in the PLGA@MBds by the hydrogel template method and to mimic the loading of the MSNPs with a chemotherapy drug, MSNPs of around 56±8 nm were loaded with Orange 2 (**Scheme 12**). After, TGA analysis showed a drug loading of 12.2 % of the Orange 2 (**Figure 2.42**). **Figure 2.43** shows the IR spectra of the Orange 2 dye, the NPs loaded with the dye and the IR of this particles after TGA, we can observe with this analysis the presence of the dye in the particles and the absence of this after its calcination in TGA.
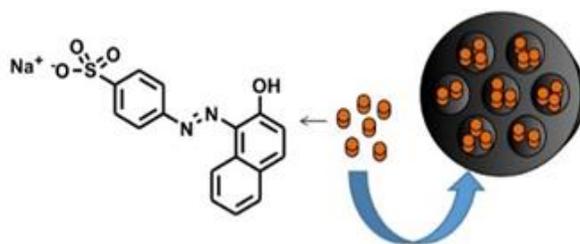
Scheme 2.12. Representation of the loading of NPs with Orange 2.
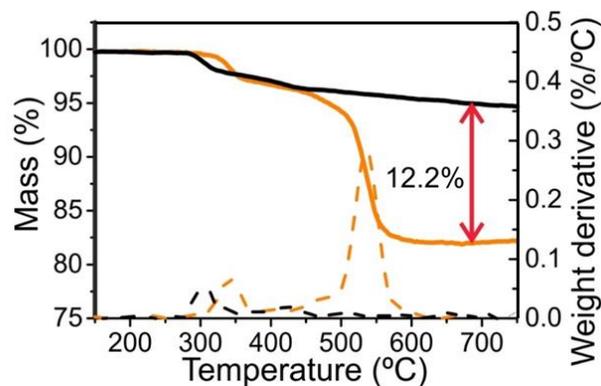
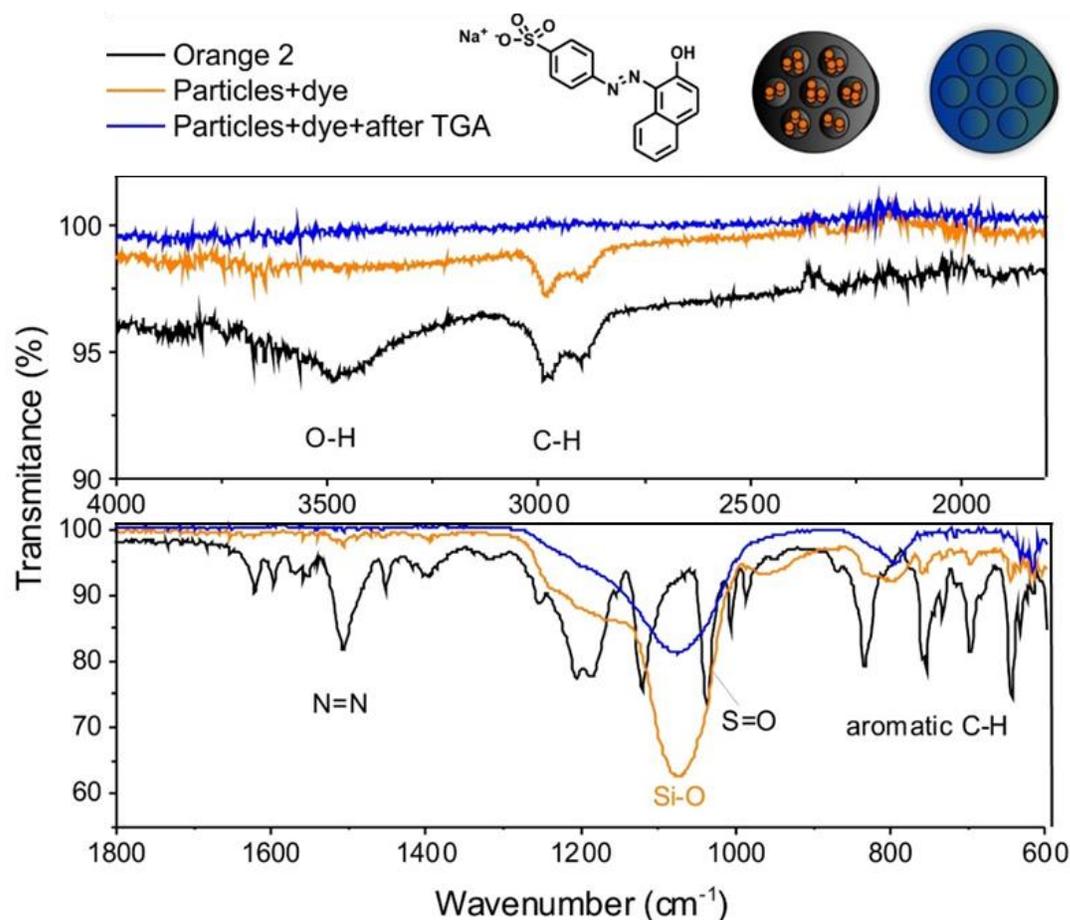**Figure 2.42.** TGA of the Orange 2 loaded in the NPs.

Figure 2.43. IR spectra of Orange 2 dye, particles loaded with Orange 2 and particles loaded after TGA; line black, orange and blue, respectively.

Furthermore, photophysics studies of the MSNPs loaded with Orange 2 were done. The absorbance, emission and excitation spectra of the Orange 2 and the MSNPs loaded with the dye were taken (**Figure 2.44 A** and **B**, respectively). It is observable the same absorbance at λ_{max}=480 nm), emission (at λ_{max}=480 nm) and excitation band (at λ_{max}=550 nm) for the dye and the particles loaded. Showing then another probe that the dye was successfully loaded in the MSNPs.
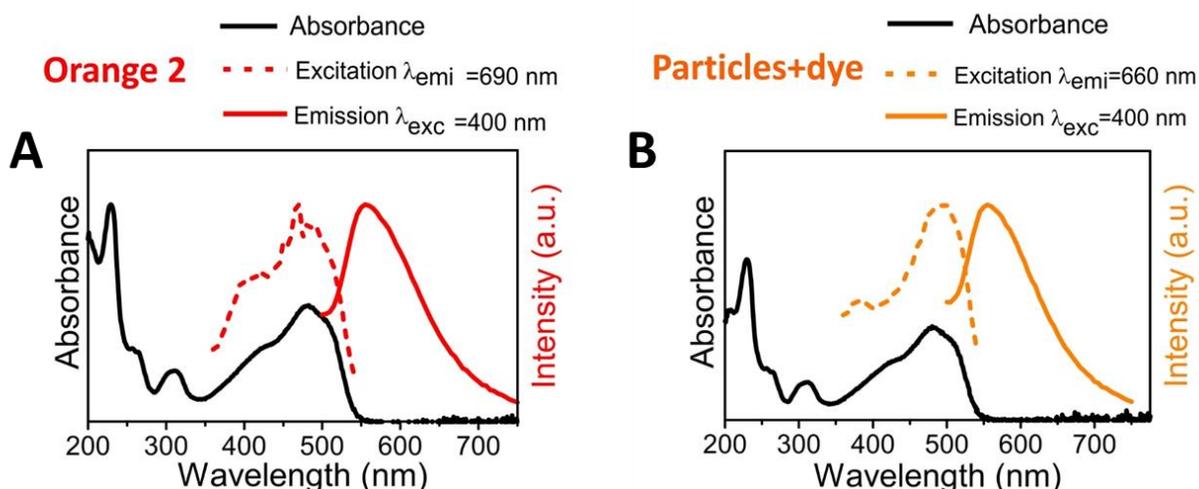
Figure 2.44. A) Absorption, Excitation and Emission spectra of **A)** Orange 2 and **B)** MSNPs loaded with Orange 2.

Finally, this MSNPs loaded with Orange 2 were included in the PLGA@MBds (**Scheme 13**). To characterize the system NPs@PLGA-MBd, confocal images were taken using 10x and 63x objectives. The fluorescence, PMT, superimposition and the lambda mode of the material is shown in **Figure 2.45**. Z- stack measurement was performed using the 63x objective (**Figure 2.46**), the morphology of this material is shown in these pictures and how the NPs are uniformly distributed along the entire MBds. It can be said that the PVA template material is stable as the NPs-PLGA solution is not diffusing outside the bead hole when it is doing the sol-gelation process. With SEM images (**Figure 2.47**), it is observed the incorporation of the NPs, which also remains on the surface of the MBds. Finally, TGA studies were performed to know the mass loss of the material as it can be seen in **Figure 2.48** is presented the TGA of NPs@PLGA-MBd, the NPs loaded with the dye Orange 2, and the NPs and the Orange 2 dye**.** The NPs@PLGA-MBd mass lost is 91.5% while in the NPs with dye is 12.2%, due to those values it can be assumed that there is 79.3% of polymer in the NPs@PLGA-MBd.
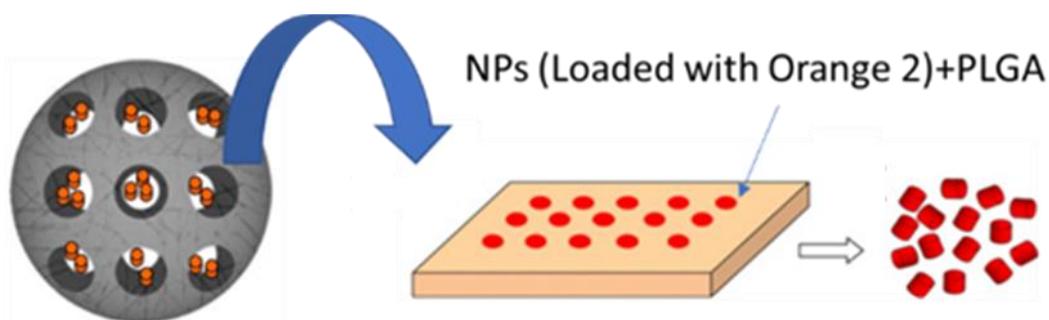
Scheme 2.13. Representation of the loading of NPs in the PLGA@MBds by the hydrogel template method.
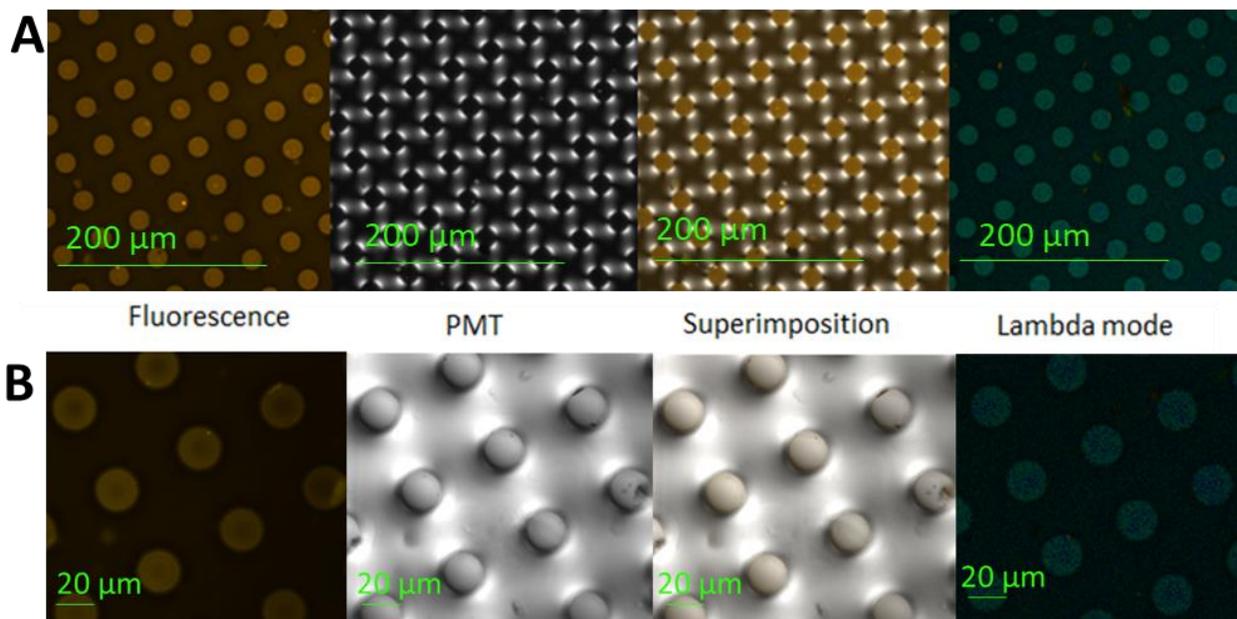
Figure 2.45. Confocal microscope images of the hydrogel filled by the polymer with NPs using **A)** 10x and **B)** 64x objective (scale bar 200 and 20 μm, respectively).
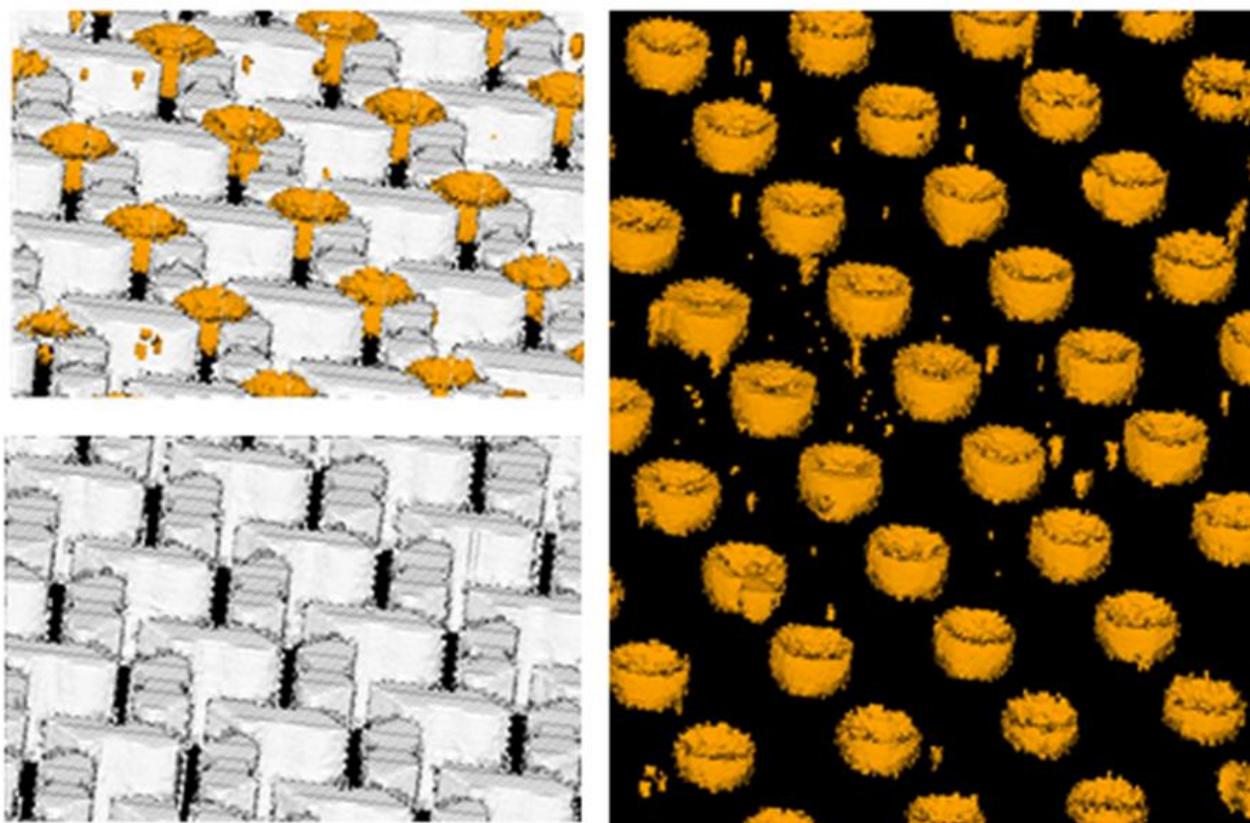

Figure 2.46. Z-stack analysis of the hydrogel filled by the polymer with NPs using 63x objective.
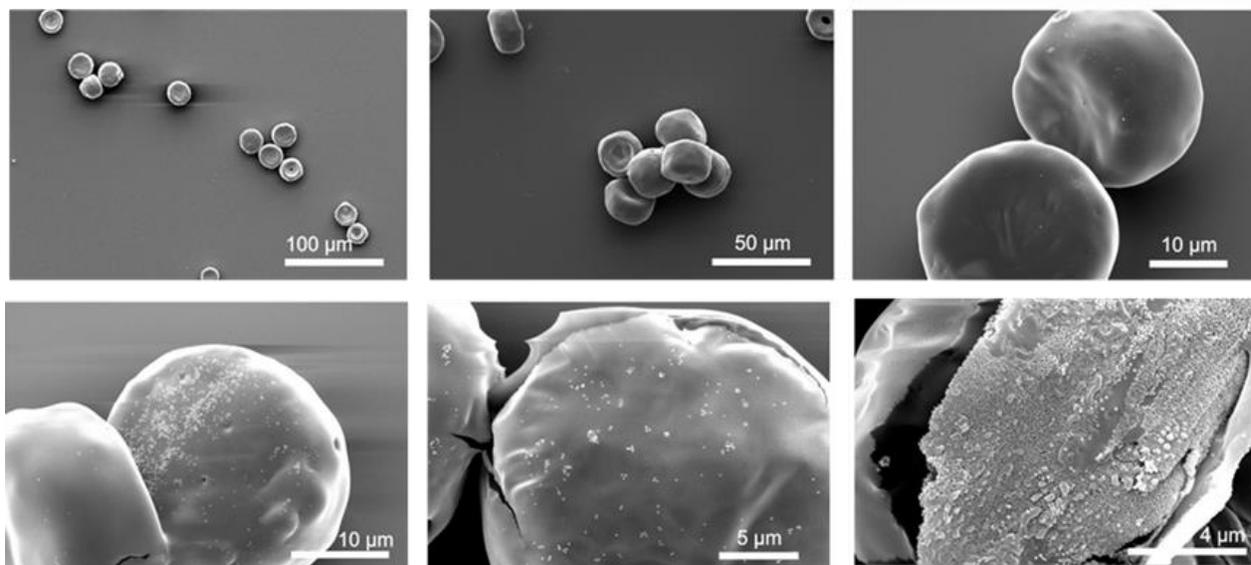
155

Figure 2.47. SEM images of the NPs-PLGA@MBds microparticles containing NPs and loaded with orange 2 (Scale bars 100, 50, 10, 5 and 4 µm).
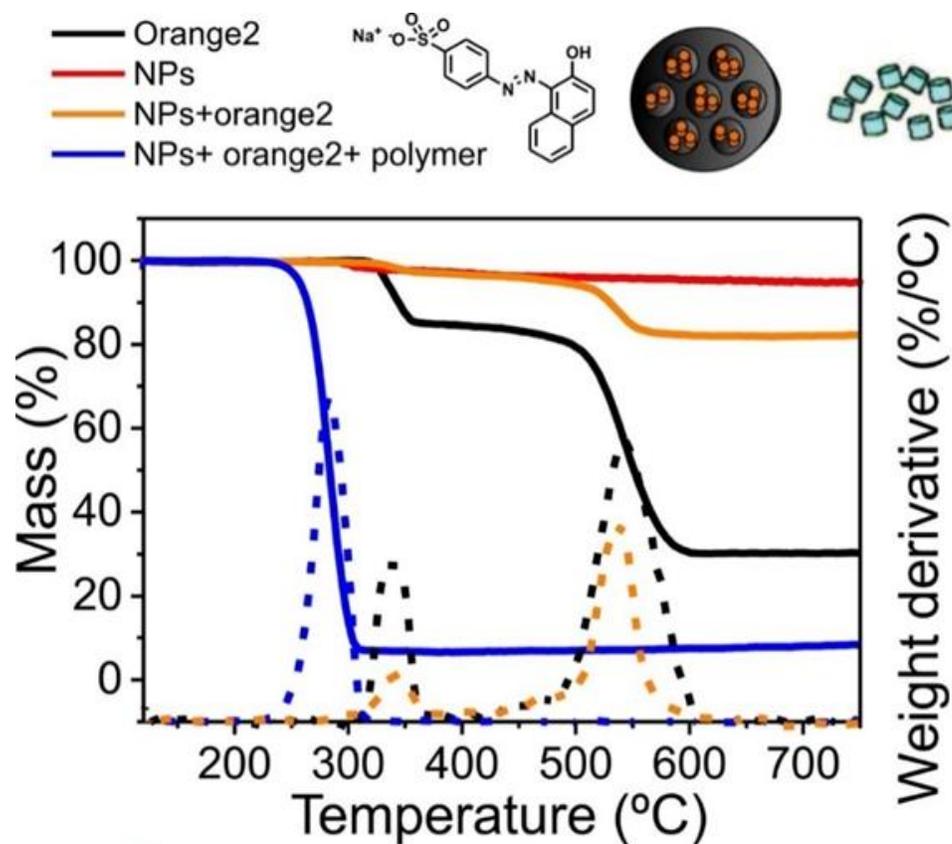

Figure 2.48. TGA analysis of the microparticles containing NB-NPs loaded with orange dye (line blue), and the comparation with NB-NPs (line red), NPs loaded with orange 2 (line orange) and the dye (line black).

As a conclusion, the hydrogel template methodology is a procedure in which particles of any size and morphology can be done, with a lot of possibilities of inclusion of different materials at a high loading of contents without losing its morphology and monodispersity. NPs-PLGA@MBds and CBds-PLGA@MBds are the platforms to know that indeed CBds-NPs-PLGA@MBds can be done using this methodology.

2.2.3.3.3. Breakability test of the PLGA@MBds

Breakability test was performed in the PLGA@MBds system. The degradation rate and the drug release of the PLGA-based polymer is influenced by many factors, such as the initial molecular weight (Mw), monomer composition ratio of PLGA matrix (i.e., LA/GA ratio), drug type, processing method, and pH value of the release medium.[92]

Then, the degradation of the PLGA@MBds loaded with Nile Red was studied in three different media: water, PBS (pH 7.4) and in an acetate buffer (pH 5.2) (**Figures 2.49**, **2.50** and **2.51**, respectively) for 20 days at 37 °C , giving different types of degradation of the MBds depending on the media. In water (**Figure 2.49**), the process starts with the apparition of holes after 3 days of the study, which incremented in number over time, making then the breakability of the material (after 10 days) and the post deformation of the MBds after 20 days. In buffer PBS (**Figure 2.50**), after 5 days of production, the material starts to crack making the deformation of the beads and the degradation starts to be visible after 20 days. On the other hand, in acetate buffer (**Figure 2.51**), since one day, the deformation of the material started not only giving smaller sizes of the MBds each time but also the degradation seemed to cause the fusion of the material in aggregates after 7 days of the study, that after appeared in small pieces.

As a conclusion in this part, it has been studied that the PLGA@MBds done are able to degrade in different media after 20 days, what makes them a good platform as a long drug delivery system.
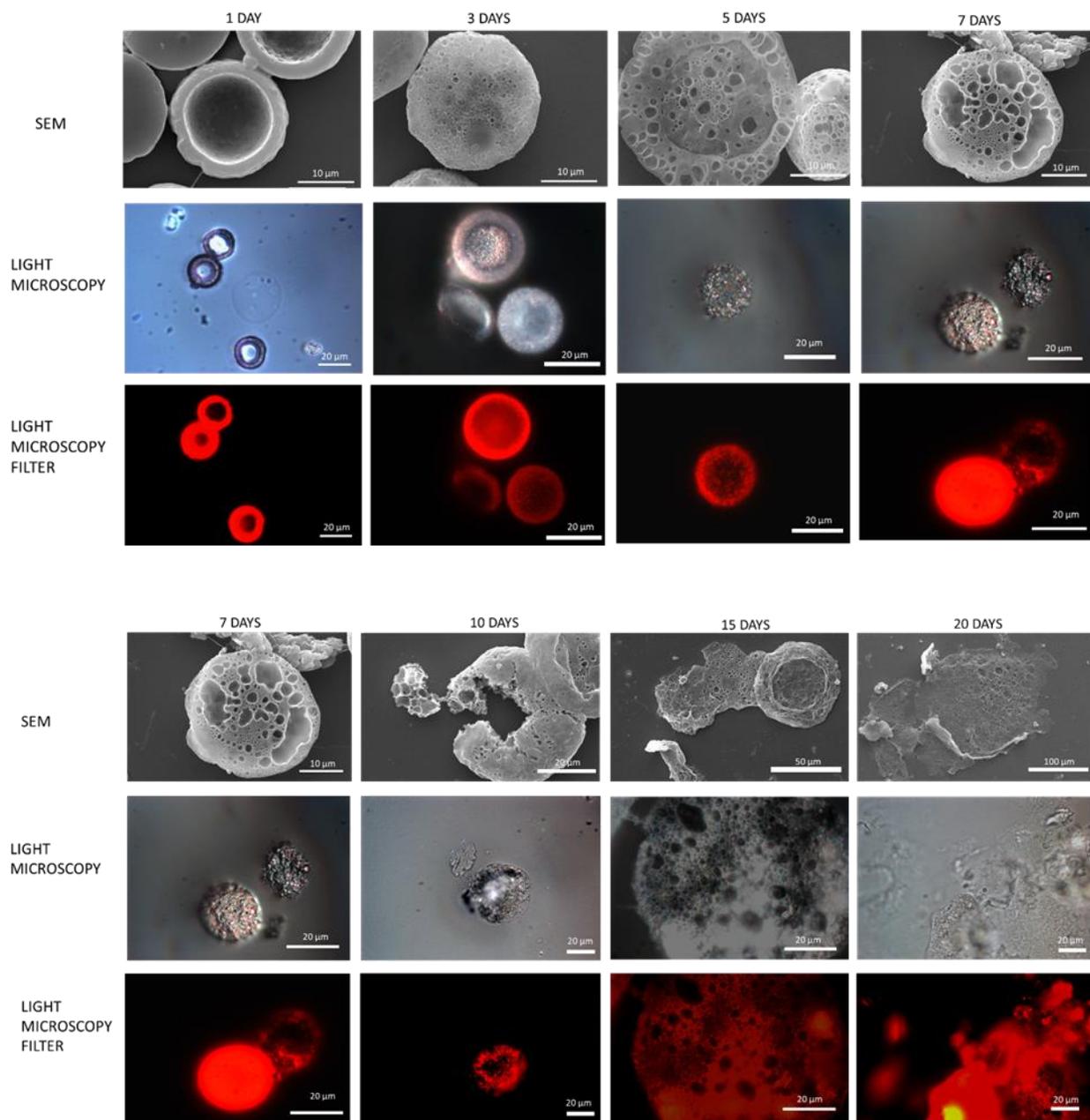
Figure 2.49. SEM, Light microscopy, and light microscopy using a filter of the degradation of the PLGA@MBds loaded with Nile Red in water media (pH 5.2) and 37 °C, followed during the time for 20 days.
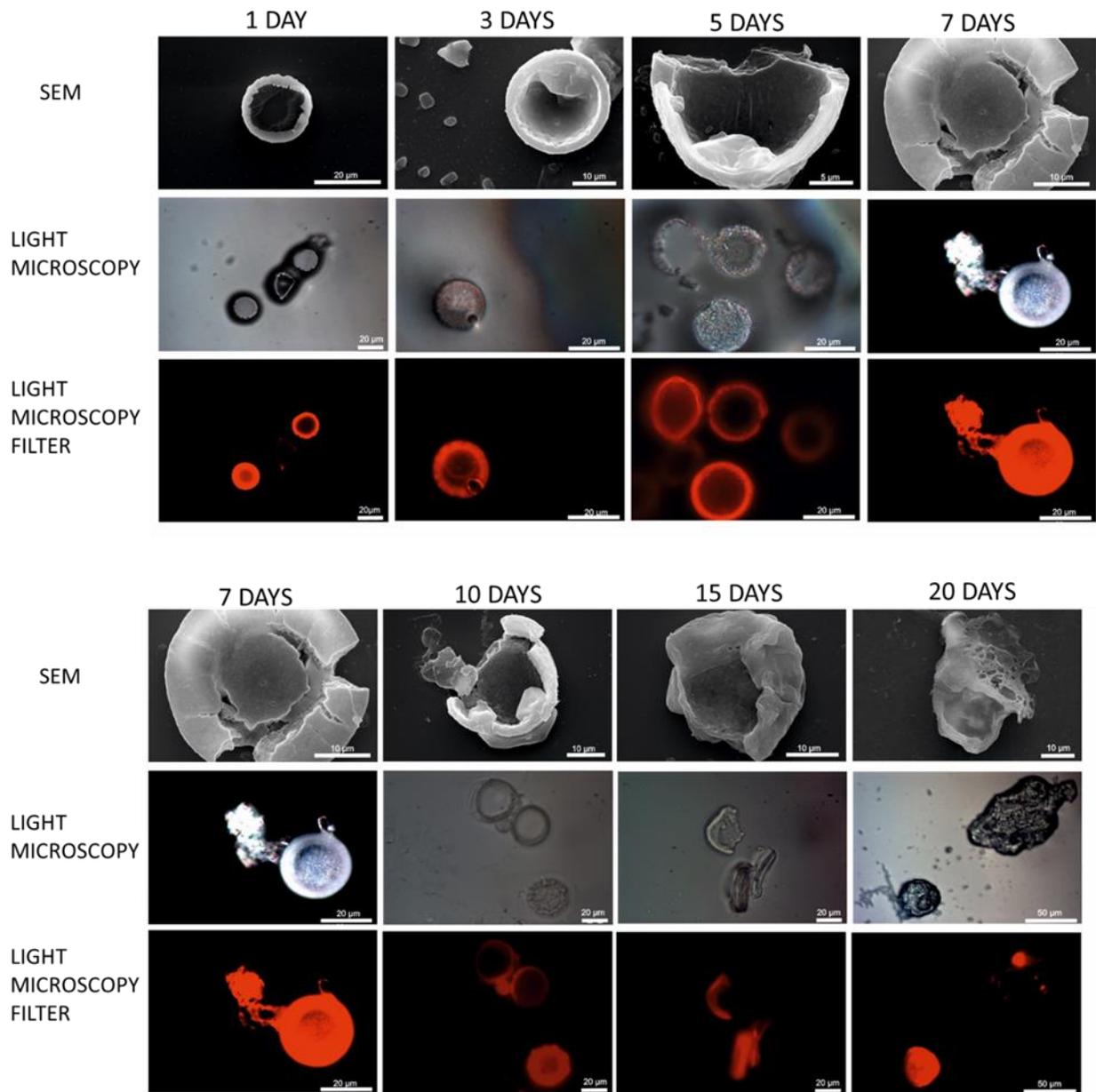
Figure 2.50. SEM, Light microscopy, and light microscopy using a filter of the degradation of the PLGA@MBds loaded with Nile Red in PBS pH 7 media and 37 °C, followed during the time for 20 days.
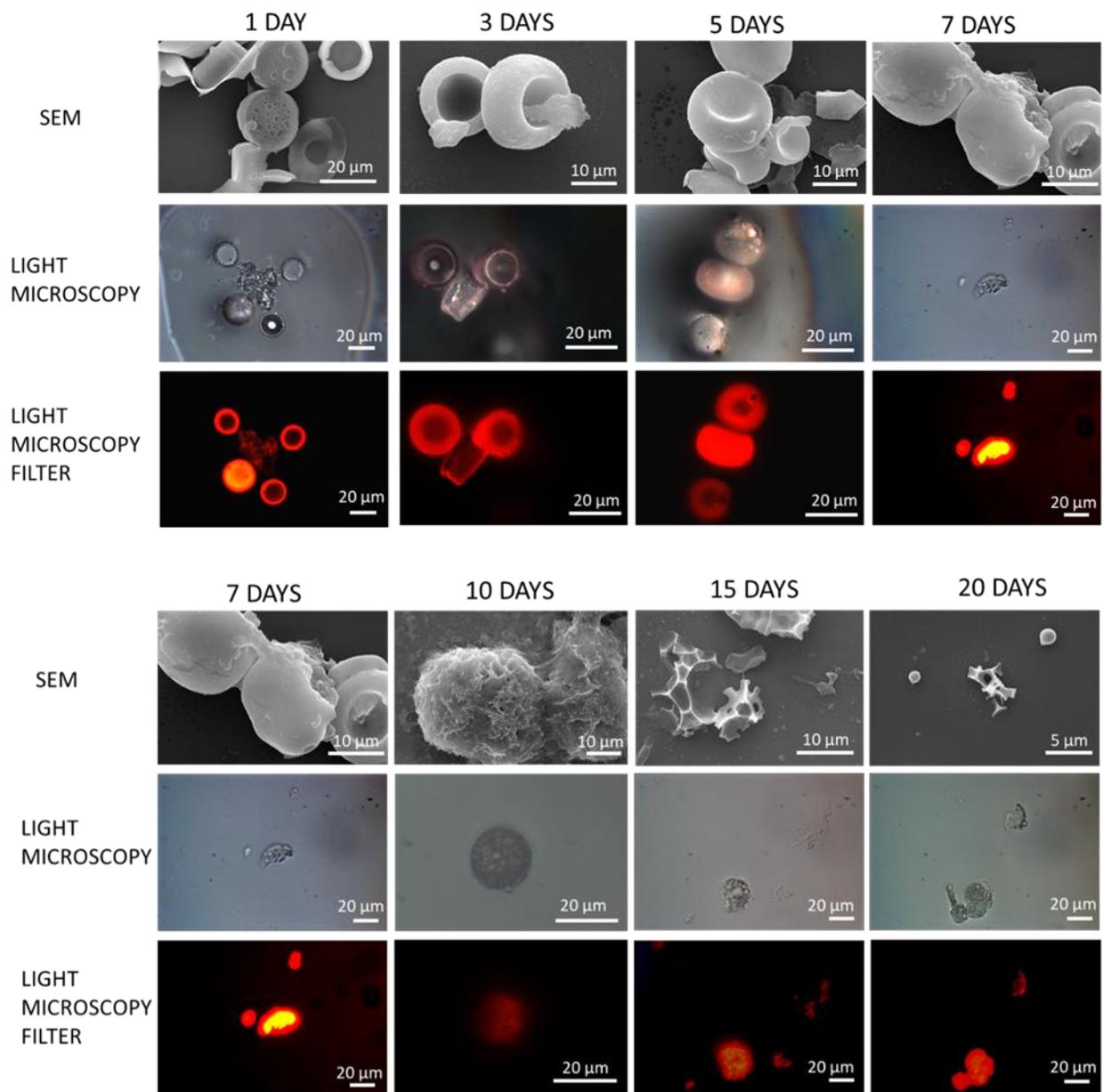
Figure 2.51. SEM, Light microscopy, and light microscopy using a filter of the degradation of the PLGA@MBds loaded with Nile Red in Acetates buffer media (pH 5.2) and 37 °C, followed during the time for 20 days.

2.3. Conclusions

N-(2-hydroxy ethyl) oleamide (2HEO) and Anandamide (2HEA), as analog and active endocannabinoids, were synthesized and characterized by NMR, IR, HR ESI-TOF-MS.

Different kinds of MSNPs were synthesized as an example of all the varieties of materials that can be included in the PLGA@vehicles. Fully characterization of non-breakable and breakable MSNPs with different constructions are presented.

Different techniques were used to synthesize the PLGA@vehicles as the solvent evaporation method, self-organized precipitation route (SORP) and the hydrogel template method.

By the solvent evaporation method, PLGA@MS were obtained with two main diameter size distributions of around 1.47±0.37 μm and 14.9±3.7 μm. The inclusion of MSNPs can be done but the polydispersity of the system gave the information that this methodology was not the best to continue the studies.

Using the SORP methodology, PLGA spheres of around 600 nm and 1 μm can be done with a free surfactant. The incorporation of MSNPs gives agglomerations of the PLGA@MS with 20 and 5% w/w. On the other hand, the incorporation of an endocannabinoid perturbs the formation of the spheres even at low loading (5% w/w).

On the other hand, homogeneous cylindrical PLGA microparticles (PLGA-MBds) were fabricated with a size of 20 μm using the hydrogel template method (HTM) and Nile Red as a dye. The material was characterized by confocal microscopy SEM and Light Microscopy. Additionally, 2HEO or AEA were loaded in high % (20% w/w) in the PLGA@MBds giving CBds-PLGA@MBds systems using the HTM. Confocal images show the conservation of the PLGA-MBds morphology. No breakable Nanoparticles (NB-NPs) loaded with Orange 2 were selected to mimic the loading of MSNPs inside the PLGA@MBds, showing that the material can be prepared also with this methodology giving vehicles with monodispersity in size and shape.

The degradation breakability test of the PLGA@MBds in different media was also tried, giving the information that they can be broken after 20 days.

2.4. Materials and Methods

2.4.1. Materials. All commercial solvents and reagents were used as received, without further purification. Tetraethyl orthosilicate (TEOS), bis(triethoxysilyl-propyl)disulfide (BTSPD), Glutathione (GSH), Cetyltrimethylammonium bromide (CTAB, ultra for molecular biology) Orange2 and Nile Red were purchased from Sigma Aldrich. The PDMS template for the Hidrogel template method, PLGA (75:25 LA:GA, Mn 15K-25k Da and 50:50 LA:GA, Mn 15K-25k Da) was purchase from PolyScitech®.

2.4.2. Synthesis

2.4.2.1. Synthesis of N-(2-fluoroethyl)oleamide (2FEO)

HBTU (*N,N,N',N'*-Tetramethyl-*O*-(1*H*-benzotriazol-1-yl)uronium hexafluorophosphate, 0.834 g, 2.2 mmol) was dissolved in anhydrous DMF (5 mL) under nitrogen atmosphere. A solution of oleic acid (0.565 g, 2 mmol) in anhydrous DMF (5 mL) was added to the HBTU solution. To the mixture was added DIPEA (*N,N*-Diisopropylethylamine, 2 mL), and the mixture was let to stir at RT for 5 min. Then (2-fluoroethyl)amine hydrochloride (0.419 g, 4.2 mmol) was added at once. The mixture was let to stir at RT for 2 days (Scheme 2). The reaction mixture was diluted with DCM (30 mL) and was extracted with a saturated solution of NaHCO$_3$ (3 × 30 mL). The organic phase was dried over Na$_2$SO$_4$, and the solvents were evaporated under reduced pressure. Toluene was used to remove all traces of DMF. The compound was purified by flash chromatography (SiO$_2$/DCM 95:5 MeOH) to give a white waxy solid. Yield 455 mg (69 %) (**Scheme 14**). The N-(2-fluoroethyl)oleamide was characterized by IR, ^{1}H (**Figure 2.52**), ^{13}C (**Figure 2.53**) and ^{19}F NMR (**Figure 2.54**). IR and HR ESI-TOF-MSC (**Figures 2.55** and **2.56**, respectively).

^{1}H-NMR (400 MHz, CDCl$_3$, , δ ppm, J Hz): δ = 5.80 (bs, 1H, N–*H*), 5.34 (m, 2H, =C–*H*), 4.49 (dt, 2H, ^{2}J(^{19}F) = 48 Hz, ^{3}J = 4Hz, –C*H$_2$*F), 3.56 (ddt, 2H, ^{3}J$_1$(^{19}F) = 32 Hz, ^{3}J$_2$ = ^{3}J$_3$ = 4 Hz, –C*H$_2$*–CH$_2$F), 2.20 (t, 2H, ^{3}J = 8 Hz, –C*H$_2$*–C=O), 2.00 (m, 4H, =CH–C*H$_2$*–), 1.62 (m, 2H, –C*H$_2$*–CH$_2$–C=O), 1.28 (m, 20H, –C*H$_2$*–), 0.88 (t, 3H, ^{3}J = 4 Hz, –C*H$_3$*).

^{13}C-NMR (100.58 MHz, CDCl3, δ ppm, J Hz): δ = 173.5 (*C*=O), 130.1 (–H*C*=CH–), 129.9 (–HC=*C*H–), 83.8 (d, ^{1}J(^{19}F) = 166 Hz, –*C*H$_2$F), 39.96 (d, ^{2}J(^{19}F) = 20 Hz, –*C*H$_2$–CH$_2$F), 36.8 (–*C*H$_2$–C=O), 32.0, 29.9, 29.8, 29.6, 29.4, 29.4, 29.2, 27.4, 27.3, 25.8, 22.8, 14.2 (–*C*H$_3$).

^{19}F-NMR (376 MHz, CDCl$_3$, δ ppm, J Hz): δ = -224.3 (tt, 1F, ^{2}J(^{1}H) = 48 Hz, ^{3}J(^{1}H) = 32 Hz).

IR   (solid, cm⁻¹): $\bar{v}$ = 3304 (N–H), 2916 (C–H), 2849 (C–H), 1643 (C=O), 1555, 1038,
                719.

HR ESI-TOF-MS m/z = 350.2832 (calc. 350.2830), 351.2858 (calc. 351.2863), 352.2929 (calc.
                352.2897)
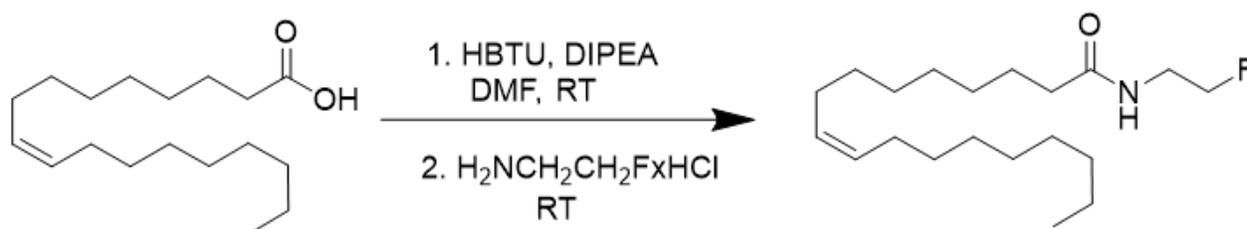
Scheme 2.14. Synthesis of N-(2-fluoroethyl)oleamide, analogue of the endocannabinoid.
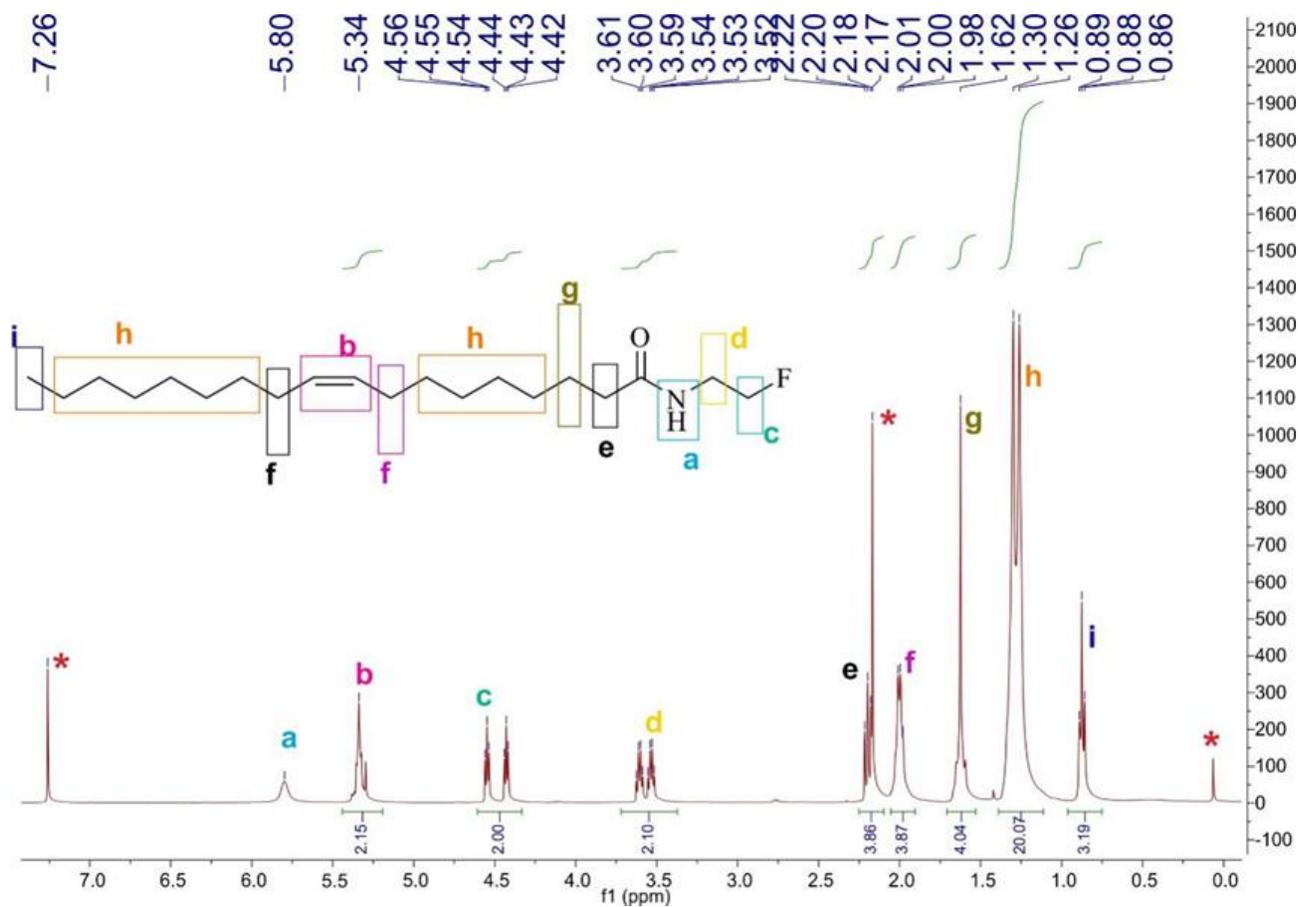

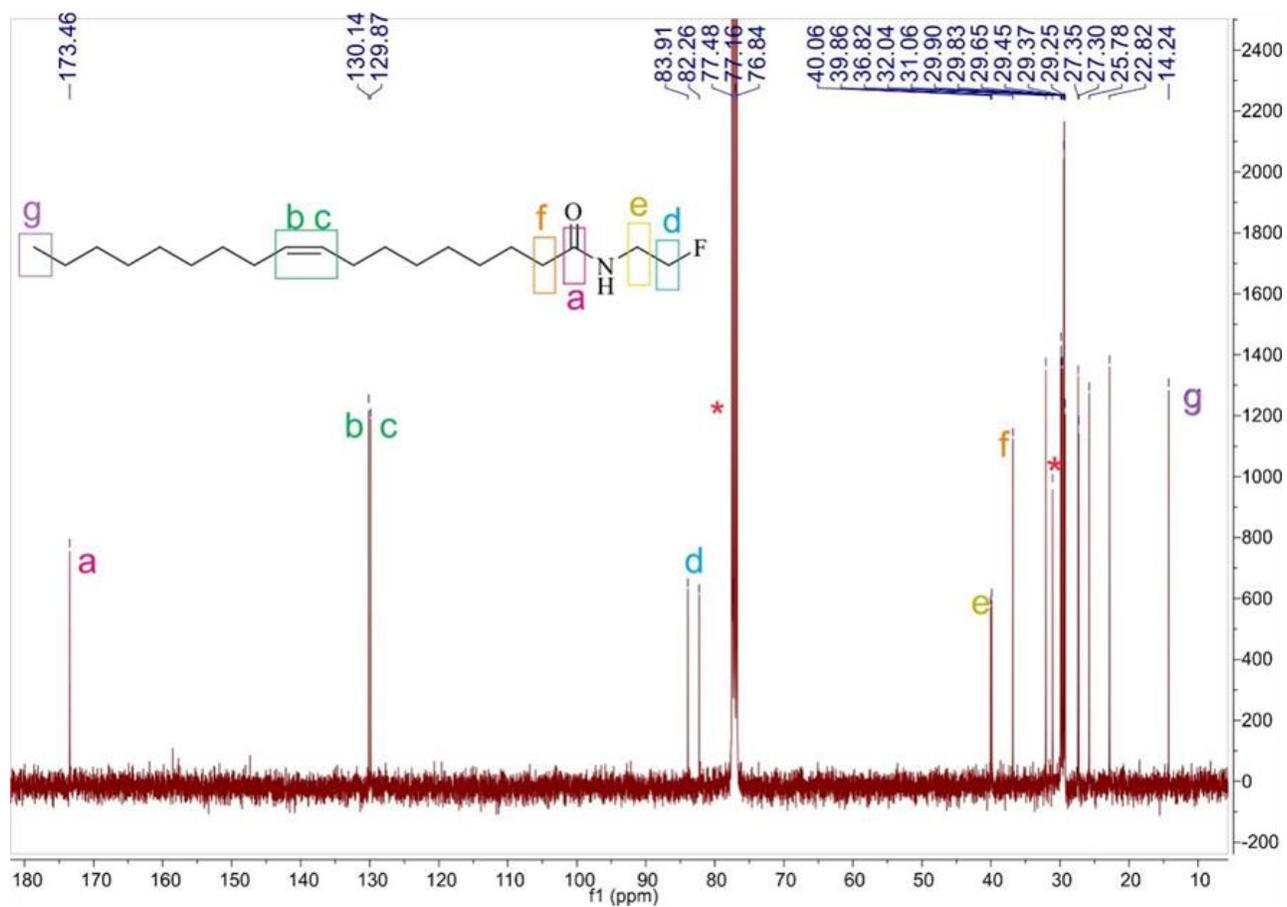**Figure 2.52.** ¹H NMR spectrum of N-(2-fluoroethyl)oleamide.

Figure 2.53. ^{13}C NMR spectrum of N-(2-fluoroethyl)oleamide.
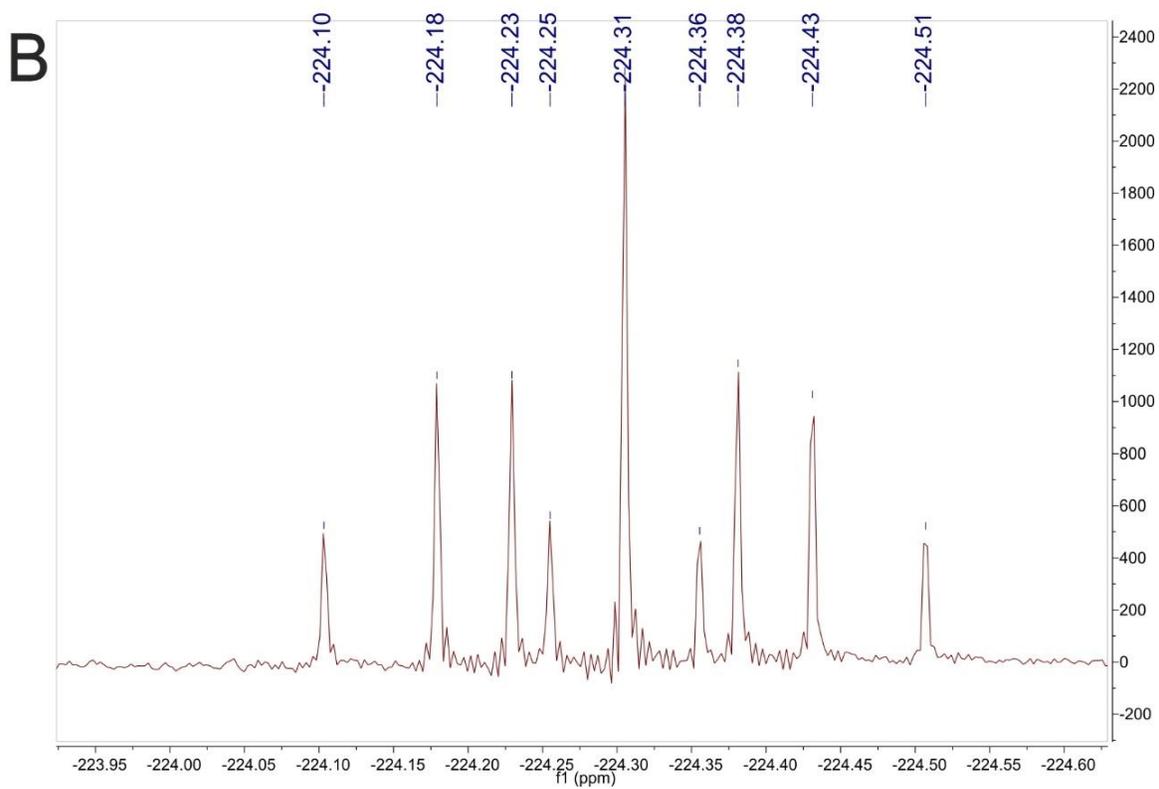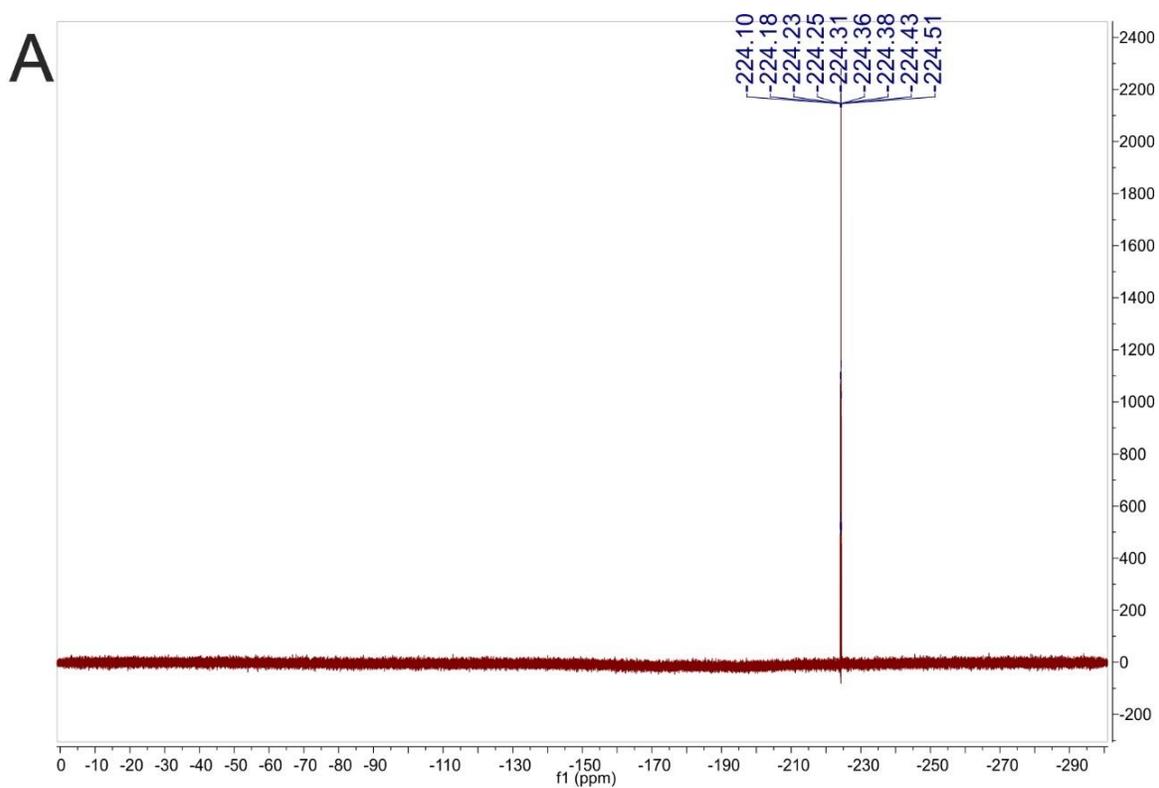
Figure 2.54. ^{19}F NMR Spectra of N-(2-fluoroethyl)oleamide.
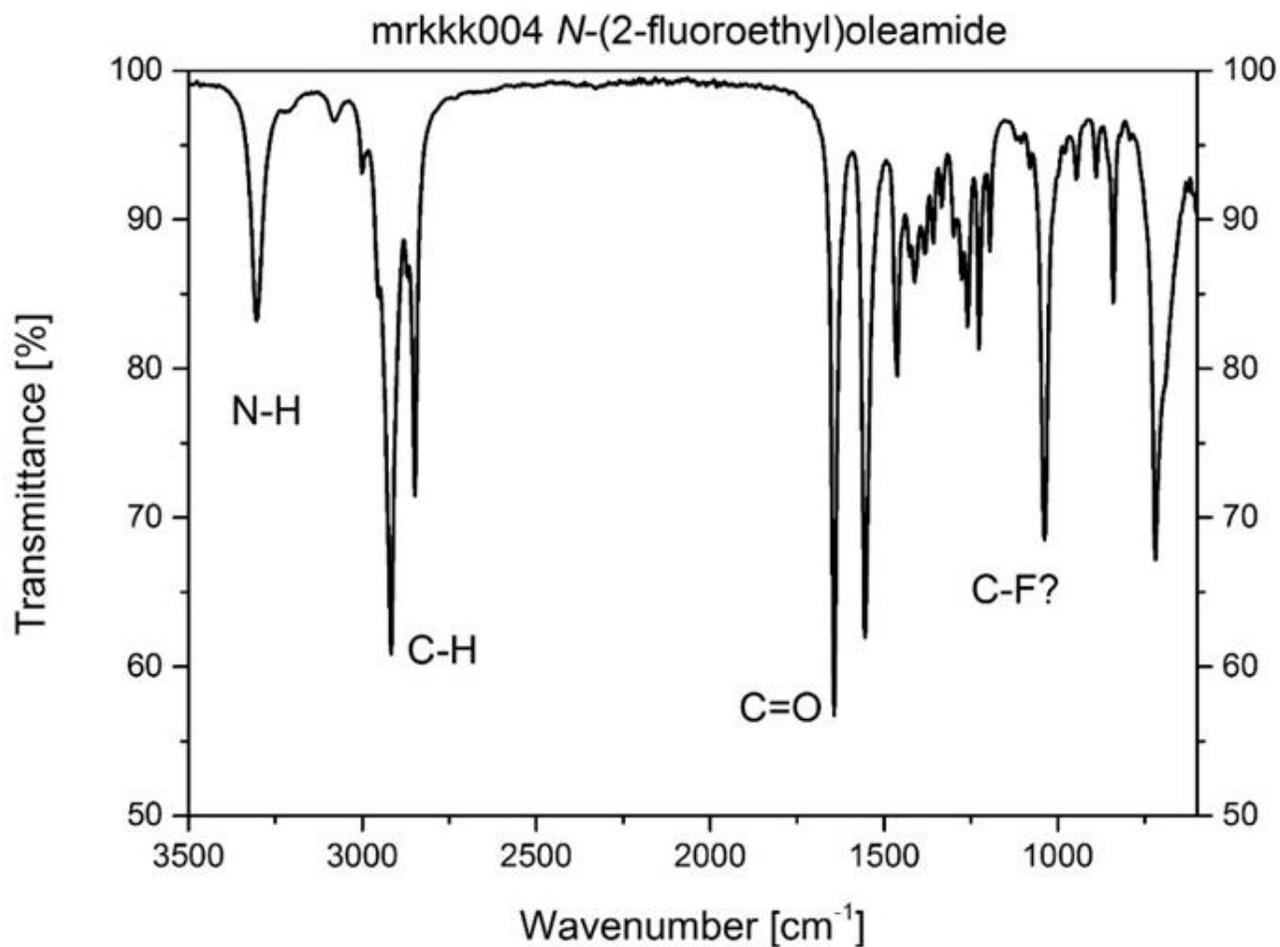
Figure 2.55. IR spectrum of N-(2-fluoroethyl)oleamide.
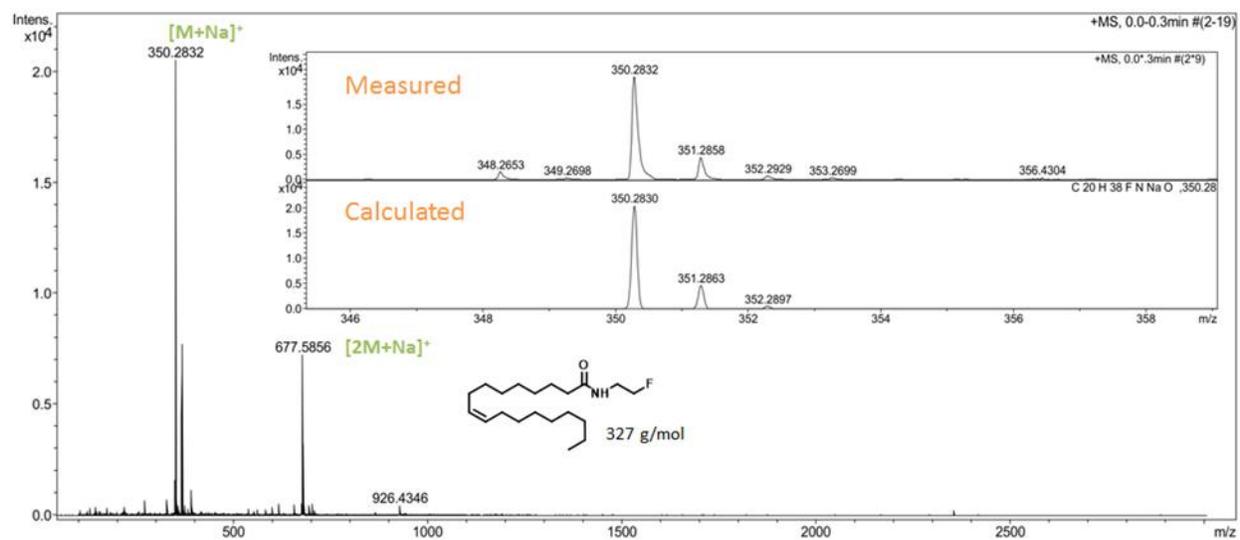

Figure 2.56. HR ESI-TOF-MS spectra of N-(2-fluoroethyl)oleamide.

2.4.2.2. Synthesis of N-(2-hydroxy ethyl) oleamide (2HEO)

The synthesis of N-(2-hydroxy ethyl) oleamide (2HEO) was synthetized as analog of endocannabinoids (**Scheme 2.15**). The reaction was divided in two steps: 1) Synthesis of the methyl oleate (**Scheme 2.16**) and 2) Synthesis of N-(2-hydroxy ethyl) oleamide from the ester (**Scheme 2.17**).
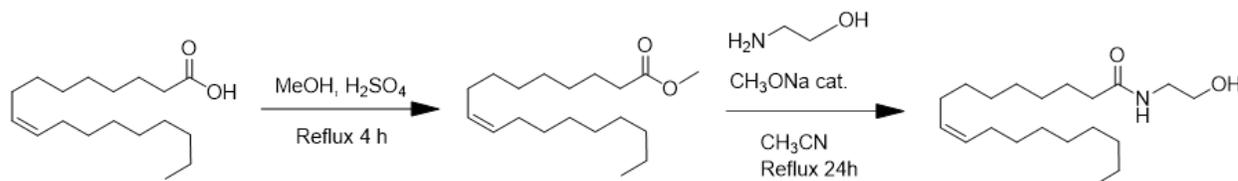

Scheme 2.15. Synthesis route of 2HEO from oleic acid.

1) Synthesis of methyl oleate

Oleic acid (4.282 g, 15 mmol) was dissolved in 50 mL of MeOH and 3 drops of Sulfuric acid (concentrated) was added. The mixture was refluxed for 4 h. The reaction mixture was diluted in water (30 mL) and was extracted with DCM (3 × 30 mL). The organic phase was dried over Na_2SO_4, and the solvents were evaporated under reduced pressure. The compound obtained was a yellow oil/solid. Yield 4.478 g (99.7%) (**Scheme 2.16**). Methyl oleate was characterized by ^{1}H (**Figure 2.57**), and IR (**Figure 2.58**).

^{1}H-NMR   (400 MHz, CDCl$_3$, , δ ppm, J Hz): δ = 5.33 (m, 2H, =C–*H*), 3.65 (s, 3H, O-CH$_3$), 2.29 (t, 2H, ^{3}J = 8 Hz, –C*H$_2$*–C=O), 1.99 (m, 4H, =CH-C*H2*-), 1.61 (m, 2H, –C*H$_2$*–CH$_2$–C=O), 1.28 (m, 20H, –C*H$_2$*–), 0.87 (t, 3H, ^{3}J = 8 Hz, –C*H$_3$*).

IR   (solid, cm^{-1}): $\bar{v}$ = 2924 (C–H), 2852 (C–H), 1739(C=O), 1435, 1168, 721.
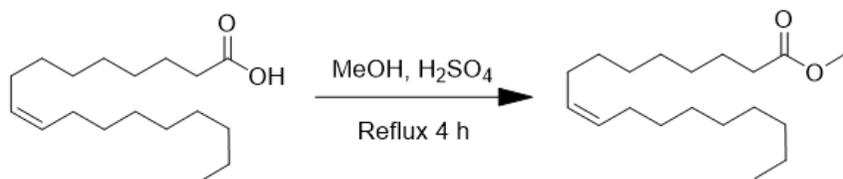
Scheme 2.16. Synthesis of methyl oleate from oleic acid.
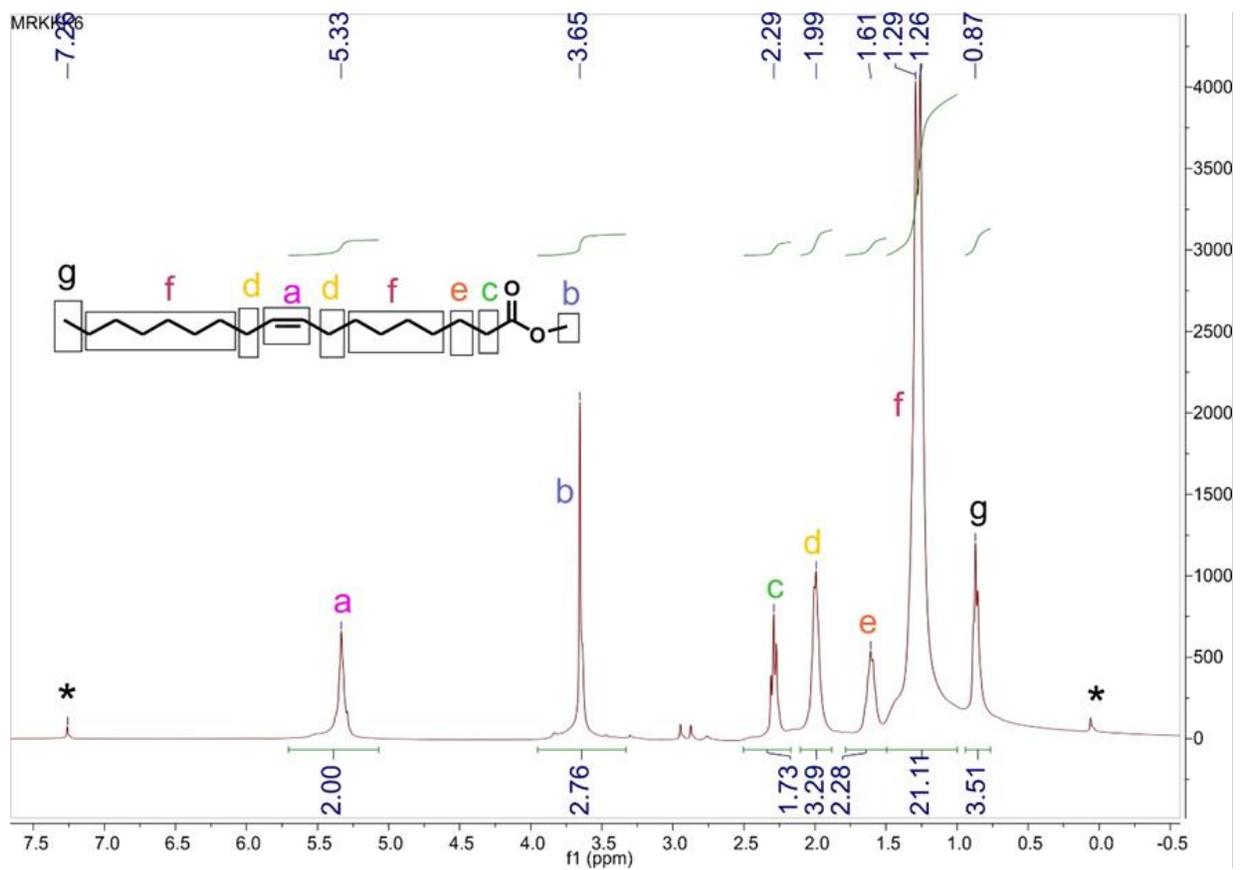
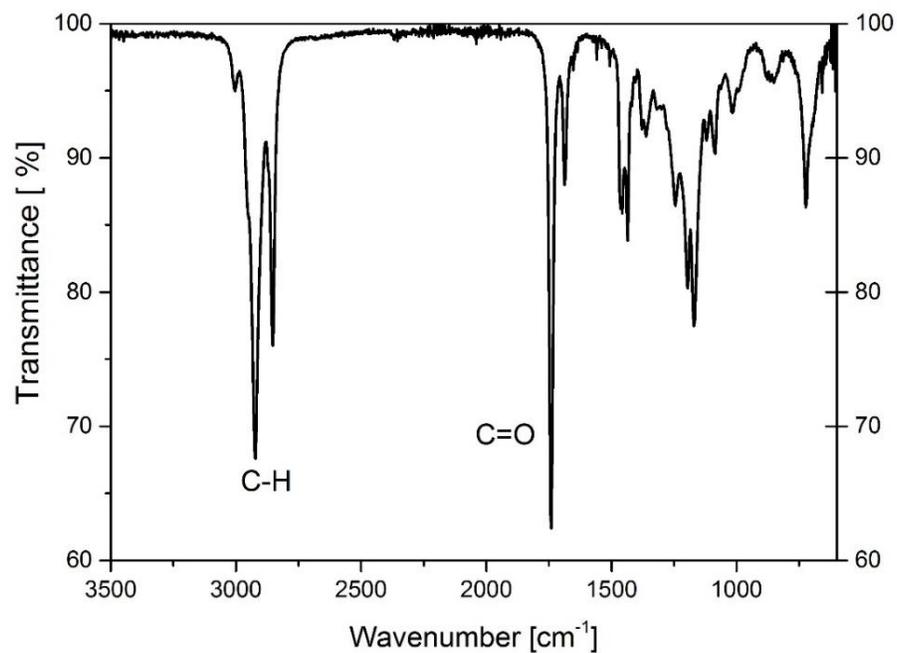**Figure 2.57**. ^{1}H NMR spectrum of methyl oleate.

Figure 2.58. IR spectrum of methyl oleate.

2) Synthesis of N-(2-hydroxy ethyl) oleamide (2HEO)

Methyl oleate (1.02 g, 3.4mmol) and ethanolamine (1.24 mL, 20 mmol) were dissolved in 14 mL Acetonitrile. To the mixture was added Sodium methoxide (0.026g, 0.4 mmol). The mixture was refluxed for 24 h. The reaction mixture was evaporated under reduced pressure to have less volume and then the compound was purified by flash chromatography (SiO$_2$/DCM 97:3 MeOH) to give a yellow waxy solid. Yield (86.5%) (**Scheme 2.17**). *N*-(2-hydroxy ethyl) oleamide was characterized by ^{1}H NMR (**Figure 2.59**), ^{13}C (**Figure 2.60**), IR (**Figure 2.61**) and HR ESI-TOF-MSC (**Figure 2.62**). In **Figure 2.63** is presented the IR spectra of methyl oleate and *N*-(2-hydroxy ethyl) oleamide.

This reaction was repeated one more time giving a yield of 86.9%.

^{1}H-NMR (400 MHz, CDCl$_3$, δ ppm, J Hz): δ = 5.87 (bs, 1H, N–*H*), 5.34 (m, 2H, =C–*H*), 3.73 (t, 2H, ^{3}J = 4Hz, –C*H$_2$*OH), 3.425 (q, 2H, ^{3}J= 6Hz , –C*H$_2$*–CH$_2$OH), 2.20 (t, 2H, ^{3}J = 8 Hz, –C*H$_2$*–C=O), 2.00 (m, 4H, =CH–C*H$_2$*–), 1.63 (m, 2H, –C*H$_2$*–CH$_2$–C=O), 1.28 (m, 20H, –C*H$_2$*–), 0.88 (t, 3H, ^{3}J = 4 Hz, –C*H$_3$*).

^{13}C-NMR (100.58 MHz, CDCl3, δ ppm, J Hz): δ = 174.66 (*C*=O), 130.17 (–H*C*=CH–), 129.89 (–H*C*=CH–), 62.88 (–*C*H$_2$OH), 42.65 (–*C*H$_2$–CH$_2$OH), 36.82 (–*C*H$_2$–C=O), 32.05, 29.92, 29.85, 29.67, 29.46, 29.40, 29.27, 27.37, 27.32, 25.85, 22.83, 14.26 (–*C*H$_3$).

IR (solid, cm^{-1}): $\bar{v}$ = 3294 (N–H), 2916 (C–H), 2848(C–H), 1643 (C=O), 1562, 1465, 1263, 1035, 723.

HR ESI-TOF-MS *m/z* = 326.3046 (calc. 326.3054), 327.3076 (calc. 327.3087), 328.3151 (calc. 328.3117).
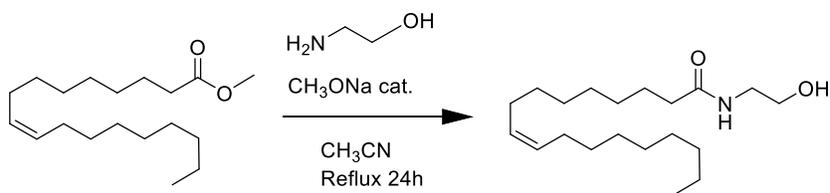
Scheme 2.17. Synthesis of *N*-(2-hydroxy ethyl) oleamide from methyl oleate.
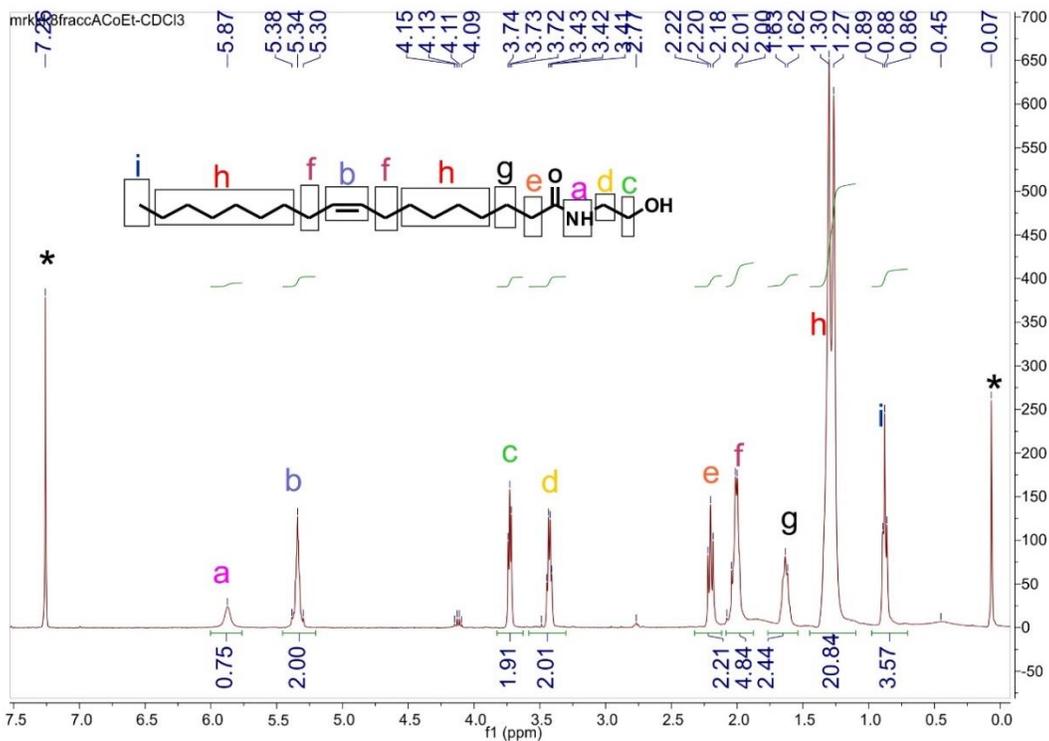
Figure 2.59. ¹H NMR spectrum of *N*-(2-hydroxy ethyl) oleamide.
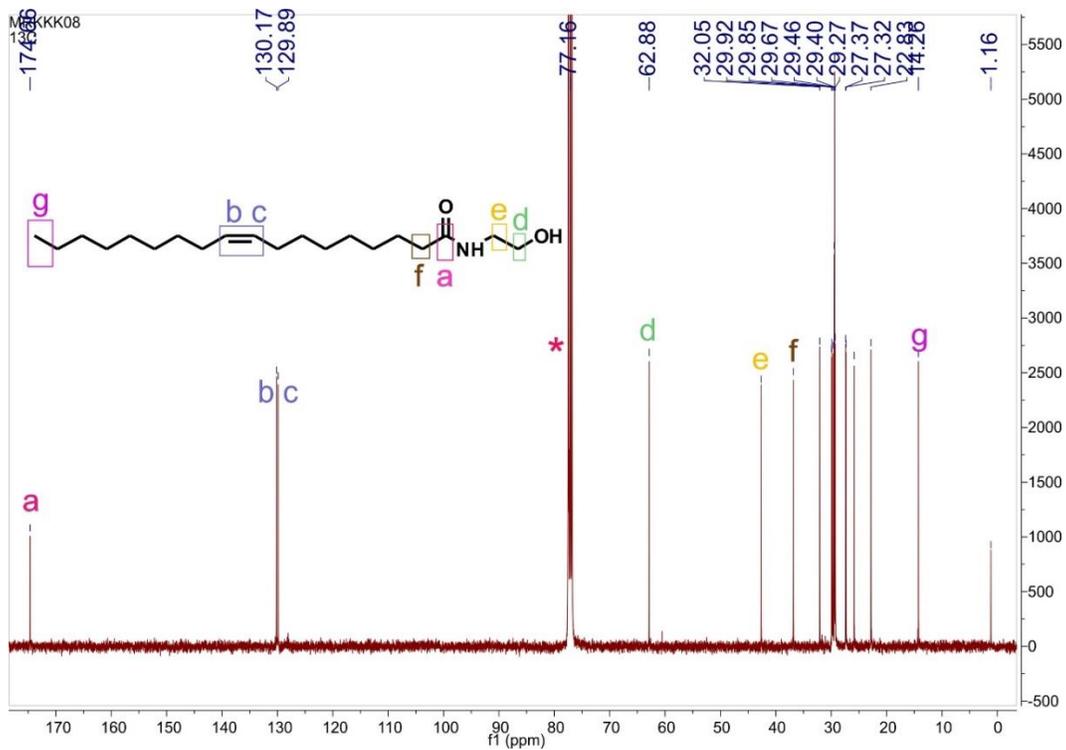
Figure 2.60. ¹³C NMR spectrum of *N*-(2-hydroxy ethyl) oleamide.
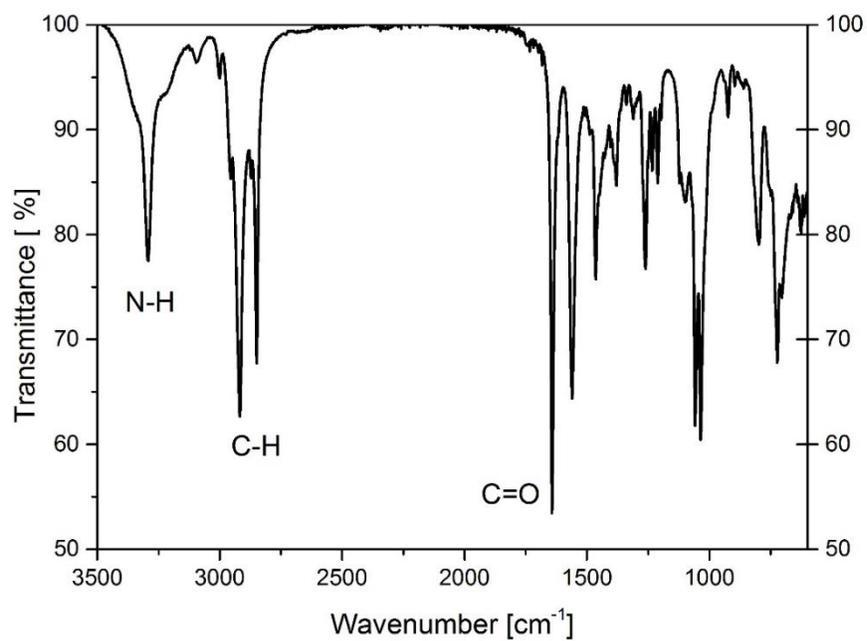
Figure 2.61. IR spectrum of *N*-(2-hydroxy ethyl) oleamide.
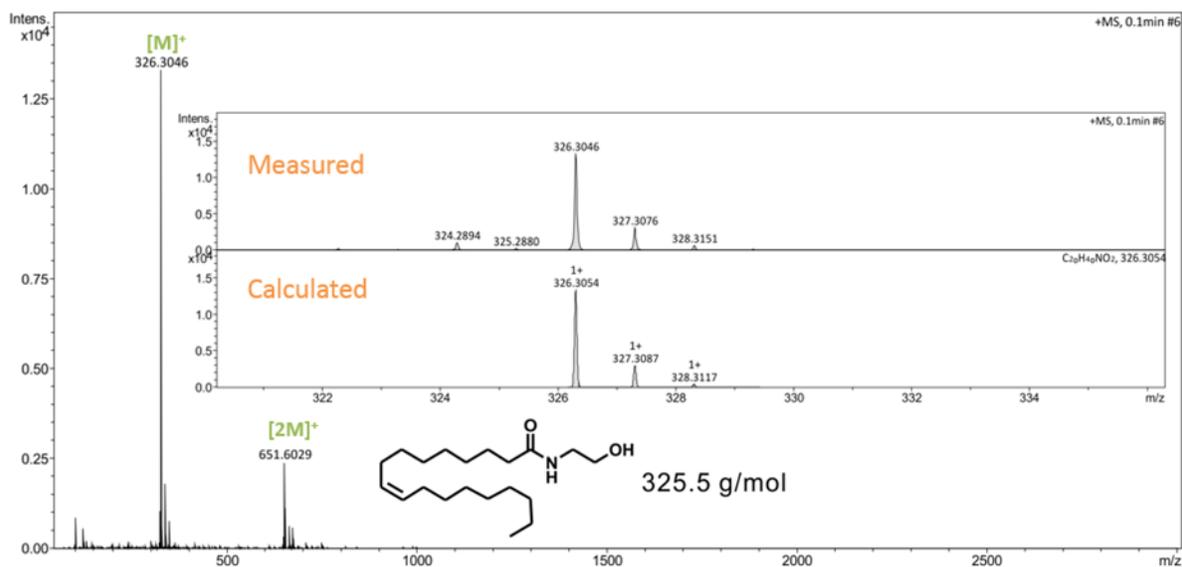
Figure 2.62. HR ESI-TOF-MS spectra of N-(2-hydroxy ethyl) oleamide.

171
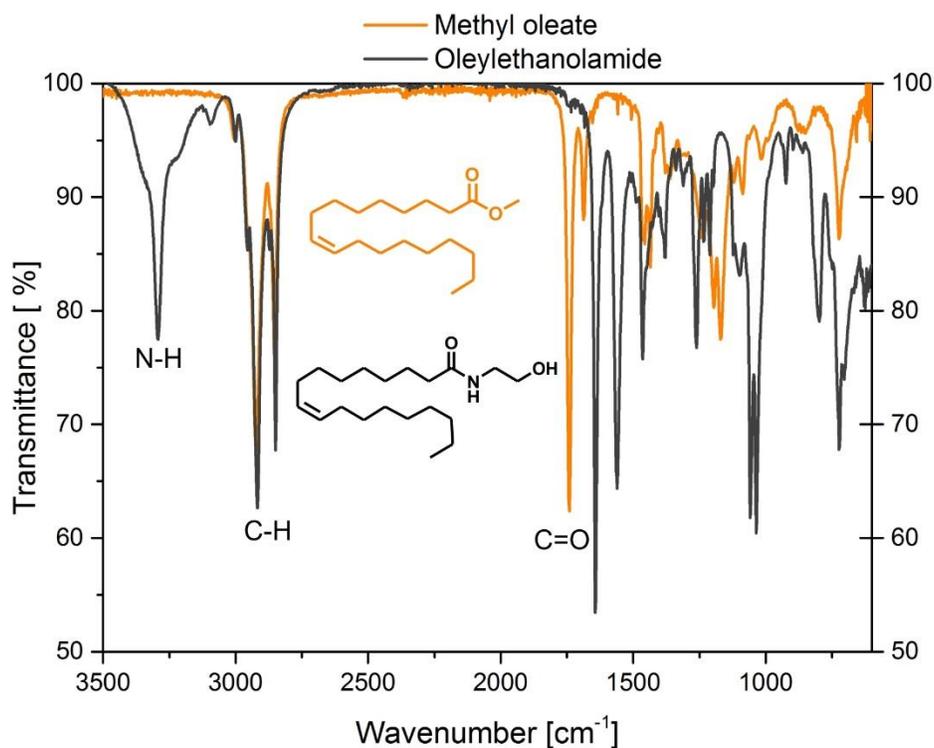
Figure 2.63. IR comparation between methyl oleate and *N*-(2-hydroxyethyl)oleamide (oleylethanolamide).

2.4.2.3. Synthesis of anandamide (AEA)

The synthesis of Anandamide (2HEA) was done in two step reaction (**Scheme 2.17**); the first step was done starting from the arachidonic acid to produce the methyl arachidonate (**Scheme 2.18**); and the second step was done using this methyl arachidonate to produce the anandamide (**Scheme 2.19**).
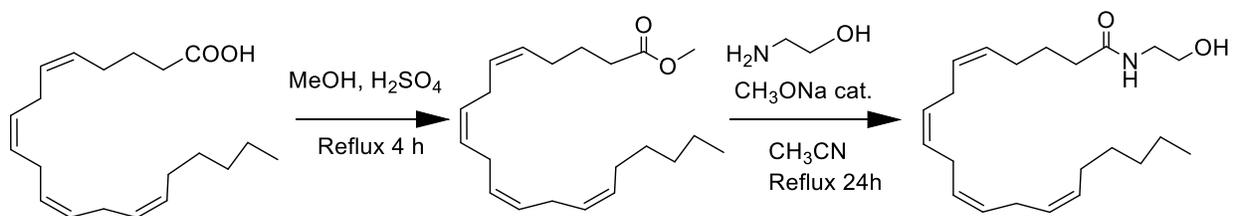
Scheme 2.17. Synthesis route of AEA from arachidonic acid.

1) Synthesis of Methyl arachidonate

Arachidonic acid (278 mg, 0.9 mmol)– was dissolved in 20 mL of MeOH and 2 drops of Sulfuric acid (concentrated) was added. The mixture was refluxed for 6 h. The reaction mixture was diluted in water (30 mL) and was extracted with DCM (3 × 30 mL). The organic phase was dried over Na_2SO_4, and the solvents were evaporated under reduced pressure. The compound was purified by flash chromatography (SiO_2/DCM 97:3 MeOH) and was collected in the first tubes (100% DCM) to give a yellow oil. Yield 223 mg (77 %). The Methyl arachidonate was characterized by, ^1H (**Figure 2.64**), ^{13}C (**Figure 2.65**), IR (**Figure 2.66**) and HR ESI-TOF-MSC (**Figure 2.67**).
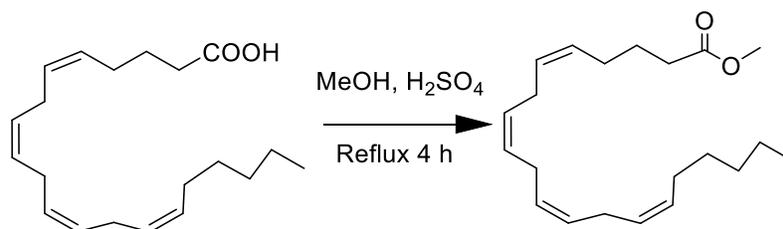
Scheme 2.18. Synthesis of methyl arachidonate from arachidonic acid.
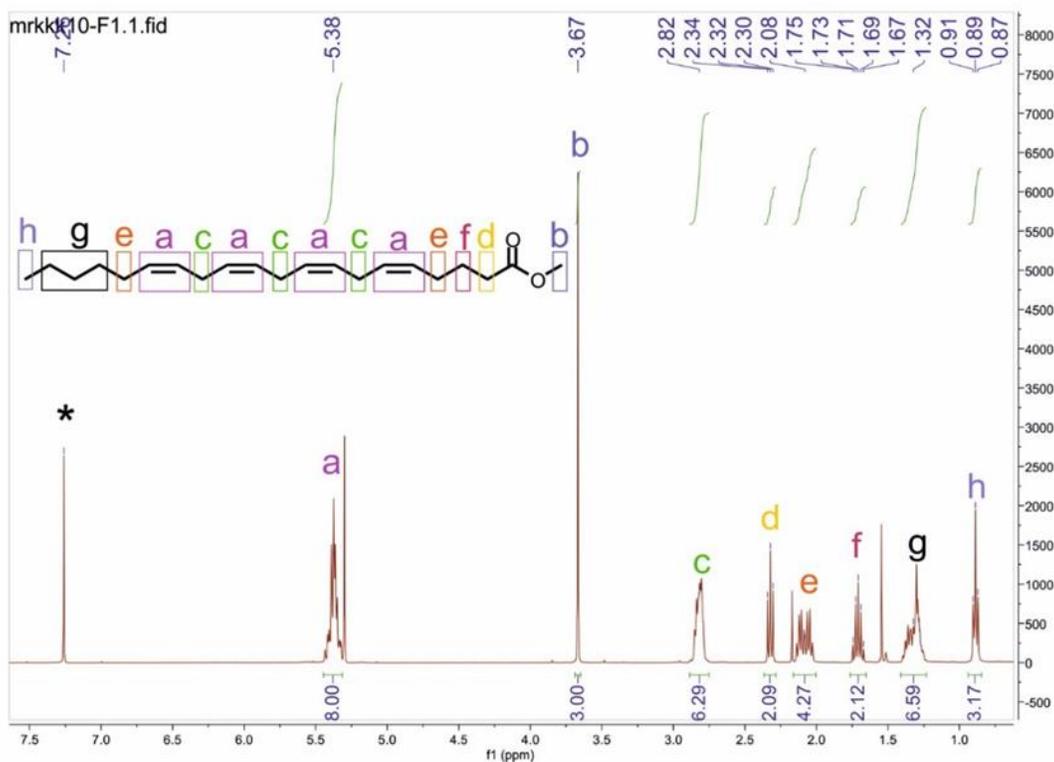
Figure 2.64. ^1H NMR spectrum of Methyl arachidonate.
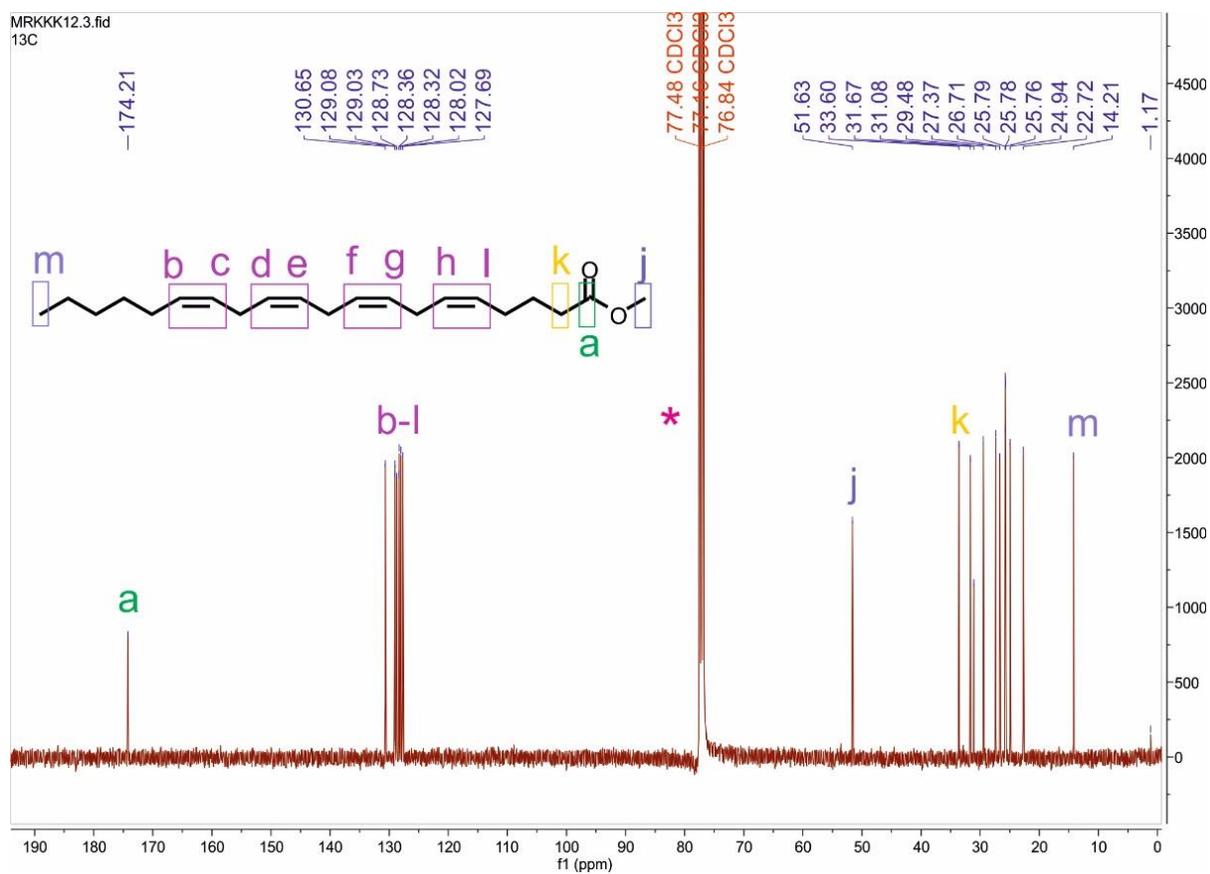
Figure 2.65. ^{13}C NMR spectrum of Methyl arachidonate.
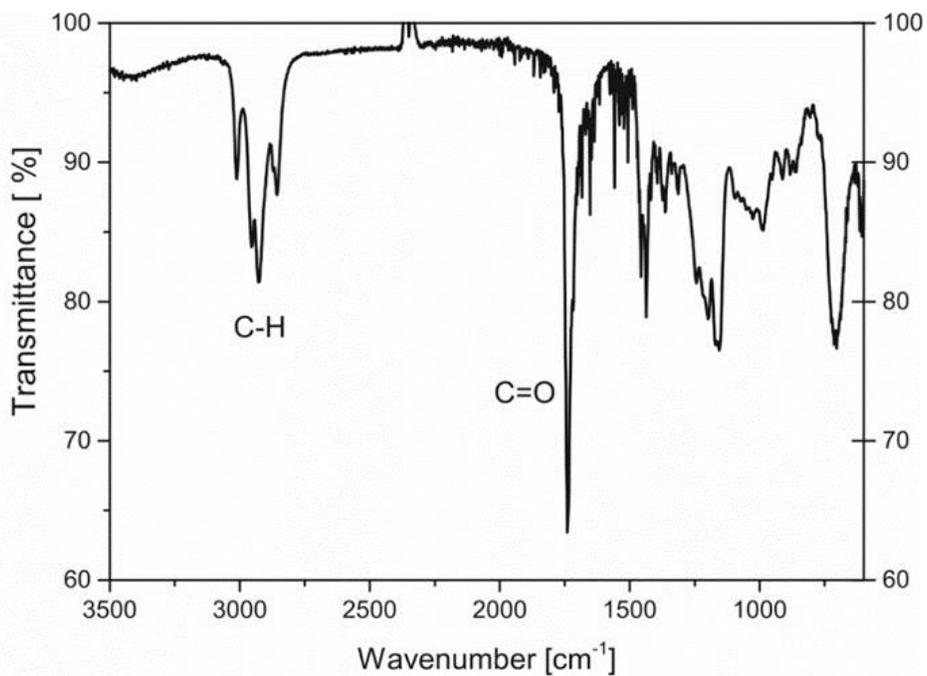
Figure 2.66. IR Methyl arachidonate.
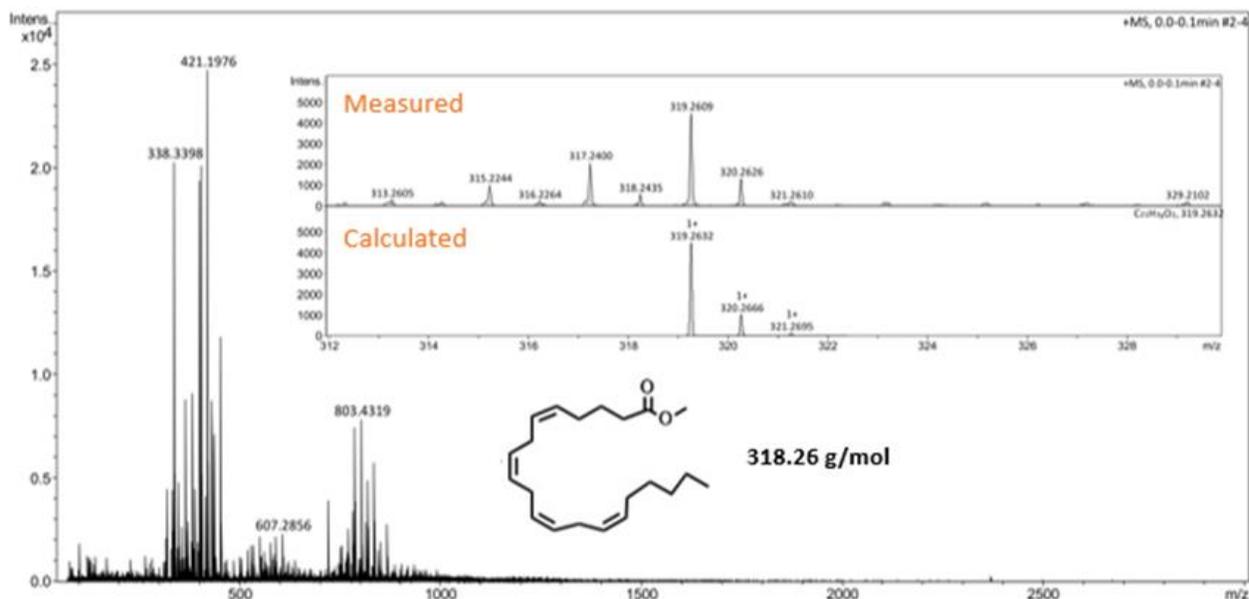
Figure 2.67. HR ESI-TOF-MS spectra of Methyl arachidonate.

2) Synthesis of Anandamide (2HEA)

Methyl arachidonate (0.412, 1.3 mmol) and ethanolamine (0.6 mL, 10 mmol) were dissolved in 10 mL Acetonitrile. To the mixture was added Sodium methoxide (15mg, 0.28 mmol). The mixture was refluxed for 24 h. The reaction mixture was evaporated under reduced pressure to have less volume and then the compound was purified by flash chromatography (SiO$_2$/DCM 95:5 MeOH) to give a brown oil (the product appears in the second fraction). Yield for the two steps (52%). Anandamide was characterized by ^{1}H NMR (**Figure 2.68**), [13]C (**Figure 2.69**), IR (**Figure 2.70**) and HR ESI-TOF-MSC (**Figure 2.71**) and. In **Figure 2.72** is shown the IR spectra of methyl arachidonate and Anandamide together.
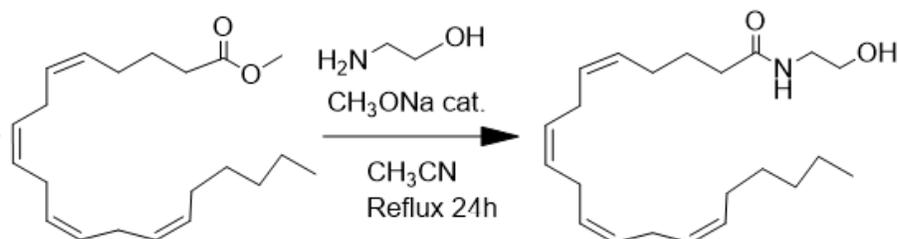
Scheme 2.19. Synthesis of *anandamide* from methyl arachidonate.
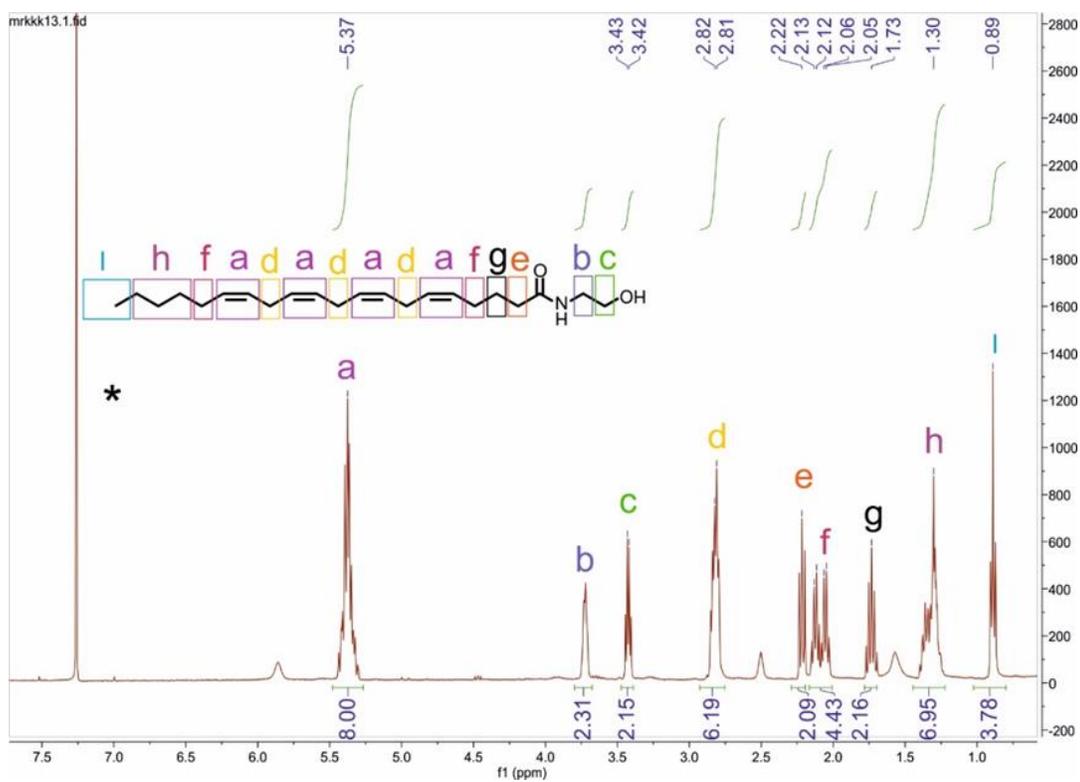
Figure 2.68. ^{1}H NMR spectrum of Anandamide.
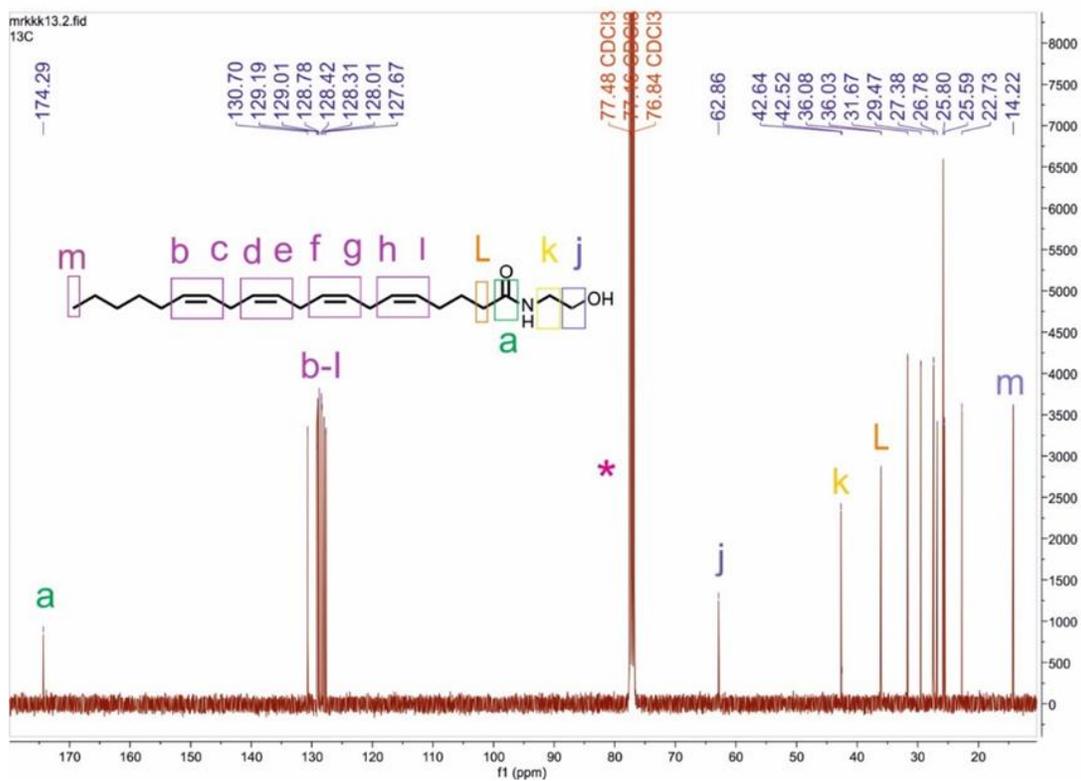
Figure 2.69. ^{13}C NMR spectrum of Anandamide.
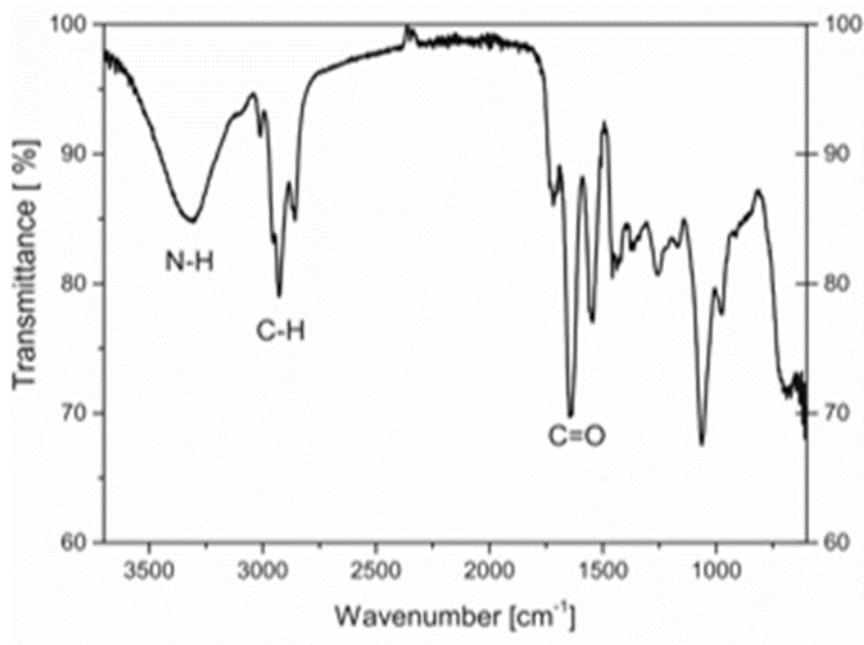
Figure 2.70. IR of Anandamide.

347.28 g/mol
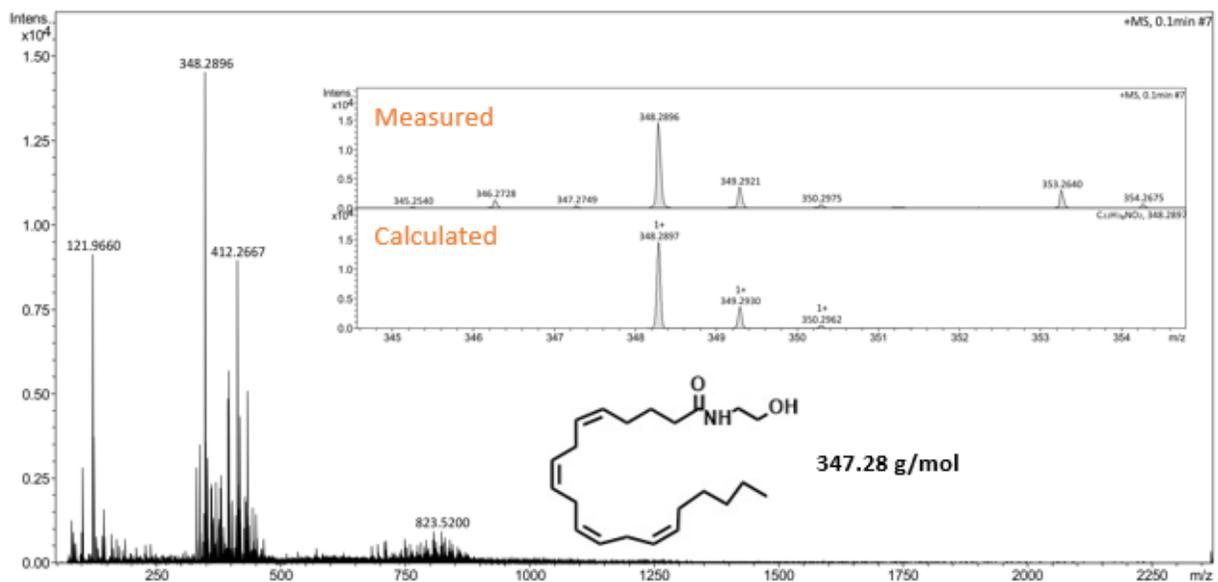
Figure 2.71. HR ESI-TOF-MS spectra of Anandamide.
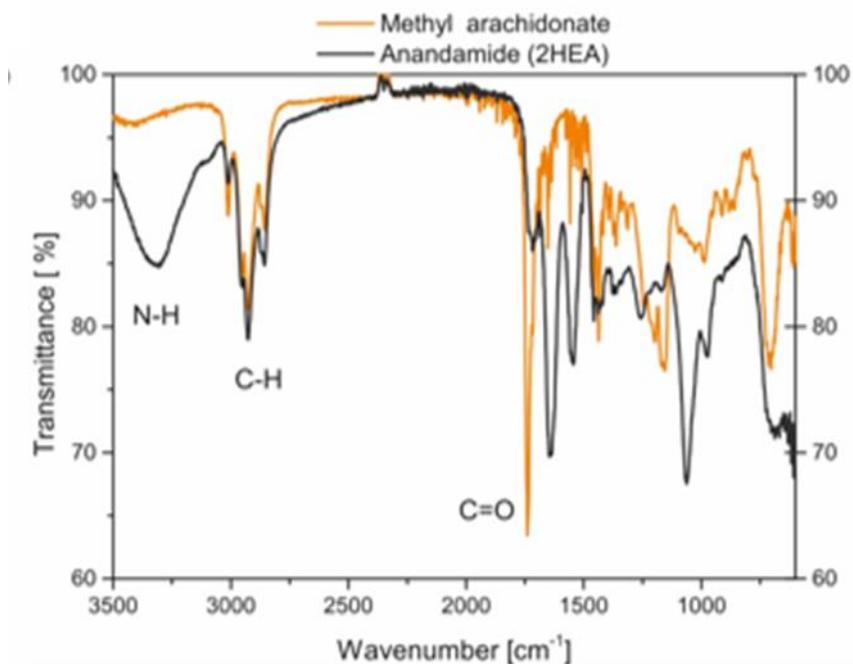
Figure 2.72. IR comparation between methyl arachidonate and Anandamide.

2.4.2.4. Synthesis and characterization of MSNPs.

2.4.2.4.1. Synthesis and characterization of Non-breakable MSNPs.

Synthesis of NB-MSNPs through micelle templating

NB-NPs nanoparticles were synthesized using the micelle template method: cetyl trimethyl ammonium bromide (CTAB, 0.6 g) and triethanolamine (0.06 g) were dissolved in water (20 mL), the solution was heated to 95 °C and stirred vigorously (100 rpm). Once the temperature of the CTAB containers was stable, TEOS (1.5 mL) was added dropwise. After 1 hour of reaction, the particles were let to cool down until r.t. and then recovered by centrifugation (20 min at 30 krpm). Immediately after this, the particles were washed through a sequence of sonication/centrifugation cycles (3×EtOH). To remove the surfactant from the pores, the particles were dissolved in acidic EtOH (100 mL, and few drops of concentrated HCl) and refluxed overnight. Then the particles were cleaned by a sequence of sonication/centrifugation cycles in EtOH (3×EtOH) and finally dried under vacuum. The particles were then characterized by SEM, EDX, IR, TGA, and N_2 adsorption.

178

Synthesis of Dodecyl-NPs through micelle templating

Synthesis of Dodecyl-NPs were synthesized using a modification of the micelle templating methodology in the following way: CTAB (0.6 g) was dissolved in a solution of distilled water (20 mL) and Triethanolamine (0.06 g), the solution was heated to 95 °C and stirred vigorously (100 rpm). On the other hand, in a vial TEOS (1.4 mL, 6.2 mmol) was mixed with Dodecyltriethoxysilane (Dodecyl-NPs) (130 μL, 0.35 mmol). Once the temperature of the CTAB containers is stabilized, the solution containing the silanes was added. After 1 hour of reaction, the particles were cooled down until r.t. and then recovered by centrifugation (20 min at 30 krpm). Immediately after this, the particles were washed through a sequence of sonication/centrifugation cycles (3X EtOH). To remove the surfactant from the pores, the particles were dissolved in acidic EtOH (100 mL, and few drops of HCl) and refluxed overnight. After this, the particles were cleaned by a sequence of sonication/centrifugation cycles in EtOH (3XEtOH) and finally dried under vacuum. The particles were then characterized SEM, STEM, DLS, EDX, XPS, IR, TGA, N_2 adsorption techniques and SAXS.

Synthesis of PFOTS-NPs through Modification of Stöber process

Synthesis of Perfluoro-Octyl nanoparticles were synthesized through Modification of Stöber process in the following way (1): CTAB (250 mg) was dissolved in a solution of distilled water (110 mL), EtOH (10 mL) and NaOH (2M, 0.875 mL), the solution was heated to 80 °C and stirred vigorously (500rpm). On the other hand, in a vial TEOS (875μL, 3.9 mmol) was mixed with PFOTS (77μL, 0.2 mmol) in EtOH (5 mL). Once the temperature of the CTAB containers is stabilized, the solution containing the silanes was added. After 6 hours of reaction, the particles were cooled down until r.t. and then recovered by centrifugation (20 min at 30 krpm). Immediately after this, the particles were washed through a sequence of sonication/centrifugation cycles (2x H_2O and 2x EtOH). To remove the surfactant from the pores, the particles were dissolved in acidic EtOH (100 mL, and few drops of HCl) and refluxed overnight. After this, the particles were cleaned by a sequence of sonication/centrifugation cycles in EtOH (4xEtOH) and finally dried under vacuum. The particles were then characterized by SEM, EDX, XPS, IR, TGA, N_2 adsorption techniques and SAXS.

Synthesis of nanoparticles with FITC moieties in the silica framework were synthesized using a change in the micellar templating method: CTAB (0.6 g) was dissolved in a solution of distilled water (15 mL). Triethanolamine was added (5 mL 0.08M, 0.06g) when the system was under stirred (400 rpm) and 95°C. In an Eppendorf, FITC (3.41 mg, 8.7×10^{-6} moles) was dissolved with 300 µL of EtOH, after 10 µL of APTES (4.27×10^{-5} moles) were added. At this point the color of the dye change from yellow to orange. The solution was stirred for 30 mins and after TEOS (1.5 mL, 6.7 mmol) was added. The solution containing the silanes was added. After 1 hour of reaction, the particles were cooled down until r.t. and then recovered by centrifugation (20 min at 23 krpm). Immediately after this, the particles were washed through a sequence of sonication/centrifugation cycles (3X EtOH). To remove the surfactant from the pores, the particles were dissolved in acidic EtOH (100 mL, and few drops of HCl) and refluxed overnight. After this, the particles were cleaned by a sequence of sonication/centrifugation cycles in EtOH (3XEtOH) and finally dried under vacuum. The particles were then characterized by SEM, EDX and N_2 adsorption techniques (1).

2.4.2.4.2. Synthesis and characterization of Breakable MSNPs

Synthesis of s-s NPs Modification of Stöber process (METHOD 1)

Synthesis of disulfide nanoparticles were synthesized in the following way (1): CTAB (250 mg) was dissolved in a solution of distilled water (110 mL), EtOH (10 mL) and NaOH (2M, 0.875 mL), the solution was heated to 80 °C and stirred vigorously (500rpm). On the other hand, in a vial TEOS (875µL, 3.9 mmol) was mixed with bis(triethoxysilyl-propyl)disulfide (BTSPD) (390 µL, 0.89 mmol) in EtOH (5mL). Once the temperature of the CTAB containers is stabilized, the solution containing the silanes was added. After 6 hours of reaction, the particles were cooled down until r.t. and then recovered by centrifugation (20 min at 30 krpm). Inmediatly after this, the particles were washed through a sequence of sonication/centrifugation cycles (2X H2O and 2xEtOH). To remove the surfactant from the pores, the particles were dissolved in acidic EtOH (100 mL, and few drops of HCl) and refluxed overnight. After this, the particles were cleaned by a sequence of sonication/centrifugation cycles in EtOH (4XEtOH) and finally dried under vacuum. The particles were then characterized by SEM, EDX and N_2 adsorption techniques.

Synthesis of s-s NPs MP-SNPs through micelle templating (METHOD 2)

Synthesis of disulfide nanoparticles with this method were synthesized in the following way (1): CTAB (0.6 g) was dissolved in a solution of distilled water (20 mL) and Triethanolamine (0.06 g), the solution was

heated to 95 °C and stirred vigorously (100 rpm). On the other hand, in a vial TEOS (1.05 mL) was mixed with bis(triethoxysilyl-propyl)disulfide (BTSPD) (0.46 mL, 1 mmol). Once the temperature of the CTAB containers is stabilized, the solution containing the silanes was added. After 1 hour of reaction, the particles were cooled down until r.t. and then recovered by centrifugation (20 min at 30 krpm). Immediately after this, the particles were washed through a sequence of sonication/centrifugation cycles (3X EtOH). To remove the surfactant from the pores, the particles were dissolved in acidic EtOH (100 mL, and few drops of HCl) and refluxed overnight. After this, the particles were cleaned by a sequence of sonication/centrifugation cycles in EtOH (3XEtOH) and finally dried under vacuum. The particles were then characterized by SEM, EDX and N_2 adsorption techniques.

Synthesis of FITC-*ss*-NPs through micelle templating

Synthesis of breakable nanoparticles with FITC moieties in the silica framework were synthesized using a change in the micellar templating method: CTAB (0.6 g) was dissolved in a solution of distilled water (15 mL). Triethanolamine was added (5 mL 0.08M, 0.06g) when the system was under stirred (400 rpm) and 95 °C. In an Eppendorf, FITC (3.41 mg, 8.7×10^{-6} moles) was dissolved with 300 µL of EtOH, after 10 µL of APTES (4.27×10^{-5} moles) were added. At this point the color of the dye change from yellow to orange. The solution was stirred for 30 mins and after TEOS (1.05 mL, 4.7×10^{-3} moles) and BTSPD (0.46 mL, 1 mmol) was added. The solution containing the silanes was added. After 1 hour of reaction, the particles were cooled down until r.t. and then recovered by centrifugation (20 min at 23 krpm). Immediately after this, the particles were washed through a sequence of sonication/centrifugation cycles (3X EtOH). To remove the surfactant from the pores, the particles were dissolved in acidic EtOH (100 mL, and few drops of HCl) and refluxed overnight. After this, the particles were cleaned by a sequence of sonication/centrifugation cycles in EtOH (3XEtOH) and finally dried under vacuum. The particles were then characterized by SEM, EDX and N_2 adsorption techniques.

2.4.2.5. Synthesis and characterization of the PLGA@carriers

Synthesis of PLGA@MS by the solvent evaporation method

First, 50:50 PLGA was dissolved in dichloromethane (DCM) at a concentration of 10% w/v. To fabricate the fluorescently labeled PLGA@carrier, Nile Red was added to the PLGA solution in DCM

at co concentration 1 mg/mL. MSVs were mixed in 1 mL of 10% w/v PLGA in DCM, then dropped into 3 mL of a solution of poly(vinyl alcohol (PVA) 2.5% (w/v) at room temperature, and was subsequently emulsified with an homogenization for 3 min at 10,000 rpm. The resulting emulsion was dropped into 40 mL of PVA 1% w/v and stirred overnight to allow DCM evaporation. The resulting microspheres (MS) suspension was centrifuged at 3,000 rpm for 3 min, and then washed 3 times with distilled water.

Notes: Sonication of the sample is possible without damage of the sample and the MS can be recollected by centrifugation and freeze-dried to be stored under vacuum.

Synthesis of NPs@PLGA@MS by the solvent evaporation method

100 mg PLGA, Nile Red, and 1 mg of NB-NPs with an average diameter 97± 10 nm were mixed together. Certain volume of this solution was put in 3 mL of PVA 2.5% and was homogenized at 10×10^3 rpm for 3 min. After, this solution was immediately transferred in 40 mL PVA 1% w/v and the solution was stirred overnight at room temperature and using 800 rpm. The sample was washed 3 times with water using cycles of centrifugation of 3000 rpm.

Synthesis of PLGA@MS by the SORP method

PLGA 2mg was first dissolved in 2 mL of THF (a good solvent for the polymer) and put it in a vial; then under gentle magnetic stirring (100 rpm) at room temperature, 2 mL of water (a precipitant for the polymer) was added slowly to the polymer solution via a syringe pump at a speed of 2 mL/h. The polymer solution remained was stirring overnight to let the THF evaporates in an open system at room temperature (25 °C). After this, the MS suspension was obtained. The MS can be recovered by centrifugation (1.2×10^4 rpm for 10 mins) to remove the supernatant, and the Ps were re-dispersed in deionized water. To prepare the MS loaded with Nile Red 0.2% w/w of this dye with respect of the polymer was put in the THF solution.

Synthesis of PLGA@MS by the SORP method big scale10x

20 mg PLGA and 2 mg Nile Red was dissolved in 20 mL of THF, under magnetic stirring (100 rpm) at room temperature (using a 100 mL flask ball and a big stirring bar), 20 mL of water was added to the polymer solution via a syringe pump at a speed of 10 mL/h. The polymer solution remained was stirring overnight to let the THF evaporates in an open system at room temperature.

After the PLGA suspension is centrifuged at a speed of 1.2×10^4 rpm for 10 min to remove the supernatant, and the Ps were re-dispersed in deionized water.

Synthesis of PLGA@MS by the SORP method scale 5x

10 mg PLGA and 1 mg Nile Red was dissolved in 10 mL of THF, under magnetic stirring (100 rpm) at room temperature (using a vial with a flat surface and a flat stirring bar), 10 mL of water was added to the polymer solution via a syringe pump at a speed of 2 mL/h. The polymer solution remained was stirring overnight to let the THF evaporates in an open system at room temperature.

After the PLGA suspension is centrifuged at a speed of 1.2×10^4 rpm for 10 min to remove the supernatant, and the Ps were re-dispersed in deionized water.

Table 2.1. Synthesis of the PLGA spheres by the SORP method.

	[PLGA]$_i$	Nile Red	THF	H$_2$O	R$_M$(ml/h)	Stirring bar used	Stirring plate/ frask	Agitation used by adding H$_2$O	Agitation of evaporation	System	Distribution size Counting	Distribution size DLS	Yield
	1mg/ml	c.a.	2ml	2ml	2ml/h		Vial 5ml	100rpm	100 rpm	Monodisperse system	639±119 nm	676±141 nm	
	1mg/ml	0.1mg	2ml	2ml	2ml/h		Vial 10 ml	100 rpm	100rpm	Monodisperse		Ø=604±135 nm	90%
	1mg/ml	0.1 mg	2ml	2ml	2ml/h		Vial 10 ml	100 rpm	100rpm	Monodisperse	689±118	Ø=710±141 nm	86.5%
	1mg/ml	0.16 mg	2ml	2ml	2ml/h		Vial 5ml	100rpm Not homogeneous stirring	No stirring	Polydisperse			
	1mg/ml	0.1 mg	2ml	2ml	2ml/h		Vial 5ml	100rpm Not homogeneous stirring	100 rpm Not homogeneous stirring	Monodisperse agglomerates			
	1mg/ml	0.13	2ml	2ml	2ml/h		Tube microwave	120rpm	120 rpm	Not good results- spheres not well formed			
	1mg/ml	0.2 mg	2ml	2ml	2ml/h		Tube microwave	120rpm	120 rpm	Spheres not well formed			
	1mg/ml	0.12mg	2ml	2ml	2ml/h		Vial 5ml	100rpm	100 rpm	Polydisperse system System with 2 size distribution	168±46 nm and 524±87 nm	236±46 nm 1312±265 nm	46.5%
	1mg/ml	0.11mg	2ml	2ml	2ml/h		Vial 5ml	100rpm	100 rpm	Polydisperse system System with 2 size distribution		233±55 nm and 650±111 nm	
	1mg/ml	0.17mg	2ml	2ml	2ml/h		Vial 5ml	1200 rpm	100 rpm	Rods and nanospheres			
Up-scale 10x	1mg/ml	0.1 mg	20 ml	20 ml	10ml/h		Flask ball 100 ml	250rpm	250 rpm	Rods and nanospheres			
Up-scale 5x	1mg/ml	2mg	10 ml	10ml	2ml/h		Vial 25ml	100rpm	100rpm	Monodisperse system		1.1±0.2 µm	70%
Up-scale 5x	1mg/ml	1mg	10 ml	10ml	2ml/h		Vial 25ml	100rpm	100rpm	Monodisperse system	1.2±0.3 µm	1.1±0.1 µm	40%

Synthesis of PLGA@MBds by the hydrogel template method

Synthesis of the hydrogel PVA template.

The hydrogel mold consisting of a film of water-soluble PVA patterned with 20 μm wells was prepared by a copying of the PDMS PolyScitech® master template. SEM images of the PVA mold can be appreciated in figure 26B, showing the cavities with a size of 20 μm.

Preparation of PLGA beads.

PLGA is dissolved in dichloromethane 0.2 g/mL and Nile Red is added to this solution. With a pipette, the solution is transferred to the patterned area of the PVA template and carefully spread the material with a glass slide, then is dried overnight at room temperature to then obtain 20% PLGA beads. Same methodology was used to obtain the 30%PLGA beads.

To obtain the microparticles out of the PVA matrix, the hydrogel is dissolved in water and recovered them by centrifugation; the material is washed 3 times with water by a sequence of sonication/centrifugation to remove all the traces of the PVA matrix.

Table 2.2. Experiments done to obtain PLGA MBds of good quality.

Experiment	PLGA 75:25	No. Layers	Passing times	Tool to make the layer	RESULT BEADS
1	20%	1	several	Razor	Bad formation (Donuts)
2	30%	1	several	Razor	Bad formation
3	30%	3	several	Razor	Beads
4	30%	6	several	Razor	Pieces of polymer formation (layers)+ beads bad quality
5	30%	1	once	Slide glass	Beads
6	20%	1	once	Slide glass	Beads

2.4.3. Incorporation of cannabinoids in the PLGA-MBds (hydrogel template method)

100 mg of PLGA were dissolved in 500 µL of CH_2Cl_2 to make 20% PLGA MBds, 20 mg of 2HEO or AEA and Nile Red (100 µL 2.75 mM) was added to the solution and then sonicated to make a homogeneous solution. After the solution is dropped in the PVA template and let it dried. Confocal images were taken to see if the beads were formed with the inclusion of 2HEO.

2.4.4. Fluorescence emission spectra of PLGA-Nile Red and PLGA-AEA (drop castle method)

To prepare the first sample, 10 mg of PLGA were dissolved in 50 µL of DCM and it was added 10 µL of Nile Red 2.75 mM; this solution was quickly put it in a glass slide to let it dry and then covered with a coverslip to then measure the emission. To prepare the second sample, 2 mg of AEA were dissolved in 50 µL of DCM and then 10 µL of Nile Red 2.75 mM was added; as the other the addition of the solvent and the Nile Red has to be fast in order to take the aliquot and put in in the glass slide to let it dry there; the sample is protected using a coverslip and after the emission is measured in a Fluorimeter.

2.4.5. Loading of the particles: MSNPs+ Orange 2

15 mg of NB-NPs particles were mixed with 15 mg of Orange 2 in 750 µL EtOH. The solution was put in a rotator-mixer for 1 day. After the particles were centrifuged and washed with 750 µL of EtOH two times.

2.4.6 Breakability test of FITC-ss-NPs

0.1 mg/mL of FITC-ss-NPs were dispersed in in PBS or acetate buffer. Glutathione (GHS) is added to have a final concentration of 10 mM. The sample is stirred and heated up to 37 °C. Duron the time, aliquots are taken and dropcasted on a TEM grid.

2.4.7. Breakability test of the PLGA@MBds

1.35 mg of PLGA@MBds (done using 20% PLGA 50:50) were put in 2 mL of media (water, PBS (pH7.4) or Buffer acetate (pH 5.2)). The solutions were agitated at 37 °C during all the experiment. SEM and optical microscopy were the techniques to characterize the material for 1,3,7,10, 15 and 20 days.

2.5. REFERENCES

(1)   Boyle, P. Global Burden of Cancer. *Lancet* **1997**, *349*, 85–94.

(2)   Massi, P.; Valenti, M.; Solinas, M.; Parolaro, D. Molecular Mechanisms Involved in the Antitumor Activity of Cannabinoids on Gliomas: Role for Oxidative Stress. *Cancers* **2010**, *2* (2), 1013–1026.

(3)   Torres, S.; Lorente, M.; Rodríguez-Fornés, F.; Hernández-Tiedra, S.; Salazar, M.; García-Taboada, E.; Barcia, J.; Guzmán, M.; Velasco, G. A Combined Preclinical Therapy of Cannabinoids and Temozolomide against Glioma. *Molecular Cancer Therapeutics* **2011**, *10* (1), 90–103.

(4)   Maggini, L.; Cabrera, I.; Ruiz-Carretero, A.; Prasetyanto, E. A.; Robinet, E.; De Cola, L. Breakable Mesoporous Silica Nanoparticles for Targeted Drug Delivery. *Nanoscale* **2016**, *8* (13), 7240–7247.

(5)   Jiang, W.; Gupta, R. K.; Deshpande, M. C.; Schwendeman, S. P. Biodegradable Poly(Lactic-Co-Glycolic Acid) Microparticles for Injectable Delivery of Vaccine Antigens. *Advanced Drug Delivery Reviews* **2005**, *57* (3), 391–410.

(6)   Pertwee, R. G. The Pharmacology of Cannabinoid Receptors and Their Ligands: An Overview. *International Journal of Obesity* **2006**, *30* (1), S13–S18.

(7)   Witasp, E.; Kupferschmidt, N.; Bengtsson, L.; Hultenby, K.; Smedman, C.; Paulie, S.; Garcia-Bennett, A. E.; Fadeel, B. Efficient Internalization of Mesoporous Silica Particles of Different Sizes by Primary Human Macrophages without Impairment of Macrophage Clearance of Apoptotic or Antibody-Opsonized Target Cells. *Toxicology and Applied Pharmacology* **2009**, *239* (3), 306–319.

(8)   Lu, F.; Wu, S. H.; Hung, Y.; Mou, C. Y. Size Effect on Cell Uptake in Well-Suspended, Uniform Mesoporous Silica Nanoparticles. *Small* **2009**, *5* (12), 1408–1413.

(9)   Gasparini, G. Metronomic Scheduling: The Future of Chemotherapy? *Lancet Oncology* **2001**, *2* (12), 733–740.

(10)   Scharovsky, O. G.; Mainetti, L. E.; Rozados, V. R. Metronomic Chemotherapy: Changing the Paradigm That More Is Better. *Current Oncology* **2009**, *16* (2), 7–15.

(11)   Jang, S. H.; Wientjes, M. G.; Lu, D.; Au, J. L. S. Drug Delivery and Transport to Solid Tumors. *Pharmaceutical Research* **2003**, *20* (9), 1337–1350.

(12)   De Souza, R.; Zahedi, P.; Allen, C. J.; Piquette-Miller, M. Polymeric Drug Delivery Systems for Localized Cancer Chemotherapy. *Drug Delivery* **2010**, *17* (6), 365–375.

(13)   Anderson, J. M.; Shive, M. S. Biodegradation and Biocompatibility of PLA and PLGA Microspheres. *Advanced Drug Delivery Reviews* **1997**, *28*, 5–24.

(14)   Pertwee, R. G. Emerging Strategies for Exploiting Cannabinoid Receptor Agonists as Medicines. *British Journal of Pharmacology* **2009**, *156* (3), 397–411.

(15)   Grimaldi, C.; Capasso, A. The Endocannabinoid System in the Cancer Therapy: An Overview. *Current Medicinal Chemistry* **2011**, *18* (11), 1575–1583.

(16)   Hermanson, D. J.; Marnett, L. J. Cannabinoids, Endocannabinoids, and Cancer. *Cancer and Metastasis Reviews* **2011**, *30* (3–4), 599–612.

(17)   Miyato, H.; Kitayama, J.; Yamashita, H.; Souma, D.; Asakage, M.; Yamada, J.; Nagawa, H. Pharmacological Synergism Between Cannabinoids and Paclitaxel in Gastric Cancer Cell Lines. *Journal of Surgical Research* **2009**, *155* (1), 40–47.

(18)   Izzo, A. A.; Camilleri, M. Cannabinoids in Intestinal Inflammation and Cancer. *Pharmacological Research* **2009**, *60* (2), 117–125.

(19)   Ezzili, C.; Otrubova, K.; Boger, D. L. Fatty Acid Amide Signaling Molecules. *Bioorganic and Medicinal Chemistry Letters* **2010**, *20* (20), 5959–5968.

(20)   Farrell, E. K.; Merkler, D. J. Biosynthesis, Degradation and Pharmacological Importance of the Fatty Acid Amides. *Drug Discovery Today* **2008**, *13* (13–14), 558–568.

(21)   Di Marzo, V.; Bisogno, T.; De Petrocellis, L.; Melck, D.; Martin, B. R. Cannabimimetic Fatty Acid Derivatives: The Anandamide Family. *Med.Chem* **1999**, *6* (8), 721.

(22)   Boger, D. L.; Patterson, J. E.; Jin, Q. Structural Requirements for 5-HT2A and 5-HT1A Serotonin Receptor Potentiation by the Biologically Active Lipid Oleamide. *Proceedings of the National Academy of Sciences of the United States of America* **1998**, *95* (8), 4102–4107.

(23)   Burstein, S.; Salmonsen, R. Acylamido Analogs of Endocannabinoids Selectively Inhibit Cancer Cell Proliferation. *Bioorganic & Medicinal Chemistry* **2008**, *16* (22), 9644–9651.

(24)   Sarfaraz, S.; Adhami, V. M.; Syed, D. N.; Afaq, F.; Mukhtar, H. Cannabinoids for Cancer Treatment: Progress and Promise. *Cancer Research* **2008**, *68* (2), 339–342.

(25)   De Petrocellis, L.; Melck, D.; Bisogno, T.; Di Marzo, V. Endocannabinoids and Fatty Acid Amides in Cancer, Inflammation and Related Disorders. *Chemistry and Physics of Lipids* **2000**, *108* (1–2), 191–

209.

(26)   Proto, M. C.; Gazzerro, P.; Di Croce, L.; Santoro, A.; Malfitano, A. M.; Pisanti, S.; Laezza, C.; Bifulco, M. Interaction of Endocannabinoid System and Steroid Hormones in the Control of Colon Cancer Cell Growth. *Journal of Cellular Physiology* **2012**, *227* (1), 250–258.

(27)   Pertwee, R. G.; Howlett, A. C.; Abood, M. E.; Alexander, S. P. H.; Di Marzo, V.; Elphick, M. R.; Greasley, P. J.; Hansen, H. S.; Kunos, G.; Mackie, K.; Mechoulam, R.; Ross, R. A. International Union of Basic and Clinical Pharmacology. LXXIX. Cannabinoid Receptors and Their Ligands: Beyond CB1 and CB2. *Pharmacological Reviews* **2010**, *62* (4), 588–631.

(28)   Fusi, C.; Materazzi, S.; Minocci, D.; Maio, V.; Oranges, T.; Massi, D.; Nassini, R. Transient Receptor Potential Vanilloid 4 (TRPV4) Is Downregulated in Keratinocytes in Human Non-Melanoma Skin Cancer. *Journal of Investigative Dermatology* **2014**, *134* (9), 2408–2417.

(29)   dos Santos, D. S.; Piovesan, L. A.; D'Oca, C. R. M.; Hack, C. R. L.; Treptow, T. G. M.; Rodrigues, M. O.; Vendramini-Costa, D. B.; Ruiz, A. L. T. G.; de Carvalho, J. E.; D'Oca, M. G. M. Antiproliferative Activity of Synthetic Fatty Acid Amides from Renewable Resources | Elsevier Enhanced Reader. *Bioorganic & Medicinal Chemistry* **2015**, *23* (2), 340–347.

(30)   Lin, S.; Khanolkar, A. D.; Fan, P.; Goutopoulos, A.; Qin, C.; Papahadjis, D.; Makriyannis, A. Novel Analogues of Arachidonylethanolamide (Anandamide): Affinities for the CB1 and CB2 Cannabinoid Receptors and Metabolic Stability. *Journal of Medicinal Chemistry* **1998**, *41* (27), 5353–5361.

(31)   Okamoto, Y.; Wang, J.; Morishita, J.; Ueda, N. Biosynthetic Pathways of the Endocannabinoid Anandamide. *Chemistry & Biodiversity* **2007**, *4* (8), 1842–1857.

(32)   Burstein, S. Cannabidiol (CBD) and Its Analogs: A Review of Their Effects on Inflammation. *Bioorganic and Medicinal Chemistry* **2015**, *23* (7), 1377–1385.

(33)   Vallet-Regi, M.; Rámila, A.; Del Real, R. P.; Pérez-Pariente, J. A New Property of MCM-41: Drug Delivery System. *Chemistry of Materials* **2001**, *13* (2), 308–311.

(34)   Vallet-Regí, M.; Colilla, M.; Izquierdo-Barba, I.; Manzano, M. Mesoporous Silica Nanoparticles for Drug Delivery: Current Insights. *Molecules* **2018**, *23* (1), 47.

(35)   Manzano, M.; Vallet-Regí, M. Mesoporous Silica Nanoparticles for Drug Delivery. *Advanced Functional Materials* **2020**, *30* (2), 1902634.

(36)   Bharti, C.; Nagaich, U.; Pal, A. K.; Gulati, N. Mesoporous Silica Nanoparticles in Target Drug Delivery System: A Review. *International Journal of Pharmaceutical Investigation* **2015**, *5* (3), 124–133.

(37)   Watermann, A.; Brieger, J. Mesoporous Silica Nanoparticles as Drug Delivery Vehicles in Cancer. *Nanomaterials* **2017**, *7* (7), 189.

(38)   Jafari, S.; Derakhshankhah, H.; Alaei, L.; Fattahi, A.; Varnamkhasti, B. S.; Saboury, A. A. Mesoporous Silica Nanoparticles for Therapeutic/Diagnostic Applications. *Biomedicine and Pharmacotherapy* **2019**, *109*, 1100–1111.

(39)   Stober, W.; Fink, A.; Ernst Bohn, D. Controlled Growth of Monodisperse Silica Spheres in the Micron Size Range 1. *Journal of colloid and interface science* **1968**, *26* (1), 62–69.

(40)   Lv, X.; Zhang, L.; Xing, F.; Lin, H. Controlled Synthesis of Monodispersed Mesoporous Silica Nanoparticles: Particle Size Tuning and Formation Mechanism Investigation. *Microporous and Mesoporous Materials* **2016**, *225*, 238–244.

(41)   Möller, K.; Kobler, J.; Bein, T. Colloidal Suspensions of Nanometer-Sized Mesoporous Silica. *Advanced Functional Materials* **2007**, *17* (4), 605–612.

(42)   Kresge, C. T.; Leonowicz, M. E.; Roth, W. J.; Vartuli, J. C.; Beck, J. S. Ordered Mesoporous Molecular Sieves Synthesized by a Liquid-Crystal Template Mechanism. *Nature* **1992**, *359* (6397), 710–712.

(43)   Forman, H. J.; Zhang, H.; Rinna, A. Glutathione: Overview of Its Protective Roles, Measurement, and Biosynthesis. *Molecular Aspects of Medicine* **2009**, *30* (1–2), 1–12.

(44)   Balendiran, G. K.; Dabur, R.; Fraser, D. The Role of Glutathione in Cancer. *Cell Biochemistry and Function* **2004**, *22* (6), 343–352.

(45)   Schafer, F. Q.; Buettner, G. R. Redox Environment of the Cell as Viewed through the Redox State of the Glutathione Disulfide/Glutathione Couple. *Free Radical Biology and Medicine* **2001**, *30* (11), 1191–1212.

(46)   Dentinger, M. Breakable Silica Nanoparticles for the in Vitro and in Vivo Delivery of Biomolecules, Doctoral dissertation, Université de Strasbourg, **2018**.

(47)   Allen, T. M.; Cullis, P. R. Drug Delivery Systems: Entering the Mainstream. *Science* **2004**, *303* (5665), 1818–1822.

(48)   des Rieux, A.; Fievez, V.; Garinot, M.; Schneider, Y. J.; Préat, V. Nanoparticles as Potential Oral

Delivery Systems of Proteins and Vaccines: A Mechanistic Approach. *Journal of Controlled Release* **2006**, *116* (1), 1–27.

(49) Kamaly, N.; Xiao, Z.; Valencia, P. M.; Radovic-Moreno, A. F.; Farokhzad, O. C. Targeted Polymeric Therapeutic Nanoparticles: Design, Development and Clinical Translation. *Chemical Society Reviews* **2012**, *41* (7), 2971–3010.

(50) Janib, S. M.; Moses, A. S.; MacKay, J. A. Imaging and Drug Delivery Using Theranostic Nanoparticles. *Advanced Drug Delivery Reviews* **2010**, *62* (11), 1052–1063.

(51) Liang, R.; Dong, L.; Deng, R.; Wang, J.; Wang, K.; Sullivan, M.; Liu, S.; Wang, J.; Zhu, J.; Tao, J. Surfactant-Free Biodegradable Polymeric Nanoparticles Generated from Self-Organized Precipitation Route: Cellular Uptake and Cytotoxicity. *European Polymer Journal* **2014**, *57*, 187–201.

(52) Park, H.; Park, K. Biocompatibility Issues of Implantable Drug Delivery Systems. *Pharmaceutical Research* **1996**, *13* (12), 1770–1776.

(53) Pillai, O.; Panchagnula, R. Polymers in Drug Delivery. *Current Opinion in Chemical Biology* **2001**, *5* (4), 447–451.

(54) Elstad, N. L.; Fowers, K. D. OncoGel (ReGel/Paclitaxel) - Clinical Applications for a Novel Paclitaxel Delivery System. *Advanced Drug Delivery Reviews* **2009**, *61* (10), 785–794.

(55) Kang, J.; Schwendeman, S. P. Comparison of the Effects of Mg(OH)2 and Sucrose on the Stability of Bovine Serum Albumin Encapsulated in Injectable Poly(D,L-Lactide-Co-Glycolide) Implants. *Biomaterials* **2002**, *23* (1), 239–245.

(56) Wang, J.; Wang, B. M.; Schwendeman, S. P. Mechanistic Evaluation of the Glucose-Induced Reduction in Initial Burst Release of Octreotide Acetate from Poly(D,L-Lactide-Co-Glycolide) Microspheres. *Biomaterials* **2004**, *25* (10), 1919–1927.

(57) Schwendeman, S. P.; Langer, R.; Tracy, M. Recent Advances in the Stabilization of Proteins Encapsulated in Injectable PLGA Delivery Systems. *Critical Reviews™ in Therapeutic Drug Carrier Systems* **2002**, *19* (1), 73–98.

(58) Zhu, G.; Mallery, S. R.; Schwendeman, S. P. Stabilization of Proteins Encapsulated in Injectable Poly (Lactide-Co- Glycolide). *Nature Biotechnology* **2000**, *18* (1), 52–57.

(59)   Wischke, C.; Schwendeman, S. P. Principles of Encapsulating Hydrophobic Drugs in PLA/PLGA Microparticles. *International Journal of Pharmaceutics* **2008**, *364* (2), 298–327.

(60)   Freiberg, S.; Zhu, X. X. Polymer Microspheres for Controlled Drug Release. *International Journal of Pharmaceutics* **2004**, *282* (1–2), 1–18.

(61)   Zhang, Y.; Wischke, C.; Mittal, S.; Mitra, A.; Schwendeman, S. P. Design of Controlled Release PLGA Microspheres for Hydrophobic Fenretinide. *Molecular Pharmaceutics* **2016**, *13* (8), 2622–2630.

(62)   Vauthier, C.; Bouchemal, K. Methods for the Preparation and Manufacture of Polymeric Nanoparticles. *Pharmaceutical Research* **2009**, *26* (5), 1025–1058.

(63)   Cleland, J. L. Solvent Evaporation Processes for the Production of Controlled Release Biodegradable Microsphere Formulations for Therapeutics and Vaccines. *Biotechnology Progress* **1998**, *14* (1), 102–107.

(64)   Yu, X.; Zhao, Z.; Nie, W.; Deng, R.; Liu, S.; Liang, R.; Zhu, J.; Ji, X. Biodegradable Polymer Microcapsules Fabrication through a Template-Free Approach. *Langmuir* **2011**, *27* (16), 10265–10273.

(65)   Kawashima, Y.; Yamamoto, H.; Takeuchi, H.; Hino, T.; Niwa, T. Properties of a Peptide Containing DL-Lactide/Glycolide Copolymer Nanospheres Prepared by Novel Emulsion Solvent Diffusion Methods. *European Journal of Pharmaceutics and Biopharmaceutics* **1998**, *45* (1), 41–48.

(66)   Jeon, H. J.; Jeong, Y. Il; Jang, M. K.; Park, Y. H.; Nah, J. W. Effect of Solvent on the Preparation of Surfactant-Free Poly(DL-Lactide-Co-Glycolide) Nanoparticles and Norfloxacin Release Characteristics. *International Journal of Pharmaceutics* **2000**, *207* (1–2), 99–108.

(67)   Mayo, A. S.; Ambati, B. K.; Kompella, U. B. Gene Delivery Nanoparticles Fabricated by Supercritical Fluid Extraction of Emulsions. *International Journal of Pharmaceutics* **2010**, *387* (1–2), 278–285.

(68)   Li, G.; Yao, L.; Li, J.; Qin, X.; Qiu, Z.; Chen, W. Preparation of Poly(Lactide-Co-Glycolide) Microspheres and Evaluation of Pharmacokinetics and Tissue Distribution of BDMC-PLGA-MS in Rats. *Asian Journal of Pharmaceutical Sciences* **2018**, *13* (1), 82–90.

(69)   Minardi, S.; Pandolfi, L.; Taraballi, F.; Wang, X.; De Rosa, E.; Mills, Z. D.; Liu, X.; Ferrari, M.; Tasciotti, E. Enhancing Vascularization through the Controlled Release of Platelet-Derived Growth Factor-BB. *ACS Applied Materials and Interfaces* **2017**, *9* (17), 14566–14575.

(70)   Acharya, G.; Shin, C. S.; McDermott, M.; Mishra, H.; Park, H.; Kwon, I. C.; Park, K. The Hydrogel Template Method for Fabrication of Homogeneous Nano/Microparticles. In *Journal of Controlled Release*; Mohapatra, S. S., Ranjan, S., Dasgupta, N., Mishra, R. K., Thomas, S., Eds.; Elsevier, **2010**; Vol. 141, pp 314–319.

(71)   Champion, J. A.; Walker, A.; Mitragotri, S. Role of Particle Size in Phagocytosis of Polymeric Microspheres. *Pharmaceutical Research* **2008**, *25* (8), 1815–1821.

(72)   Siepmann, J.; Faisant, N.; Akiki, J.; Richard, J.; Benoit, J. P. Effect of the Size of Biodegradable Microparticles on Drug Release: Experiment and Theory. *Journal of Controlled Release* **2004**, *96* (1), 123–134.

(73)   Gaumet, M.; Gurny, R.; Delie, F. Localization and Quantification of Biodegradable Particles in an Intestinal Cell Model: The Influence of Particle Size. *European Journal of Pharmaceutical Sciences* **2009**, *36* (4–5), 465–473.

(74)   Shakweh, M.; Besnard, M.; Nicolas, V.; Fattal, E. Poly (Lactide-Co-Glycolide) Particles of Different Physicochemical Properties and Their Uptake by Peyer's Patches in Mice. *European Journal of Pharmaceutics and Biopharmaceutics* **2005**, *61* (1–2), 1–13.

(75)   Gundloori, R. V.; Singam, A.; Killi, N. Nanobased Intravenous and Transdermal Drug Delivery Systems. In *Applications of Targeted Nano Drugs and Delivery Systems*; Mohapatra, S. S., Ranjan, S., Dasgupta, N., Mishra, R. K., Thomas, S., Eds.; Elsevier, **2019**; pp 551–594.

(76)   Reis, C. P.; Neufeld, R. J.; Ribeiro, A. J.; Veiga, F. Nanoencapsulation I. Methods for Preparation of Drug-Loaded Polymeric Nanoparticles. *Nanomedicine: Nanotechnology, Biology, and Medicine* **2006**, *2* (1), 8–21.

(77)   Song, C. X.; Labhasetwar, V.; Murphy, H.; Qu, X.; Humphrey, W. R.; Shebuski, R. J.; Levy, R. J. Formulation and Characterization of Biodegradable Nanoparticles for Intravascular Local Drug Delivery. *Journal of Controlled Release* **1997**, *43* (2–3), 197–212.

(78)   Quellec, P.; Gref, R.; Dellacherie, E.; Sommer, F.; Tran, M. D.; Alonso, M. J. Protein Encapsulation within Poly(Ethylene Glycol)-coated Nanospheres. II. Controlled Release Properties. *Journal of Biomedical Materials Research* **1999**, *47* (3), 388–395.

(79)   Allouche, J. Synthesis of Organic and Bioorganic Nanoparticles: An Overview of the Preparation Methods. In *Nanomaterials: A Danger or a Promise?*; Brayner, R., Fiévet, F., Coradin, T., Eds.;

Springer-Verlag London Ltd: London, **2013**; pp 27–74.

(80)   Liang, R.; Wang, J.; Wu, X.; Dong, L.; Deng, R.; Wang, K.; Sullivan, M.; Liu, S.; Wu, M.; Tao, J.; Yang, X.; Zhu, J. Multifunctional Biodegradable Polymer Nanoparticles with Uniform Sizes: Generation and in Vitro Anti-Melanoma Activity. *Nanotechnology* **2013**, *24* (45), 455302.

(81)   Zhou, S.; Deng, X.; Li, X. Investigation on a Novel Core-Coated Microspheres Protein Delivery System. *Journal of Controlled Release* **2001**, *75* (1–2), 27–36.

(82)   Derfus, A. M.; Chan, W. C. W.; Bhatia, S. N. Probing the Cytotoxicity of Semiconductor Quantum Dots. *Nano Letters* **2004**, *4* (1), 11–18.

(83)   Minardi, S.; Fernandez-Moure, J. S.; Fan, D.; Murphy, M. B.; Yazdi, I. K.; Liu, X.; Weiner, B. K.; Tasciotti, E. Biocompatible PLGA-Mesoporous Silicon Microspheres for the Controlled Release of Bmp-2 for Bone Augmentation. *Pharmaceutics* **2020**, *12* (2), 118.

(84)   Minardi, S.; Corradetti, B.; Taraballi, F.; Sandri, M.; Van Eps, J.; Cabrera, F. J.; Weiner, B. K.; Tampieri, A.; Tasciotti, E. Evaluation of the Osteoinductive Potential of a Bio-Inspired Scaffold Mimicking the Osteogenic Niche for Bone Augmentation. *Biomaterials* **2015**, *62*, 128–137.

(85)   Win, K. Y.; Feng, S. S. Effects of Particle Size and Surface Coating on Cellular Uptake of Polymeric Nanoparticles for Oral Delivery of Anticancer Drugs. *Biomaterials* **2005**, *26* (15), 2713–2722.

(86)   Sahoo, S. K.; Panyam, J.; Prabha, S.; Labhasetwar, V. Residual Polyvinyl Alcohol Associated with Poly (D,L-Lactide-Co-Glycolide) Nanoparticles Affects Their Physical Properties and Cellular Uptake. *Journal of Controlled Release* **2002**, *82* (1), 105–114.

(87)   Xiong, S.; Zhao, X.; Heng, B. C.; Ng, K. W.; Loo, J. S. C. Cellular Uptake of Poly-(D,L-Lactide-Co-Glycolide) (PLGA) Nanoparticles Synthesized through Solvent Emulsion Evaporation and Nanoprecipitation Method. *Biotechnology Journal* **2011**, *6* (5), 501–508.

(88)   Wang, S.; Dormidontova, E. E. Nanoparticle Design Optimization for Enhanced Targeting: Monte Carlo Simulations. *Biomacromolecules* **2010**, *11* (7), 1785–1795.

(89)   Liang, R.; Zhu, J. Monodisperse PLA/PLGA Nanoparticle Fabrication through a Surfactant-Free Route. *Journal of controlled release* **2011**, *152*, e129–e131.

(90)   Yabu, H. Self-Organized Precipitation: An Emerging Method for Preparation of Unique Polymer Particles. *Polymer Journal* **2013**, *45* (3), 261–268.

(91)   Yabu, H.; Higuchi, T.; Ijiro, K.; Shimomura, M. Spontaneous Formation of Polymer Nanoparticles by Good-Solvent Evaporation as a Nonequilibrium Process. *Chaos: An Interdisciplinary Journal of Nonlinear Science* **2005**, *15* (4), 047505.

(92)   Xu, Y.; Kim, C. S.; Saylor, D. M.; Koo, D. Polymer Degradation and Drug Delivery in PLGA-Based Drug–Polymer Applications: A Review of Experiments and Theories. *Journal of Biomedical Materials Research - Part B Applied Biomaterials* **2017**, *105* (6), 1692–1716.

CHAPTER 3
Silica-coated Quatsomes

ABSTRACT

In this chapter is presented the synthesis of a hybrid system based on a non-lipid based vesicle, Quatsomes (QS), covered with silica. The silica shell around the vesicles protects them, giving more structural and mechanical stability to the QS, against fusion and internal leakage during storage, transport for eventual applications. Interestingly, this shell could prevent the loss of cargo during the delivery of drugs or biomolecules. Moreover, redox-organic stimulus-responsive silica shell systems were synthetized. The use of S-S groups in the silica framework allows the breaking of the shell in presence of a reducing agent, such as glutathione inside cells. The destruction of the system results in the release of the cargo and their breaking in small pieces, preventing their accumulation in the body. These materials could therefore have a potential interest in biomedical applications.

3.1. Introduction

Liposomes are phospholipid self-assembled nano-objects that have been well studied since their discovery in 1964.[1–4] The structure of liposomes allows hydrophobic molecules to be encapsulated within the bilayers and hydrophilic molecules in the lumen. These properties have been explored to encapsulate drugs for drug delivery applications.[5–9] A major drawback of lipids assemblies is their tendency to aggregate, causing a low degree of structural homogeneity that is crucial for pharmacological purposes.[10] As a result, there is an interest in building stable monodisperse vesicles that could be used in pharmaceutical formulations.[6–10]

Recently the group of N. Ventosa developed a new kind of thermodynamically stable unilamellar vesicular structures, termed Quatsomes (QS), constructed from quaternary surfactants and sterols (with highly positive charged surfaces) (see **Figure 3.1**). QS show outstanding vesicle to vesicle homogeneity in size, lamellarity, and membrane supramolecular organization. They are stable for periods up to several years, and also maintaining stability upon dilution making them a promising platform for theragnostic nanomedicine.[11–17]
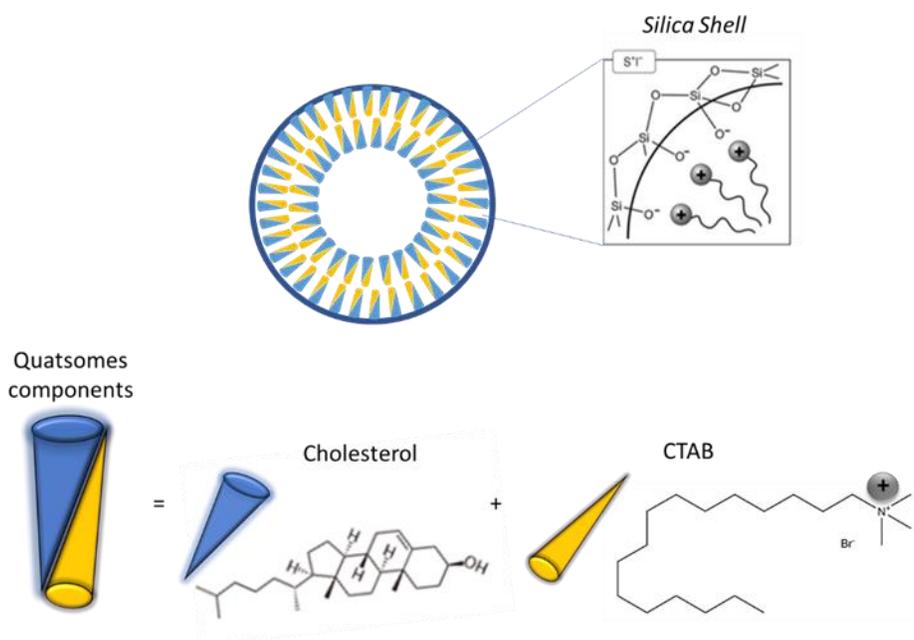

Figure 3.1. Representation of a silica-coated QS. The bilayer of the QS is formed by CTAB and cholesterol. In basic conditions electrostatic interactions make possible the interaction between the silica (negatively charged) and the QS (positive charge).

To give more structural and mechanical stability to the QS, we decided to create a silica shell around them so that a new drug delivery system could be realized (see **Scheme 3.1)**. The combination of soft and hard materials in a combined system will provide stability to the loaded QS against aggregation and internal leakage during its storage, transportation, and application. Besides this, it could introduce in the system new groups for bioconjugation.[18–20]

This work presents the strategy and the achievements in the use of silica as a stable shell for QS to prevent cargo loss.[21–24] Moreover, the synthesis of a stimulus-responsive coating to create a degradable system for delivery applications is also reported.[21] In this last case, the shell specifically breaks in the presence of a reducing environment typically found inside of cancer cells. The mechanism of degradation induces silica debris which are easily removed from the body.[25,26]
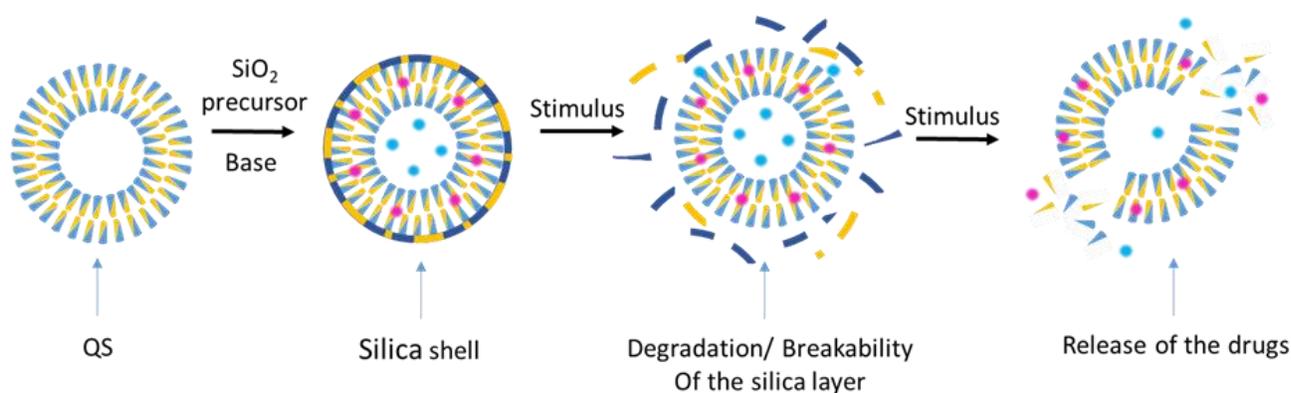
Scheme 3.1. Quatsomes coverage mechanism and drug delivery strategy employing organo-silica-coated (QS) as vehicles of drugs.

QS used throughout the initial phase of experiments were generated from cholesterol and CTAB (1:1), forming nanovesicles with a diameter of ~100 nm. These vesicles were made using the depressurization of an expanded organic solution-suspension (DELOS-SUSP) methodology.[27] The interaction between the two materials resulted from electrostatic interactions between the positively charged quaternary ammonium surfactant (CTAB) and the negatively charged silica, under basic conditions (**Figure 3.1**).[28]

3.2. Results and Discussion

3.2.1. Synthesis and characterization of silica-coated QS (SQS)

Two main hybrid materials were synthetized during this work: Non- breakable silica QS (NB-SQS) and stimuli responsive breakable silica-coated QS (B-SQS). For the B-SQS breaking was triggered by a reducing agent, since the silica contains in its network disulfide groups. For the preparation of these materials several silanes were tested: Tetraethyl orthosilicate (TEOS), Tetramethyl orthosilicate (TEMOS) and (3-aminopropyl)triethoxysilane (APTES) for the NB-SQS and the disulfide linker Bis(triethoxysilylpropyl)tetrasulfide (BTSPD) for the B-SQS (**Figure 3.2**).

1) The encapsulation of QS with SiO₂ precursors.
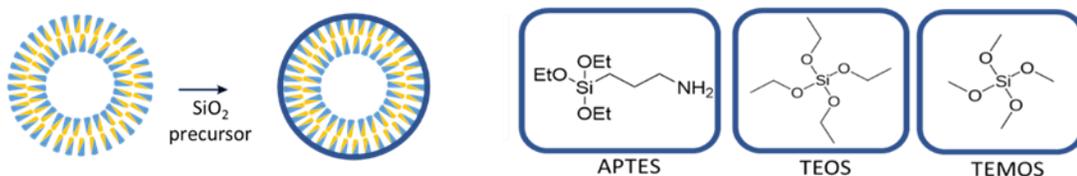
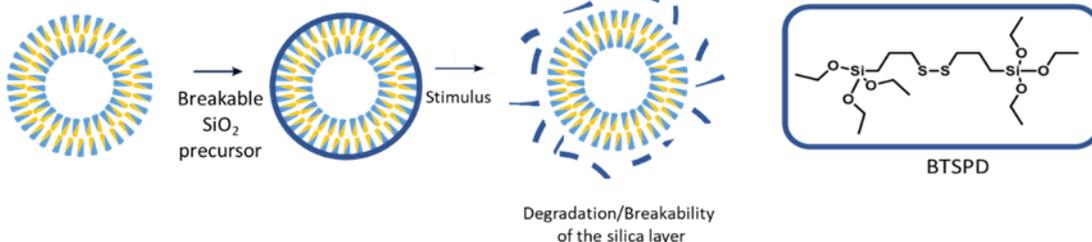2) Synthesis of stimuli responsive breakable BioMSNPs.

Figure 3.2. Synthesis of non-breakable silica and breakable coated QS and the silane precursors employed in each case.

3.2.2. Synthesis and characterization of the Non-Breakable silica-coated QS (NB-SQS)

Even though QS are stable in comparation with other non-lipidic vesicles, changes in the media solution as pH, content of solvents or even stirring can change the properties of these nanocontainers. Because of that, it is important to study under which conditions the sample maintains its properties as, homogeneous size and shape. In order to explore those conditions, a solution of QS, with a diameter of 156±37 nm (measurement done by Dynamic light scattering (DLS)) was analyzed under different % of EtOH, stirring and in presence of ammonia during time. These experiments were carried out to find the parameters in which there is not damage in the starting QS sample to then perform the reactions with the silanes.

QS in presence of EtOH

The stability of the QS in presence of EtOH was determined over a range of 20 to 40% of EtOH in water. The initial diameter of the QS was measured by DLS showed a size distribution of 156±37 nm. The **Figure 3.3** shows the DLS results increasing the % of EtOH, where it is observed that at 20% of EtOH the Quatsomes was still stable (reporting a size 150±33 nm) but the addition of more EtOH, modified then the equilibrium of the Quatsomes solution and a re-organization of the QS was produced, giving assemblies of bigger sizes. At 30% EtOH the size observed was of 197±45 nm, and with 40% EtOH two population of QS were observed: one of 216±54 nm and another of 710±151 nm. These results suggest that not more than 20% of EtOH can be used without changing the homogeneity of the sample. In other words, for the synthesis of the silica shell, the maximum amount of EtOH that can be used is 20%.
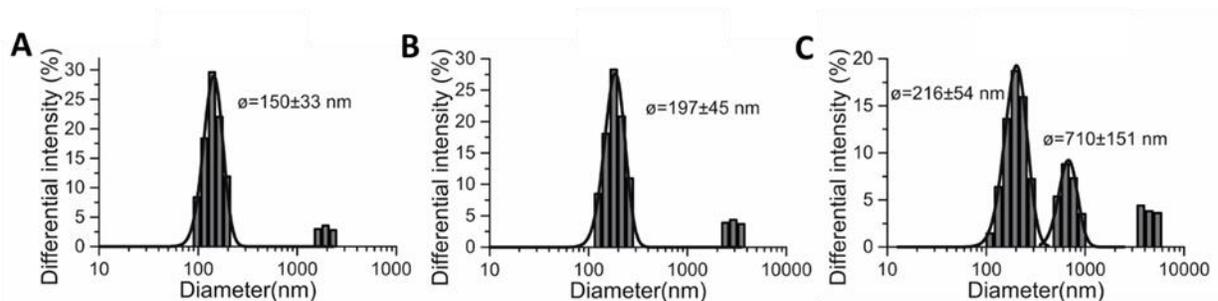

Figure 3.3. Size of the QS was measured by DLS at three different % of EtOH **A)** 20, **B)** 30 and **C)** 40 %.

QS during stirring

The stability experiments of QS under stirring over time were performed at the lowest achievable stirring rate (using a stirring of 375 rpm, in which all the solution was observed to be homogeneous). **Figure 3.4** showed how the size of QS was evaluated after 0, 1, and 3h of continuous stirring (measurements done by DLS); it was observed that the majority of the QS were not destroyed because of stirring; though a new population was observed after 3h. The size reported at time 0 h was 158±36 nm, at time 1h is 153±34 nm and a time 3h one population was 131±29 nm and the new one reported was 377±71 nm. From these results, stirring with this speed was started to be used in the synthesis of the silica shell in the QS.

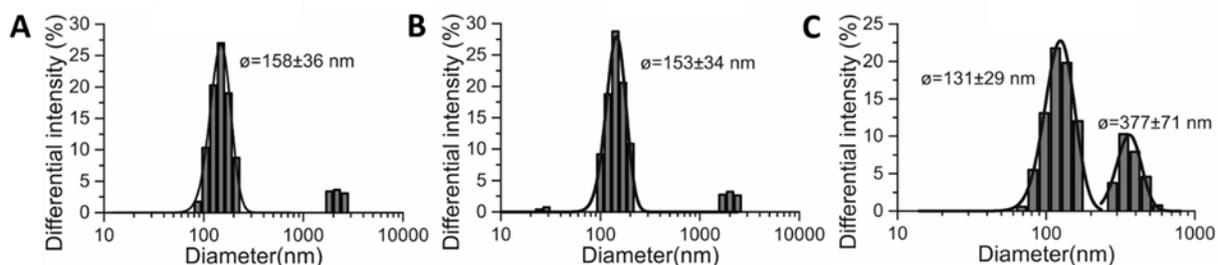**Figure 3.4.** Size distribution of QS under stirring at 375 rpm and 20% of EtOH at different time of stirring **A)** 0h, **B)** 1h and **C)** 3h.

QS in presence of base

The addition of base is often used to trigger silica polymerization. The stability of QS in the presence of ammonia was investigated. QS of diameter 127±29nm in water was treated with a base (6 mM ammonia), 10% EtOH was added and the stirring rate was set at 375 rpm. The system was analyzed by DLS and the size of the QS was quantified over 3 h, **Figure 3.5**. At time 0h, the size was 136±31 nm, after 1h was 126±29 nm and after 3h appeared two populations: 109±26 nm and 424±107 nm. Even though a new population was appearing after time, the initial population still remained (It has to be explained that bigger particles scatter more in DLS, meaning that the number of particles with bigger sizes is low). In conclusion, ammonia can be used up to this concentration for the synthesis of silica on the surface of the QS.
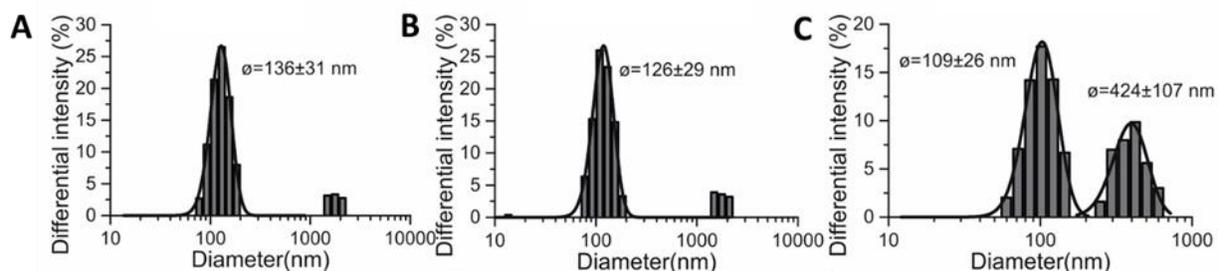

Figure 3.5. Size distribution of QS in the presence of ammonia 6 mM, under 375 rpm and 10% EtOH at different time of stirring **A)** 0h, **B)** 1h and **C)** 3h.

3.2.2.1. Synthesis and characterization of the Non-Breakable silica-coated QS (NB-SQS) using APTES

Beloglazova *et al.* previously explored the possibility of making silica-coated liposomes loaded with quantum dots as labels for multiplex fluorescent immunoassay. [18] The silica coverage was meant to ensure the stability of the loaded liposomes against aggregation and internal leakage during storage. Additionally, the silica surface can be functionalized by a silane containing a terminal amino group that allows for further bioconjugations.[18] In the paper was also proposed to use APTES for the encapsulation of the liposomes (**Figure 3.6**). This silane reagent can individually encapsulate the vesicles, as the positive charges of the amino group make repulsive electrostatic interaction between the particles which helps to avoid the formation of agglomerations (**Figure 3.6B** shows the representation of the amino groups pointing outside). **Figure 3.6C** from the scheme shows the Transmission electron microscopy (TEM) image of this material.
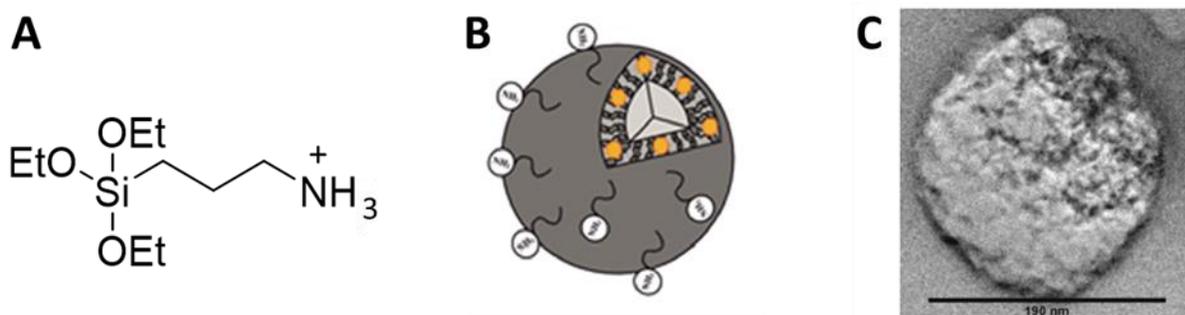

Figure 3.6. A) Silane used to encapsulate the liposomes (APTES) **B)** Schematic representation of the encapsulation of the liposomes, and **C)** TEM image of a liposome cover with APTES. Adapted with permission from ref. 18 (Copyright 2006, Wiley-VCH Verlag GmbH & Co. KGaA, Weinheim)

With this previous work, we then used a modified procedure from Beloglazova *et al.*, [18] which prevented precipitation of the material and improved surface coverage of the QS with silica. **Figure 3.7** shows the DLS spectra of the SQS samples after 2h, overnight (around 12 hours), and 2 days of stirring. From these data, SQS formation occurred within the first two hours and are stable thereafter based on the size change from 114±26 nm at t = 0 to 193±49 nm after 2 h. No change was observed after this time period.
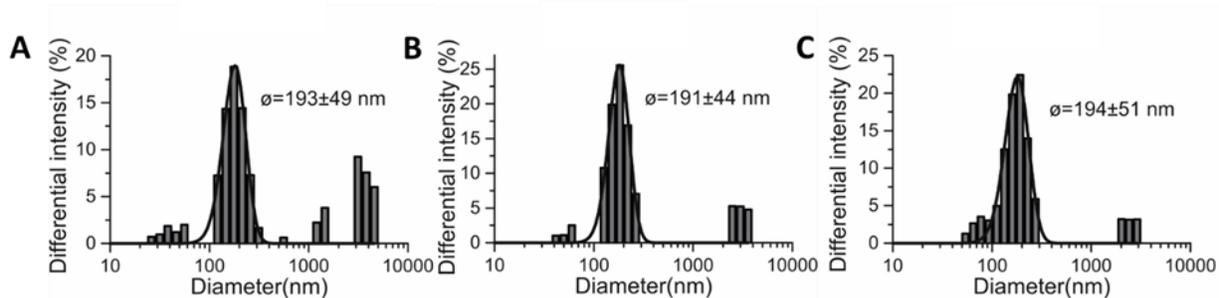
Figure 3.7. The DLS measurement of the SQS using APTES after **A)** 2h, **B)** overnight and **C)** 2 days of stirring.

Images of **Figure 3.8** was taken from a scanning electron microscope (SEM) of the sample after overnight stirring (**Figure 3.8**). The images reveal that silica QS were broken due to the vacuum applied during the sample preparation (top left of **Figure 3.8**). Despite this, some QS were able to see. **Figures 3.8** and **3.9** show the formation of spheres which were attributed to the formation of the silica around the QS. **Figure 3.9** shows that the SEM size distribution, count performed on 300 nanoparticles, gave an average diameter of 140±23nm SQS particles.
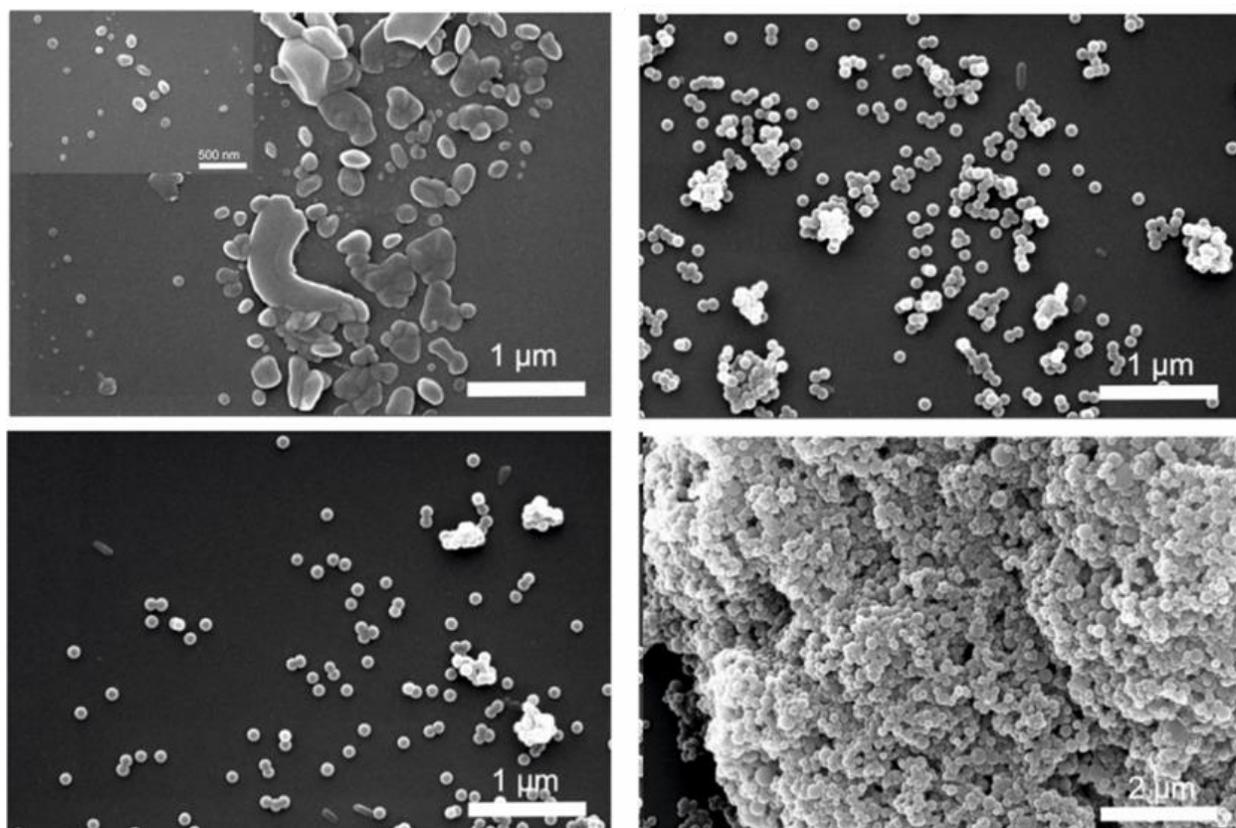

Figure 3.8. SEM pictures of the SQS after overnight of stirring (Scale bar of top left is 1 μm and inset is 500 nm, top right and down left are 1μm and down right is 2μm).
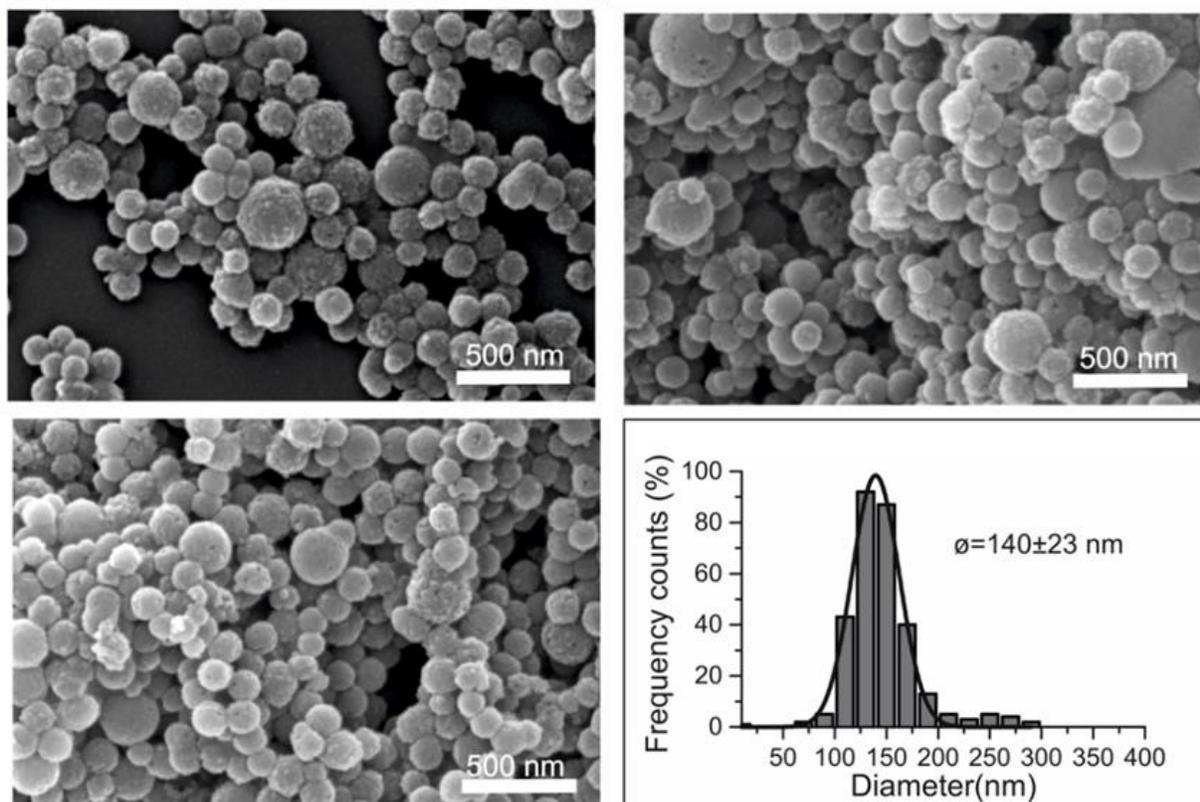
204

Figure 3.9. SEM pictures of the SQS after overnight stirring (scale bar 500 nm). Down right: SEM size distribution (count performed on 300 nanoparticles; average diameter 140±23 nm).

In order to know if the reaction could be run in a concentrated system of QS, a second methodology was tested to prepare the sample. The new methodology involved the non-dilution of the system and the addition of more base (25 times more ammonia) in comparation with the previous methodology. **Figure 3.10** shows the DLS of the QS covered with silica (SQS), 1 h and overnight after the addition of base (6 mM ammonia) while stirring with the APTES. The 114±26 nm QS were found to increase in size after the addition of base, 123±26 nm and continued to grow after 1 hour (174±41 nm) and overnight (194±26 nm). **Figure 3.11** shows the SEM and size distribution after overnight stirring that yielded an average diameter of 142±24 nm SQS particles. It should be noted that particle degradation made average particle size quantification difficult (see **Figure 3.11** top-right); these particles were found outside the drop casting, while in the interior of the drop mostly all the sample was broken as is represented in **Figure 3.12**.
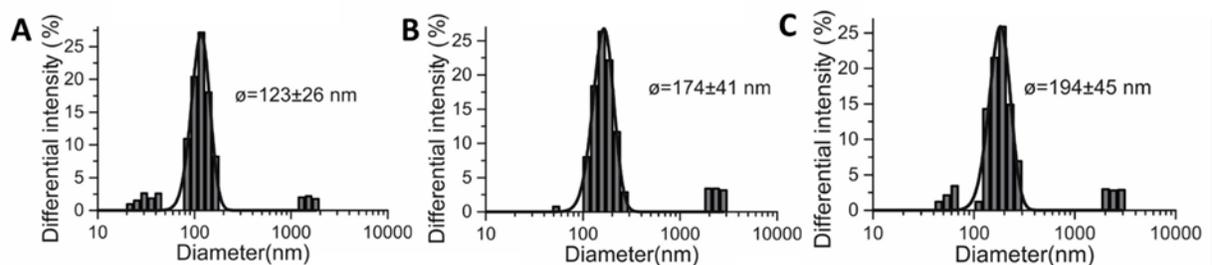
Figure 3.10. DLS measurements of the silica covered Quatsomes (SQS) **A)** after putting base (6 mM ammonia) and stirring during **B)** 1 h and **C)** overnight.
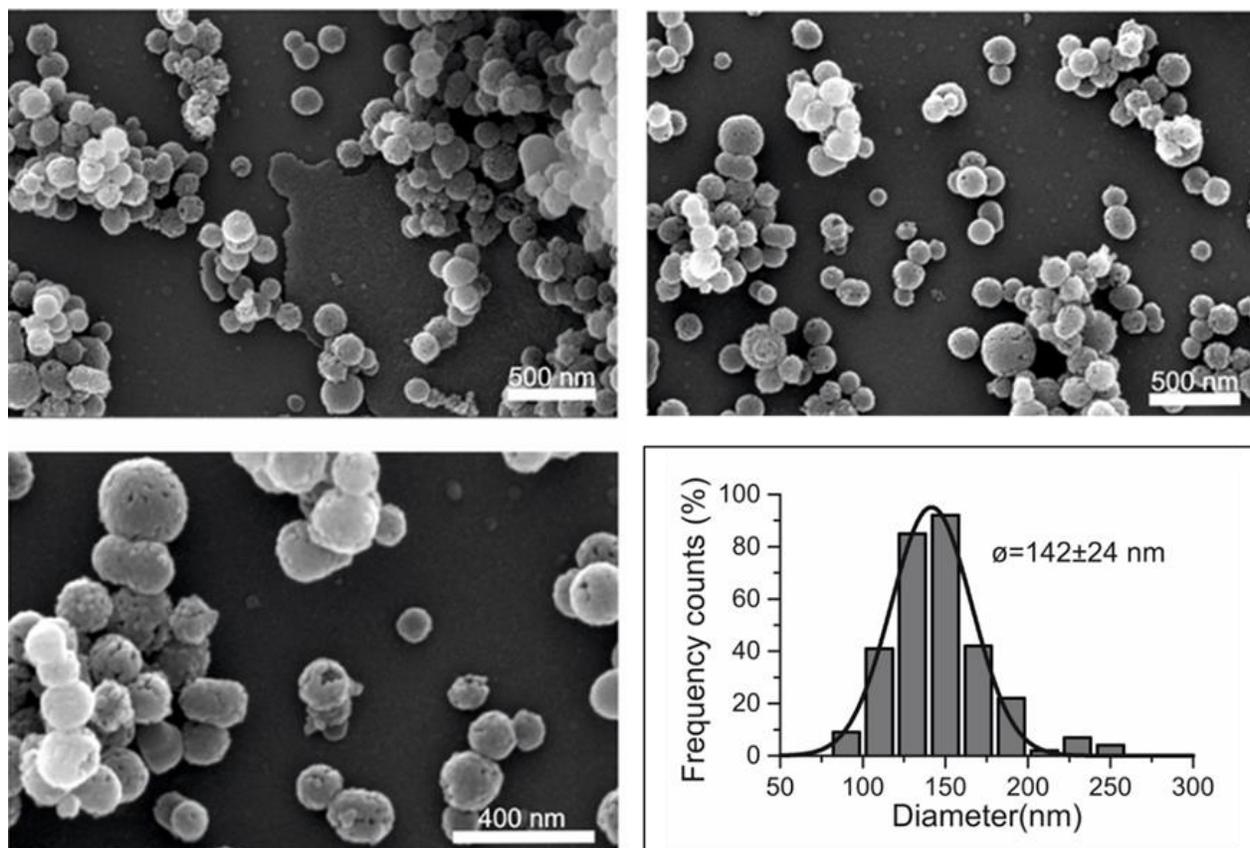

Figure 3.11. SEM pictures of the silica covered Quatsomes (SQS) after overnight of stirring (scale bar 500 nm and 400 nm) using a concentrated methodology to produce them. Down right: SEM size distribution (count performed on 300 nanoparticles; average diameter 142±24 nm).
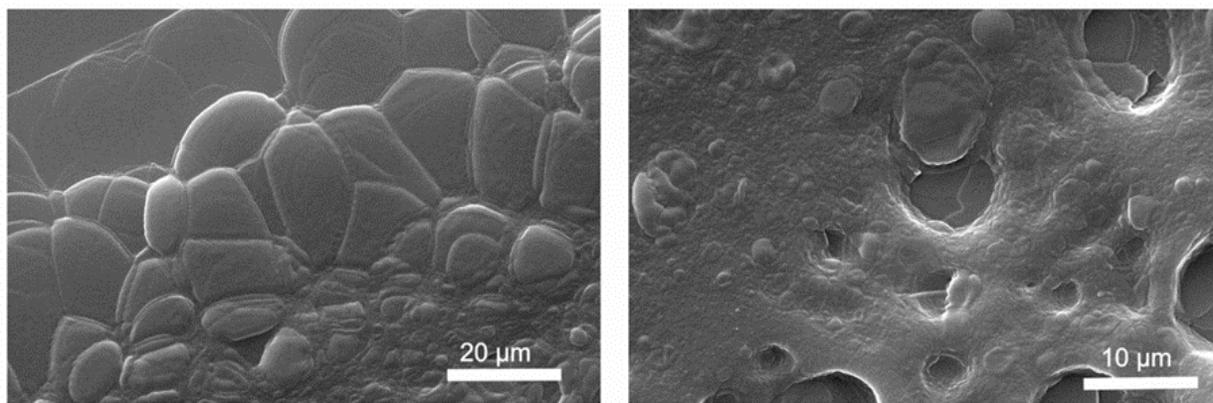
Figure 3.12. SEM pictures of the drop casting silica covered Quatsomes (SQS) after overnight of stirring (scale bar: 20 and 10 μm); in the interior of the drop; all the sample is broken due to the vacuum of the SEM equipment.

Non-Breakable silica-coated QS (NB-SQS) using APTES at 0 °C-7 DAYS

Another methodology of synthesis described in the literature by Zhang[29] *et al*. was explored. This methodology involved the use of a buffer of ascorbic acid and ammonia to set the reaction at pH 9 and to run it at 0 °C. At time 0h, the starting material of QS had a size of 84±1 nm, a Pdl of 0.23±0.01 and a Zeta Potential of 84±2 mV. After 2 days the pH of the reactions was measured giving a value of 9.64 and a size of 78±1 nm, Pdl of 0.21±0.01 and Zeta Potential of 53±3 mV. After, 3 mL of the solution was held separately, and 5.2 μL of APTES was added directly to the remaining reaction. The size of the QS was 81±2 nm after 4 days of stirring, with a Pdl of 0.22±0.01 and Zeta Potential of 54±3 mV (see **Figure 3.13C**); and to the seventh day, the size reported was still constant 81±2 nm, with Pdl of 0.24±0.01 and with a little decrease of the Zeta Potential to 52±1 mV (**Figure 3.13A** and **3.13B** which showed that the change of size and Zeta Potential of the reaction during the time). Due to the size stability after 7 days (not presence of agglomerations was observed), no dialysis of the material was performed to stop the reaction. IR was performed to reveal the existence of silica formed around the material and **Figure 3.13D** shows the Si-O band at 1175 cm^{-1} due to the presence of the silica polymerization on the QS.
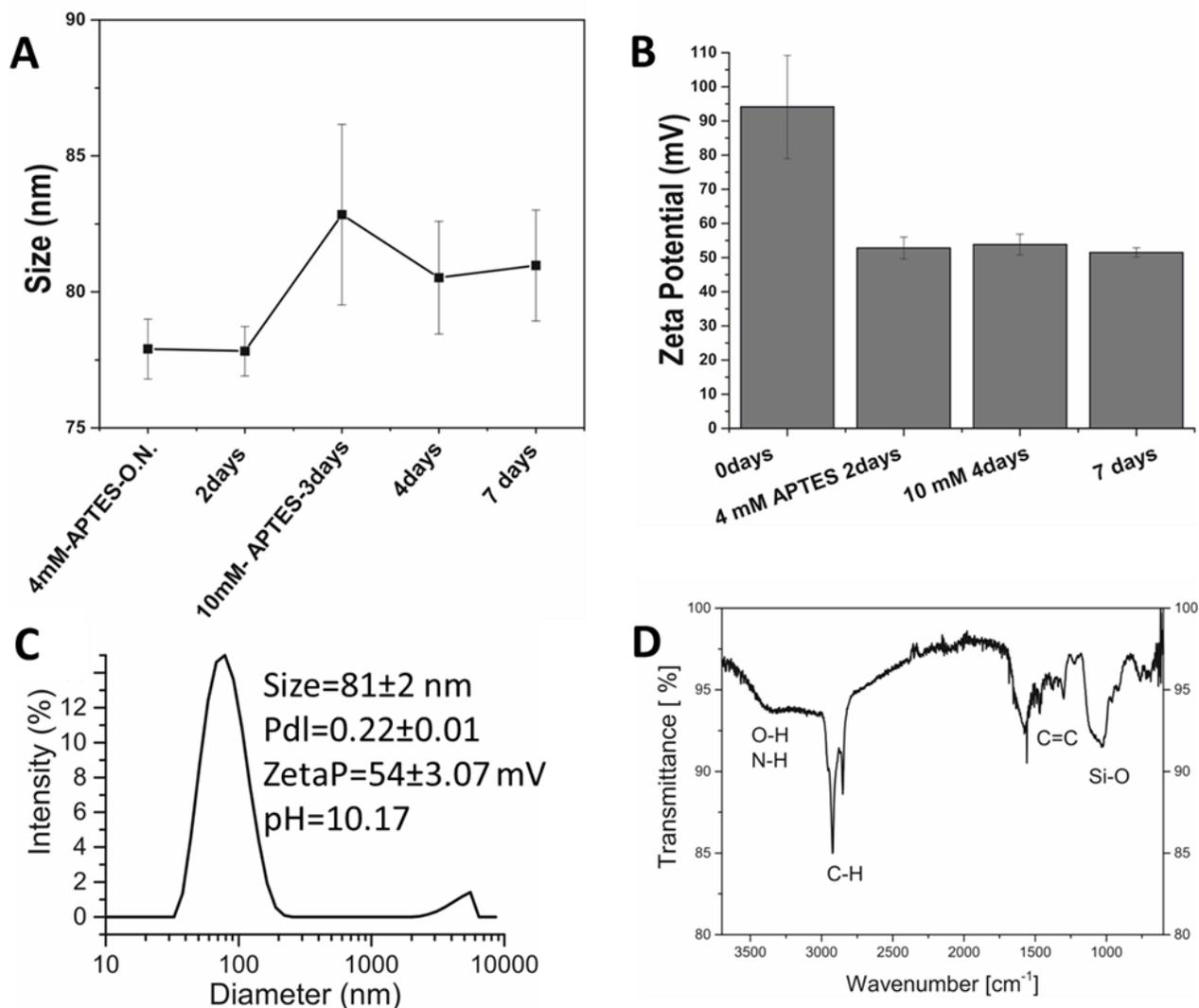
Figure 3.13. A) DLS measurements and **B)** Zeta Potential measurement of the reaction over time of TEOS silica-coated QS at 0 °C for 7 days. **C)** DLS measurements after 4 days of reaction the NB-QS-TEOS. **D)** IR spectra of silica-coated QS. The starting material has a size of 84±1 nm a PdI of 0.23±0.01 and a Zeta Potential of 84±2 mV.

3.2.2.2. Synthesis and characterization of the Non-Breakable silica-coated QS (NB-SQS) using TEOS

The encapsulation of the Quatsomes using the silane TEOS was done following the Hubert,[30] and Zhang[29] procedures, where Hubert H. *et al.*, reported the use of TEOS and TEMOS as silica precursors for the encapsulation of liposomes.[30] During their synthesis, the authors avoided the use of EtOH in the synthesis, while setting the reaction at pH 8 with the addition of diluted ammonia. The concentration of TEOS used was six and 32 times the concentration of vesicles

(with the QS the high addition of TEOS produces immediately a formation of precipitates; no covering of the QS was observed) but they reported long synthesis time of reaction (7days) and the pH adjusted at any desired time with the addition of extra ammonia to let the reaction continue. In contrast, Zhang *et.al.*, reported the cover of lipid vesicles using TEOS and working with an ascorbic-acid-based buffer and the solution of ammonia to set the pH of the reaction; also two different temperatures 8 °C and 20 °C were tested in the experiments reported, observing one and two different populations of cover vesicles at these temperatures, respectively.[29]

For our first experiments, the Zhang[29] methodology was used with some modifications in order to cover the QS with silica: 6.5 mL of water and 1 mL QS (final concentration of QS was 2 mM) were placed in 10 mL flask under 375 rpm stirring. A 200 µL portion of an ascorbic acid solution (with an initial concentration of 50 mM) and 375 µL of diluted ammonia (0.134 M) were added to obtain a pH around 9. Finally, 8 µL of TEOS was added directly to the solution ([TEOS]=4.4 mM). The experiment was performed at two different temperatures: 0 °C and room temperature. The following day the pH of the reactions was measured, the reaction that was at 0 °C reported a pH of 7.8 while the one performed at room temperature was 7.13. From DLS measurements, the initial QS size was 82±1 nm, with a Pdl of 0.22±0.01 and Zeta Potential of 88±1 mV. After one night reacting at 0 °C and pH of 7.8, particles with a size of 90±1 nm, a Pdl of 0.16±0.01 and Zeta Potential of 54±3 mV were obtained while the reaction at 20 °C and pH of 7.13 resulted in particles with a size distribution of 79.3±1 nm, Pdl=0.2±0.01 and Zeta Potential of 52±1 mV. To both reactions, ammonia was again added to set the pH value around 8 (at this point the pH of the reaction at 0 °C and 20 °C measured is 8.18 and 8.1, respectively). Immediately afterward, 10 µL of TEOS was added (obtaining a final concentration of TEOS of 10 mM) to both reactions, and the day after the reaction at 0 °C and pH of 7.13, yielded particles with a size distribution of 155±3 nm, Pdl of 0.18±0.01 and Zeta Potential of 32±0.59 mV, while the reaction at 20 °C and pH of 7.17, shows a size distribution of 98±1 nm, Pdl of 0.09±0.02 and Zeta Potential of 46±2 mV. The reaction was stopped by dialysis using a membrane of 14 KDa. 5.5ml of the sample was washed by replacing the water solution ever 15 mins over an hour. The final product was measured by DLS, and a size distribution of 159±3 nm, Pdl of 0.2±0.01 and Zeta Potential of 29±1 mV were obtained for the reaction at 0 °C. While that for the reaction at 20 °C the size distribution was

97±2 nm, Pdl of 0.1±0.01 and the Zeta Potential of 41±2 mV. **Figure 3.14A** and **3.14D** contains the monitoring of the change size silica-coated QS during the reaction of these experiments at 0 °C and 20 °C, respectively. In both cases, the second addition of silica caused a large size increase after stirring overnight (**Figure 3.14C** and **Figure 3.14F** for the reaction at 0 °C and 20 °C, respectively). It seems that the reaction at 0 °C doubled in size while the reaction at 20 °C increased only 25%. This could be also due to the higher value of pH. **Figure 3.14B** and **3.14D** shows the change of Zeta Potential in both reactions (0 and 20 °C) giving us information about the homogeneity of the silica shell and the thickness; the thicker is the silica shell, the lower is the value of Zeta Potential due to the negative charges of the silica.
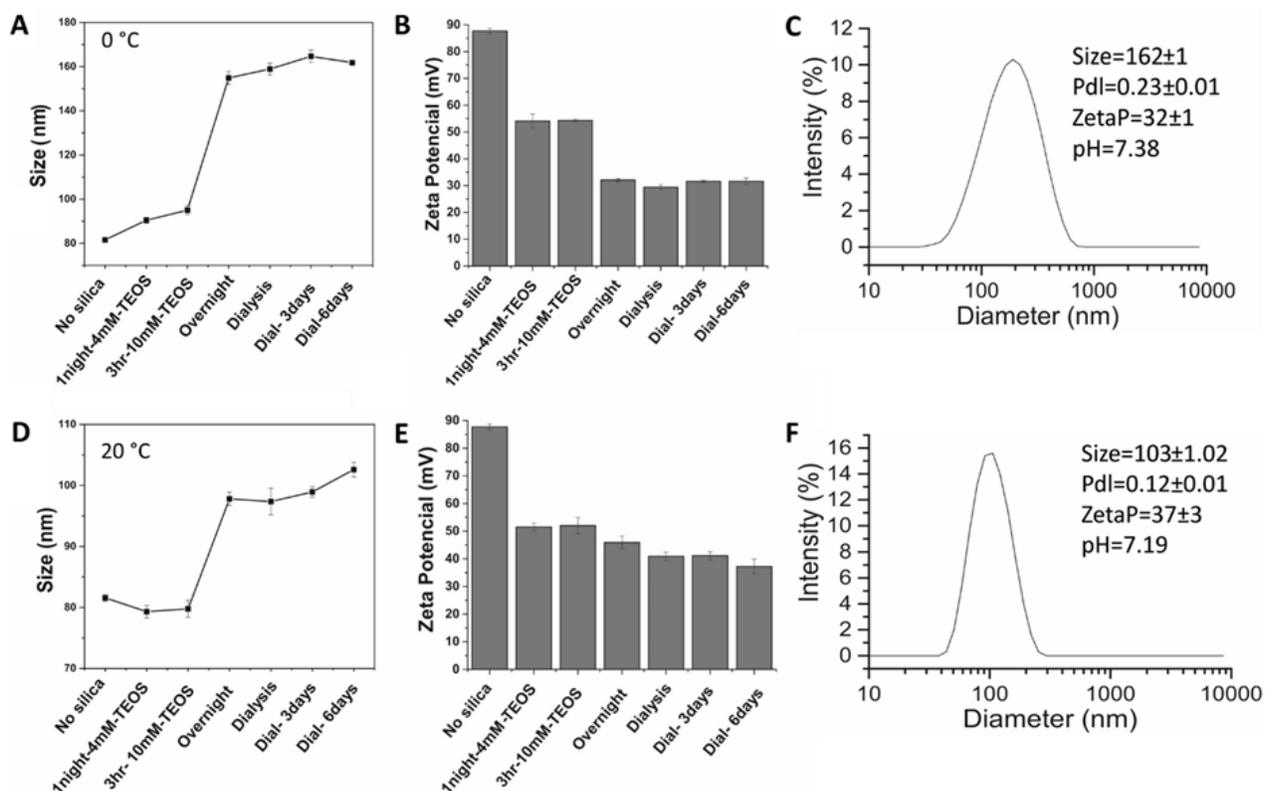
Figure 3.14. DLS-Size distribution of the reaction over time of TEOS silica-coated QS at **A)** 0 °C and **D)** 20 °C that was carried out by DLS. Zeta Potential of the reaction over time of TEOS silica-coated QS at **B)** 0 °C and **E)** 20 °C. DLS- measurement after dialysis of the NB-QS-TEOS at **C)** 0 °C and **F)** 20°C. The starting material has a size of 82±1 nm a Pdl of 0.22±0.01 and a Zeta Potential of 88±1 mV.

Figure 3.15 and **3.16** show the cryogenic transmission electron microscopy (Cryo-TEM) images of the samples prepared at 0 °C and 20 °C, respectively. An external material was observed on the

surface of the QS, as indicated by the darker zones in the QS that demonstrate the interaction between the silica and the QS. However, the deposition of silica was not uniform meaning that the QS were not completely covered by the silica in both experiments. This also agrees with the positive Zeta Potential values for the reaction at 0 °C and 20 °C of 29±1 mV and 41±2 mV, respectively. Negatively charged material formed could give an indication that the positive charge of the QS is neutralized by the silica. For these results, the material must be improved to then have a homogeneous silica coating on the QS. The concentration of TEOS in the reaction and the total synthesis time has then to be varied to improve surface coverage by using this silane.
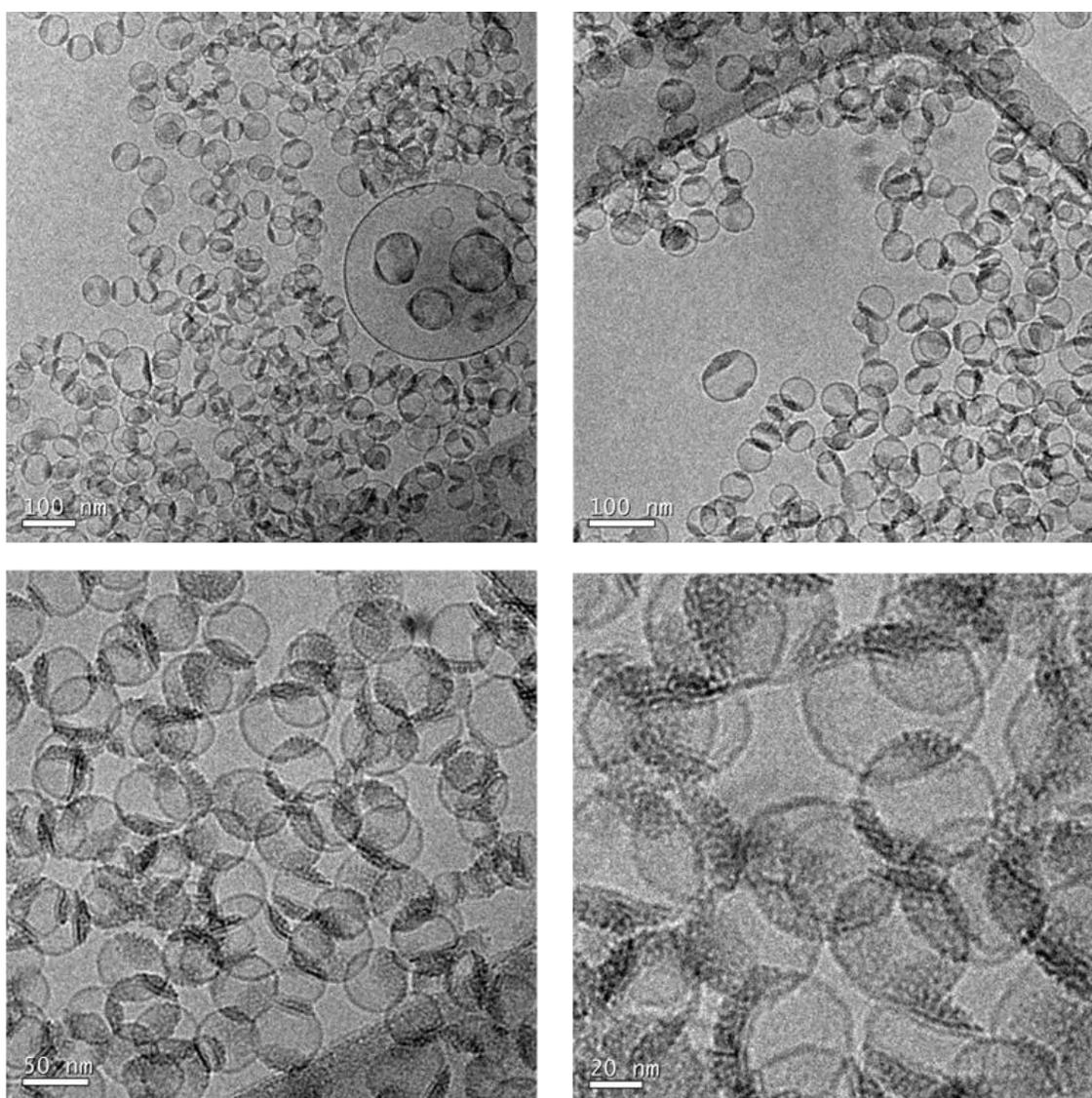

Figure 3.15. Cryo-TEM images of the 10 mM TEOS silica-coated QS at 0 °C after dialysis. Scale bars, 100, 50 and 20 nm.
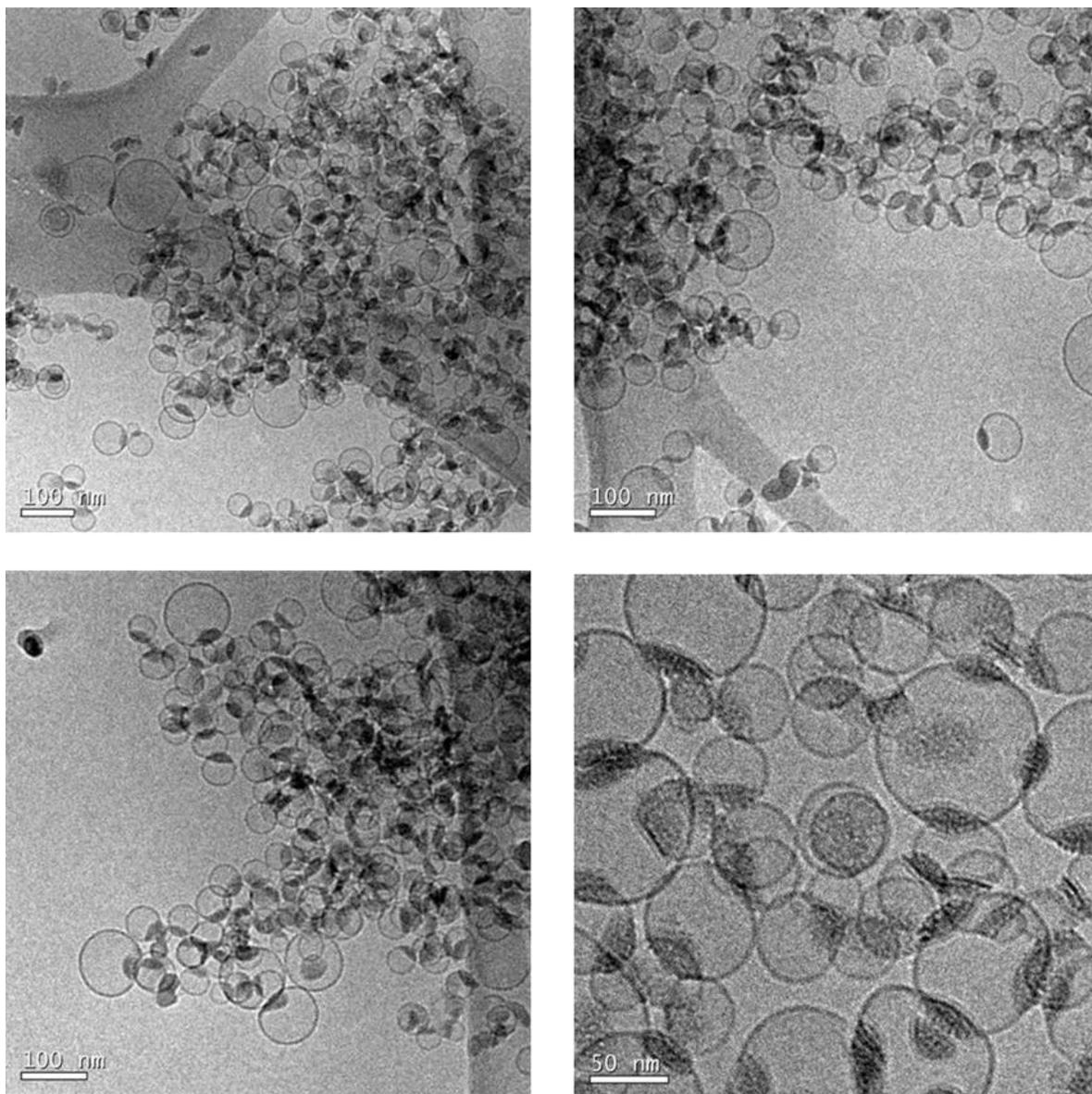
Figure 3.16. Cryo-TEM images of the 10 mM TEOS silica-coated QS at 20 °C after dialysis. Scale bars, 100 and 50 nm.

Observing the images at 0 °C and 20 °C, we can see that the reaction at 0 °C, which gives a bigger change in size (data observing by DLS), had in fact more surface covered by the silica. However, further experiments must be done to know if an effect of the temperature, pH or the combination of both parameters was the cause of those observations.

To know if the dark zones of the QS in the Cryo-TEM images the silica was interacting with the QS, IR experiments were performed on both samples. **Figure 3.17** shows an intense band around

1175 cm^{-1} attributed to the Si-O which means there was the formation of silica on the surface of the QS.

Figure 3.17. IR spectra of TEOS silica-coated QS at **A)** 0 °C and **B)** 20 °C.
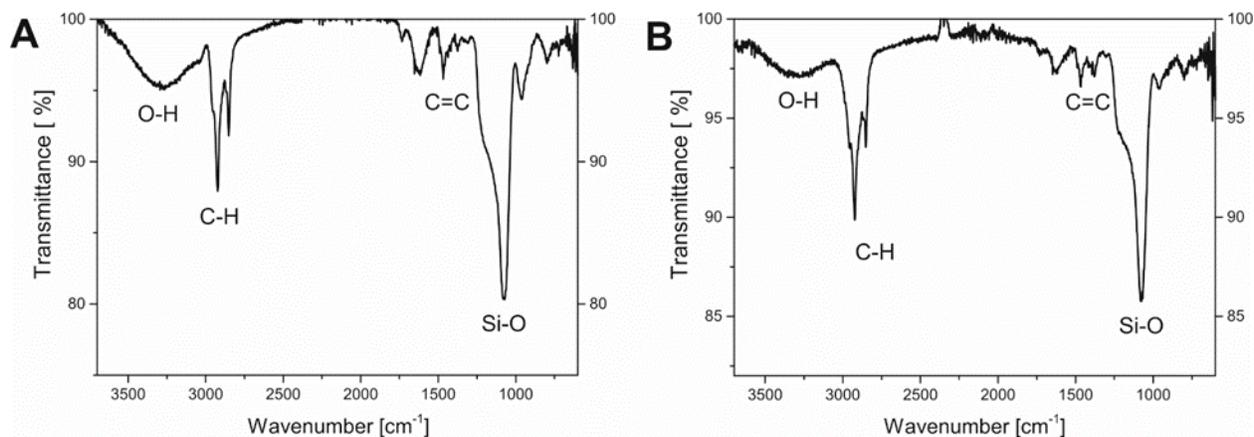
Non-Breakable silica-coated QS (NB-SQS) using TEOS at 0 °C and longer times

Based on these last results, the TEOS based synthesis was modified with longer synthesis times [30] at 0 °C, in ice bath.[29] The starting conditions of the reaction was as well, 2 mM of QS at pH of 9.03, the first addition of TEOS (4 mM) was added and after 2 days a second addition of TEOS was done to have a final concentration of 10 mM. At time 0h, the reported size distribution was 85±2 nm, with a Pdl of 0.24±0.01 and Zeta Potential of 94±15 mV. After 2 days the pH was measured giving a value of 7.38 and a size distribution of 86±1 nm, Pdl of 0.22±0.01 and Zeta Potential of 56±2 mV. After these two days, 3 mL of the solution were extracted to storage and 5 µL of TEOS were added directly to the reaction media and after another day the size of the QS was changing to a size of 91±1 nm, with a Pdl of 0.22±0.01; to the 4 day ago of the starting addition, the size was 95±1 nm, Pdl of 0.22±0.01 and Zeta Potential of 51±3 mV. After 7 days of the starting addition, the reaction was stopped by dialysis giving a material with a size of 104±2 nm, a Pdl of 0.21±0.1 and a Zeta Potential of 41±3 mV. **Figure 3.18A** shows the increasing of the size over the time adding TEOS; measured by DLS and the **Figure 3.18B** displays how the Zeta Potential was decreasing until the end of the reaction. A negative Zeta Potential of the nanosystem provided us information about the homogeneity of the silica coverage. With these results, we believe that there are zones in the material where the silica does not cover the QS. For this, another

methodology must be investigated to improve the reaction. **Figure 3.18C** shows the DLS-Size distribution measurement after 4 days of reaction and in **Figure 3.18D** the IR spectra.
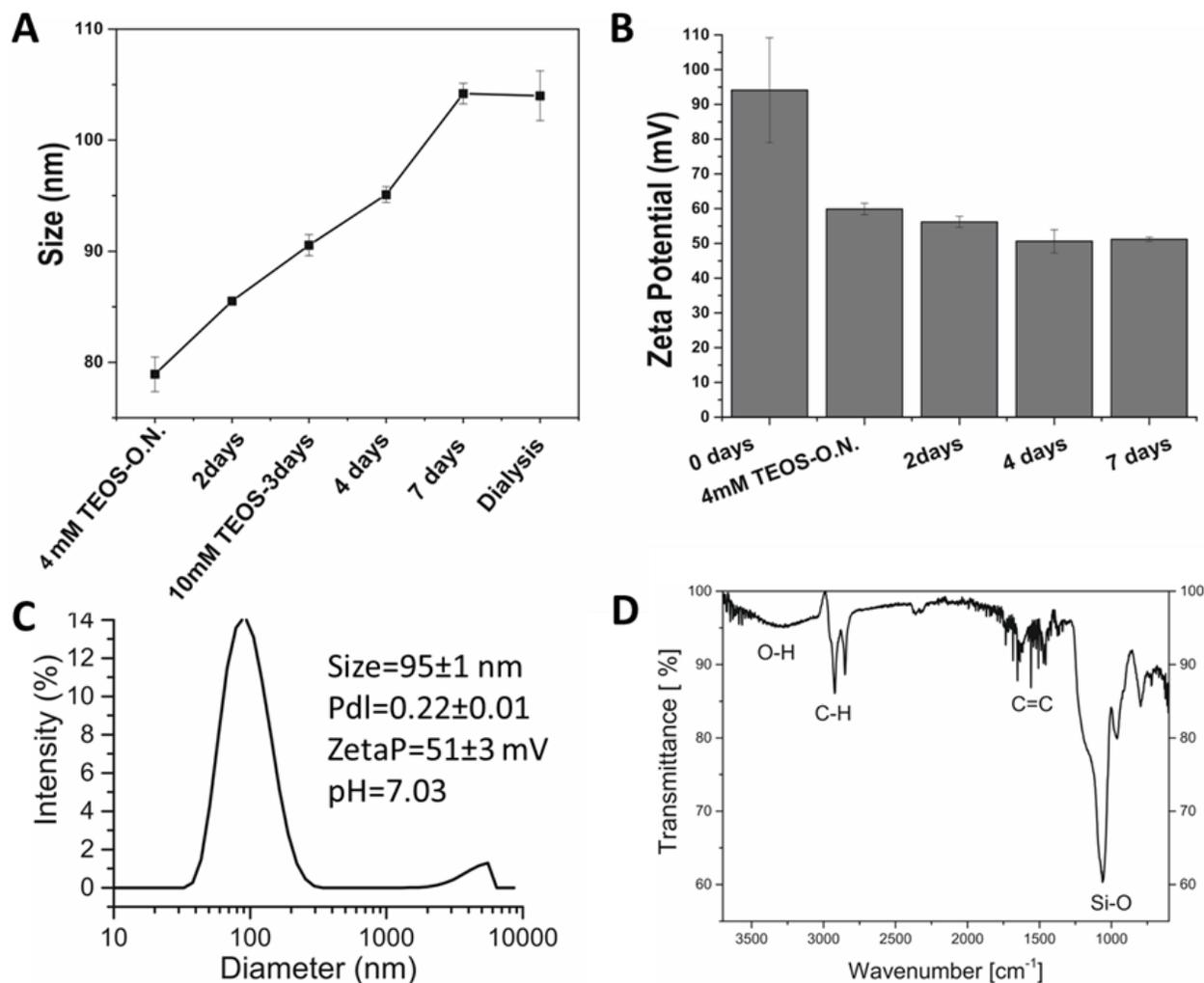
Figure 18. A) DLS-Size and **B)** Zeta Potential measurement of the reaction over time of TEOS silica-coated QS at 0 °C for 7 days. **C)** DLS-Size distribution measurement after 4 days of reaction the NB-QS-TEOS. **D)** IR spectra of silica-coated QS. The starting material has a size of 84±1 nm a Pdl of 0.23±0.01 and a Zeta Potential of 84±2 mV.

Non-Breakable silica-coated QS using TEOS and Dodecylsilane-QS (NBS-Dodecylsilane-QS)

A different strategy to favor a homogeneous shell could be to have the silica precursor already in place in the Quatsomes. Therefore, we decided to use a silica precursor that could be acting as a surfactant inserted in the QS membrane to then perform the reaction. Dodecyl(trimethoxy)silane (dodecyl-silane) was added to the membrane at 5% and 10% wt during the synthesis of QS (**Figure**

3.19A). Figure **3.19B** and **3.19C** show the size distribution of both systems; 10% and 5% dodecyl-silane QS prepared for the following coating of silica which show the following parameters, a size distribution of 62±1 nm, Pdl of 0.23±0.01 and Zeta Potential of 80±5 mV and a size distribution of 65±1 nm, Pdl of 0.25±0.01 and Zeta Potential of 83±3 mV, respectively.
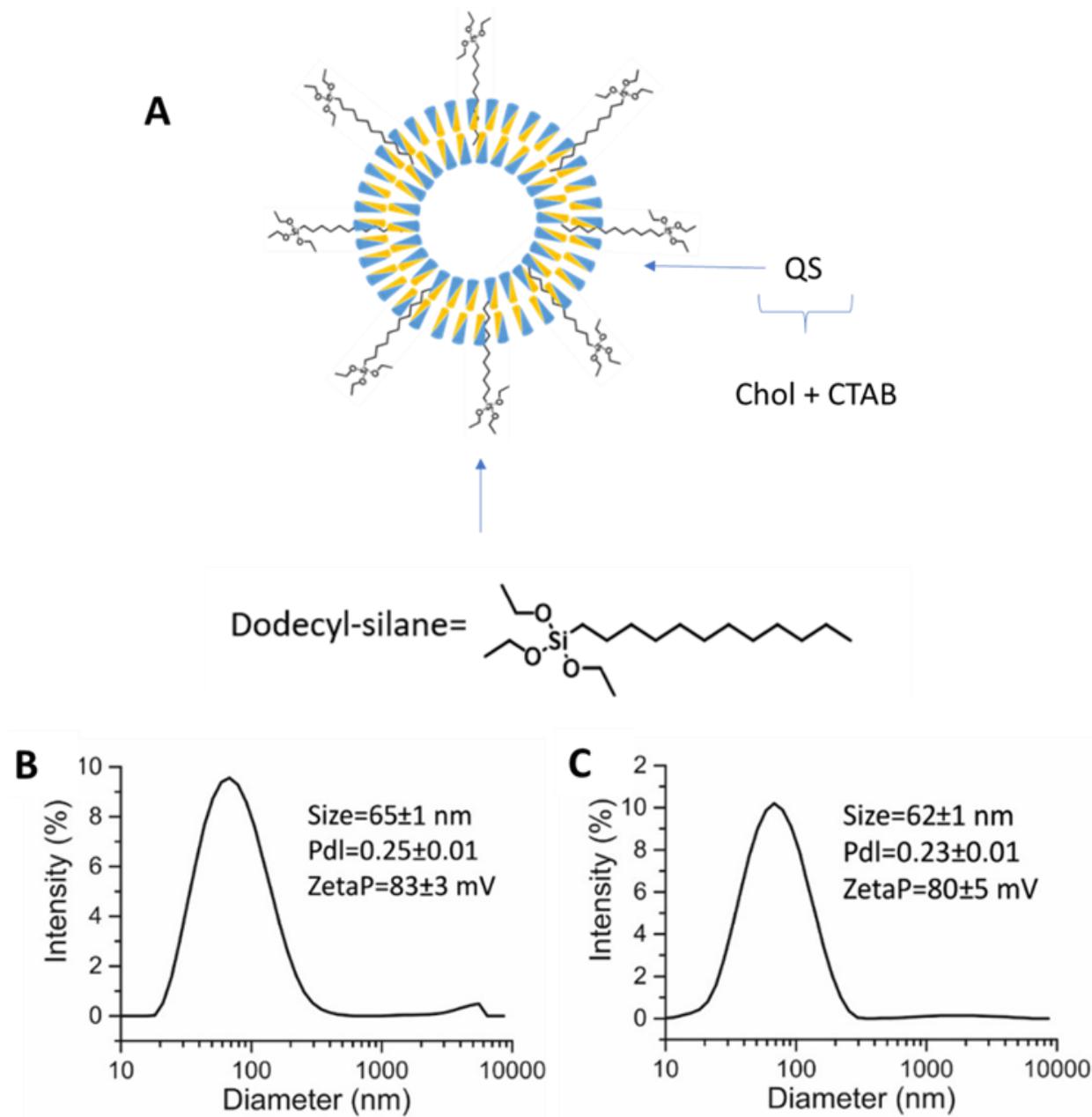

Figure 3.19. A) Representation of the Dodecyl-silane-QS and their DLS-Size distribution measurement of **B)** 5% **C)** 10% wt Dodecyl silica QS.

To continue with the silica deposition on the QS, from the two Dodecyl-silane-QS systems done, the one with 10% wt was selected to proceed with the synthesis with TEOS; this because it has the lowest Pdl value, which means it is a sample with more homogeneity in terms of size distribution. Moreover, more Dodecyl silane is inserted in the QS membrane easier should be the condensation. The reaction was run using TEOS as the silane precursor (**Figure 3.20**). The initial QS was measured by DLS and provide a size distribution of 62±1 nm with a Pdl of 0.23±0.01, and a Zeta Potential of 80±5 mV. After one day, the pH of the reaction was measured giving a value of 7.6 and a size distribution of 69±3 nm.
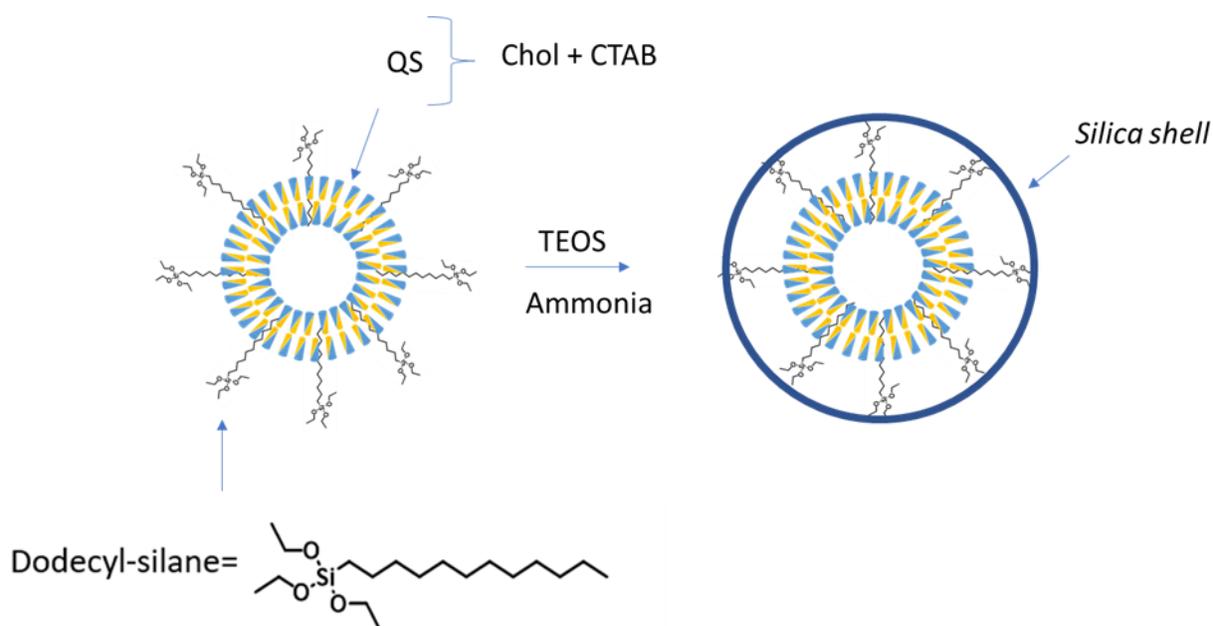
Figure 3.20. Representation of the Dodecyl-silane QS covered with a shell of silica form.

An 80 µL portion of ammonia with a concentration of 0.134 M was added to the solution to adjust the pH to basic conditions, giving a pH of 8.35. The following day the size reported by DLS was 76±2 nm with a Pdl of 0.18±0.01 and Zeta potential of 49±1 mV (see **Figure 3.21A**). Cryo-TEM images (**Figure 3.22**) displayed the interaction of the silica in the QS, despite the QS not being completely encapsulated. As a result, the reaction could run for additional time. After 5 days, the size distribution of the QS system reaction was 170±2 nm, Pdl of 0.2±0.01 and Zeta Potential of 32±1 mV; at this point some volume of the reaction was stopped and purified by dialysis, giving at the end the same size 170±2 nm, a Pdl of 0.19±0.01 and Zeta Potential of 34±2 mV. **Figure 3.23** shows SEM images collected from the material after 5 and 13 days of reaction. Some

nanoparticles around 50 nm could be observed in the 5-day sample, while that the agglomerations were more prevalent in the 14-day sample, but also this could be produced when the material is exposed to the vacuum at the time that is covered with gold and inside the SEM equipment. Further Cryo-TEM experiments have to be done in order to know if after the time the QS present a more homogeneous coverture of silica maintaining the QS as a separate identity (without agglomerations). IR spectrum of the sample was taken (**Figure 3.21B**), which reveals a band around 1175 cm^{-1} which is assigned to the presence of Si-O bonds.
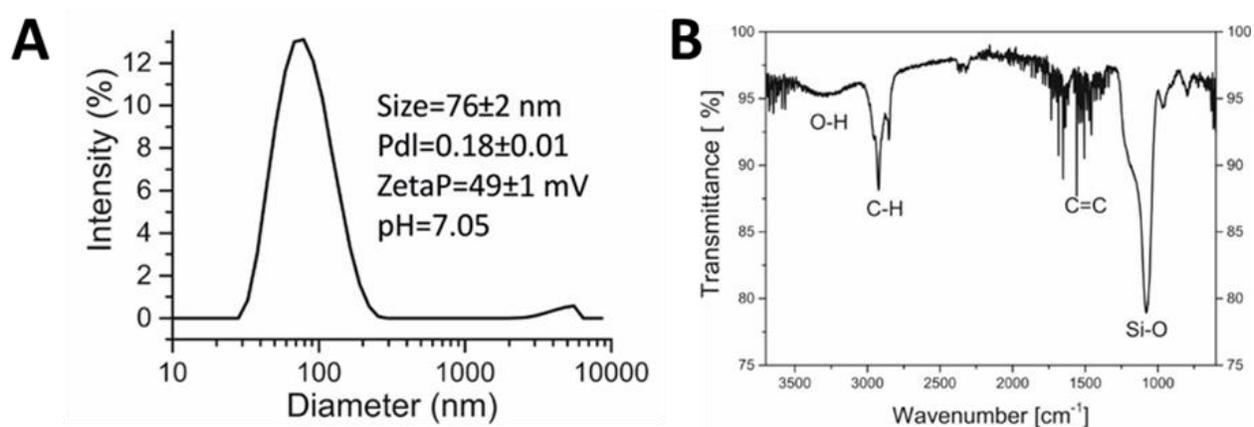

Figure 3.21. A) Size distribution of the 10% Dodecyl silane QS covered with TEOS after 2 days of reaction and **B)** IR spectra of silica dodecyl silane QS.
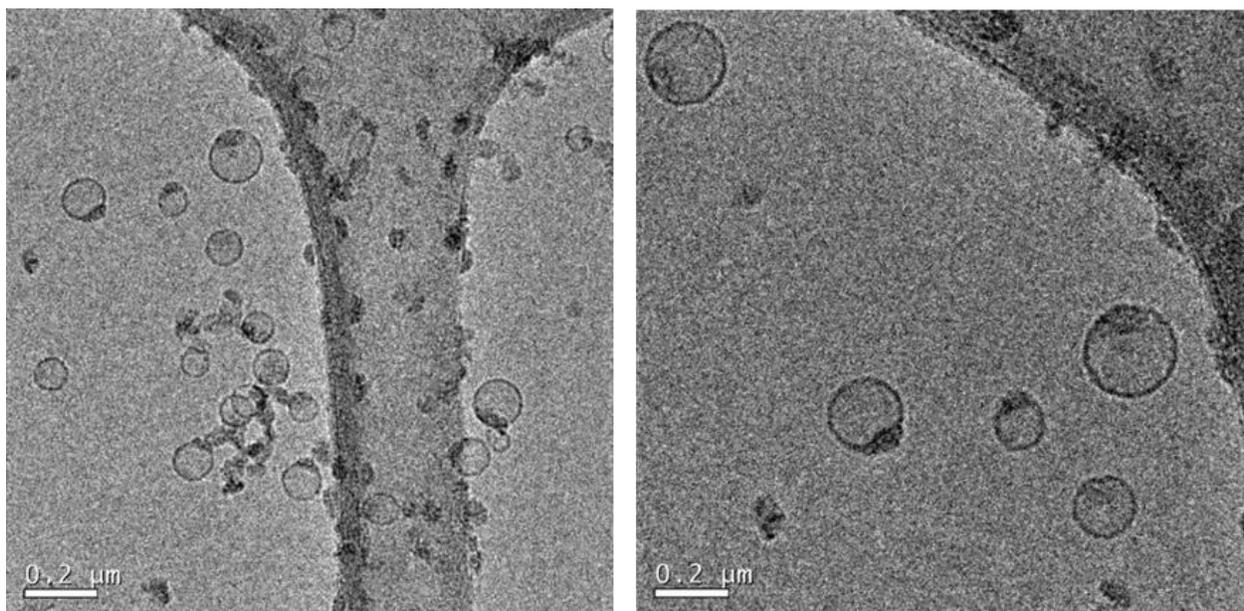
Figure 3.22. Cryo-TEM images of 10% silica-coated Dodecyl silane QS. Scale bar 0.2 μm.
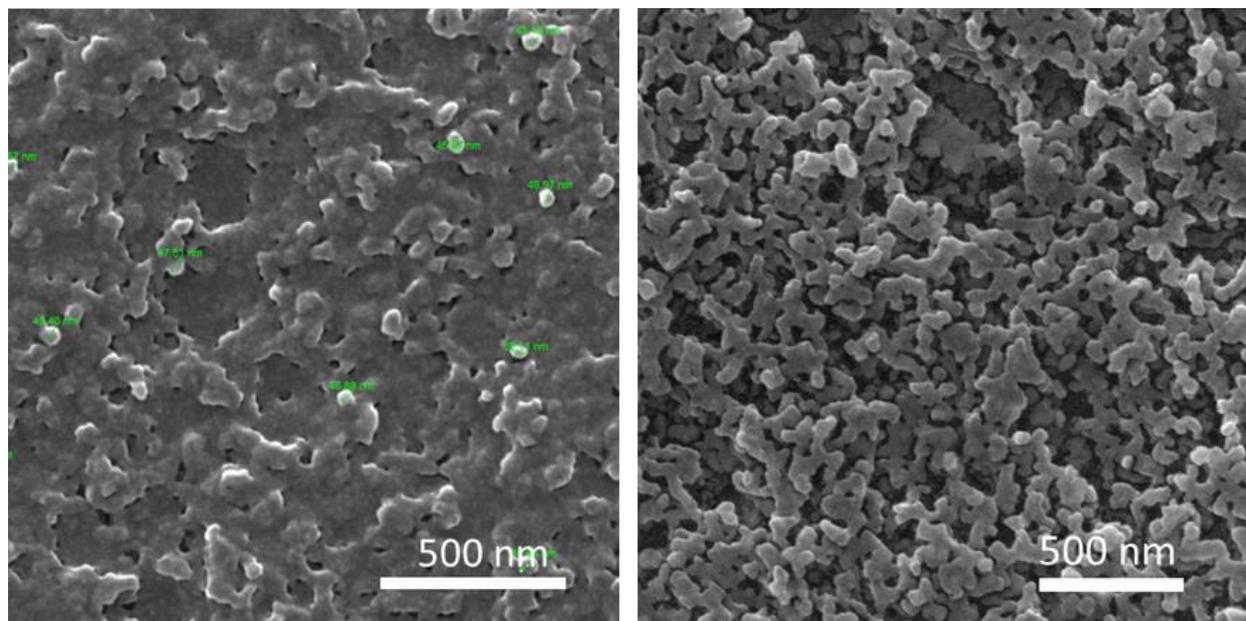
Figure 3.23. SEM images of 10% silica-coated Dodecyl silane QS after 5 days (reaction stopped by dialysis) and after 13 days (reaction still continue). Scale bar 500 nm.

The reaction was stopped after 5 days and it was analyzed by TEM, Cryo-STEM, Energy-dispersive X-ray spectroscopy (EDX) and X-ray photoelectron spectroscopy (XPS) to characterize the sample. After this time of reaction with TEOS, the sample shows a complete silica covered shell (see **Figure 3.24**). Also, with this technique it is appreciable that the silica around the QS has porosity which agrees with the last Cryo-TEM images taken after 2 days, where patches of silica where started to cover the QS with dodecyl silane moieties.

Figure 3.25A shows the Cryo-scanning transmission electron microscopy (Cryo-STEM) analysis from the 10% silica-coated Dodecyl silane QS after 5 days, where is shown again the porosity of the material; EDX in two different areas of the sample (1 and 2 in the **Figure 3.25A**) showed the presence of silicon (**Figure 3.25B**), probe of the formation of the silica shell around the QS.
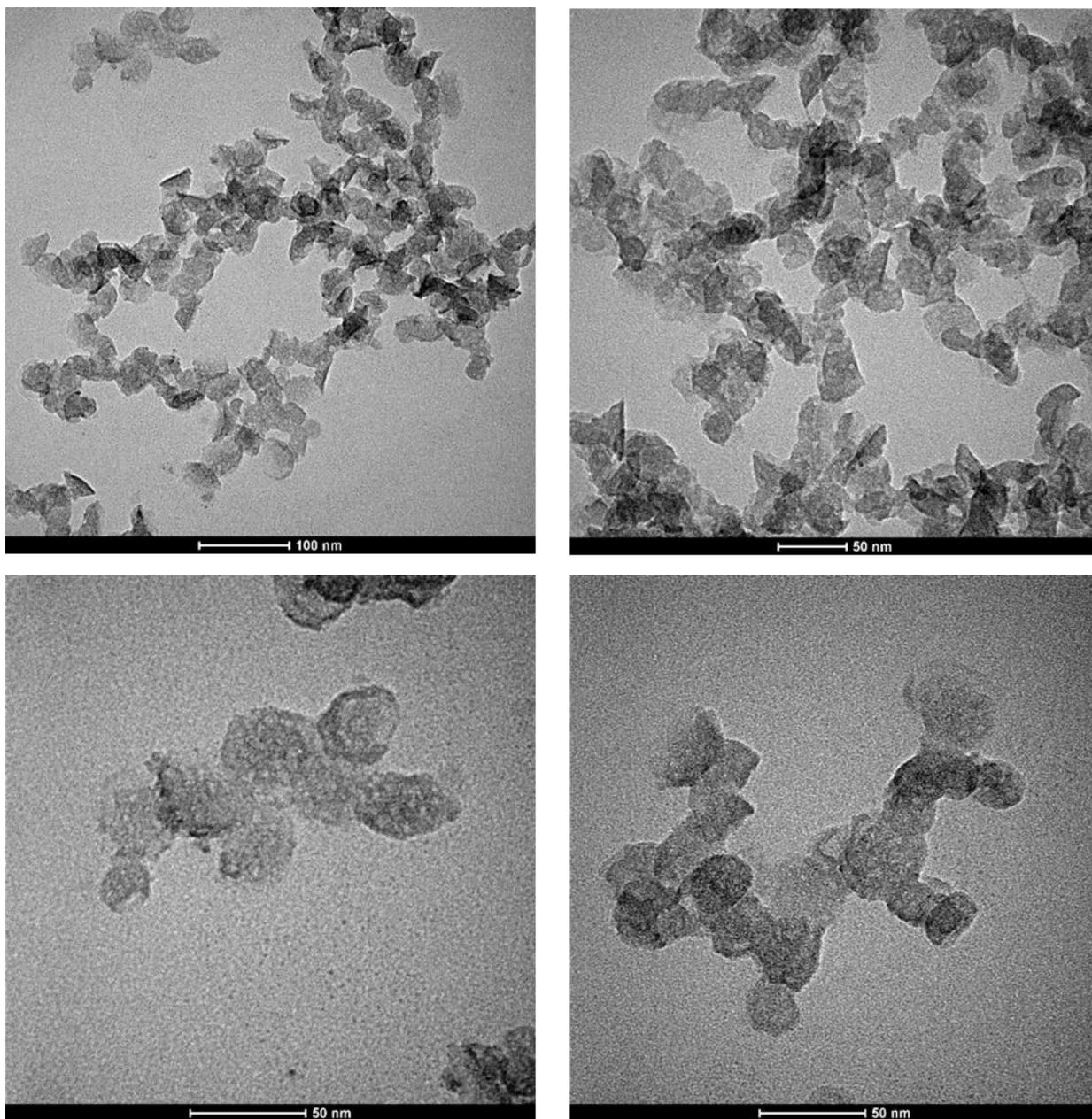
Figure 3.24. TEM images of 10% silica-coated Dodecyl silane QS after 5 days (reaction stopped by dialysis). Scale bar 100 and 50 nm.
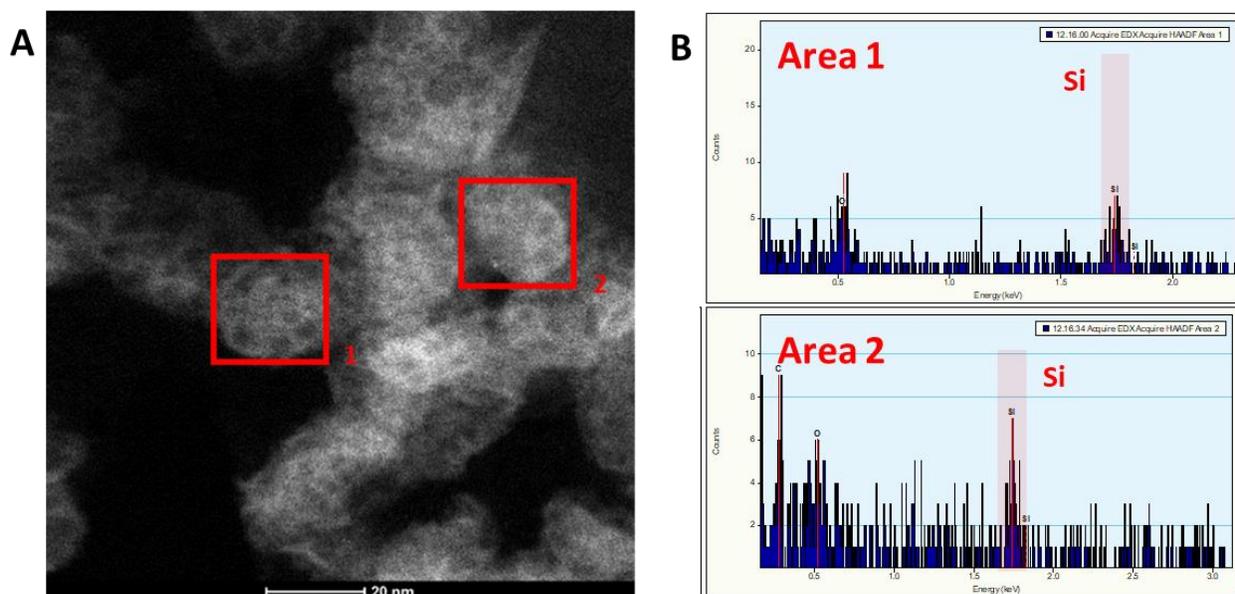
Figure 3.25. **A)** Cryo-STEM image of 10% silica-coated Dodecyl silane QS after 5 days (reaction stopped by dialysis). Scale bar 20 nm and **B)** EDX of the sample in two different areas (zone 1 and 2 of the Cryo-STEM image).

X-Ray Photoelectron Spectroscopy (XPS) spectra analysis was carried out to confirm the presence of silica in the material. **Figure 3.26A** shows the analysis of the surface of the sample of 10% silica-coated QS reacted for 5 days, where was visible the presence of carbon, oxygen and silicon. In **Figure 3.26B** is represented the deconvolution of the C1s core level showing the presence of C-C, C-O, C=O bonds, belonging to the components of the QS (CTAB, Cholesterol and Dodecyl Silane). **Figure 3.26C** shows the XPS of the silicon analysis, where its deconvolution of the Si2p core level showing the presence of Si-C and Si-O bonds, belonging to the dodecyl silane moieties and for the formation of the silica shell around the QS.
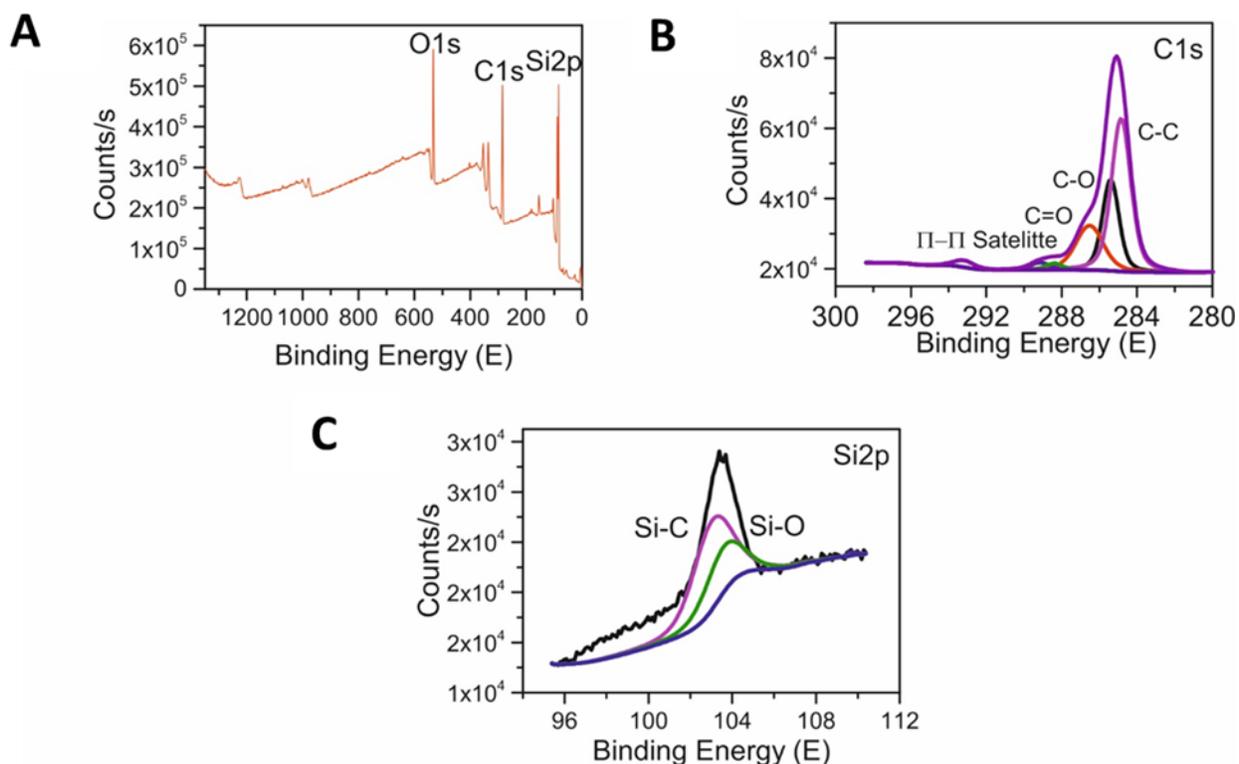
Figure 3.26. A) Representative X-Ray Photoelectron Spectroscopy (XPS) spectra analysis of the surfaces of 10% silica-coated Dodecyl silane QS after 5 days, **B)** Carbon analysis, deconvolution of the C_{1s} core level spectra and **C)** Silicon analysis, deconvolution of the Si2p core level.

In contrast, the curiosity to explore the system, make us analyze the sample in which the reaction was never stopped by dialysis (after several months). 10% silica-coated Dodecyl silane QS without post-treatment was analyzed with TEM. In **Figure3.27** is visible the QS covered by silica; it could be seen the same porous structure as observable using this TEOS silane in previous experiments. This porosity could be attributed either to the fact that the silane was all consumed and not all the areas are covered; giving then these porous areas or due that the silica arranges in a way that brings these porosity structures of polymerization. From the **Figure 3.27** images, where the silica shell was starting to form around the QS (Cryo-TEM). We observe that the porosity was already existing even when more silane was presented in the solution. Even though, not much more silane was put to see if a complete silica shell without porous was formed; so further investigations must be done to explain the pattern.
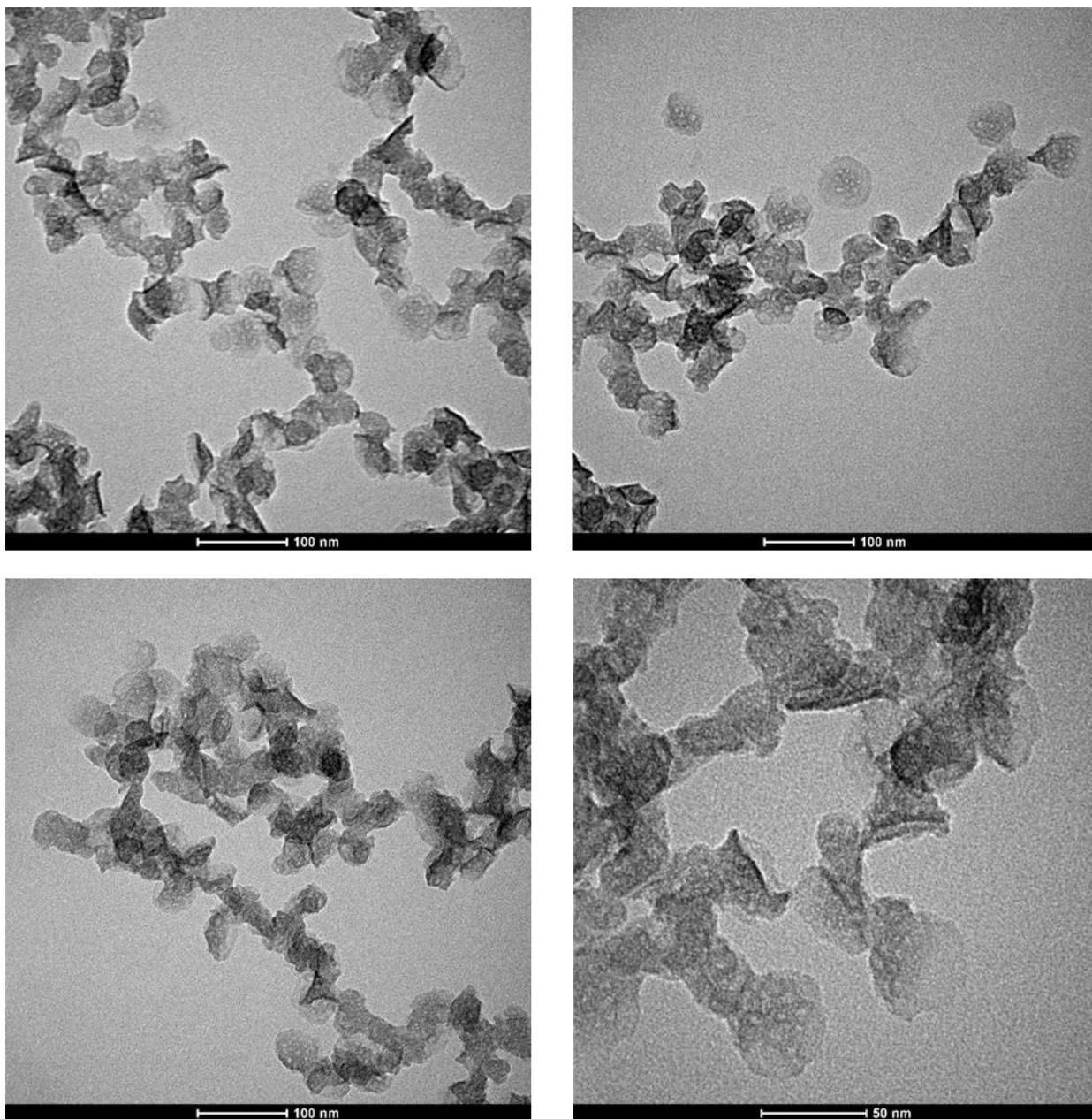
Figure 3.27. TEM images of 10% silica-coated Dodecyl silane QS with not pos-treatment to the reaction. Scale bar 100 and 50 nm.

3.2.2.3. Synthesis and characterization of the Non-Breakable silica-coated QS (NB-SQS) using TEMOS

The pH of the reaction after 2 days was 7.55 with a size distribution of 98±2 nm, Pdl of 0.16±0.01 and Zeta Potential of 42±1 mV. After these 2 days, 3 mL of the reaction were extracted and the rest of the reaction (4.5 mL) was added to 3.3 µL of 4.4 mM TEMOS. After 2h, the size distribution

of the reaction was 108±8 nm with a PdI of 0.18±0.02. Stirring overnight the solution caused precipitation of the NPs. Because of that, we continue analyzing the 3 mL of the sample that was stored before the second TEMOS addition (4.4 mM). The reaction after 4 days gives a size distribution of 105±3 nm, a Pdl of 0.2±0.01 and Zeta Potential of 37±1mV (**Figure 3.28C**). In this point, Cryo-TEM images of the sample were taken (**Figure 3.29**). The QS showed a thin layer around them, these contrasting areas were attributed to the polymerization of the silica around the QS. To corroborate this statement, IR of the sample was performed, and **Figure 3.28D** showed the Si-O band of the silica at 1175 cm^{-1}. After 7 days, the reaction was stopped using dialysis, DLS analysis showed a silica-coated QS increase of size to 116±3 nm, a Pdl of 0.23±0.01 and Zeta Potential of 36±3 mV. **Figure 3.28A** and **3.28B** show the size increase of the material and the decrease of the Zeta Potential over time.
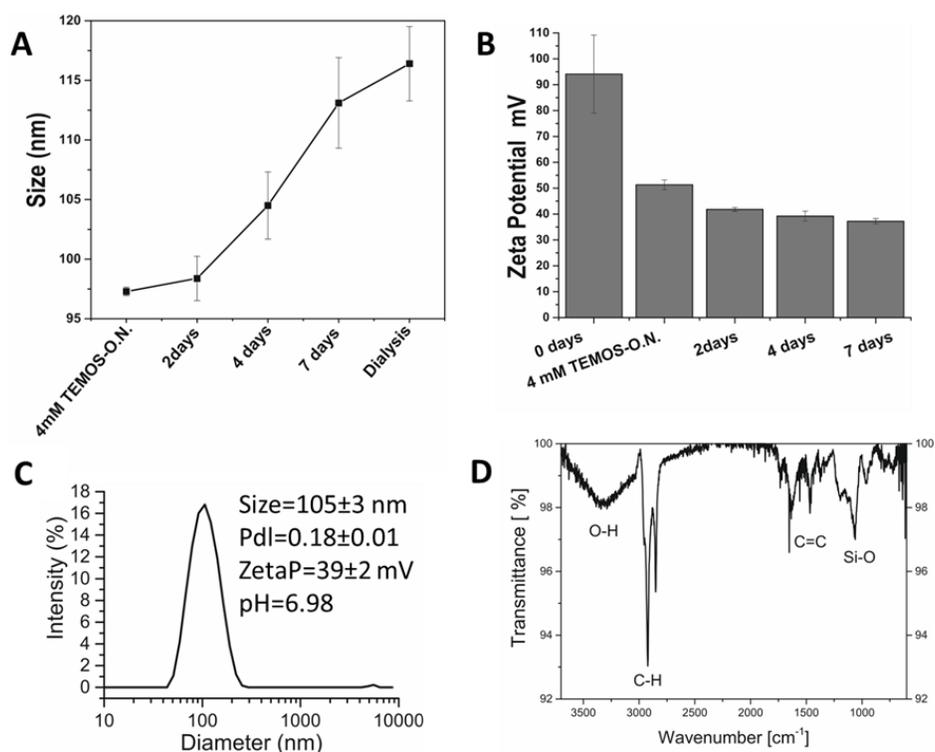
Figure 3.28. A) DLS size distribution measurement of the samples and **B)** Zeta Potential measurement of the reaction over time of TEMOS silica-coated QS at 0 °C for 7 days. **C)** DLS-Size distribution measurement after 4 days of reaction the NB-QS-TEOS. **D)** IR spectra of silica-coated QS. The starting material has a size of 84±1 nm a Pdl of 0.23±0.01 and a Zeta Potential of 84±2 mV.
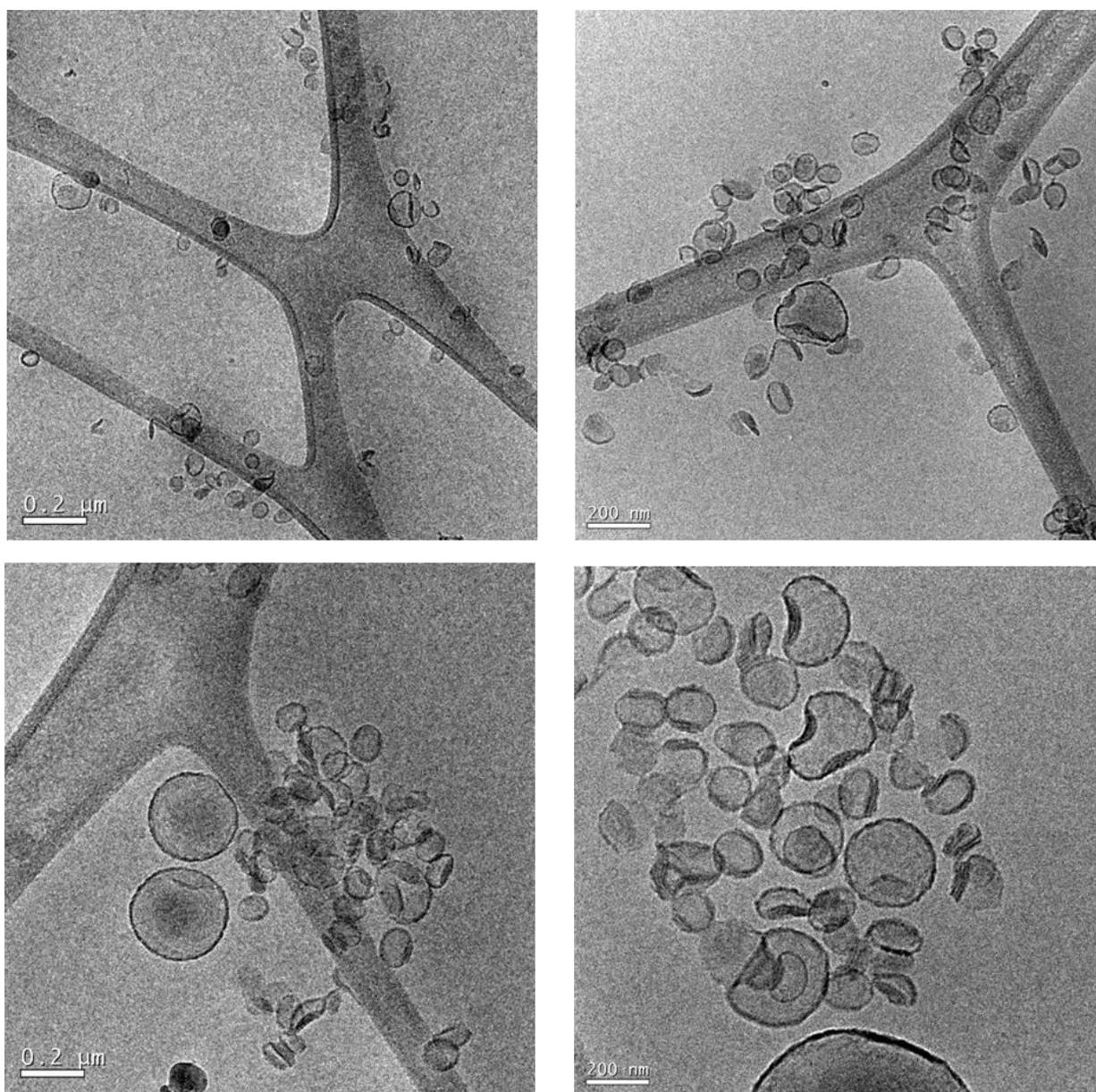
Figure 3.29. Cryo-TEM images of the 4.4 mM TEMOS silica-coated QS after 4 days of reaction. Scale bars, 200 nm.

3.2.3. Synthesis and characterization of the Breakable silica-coated QS (B-SQS)

In order to make stimulus-response silica-coated QS, we explored the possibility to make a redox response silica shell containing disulfide (S–S) bridges in the framework, where cleavage of the S-S bond in the presence of reducing agent leads to particle degradation and cargo release (**Scheme 3.2**).[25] This breakable property brings a faster exocytosis of the silica that enhances its potentiality for *in vivo* theragnostic applications.

224

Three different methodologies to make these breakable silica QS were explored by using APTES, TEOS and TEMOS as silanes in a combination with the disulfide linker (redox response) BTSPD.
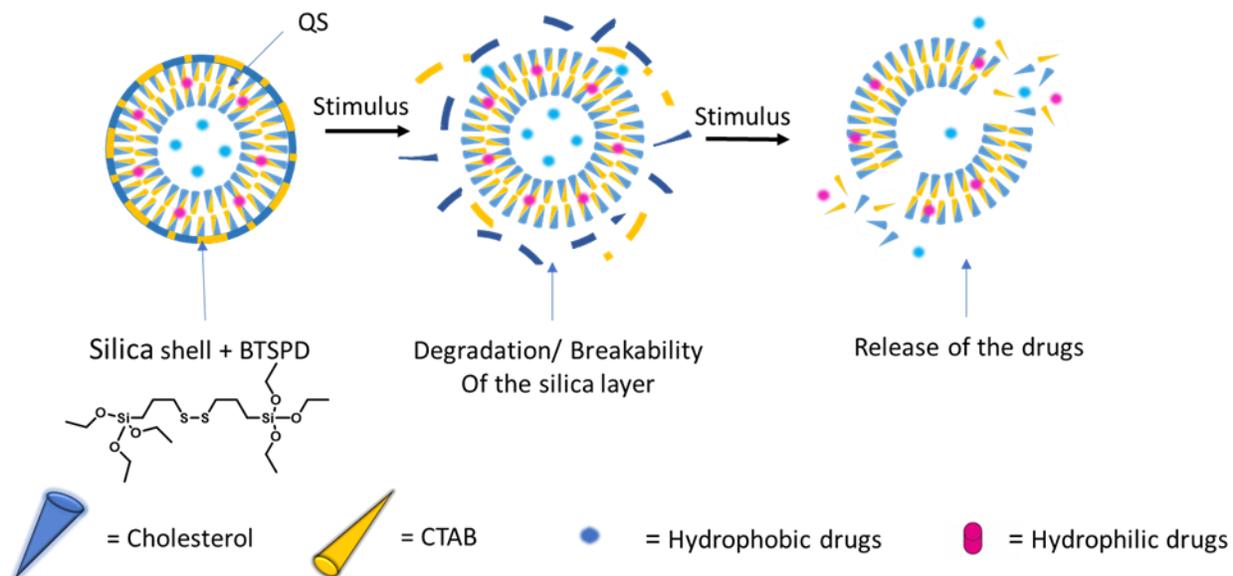
Scheme 3.2. Breakable silica-coated QS as a stimulus response vehicle for drug release.

3.2.3.1. Synthesis and characterization of the Breakable silica-coated QS (BS-QS) using APTES and BTSPD.

Breakable silica shells were prepared from a mixture of APTES and BTSPD. **Figure 3.30** shows the DLS measurements of the silica (SQS) after the addition of silanes. Which grown from 114±26 nm (starting size of the QS) to 168±42 nm and showed a second population at 468±110 nm probably due to the formation of agglomerations. After 1 h, two size distributions were showed at 87±19 nm and 273±73 nm; after this time seemed that the reaction was over as after overnight the size distributions were maintained around the values after 1h. After 1h, the size distributions were 68±12 nm and 208±50nm.

SEM pictures of the sample left stirring overnight are shown in the **Figure 3.31**. SEM size distribution, count performed on 300 nanoparticles, gave an average diameter of 143±19 nm BS-QS particles (**Figure 3.31** down-right).
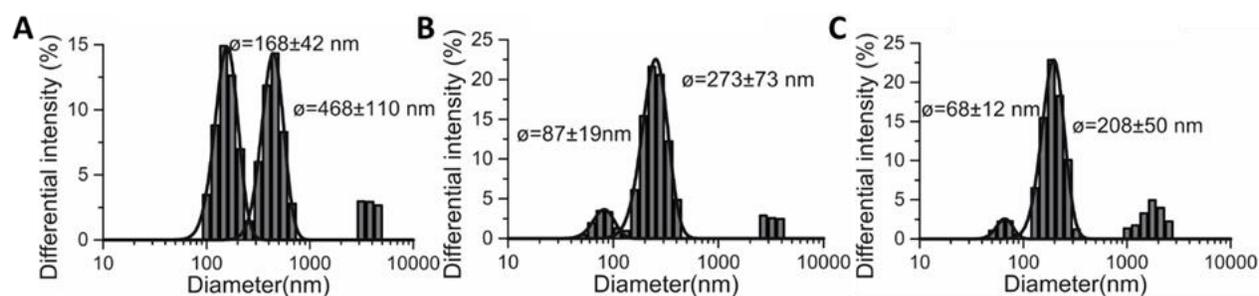
Figure 3.30. DLS experiments of the silica covered Quatsomes (SQS) **A)** after the addition of silanes, **B)** 1 h, **C)** overnight.
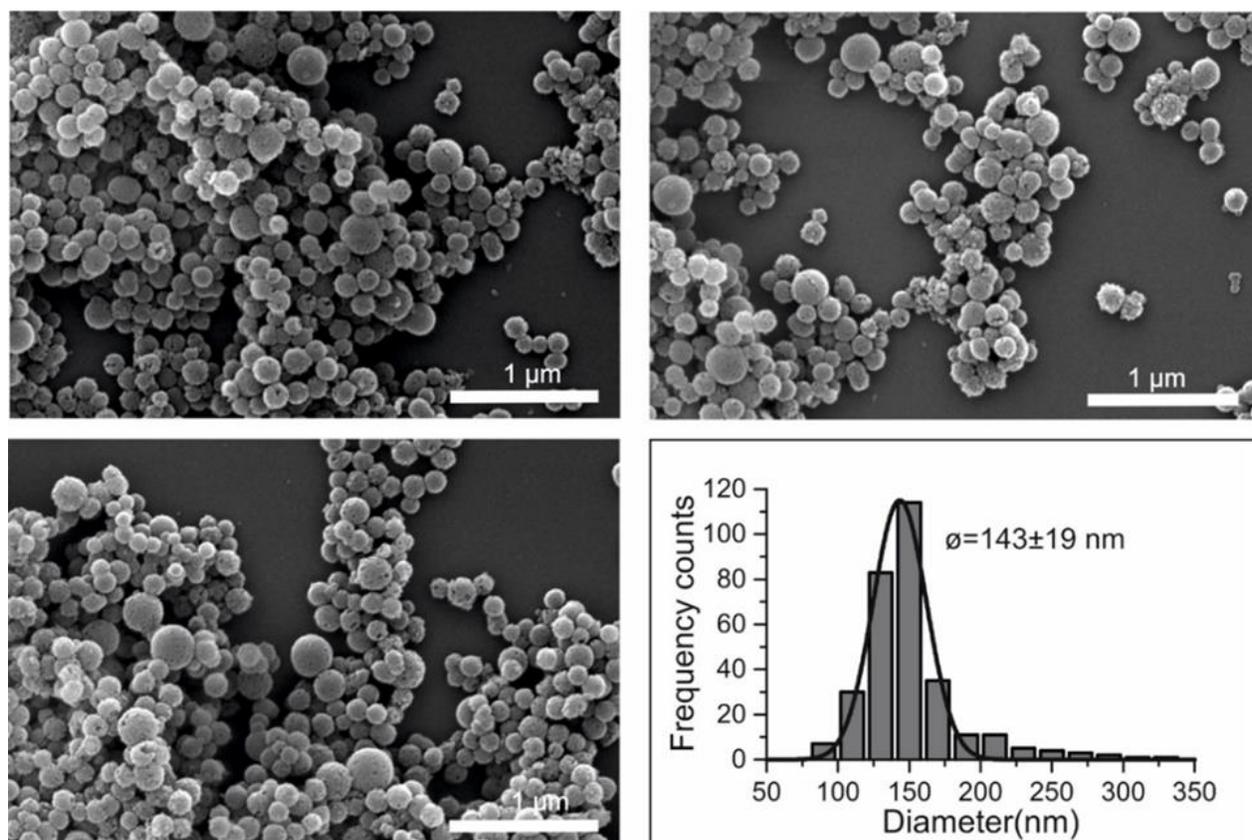
Figure 3.31. SEM pictures of the Breakable Silica covered Quatsomes (B-SQS) after overnight of stirring (scale bar 1 μm). Down right: SEM size distribution (count performed on 300 nanoparticles; average diameter 143±19nm).

Smaller QS (size distribution of 58±1, PdI of 0.23±0.01 and Zeta Potential of 83.5±2.1 mV) were covered using the same methodology. TEM images were taken to characterize the system (**Figure 3.32**) which shows the presence of silica as a shell around the QS. An average diameter of 32±6

nm was obtained by counting 200 nanoparticles, while a shell thickness of 9±2 nm was extracted (**Figure 3.33A** and **3.33B**).
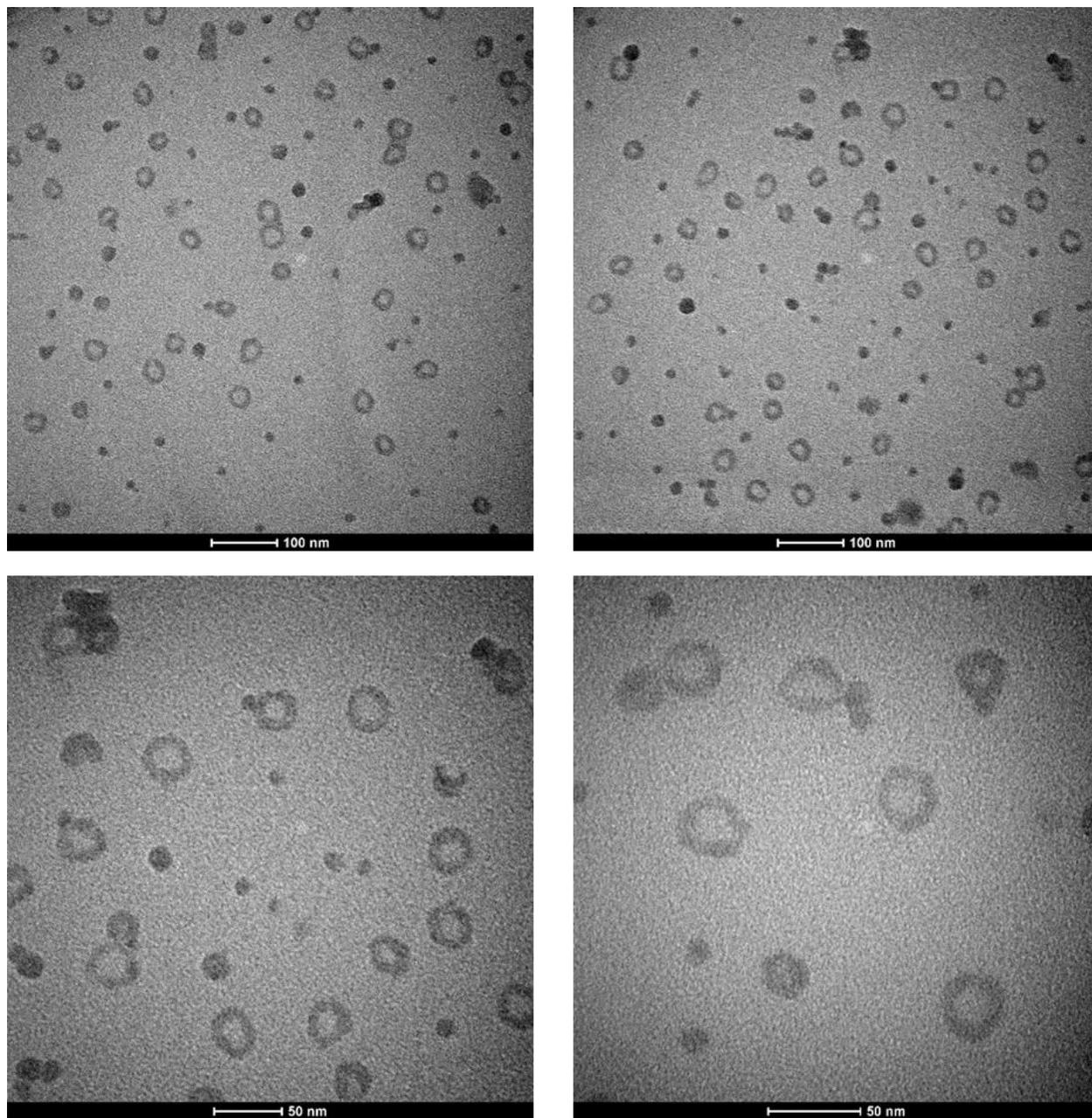
Figure 3.32. TEM images of breakable silica-coated QS (APTES+BTSPD). Scale bar 100 and 50 nm.
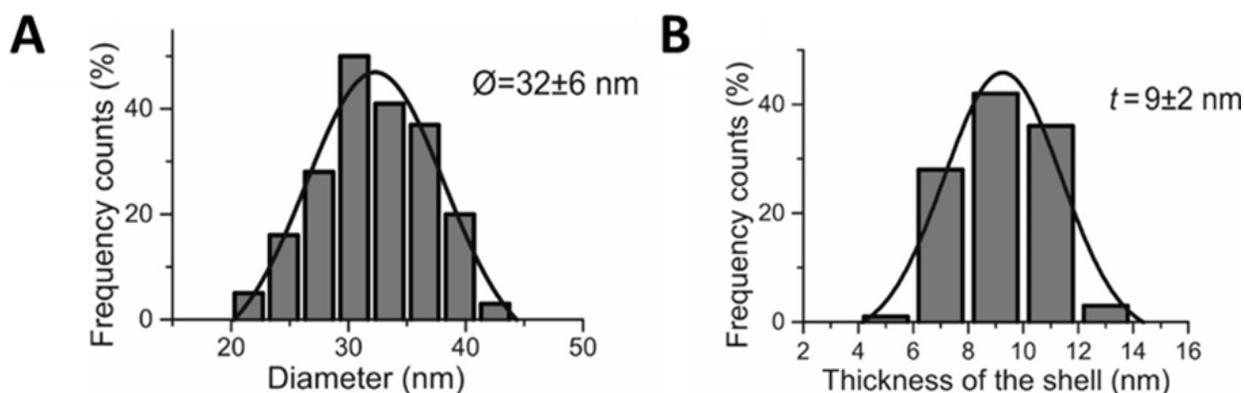
Figure 3.33. **A)** TEM size diameter distribution (count performed 200 silica-QS particles; average diameter 32±6 nm) and **B)** TEM size Thickness of the shell distribution (count performed in 100 silica-QS particles; average thickness of the shell 9±2nm).

X-Ray Photoelectron Spectroscopy (XPS) spectra analysis was measured to the sample to confirm the presence of silica and sulfur in the material. **Figure 3.34A** shows the analysis of the surface of the sample, where is visible the presence of carbon, oxygen, silicon, and sulfur. **Figure 3.34B** shows the XPS of the silicon analysis, and in **Figure 3.34C** is represented the deconvolution of the S2p core level showing the characteristic.
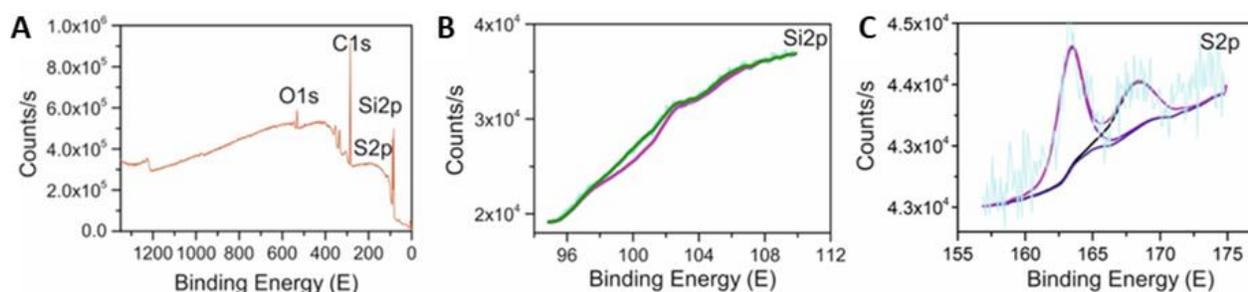
Figure 3.34. **A)** Representative X-Ray Photoelectron Spectroscopy (XPS) spectra analysis of the surfaces of B-SQS **B)** Silicon analysis, deconvolution of the Si2p core level spectra and **C)** Sulfur analysis, deconvolution of the S2p core level.

Cryo-STEM images were taken to see the three-dimensionality of the material (**Figure 3.35**). From these images, we could see the cavity that corresponded to the QS and the whiter areas which belong to the silica-shell around this material. In **Figure 3.36A** is the characterization using SEM, and in **Figure 3.36B** is represented the EDX analysis from the area represented (red box), where

is clear that the sample was constituted by atoms of silicon which came from the silica structure of the shell around the QS. Further experiments were planned to be done as breakable silica-coated QS with a fluorescent dye, and QS labeled with a dye and coated with silica to have more information about this silica coating, as how long it took to break in presence of the reducing agent. In the **Figure 3.37** is shown the IR of the sample, the revels a band around 1175 cm^{-1} which was assigned to the presence of Si-O bonds.
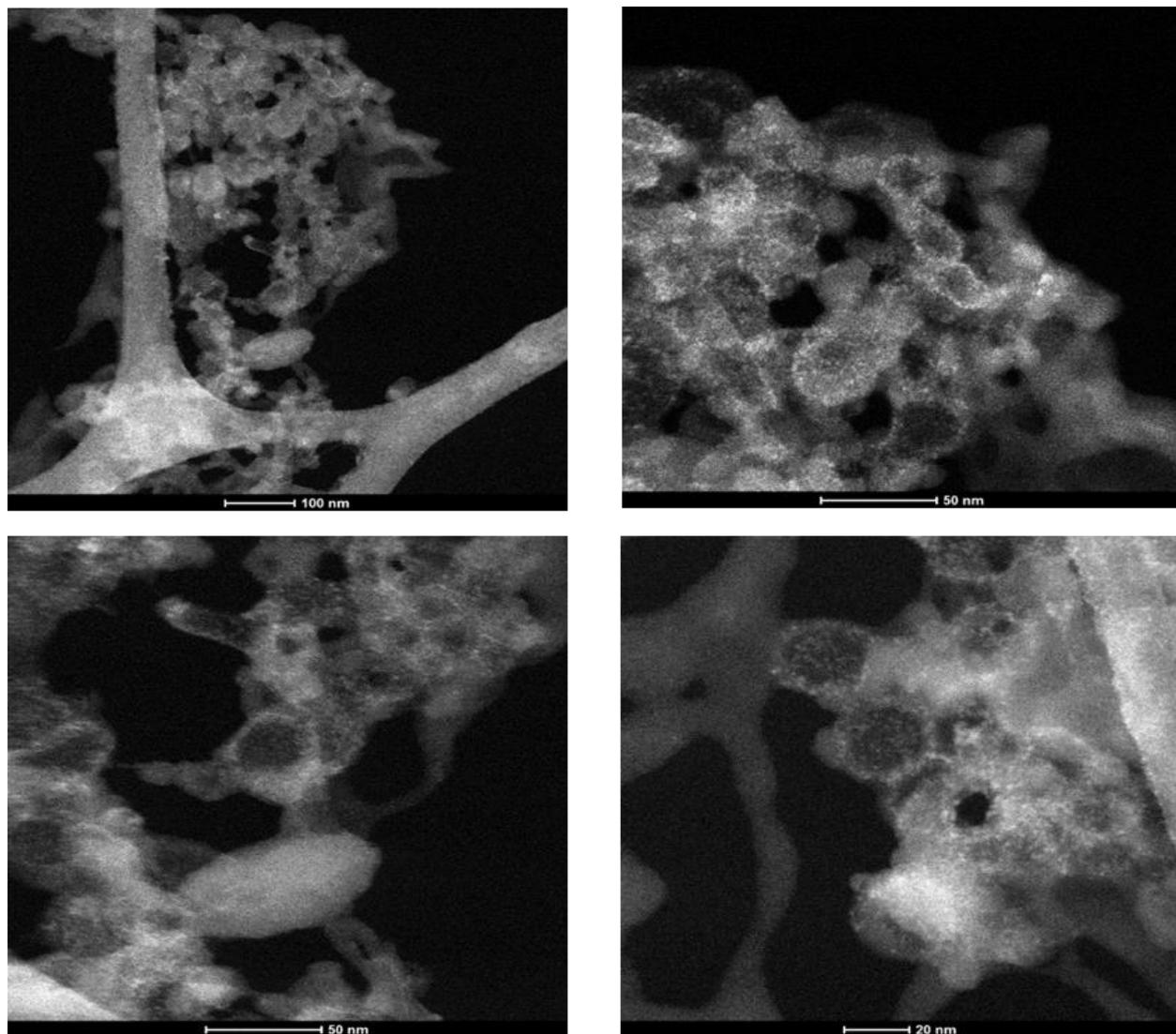
Figure 3.35. Cryo-STEM image of breakable silica-coated QS (APTES+BTSPD). Scale bar 100, 50 and 20 nm.
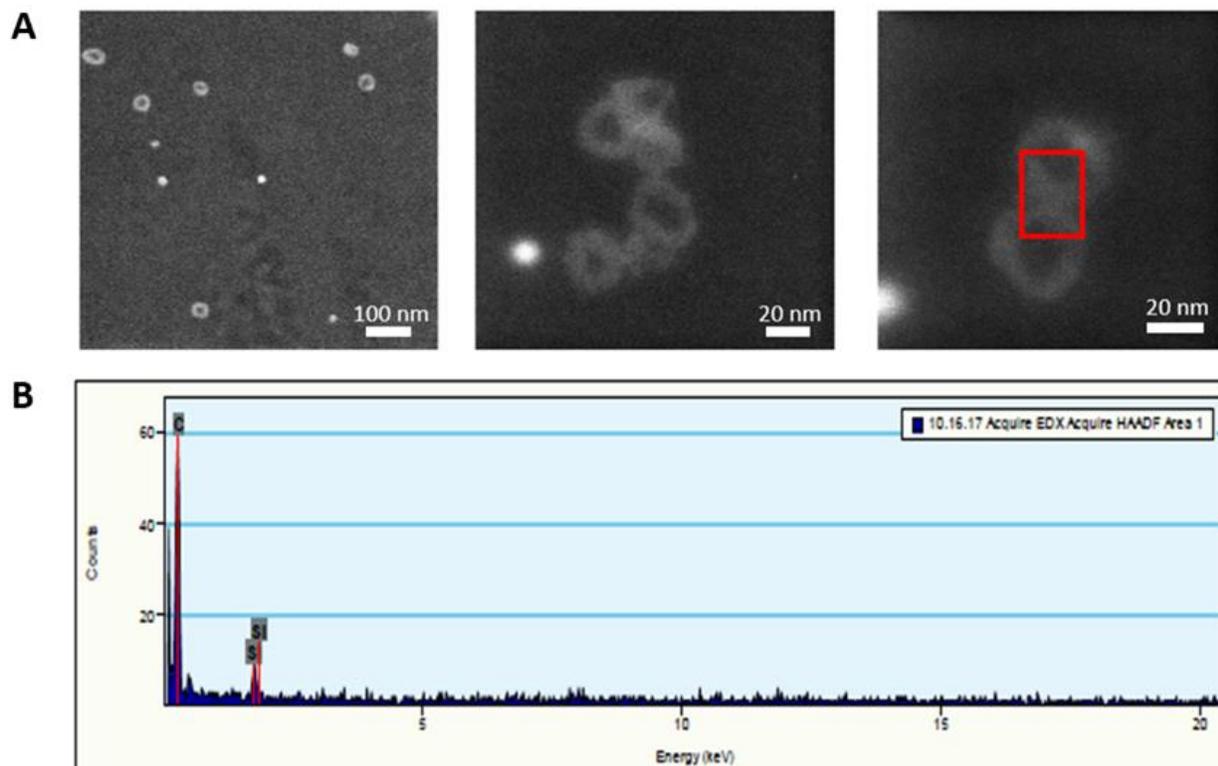
Figure 3.36. A) SEM image of breakable silica-coated QS. Scale bar 100, and 20 nm and **B)** EDX of the B-SQS sample.
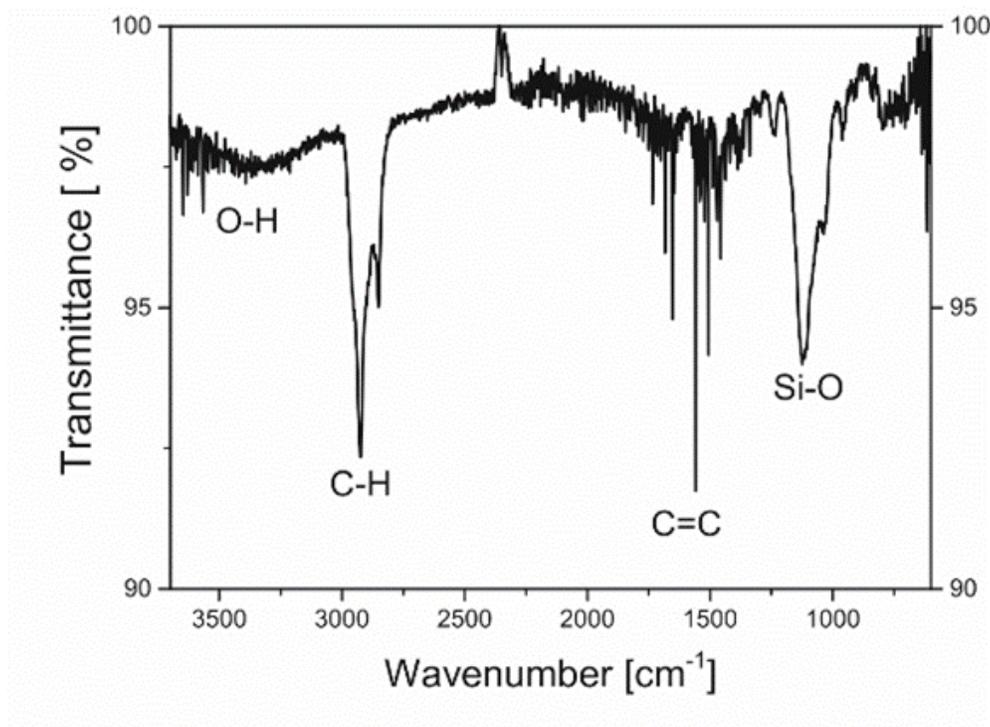
Figure 3.37. IR spectra of the B-SQS.

3.2.3.2. Synthesis and characterization of the Breakable silica-coated QS (BS-QS) using TEOS and BTSPD

A procedure by Zhang *et al*. was used to prepare BS-QS. [29] At time 0, the starting solution of QS diameter size was 84±1 nm, a Pdl of 0.23±0.01 and a Zeta Potential of 84±2 mV. After 2 days, the pH of the reaction was 7.7, the size distribution of the material increased to 87±1 nm, Pdl of 0.33±0.02 and Zeta Potential of 61±1 mV (**Figure 3.38C**). After these 2 days, 3 mL of the reaction were extracted and the rest of the reaction (4.5 mL) was added 3.5 µL of TEOS and 1.5 µL BTSPD previously mixed. 2 hours later, the reaction solution started to present some precipitate, so the reaction was stopped by dialysis; the material showed a size distribution of 102±3 nm and a Pdl of 0.5±0.03. To remove the precipitate, the sample was centrifugated for 15 mins at 6000 rpm, the supernatant phase had QS with a size of 76±2 nm, Pdl of 0.19±0.01 and Zeta Potential of 45±2 mV and the bottom phase a size of 177±3 and a Pdl of 0.77±0.02. At these conditions of centrifugation, we can say that probably the QS that are not covered by silica stayed in the supernatant and the QS with silica went to the bottom. The big change of size distribution from the sample before and after centrifugation probably was due that the silica-coated QS that precipitate formed agglomerations. Because of these results, the sample that was stored before the second addition was following under time (**Figure 3.38A** and **3.38B**). The Cryo-TEM images of the sample were taken (**Figure 3.39**), but again the material showed just a few zones of silica polymerization; more silica precursor was needed in order to make a homogenous silica-coated QS. IR experiment was done (**figure 3.38D**), which shows the Si-O band of the silica at 1175 cm^{-1}.
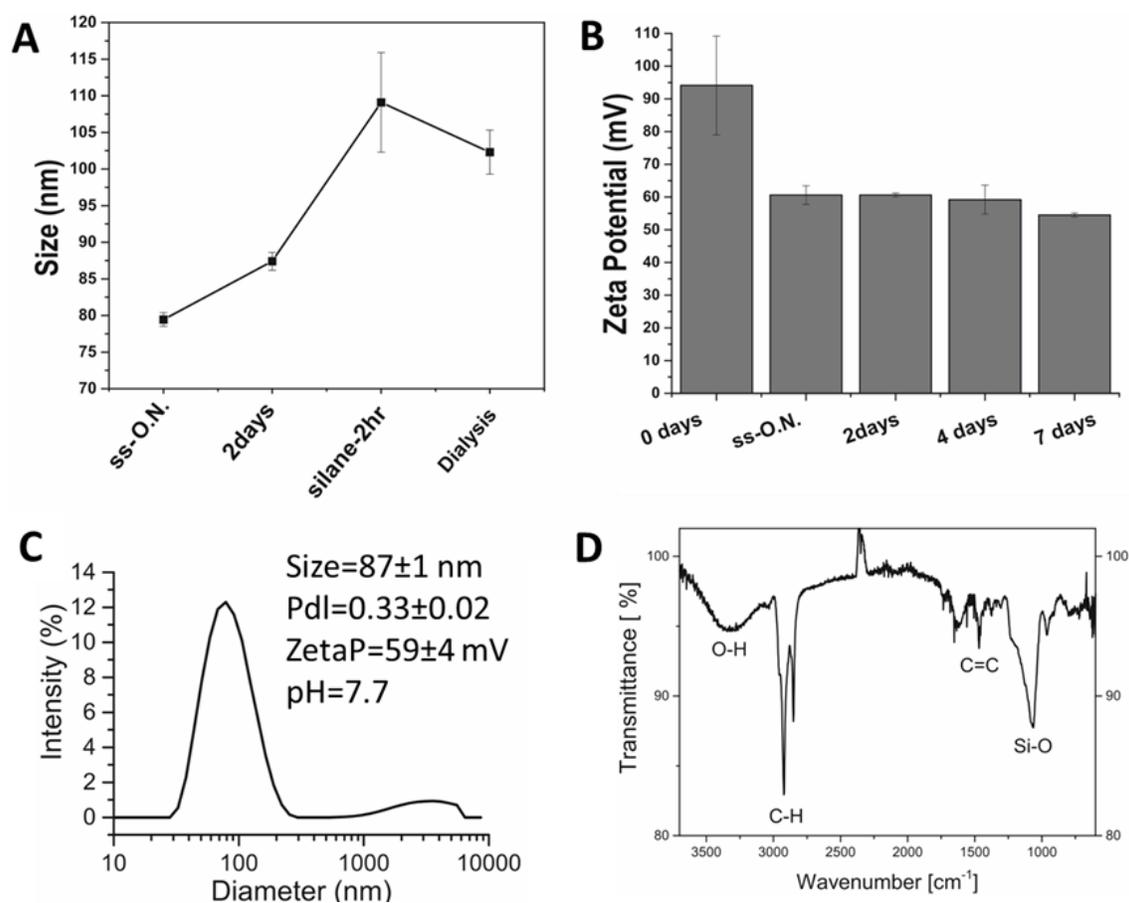
Figure 3.38. A) DLS-Size and **B)** Zeta Potential measurement of the reaction over time of for the breakable silica-coated QS at 0 °C for 2 days. **C)** DLS-Size distribution measurement after 2 days of reaction. **D)** IR spectra of silica-coated QS. The starting material has a size of 84±1 nm a PdI of 0.23±0.01 and a Zeta Potential of 84±2 mV.
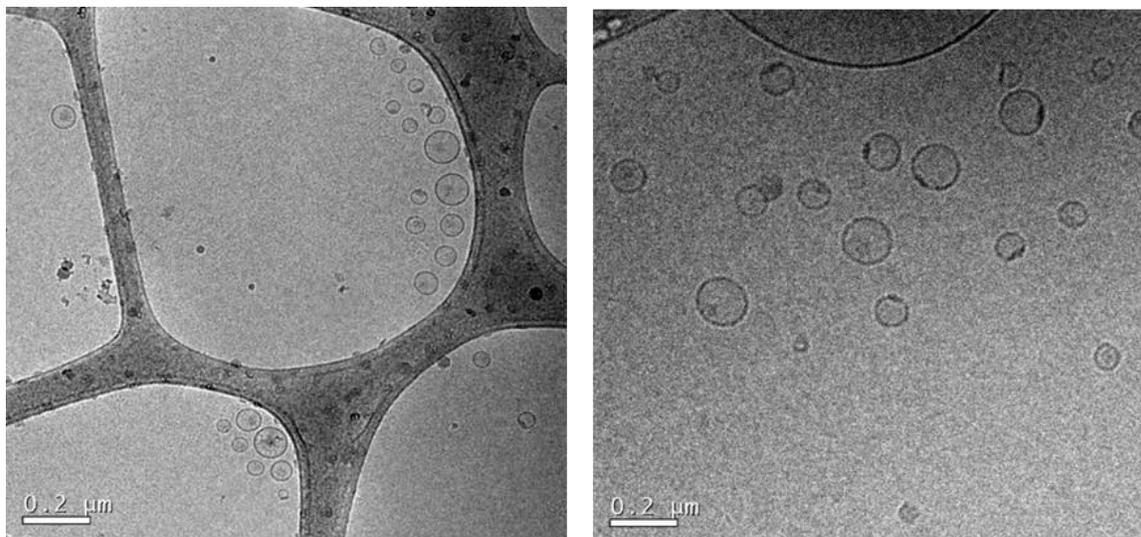
Figure 3.39. Cryo-TEM images of the responsible redox (BTSPD) silica-coated QS after 4 days of reaction. Scale bar 0.2 µm.

3.2.3.3. Synthesis and characterization of the Breakable silica-coated QS (BS-QS) using TEMOS and BTSPD

Figure 3.40A shows the DLS-size measurement with a size distribution of 95±21 nm. IR of the sample (**Figure 3.40 B**) revealed a band around 1175 cm^{-1} which was assigned to the presence of Si-O bonds. **Figure 3.41** shows TEM images of the QS cover with breakable silica using the methodology previously described. It was observable a rim of silica. The thickness of the coating from the pictures was around 10 nm (counting 12 silica-coated QS).
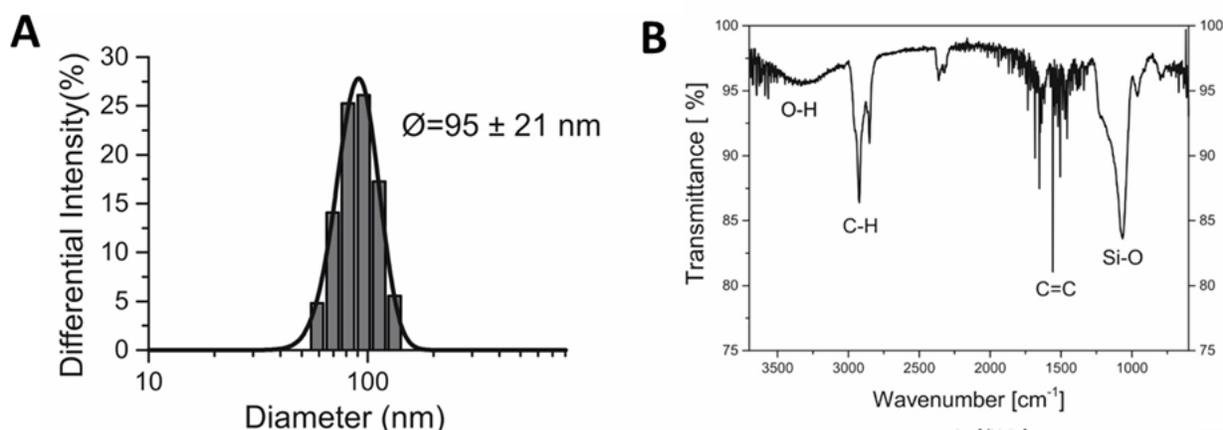
Figure 3.40. A) DLS measurement and **B)** IR spectra of the B-SQS.

On the other hand, TGA analysis of the QS and the breakable silica QS were performed. Between 200-270 °C, CTAB was decomposed (decomposition temperature >235 °C) while the cholesterol decomposed between 270-350 °C. The mass loss of each compound was around 50% which corroborates with the fact that the composition of the QS is 1:1 Chol:CTAB (**Figure 3.42A**). Analyzing the TGA of the breakable silica QS, the total mass loss of the sample was 70%. From this total mass lost, 42% was from the CTAB, and 58% was from the cholesterol and the disulfide linker. From this data then was calculated the % of disulfide linker as it is known the relation QS:CTAB was 1:1 giving then a value of 16% of mass lost (**Figure 3.42B**).
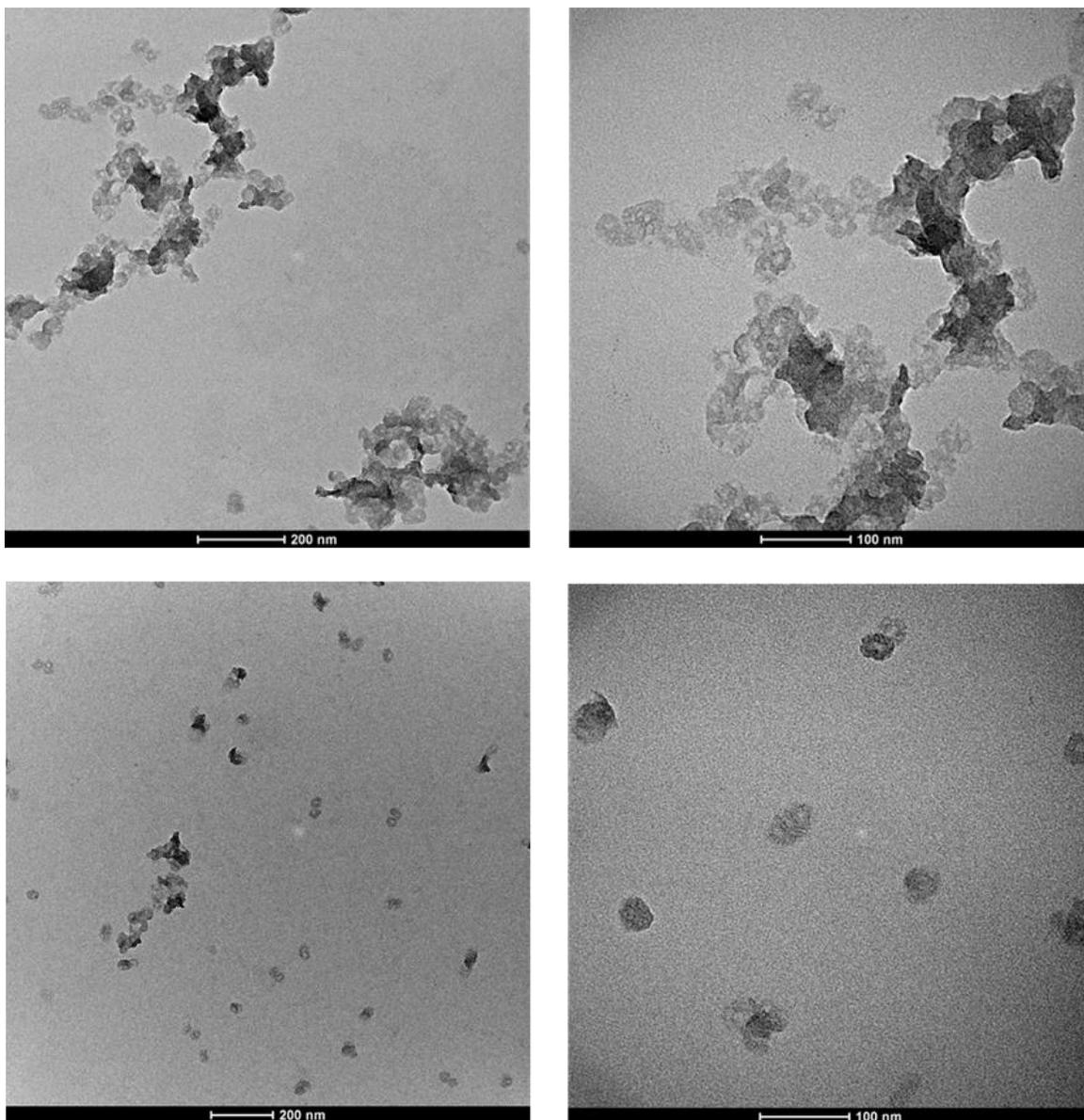
Figure 3.41. TEM images of breakable silica-coated QS (TEMOS+BTSPD). Scale bar 200 and 100 nm.
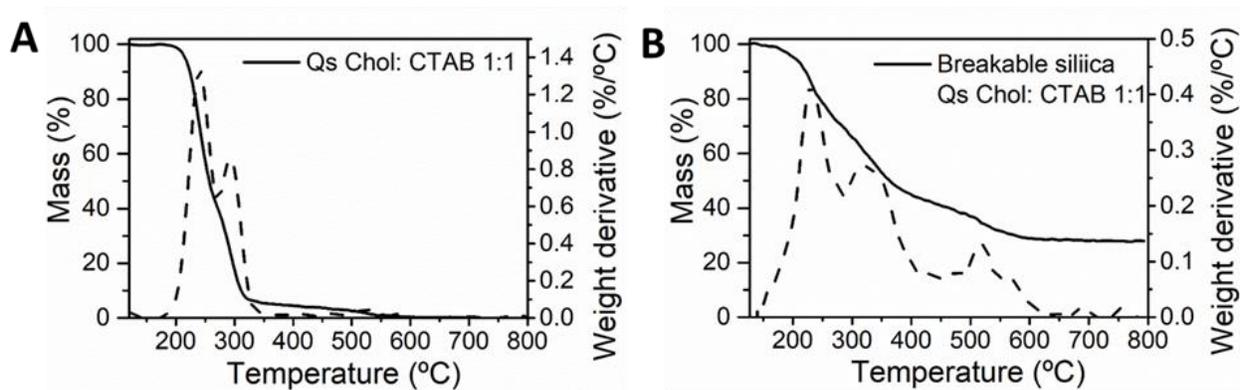
Figure 3.42. TGA of the **A)** QS and **B)** breakable silica QS.

3.3. Conclusions

Coated silica QS were performed using several silanes and different methodologies. Using DLS measurements and Cryo-TEM analysis were found that TEMOS and TEOS precursors showed to be the best silanes to coat the QS. It was observed that many variants play a role in the reaction as temperature, pH, silane, concentration of silane, and solvent.

On the other hand, breakable silica-coated QS were performed using three different techniques; the combination of the disulfide linker with APTES, TEOS and TEMOS were investigated giving the formation of a breakable shell around the QS. The systems were characterized by SEM, Cryo-SEM, TEM, EDX, XPS, and IR. Using APTES and BTSPD, the sample shows particles of around 32±6 nm with a shell of 9±2.

Breakable silica-coated QS with a fluorescent dye and QS loaded with dye and covered with breakable silica were formed to continue the studies.

3.4. Materials and Methods

3.4.1. Materials

All commercial solvents and reagents were used as received and without further purification. Tetraethyl orthosilicate (TEOS), Tetramethyl orthosilicate (TEMOS)(3-Aminopropyl)triethoxysilane (APTES), bis(triethoxysilyl-propyl)disulfide (BTSPD), Glutathione (GSH), was purchased from Sigma Aldrich.

5-Cholesten-3β-ol (Chol, purity 95%) was obtained from Panreac (Barcelona, Spain). Cetyltrimethylammonium bromide (CTAB, ultra for molecular biology) was purchased from Fluka-Aldrich and without further purification.

1,1'-dioctadecyl-3,3,3',3'-tetramethyl-indocarbocyanine perchlorate (DiI), and cyanine5 NHS ester were purchased from Life Technologies (Carlsbad, USA) and Lumipro, respectively.

MilliQ water was used for the sample preparation (Millipore Ibérica, Madrid Spain), EtOH (Teknochroma, Sant Cugat del Vallès, Spain). Carbon dioxide (99.9% purity) purchased by Carburos Metálicos S.A. (Barcelona, Spain).

3.4.2. Synthesis

3.4.2.1. Synthesis of Quatsomes (QS)

DELOS-SUSP Methodology, Depressurization of an Expanded Organic Solution-Suspension (DELOS-SUSP) method is a compressed fluid (CFs)-based to produce multifunctional small unilamellar vesicles (SUVs). In the last 25 years, several CFs-based methodologies have been developed,[12,31,32] giving advantages to produce homogeneous nanovesicles, in one-pot technology (no post-formation steps), with reproducibility, and easy to scale up.[33] Moreover, the extensive use of organic solvents is reduced; improving the toxicological profile of the particles produced. The most widely used CF is CO_2, which is nontoxic, non-flammable and easy recyclable. The moderate critical parameters of CO_2 (P_c = 7.4 MPa; T_c = 304.1 K). Most of the methods using compressed CO_2 for L-NV production involve the formation of a mixture of this dense gas, the vesicle membrane constituents, and an organic solvent at a certain pressure and temperature; vesicles are usually produced upon contact between this organic phase and an aqueous phase.[32,34]

In 2008, a CF-based method, called DELOS-SUSP (Depressurization of an Expanded Liquid Organic Solution), for the preparation of colloidal nanomaterials was developed.[27] Involves the

depressurization of a CO_2- expanded liquid solution of the lipids into an aqueous phase; uses a simple set-up and mild conditions of pressure (10 MPa) and temperature (35 °C) to make one-step preparation to produce controlled size distribution, with uniform shapes and good shell stability of vesicles. The whole procedure includes (a) the loading of an organic solution of the lipidic membrane components and the desired hydrophobic active compounds/molecules into an autoclave at a working temperature (Tw) and atmospheric pressure; (b) the addition of CO_2 to produce a CO_2-expanded solution, where the hydrophobic active and membrane components remain dissolved; and finally, (c) the depressurization of the expanded solution over an aqueous solution, which might contain membrane surfactants and hydrophilic biomolecules, to produce an aqueous dispersion of the nanovesicle bioactive(s) hybrids (**Figure 3.43**).[12]
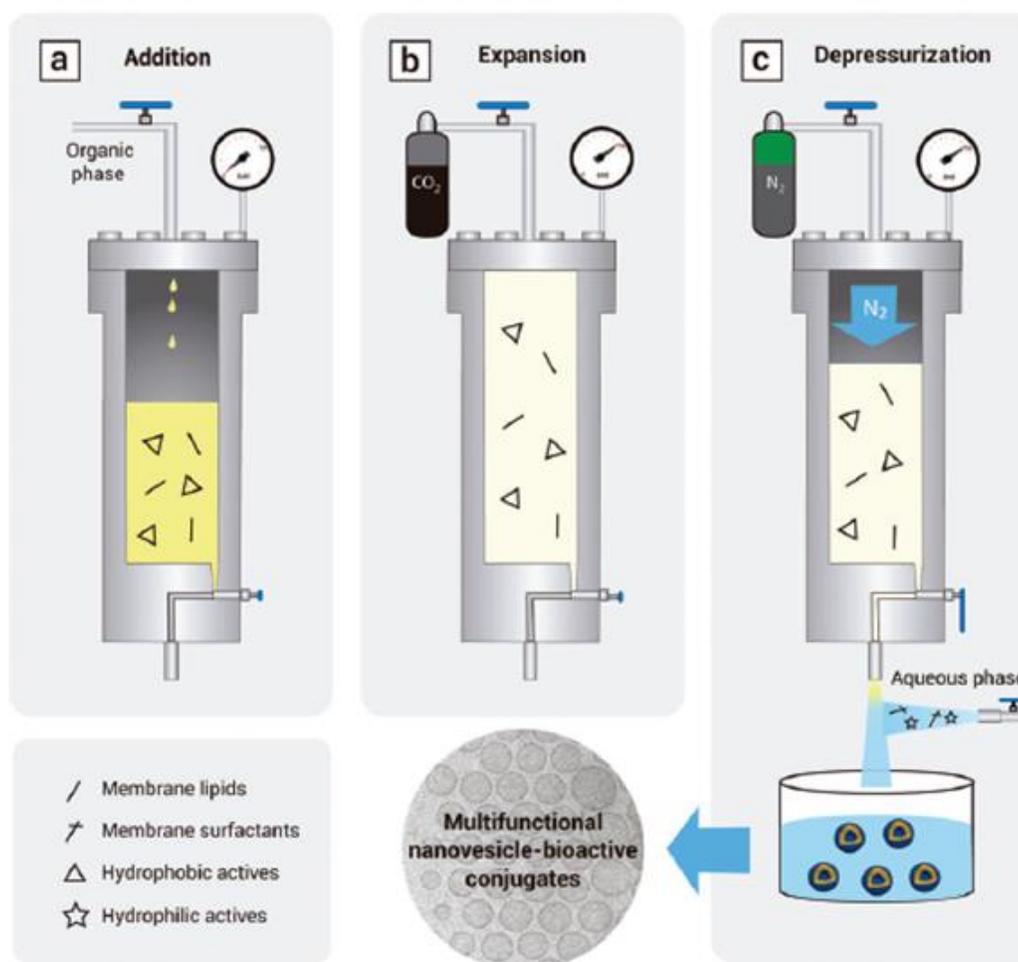
Figure 3.43. A) Schematic representation of the DELOS-SUSP method for the efficient preparation of multifunctional nanovesicle–bio-active hybrids. Extracted from ref. [12] Copyright 2013, with permission from American Chemical Society.

3.4.2.1.1. Synthesis of CTAB/CHOL QS (QS) and CTAB/CHOL/DiI QS (QS-DiI).

QS and QS-DiI were made by Cholesterol and CTAB and were prepared by the CO2-based method, DELOS-SUSP.

For the QS, cholesterol was dissolved in EtOH and then added to a high-pressure vessel, while the QS-DII were formed by mixing Cholesterol with DiI in a solution of EtOH before been added to the high-pressure vessel. In each case this vessel is previously heated at Tw = 308 K and after the addition of the EtOH solution, CO2 was added until reaching the working pressure (Pw = 10 MPa), to obtain a CO2-expanded solution of the compounds.

Afterward, The QS are formed by depressurizing the CO2-expanded solution over an aqueous solution of the surfactant (CTAB).

3.4.2.1.2 Synthesis of CTAB/CHOL/10% DODECYL-SILANE QS

This QS were prepared using the same methodology used to produce CTAB/CHOL QS. 10% in weight of Dodecyl silane was added in the inorganic phase mixed with the Cholesterol.

Synthesis of 10% and 5% dodecyl-silane QS (1:1 Chol:CTAB): 85.8 mg of cholesterol were mixed with 16 or 8 mg of dodecyl(trimethoxy)silane (to produce the 10% and 5%, respectively) in 2.89 mL of EtOH using a vial; the solution was stirred and heated at 37 °C until the components were in a homogeneous solution. After, the mixture was putted in the reactor and 200 μL of EtOH were used to clean the vial to then recover all the material left in it. The components in the reactor were inside one hour at 308K and 10 MPa with CO_2, to produce the supercritical fluid. In another vial, 73.90 mg of CTAB was dissolved in 25.8 mL of water using a stirring bar and a temperature of 37 °C. This solution was verted in a bigger container to then make the depressurization of the supercritical fluid (the organic solution) in this aqueous phase using N_2 in a slowly addition. Scheme 5 shows the representation of the DELOS methodology used to prepare the QS.

3.4.2.2. Synthesis of silica-coated QS

3.4.2.2.1. Synthesis of non-breakable silica-coated QS

3.4.2.2.1.1. Synthesis of Non-Breakable APTES-silica-coated QS (NB-APTES-QS)

Synthesis using APTES: 4 mL of water and 0.5 mL of EtOH were putted in 25 mL ball flask under 375 rpm stirring, 0.5mL of Quatsomes (size distribution of 114±26 nm) and after 4 µL the ammonia 28% are added in that order. Finally, Eppendorf 3.4 µL of APTES was dissolved in 0.5 mL of EtOH and added to the ball flask in aliquots of 30 µL, each 5 minutes (each 30 µL was added in 3x 10µL shoot to avoid agglomerations of the silica).

Synthesis using APTES (Concentrate QS): 1 mL of QS was put in the 10 mL ball flask and 20 µL of Ammonia 28% was put; after 200µL of a 0.012M APTES (2 mM APTES) (flask in aliquots of 30 µL each 5 minutes (each 30µL is added in 3x 10µL shoot to avoid agglomerations of the silica).

Synthesis using APTES (Zhang *et al.* procedure): 6.5 mL of water and 1 mL QS (size distribution of 85±2 nm, Pdl of 0.24±0.004 and Zeta Potential of 94±15 mV) were putted in 10 mL ball flask under 500 rpm stirring, 200 µL of Ascorbic acid (50 mM) and 300 µL of ammonia (0.134 M) were added to obtain a final pH of 9.25. After, 8.4 µL of APTES (4.4 mM) were added directly in the solution. The experiment was run at 0 °C (ice bath during the day and during the night at room temperature (around 20 °C).

3.4.2.2.1.2. Synthesis of Non-Breakable TEOS-silica-coated QS (NB-TEOS-QS).

Non-Breakable silica-coated QS (NB-SQS) using TEOS at 0 °C and longer times. 6.5 mL of water and 1 mL QS (size distribution of 85±2 nm, Pdl of 0.24±0.004 and Zeta Potential of 94±15 mV) were putted in 25 mL ball flask under 500 rpm stirring, 200 µL of Ascorbic acid (50 mM) and 260 µL of ammonia (0.134 M) were added to obtain a final pH of 9.03. Finally, 8 µL of TEOS (4.4 mM) were added directly in the solution. The experiment was run at 0 0 °C (ice bath) during the day and during the night at room temperature (around 20 °C).

3.4.2.2.1.3 Synthesis of Non-Breakable TEMOS-silica-coated QS (NB-TEMOS-QS)

Synthesis using TEMOS: 1 mL of QS 5.35 mg/mL (size distribution of 85±2 nm, Pdl of 0.24±0.004 and Zeta Potential of 94±15 mV) was added to 6.5mL of water, 200 µL of Ascorbic acid (50 mM)

and 300 µL of ammonia (0.134 M) were added to obtain a pH of 9.2. After, 5.3 µL of TEMOS (4.4 mM) were added directly in the solution. The experiment was performed at 0 °C (ice bath) the firsts hours of reaction. The reaction was stopped after 7 days by dialysis.

3.4.2.2.1.4. Synthesis of Non-Breakable TEOS-silica-coated QS (NB-TEOS-QS)

Synthesis using TEOS: 1 mL of QS 5.35 mg/mL (size distribution of 85±2 nm, Pdl of 0.24±0.01 and Zeta Potential of 94±15 mV) was added to 6.5 mL of water, 200 µL of Ascorbic acid (50 mM) and 300 µL of ammonia (0.134 M)were added to obtain a pH of 9.2. After, 8 µL of TEOS (4.4 mM) were added directly in the solution. The experiment was performed at 0 °C (ice bath), the firsts hours of reaction. After 2 days of reaction, another addition of TEOS was done to obtain a final concentration of 8.9 mM in the solution. The reaction was stopped after 7 days by dialysis.

3.4.2.2.1.5. Synthesis of Non-Breakable TEOS-silica-coated QS (NBS-Dodecylsilane-QS)

Synthesis of silica-coated Dodecyl-silane QS: 6.5 mL of water and 1 mL of 10% Dodecyl silica QS (size distribution of 62±1 nm, Pdl of 0.23±0.01 and Zeta Potential of 80±5 mV) were putted in 25 mL ball flask under 625 rpm using a bar stirring bar, 200 µL of Ascorbic acid (50 mM) and 260 µL of ammonia (0.134 M) were added to obtain a pH of 9.03. After, 8 µL of TEOS (4.4mM) were added directly in the solution. The experiment was run at 0 °C (ice bath) during the day and during the night at room temperature (around 20 °C).

3.4.2.2.2. Synthesis of Breakable silica-coated QS (BS-QS)

3.4.2.2.2.1. Synthesis of Breakable BTSPD-silica-coated QS (BS-QS-APTES/BTSPD)

Synthesis using APTES/BTSPD: 0.5 mL of QS (5.35 mg/mL) was added to 4 mL of water and 0.5 mL of EtOH, 4 µL of Ammonia 28% was added. Separately, 3.4 µL of APTES, 2 µL BTSPD were mixed in 500µL of EtOH. From this solution, 320 µL are added to the QS slowly (40µL each 5 mins).

3.4.2.2.2.2. Synthesis of breakable silica-coated QS(BS-QS-TEOS/BTSPD)

Synthesis using TEOS/BTSPD: 6.5 mL of water and 1 mL QS (size distribution of 85±2 nm, Pdl of 0.24±0.004 and Zeta Potential of 94±15 mV) were putted in 10 mL ball flask under 500 rpm stirring, 200 µL of Ascorbic acid (50 mM) and 310 µL of ammonia (0.134 M) were added to obtain

a pH of 9.1. In an Eppendorf 6 µL of TEOS were mixed with 2.5 µL of BTSPD and putted in the reaction ([TEOS]=3.37 mM and [BTSPD]=0.07 mM). The experiment was performed at 0 °C (ice bath) during the day and at room temperature during the night (around 20 °C).

3.4.2.2.2.3. Synthesis of Breakable BTSPD-silica-coated QS (BS-QS-TEMOS/BTSPD)

Synthesis using TEMOS/BTSPD: 1 mL of QS 5.35 mg/mL (size distribution of 85±2 nm, Pdl of 0.24±0.004 and Zeta Potential of 94±15 mV) was added to 6.5 mL of water, 200 µl of Ascorbic acid (50 mM) and 300 µL of ammonia (0.134 M) were added to obtain a pH of 8. In an Eppendorf, 4µL of TEMOS and 2.5 µL of BTSPD were mixed with 300 µL of EtOH and added to the reaction ([TEMOS]=3.37 mM and [BTSPD]=0.07 mM). The experiment was performed at 0 °C (ice bath) during the day and at room temperature during the night (around 20 °C). After 2 days, a second addition of silanes was made; 4.6 µL of TEMOS and 3 µL of BTSPD in 200µL of EtOH are mixed in the solution. After 2h the reaction is stopped by dialysis.

3.5. REFERENCES

(1)   Antonietti, M.; Förster, S. Vesicles and Liposomes: A Self-Assembly Principle Beyond Lipids. *Advanced Materials* **2003**, *15* (16), 1323–1333.

(2)   Bangham, A. D.; Horne, R. W. Negative Staining of Phospholipids and Their Structural Modification by Surface-Active Agents as Observed in the Electron Microscope. *Journal of Molecular Biology* **1964**, *8* (5), 660–668.

(3)   Sawant, R. R.; Torchilin, V. P. Challenges in Development of Targeted Liposomal Therapeutics. *AAPS Journal* **2012**, *14* (2), 303–315.

(4)   Bangham, A. D.; De Gier, J.; Greville, G. D. Osmotic Properties and Water Permeability of Phospholipid Liquid Crystals. *Chemistry and Physics of Lipids* **1967**, *1* (3), 225–246.

(5)   James, N. D.; Coker, R. J.; Tomlinson, D.; Harris, J. R. W.; Gompels, M.; Pinching, A. J.; Stewart, J. S. W. Liposomal Doxorubicin (Doxil): An Effective New Treatment for Kaposi's Sarcoma in AIDS. *Clinical Oncology* **1994**, *6* (5), 294–296.

(6)   Batist, G.; Ramakrishnan, G.; Rao, C. S.; Chandrasekharan, A.; Gutheil, J.; Guthrie, T.; Shah, P.; Khojasteh, A.; Nair, M. K.; Hoelzer, K.; Tkaczuk, K.; Park, Y. C.; Lee, L. W. Reduced Cardiotoxicity and Preserved Antitumor Efficacy of Liposome-Encapsulated Doxorubicin and Cyclophosphamide Compared with Conventional Doxorubicin and Cyclophosphamide in a Randomized, Multicenter Trial of Metastatic Breast Cancer. *Journal of clinical oncology* **2001**, *19* (5), 1444–1454.

(7)   Stathopoulos, G. P.; Boulikas, T. Lipoplatin Formulation Review Article. *Journal of Drug Delivery* **2012**, *2012*, 581363.

(8)   Kaposi's Sarcoma: DaunoXome Approved. *AIDS Treat News* **1996**, No. 79, 3–4.

(9)   Salehi, B.; Selamoglu, Z.; Mileski, K. S.; Pezzani, R.; Redaelli, M.; Cho, W. C.; Kobarfard, F.; Rajabi, S.; Martorell, M.; Kumar, P.; Martins, N.; Santra, T. S.; Sharifi-Rad, J. Liposomal Cytarabine as Cancer Therapy: From Chemistry to Medicine. *Biomolecules* **2019**, *9* (12), 773.

(10)   Kirby, C.; Clarke, J.; Gregoriadis, G. Effect of the Cholesterol Content of Small Unilamellar Liposomes on Their Stability in Vivo and in Vitro. *The Biochemical journal* **1980**, *186* (2), 591–598.

(11)   Ferrer-Tasies, L.; Moreno-Calvo, E.; Cano-Sarabia, M.; Aguilella-Arzo, M.; Angelova, A.; Lesieur, S.; Ricart, S.; Faraudo, J.; Ventosa, N.; Veciana, J. Quatsomes: Vesicles Formed by Self-Assembly of Sterols and Quaternary Ammonium Surfactants. *Langmuir* **2013**, *29* (22), 6519–6528.

(12)   Cabrera, I.; Elizondo, E.; Esteban, O.; Corchero, J. L.; Melgarejo, M.; Pulido, D.; Córdoba, A.; Moreno, E.; Unzueta, U.; Vazquez, E.; Abasolo, I.; Schwartz, S.; Villaverde, A.; Albericio, F.; Royo, M.; García-Parajo, M. F.; Ventosa, N.; Veciana, J. Multifunctional Nanovesicle-Bioactive Conjugates Prepared by a One-Step Scalable Method Using CO2-Expanded Solvents. *Nano Letters* **2013**, *13* (8), 3766–3774.

(13)   Cano-Sarabia, M.; Angelova, A.; Ventosa, N.; Lesieur, S.; Veciana, J. Cholesterol Induced CTAB Micelle-to-Vesicle Phase Transitions. *Journal of Colloid and Interface Science* **2010**, *350* (1), 10–15.

(14)   Elizondo, E.; Moreno, E.; Cabrera, I.; Córdoba, A.; Sala, S.; Veciana, J.; Ventosa, N. Liposomes and Other Vesicular Systems: Structural Characteristics, Methods of Preparation, and Use in Nanomedicine. In *Progress in Molecular Biology and Translational Science*; Academic Press, **2011**; Vol. 104, pp 1–52.

(15)   Vargas-Nadal, G.; Muñoz-Ubeda, M.; Alamo, P.; Arnal, M. M.; Céspedes, V.; Köber, M.; Gonzalez, E.; Ferrer-Tasies, L.; Vinardell, M. P.; Mangues, R.; Veciana, J.; Ventosa, N. MKC-Quatsomes: A Stable Nanovesicle Platform for Bio-Imaging and Drug-Delivery Applications. *Nanomedicine: Nanotechnology, Biology, and Medicine* **2020**, *24*, 102136.

(16)   Liu, X.; Ardizzone, A.; Sui, B.; Anzola, M.; Ventosa, N.; Liu, T.; Veciana, J.; Belfield, K. D. Fluorenyl-Loaded Quatsome Nanostructured Fluorescent Probes. *ACS Omega* **2017**, *2* (8), 4112–4122.

(17)   Ardizzone, A.; Kurhuzenkau, S.; Illa-Tuset, S.; Faraudo, J.; Bondar, M.; Hagan, D.; Van

Stryland, E. W.; Painelli, A.; Sissa, C.; Feiner, N.; Albertazzi, L.; Veciana, J.; Ventosa, N. Nanostructuring Lipophilic Dyes in Water Using Stable Vesicles, Quatsomes, as Scaffolds and Their Use as Probes for Bioimaging. *Small* **2018**, *14* (16), 1703851.

(18) Beloglazova, N. V.; Goryacheva, O. A.; Speranskaya, E. S.; Aubert, T.; Shmelin, P. S.; Kurbangaleev, V. R.; Goryacheva, I. Y.; De Saeger, S. Silica-Coated Liposomes Loaded with Quantum Dots as Labels for Multiplex Fluorescent Immunoassay. *Talanta* **2015**, *134*, 120–125.

(19) Hameed, S.; Bhattarai, P.; Dai, Z. Cerasomes and Bicelles: Hybrid Bilayered Nanostructures with Silica-like Surface in Cancer Theranostics. *Frontiers in Chemistry* **2018**, *6*, 127.

(20) Li, C.; Zhang, Y.; Su, T.; Feng, L.; Long, Y.; Chen, Z. Silica-Coated Flexible Liposomes as a Nanohybrid Delivery System for Enhanced Oral Bioavailability of Curcumin. *International Journal of Nanomedicine* **2012**, *7*, 5995–6002.

(21) Corma, A.; Díaz, U.; Arrica, M.; Fernández, E.; Ortega, Í. Organic-Inorganic Nanospheres with Responsive Molecular Gates for Drug Storage and Release. *Angewandte Chemie International Edition* **2009**, *48* (34), 6247–6250.

(22) Kesarkar, S.; Rampazzo, E.; Valenti, G.; Marcaccio, M.; Bossi, A.; Prodi, L.; Paolucci, F. Iridium(III)-Doped Core-Shell Silica Nanoparticles: Near-IR Electrogenerated Chemiluminescence in Water. *ChemElectroChem* **2017**, *4* (7), 1690–1696.

(23) Rampazzo, E.; Boschi, F.; Bonacchi, S.; Juris, R.; Montalti, M.; Zaccheroni, N.; Prodi, L.; Calderan, L.; Rossi, B.; Becchi, S.; Sbarbati, A. Multicolor Core/Shell Silica Nanoparticles for in Vivo and Ex Vivo Imaging. *Nanoscale* **2012**, *4* (3), 824–830.

(24) Huo, Q.; Liu, J.; Wang, L. Q.; Jiang, Y.; Lambert, T. N.; Fang, E. A New Class of Silica Cross-Linked Micellar Core-Shell Nanoparticles. *Journal of the American Chemical Society* **2006**, *128* (19), 6447–6453.

(25) Maggini, L.; Cabrera, I.; Ruiz-Carretero, A.; Prasetyanto, E. A.; Robinet, E.; De Cola, L. Breakable Mesoporous Silica Nanoparticles for Targeted Drug Delivery. *Nanoscale* **2016**, *8* (13), 7240–7247.

(26) De Cola, L.; Maggini, L.; Adi, E. Matériau d'oxyde Organométallique Poreux Désintégrable. IP 14151167.5, **2014**.

(27) Cano-Sarabia, M.; Ventosa, N.; Sala, S.; Patiño, C.; Arranz, R.; Veciana, J. Preparation of Uniform Rich Cholesterol Unilamellar Nanovesicles Using CO 2-Expanded Solvents. *Langmuir* **2008**, *24* (6), 2433–2437.

(28) Hoffmann, F.; Cornelius, M.; Morell, J.; Fröba, M. Silica-Based Mesoporous Organic-Inorganic Hybrid Materials. *Angewandte Chemie International Edition* **2006**, *45* (20), 3216–3251.

(29) Zhang, L.; Li, P.; Liu, X.; Du, L.; Wang, E. The Effect of Template Phase on the Structures of As-Synthesized Silica Nanoparticles with Fragile Didodecyldimethylammonium Bromide Vesicles as Templates. *Advanced Materials* **2007**, *19* (23), 4279–4283.

(30) Hubert, D. H. W.; Jung, M.; Frederik, P. M.; Bomans, P. H. H.; Meuldijk, J.; German, A. L. Vesicle-Directed Growth of Silica. *Advanced Materials* **2000**, *12* (17), 1286–1290.

(31) Byrappa, K.; Ohara, S.; Adschiri, T. Nanoparticles Synthesis Using Supercritical Fluid Technology - towards Biomedical Applications. *Advanced Drug Delivery Reviews* **2008**, *60* (3), 299–327.

(32) Elizondo, E.; Veciana, J.; Ventosa, N. Nanostructuring Molecular Materials as Particles and Vesicles for Drug Delivery, Using Compressed and Supercritical Fluids. *Nanomedicine* **2012**, *7* (9), 1391–1408.

(33) Grimaldi, N.; Andrade, F.; Segovia, N.; Ferrer-Tasies, L.; Sala, S.; Veciana, J.; Ventosa, N. Lipid-Based Nanovesicles for Nanomedicine. *Chemical Society Reviews* **2016**, *45* (23), 6520–6545.

(34) Otake, K.; Imura, T.; Sakai, H.; Abe, M. Development of a New Preparation Method of Liposomes Using Supercritical Carbon Dioxide. *Langmuir* **2001**, *17* (13), 3898–3901.

ABSTRACT

Fluorescent molecules have been loaded in the system silica-coated QS to produce *labeled silica shell QS* for different objectives. These systems act as luminescent bio-probes and their study go for research on the potentiality of these materials as a drug delivery system. Moreover, labeled stimulus-response systems were synthesized to make delivery particles in which under reducing agents, the material would break in small pieces, releasing the cargo and having better elimination from the body, making them good prospects for biological applications.

In this chapter, labeled silica shell QS permit us to confirm the formation of the silica shell on the QS by performing systems with combinations of dyes (loaded in the QS membrane and inserted covalently in the silica shell) in which the fluorescence resonance energy transfer (FRET) is presence. Fluorescence spectroscopy, confocal microscopy and stochastic optical reconstruction microscopy (STORM) studies were the techniques to study these systems. Furthermore, breakability and permeability tests were performed to study the potentiality of those systems to be able to act as a stimulus-responsive drug delivery carrier.

4.1. Introduction

For many years, fluorescence has been a methodology used as a primary research tool in biochemistry and biophysics. Fluorescence has been used in biotechnology, flow cytometry, medical diagnostics, DNA sequencing, genetic analysis, etc, due to its high detection sensibility and low-cost in comparison to other detection analytical techniques.[1] An increase in attention has become to use fluorescence for cellular and molecular imaging.[2–8] This technique can reveal the localization of molecules intracellularly, sometimes in a single-molecular detection.[1,9]

Luminescence is the emission of light from any substance and occurs from electronically excited states. Luminescence is formally divided into two categories -fluorescence and phosphorescence- depending on the nature of the excited state.[1] Prof. Alexander Jablonski, regarded as the father of fluorescence spectroscopy illustrated various molecular processes for the phenomena on the named Jablonski diagram (**Figure 4.1**).[1] The single ground, first and second electronic states are depicted by S_0, S_1 and S_2. And each of the electronic energy levels, the fluorophores can exist in a number of vibrational energy levels, denoted by 0, 1, 2, etc.

Absorption typically occurs from molecules with the lowest vibrational energy level between S_0 to either S_1 or S_2. Larger energy difference between S_0 and S_1 excited states is too large for thermal population of S_1, for that reason light and not heat is required to induce fluorescence. After light absorption, electrons in the S_2 vibrational level rapidly relax to the S_1. This process is called internal conversion and generally occurs in 10^{-12} s. Fluorescence is then the emission of light which results in the return of the electron from the $S_{1\,excited}$ state to the ground state orbital S_0 (with emission rates of 10^{-8} s). On the other hand, phosphorescence is the emission of light from a triplet excited state T_1 (with lower energy than the S_1) to the S_0 state. This transition is forbidden and as a result, emission rates are slower, typically milliseconds to seconds (10^3 to 10 s^{-1}). Electrons in the S_1 state can have a spin conversion to the T_1, phenomena called intersystem crossing.[1]
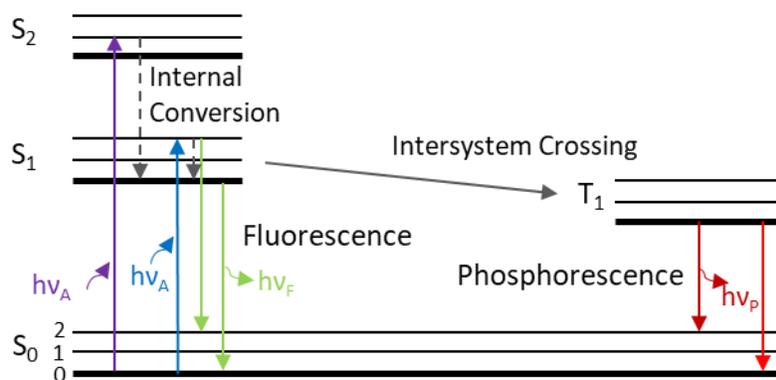
Figure 4.1. Jablonski diagram, florescence and phosphorescence phenomena.

Resonance Energy Transfer (RET), sometimes called fluorescence resonance energy transfer or Förster Resonance Energy Transfer (FRET), was described originally by the scientist Theodor Förster.[10–12] It is another important process that occurs in the excited state, which involves a transfer of energy from one fluorophore in an excited state to a second nearby molecule through a nonradiative process.[13] The phenomenon occurs when the emission of a fluorophore (whenever the emission spectrum is), called the donor, overlaps with the absorption spectrum of another molecule, called acceptor (do not have to be fluorescent).[14–17] In this case, the donor and the acceptor are coupled by dipole-dipole interaction. The extent of energy is determined by the distance between the donor and the acceptor and the extent of spectral overlap.[1] Then, for efficient FRET to occur, a substantial overlap between the donor fluorescence emission spectra and the acceptor fluorescence excitation (or absorption) must exist.[18,19] Moreover, FRET measurements are often named as "spectroscopic ruler" or "molecular rulers" because FRET is only efficient when two fluorophores are within 2-10 nm of one another.[1,13] The distance between a donor and acceptor can be calculated from the transfer energy:

$$E = \frac{R_O^6}{R_O^6 + r^6}$$

where E is the efficiency of energy transfer, R_0 is Förster distance and r is distance between the donor (D) and acceptor (A). **Figure 4.2** summarizes the three conditions to observe FRET which

are 1) a proper spectral overlap, 2) a distance <10 nm and 3) and a correct orientation of the fluorescent molecules.
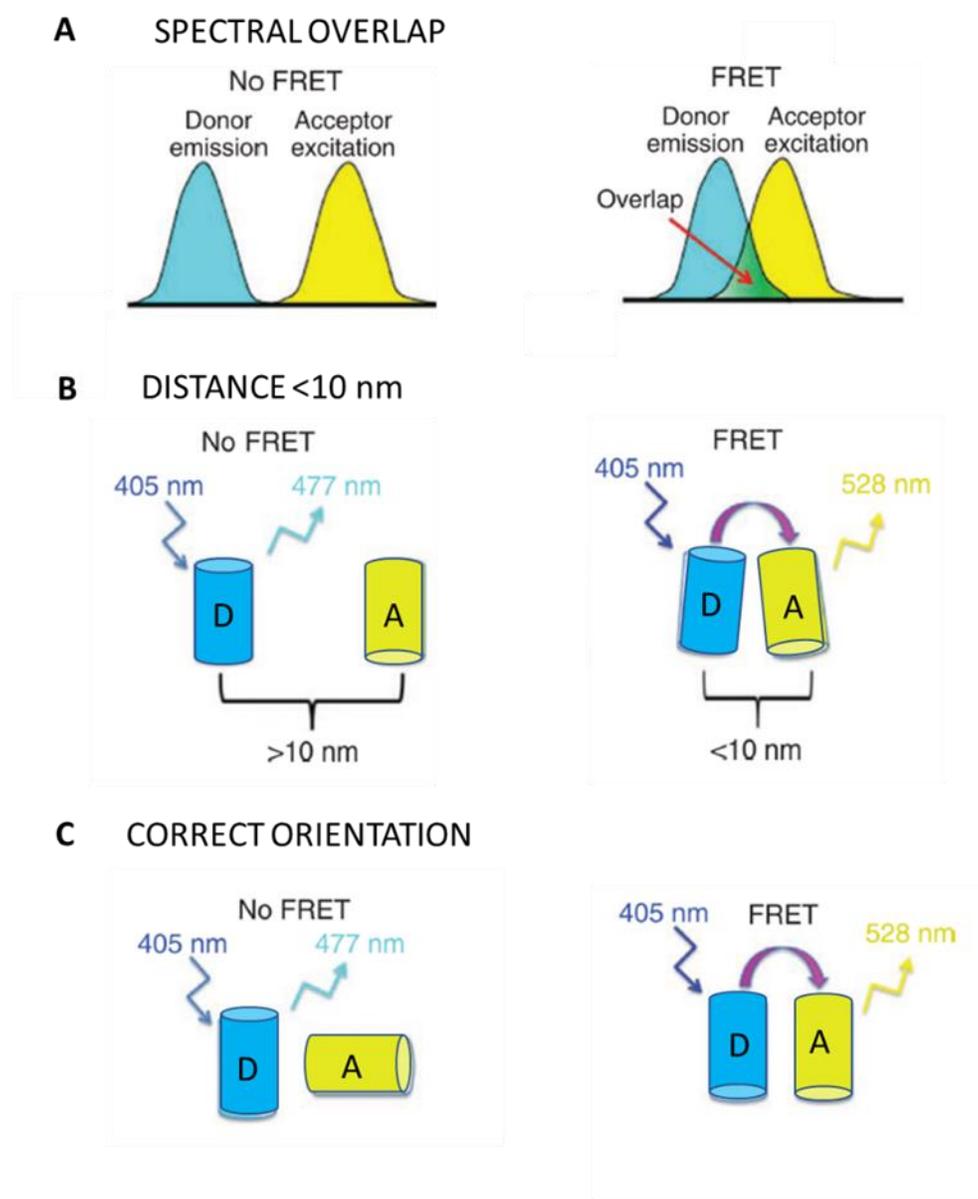
Figure 4.2. Representation of the three conditions that must be for an efficient FRET. **A)** *The spectral overlap*: the emission spectrum from the donor (D) fluorophore must overlap with the excitation spectrum of the acceptor (A) fluorophore. **B)** *Distance <10 nm*: If the FRET donor and acceptor are more than 10nm apart, then no FRET occurs, and the donor emits fluorescence. If the donor and acceptor are within ~10 nm of one another, then energy transfer can occur from the donor to the acceptor. **C)** *Correct orientation*: If the donor and acceptor fluorophore dipoles are perpendicular to one another, then the donor molecule will emit fluorescence. However, if the dipoles are parallel to each other, FRET will occur. Reprinted with permission from ref 13. (Copyright 2013, Macmillan Publishers Limited)

4.2. Results and discussion

4.2.1. Photophysical characterization of the Labeled Breakable silica QS

The fluorescent labeling of silica shell QS permits us to do several studies.[20] One of these studies was the confirmation of the formation of the silica shell on the QS. This was achieved by performing systems with combinations of dyes leading FRET such as loading the dye which acts as a donor in the QS membrane and another dye covalently linked in the silica shell, as the acceptor. This provides a system in which fluorescence resonance energy transfer (FRET) is present if the two dyes are close enough.[21] Moreover, breakable silica shell around the QS was done to make them stimuli-responsive for potential biomedical applications.[22]

To produce FRET breakable silica QS, four systems were tested. 1) Quatsomes loaded with (1,1'-dioctadecyl-3,3,3'3'-tetramethylindocarbocyanine perchlorate) (DiI) in their membrane, acting as a donor dye in the future FRET system (QS-DiI)[23] 2) Quatsomes loaded with DiI in the membrane and coated with breakable shell (BS-QS-DiI), 3) Quatsomes with a labeled breakable shell, for this Cyanine5 NHS ester (Cy5) was used to be covalently linked in the silica shell (Cy5-BS-QS), acting as a future acceptor dye in the FRET system. 4) Quatsomes loaded with DiI and coated with labeled Cy5 breakable shell to produce the FRET system (Cy5-BS-QS-DiI) (**Figure 4.3**). Complete photophysics studies were done to those materials.
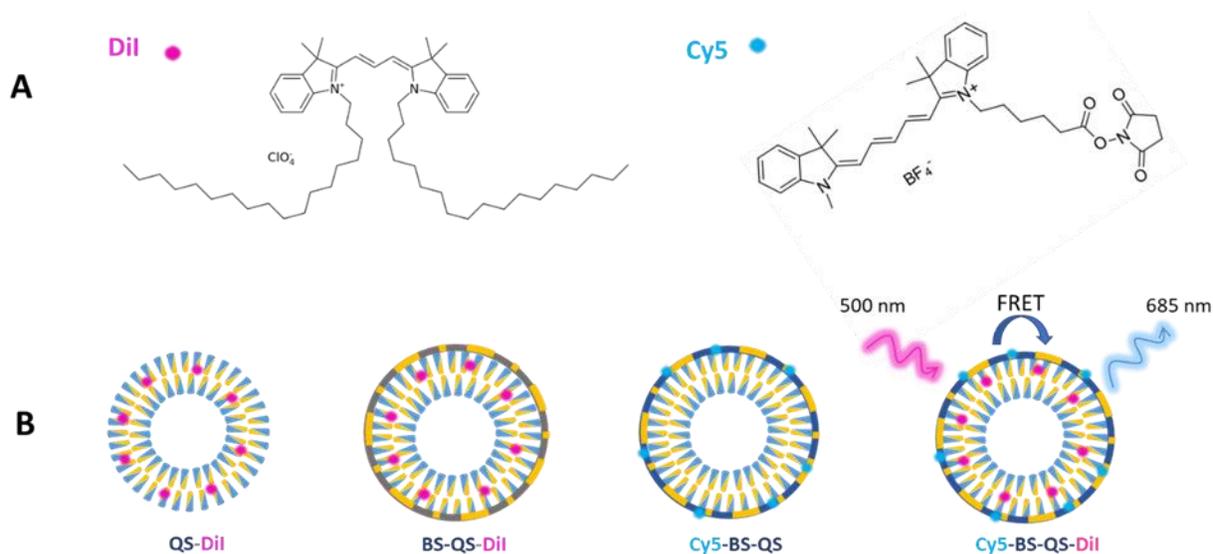
Figure 4.3. A) Dyes using for the labeled silica QS to produce the FRET system. **B)** Different systems for the labeled silica-coated QS to produce the Breakable labeled silica-coated QS with FRET.

To optically characterize the systems, absorbance spectra were first measured (**Figure 4.4**). It is observed the characteristics bands for the absorbance of the DiI and Cy5 dyes for each system (with λ_{max}= 551 nm and 659 nm, respectively). The Cy5-BS-QS-DiI, presents both absorbance bands due to the presence of DiI and Cy5.
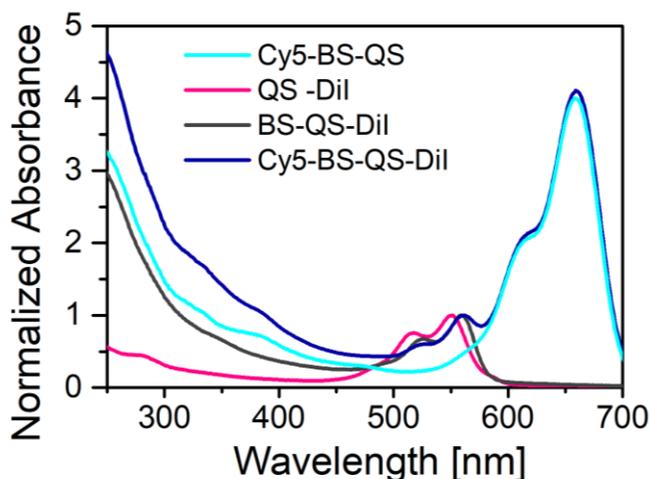
Figure 4.4. Absorbance of the different labeled silica-coated QS systems in the range of 200 to 700 nm.

After, fluorescence studies were done for the three different systems BS-QS-DiI, Cy5-BS-QS and Cy5-BS-QS-DiI. **Figure 4.5A** shows the spectroscopic parameters to obtain the emission and excitation spectra of the systems using a fluorometer. In **Figure 4.5B** is shown the emission and excitation spectra of Breakable QS loaded with DiI (pink lines) in which the wavelength of excitation and emission were 525 and 625 nm, respectively. Moreover, for its overlap with the emission and excitation spectra of Cy5 Breakable QS (blue lines), excitation and emission wavelengths at 600 and 750 nm were respectively used. In this spectra, we can observe that the emission of the donor (the QS with the DiI dye) is overlaping with the excitation spectra of the acceptor (QS done with Cy5 dye shell) which brings the possibility to have FRET in the system based on the DiI and Cy5 mixture. In **Figure 4.5C** is shown the emission and excitation spectra of the Cy5-BS-QS-DiI system where both dyes exist in one system; the DiI is inside of the QS (in the hydrophobic part) and the Cy5 is in the silica shell around the QS. To obtain the emission spectra, the sample was excited at 500 nm were the DiI acts like a donor and Cy5 as the acceptor. On the other hand, to obtain the excitation spectra, the sample was irradiated at 750 nm in which the

Cy5 pass the energy to the DiI. Since in the emission spectra of Cy5-BS-QS-DiI two emission band are clearly appreciated (569 nm and 686 nm for DiI and Cy5, respectively) this evidently indicates the incorporation of both dyes into the nanostructure. Moreover, it noticeably shows the presence of FRET since the excitation wavelength employed only excites the DiI, although the main emission band of Cy5 is displayed intensively at 570 nm. These results corroborated the presence of FRET in the sample, which also reveals that the two dyes are in a distance less than 10 nm, confirming the formation of silica around the QS.

Figure 4.5. A) Representative diagrams of the fluorescent QS and the schematic representation of the emission of the dyes present in the three systems, BS-QS-DiI, Cy5-BS-QS and Cy5-BS-QS-DiI**. B)** Emission and excitation spectra of Breakable Silica QS loaded with DiI (BS-QS-DiI) (pink lines); Wavelength of excitation and emission were 525 and 625 nm, respectively. And its translapation with the Emission and excitation spectra of Cy5 Breakable Silica QS (Cy5-BS-QS) (blue lines); excitation and emission wavelenth at 600 and 750 nm, respectively. **C)** Emission and Excitation spectra of the Cy5-Breakable silica-coated DiI-QS (Cy5-BS-QS-DiI) exiting at 500 nm and emitting at 750 nm.

To continue characterizing the labeled breakable silica system, photophysics studies of the QS loaded with DiI (QS-DiI) *vs* these vesicles coated with breakable silica shell (BS-QS-DiI) were done. As shown in **Figure 4.6**. **Figure 4.6B,** the absorbance of the DiI appears in both samples, without

coating and coated QS-DiI (pink and gray lines, respectively). It is appreciable a small red-shift of 9 nm, from 550 to 559 nm, from the material without and with silica coating, respectively. Also, it is observable a stronger light scattering at 200-400 nm wavelength on the BS-QS-DiI sample, attributed to the presence of silica. To continue studying these systems, emission and excitation spectra were taken (**Figure 4.6C**). The emission spectra of the two samples were taken by the excitation at 520 and 525 nm for the QS-DiI (pink lines) and BS-QS-DiI (gray lines), observing a red-shift of 8 nm from 570 to 578 nm for the QS-DiI to the BS-QS-DiI sample (**Figure 4.6A**). On the other hand, from the excitation spectra, we can also observe the shifting with the absorbance results. This shift of around 10 nm is shown from 550 to 560 nm, from the sample QS-DiI and BS-QS-DiI (pink and gray slash lines), respectively with an emitting wavelength of 625 nm. From these results, it is clear that the silica shell is inducing a change in the photophysical properties of the material, indicating then the proper formation of silica shells in the QS.

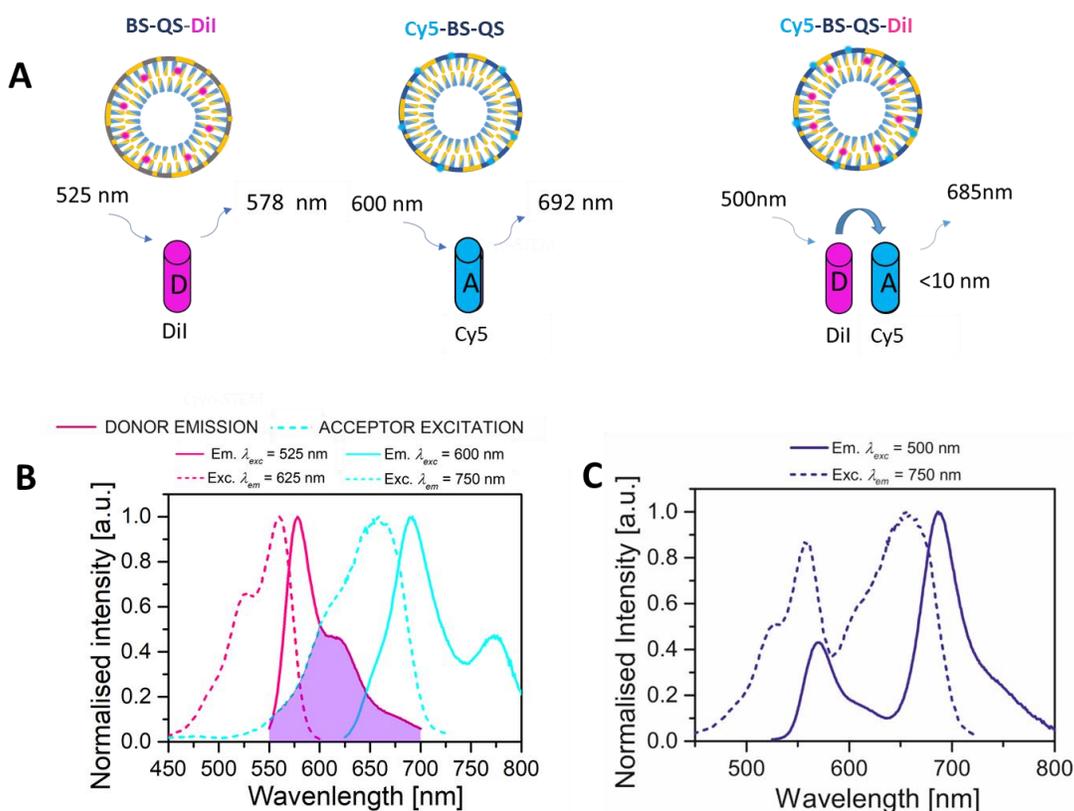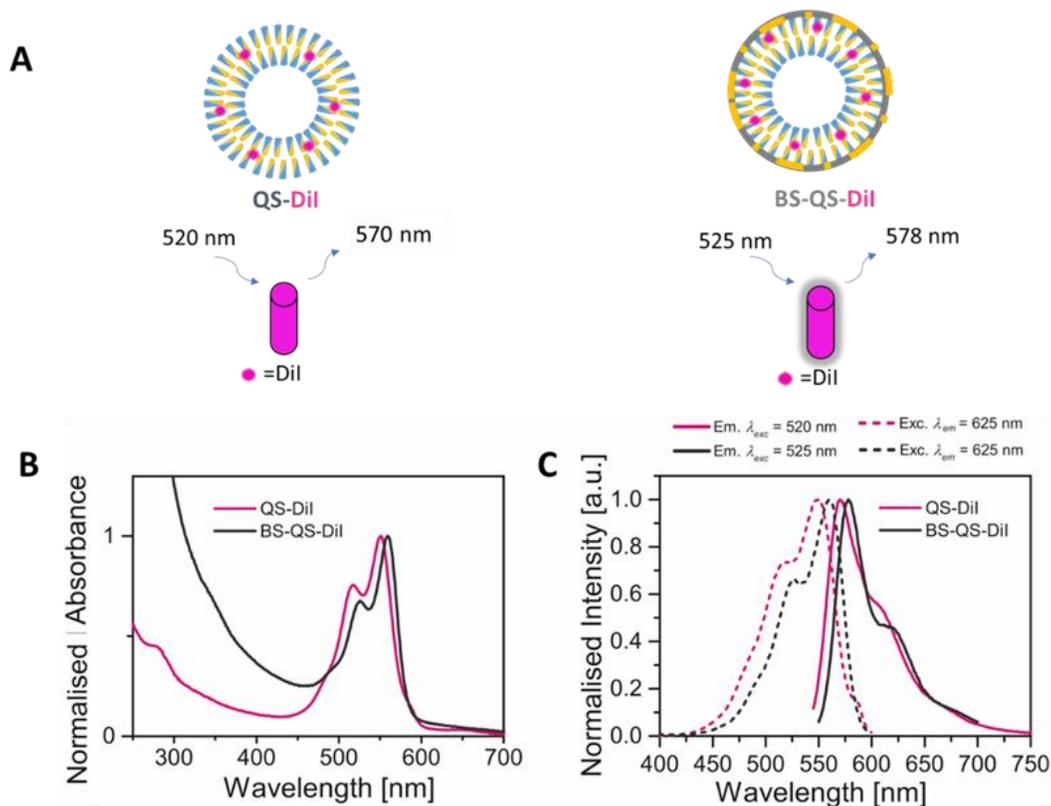**Figure 4.6. A)** Representative diagrams of the fluorescent QS and the schematic representation of the emission of the DiI without and with the breakable silica shell, QS-DiI and BS-QS-DiI, respectively. **B)** Absorbance of the QS-DiI and BS-QS-DiI (pink and gray lines) and **C)** Emission (solid lines) and excitation (slash lines) spectra of the QS-DiI (pink lines) and BS-QS-DiI (gray lines). Wavelength of excitation and emission were 520 and 625 nm, for the QS-DiI system and 525 and 625 nm for the BS-QS-DiI material.

4.2.1.1. Confocal test for different Labeled Coated QS

Different fluorescent-labeled coated QS were analysed in the confocal microscope to have in detail the optical characterization of the systems. Breakable silica-coated QS loaded with DiI (BS-QS-DiI), Cy5 breakable QS (Cy5-BS-QS), Cy5 breakable QS loaded with DiI (Cy5-BS-QS-DiI), and QS with a breakable shell linked covalently with rhodamine B isothiocyanate QS (Rh.B-BS-QS) (**Figure 4.7**) were synthetized and analysed by FRET. Rhodamine B was used as an example of a hydrophilic dye incorporated in the silica shell (excitation and emission wavelength at 546 and 568 nm, respectively).
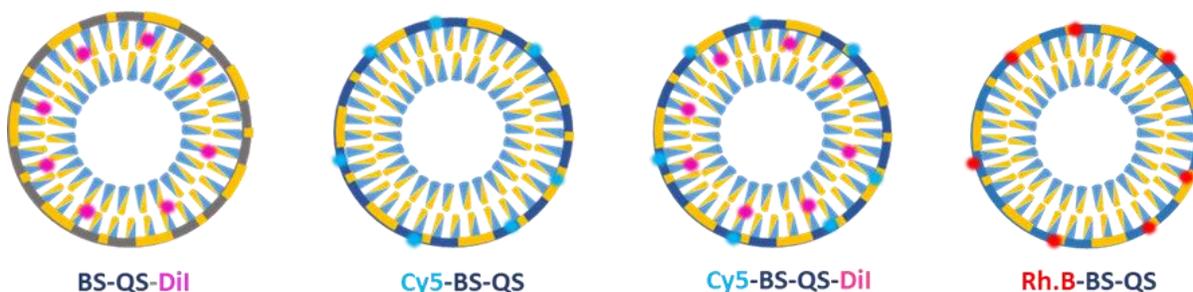
Figure 4.7. Schema of the structure of the labeled silica-coated QS analysed in the confocal microscope.

Figure 4.8 shows the confocal images of the lambda mode of these different labeled silica-coated QS systems. The excitation wavelength used for these experiments was 488 nm. As it is observable from the confocal images and the emission spectra, the systems indeed encapsulated or/and linked the fluorescent molecule in the QS or/and in the silica shell. BS-QS-DiI and Cy5-BS-QS have a maximum emission wavelength at 582 and 689 nm (**Figure 4.8A** and **4.8B** right). The sample Cy5-BS-QS-DiI presents two maximum emission bands at 572 nm and 689 nm, which corresponds to the presence of DiI and Cy5 (**Figure 4.8C**). Finally, the sample Rh.B-BS-QS showed its characteristic pick with a maximum emission wavelength at 572 nm (**Figure 4.8D**). It has to be mentioned that all these samples were synthetized to be also analysed by STORM to have a super-resolution confocal images for the materials. The confocal microscopy images point out the successful loading of the DiI into QS in the sample BS-QS-DiI and Cy5-BS-QS-DiI, and the successful attachment of the Cy5 or Rh.B in the silica shell structure in the Cy5-BS-QS, Cy5-BS-QS-DiI and Rh.B-BS-QS.
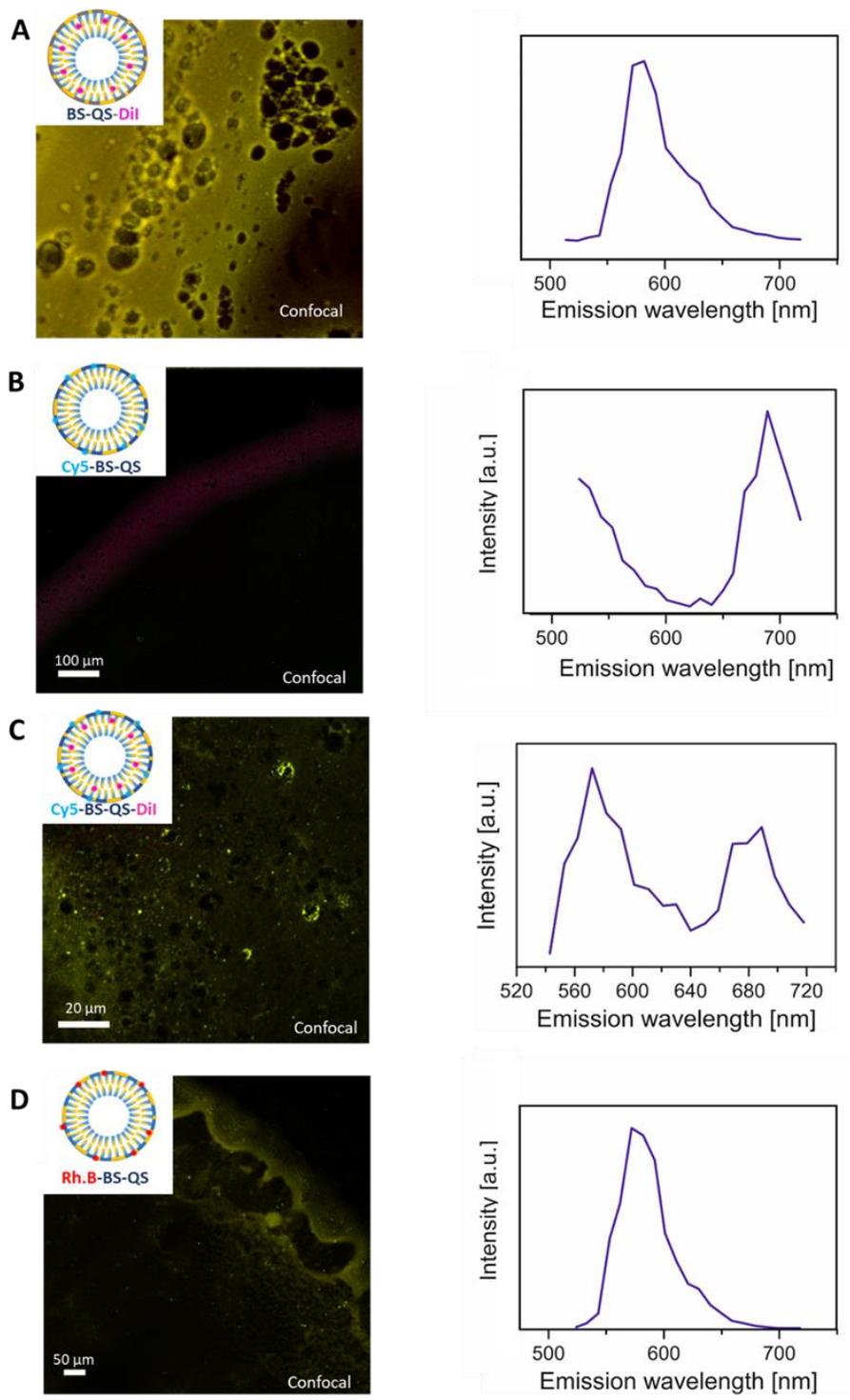
Figure 4.8. Image of the lambda mode and the emission spectra of the **A)** BS-QS-DiI, **B)** Cy5-BS-QS, **C)** Cy5-BS-QS-DiI and **D)** Rh.B-BS-QS. Using the Confocal microscope with a 64x Object. Excitation wavelength: 488 nm.

4.2.1.2. Stochastic Optical Reconstruction Microscopy-STORM ANALYSIS

Fluorescence microscopy is a technique to visualize distributions of fluorescently labeled molecules within a sample in a non-invasive and specific way and is also compatible with complex biological systems like cells or tissues. However, the resolution is limited by the diffraction limit of light to about 200 nm in the lateral imaging plane and to >500 nm in the axial plane.[24] In the past years, a variety of super-resolution techniques were developed circumventing the diffraction limit.[25–29]

Stochastic optical reconstruction microscopy (STORM) is a method for super-resolution imaging based on the high accuracy localization of individual fluorophores. It uses optically switchable fluorophores: molecules that can be switched between a nonfluorescent and a fluorescent state by exposure to light.[30] This "blink" is the activation from an off or dark state, to an on or emission state, quickly followed by a switch back to a dark state or photobleaching (**Figure 4.9**).

The process is called photoswithing[31,32] or photoactivating fluorescent probes, which enables single-molecule detection; in STORM only a small subset of fluorophores is excited in the field at a given time, but the process is repeated thousands of times to compile a full image by stacking sequential frames (imaging cycles). These images have an enhanced resolution about 20 nm.
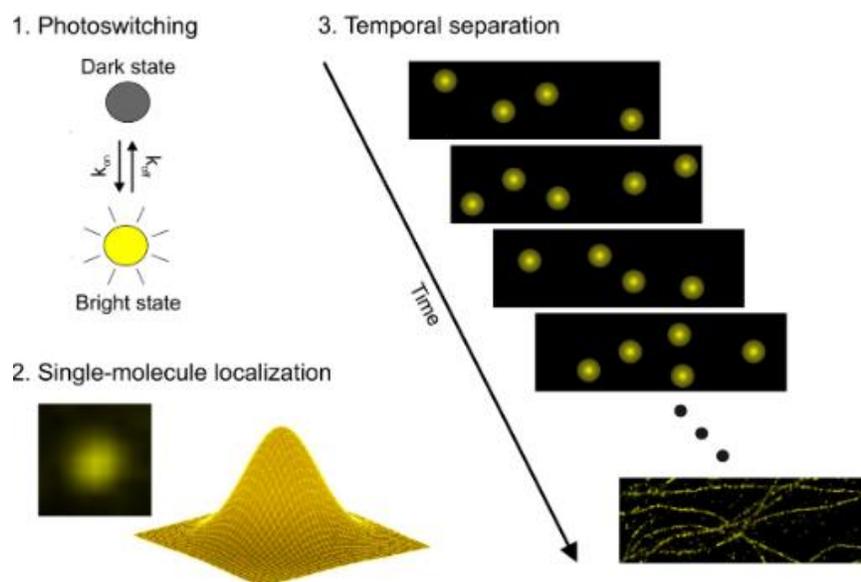
Figure 4.9. STORM analysis. Reconstruction of an image with super-resolution using the photoswitching of fluorophores between a dark site and a bright state. The position of the fluorophores can be then determined in an accurate way during the time; after several cycles of photobleaching the images can then overlap to complete the construction of the full image. Reprinted with permission from the Goethe University. Institute of Physical and Theoretical Chemistry. (Copyright 2015, Goethe University)

The best results taken with this technique was using the system: Cy5-BS-QS-DiI. Briefly, the Cy5-Breakable QS solution was first diluted 1:100. Then, the sample was irradiated with a power laser of 642 nm and the images were recollected during an interval of time.[28] In **Figure 4.10,** the obtained STORM images are shown, where the Cy5 was the dye which was excited using the 642 nm laser. From these results, it is observable that the sample is based on vesicles less than 300 nm, although vesicles around 50 nm were expected. This difference in size could be related to the high brightness of Cy5 dye, and also to its high loading (high local concentration of Cy5 at QS). Considering that STORM is based on the analysis of the photoswitching of one event, the fact of having several dyes blinking at the same time is unfavourable. In order to improve those measurements, another dye should be attached to the silica shell, for instance, Alexa 647. To continue the experiments, breakability tests and permeability tests were done to study these properties in the systems.
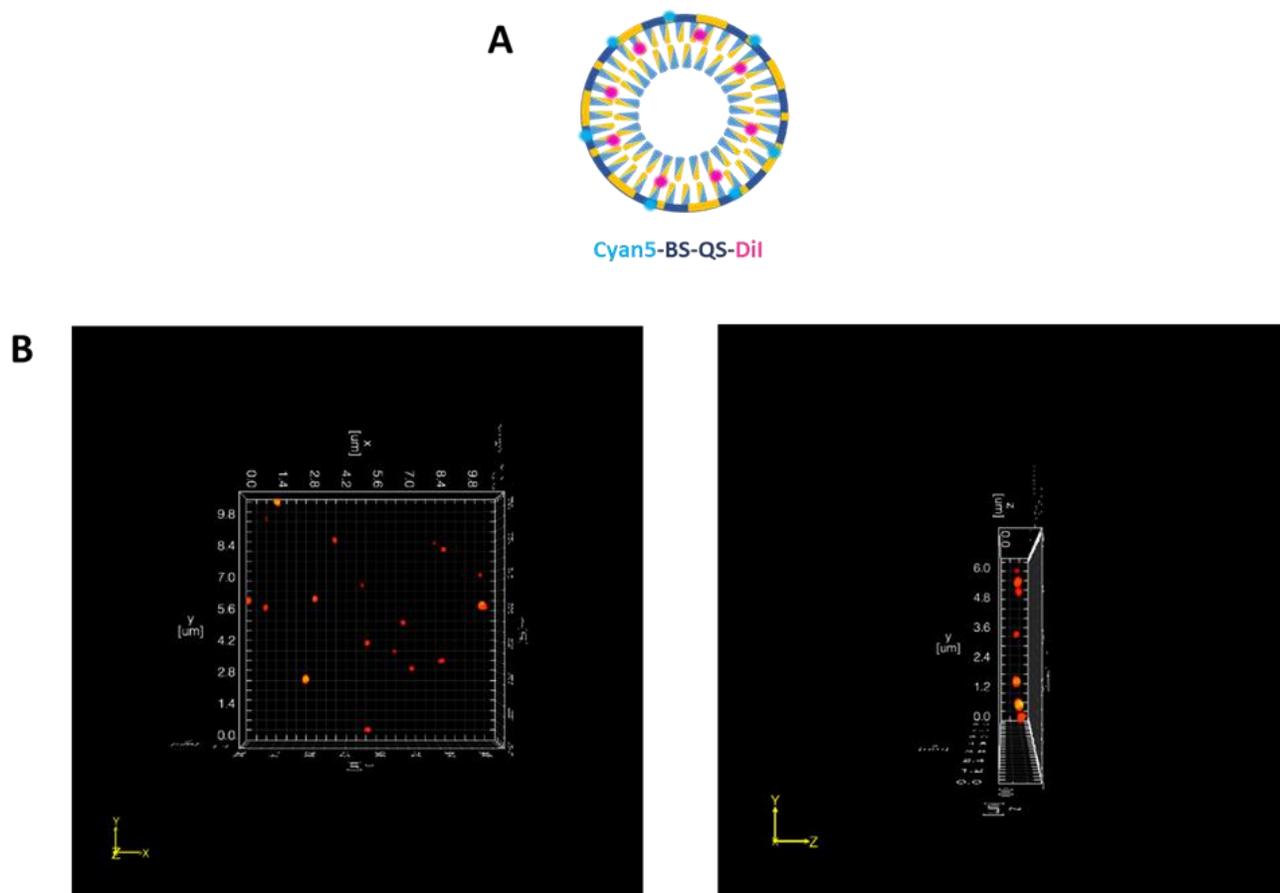
Figure 4.10. A) Scheme of the Breakable QS used for STORM analysis (Cy5-BS-QS-DiI). **B)** STORM images of the of Cy5-Breakable QS (u.m. micrometer).

4.2.2. Breakability test of the Labeled Breakable Coated QS

Cyanine5 breakable silica QS (Cy5-BS-QS) and Cyanine5-Breakable silica-coated DiI-QS (Cy5-BS-QS-DiI) (**Figure 4.11**), were tested in a breakability test in presence of glutathione, called "open system". During 18 days, a solution containing the QS was put in a cellulose membrane of 14 KDa and then, this dialysis membrane was put in a beaker which was containing 10 mM of Glutathione (a reducing agent) where the silica motif with disulfide linkers will consequently break. Then, the small particles of silica coming from the broken silica shell will pass the membrane through the exterior (**Figure 4.12A** and **4.12B**). Additionally, each day of the experiment, an aliquot of the sample contained inside of the dialysis membrane was taken and analysed. For the Cy5-BS-QS system, a decrease of the Cy5 absorbance intensity value was observed. On other hand, in the case of the Cy5-BS-QS-DiI system a decrease of the FRET signal was detected.

Additionally, in **Figure 4.13**, the evolution of the absorbance spectra on time of the Cy5-Breakable silica QS sample during the time experiment is displayed, showing how the main absorption band (λ~659 nm) progressively decreases from 0 to 18 days (**Figure 4.13B**). If the absorbance values at 659 nm are plotted against time, it is observed the decrease of the Cy5 band at 659 nm. After 12 days of exposition of Glutathione, all the Cyanine has gone outside the dialysis membrane. These results provide us a lot of information about the degradation of the breakable system, showing that after 3 weeks, the silica shell was totally broken since Cy5 absorption is vanished due to its degradation in presence of GSH in aqueous media.
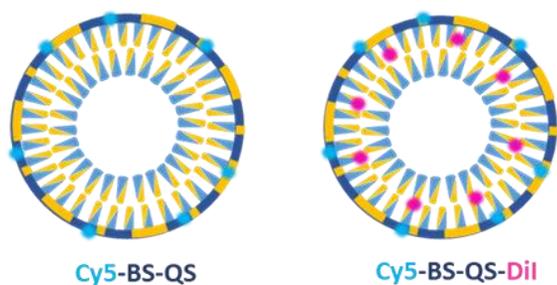
Figure 4.11. Schema of the labeled silica-coated QS used for the breakability test.
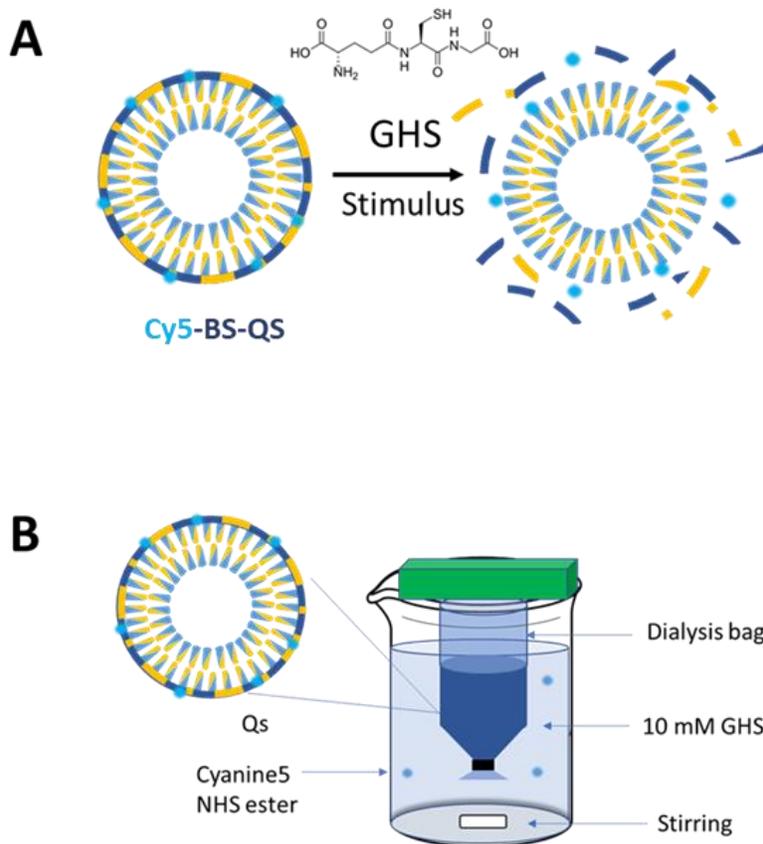
Figure 4.12. A) Bribability picture of the silica shell of the QS under the reducing agent glutathione (GSH**) B)** Experiment diagram for the breakability test (open system).
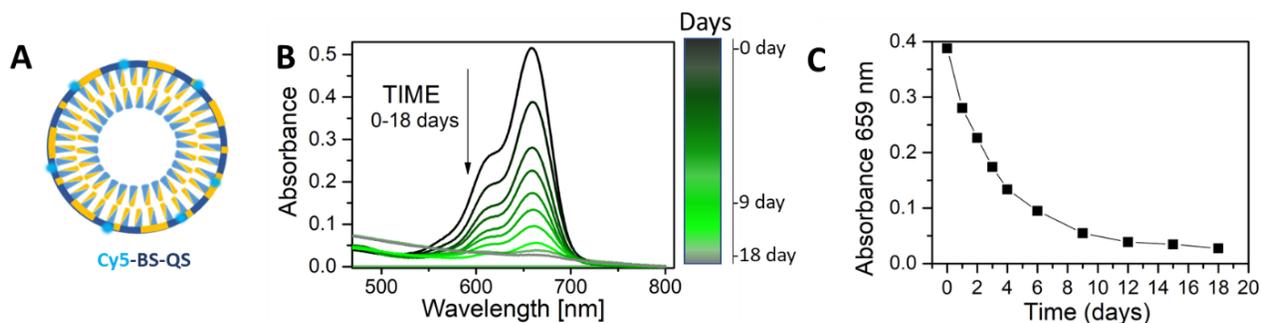
Figure 4.13. A) Scheme of the Cyanine5 Breakable Silica QS (Cy5-BS-QS) **B)** Absorbance spectra of the Cy5-Breakable QS after the time in the presence of 10 mM Glutathione. **C)** Absorbance spectra at 659nm through the time of the Cy5-Breakable QS.

In **Figure 4.14** is presented the results using Cy5-Brekable QS loaded with DiI where the absorbance spectra during the time was plotted to follow the evolution of the band when the Cy5-Brekable QS loaded with DiI was exposed to Glutathione (**Figure 4.14B**), showing an absorbance band decrease during time, from 0 to 18 days. At the same time, **Figure 4.14C** and

4.14D show the plotting graphing at 659 and 562 nm, where it can be observed that after 12 days, the band of 659 nm (related to the presence of Cy5 in the sample) decreases as the dye goes outside of the membrane when the shell was breaking. It is observable that at 562 nm (wavelength attributed to the DiI dye) also decreases by the time. This could be since in the presence of glutathione, the breakable shell of the QS was broken, releasing the Cy5 dye. Then, the Cy5 dye passed outside to the dialysis membrane until it reached an equilibrium (decreasing then the concentration of the dye in all the solution). A possible hypothesis that explains the decrease of DiI is that at the moment that the silica shell is breaking, the shell is not protecting anymore the molecule inside the QS, so having an exchange through the media and consequently, decreasing the absorbance of the band related to the DiI. However, it is not exclusive to think that this decrease of the DiI absorbance band is because of the escape of the DiI-QS outside of the dialysis membrane when doing dialysis over time. As these nanoparticles belong to soft materials, it could be possible that they can be flexible. Then, this flexibility could affect their morphology and consequently, they could cross the membrane.
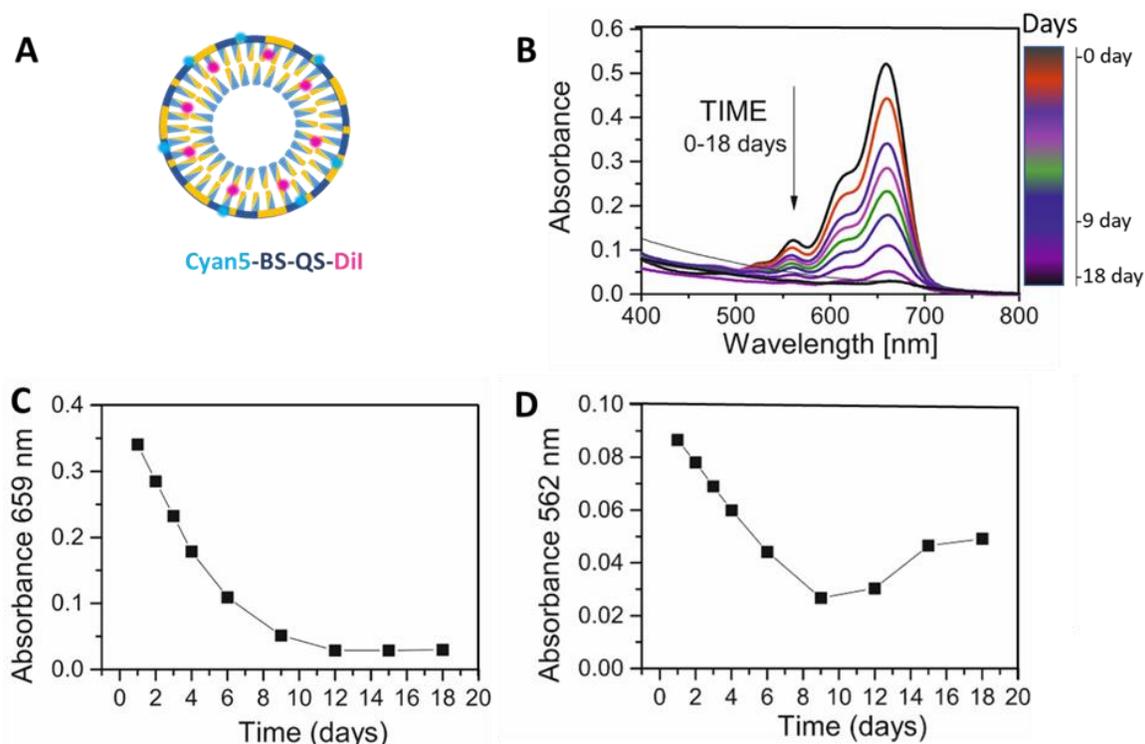
Figure 4.14. A) Scheme of the Cy5-Breakable silica-coated DiI-QS (Cy5-BS-QS-DiI), **B)** Absorbance spectra of the Cy5-BS-QS-DiI after the time in the presence of 10 mM GSH and **D)** Absorbance spectra at 659 nm and 562 nm through the time of the Cy5-Breakable QS loaded with DiI.

To rule out this possibility, the experiment was changed to a named "close system" in which the QS were placed in a quartz cuvette. The experiment was done using Cy5-Breakable QS loaded with DiI and directly putting the Glutathione (10 mM) (**Figure 4.15**). In this experiment, a change of the emission was observed, presenting an increase of the intensity over time (**Figure 4.16A**). The spectra were normalized using the DiI band (562 nm), where the signal of the Cy5 showed an increase in signal over time (**Figure 4.16B**). On the other hand, if the normalization is from the Cy5 maximum emission wavelength (659 nm), the emission corresponding to the DiI also decreases (**Figure 4.16C**). In **Figure 4.16D** is plotted the normalised intensity emission at 562 and 659 nm.
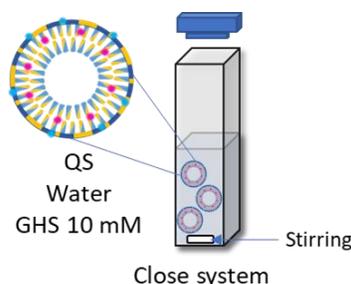
Figure 4.15. Experiment diagram for the breakability test (close system).
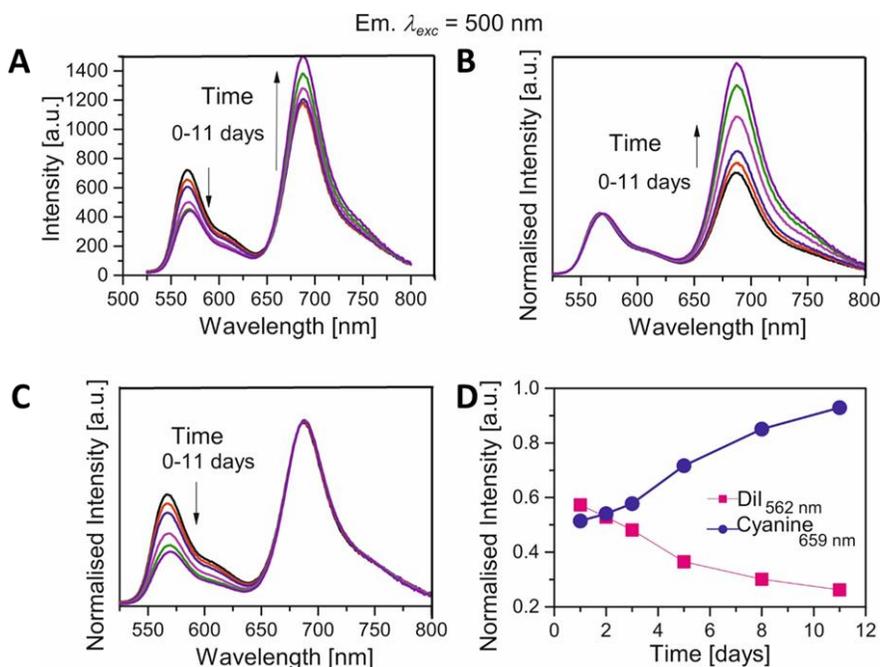
Figure 4.16. A) Emission spectra of Cy5-Breakable QS loaded with DiI after the time in the presence of 10 mM Glutathione. **B)** and **C)** Normalised Intensity of the Emission of Cy5-Breakable QS loaded with DiI normalised by the DiI and the Cy5, respectively. **D)** Normalised intensity of the emission at 562 and 659 nm representing the DiI and the Cyanine5.

Figure 4.17 shows the normalized intensity of the emission at 562 and 659 nm representing the DiI and the Cyanine5 in the Cy5-Breakable QS loaded with DiI after the exposition of Glutathione (10 mM) at different time reactions, 24 and 44 days, and its Acceptor/Donor ratio (A/D, emission wavelength) of the sample at that times. It can be observed that during the reaction time, the maximum emission wavelength of the donor (DiI) decreases while conversely, the emission intensity of the acceptor (Cy5) increases. Additionally, the ratio A/D increases, which means that the energy transfer between them is also enhanced. This observation can be explained as follows: when the silica shell is being broken in the presence of GSH, the Cy5 is released in the medium (detached from the silane matrix) and then, internalized in the hydrophobic part of the QS where the DiI is loaded. Then, it could be detected that both dyes are closer between each other, meaning that shortening the distance between donor and acceptor has shown to have an impact on the energy transfer process producing an increment of FRET (**Figure 4.18**).
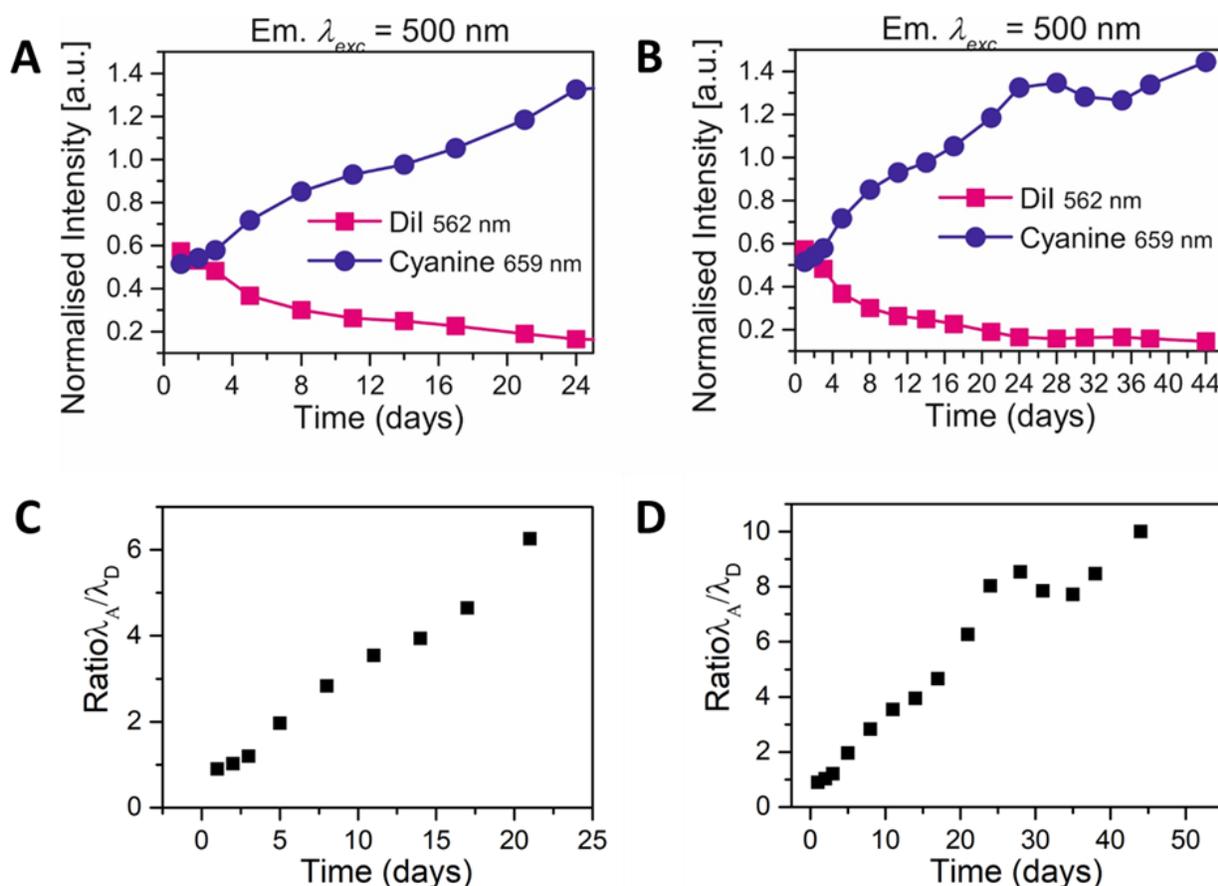
Figure 4.17. A) and **B)** Normalised intensity of the emission at 562 and 659 nm representing the DiI and the Cyanine5 in the Cy5-Breakable QS loaded with DiI after the time in the presence of 10 mM Glutathione after 24 and 44 days, respectively. **C)** and **D)** Ratio Acceptor/Donor of the sample after 24 and 44 days.
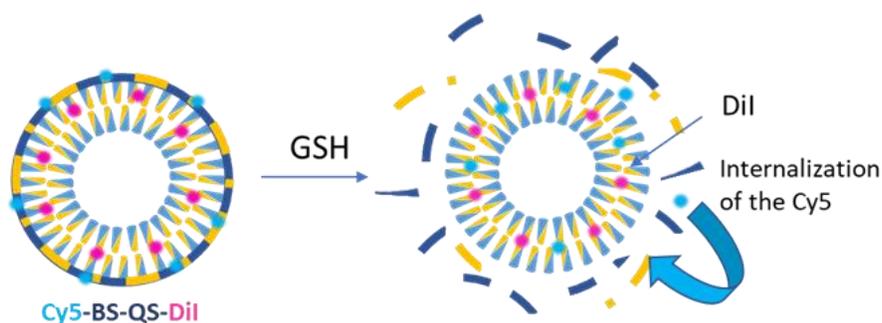
Figure 4.18. Breakability representation of the Cyanine5 Breakable QS loaded with DiI after the presence of Glutathione (GSH).

4.2.3. Permeability test of the Labeled coated QS

In order to know if the Cy5 was entering into the QS, permeability tests were carried out. Then, four systems were compared to identify if the dye was able to permeate the silica shell around the QS. QS loaded with DiI (QS-DiI) were used as a control, two different non-breakable silica coating with QS loaded with DiI and covered with TEOS (TEOS-QS-DiI) and TEMOS (TEMOS-QS-DiI) were employed, and for the breakable system (QS loaded with DiI and covered with BTSPD (Bs-QS-DiI); QS made with TEMOS and BTSPD 30% mol) (**Figure 4.19**). In this case, QS coated with non-breakable silica, using TEMOS, should not incorporate the dye, however, with the system using TEOS, from Cryo-TEM images, it can be observed certain porosity (see **Figure 3.24**). This study provided us information about the porosity of the samples. On the other hand, the system with a breakable silica shell could be more permeable than the system with the non-breakable coating using TEMOS due to its structure, as is less compact due to the BTSPD linker.
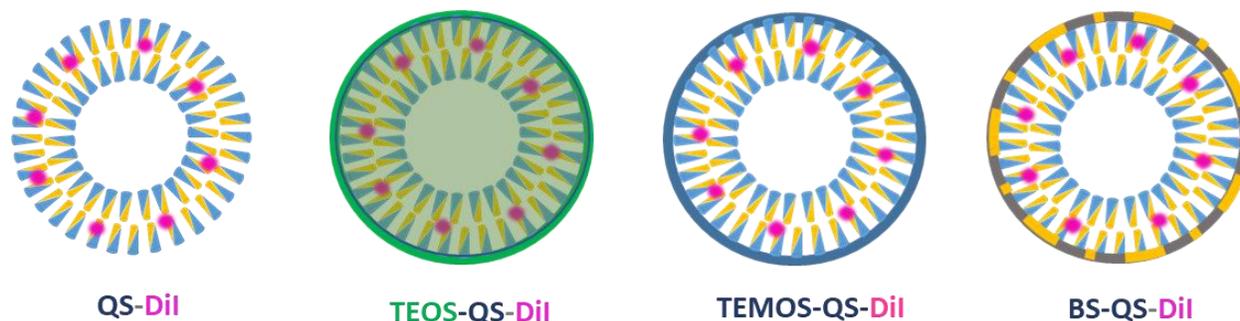
Figure 4.19. Labeled silica-coated QS used for the permeability test. From left to right: QS loaded with DiI, QS loaded with DiI and coated with TEOS (non-breakable shell), QS loaded with DiI and coated with TEMOS (non-breakable shell) and QS loaded with DiI and covered with BTSPD and APTES (breakable silica shell).

263

These different type of QS were put in quartz cuvettes in presence of 10 mM of GSH (same conditions used in the breakability test) and a solution of Cyanine5 NHS ester was added (to have the same concentration as the calculated for the loaded QS covered with Cyanine5 silica shell) (**Figure 4.20**).
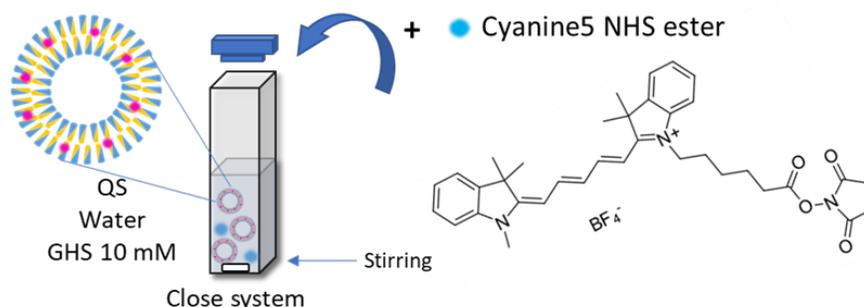
Figure 4.20. Experiment diagram for the permeability test.

Figure 4.21 shows a schema of how permeability tests were carried out and the results obtained for the QS loaded with DiI and not covered with silica under the same conditions used for the breakable systems tested previously in the section 4.2.2. The QS-DiI were introduced in water and 10 mM of GSH in a close system in presence of Cyanine5 NHS ester. This experiment was done in order to study the permeability of the Cy5 to the interior of the QS (**Figure 4.21A**). This study was proposed to understand the interaction observed before between the labeled breakable shell and the Cy5 (interaction caused when the silica shell was breaking in presence of GSH, making then a stronger FRET between the loaded DiI dye and the Cy5). The experiment was carried out for 23 days and the emission spectra was obtained exciting the sample at a wavelength of 500 nm (wavelength chosen to see FRET in the Cy5-Breakable silica-coated DiI-QS (Cy5-BS-QS-DiI)). Additionally, in **Figure 4.21B** and **4.21C** the emission spectra of the sample is shown where the intensity of the DiI and Cy5 is normalised, respectively. The plot in **Figure 4.21B** (normalisation at the Cy5 emission band 664 nm), shows how the emission pick of the DiI (566 nm) is increasing over time, while in **Figure 4.21C** (normalised at the DiI emission band 566 nm), in this case, the emission peak (664 nm) is decreasing over time. The different behavior showed for the previous systems at 566 (DiI) and 664 (Cy5) nm was also plotted in **Figure 4.21D** in which an opposite trend is observed, presenting an increment of intensity for the DiI band and a

decrease in the intensity in the Cy5, meaning that the FRET effect is a decreased over time. On the other hand, in **Figure 4.21E** is shown the evolution of the Ratio Acceptor/Donor of the sample after 24 days. These obtained results are the opposite of hypothesized since if there is not a shell covering the QS, the permeability of the Cy5 might occur and the FRET should increase over time as the two dyes could be closer to each other in the membrane to make a good energy exchange. However, we observed an opposite trend which has an explanation. Moreover, it can believed that the permeation of the Cy5 to the membrane is so fast that when the measurements start, the system is already in a saturation regime (maximum intensity) achieving a maximum FRET effect at the starting point of the study. Additionally, if one of the dyes starts to degrade, like is believed in DiI, that could produce a diminution of the energy transfer to the Cy5.

Figure 4.21. A) Experiment diagram for the permeability test using QS-DiI (without silica coating). **B)** and **C)** Normalised Intensity of the Emission of the QS-DiI; normalised by the Cyanine5 and the DiI, respectively. **D)** Normalised intensity of the emission at 566 and 664 nm representing the DiI and the Cyanine5. **E)** Ratio Acceptor/Donor of the sample after 24 days.

The second hypothesis could be that with time the DiI migrates outside of the QS shell (to have an interchange with the exterior) and then consequently the FRET deceases. When the migration occurs, the distance between the two dyes increase and the energy transfer is not observed. Although a clear conclusion is not possible with these preliminary experiments, additional

experiments and simulations would be needed to enlighten the behaviour of Cy5 under these conditions.

In **Figure 4.22** is shown the permeability results using the QS loaded with DiI and covered with TEOS (TEOS-QS-DiI). These studies were carried out under the same conditions that the previous experiment (QS in water and 10 mM of GSH in a close system) (**Figure 4.22A**). The experiment was monitored for 7 days because almost no change was shown in the emission band for the DiI and the Cyanine5, exciting at 500 nm. **Figure 4.22B** and **4.22C** shows the normalised intensity of the emission spectra of the TEOS-QS-DiI normalised at the Cy5 and the DiI, respectively. In this case, there is not a major change in the emission spectra, even though, a tendency is observed. However, the emission band of the DiI (maximum wavelength at 566 nm) is slightly increasing over time while in **Figure 4.22C** (normalised by the DiI) the emission peak of Cy5 is decreasing (maximum wavelength at 669 nm). In **Figure 4.22D** is plotted the normalised intensity of the emission at 566 and 669 nm in which the DiI and the Cy5 plots show a little bit of increase and decrease of the DiI and the Cy5 band, respectively. On the other hand, **Figure 4.22E** shows the ratio between the acceptor and the donor of the sample after 7 days. If the data are graphed at the same scale that was used for the permeability test for the QS-DiI, it can be observed that the FRET effect remains constant. In this case, FRET effect was helpful to understand the behaviour of this material, since the silica is permeable and it could contain the dye in the porous. Also, the results provide enough information to validate our hypothesis in which the Cyanine5 permeates in the shell and it is enough close (<10nm) to interact with the DiI. For this reason, the FRET signal is kept constant and a decrease or increase of the FRET is not observed, meaning that the non-breakable silica shell containing TEOS protects the interchange of Dyes and their stability in the QS.
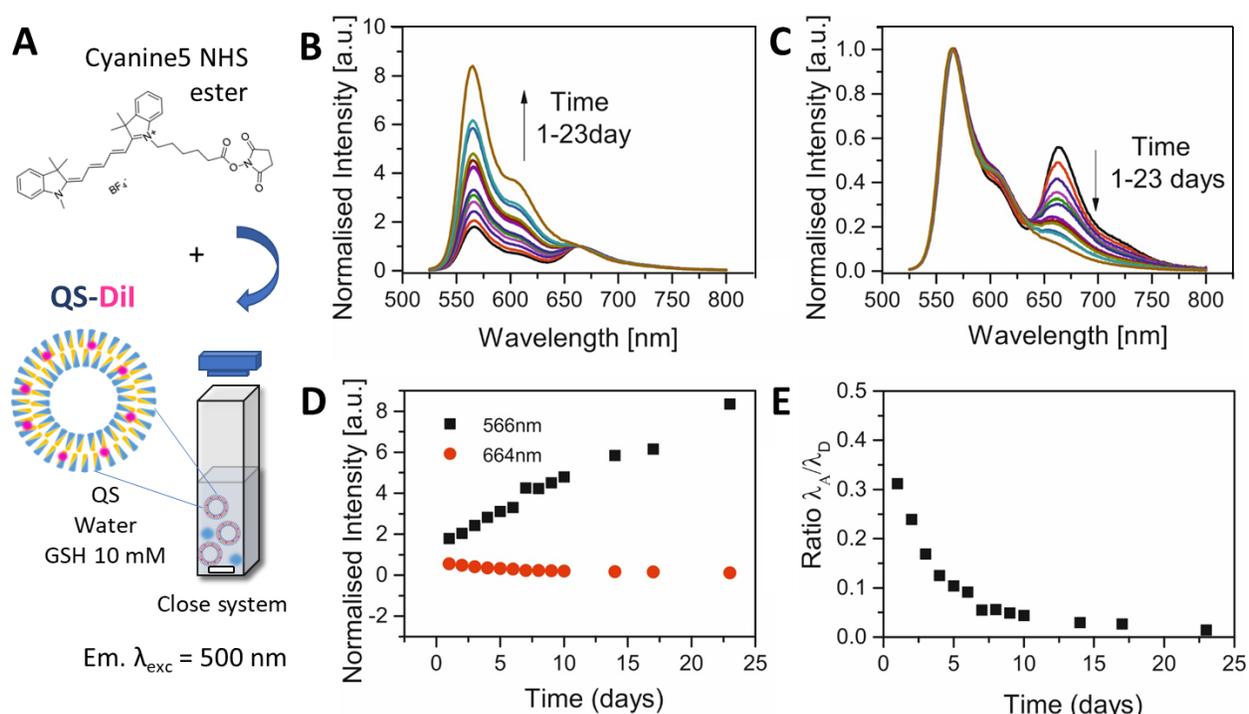
Figure 4.22. A) Experiment diagram for the permeability test using TEOS-QS-DiI (non-breakable). **B)** and **C)** Normalised Intensity of the Emission of the TEOS-QS-DiI; normalised by the Cyanine5 and the DiI band, respectively. **D)** Normalised intensity of the emission at 566 and 669 nm representing the DiI and the Cyanine5. **E)** Ratio Acceptor/Donor of the sample after 7 days.

To study the permeability test in other non-breakable silica shell system, the shell synthesized using TEMOS (in which Cryo-TEM images presented like a ring outside the QS) was studied. Also, the same conditions of the previous experiment were carried out. To carried out, a solution of Cyanine5 NHS ester was put in QS, 10 mM of GSH in water and under stirring. The solution was monitored for 7 days by fluorescence, analysing the emission exciting the sample at 500 nm (**Figure 4.23A**). Normalised intensity of the emission of the TEMOS-QS-DiI was plotted, normalised by the Cy5 and the DiI as it can be seen in **Figure 4.23B** and **4.23C**, respectively, in which small changes in the DiI and Cy5 band were monitored over the time. These figures show that when the spectrum was normalised by the maximum at 663 nm, the band at 565 nm increases. However, when the spectrum was normalised by the maximum at 565 nm, the band at 663 decreases. In **Figure 4.23D** is displayed the normalised intensity of the emission at 565 and 663 nm representing the DiI and the Cy5 evolution. The results were represented in the **Figure 4.23E**, the value obtained from the ratio Acceptor/Donor of the sample after 7 days decreases

267

over time. With all these data, we concluded that the non-breakable silica shell protects the two dyes (the Cy5 is in equilibrium). Over time, the DiI dye could be degraded or forming agglomerates outside the QS (precipitates), which could explain why the FRET starts to decrease, reflecting in a lower energy transfer between the DiI to the Cy5. However, we believe that is important to consider the slight change on these emission bands which could confirm that the silica shell is protecting the fluorescent QS, and thus, DiI is being protected from degradation and also the exchange DiI-Cy5 is avoided.
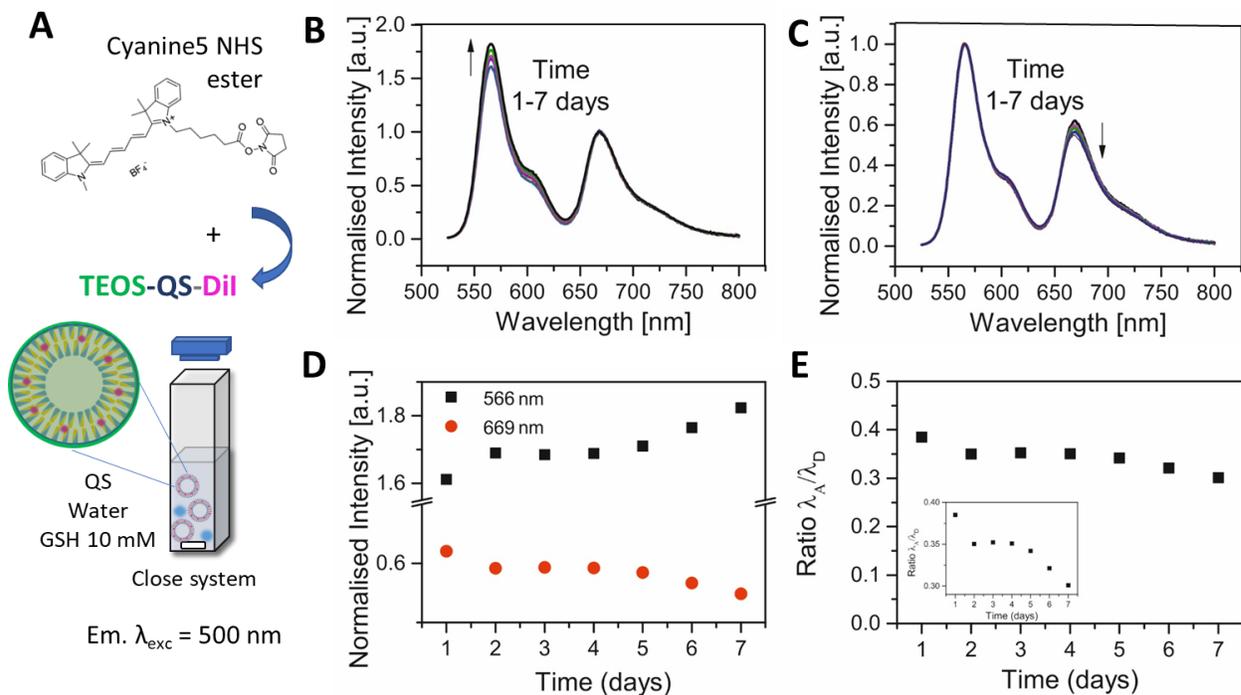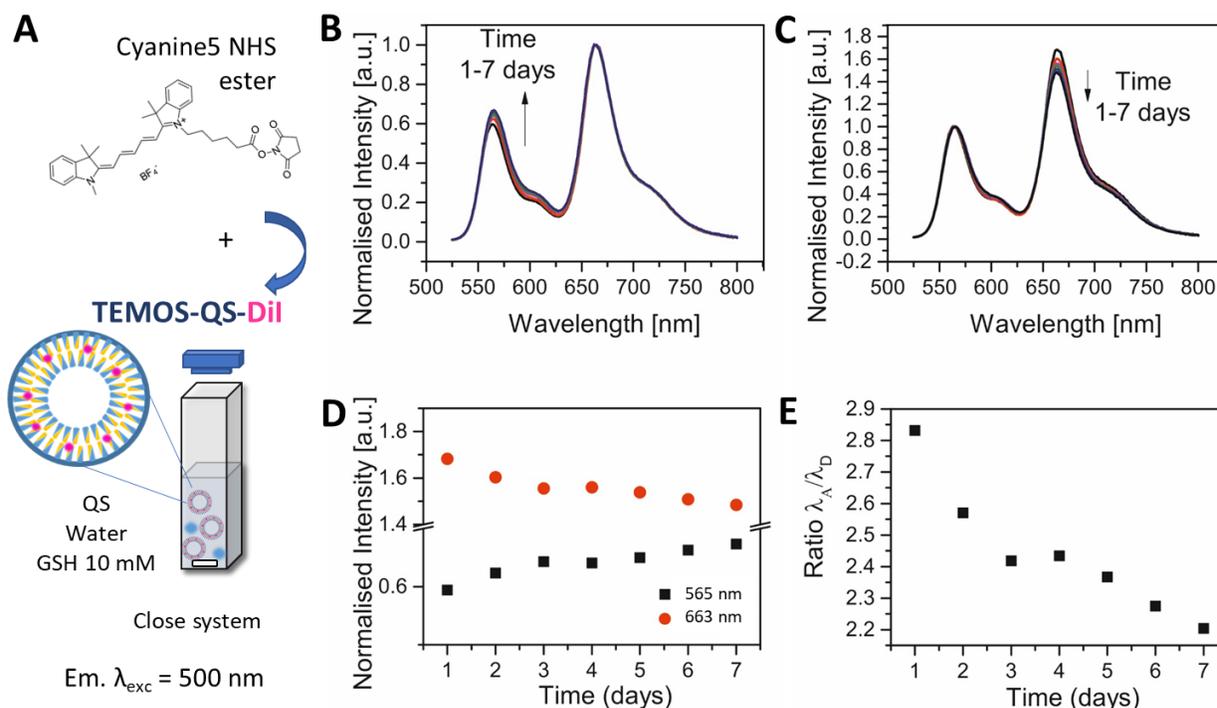

Figure 4.23. A) Experiment diagram for the permeability test using TEMOS-QS-DiI (non-breakable). **B)** and **C)** Normalised Intensity of the Emission of the TEMOS-QS-DiI; normalised by the Cyanine5 and the DiI band, respectively. **D)** Normalised intensity of the emission at 565 and 663 nm representing the DiI and the Cyanine5. **E)** Ratio Acceptor/Donor of the sample after 7 days.

Finally, to conclude this set of experiments, another system was run in parallel and its results will be discussed. Permeability test using a breakable silica shell of QS loaded with DiI was studied (BTSPD-QS-DiI) following the previous experimental conditions (see **Figure 4.24A**) for 7 days. **Figure 4.24B** and **4.24C** shows the normalised intensity of the emission of the sample (exciting at 500 nm) and normalised by the Cy5 and the DiI, respectively, which could be seen as in the

previous cases, that the increase of the DiI pick (normalising at 678 nm) and the decrease of the Cy5 band (normalising at 575 nm) is small (**Figure 4.24D**). However, the change in the acceptor/donor ratio is the biggest observed from the samples tested in this experiment (changing from 18.2 to around 15). Also, it is observed a decrease in the FRET effect (**Figure 4.24E**) over time. It has to be highlighted that, from all the silica shell QS, the BTSPD-QS-DiI system showed the strongest energy transfer in the first steps of the reaction (the band at 678 is much bigger than the band at 575 nm) (see **Figure 4.24B**, **4.22** and **4.23B**). This could be since the shell is breakable, so, the Cy5 and DiI are more prompt to interact, and thus, giving a higher energy transfer.
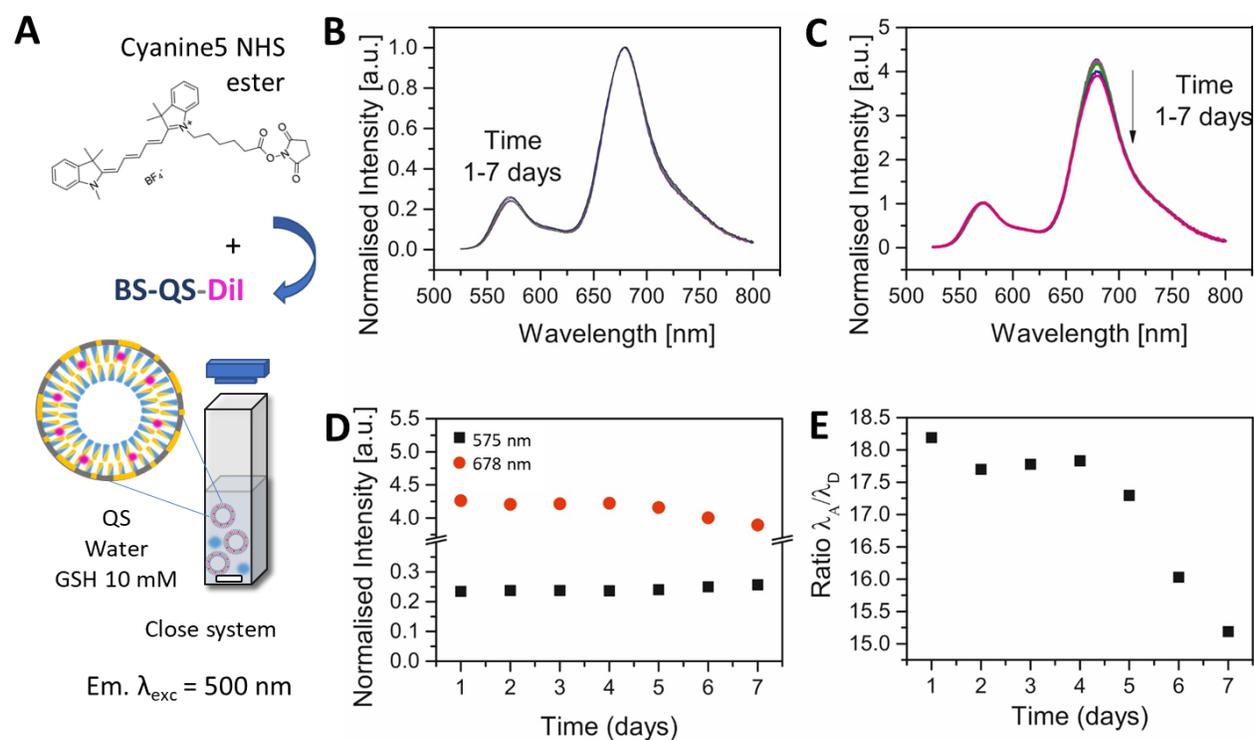
Figure 4.24. A) Experiment diagram for the permeability test using BTSPD-QS-DiI (breakable shell). **B)** and **C)** Normalised Intensity of the Emission of the BTSPD-QS-DiI; normalised by the Cyanine5 and the DiI band, respectively. **D)** Normalised intensity of the emission at 575 and 678 nm representing the DiI and the Cyanine5. **E)** Ratio Acceptor/Donor of the sample after 7 days.

On the other hand, comparing the emission bands of the different silica shell QS systems (**Figure 4.22B, 4.23B** and **4.24B**), from the TEOS-QS-DiI, TEMOS-QS-DiI, and BTSPD-QS-DiI systems, it can be observed that from the non-breakable silica QS (TEOS-QS-DiI and TEMOS-QS-DiI), the TEMOS-

QS-DiI shows a stronger FRET effect (the ratio of the Cy5 pick in relation with the DiI pick is bigger). In this case, the acceptor/donor ratio value was 2.8 for the TEMOS-QS-DiI system, while for the TEOS-QS-DiI ratio value was 0.4. This could give an idea about the thickness of the shell since if there is a stronger FRET effect, then the thickness of the shell should be smaller than the lower FRET respond, because the dyes have a higher interaction giving higher energy transfer. It has to be remembered that from the TEM and Cryo-TEM images of the TEOS and the TEMOS shell, a different kind of deposition around the QS was observed. This different deposition could give the idea that the TEOS shell is thicker than the TEMOS shell. The explanation for this hypothesis is that the contrast of the image reveals that dark porous spheres represent a thicker shell around the QS while the thin shell is present as a ring outside the QS (see **Figure 3.24** and **3.29** for the formation of the silica shell using TEOS and TEMOS, respectively).

As a conclusion of this experimental part, it can be seen that the silica shell with TEOS-QS-DiI, TEMOS-QS-DiI, and BTSPD-QS-DiI protects the dyes entrapped at the QS nanostructure (**Figure 4.22B**, **4.23B** and **4.24B**), while that the no-coated QS are present a big change in the emission bands (DiI and Cyanine) during the test. For that reason, it should be recommended to study in further experiments the reason why the FRET in the system without shell shows a decrease over time (**Figure 4.21C**), since up to now, one of our main hypotheses is related to the higher degree of DiI degradation when is unprotected.

Doing a complementary study, the QS loaded with DiI in PBS and stirred was also analysed during 391h (during almost 16 days). In this experiment, only DiI was present in the sample, thus, its emission band was followed on time demonstrating a progressive decrement in the absorbance band (**Figure 4.25**). This means that under experimental conditions, the emission of the DiI is quenched, probably it due to DiI degradation or quenching, as explained below:

a) The dye is degrading because of the experimental conditions (i.e stirring conditions, media...)

b) Considering that DiI is a hydrophobic dye, once it is placed in aqueous media, it tends to form aggregates due to the strong π-π interactions. Thus, if the QS are broken and DiI is released, it makes sense to conclude that aggregates could be formed in the reaction media causing a lost in its fluorescent properties.

At the same time, although there exist enough evidence to understand the behaviour of the QS-DiI, which can break under the tested experimental conditions a better experiment should be carried out to comprise the stability of these systems under GSH in the presence or not of PBS media. These experiments could give more information of these vesicles behaviour and could be extrapolated to the fact that the QS with non-breakable silica shell do not present a significant change of FRET, meaning that the silica shell protects the QS from breaking.
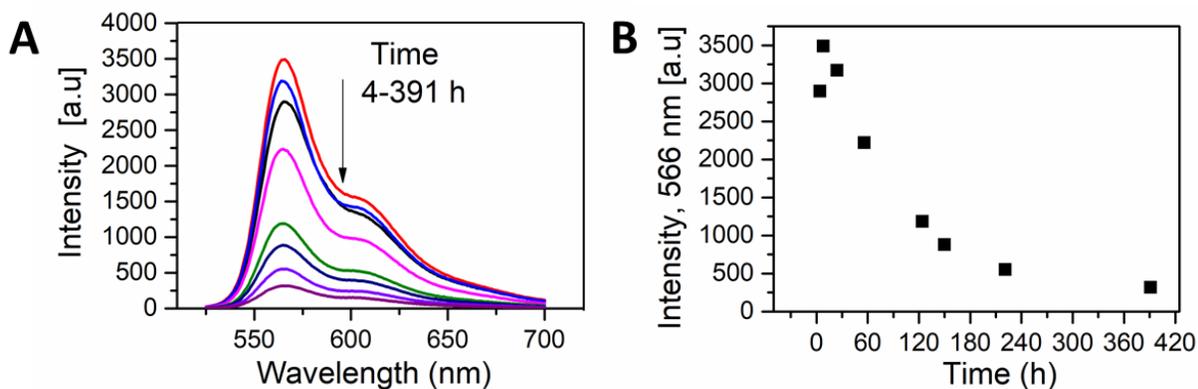
Figure 4.25. A) Emission of the QS loaded with DiI and put them in PBS and stirring up 391 h. **B)** Intensity at 566 nm of the QS-DiI during the time.

4.2.4. Breakability test of the Labeled Breakable Coated QS using metabolic conditions

The breakability test using metabolic conditions; breakable QS were studied in presence of PBS, with 10 mM GSH and at 37 °C in a close system. The breakable silica shell QS studied were the QS loaded with DiI and covered with a breakable silica shell labeled with Cy5 NHS ester (Cy5-BS-QS-DiI) and QS loaded with DiI and covered with breakable silica labeled with Sulfocyanine5 NHS ester (Sulfo-Cyan5-BS-QS-DiI). The sulfo-cyanine5 dye was studied as more hydrophilic dye to compare with the Cyanine5 due to the sulfo groups, which may change the behaviour after the shell breaks into the hydrophobic layer due to the internalization of the dye. Non-breakable sulfo-Cyanine silica shell QS loaded with DiI (Sulfo-Cyan5-TEMOS-QS-DiI) were also synthesized and analysed in parallel with these experiments as a control in the presence GSH or not in the same conditions (**Figure 4.26**).
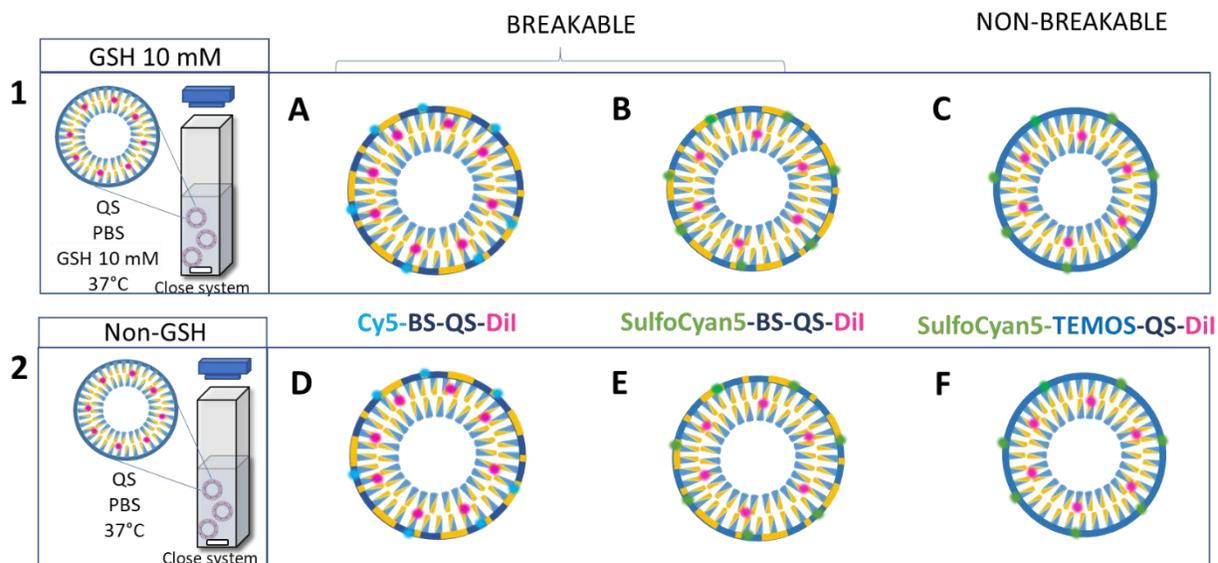
Figure 4.26. Breakability test under metabolic conditions PBS and at 37 °C in **1)** presence of GSH and **2)** non-GSH for breakable and non-breakable silica QS shell A) and B) and C), respectively for Cy5-BS-QS-DiI, Sulfo-Cyan5-BS-QS-DiI and Sulfo-Cyan5-TEMOS-QS-DiI.

The experiment was carried out for 9 days and the emission of the sample was taken exciting at 500 nm. Then, after analysing the results, breakable silica shell QS showed two different tendencies:

a) From 0 to 6 days (for the experiments in the presence and absence of GSH) is observed a decrease in the DiI band at 568 nm and an increase in the Cyanine5 band at 686 nm.

b) From 6 to 9 days is observed an opposite behaviour compared to the previous, an increase in the DiI band and a decrease in the Cyanine5 band was detected, as it can be seen in **Figure 4.27**, **4.28A** and **4.28D**.

Similar tendency is presented using the sulfo-cyanine5 breakable silica shell QS. In presence of GSH, there is a decrease in the emission band for the DiI at 559 nm from 0 to 4 days, while the sulfo-cyanine band (687 nm) increases up. After 6 days, the trend is the opposite, showing an increase of the DiI band and a decrease of the sulfo-cyanine band (**Figure 4.27** and **4.28B**). For these systems in absence of GSH, the band for the DiI emission decreases from 0 until 6 days and after this time increases, while the band for the sulfo-cyanine in from 0 to3 days increases and after 3 days decreases (**Figure 4.27** and **4.28E**).
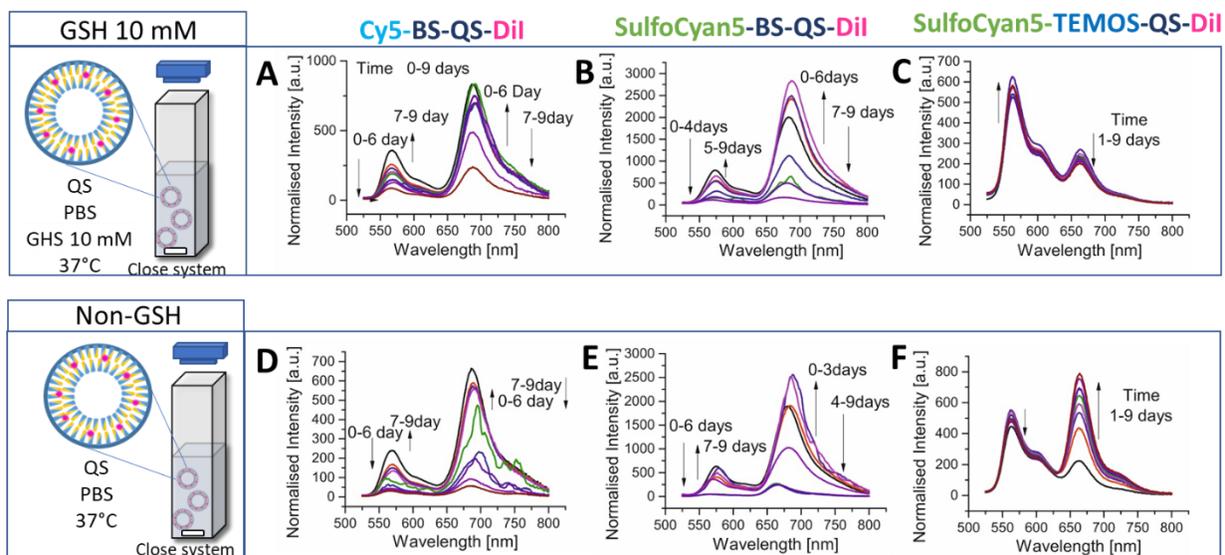
Figure 4.27. Emission (excitation wavelength 500 nm) for the Cy5-BS-QS-DiI, Sulfo-Cyan5-BS-QS-DiI, and Sulfo-Cyan5-TEMOS-QS-DiI in presence of GSH **A), B)** and **C)**; and with non-GSH **D), E)** and **F)**, respectively.

The consistency of this observation for the different systems seems to indicate that at the first steps there is an increment in the FRET signal (**Figure 4.29A, 4.29B, 4.29D** and **4.29E**), while after approximately 6 days; there is a diminution of the FRET signal. This suggests that two different processes are going on. In the beginning, it was thought that the increment in the FRET signal was because the shell was breaking and the cyanine5 was getting inside of the hydrophobic membrane (**Figure 4.29A**). Likewise, the sulfo-cyanine produces an increase even it is more hydrophilic and is negatively charged which can interact with the positive charge of the CTAB of the QS, increasing then the FRET signal (**Figure 4.29B**). After some time, the second process appears presenting a decrease of the FRET signal that could be due to the DiI degrading/forming aggregates (**Figure 4.25**). The QS in presence of PBS can break causing then the aggregation of the dye and the subsequently quenching and finally precipitation. **Figure 4.30, 4.31** and **4.32** show the absorption taken by UV-Vis, the plotted for the cyanine band and the pictures after time, where is visible how the absorbance of all these systems decreases over time due to the precipitation (**Figure 4.32A** and **4.32B**). The same fact is observed for the vesicle systems based on Cy5-BTSPD-QS-DiI and SulfoCyan5-BTSPD-QS-DiI in absence of GSH (**Figure 4.28** and **4.32D** and **4.32E**), pointing out that the most probable thing is that the PBS is playing a role in the

273

breakability of the system. Consequently, it can be suggested that probably the QS are unstable under these experimental conditions and that the shell is thin enough to be broken. Then, the PBS could produce the release of the QS after some time and also the DiI precipitation causing a decrease in the FRET effect.
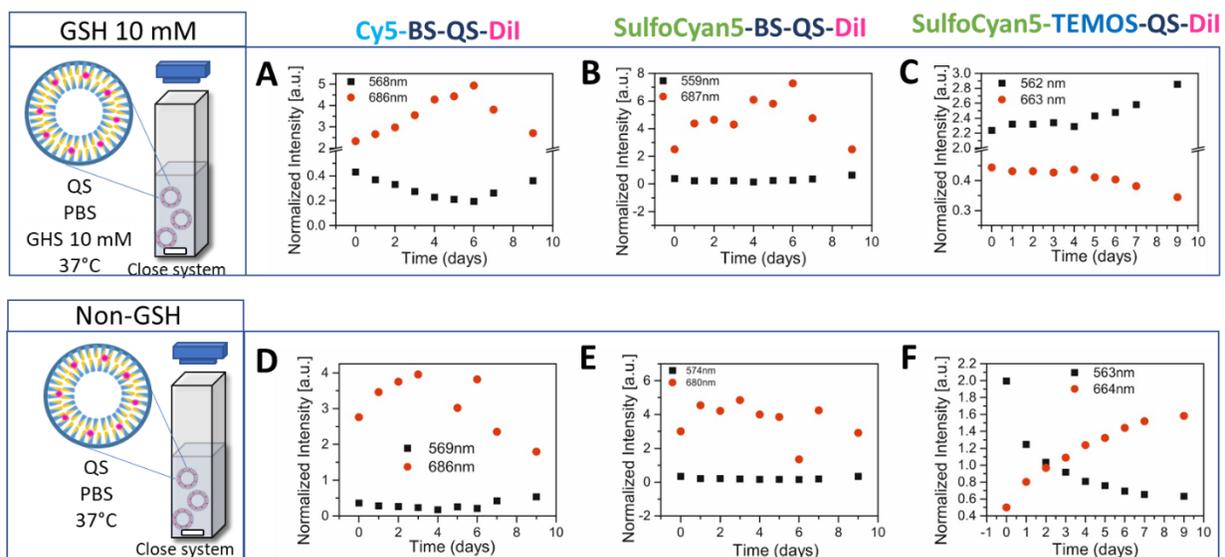
Figure 4.28. Normalised intensity of the emission at the maximum wavelength for the DiI and Cyanine5 for the Cy5-BS-QS-DiI, Sulfo-Cyan5-BS-QS-DiI, and Sulfo-Cyan5-TEMOS-QS-DiI in presence of GSH **A), B)** and **C)**; and with non-GSH **D)**, **E)** and **F)**, respectively.

Moreover, it must be discussed that the breakability of the QS can take some time, around 6 days, and during this period the silica shell protects the QS. The explanation to understand the experiment of the permeability of the Cyanine done just for the QS loaded with DiI and without any silica shell (**Figure 4.21**) is that, without the silica shell, the QS are breaking and releasing the DiI, so a diminution of the FRET effect is observed.

Returning to the breakability experiment, a control was also prepared. Non-breakable silica shell was prepared with TEMOS (presenting a ring outside the QS seen by Cryo-TEM images (see **Figure 3.29**). Additionally, Sulfo-Cyan5-TEMOS-QS-DiI was analysed in the presence and absence of GSH (**Figure 4.27-4.32C** and **4.32F**). The emission of the QS in presence of GSH shows a very small change up the time, increasing the emission pick for the DiI at 562 and decreasing in the emission pick of the Cy5 band at 663 nm (**Figure 4.28C**). The acceptor/donor plot does not show any change, so the FRET is stable up the time (**Figure 4.29C**) since is consistent with the idea that under

these conditions, non-breakable silica shell should not break (see **Figure 4.31C**, UV-Vis results for this sample). The pictures of the **Figure 4.32C** show homogeneity of the solution where it is not visible any precipitate due to the fact that QS with TEMOS are not breaking.

Figure 4.29. Acceptor/Donor ratio of the sample after 9 days for the Cy5-BS-QS-DiI, Sulfo-Cyan5-BS-QS-DiI, and Sulfo-Cyan5-TEMOS-QS-DiI in presence of GSH **A), B)** and **C)**; and with non-GSH **D)**, **E)** and **F)**, respectively.

Finally, the system of Sulfo-Cyan5-TEMOS-QS-DiI in absence of GSH was also analysed. Surprisingly, this system shows a decrease in the DiI band at 563 nm and an increase in the sulfo-cyanine band at 664 nm as seen in **Figure 4.27E** and **4.28E**. Additionally, an increase of the FRET signal appeared (**Figure 4.29E**), which was not expected as these systems are non-breakable. Analysing the **Figure 4.31E** and **4.32E,** the sulfo-cyanine5 response does not change over time and any presence of precipitation was observed.

Up to this point, it can be concluded that the labeled breakable silica shell, under metabolic conditions, breaks giving different trends of FRET signal during the time depending on the experimental conditions. However, this part of the work is not already closed and new experiments will be carried on to understand the breakability of the system which will be analysed by DLS, Z-potential and Cryo-TEM.
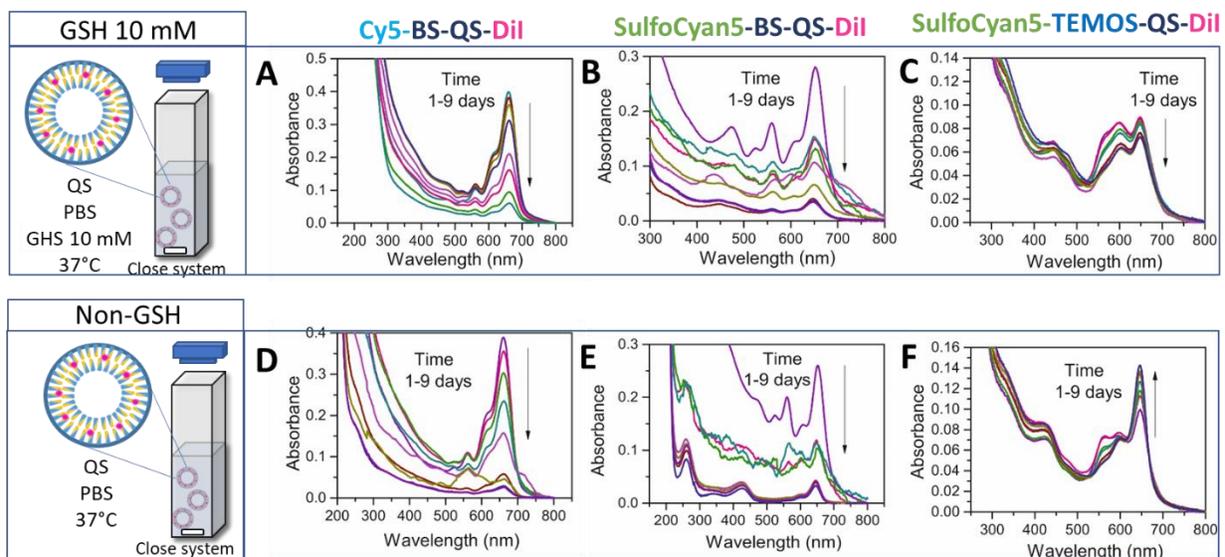
Figure 4.30. Absorbance of the sample during 9 days for the Cy5-BS-QS-DiI, Sulfo-Cyan5-BS-QS-DiI, and Sulfo-Cyan5-TEMOS-QS-DiI in presence of GSH **A), B)** and **C)**; and with non-GSH **D)**, **E)** and **F)**, respectively.
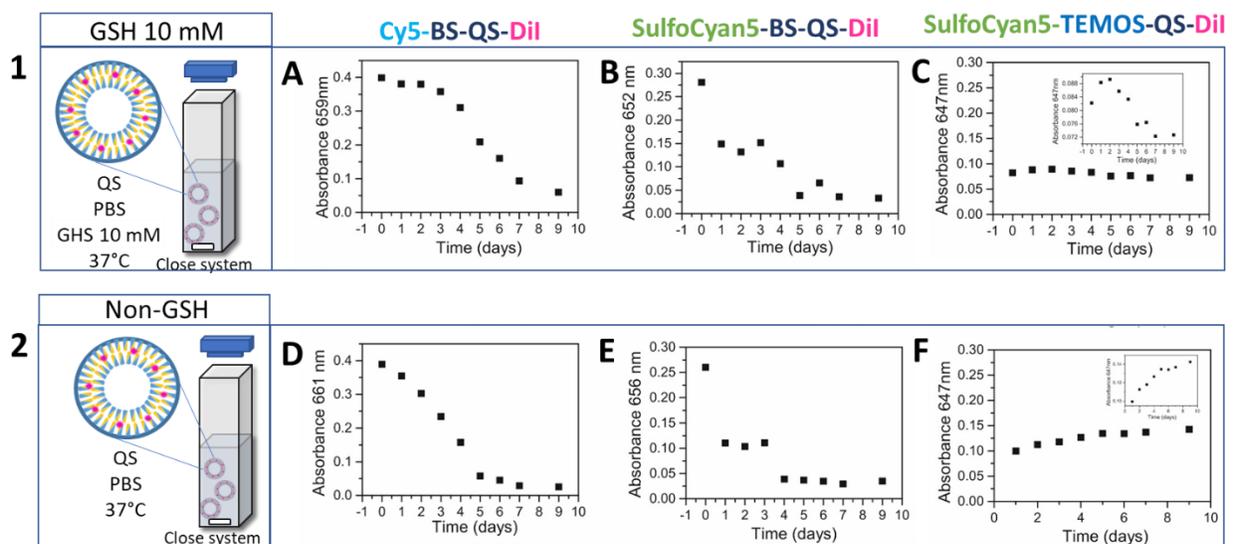
Figure 4.31. Absorbance of the maximum wavelength (Cy5) during 9 days for the Cy5-BS-QS-DiI, Sulfo-Cyan5-BS-QS-DiI, and Sulfo-Cyan5-TEMOS-QS-DiI in presence of GSH **A), B)** and **C)**; and with non-GSH **D)**, **E)** and **F)**, respectively.
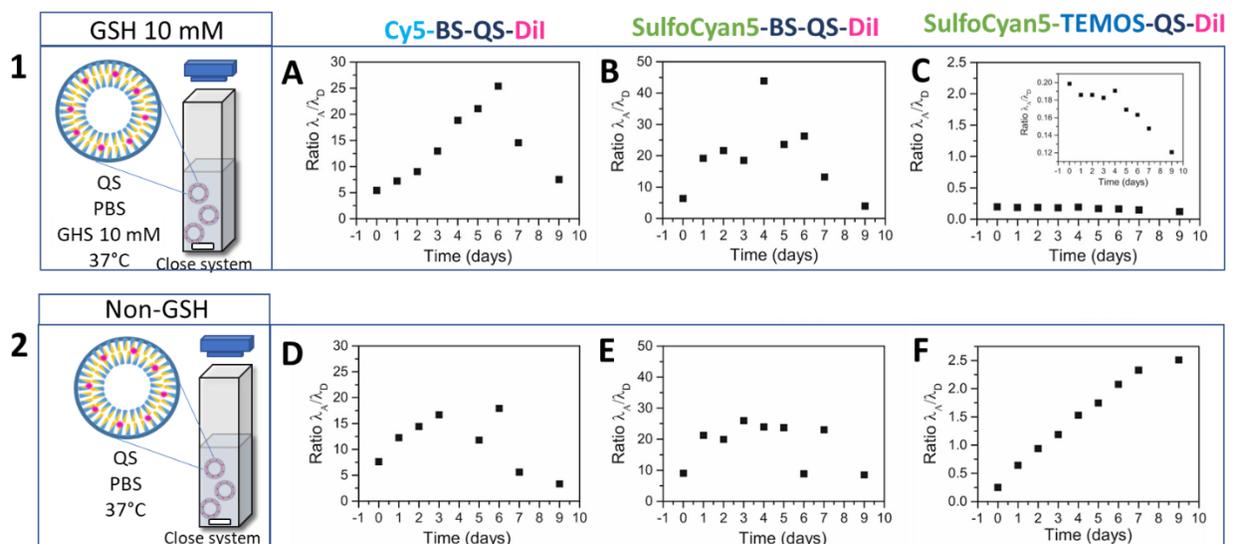
276
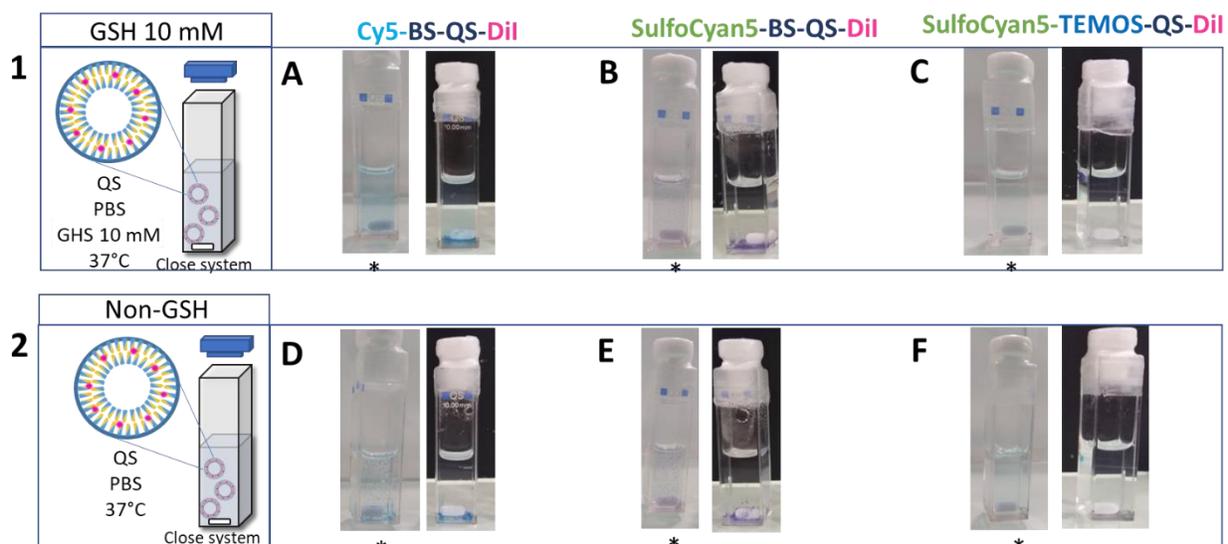
Figure 4.32. Pictures of the samples after 9 days for the Cy5-BS-QS-DiI, Sulfo-Cyan5-BS-QS-DiI, and Sulfo-Cyan5-TEMOS-QS-DiI in presence of GSH **A), B)** and **C)**; and with non-GSH **D), E)** and **F)**, respectively.*Images were taken after shaking the samples.

4.2.5. Release experiment of the Labeled silica-coated QS systems

The silica shell avoid the (uncontrolled) release of DiI: The impact of a breakable and non-breakable silica shell on the protection of a hydrophobic molecule loaded in the QS membrane was studied; in particular the release of DiI has been monitored over time in three different systems: 1) The QS loaded with DiI (QS-DiI), 2) QS loaded with DiI and coated with a breakable shell (BS-QS-DiI) and 3) QS loaded with DiI and coated with non-breakable silica shell (NB-QS-DiI) (**Figure 4.33A**). The last two systems, BS-QS-DiI and NB-QS-DiI, were coated with TEMOS as the precursor to form the silica layer. Then, in order to do the release experiment with DiI-loaded QS (with or without silica-shell), they were placed in a semi-permeable membrane tubing (with a pore cut-off size of 3.5 kDa), and the emission of DiI was evaluated at 500 nm outside the reservoir for a period time of 400 h (**Figure 4.33B**).[33–35]

Initially, the emission was practically zero, due to the absence of DiI molecules outside the reservoir, but after 5 hours, the emission increased for both systems (coated and uncoated QS) (**Figure 4.33C**) in comparison with non-coated QS (QS-DiI). However, silica-coated QS with breakable and non-breakable shell (BS-QS-DiI and NB-QS-DiI) showed a reduction in the emitted

light intensity of 63%. Therefore, the release of DiI was avoided by the silica shell, and in the first hours, the shielding worked equally well for both breakable and non-breakable shells. After longer times (>124 h), the breakable silica shell started to release more DiI than the non-breakable (**Figure 4.33D**), showing 3 times higher emission after 16 days.

It is important to remark that a hydrophilic molecule could be better for a model of a hydrophilic drug, which could provide to see a higher release of the load from the QS system. Considering that DiI is a hydrophobic molecule, it is stable inside the membrane of the QS, observing then less than 10% of the total dye encapsulated in the QS which has been released.
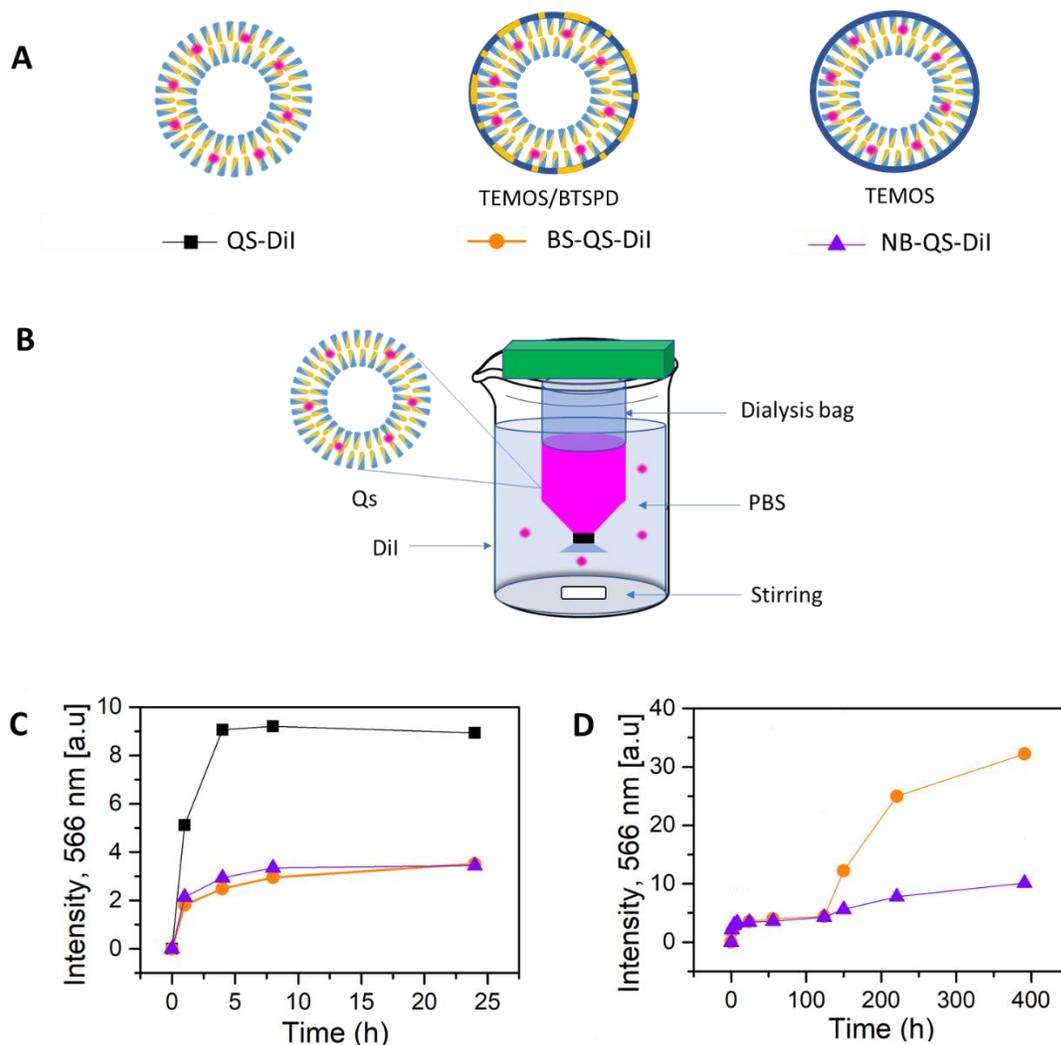
Figure 4.33. A) Representation of the release experiment **B)** Schematic representation of the QS loaded with DiI, BS-QS and NB-QS loaded with DiI. **C)** Release study of the QS-DiI (black), BS-QS-DiI (yellow) and NB-QS-DiI (purple) run for 25 h and **D)** for 400 h. The intensity emission at 566 nm was measured over the time (λ_{exc}= 500 nm).

4.3. Conclusions

Fluorescent labeled silica-coated QS were synthesized in order to have an additional characterization demonstration of the formation of the silica shell and its advantages and disadvantages in terms of stability and permeability drug-release of the nanostructure. Breakability, permeability, confocal microscopy, STORM and release studies were carried out with these systems.

Fluorescence spectroscopy characterization exploiting FRET (Fluorescence Resonance Energy transfer) studies were done for the loaded QS, revealing that the distance between the dyes inside the QS and the dye in the silica shell is less than 10 nm. Additionally, confocal and STORM images were exploited to characterize the silica shell. Successfully, the silica shell was observable at the Cryo-TEM images in all systems based on QS in both breakable and non-breakable silica shells, (TEOS; TEMOS, and TEMOS/BTSPD, respectively). Moreover, confocal microscopy and STORM helped us to corroborate the presence of the silica shell via fluorescence emission.

Furthermore, breakability tests were done to study the breakability of the sample in presence of a reducing agent (GSH). Using several methodologies, open and close systems, it was revealed that the breakability of the silica shell modifies the FRET signal in the system over time. Indeed, FRET emission signal between the dye inside the membrane QS (donor) and the one located at the silica shell (acceptor) has provided a lot of information for being used as a monitoring tool for breakability tests.

Permeability tests were done to see the interchange of compounds inside and outside the QS in the presence or not of silica shell, which resulted to be an observable protection role of the silica shell over QS when those are coated.

At the same time, labeled breakable silica shell, under metabolic conditions, presented a breaking, giving an increase and a decrease of FRET over time. However, more experiments must be done to study the breakability of the system by using DLS, Z-potential and Cryo-TEM to corroborate the versatility of this approach in biological conditions.

What is more, the release studies have shown a protection of 62% of the loaded drug using a hydrophobic dye as a model drug under the first 25h of release. In the future, new investigations

should be carried out to validate and study the release test of hydrophilic drugs employing this kind of systems and under the conditions previously studied.

Overall, it can be concluded that QS coated with silica shell shows a great potential for future applications not only for further protection of the nanostructure if needed but also for required controlled release. Nevertheless, further studies should be carried out in order to improve the understanding of such novel combined nanomaterials.

4.4. Materials and Methods

4.4.1. Materials

All commercial solvents and reagents were used as received, without further purification. Tetraethyl orthosilicate (TEOS), Tetramethyl orthosilicate (TEMOS)(3-Aminopropyl) triethoxysilane (APTES), bis(triethoxysilyl-propyl)disulfide (BTSPD), Glutathione (GSH), was purchased from Sigma Aldrich.

5-Cholesten-3β-ol (Chol, purity 95%) was obtained from Panreac (Barcelona, Spain). Cetyltrimethylammonium bromide (CTAB, ultra for molecular biology) was purchased from Fluka-Aldrich.

1,1'-dioctadecyl-3,3,3',3'-tetramethyl-indocarbocyanine perchlorate (DiI), and cyanine5 NHS ester were purchased from Life Technologies (Carlsbad, USA) and Lumipro, respectively.

MilliQ water was used for the sample preparation (Millipore Ibérica, Madrid Spain), EtOH (Teknochroma, Sant Cugat del Vallès, Spain). Carbon dioxide (99.9% purity) purchased by Carburos Metálicos S.A. (Barcelona, Spain).

4.4.2. Synthesis

4.4.2.1 Synthesis of Quatsomes (QS)

4.4.2.1.1 Synthesis of CTAB/CHOL QS (QS) and CTAB/CHOL/DiI QS (QS-DiI)

QS and QS-DiI were made by Cholesterol and CTAB and were prepared by the CO_2-based method, DELOS-SUSP.

For the QS, Cholesterol was dissolved in EtOH and then added to a high-pressure vessel, while the QS-DII were formed by mixing Cholesterol with DiI in a solution of EtOH before been added to the high-pressure vessel. In each case this vessel is previously heated at Tw = 308 K and after the addition of the EtOH solution, CO_2 was added until reaching the working pressure (Pw = 10 MPa), to obtain a CO_2-expanded solution of the compounds.

Afterward, The QS are formed by depressurizing the CO_2-expanded solution over an aqueous solution of the surfactant (CTAB).

4.4.2.1.2 Synthesis of CTAB/CHOL/10% DODECYL-SILANE QS

This QS were prepared using the same methodology used to produce CTAB/CHOL QS. 10% in weight of Dodecyl silane was added in the inorganic phase mixed with the Cholesterol.

4.4.2.2. Synthesis of silica-coated QS for the permeability test

4.4.2.2.1. Synthesis of non-breakable silica-coated QS Labeled with DiI

4.4.2.2.1.1. Synthesis of Non-Breakable TEOS-silica-coated QS (NB-TEOS-QS-DiI)

Non-Breakable silica-coated QS (NB-SQS) using TEOS at 0 °C and longer time reaction. 6.5 mL of water and 1 mL QS loaded with DiI were putted in 25 mL ball flask under 460 rpm stirring, 200 µL of Ascorbic acid (50 mM) and 260 µL of ammonia (0.134 M) were added to obtain a pH of 9. Finally, 8 µL of TEOS were added directly in the solution ([TEOS]=4.4 mM). The experiment was run at 0 °C (ice bath) during the addition. After 2 days the pH was readjusted to pH of 8 and after 6 days the reaction was stopped by dialysis.

4.4.2.2.1.2. Synthesis of Non-Breakable TEMOS-silica-coated QS (NB-TEMOS -QS-DiI)

0.5 mL of QS (5.35 mg/mL) loaded with DiI was added to 4 mL of water and 0.5 mL of EtOH, 4 µL of Ammonia 28% was added. Separately, 3.4 µL of APTES, and 1.2 µL TEMOS were mixed in 400 µL of EtOH, and 2 µL APTES 0.142 M, 88 µL of Cynine5 NHS ester (3 mM) were mixed with 10 µL of EtOH. These two solutions were combined and 320 µL of the mixed solution was added to the QS flask. After 2 days the reaction was stopped by dialysis.

4.4.2.2.2. Synthesis of Labeled Breakable silica-coated QS

4.4.2.2.2.1 Breakable BTSPD-silica-coated DII-QS (BTSPD-QS-DiI)

Synthesis using APTES/BTSPD: 0.5 mL of QS (5.35 mg/mL) loaded with DiI was added to 4 mL of water and 0.5 mL of EtOH, 4 μL of Ammonia 28% was added. Separately, 3.4 μL of APTES, 2 μL BTSPD were mixed in 500 μL of EtOH. From this solution, 320 μL are added to the QS and the reaction was stopped after 2 days by dialysis.

4.4.2.2.2.2 Breakable Cyanine5-BTSPD-Silca coated -QS (Cy5-BS-QS)

Synthesis using APTES/BTSPD: 0.5 mL of 10% Dodecylsilane QS (5.35 mg/mL) was added to 4 mL of water and 0.5 mL of EtOH, 4 μL of Ammonia 28% was added. Separately, 3.4 μL of APTES, 2 μL BTSPD were mixed in 400 μL of EtOH, and 2 μL APTES 0.142 M, 88 μL of Cynine5 NHS ester 3 mM were mixed with 10 μL of EtOH. These two solutions were combined and 320μL of the mixed solution was added to the QS ball flask. After 2 days the reaction was stopped by dialysis.

4.4.2.2.2.3 Breakable Cyanine5-BTSPD-Silca coated -QS (Cy5-BS-QS-DiI)

Synthesis using APTES/BTSPD: 0.5 mL of QS (5.35 mg/mL) loaded with DiI was added to 4 mL of water and 0.5 mL of EtOH, 4 μL of Ammonia 28% was added. Separately, 3.4 μL of APTES, 2 μL BTSPD were mixed in 400 μL of EtOH, and 2 μL APTES 0.142 M, 88 μL of Cynine5 NHS ester 3 mM were mixed with 10 μL of EtOH. These two solutions were combined and 320 μL of the blend was added to the QS ball flask. After 2 days the reaction was stopped by dialysis.

4.4.2.2.2.3. Release experiments

For the release of DiI in the QS-DiI:125 μL of the solution of QS was diluted with water to have a total volume of 3 mL. For the release of DiI in the QS-DiI with breakable and non-breakable silica shell: 1 mL of the solution of the silica-coated QS was diluted to have a total volume of 3 mL. The solutions were put in different dialysis membranes of 3.5 KDa, and these bags were put in baker glasses containing 50 mL of PBS at 37 °C and 200 rpm and closed with parafilm. The emission of the PBS solution was monitored during the time.

4.4.3. STORM analysis

4.4.3.1. Preparation of the sample

Cy5-Breakable QS solution was diluted 1:100 in distilled water and drop casted it in a coverslip. After it is dried, this glass is attached to a glass slide with tape. Before the analysis 10 µL drop of a buffer switching medium (composed by a mixture of 20% Vectashield (H-1000, Vector Laboratories) and TRIS-Glycerol (5%v/v TRIS 1 M pH 8 in Glycerol)) was deposited between the microscope slide and the cover-glass (our sample) to induce the photobleaching. The sample was irradiated with a power laser of 672nm and the images were recollected during an interval of time (20,000 time points).

4.4.3.2. Setup and imaging

Super-resolution localization microscopy imaging was performed on a home-built setup based on a Nikon Eclipse Ti microscope with 100x 1.49 NA oil-immersion objective. The laser line at 642 nm (Oxxius) were used for excitation of Cy5. Laser power during the experiments was set to 130 mW, that results in 5.2 kW/cm2 excitation intensity. Emission from the sample was spectrally filtered with the help of notch filter (642 nm StopLine single-notch filter: NF03-642E-25, Semrock; in order to remove the scattered laser light), and then was imaged on an EM-CCD camera from Hamamatsu (ImagEM). An additional lens was used to obtain a final magnification of 150X corresponding to a pixel size of 106.67 nm.

4.4.3.3. Data analysis

A stack of 10000–20000 images of 512 * 256 pixels (two channels together) was analysed with the Thunder STORM plugin in ImageJ. The following parameters were used to find and fit the signal of each particle: image filtering – Difference-of-Gaussians filter (sigma 1 = 1.0 and sigma 2 = 1.6); approximate localization of molecules – Local maximum (peak intensity threshold: std, connectivity: 8-neighbourhood); sub-pixel localization of molecules – Integrated Gaussian (fitting radius: 4 px, fitting method: Least squares, initial sigma: 1.3 px). Results were filtered by sigma and localization precision values: 120 nm < sigma < 180 nm, precision < 25 nm. Drift correction: with fiducial markers Max distance – 100 nm, Min marker visibility ratio– 0.15, Trajectory smoothing – 0.03.

4.5. REFERENCES

(1)   Lakowicz, J. R. Introduction to Fluorescence. In *Principles of Fluorescence Spectroscopy*; Springer US: Boston, MA, **1999**; pp 1–23.

(2)   Reisch, A.; Klymchenko, A. S. Fluorescent Polymer Nanoparticles Based on Dyes: Seeking Brighter Tools for Bioimaging. *Small* **2016**, *12* (15), 1968–1992.

(3)   Kaeser, A.; Schenning, A. P. H. J. Fluorescent Nanoparticles Based on Self-Assembled π-Conjugated Systems. *Advanced Materials* **2010**, *22* (28), 2985–2997.

(4)   Aliprandi, A.; Mauro, M.; De Cola, L. Controlling and Imaging Biomimetic Self-Assembly. *Nature Chemistry* **2016**, *8* (1), 10–15.

(5)   Tang, J.; Kong, B.; Wu, H.; Xu, M.; Wang, Y.; Wang, Y.; Zhao, D.; Zheng, G. Carbon Nanodots Featuring Efficient FRET for Real-Time Monitoring of Drug Delivery and Two-Photon Imaging. *Advanced Materials* **2013**, *25* (45), 6569–6574.

(6)   Sun, G.; Berezin, M. Y.; Fan, J.; Lee, H.; Ma, J.; Zhang, K.; Wooley, K. L.; Achilefu, S. Bright Fluorescent Nanoparticles for Developing Potential Optical Imaging Contrast Agents. *Nanoscale* **2010**, *2* (4), 548–558.

(7)   Jenkins, R.; Burdette, M. K.; Foulger, S. H. Mini-Review: Fluorescence Imaging in Cancer Cells Using Dye-Doped Nanoparticles. *RSC Advances* **2016**, *6* (70), 65459–65474.

(8)   Terai, T.; Nagano, T. Fluorescent Probes for Bioimaging Applications. *Current Opinion in Chemical Biology* **2008**, *12* (5), 515–521.

(9)   Albrecht, C. Joseph R. Lakowicz: Principles of Fluorescence Spectroscopy, 3rd Edition. *Analytical and Bioanalytical Chemistry* **2008**, *390* (5), 1223–1224.

(10)   Förster, T. Delocalized Excitation and Excitation Transfer. Bulletin No. 18 (No. FSU-2690-18), Florida State University, Tallahassee. Dept. of Chemistry, **1965**.

(11)   Sun, Y.; Wallrabe, H.; Seo, S. A.; Periasamy, A. FRET Microscopy in 2010: The Legacy of Theodor Förster on the 100th Anniversary of His Birth. *ChemPhysChem* **2011**, *12* (3), 462–474.

(12) Periasamy, A.; Vogel, S. S.; Clegg, R. M. FRET 65: A Celebration of Förster. *Journal of Biomedical Optics* **2012**, *17* (1), 011001.

(13) Broussard, J. A.; Rappaz, B.; Webb, D. J.; Brown, C. M. Fluorescence Resonance Energy Transfer Microscopy as Demonstrated by Measuring the Activation of the Serine/Threonine Kinase Akt. *Nature Protocols* **2013**, *8* (2), 265–281.

(14) He, J. H.; Cheng, Y. Y.; Zhang, Q. Q.; Liu, H.; Huang, C. Z. Carbon Dots-Based Fluorescence Resonance Energy Transfer for the Prostate Specific Antigen (PSA) with High Sensitivity. *Talanta* **2020**, *219*, 121276.

(15) Wagh, A.; Jyoti, F.; Mallik, S.; Qian, S.; Leclerc, E.; Law, B. Polymeric Nanoparticles with Sequential and Multiple FRET Cascade Mechanisms for Multicolor and Multiplexed Imaging. *Small* **2013**, *9* (12), 2129–2139.

(16) Chen, J.; Zhang, P.; Fang, G.; Yi, P.; Zeng, F.; Wu, S. Design and Synthesis of FRET-Mediated Multicolor and Photoswitchable Fluorescent Polymer Nanoparticles with Tunable Emission Properties. *Journal of Physical Chemistry B* **2012**, *116* (14), 4354–4362.

(17) Algar, W. R.; Hildebrandt, N.; Vogel, S. S.; Medintz, I. L. FRET as a Biomolecular Research Tool — Understanding Its Potential While Avoiding Pitfalls. *Nature Methods* **2019**, *16* (9), 815–829.

(18) Chen, Y.; Mills, J. D.; Periasamy, A. Protein Localization in Living Cells and Tissues Using FRET and FLIM. *Differentiation* **2003**, *71* (9–10), 528–541.

(19) Citovsky, V.; Gafni, Y.; Tzfira, T. Localizing Protein-Protein Interactions by Bimolecular Fluorescence Complementation in Planta. *Methods* **2008**, *45* (3), 196–206.

(20) Liu, X.; Ardizzone, A.; Sui, B.; Anzola, M.; Ventosa, N.; Liu, T.; Veciana, J.; Belfield, K. D. Fluorenyl-Loaded Quatsome Nanostructured Fluorescent Probes. *ACS Omega* **2017**, *2* (8), 4112–4122.

(21) Morla-Folch, J.; Vargas-Nadal, G.; Zhao, T.; Sissa, C.; Ardizzone, A.; Kurhuzenkau, S.; Köber, M.; Uddin, M.; Painelli, A.; Veciana, J.; Belfield, K. D.; Ventosa, N. Dye-Loaded Quatsomes Exhibiting FRET as Nanoprobes for Bioimaging. *ACS Applied Materials & Interfaces* **2020**,

12 (18), 20253–20262.

(22)   Maggini, L.; Cabrera, I.; Ruiz-Carretero, A.; Prasetyanto, E. A.; Robinet, E.; De Cola, L. Breakable Mesoporous Silica Nanoparticles for Targeted Drug Delivery. *Nanoscale* **2016**, *8* (13), 7240–7247.

(23)   Ardizzone, A.; Kurhuzenkau, S.; Illa-Tuset, S.; Faraudo, J.; Bondar, M.; Hagan, D.; Van Stryland, E. W.; Painelli, A.; Sissa, C.; Feiner, N.; Albertazzi, L.; Veciana, J.; Ventosa, N. Nanostructuring Lipophilic Dyes in Water Using Stable Vesicles, Quatsomes, as Scaffolds and Their Use as Probes for Bioimaging. *Small* **2018**, *14* (16), 1703851.

(24)   Pawley, J. *(Ed.) Handbook of Biological Confocal Microscopy (Vol. 236)*; Springer Science & Business Media: New York, **2006**.

(25)   Hartland, G. V. Virtual Issue on Super-Resolution Far-Field Optical Microscopy. *Journal of Physical Chemistry A* **2020**, *124* (9), 1669–1672.

(26)   Huang, B.; Bates, M.; Zhuang, X. Super-Resolution Fluorescence Microscopy. *Annual Review of Biochemistry* **2009**, *78*, 993–1016.

(27)   Huang, B.; Babcock, H.; Zhuang, X. Breaking the Diffraction Barrier: Super-Resolution Imaging of Cells. *Cell* **2010**, *143* (7), 1047–1058.

(28)   Glushonkov, O.; Réal, E.; Boutant, E.; Mély, Y.; Didier, P. Optimized Protocol for Combined PALM-DSTORM Imaging. *Scientific Reports* **2018**, *8* (1), 8749.

(29)   Tillberg, P. W.; Chen, F. Expansion Microscopy: Scalable and Convenient Super-Resolution Microscopy. *Annual Review of Cell and Developmental Biology* **2019**, *35* (1), 683–701.

(30)   Bates, M.; Jones, S. A.; Zhuang, X. Preparation of Photoswitchable Labeled Antibodies for STORM Imaging. *Cold Spring Harbor Protocols* **2013**, *8* (6), 540–541.

(31)   Rust, M. J.; Bates, M.; Zhuang, X. Sub-Diffraction-Limit Imaging by Stochastic Optical Reconstruction Microscopy (STORM). *Nature Methods* **2006**, *3* (10), 793–795.

(32)   Bates, M.; Huang, B.; Dempsey, G. T.; Zhuang, X. Multicolor Super-Resolution Imaging with Photo-Switchable Fluorescent Probes. *Science* **2007**, *317* (5845), 1749–1753.

(33) Hu, K.; Cao, S.; Hu, F.; Feng, J. Enhanced Oral Bioavailability of Docetaxel by Lecithin Nanoparticles: Preparation, in Vitro, and in Vivo Evaluation. *International Journal of Nanomedicine* **2012**, *7*, 3537–3545.

(34) Yoon, H. Y.; Kwak, S. S.; Jang, M. H.; Kang, M. H.; Sung, S. W.; Kim, C. H.; Kim, S. R.; Yeom, D. W.; Kang, M. J.; Choi, Y. W. Docetaxel-Loaded RIPL Peptide (IPLVVPLRRRRRRRRC)-Conjugated Liposomes: Drug Release, Cytotoxicity, and Antitumor Efficacy. *International Journal of Pharmaceutics* **2017**, *523* (1), 229–237.

(35) Hamedinasab, H.; Rezayan, A. H.; Mellat, M.; Mashreghi, M.; Jaafari, M. R. Development of Chitosan-Coated Liposome for Pulmonary Delivery of N-Acetylcysteine. *International Journal of Biological Macromolecules* **2020**, *156*, 1455–1463.

CHAPTER 5

Myristalkonium chloride (MKC), a non-toxic surfactant for QS covered with silica and Mesoporous silica NPs

ABSTRACT

In the first part of the chapter is studied the formation of a stimulus redox-response breakable silica shell in a new kind of Quatsomes made by Myristalkonium chloride (MKC). MKC is a non-toxic surfactant which is one of the membrane constitutions. These materials are synthetized in prove of the formation for a more biocompatible system for further drug delivery proposes.

In the second part, the use of the MKC surfactant is proposed to be included in the synthesis of mesoporous silica nanoparticles as a template for their formation. Non-Breakable silica nanoparticles and Breakable silica nanoparticles were prepared. Stimulus redox-response particles are made using a disulfide linker as an organic functional group. Moreover, high porosity breakable mesoporous silica nanoparticles were created using MKC surfactant as a template. More biocompatible systems could arrive from this work.

5.1. Introduction

In this small introduction, different families of organic surfactants (tetrasubstituted ammonium compounds) are introduced. Here is presented some advantages and disadvantage of this compounds, and their possible applications.

5.1.1. Tetrasubstituted ammonium compounds

Tetradecyl dimethyl benzyl ammonium chloride, commonly named Myristalkonium chloride (MKC), is a quaternary ammonium compounds (QACs). QACs are cationic surfactants that contain a positively charged quaternary ammonium "head" bearing four bonds; with an alkyl or heterocyclic substituent. A common characteristic is the presence of a single long chain hydrophobic alkyl group. QACs have been used such as surfactants, dyes, neuromuscular blocking agents and desinfectants.[1] In 1988, the Environmental Protection Agency (EPA) suggested that QACs classified into one of four groups (Figure 5.1): [2]

- Group I: Straight-chain alkyl or hydroxyalkyl QACs, such as tetradecyl trimethyl ammonium bromide, hexadecyl trimethyl ammonium bromide (CTAB), octadecyl trimethyl ammonium chloride and dodecyl trimethyl ammonium bromide (**Figure 5.1A**).

- Group II: Alkyl dimethyl benzyl ammonium compounds such as Tetradecyl dimethyl benzyl ammonium chloride (Benzalkonium chloride) and Hexadecyl dimethyl benzyl ammonium chloride (**Figure 5.1B**).

- Group III: Alkyl [di- and tri- chlorobenzyl] dimethyl ammonium compounds as Tetradecyl dimethyl dichlorobenzyl (**Figure 5.1C**).

- Group IV: Heterocyclic ammonium compounds as 1-Hexadecylpyridinium chloride (cetylpyridinium chloride) (**Figure 5.1D**).
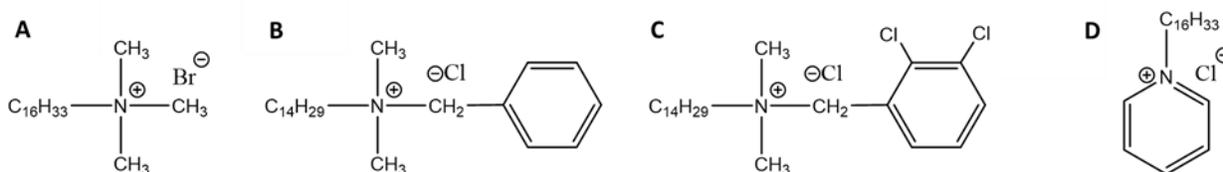
Figure 5.1. Representative quaternary ammonium compounds for the four groups. **A)** Group I: Hexadecyl trimethyl ammonium bromide (CTAB), **B)** Group II: Tetradecyl dimethyl benzyl ammonium chloride, **C)** Group III: Tetradecyl dimethyl dichlorobenzyl and **D)** Group IV: cetylpyridinium chloride.

5.1.2. Benzalkonium chlorides compounds

Benzalkonium chlorides (BACS) were reported for the first time in 1935 by Gerhard Domagk.[3] Several examples of BACS compounds include, alkyl dimethyl (phenylmethyl) quaternary ammonium chlorides, ammonium alkyl dimethyl (phenylmethyl) chlorides, or ammonium alkyl dimethyl benzyl chlorides, which have been used in a lot of applications in the nanotechnology and nanomedicine field. BACs have a broad-spectrum antimicrobial properties against bacteria; fungi, and viruses,[4] disinfectant[5], antiseptics,[3] bactericides, fungicides, sanitisiers and softeners have been developed with BACs. They are usually commercialized as a mixture of compounds with different lengths for the alkyl chain, ranging from C_8 to C_{18}, with higher biocide activity for C_{12} and C_{14} derivatives (**Figure 5.2A**).[6]
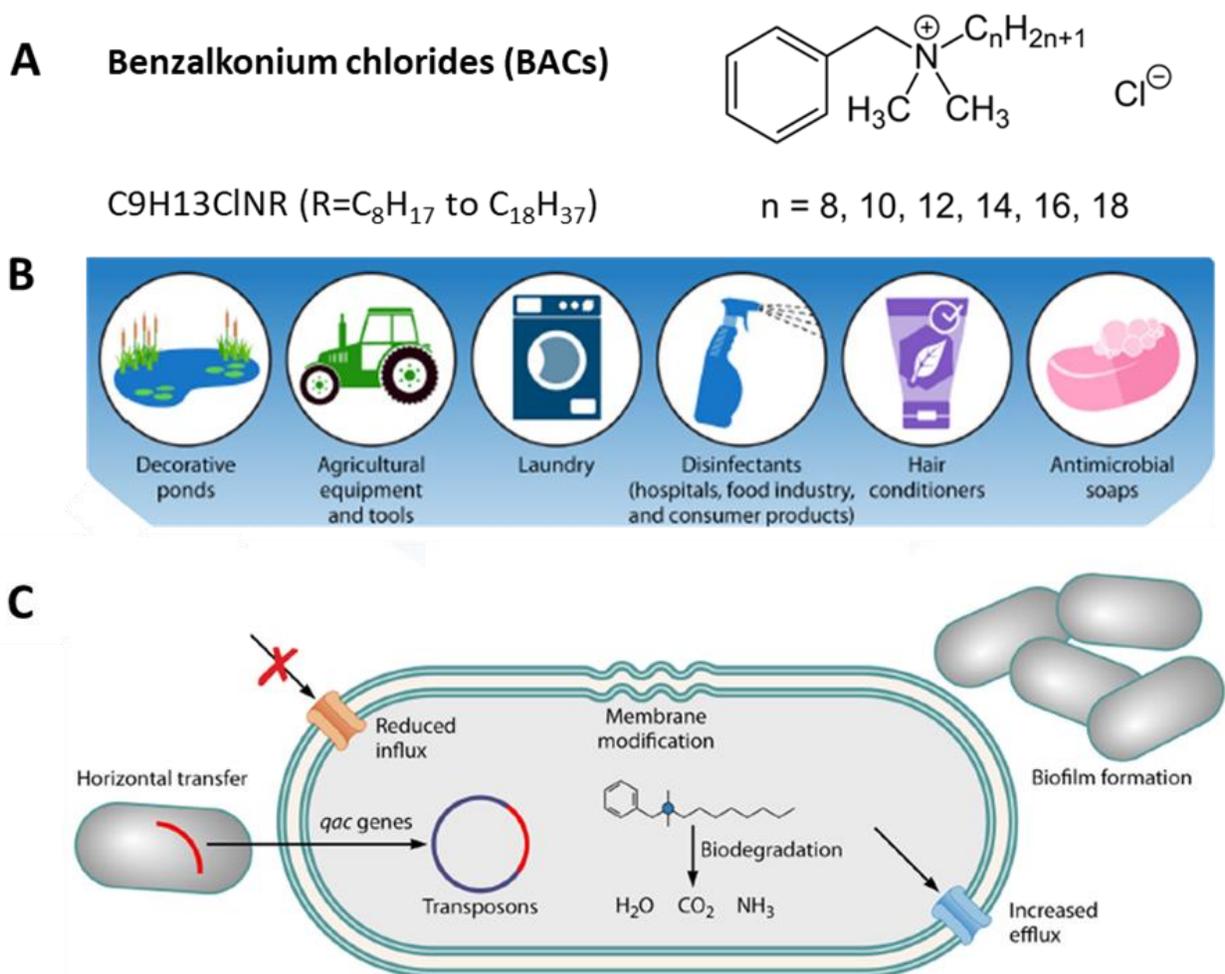
Figure 5.2. A) Benzalkonium chloride (BACs) formula and structure. **B)** Most common uses for BACs and **C)** types of mechanisms of microbial resistance to BACs. Adapted with permission from ref 4. (Copyright 2019, American Society for Microbiology)

In 1947, the first product containing BACs was registered with the EPA in the United States.[7] Since then, they have been used in a wide variety of products in the agriculture, industrial, and clinical field. They have also found their way into domestic applications such as personal hygiene and cosmetic products (**Figure 5.2B**).[5,8] The concentration recommended for the BACs depends on the application,[4] but normally these compounds are applied in concentrations between 0.01 and 1% wt. Concentrations in the low range are used in pharmaceutical products as topical antiseptics (skin, conjunctivae and mucous membranes).[9] Benzalkonium chloride is a common used preservative in ophthalmic and medications that use the nasal route of delivery.[10] The mechanism of microbial tolerance for the QACs, including the BACs involves the perturbation and disruption of the membrane bilayers by the alkyl chains and disruption of charge distribution of the membrane by the charged nitrogen, through different mechanism related to the cell membrane. Those include downregulation of porins, overexpression or modification of efflux pumps, horizontal gene transfer of transposon elements and stress factors, biofilm formation, and biodegradation (**Figure 5.3C**).[4]

5.1.3. Dimethyl benzyl ammonium chloride/ Myristalkonium chloride (MKC)

It is known that the most studied BACs compound is the alkyl dimethyl benzyl ammonium chloride also named Myristalkonium chloride (MKC) (**Figure 5.1B**). The benzyl dimethyl tetradecyl-ammonium chloride is used as a surfactant and detergent. It is registered as a US pesticide that is used as an algicide, bactericide, wood preservative, fungicide, virucide, insecticide, microbicide, deodorant, disinfectant, and sanitizer.[7] In animal studies, it has been seen that the compound is corrosive in rabbit dermal test, but It is not carcinogenic, not mutagenic or genotoxic (based studies in rats and mice) and are highly active in causing hemolysis of rabbit erythrocytes.[11]

5.1.4. MKC-Quatsomes: stable vesicles for drug delivery applications

Taking the advantage from the MKC properties as a non-toxic (in QS experimental conditions) quaternary ammonium surfactant, Ventosa and coworkers have develop a novel type of

Quatsomes (QS) composed of Cholesterol and Myristalkonium chloride instead of using the conventional CTAB for the formation of the membrane (**Figure 5.3A** and **5.3B**).[12] The new formulation of QS confirmed a stability for 18 months in aqueous media in terms of size, morphology and lamellarity (**Figure 5.3C** and **5.3B**), and as well as in human serum present stability for 24 hours. The MKC-QS show good cell viability in experiments with epithelial colorectal carcinoma cell line, among others, with a high selectivity toward cell lysosomes with respect to other organelles like mitochondria.[13]
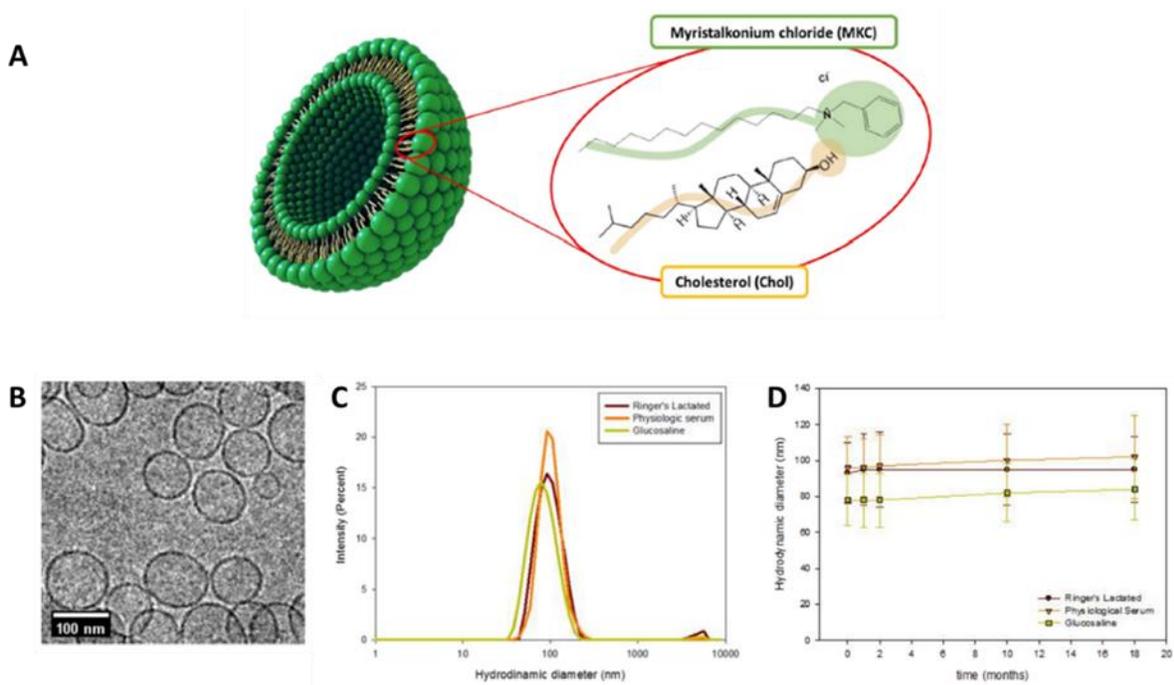
Figure 5.3. A) MKC-Quatsomes composed by the association of Myristalkonium chloride (MKC)and cholesterol, **B)** Cryo-TEM images of the MKC-Quatsomes. **C)** Hydrodynamic diameter distribution obtained by DLS for MKC-Quatsomes in Ringer's Lactate(redline), physiologic serum (orange line) and glucosaline buffer (green line). Cumulant hydrodynamic diameter and polydispersity of MKC-Quatsomes in Ringer's Lactate(red), physiological serum(orange)and glucosaline buffer (green) over a time span of 18 months. Adapted with permission from ref 12. (Copyright 2020, Elsevier)

MKC-QS vesicles are a promising nanocarriers for the encapsulation and deliver of small drugs and large biomolecules such as peptides, proteins and enzymes.[14–16] It has been demonstrated through *in vitro* studies that MKC-QS can entrap negatively-charged, small RNA molecules, like miRNA or siRNA, through electrostatic interactions of the positively-charged vesicle surface. The complex of MKC-QS and small RNA is able to halt the growth of cancer cells, particularly in cellular models of high-risk neuroblastoma.[17,18] *In vitro* cell-culture based cytotoxicity assays were

performed using MKC-QS in human fibroblast cell lines were tested using two different assays to probe the integrity of the mitochondrial compartment (MTT) and the lysosomal and cell membrane damage (NRU). The results show that the MKC-QS do not affect the integrity of the cell membrane, as the cell viability in the NRU assay was not majorly affected. The MTT assay displayed decrease of cell viability, following a dose-response behavior with an IC_{50} of 12.7μg/mL. MKC-QS label with the fluorescent dye 1,1'-Dioctadecyl-3,3,3',3'-Tetramethylindotri-carbocyanine Iodide (DiR) were injected intravenously into mice to monitor their biodistribution. Therefore, DiR-labeled MKC-Quatsomes were found to accumulate in tumor, liver, spleen and kidney tissues. Histological experiments show no alteration or toxicity in these organs (**Figure 5.4**).[12]
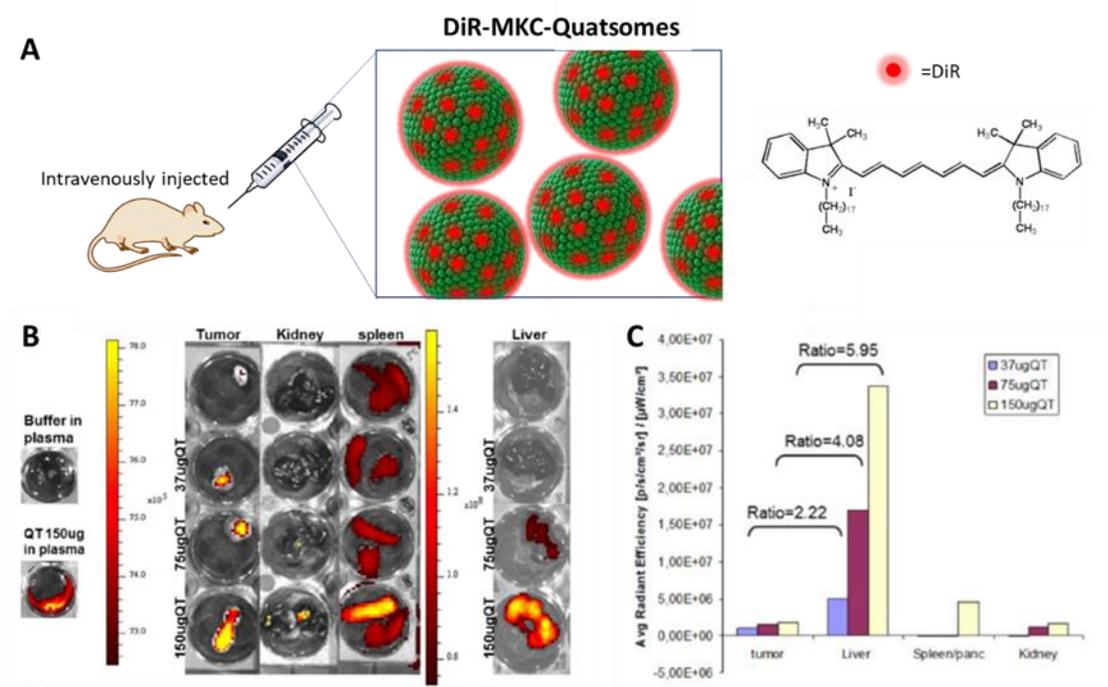

Figure 5.4. A) Schematic representation of the DiR-labeled MKC-Quatsomes injected in mice to study their biodistribution. **B)** and **C)** Biodistribution and lack of toxicity of MKC-Quatsomes after intravenous injection in the SW1417 subcutaneous colorectal cancer model. Adapted with permission from ref 12. (Copyright 2020, Elsevier)

5.2. Results and discussion

5.2.1. Synthesis of Breakable Silica-coated shell using MKC-QS (BS-MKC-QS)

As it was said before, MKC-Quatsomes formulation avoid certain limitations that the conventional Quatsomes made by CTAB present, as safety concerns, particularly for their *in vivo* use beyond topical administration. The new formulation opens a new horizon for parenteral administration.[12] For that reason, the breakable silica-coated MKC QS was synthetized and reported in this chapter.

The coating of the MKC-QS with breakable silica was carried out by a combination of silanes. Tetramethoxysilane (TEMOS) and bis(triethoxysilyl-propyl)disulfide (BTSPD) were mixed and added in two steps to prevent the agglomeration and precipitation of silica. The methodology used here was adapted from the synthesis of breakable silica shell reported in Chapter 3 of this thesis. Some modifications were implemented in this synthesis. The first one was to increase the load of base to achieve a pH of 8, and the second one was to short the time reaction after the second addition of silanes. Precipitation of the silica nanoparticles was observed if the reaction was followed for 2 hours, it is necessary to stop the reaction before the two hours of reaction have been exceeded. These changes of the synthesis were incorporated and tested: 1) decreasing the value of time reaction after the second addition and 2) decreasing the amount of silica added in the second addition and 3) decreasing the time of reaction after this.

Initially, the reaction was carried out for one hour after the second addition of silanes. However, using MKC-QS, silica NPS precipitated, the second step was reducing the reaction time to 20 minutes after the second addition, in this case was possible to maintain a homogenous suspension. DLS measurements were taken to measure the diameter size of the sample before the reaction, after the first addition and 1 day of reaction, and after 20 mins of the second addition.

The reaction was stopped (20 mins after the second addition) by dialysis. The DLS measurements revels two different size distributions: 26±19 nm and 81±19 nm (**Figure 5.5A**) for the MKC-QS suspension, after the first addition the size values increased to 81±18 nm and 401±89 nm (**Figure 5.5B**) and finally after the second addition and dialysis, the size distribution was of 39±9 nm and 122±26 nm (**Figure 5.5C**). Analyzing these data, we observe that the MKC-QS with the reactive

media (ammonia, ascorbic acid and excess of silane) gives a size distribution value which could be attributed to the aggregation of the particles, but after a cleaning process an increase of the size is observable. **Figure 5.5D** report the Cryo-TEM image of these sample after dialysis; darker zones were attributed to the formation of silica shell around the QS.

Figure 5.5. DLS meassurements for the Breakable silica-coated MKC-QS. Using TEMOS and BTSPD-first change in methodology.**A)** Initial MKC-QS, **B)** After the first addition of the mixture of silanes and 1 day of reaction**, C)** after the second addition and 20 mins of reaction before dialysis stopped the reaction and **D)** Cryo-TEM images of the final sample.

The second assay was decreasing the amount of silica added in the second addition (to the half) and decreasing the time of reaction (to the half) compared to the methodology used for the Chol:CTAB QS. Here the DLS measurements provide the following results: the initial material (QS) displayed a size distribution of 26±19 nm and 81±19 nm (**Figure 5.5A**), the size distribution after 4 hours of reaction (first addition) was 50±9 nm and 251±65 nm (**Figure 5.6A**), after one day of reaction the value was 55±14 nm and 237±62 nm (**Figure 5.6B**). These results give us information about the evolution of the reaction, after 4 hours, the size of the particles did not change, all the the silane for the silica shell had reacted. Meaning that the time of this first step can be decreased at least to this value of time. **Figure 5.6C** shows the DLS measurements after 1 hour of reaction

of the second addition, the size distribution of these system was 64±14 nm and 221±57 nm. Note that a big change in size was not observable after this second addition, (concentration of silanes was decreased to the half in comparison to the reported one). Cryo-TEM images are showed in **Figure 5.6D** in order to study the morphology of the sample using these variations in the synthesis of the breakable silica shell. The darker zones around the QS were due to the formation of the silica coating on the MKC-QS. Mostly all the QS present a ring (coating), particularly we observe this ring when TEMOS is used in the synthesis of the silica shell.

As a conclusion of this preliminary part, we can conclude that the formation of the breakable silica shell around the MKC-QS could be done using both modifications in the reported methodology (chapter 3) used for the Chol:CTAB QS. These changes allowed to obtain a similar system that the Chol:CTAB QS, with only small change in the base addition to achieve the desired pH, silane addition and reaction time. We believe that more experiments could be done in order to complete and optimize the characterization of this material as the breakability test.
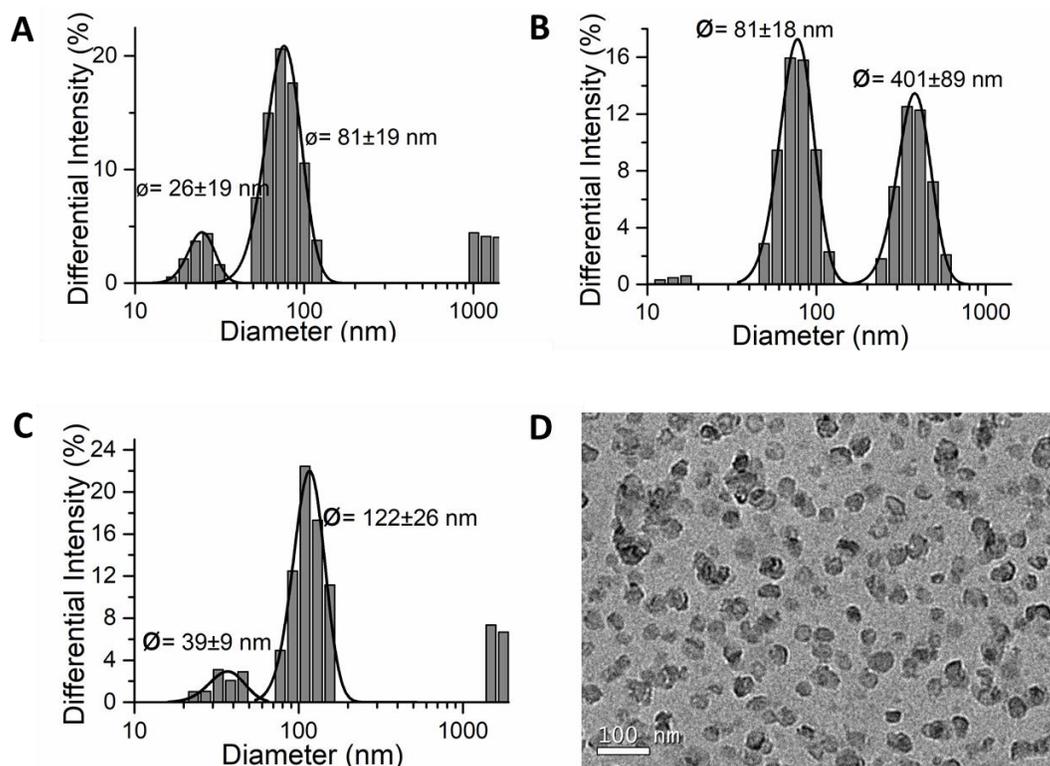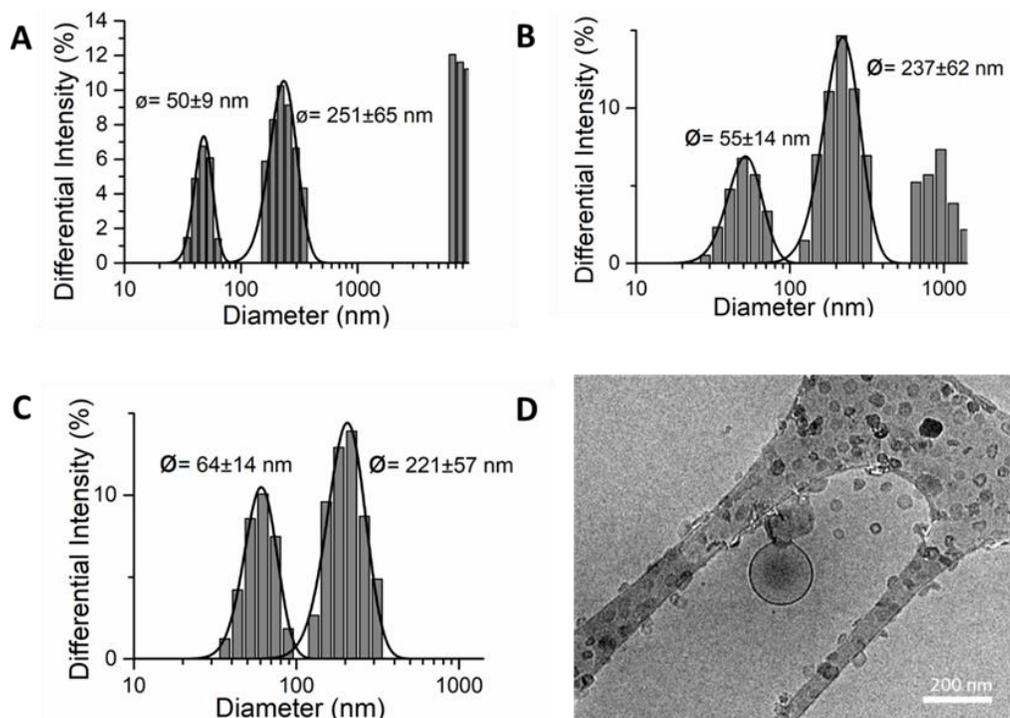

Figure 5.6. DLS meassurements for the Breakable silica-coated MKC-QS. Using TEMOS and BTSPD-first change in methodology. Initial MKC-QS has a size of 26±19 nm and 81±19 nm. **A)** After the first addition of the mixture of silanes and 4 h of reaction**, B)** after the first addition and 1 day of reaction **C)** after the second addition and 1 h of reaction before dialysis stopped the reaction and **D)** Cryo-TEM images of the final sample.

297

5.2.2. Mesoporous silica Nanoparticles (MSNPs) with Myristalkonium chloride (MKC), as a non-toxic surfactant

Mesoporous silica Nanoparticles (MSNPs) has been developed as suitable host materials for many types of pharmaceuticals (as anticancer drugs) and biologically active molecules (as proteins and nucleotides). Their mesoporous sizes, large pore volumes, high surface areas, capacity for facile multi-functionalization and excellent physicochemical stability are an excellent benchmark to develop a powerful drug delivery system.[19–23]

Several different biological and medical studies have been carried out to study the potential application of these carriers in biological systems for drug delivery, bioimaging, biosensing, biocatalysis, etc. MSNPs with specific morphology and surface functional groups have been developed to be biocompatible over specific concentration ranges.[24–28] However, despite many *in vivo* and *in vitro* studies, including those on animals models and tissues, in the non-human tests had been observed that there are a lot of parameters in the synthesis of the MSNPs that cause variations, in terms of size, shape, dosages, pore structures, composition etc., which makes the MSNPs a very complex system to carry out for fully probes in biological systems.[29]

For biomedical applications, MSNPs are used as carriers in controlled drug delivery systems (DDS). For these cases, drug molecules must be loaded into the pores of MSPNs after the surfactant template is removed from them.[30–34] CTAB has been the most commonly used surfactant as a structure-directing agent to make a good template to form the pores of the particles.[30–36] This quaternary ammonium surfactant is cataloged as toxic on the skin, eyes and respiratory system and well as having a negative environmental impact. Lingxia Zhang and coworkers have been taking the advantage of these toxicity to study the complex surfactant-MSNPs as a potential pharmaco-carrier to avoid the use of expensive anticancer drugs.[23] They compare the use of different surfactant to make the MSNPAS (Surf@MSNPs) containing CTAB, SDBS, and Triton X-100 (as a cationic, anionic and nonionic SDA, respectively). All of them are known as cytotoxic substances even at low concentrations. As a control, they studied NPs loaded with hydrochloride trihydrate (CPT-11), a common water-soluble anticancer drug. All the studies were carried out in presence of MCF-7 cells. The results showed that the toxicity follow the next order CTAB@MSNPs, SDBS@MSNPs and Triton@MSNPs, where the CTAB@MSNs were the most toxic (test done with MCF cells). Moreover, the CTAB-contained MSPNs (CTAB@MSNPs) showed

remarkably higher long-term anticancer efficacy than CPT-11-loaded surfactant-free MSPNs (CPT@MSNPs), even at very low concentrations of 2–15 mgmL^{-1}.[23]

-Even though these nanocarriers are good to kill cancerogenic cells, the cytotoxicity of these NPs in non-tumorigenic tissues should be consider. To avoid this toxicity, MSNPs must be synthetized from non-toxic surfactants in order to produce carriers for drug delivery that can be biocompatible. The production of MKC-QS done by the Nora Ventosa's group in which the CTAB was replaced by the MKC surfactant shows the same morphology and size that the CTAB-QS.[12] For this reason, in this work, MKC was used to produce MSNPs, and the incorporation of the non-toxic surfactant to produce the pores in the synthesis in both systems, non-breakable and breakable MSNPs was done. Moreover, in this thesis is explored the synthesis of long-pores breakable silica NPS as a proof of concept that the MKC surfactant can be used to produce this new material to expand the dimension of the pores (higher load capacity) to then increase the load drug amount.

5.2.2.1. Synthesis and characterization of non-breakable MSNPs with MKC as surfactant

The preparation of non-breakable mesoporous silica NPs was achieved through the micelle templating method,[37] where the CTAB surface was simply exchanged for MKC. MKC-MSNPs were dried under vacuum after the synthesis and centrifugation before the cleaning procedure was carried out. The morphology of the particles was characterized by SEM, showing a homogeneous spherical morphology (**Figure 5.7A**). The monodispersity of the sample was analyzed by measuring the diameter size of 300 particles and fitting the results (gaussian distribution function), where the maximum (vertex) represented the average particle size. The particles obtained using the micelle templating method showed a size distribution around 105±9 nm (**Figure 5.7B**). The size of the silica NPs were also characterized by DLS, the size distribution of the NPS(Gaussian fitting of the data) was 155±40 nm which is similar to the obtained value using the counting of the NPs by SEM. TGA measurements were performed on the MKC NB- silica-NPs (**Figure 5.8A**).The TGA reveal that 21% mass was loss between 200 and 300 °C which was attributed to the presence of the MKC surfactant that was content in the pores of the mesoporous silica NPs. To confirm this hypothesis, TGA data was generated on the MKC surfactant. **Figure 5.8B** showed a significant mass loss in this range of temperature. After cleaning

the particles with chloridric acid, the sample was centrifuged with water and EtOH washing cycles, to remove the MKC. To verify that the MKC had been completely removed, the particles were burned in the TGA equipment to then confirm that they were free of surfactant (**Figure 5.8A**). The characterization of the porosity of the samples was carried out using different techniques as N_2 adsorption measurements and SAXS analysis (**Figure 5.9**). These analyses showed that the NPs have a total pore volume of 0.977 cm^3 g^{-1} and a surface are of 876.31 m^2 g^{-1} with an average pore size of 3 nm (**Figure 5.9B**). With SAXS measurements, one broad peak is observed at q = 1.3 nm^{-1}. The calculated d spacing is 4.8 nm (Figure 3-C) which correspond to the pore-to-pore distance. The pore size was calculated being from 3.2 nm, which coincides with the value estimated using N_2 adsorption measurements. EDX studies from STEM analysis confirmed the presence of Si in the sample (**Figure 5.10**).

Figure 5.7. A) SEM pictures of non-breakable NPs prepared with a non-toxic surfactant (MKC). **B)** SEM counting of 300 NPs (size distribution 105±9 nm) and **C)** DLS distribution (155±40 nm) of the particles.
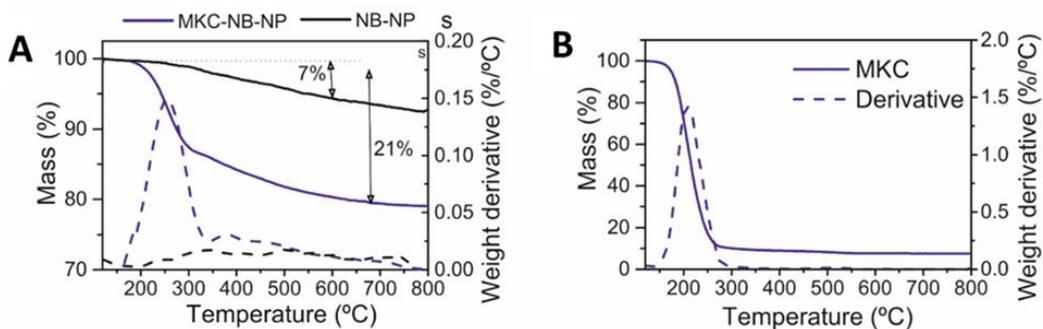
Figure 5.8. A) TGA of the Non-breakable MKC NPs before and after the extraction of the MKC and **B)** MKC surfactant.
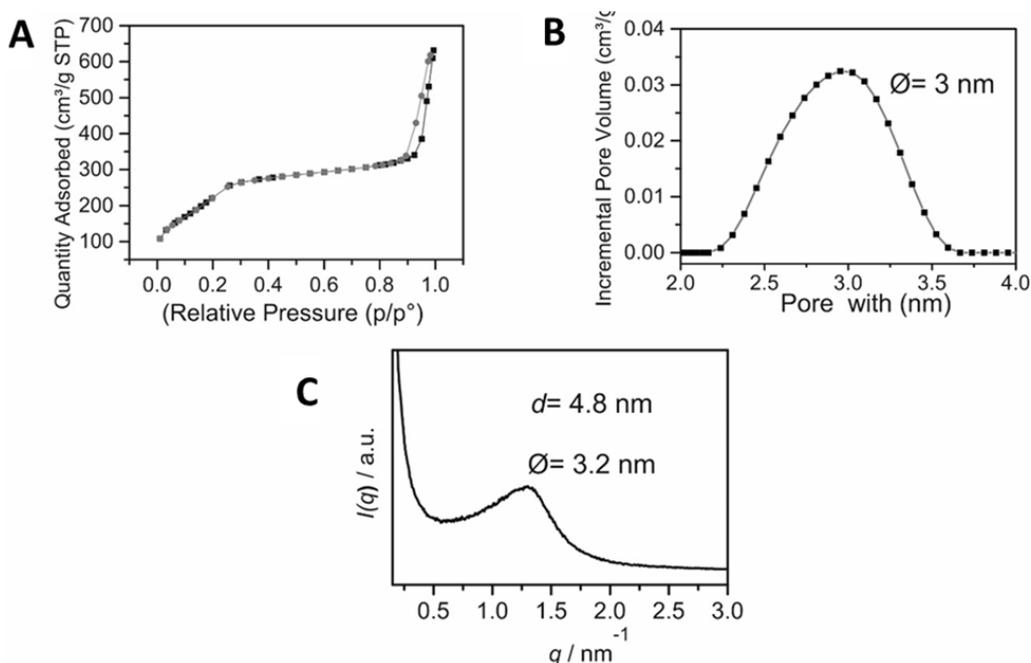
Figure 5.9. A) N$_2$ adsorption-desorption isotherm of the prepared bulk, **B)** mesopore-size distribution and **C)** Small-angle X-ray scattering (SAXS) profile of the obtained mesoporous silica bulk.
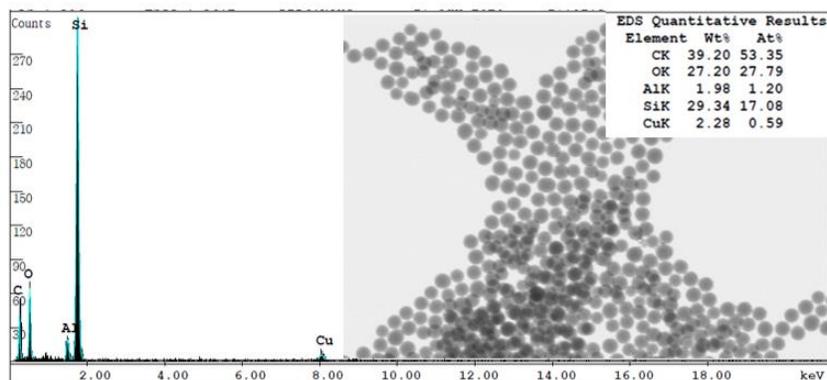
Figure 5.10. EDX of the Non-breakable MKC NPs.

5.2.3. Synthesis and characterization for the breakable MSNPs with MKC as surfactant

5.2.3.1. Synthesis and characterization for the breakable MSNPs with MKC as surfactant using the Micelle templating method

Breakable disulfide mesoporous silica NPs were prepared using the non-toxic surfactant (MKC) with the micelle templating method. The NPs formed during this synthesis were different than those obtained using just TEOS (to produce the Non-breakable NPS). For example, these NPS shows less monodispersity, the morphology of the NPs is spherical but some of them looks oval (**Figure 5.11A**). The different morphology could be due to inadequate stirring that was not able to produce a monodisperse system or the presence of too much disulfide linker in the synthesis (18 % molar BTSPD). The size of the particles was extracted by counted of 300 NPs and fitting of the data (Gaussian distribution function). The plot shows a size distribution of 62±6 nm (**Figure 5.11B**) which is smaller than the size distribution obtained to produce the NB-silica-NPs (which were produced using the same reaction condition and same mols of silane). The change of the size distribution could be attributed to the presence of the disulfide linker in the reaction. For DLS measurements, the Gaussian fitting gives a size distribution of 172±38 nm (**Figure 5.11C**). This value could be due to the agglomeration of particles. Additionally, the characterization of the organic material inside of the NPs was carried out by TGA measurements. The measurement was run for the particles before and after remove the MKC surfactant. Breakable disulfide mesoporous silica NPs with a non-toxic surfactant reveals two steps of loss of organic material, the first step occurs between 200 and 300 °C and corresponds to temperature in which the MKC burns (**Figure 5.12B**), while the second step occurs between 300 and 400 °C which the disulfide linker calcines (**Figure 5.12**). The total lost mass reported is 30.6 %. On the other hand, the NPs that were without surfactant, a total loss of mass was for 12.4%, which was attributed to the disulfide linker. The comparative between the two systems (washed and no-washed) provide more information about the loading of organic material that is of 18.2% in the MKC-Breakable-NPs which corresponds to the surfactant inside of the pores. The pores of the NPs were characterized by N_2 adsorption measurements (**Figure 5.13**). The isotherms reveal a total pore volume of 1.0793 $cm^3 g^{-1}$ and a surface area of 755.94 $m^2 g^{-1}$ with an average pore size of 2.4 nm (**Figure 5.13A** and **5.13B**). The SAXS measurements display one broad peak at q = 1.3 nm^{-1} and

the *d* spacing was calculated, the value of *d* spacing was of 4.8 nm (**Figure 5.13C**). The pore size calculated was of 3.2, which is close to the value estimated using N_2 adsorption measurements.
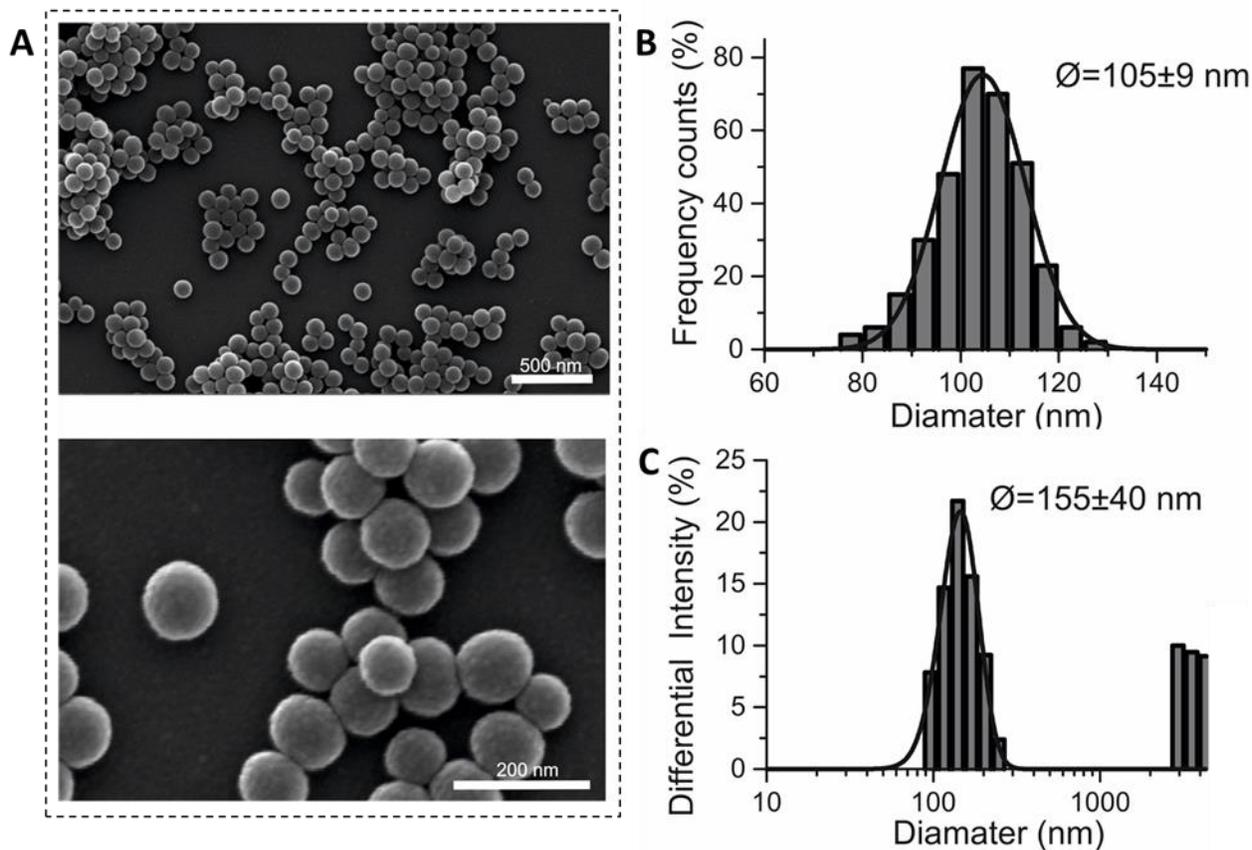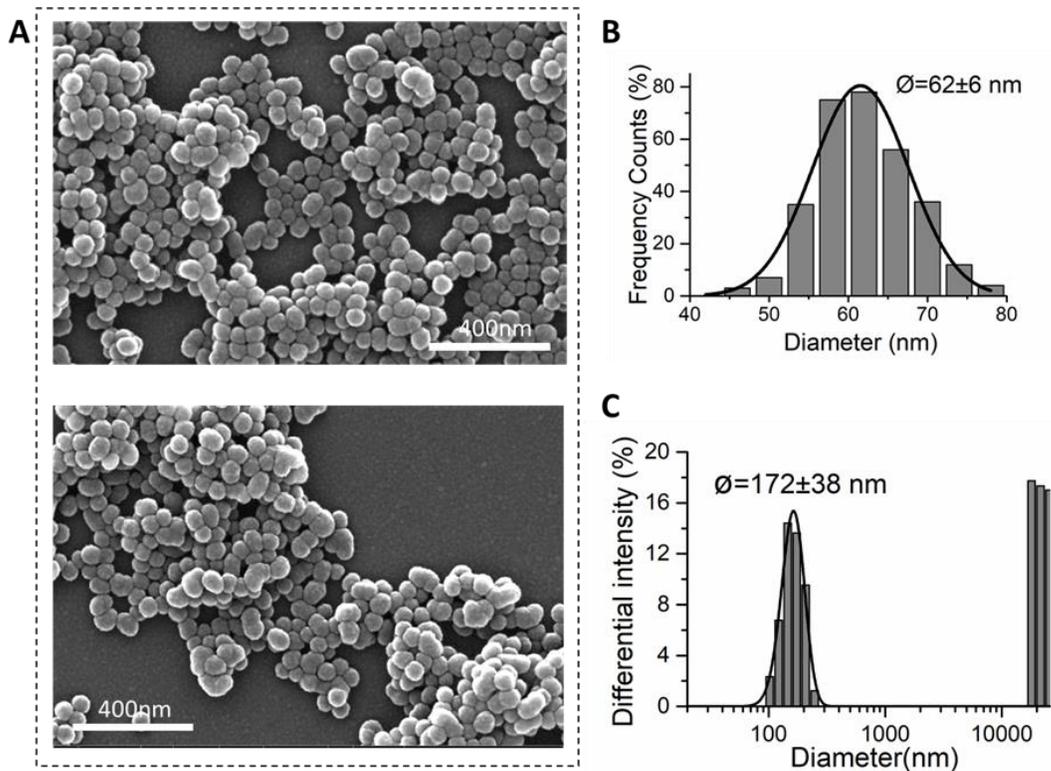

Figure 5.11. A) SEM pictures of non-breakable NPs prepared with a non-toxic surfactant (MKC). **B)** SEM counting of 300 NPs (size distribution 62±6 nm) **C)** DLS distribution 172±38 nm.

Figure 5.12. A) TGA of the Breakable MKC NPs before and after the extraction of the MKC and **B)** MKC surfactant.
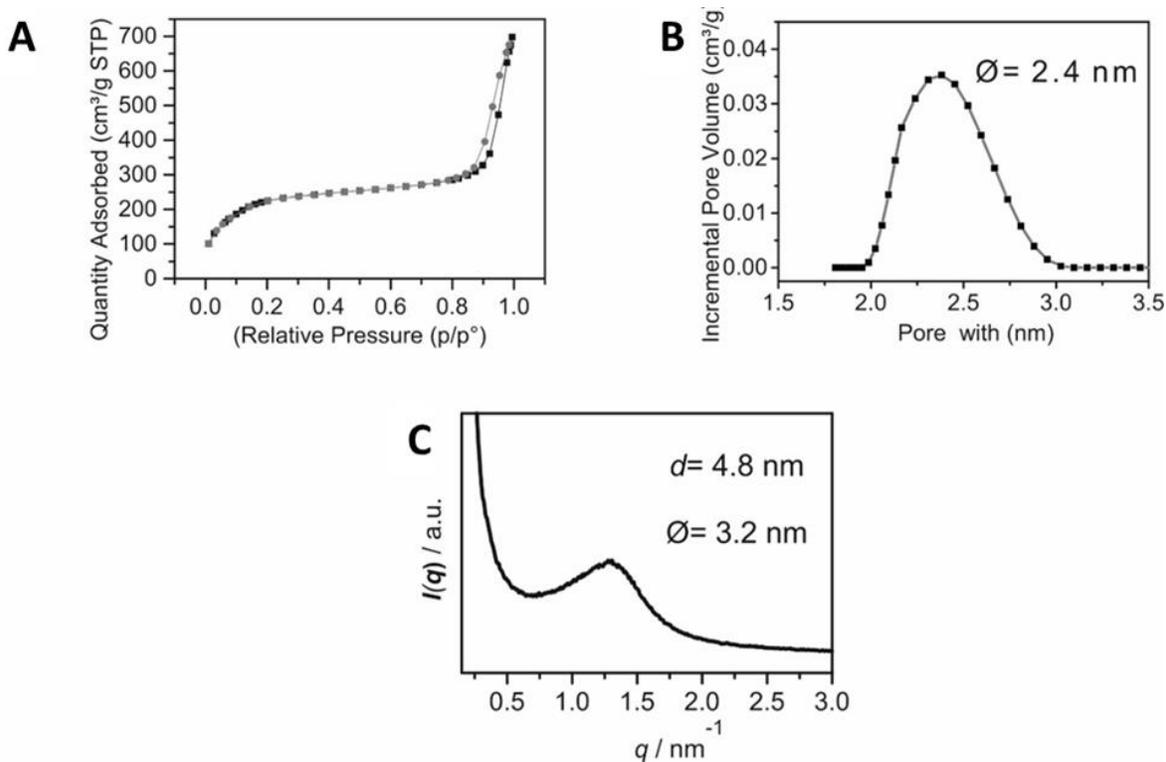
Figure 5.13. A) N_2 adsorption-desorption isotherm of the Breakable NPs done with MKC, **B)** mesopore-size distribution and **C)** Small-angle X-ray scattering (SAXS) profile of the obtained mesoporous silica bulk.

5.2.3.2. Synthesis and characterization for the breakable MSNPs with MKC as surfactant using the Micelle templating method increasing the stirring

The morphology of the NPs was optimized by varying synthetic parameters. Firstly, the centrifuge speed was reduced to 200 rpm, that cause that the NPs synthesized under this new conditions showed a size distribution of 57±6 (value obtained from the counting of 300 NPs in SEM) and a size distribution of 116±28 nm measured with DLS (**Figure 5.14**). Comparing previous data obtained with the synthesis using 100 rpm (protocol described in the methodology in the 2.2.2 section), it is observable that increasing the stirring, the size distribution of the NPs decrease a bit from 62±6 nm to 57±6, which is very small and is practically the statistical error. If we compare this observation with the results reported by Xun Lv and collaborators,[37] in which they observed the same behavior when the stirring speed is reduced, they report that the synthesis of the Non-breakable NPs stirring at 100 rpm and 200 rpm provide different size distributions, from 111±13 to 95±10 nm; respectively. Here, we could see the influence of the stirring speed which increases

the size distribution. The stirring speed control the concentration of silica-surfactant micelles that minimizes the growth of NPs, giving as a result different size distribution of NPs.[37]

Figure 5.14. **A)** SEM pictures of Breakable NPs prepared with a non-toxic surfactant (MKC). **B)** SEM counting of 300 NPs (size distribution 57±6 nm) **C)** DLS distribution 116±28 nm.
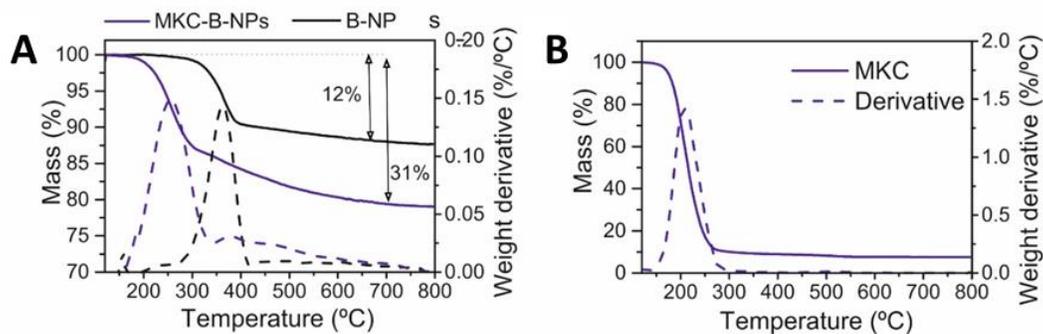
5.2.3.3. Synthesis and characterization for the breakable MSNPs with MKC as surfactant using the Micelle templating method and putting less BTSPD

The second approach was to modify the concentration of the precursors, the quantity of disulfide linker was reduced from 30% w/w to 24% w/w with respect of the TEOS reported synthesis conditions, that was varied in an effort to improve the particle morphology and increase the time reaction. More specifically, 1.15 mL of TEOS (5 mmol) were mixed with 0.36 mL of BTSPD (0.8 mmol) and then added to the solution that was containing the MKC and triethanolamine (TEA). The reaction was run for 2h and 45 min to then improve the morphology of the NPs as is shown in **Figure 5.15**. The size of the NPs developed with this new approach (24% of BTSPD) increased compared with the previous ones synthetized using 30% of BTSPD (from 62±6 nm to 76±8 nm). It is interesting to observe that non-breakable NPs synthetized only with TEOS showed a size

distribution of 105±9 nm in size and that the more quantity of TEOS you add in relation with the BTSPD (even when the equivalents of Si in the reaction are the same), the bigger size you will obtain for the NPs. This theory must be corroborated making a study of the influence of TEOS/BTSPD ratio, because the observation of the size change could also be attributed to the longer reaction time. Variations in the TEOS/BTSPD ratio could be done at the same temperature and reaction time to see the influence in the size distribution. Additionally, the size distribution of these kind of NPs was 119±28 nm.

From TGA analysis, the NPs with surfactant in the interior of the pores presented a mass loss of 23%, and the NPs without was 9% of organic material due to the disulfide linker present in the silica. From these values, the quantity of MKC present in the sample before the washing could be estimated, which was of 14% MKC wt. With this data, another comparation could be carried out; the comparative between the mass lost by both systems (30% and 24%) could give idea about the relationship between the TEOS/BTSPD and the real load of BTSPD in the system. (**Figure 5.16**).

From the N_2 adsorption measurements, the total pore volume of the samples was extracted, which was of 0.86 cm^3 g^{-1} and a BET surface are of 737.1645 m^2/g with an average pore size of 2.3 nm which are close to the values using more BTSPD (**Figure 5.17**). The small changes in the quantity of disulfide linker does not change the porosity of the NPs. Comparing this value with the one obtained with the non-breakable-NPs (using just TEOS). The average pore size was slightly bigger (around 3 nm). One possible explanation of why the pore size decreases in the presence of the disulfide linker is that the hydrolysis of ethoxy group allows the BTSPD to be inserted through condensation of the hydrolyzed silane, even though, before insertion in the surface of the pores, the BTSPD could make oligomerization, a reaction between a non-hydrolyzed neighbor species or between two hydrolyzed neighbor species makes longer then the chain and closes the pore of the NPs (**Figure 5.18**).[38]

With SAXS measurements, the main peak is observed at q = 1.27 nm^{-1}. The calculated d spacing is 5 nm and the pore size calculated is 3.3 nm (**Figure 5.17D**), which is close to the value obtained by N_2 adsorption measurements. If we compare this value with the non-breakable and breakable done before using the micellar methodology, we don not observe big differences in the pore size, which means that once the surfactant packing is done, the silica polymerization around them do

not change this organization. **Figure 5.19** are shown the TEM images of these NPs. EDX studies from STEM analysis confirms the presence of Si and S in the sample (**Figure 5.20**).
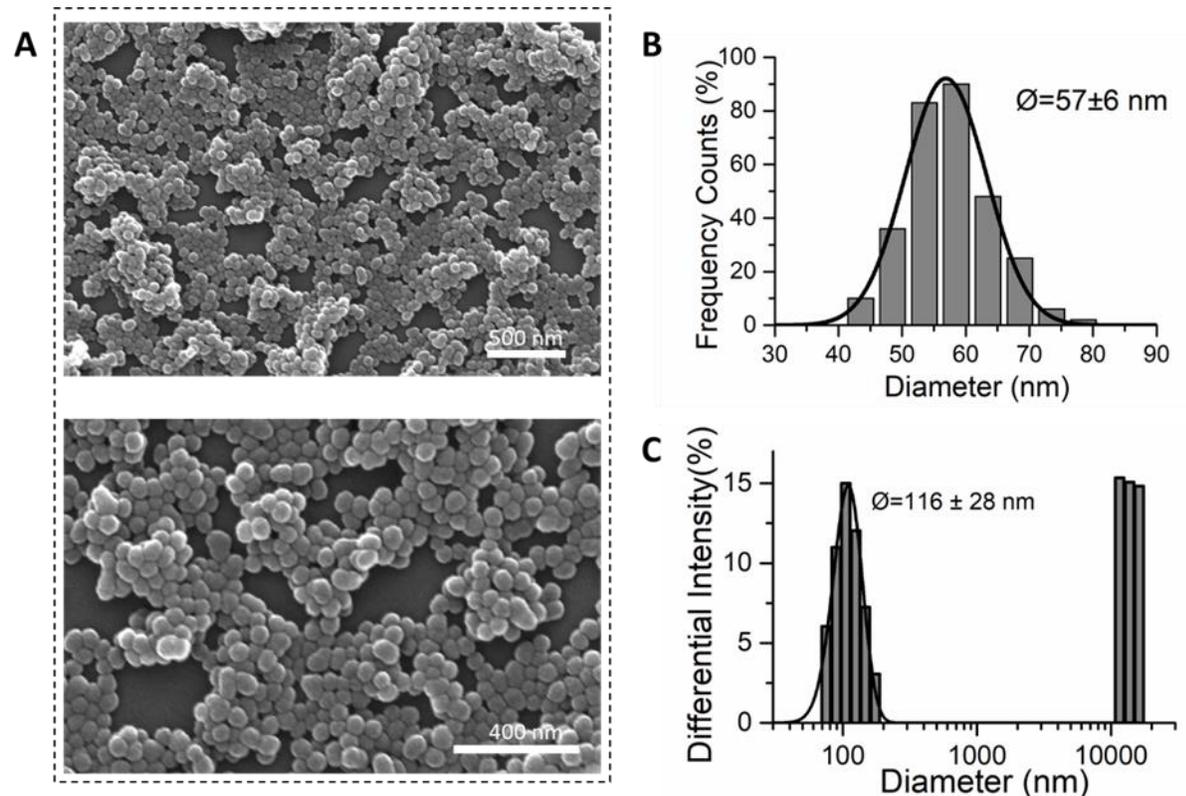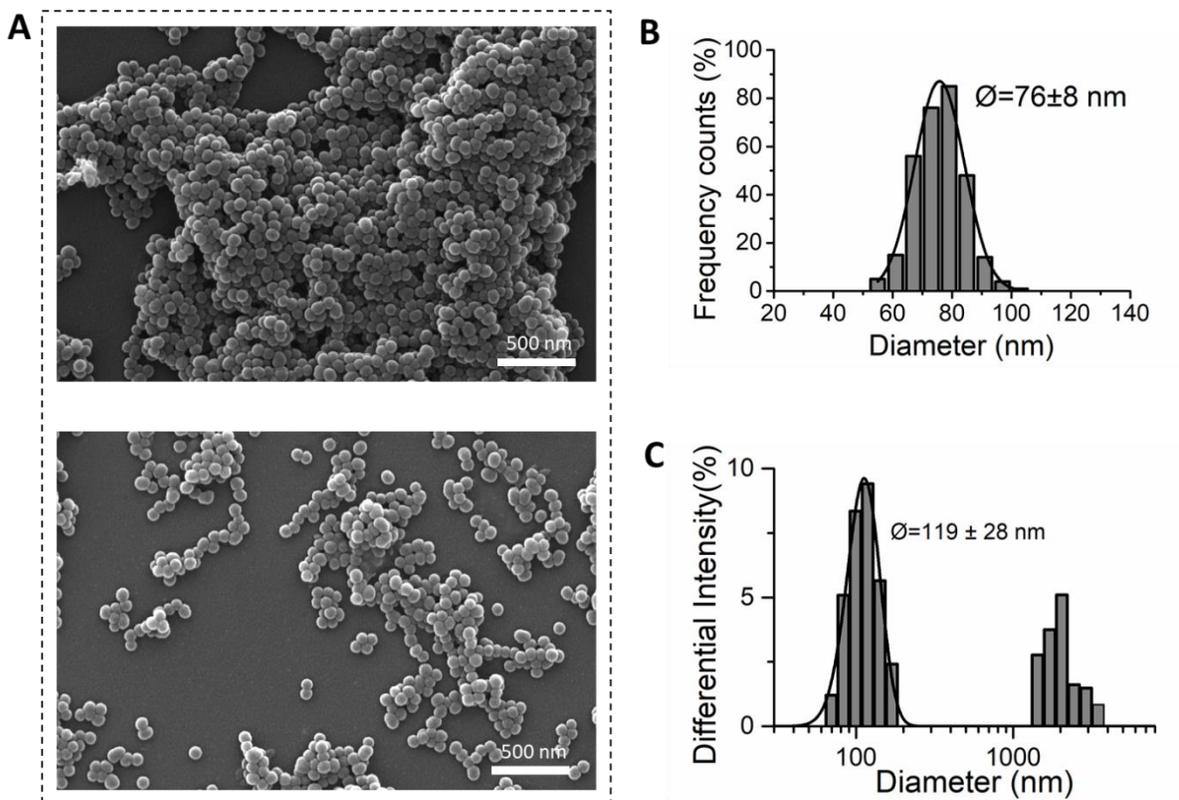

Figure 5.15. a) SEM pictures of breakable NPs prepared with a non-toxic surfactant (MKC). **b)** SEM counting of 300 NPs (size distribution 76±8 nm) **c)** DLS distribution 119±26 nm.
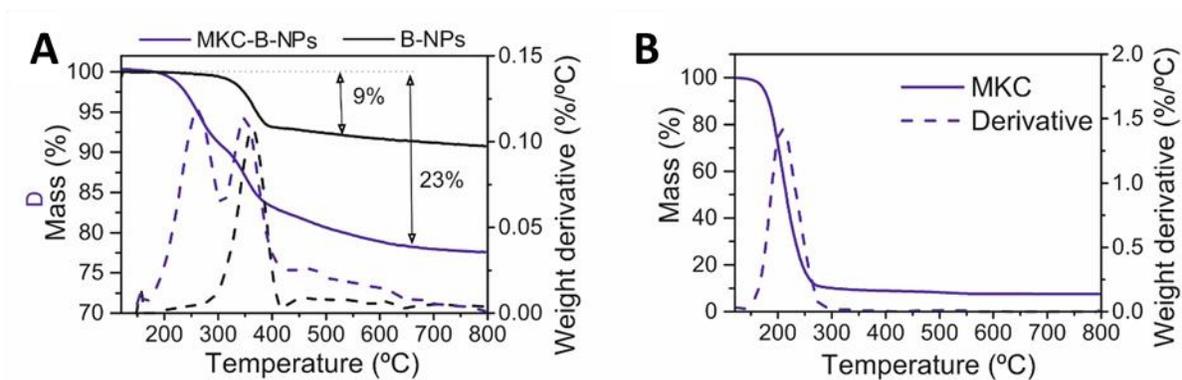
Figure 5.16. A) TGA of the Breakable MKC NPs before and after the extraction of the MKC and **B)** MKC surfactant (Micellar templating method).

Figure 5.17. A) N$_2$ adsorption-desorption isotherm of the Breakable NPs done with MKC, **B)** and **C)** mesopore-size distribution, **D)** Small-angle X-ray scattering (SAXS) profile of the obtained mesoporous silica bulk.
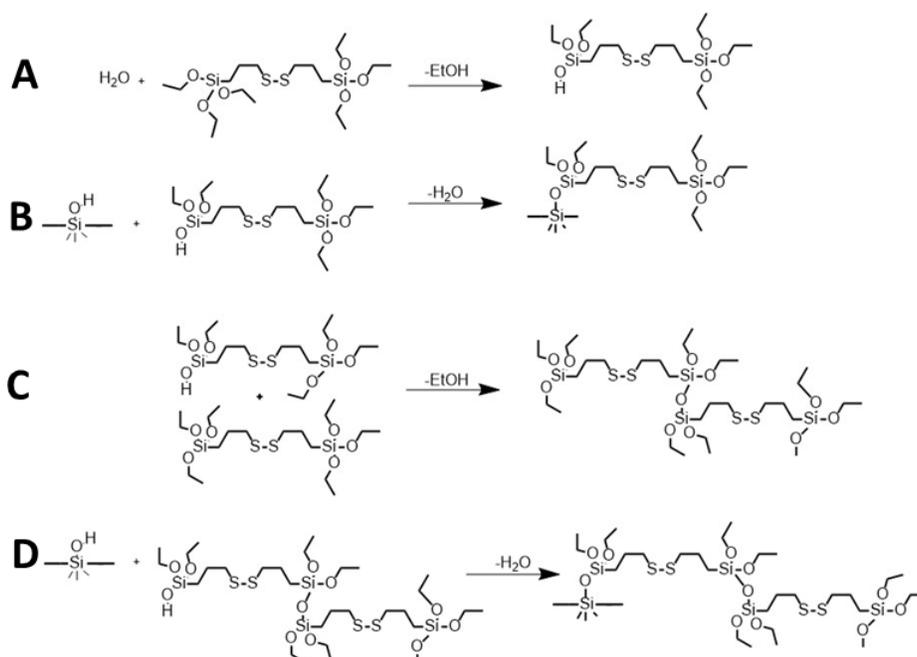
Figure 5.18. A) Hydrolysis of One Ethoxy group of BTSPD **B)** Grafting through condensation of hydrolyzed silane and silica silanols, **C)** Oligomerization trough reaction between a nonhydrolyzed and a hydrolyzed species, **D)** Grafting of the oligomerized BTSPD to the silica framework. Adapted with permission from ref 38. (Copyright 2014, American Society for Microbiology)
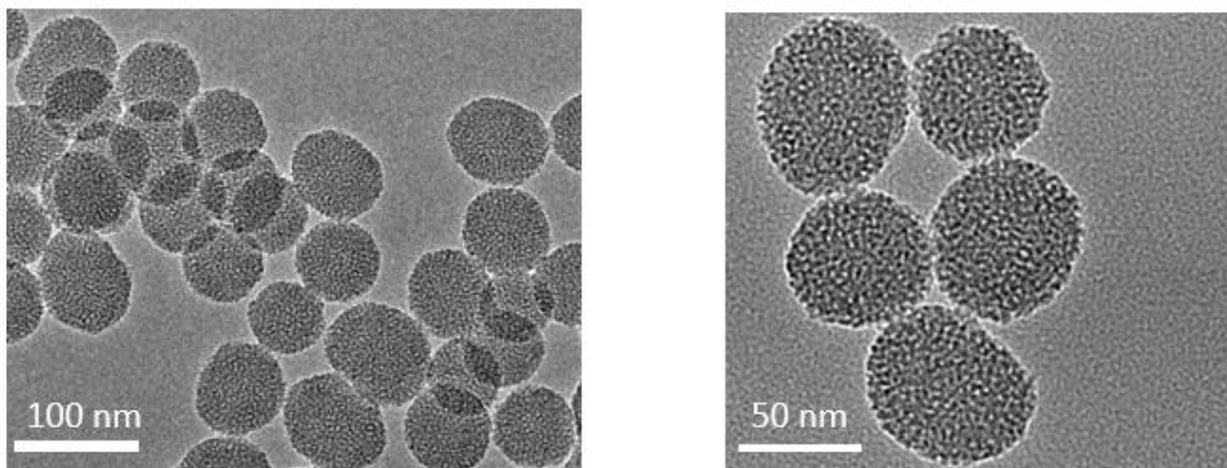
Figure 5.19. TEM images of the Breakable NPs done with MKC (Scale bar 100 and 50 nm).
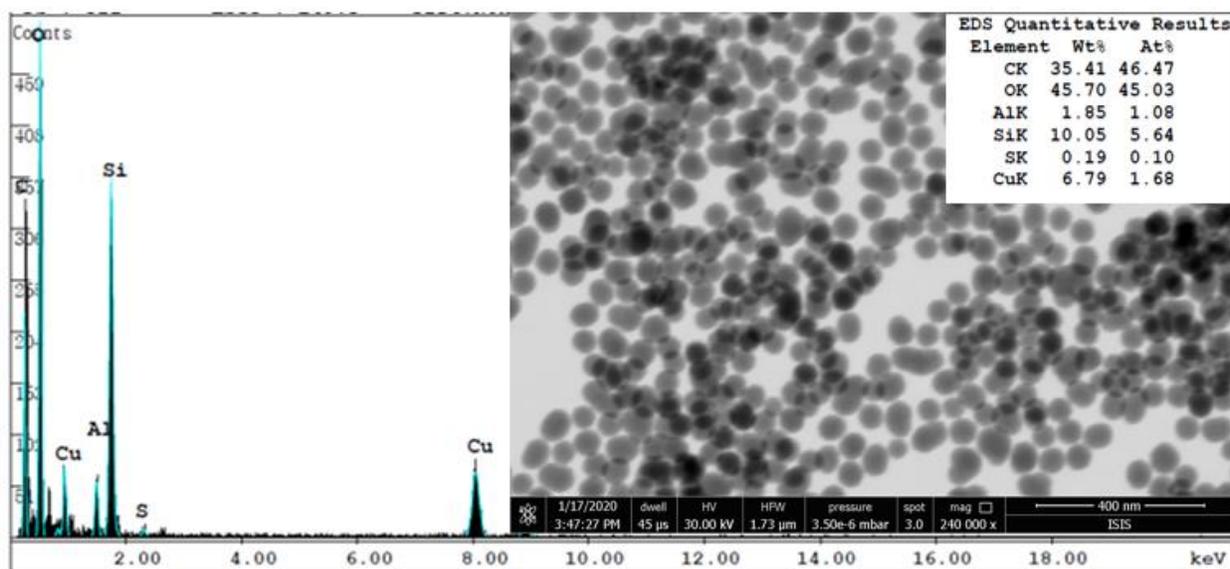
Figure 5.20. EDX of the Breakable MKC NPs.

5.2.3.4. Synthesis and characterization for the breakable MSNPs with MKC as surfactant using the Stöber method

Another approach to test a new procedure to synthesis breakable disulfide mesoporous silica NPs with a non-toxic surfactant (MKC) was developed. The NP were prepared following the Stöber method,[39] which was carried out as is described in the methodology of this chapter. The diameter size distribution of the particles is 169±24 nm (obtained by the counting of 300 NPs from SEM images). The morphology of the NPs was not improved comparing with the NPS

synthetized by the micelle templating method. As is observed in **Figure 5.21**, most of the NPs have spherical morphology but also there are some with oval morphology and aggregates. The DLS measurement of these NPs was carried out and a size distribution of 253±63 nm was obtained. After remove the surfactant, the TGA analysis was carried out to obtain the load of disulfide linker present in the matrix of the silica NPs, the measurement reveals a mass loss of 24% between 300-400 °C (**Figure 5.22**), which corresponds to disulfide linker.

The porosity of the system was analyzed by different physical techniques, N_2 adsorption measurements and SAXS analysis were performed on the NPs (**Figure 5.23**). These analysis shows that the NPs have a total pore volume of 1.03 $cm^3 g^{-1}$ and a surface are of 1347.99 $m^2 g^{-1}$ with an average pore size of 2.4 nm (**Figure 5.23A** and **5.23B**). With SAXS measurements, one broad peak is observed at q = 1.9 nm^{-1}. The calculated d spacing is 3.3 nm and the pore size calculated is 2 nm (**Figure 5.23C**), which coincides to the value obtained by N_2 adsorption measurements.

Figure 5.21. A) SEM pictures of Breakable NPs prepared with a non-toxic surfactant (MKC) and Stöber methodology. **B)** SEM counting of 300 NPs (size distribution 169±24 nm) **C)** DLS distribution 253±63 nm.
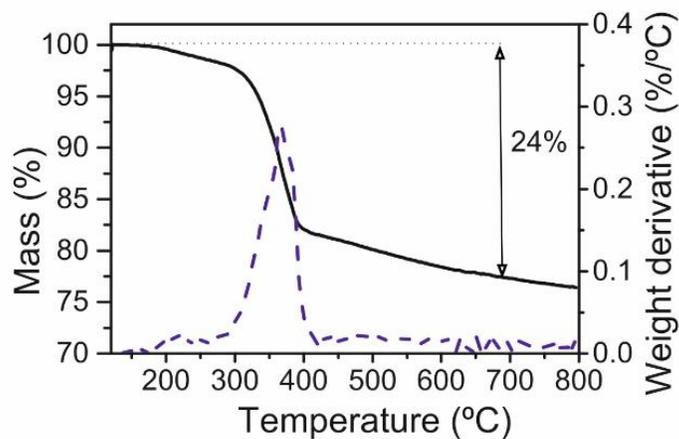
Figure 5.22. A) TGA of the Breakable MKC NPs after the extraction of the MKC (Stöber process).
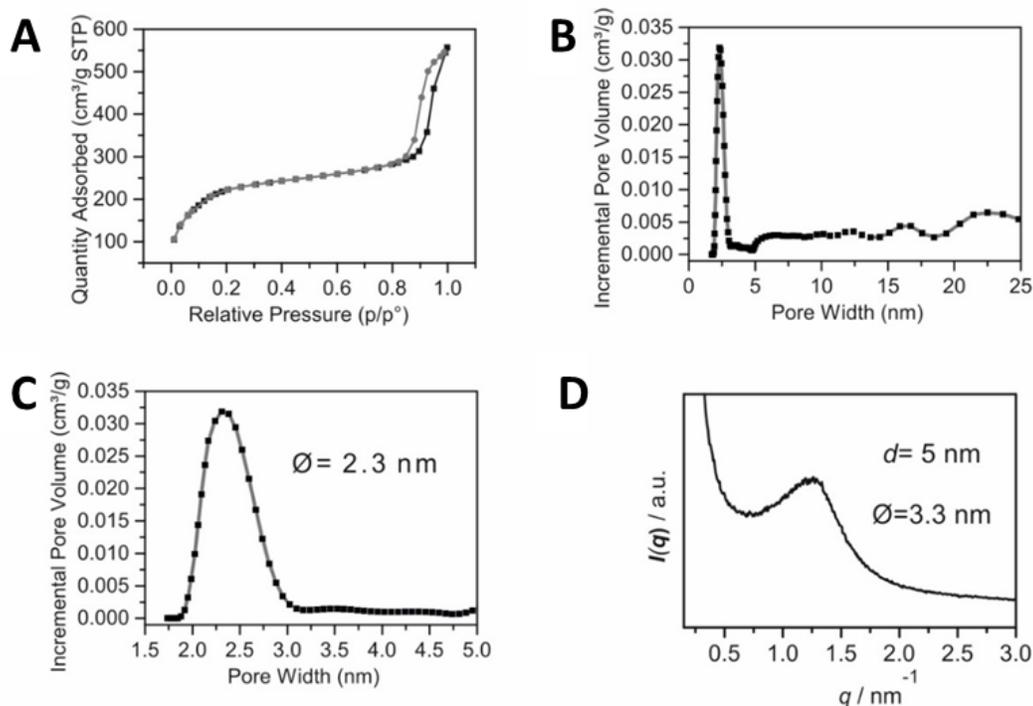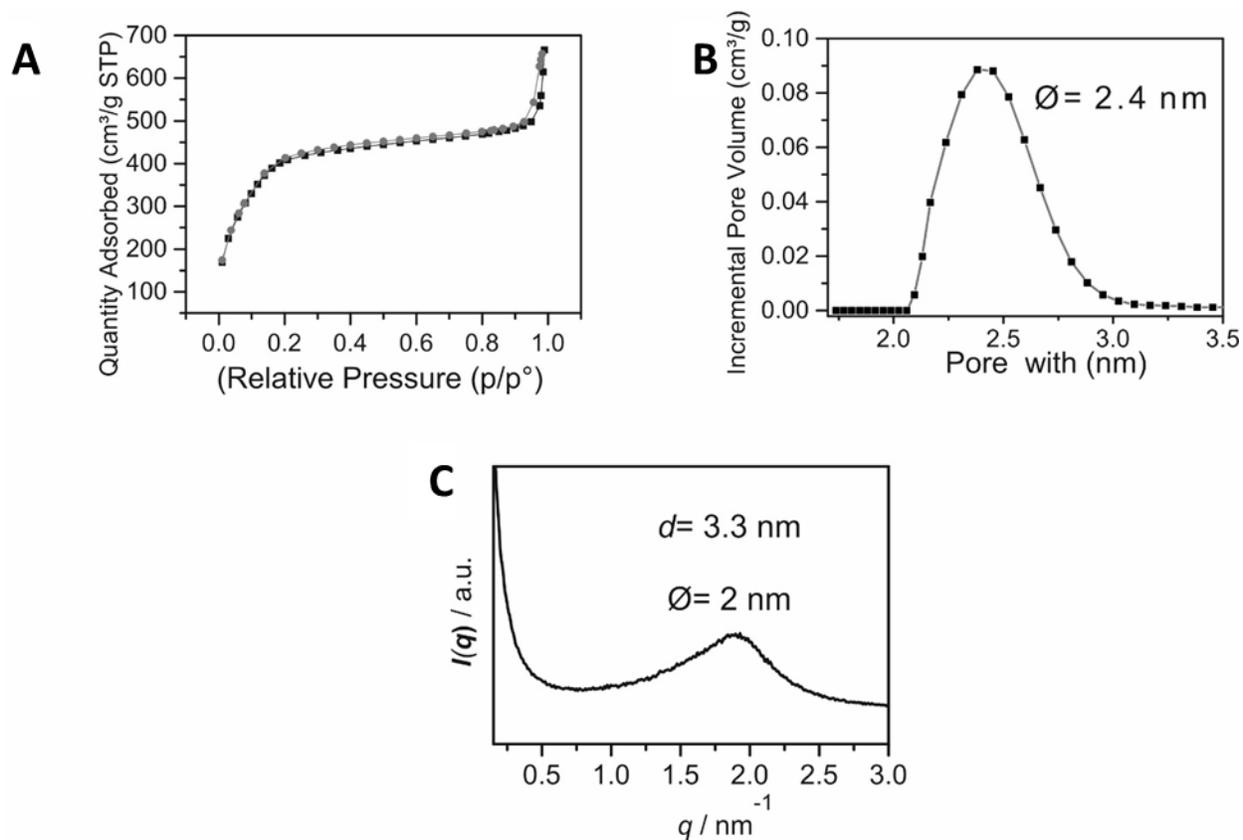

Figure 5.23. A) N_2 adsorption-desorption isotherm of the Breakable NPs done with MKC, **B)** mesopore-size distribution and **C)** Small-angle X-ray scattering (SAXS) profile of the obtained mesoporous silica bulk.

5.2.3.5. Synthesis and characterization for the long Pores breakable MSNPs with MKC as surfactant

The MKC surfactant could be used to obtain big pores for the mesoporous silica NPs, theses has been reported by Kim *et al.*[40] Therefore, the synthesis to produce the large pores silica NPs was carried out first by using the same conditions of the optimized breakable nanoparticles (24% BTSPD, see first part of the experimental part 2.2.3) using the micellar templating method. After their synthesis and before the extraction of the surfactant, the NPs were dispersed in EtOH and followed by the addition of a mixture of H_2O and Trimethylbenzene (TMB). The mixture was placed in the oven at 160 °C for 3 days without stirring and finally after this time the particles are washed and recollected with water and EtOH using cycles of centrifugation. To remove the MKC from the pores, the particles are dispersed in EtOH and chloridric acid is added to reflux overnight. All the process finish after cleaning the NPs wit EtOH by a sequence of sonication/centrifugation cycles and dried them under vacuum.

The particles obtained presented a monodisperse and spherical shape with a size distribution of 76±8 nm (counting from 300 NPs from SEM pictures (**Figure 5.24B**)) and by DLS a size distribution of 137±34 nm (**Figure 5.24A** and **5.24C**). Both size distribution presented similar size distribution.

TGA measurement was performed on the NP before and after washing, which showed 11% mass loss in the in MKC-breakable-silica NPs before cleaning and 25% mass loss in MKC-breakable-silica NPs with disulfide linker. There result allowed to calculate that the 14% were MKC inside of the pores (**Figure 5.25**). Through physical measurements was possible to obtain storage capacity, porosity and surface values. The N_2 adsorption measurements were carried out to test the porosity of the system (**Figures 5.26**). The sample contains mesoporosity (average pore size of 2.2 nm) but also presents a quite long distribution pore size from 5 to 35 nm with a maximum peak between 25 and 35 nm (**Figure 5.26A** and **5.26C**). Note that this last value can also be attributed to the space between the NPs.

With SAXS measurements, a broader peak is observed at q = 1.24 nm^{-1}. The calculated d spacing is 5.1 nm and the pore size calculated is 3.4 nm (**Figure 5.26D**), this value is close to the one obtained by N_2 adsorption measurements. Comparing this value with the non-breakable and breakable NPs synthesis using the micellar methodology, which was consistency in the value

among them. Finally, in **Figure 5.27**, the TEM images of these NPs show their homogeneity in size and shape.
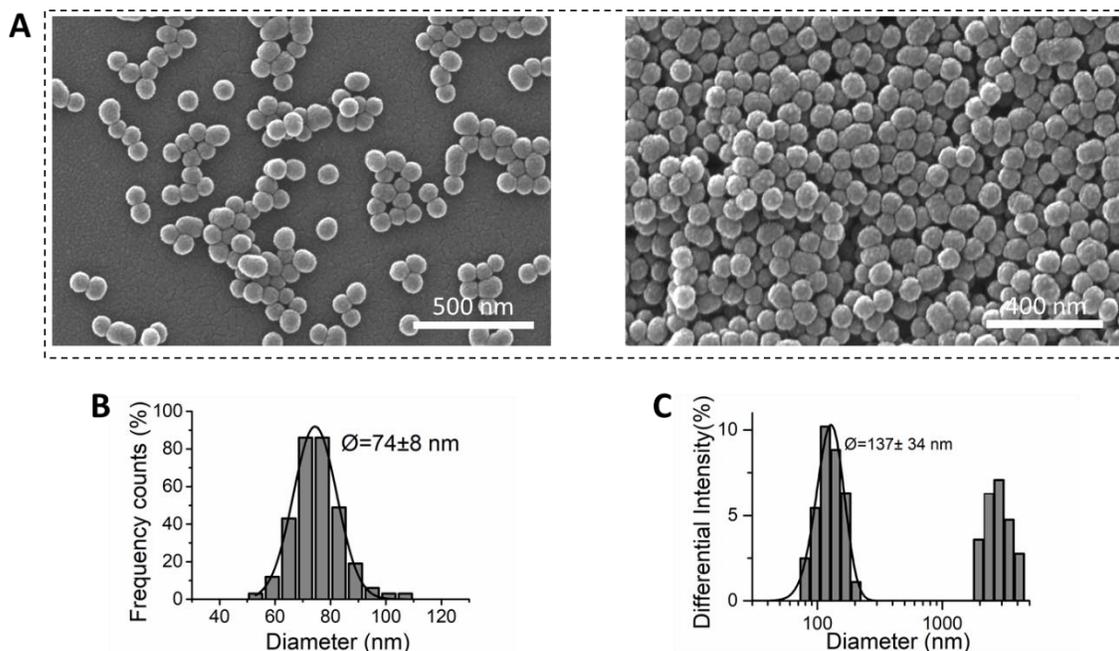
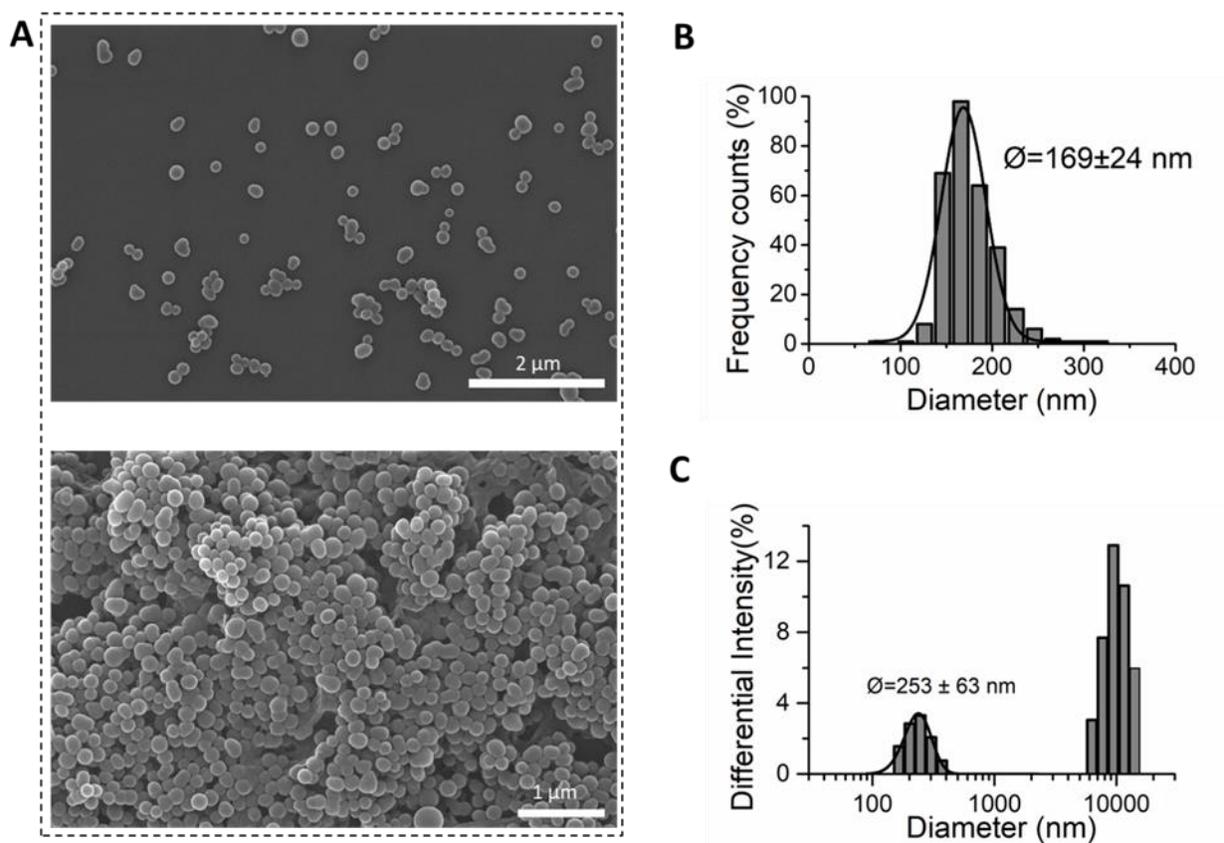**Figure 5.24. A)** SEM pictures of Long Pore-Breakable NPs prepared with a non-toxic surfactant (MKC). **B)** SEM counting of 300 NPs (size distribution 74±8 nm) and **C)** DLS distribution 137±34 nm.
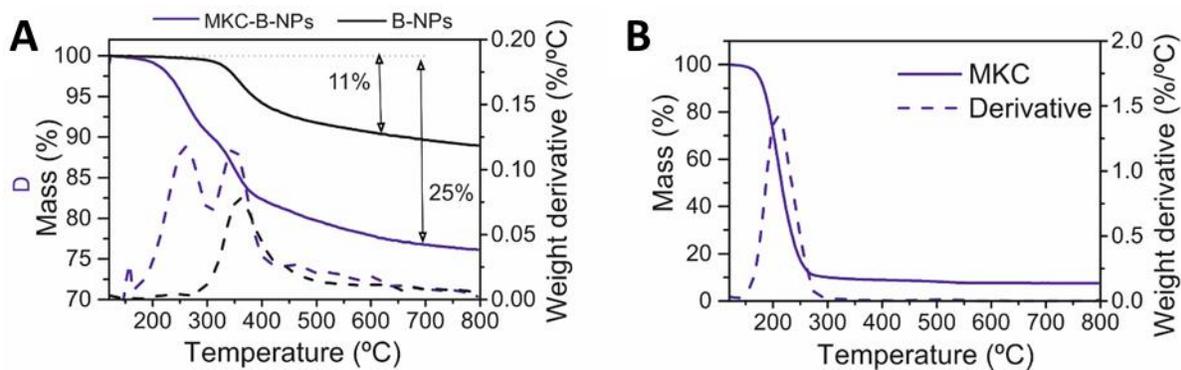
Figure 5.25. A) TGA of the Long Pore- Breakable MKC NPs before and after the extraction of the MKC and **B)** MKC surfactant.
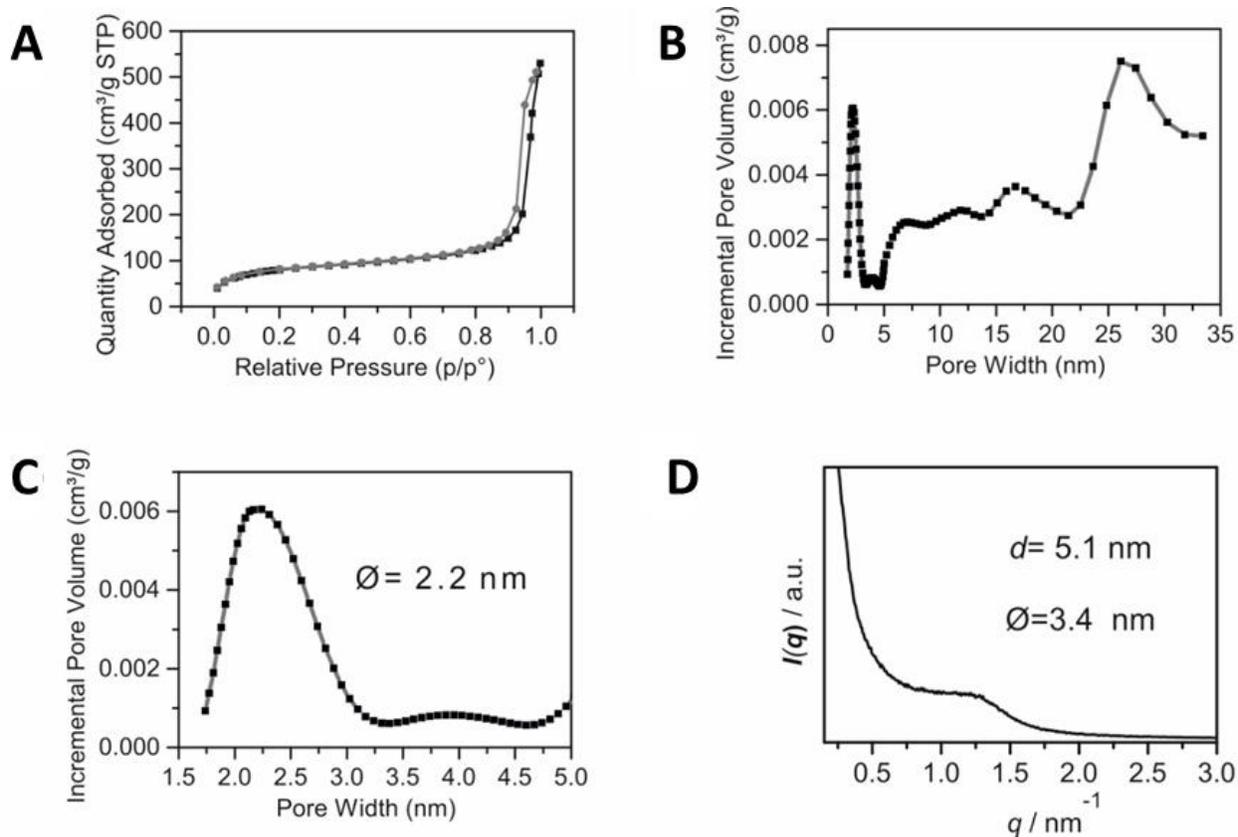
Figure 5.26. A) N$_2$ adsorption-desorption isotherm of the Long Pore- Breakable NPs done with MKC, **B)** and **C)** mesopore-size distribution, **D)** Small-angle X-ray scattering (SAXS) profile of the obtained mesoporous silica bulk and.
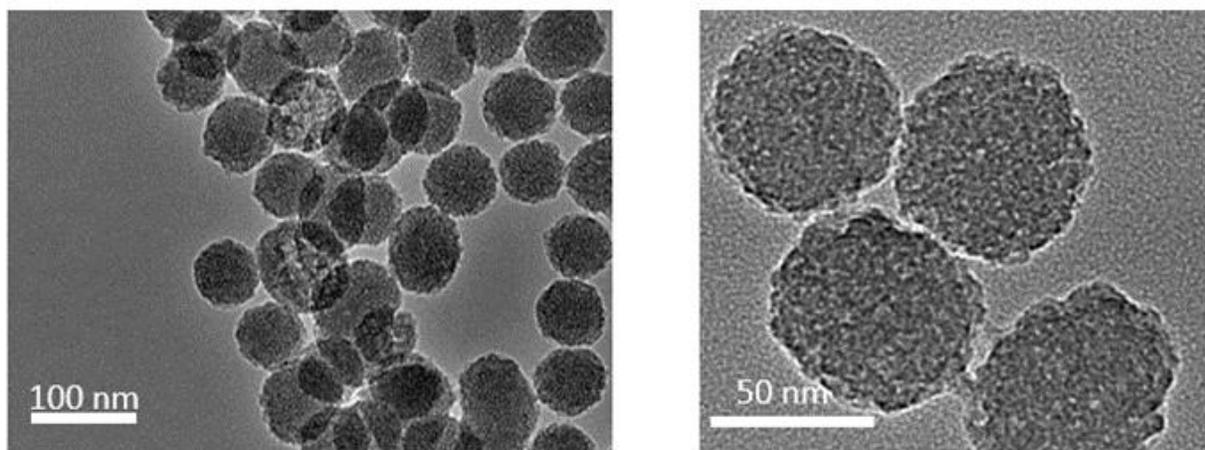
Figure 5.27. TEM images of the Breakable NPs done with MKC (Scale bar 100 and 50 nm).

5.2.3.6. Breakability test for the breakable MSNPs done with MKC as surfactant

One important part of this work was testing the breakability properties of this platform. The breakability test was carried out by taking 0.3 mg of non-breakable and breakable NPs (24% w/w BTSPD) performed with MKC surfactant in presence of 10 mM of Glutathione in PBS and stirring (200 rpm) (**Figure 5.28**) for 7 days. The degradation of the NPs was observed to begin at day 3 and while at day 7, the NPs start to agglomerate and break. As a control, the non-breakable NPs were tested in parallel and we check the different behavior; after 3 days in presence of GSH the core of NPS looks less dense (is observable a core in the center of the NPs with time in this conditions). A new batch of these non-breakable must be tested to check this hypothesis to confirm these observations. We suppose that the GSH could be superficially degrading the NPs, but the non-breakable NPs don't show any signal of agglomerate or breakability.
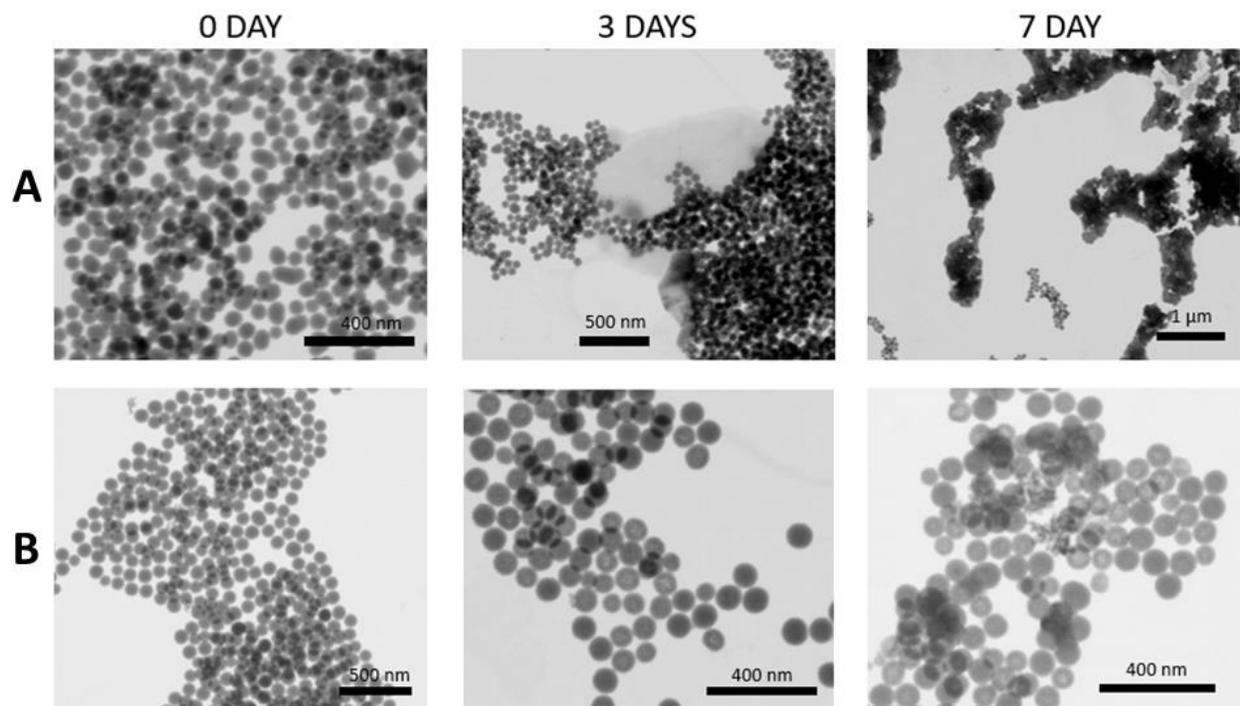
Figure 5.28. STEM pictures of the breakability test of **A)** Breakable NPs done with BTSPD 24% w/w with respect of TEOS and **B)** Non-breakable NPs.

5.2.3.7. Cell viability test for the non-breakable and breakable MSNPs done with MKC as surfactant

The non-breakable silica nanoparticles (**NB**-MSNPs) and the breakable redox-responsive silica nanoparticles (**B**-MSNPs) synthetized by MKC as a template were tested to study the cell viability in the presence of these systems. Cell viability test was performed using 3 different cell lines, HeLa (cervical cancer cells) and C6 (glioma cells) cells[41] were studied as tumorigenic lines, and MCF10 as a non-tumorigenic. And 3 different concentrations of silica NPs were also tested, 10, 50 and 100 µg/mL. Additionally, the influence of the washing was check, the NPs with and without surfactant (after its removed) were using in this experiment to understand the effect of the Residual MKC (**Figure 5.29**).

MSNPs breakable and non-breakable synthesized by MKC as surfactant and after the washing process (remove MKC) provide a good cell viability (100%, or more due the effect of cell growing) with all cell lines, MCF10, C6 and HeLa, and regardless of the concentration that was tested, which says that indeed the NPs could be good candidates for biological applications. On the other hand, the NPs without any post-treatment (+MKC), in which the pores are still containing the MKC surfactant. The breakable NPs have a better cell viability that the non-breakable, 2.6 times better viability at concentrations of 10 µg /mL (31% and 82% cell viability for NB and B, respectively, in MCF10 cells.

At this same concentration, using the C6 and HeLa lines cells, no significative statistical difference is observed (cell viability ~76% and ~86%, respectively for the B-NPs). These observations provide says that at low concentrations, NB-NPs cause more damage to the healthy cells (MCF10) that the tenogenic cells. Increasing the concentration to 50µg/mL and 100 µg/mL, a decrease of the cell viability is observed, for the B and NB-NPs in all cell lines.

The cell viability went down until 9, 2 and 5% for the B-NPs at 100µg/mL. At this concentration not significative statistical difference is observed between B and NB in all cell lines. Therefore, all cells die at 100µ/mL using NPs containing MKC. It has to be noted that at all the concentrations, B-NPs have a better cell viability that the non-breakable. This effect could be explained with the pore size diameter distribution; breakable NPs have a diameter size pore of 2.3 while non-

breakable have 3.2 nm this could bring the idea that more surfactant is here exposed in the surface of the NPs, bringing more toxicity to the cell.
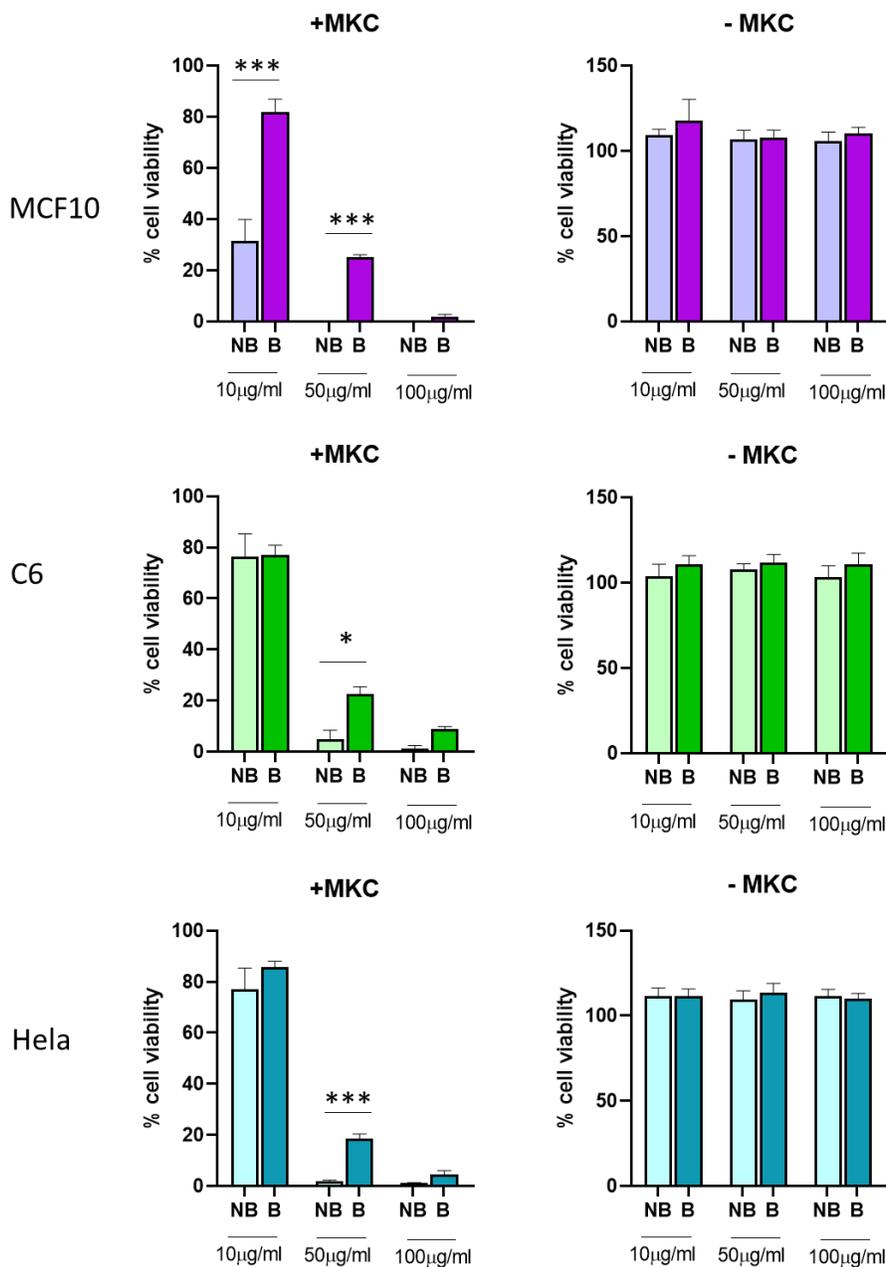
Figure 5.29. Viability assay of MCF10, C6 and HeLa cells exposed to different concentrations of NPs; non-breakable, and breakable (NB and B, respectively), with MKC and w/o MKC for 24 hours. Values are normalized to untreated cells and expressed in % of viable cells. All data are represented as mean ± S.D., statistical analysis were performed by One-way ANOVA and Turkey's post hoc test. For MCF01: *$p< 0.005$, *** $p< 0.0005$ NB vs B. $p < 0.005$ NPs+ MKC treated vs untreated cells, n.s NPs- MKC treated vs untreated cells. For C6:* *$p< 0.005$, *** $p< 0.0005$ NB vs B. $p < 0.05$ treated vs untreated cells. For HeLa:*$p< 0.005$, *** $p< 0.0005$ NB vs B. $p < 0.0005$ treated vs untreated cells except for 10μg/mL.

5.3. Conclusions

MKC-QS are vesicles capable to be coated with silica shell (breakable and non-breakable); the methodology used to coat these type of QS in contrast of the CTAB:Chol QS was a bit different in the amount of base added, the quantity of silane addition in the second addition, and the reaction time after the second addition.

MKC is a non-toxic quaternary ammonium surfactant which was tested to synthesis a new generation of mesoporous silica NPS which showed excellent characteristics to be used as drug transporters or releasers. Depending on the synthesis conditions, the characteristics of these nanoparticles could be slightly tuned and adapted to new systems. Non-breakable, breakable and Long-Pores Breakable NPs were synthetized using the MKC as a templet to produce mesoporous silica NPs, where the synthesis conditions played a critical role in the pore dimensions.

Two different methodologies were tasted to make the breakable silica NPs (Stöber and micellar templating method) in order to perform a better morphology of the NPs. The micellar method provides better morphology, but less organic material is observable analyzing TGA results.

Additionally, the improvement of the morphology was obtained using the micellar templating method if the quantity of organic material (BTSPD) is used during the synthesis. The use of mixtures between precursor (TEOS and BTSPD) helps to improve the morphology of the nanoparticles.

All the NPs characterized using this methodology present a similar porosity and NPS synthetized with the long pores produced an excellent mesoporous silica NPs with a longer distribution of pore sizes.

The breakability test was carried out employing the breakable silica NPs synthesized using 24% w/w of BTSPD in ratio of the TEOS. The breakable silica NPs could be used as a drug delivery system, this system could release the content using GSH or another reducing agent. The long pores breakable NPs should be tasted under these conditions to compare the breakability of these two systems.

The last part of the chapter was the cell viability test of the silica NPs, here was observed that breakable and non-breakable NPs synthesized by the MKC surfactant and cleaned (so that they

do not contain MKC) showed a good cell viability. Any signal of toxicity was detected at 10, 50 and 100µg/mL (100% of cell viability) with MCF10, C6 and HeLa cell lines. These observations suggest that MKC could be a good option to prepare MSNPs for biological applications.

The last step should be the loading of the NPs in order to demonstrate that this silica NPs could work as a drug delivery system in a close future.

5.4 Materials and methods

5.4.1. Materials.

All commercial solvents and reagents were used as received, without further purification. Tetraethyl orthosilicate (TEOS), Tetramethyl orthosilicate (TEMOS)(3-Aminopropyl)triethoxysilane (APTES), bis(triethoxysilyl-propyl)disulfide (BTSPD), Glutathione (GSH), was purchased from Sigma Aldrich.

5-Cholesten-3β-ol (Chol, purity 95%) was obtained from Panreac (Barcelona, Spain). Cetyltrimethylammonium bromide (CTAB, ultra for molecular biology) was purchased from Fluka-Aldrich.

1,1'-dioctadecyl-3,3,3',3'-tetramethyl-indocarbocyanine perchlorate (DiI), and cyanine5 NHS ester were purchased from Life Technologies (Carlsbad, USA) and Lumipro, respectively.

MilliQ water was used for the sample preparation (Millipore Ibérica, Madrid Spain), EtOH (Teknochroma, Sant Cugat del Vallès, Spain). Carbon dioxide (99.9% purity) purchased by Carburos Metálicos S.A. (Barcelona, Spain).

5.4.2. Synthesis

5.4.2.1 Synthesis of MKC-Quatsomes (QS)[12]

MKC-Quatsomes were prepared using the DELOS-SUSP method which has been previously described for the synthesis of CTAB:Chol QS into an aqueous phase using mild conditions of pressure (10 MPa) and temperature (308 K). MKC-Quatsomes was synthetized following the next protocol: 25.32 mg of cholesterol was added to 2.88 mL of ethanol, and then the supercritical CO_2 was added, reaching one-phase in the reactor containing the three components. The reaction was run for 1 hour, and then the solution was depressurized over a solution of 24.10 mg of MKC suspended in 24 mL of an aqueous solution, which was either PBS buffer. Finally, the resulting suspension had a total concentration of MKC-Quatsomes of 1.84 mg/mL.

5.4.2.2. Synthesis of the breakable silica shell Quatsomes (QS)

1.-Synthesis using TEMOS/BTSPD: 1 mL of QS 5.35 mg/mL was added to 6.5 mL of water, 200 µL of Ascorbic acid 50 mM and 300 µL of ammonia 0.134 M were added to obtain a pH of 8. In an Eppendorf, 4 µL of TEMOS and 2.5 µL of BTSPD were mixed with 300 µL of EtOH and added to the QS flask. After 1 day, a second addition of silanes is made; 4.6 µL of TEMOS and 3 µL of BTSPD in 200 µL of EtOH are mixed in the solution. After 20 min the reaction is stopped by dialysis (14kDa cellulose membrane).

2.- Synthesis using TEMOS/BTSPD: 1 mL of QS 5.35 mg/mL was added to 6.5 mL of water, 200 µL of Ascorbic acid (50 mM) and 300 µL of ammonia 0.134 M were added to obtain a pH of 8. In an Eppendorf, 4 µL of TEMOS and 2.5 µL of BTSPD were mixed with 300 µL of EtOH and added to the QS flask. After 1 day, a second addition of silanes is made; 4.6 µL of TEMOS and 3 µL of BTSPD in 200 µL of EtOH are mixed in the solution. Just 100 µL of this mixture is added to the sample. After 1h the reaction is stopped by dialysis (14kDa cellulose membrane).

5.4.2.3 Synthesis of MKC-MSNPs

5.4.2.3.1. Synthesis of Non-Breakable silica NPs with a non-toxic surfactant (MKC)

Micelle templating method[37] : Myristalkonium chloride (MKC) (0.6 g) was dissolved in a solution of distilled water (16 mL) and 4 mL of a solution of Triethanolamine (0.1 M,0.06 g) were added, the mixture was heated to 95 °C and stirred under 100 rpm in a ball flask of 50 mL. When the temperature of the MKC flask is stable, 1.5 mL of TEOS is added slowly to the reaction. After 1 hour of reaction, the particles were cooled down until room temperature and then 20 mL of EtOH is added. After, the NPs were cleaned by centrifugation (15 min at 20 krpm). Immediately after, the particles were washed through a sequence of sonication/centrifugation cycles (3X EtOH).

To remove the surfactant from the pores. The particles were dispersed in 100 mL of EtOH, and few drops of HCl were added, finally the solution was refluxed overnight. The last steps were to clean the particles by a sequence of sonication/centrifugation cycles in EtOH (3XEtOH) and finally dried under vacuum. The particles were then characterized by SEM, TGA, DLS and N2 adsorption techniques.

5.4.2.3.2. Synthesis of Breakable disulfide mesoporous silica NPs with a non-toxic surfactant (MKC) [42,43]

Micelle templating method [37] : Myristalkonium chloride (MKC) (0.6 g) was dissolved in a solution of distilled water (16 mL) and 4 mL of a solution 0.1 M of Triethanolamine were added. The mixture was heated to 95 °C and stirred at 100 rpm in a ball flask of 50 mL. In parallel, 1.05 mL of TEOS were mixed with 0.46 mL of BTSPD, and then was added to the MKC flask, when the temperature of the reaction flask was stabilized. After 1 hour of reaction, the particles were cooled down until room temperature and then 20 mL of EtOH were added. The particles were recollected from the dispersion by centrifugation (15 min at 20 krpm) and cleaned through a sequence of sonication/centrifugation cycles (3X EtOH). The surfactant was removed from the pores. The particles were dispersed in 100 mL of EtOH in a 250 mL ball flask, and 2 drops of HCl were added, and then the solution was refluxed overnight. After this, the particles were washed from the acid solution by a sequence of sonication/centrifugation cycles in EtOH (3XEtOH) and finally dried under vacuum. The particles were then characterized by SEM, TGA, DLS and N_2 adsorption techniques.

Stöber process [39,44] : MKC (250 mg) was dissolved in a solution of distilled water (110 mL), EtOH (10 mL) and NaOH (2M, 0.875 mL). The solution was heated to 80 °C and stirred vigorously (500 rpm). In parallel, in a vial, 875µL of TEOS was mixed with 390 µL of BTSPD in 5 mL of EtOH. When the temperature of the MKC solution is stabilized, the solution containing the silanes was added. After 6 hours of reaction, the particles were cooled down until room temperature and then recovered by centrifugation (20 min at 30 krpm). Immediately after this, the particles were washed through a sequence of sonication/centrifugation cycles (2x H_2O and 2x EtOH). The surfactant was removed from the pores, the particles were dissolved in acidic EtOH (100 mL, and few drops of HCl) and refluxed overnight (Scheme 2). After this, the particles were cleaned by a sequence of sonication/centrifugation cycles in EtOH (4xEtOH) and finally dried under vacuum. The particles were then characterized by SEM, EDX and N_2 adsorption techniques.

5.4.2.3.3. Long Pores NPs-Micellar templating method[40] to produce Breakable disulfide mesoporous silica NPs with a non-toxic surfactant (MKC)

Myristalkonium chloride (MKC) (0.6 g) was dissolved in a solution of distilled water (16 mL) and 4 mL of a solution 0.1 M of Triethanolamine were added, the mixture was heated to 95 °C and stirred under 100 rpm in a ball flask of 50 mL. In parallel, 1.15 mL of TEOS were mixed with 0.36 mL of BTSPD, the mixture was added to the MKC flask when the temperature of the reaction was stabilized. After 2 hour and 45 min of reaction, the particles were cooled down until room temperature and then 20 mL of EtOH were added. The particles were recollected from the dispersion by centrifugation (15 min at 20 krpm) and cleaned through a sequence of sonication/centrifugation cycles (3X EtOH).

100 mg of silica NPs were dispersed in 10 mL of EtOH by sonication for 30 min, followed by the addition of 20 mL of a mixture H_2O and TMB (Trimethylbenzene) (1:1). The mixture was placed in the oven at 160 °C for 3 days without stirring. After this time, the NPs are collected and washed with water and EtOH (1 and 3 respectively). The surfactant was removed from the pores. The particles were dispersed in 100 mL of EtOH in a 250 mL ball flask, and 2 drops of HCl were added to reflux overnight. After this, the particles were washed from the acid solution by a sequence of sonication/centrifugation cycles in EtOH (3XEtOH) and finally dried under vacuum. The particles were then characterized by SEM, TGA, DLS and N_2 adsorption techniques.

5.4.3. Breakability test [42]

0.3 mg of breakable and non-breakable NPs were dispersed in 2 mL of a solution of Glutathione (10 mM) in PBS and 200 rpm of stirring for 7 days. Aliquots of the solution were taken at 0, 3 and 7 days to see the breakability of the NPs during the time using STEM techniques.

5.4.4. Cell viability test

5.4.4.1. Cell lines and culture conditions

HeLa (Human cervical cancer cells), C6 (rat glia cells) were grown in DMEM-Low glucose (Dulbecco's Modified Eagle Medium with pyruvate and L-glutamine, GIBCO) supplemented with

10% fetal bovine serum (FBS, GIBCO), 100 U/mL penicillin and 0.1 mg/mL streptomycin. MCF10 (human breast non tumorigenic cells) were grown in DMEM-Low glucose (Dulbecco's Modified Eagle Medium, pyruvate and L-glutamine, GIBCO) supplemented with 10% of FBS, 100 U/mL penicillin, 0.1 mg/mL streptomycin, 100 ng/mL cholera toxin (Sigma-Aldrich) and 10 µg/mL human insulin (Sigma-Aldrich). Cells were maintained at 37 °C in a 5% CO_2 humidified atmosphere.

5.4.4.2. MTS assay

In order to evaluate the cytotoxicity of the NPs, the cell viability assay (CellTiter96® Aqueous One solution Cell Proliferation Assay, Promega) was carried out on HeLa, C6, and MCF10. Cells, that were seeded at 20000 cells/well into 96-well plate. The fresh medium containing NPs at 10-50 and 100 µg/mL was added 24 h after the seeding. Cells were incubated with the treatment for 24 h. CellTiter96® Aqueous reagent (20 µL/well) was added and incubated for 2 h. At least, plates were placed in a microplate reader (Multiskan GO, Thermo Scientific) to measure the absorbance at 490 nm, and the cytotoxicity was express as % of cell viability compared to control.

5.4.4.3. Statistical analysis

Statistical analysis was done using Prism Software (Prism 8.0; GraphPad Software, La Jolla, CA). One- ANOVA followed by Tukey's post hoc test was used for data analyses. A p value <0.05 was considered statistically significant.

5.5. REFERENCES

(1)   Berthelsen, P.; Beltoft, V.; Thorup, I.; Søborg, I.; Nielsen, E. Toxicological Evaluation and Limit Values for 2-Ethylhexyl Acryate , Propylene Carbonate , Quaternary Ammonium Compounds , Triglycidyl Isocyanurate and Tripropyleneglycol Diacrylate. **2000**, No. Environmental Project N°555, København.

(2)   Merianos, J. J. Quaternary Ammonium Antimicrobial Compounds. In *Disinfection, Sterilisation, and Preservation*; Lea & Febiger: USA, **1991**; pp 225–255.

(3)   Price, P. B. Benzalkonium Chloride (Zephiran Chloride) as a Skin Disinfectant. *Archives of surgery* **1950**, *61* (1), 23–33.

(4)   Pereira, B. M. P.; Tagkopoulos, I. Benzalkonium Chlorides: Uses, Regulatory Status, and Microbial Resistance. *Applied and Environmental Microbiology* **2019**, *85* (13), e00377-19.

(5)   Tezel U, Pavlostathis S, Tezel U, P. S. The Role of Quaternary Ammonium Compounds on Antimicrobial Resistance in the Environment. In *Antimicrobial resistance in the environment.*; John Wiley & Sons, Ltd: Hoboken, NJ, **2012**; pp 349–386.

(6)   EU Reference Laboratories, Fellbach, G. *European Commission EURL-SRM. **2012**. Analysis of Quaternary Ammonium Compounds (QACs) in Fruits and Vegetables Using QuEChERS and LC-MS/MS.*

(7)   U.S. Environmental Protection Agency (EPA). *Reregistration Eligibility Decision for Alkyl Dimethyl Benzyl Ammonium Chloride (ADBAC). EPA739-R-06-009.*; U.S. Environmental Protection Agency (EPA), Washington, DC., **2006**.

(8)   Choi, S. M.; Roh, T. H.; Lim, D. S.; Kacew, S.; Kim, H. S.; Lee, B. M. Risk Assessment of Benzalkonium Chloride in Cosmetic Products. *Journal of Toxicology and Environmental Health - Part B: Critical Reviews* **2018**, *21* (1), 8–23.

(9)   Jennings, M. C.; Minbiole, K. P. C.; Wuest, W. M. Quaternary Ammonium Compounds: An Antimicrobial Mainstay and Platform for Innovation to Address Bacterial Resistance. *ACS Infectious Diseases* **2015**, *1* (7), 288–303.

(10) Committee for Human Medicinal Products, (CHMP). *Questions and Answers on Benzalkonium Chloride Used as an Excipient in Medicinal Products for Human Use. EMA/CHMP/495737/2013*; European Medicines Agency, Amsterdam, The Netherlands., **2017**.

(11) PUBCHEM- Benzyldimethyltetradecylammonium chloride (Compound) https://pubchem.ncbi.nlm.nih.gov/compound/8755#section=Special-Reports (accessed Mar 5, **2020**).

(12) Vargas-Nadal, G.; Muñoz-Ubeda, M.; Alamo, P.; Arnal, M. M.; Céspedes, V.; Köber, M.; Gonzalez, E.; Ferrer-Tasies, L.; Vinardell, M. P.; Mangues, R.; Veciana, J.; Ventosa, N. MKC-Quatsomes: A Stable Nanovesicle Platform for Bio-Imaging and Drug-Delivery Applications. *Nanomedicine: Nanotechnology, Biology, and Medicine* **2020**, *24*, 102136.

(13) Liu, X.; Ardizzone, A.; Sui, B.; Anzola, M.; Ventosa, N.; Liu, T.; Veciana, J.; Belfield, K. D. Fluorenyl-Loaded Quatsome Nanostructured Fluorescent Probes. *ACS Omega* **2017**, *2* (8), 4112–4122.

(14) Grimaldi, N.; Andrade, F.; Segovia, N.; Ferrer-Tasies, L.; Sala, S.; Veciana, J.; Ventosa, N. Lipid-Based Nanovesicles for Nanomedicine. *Chemical Society Reviews* **2016**, *45* (23), 6520–6545.

(15) Elizondo, E.; Larsen, J.; Hatzakis, N. S.; Cabrera, I.; Bjørnholm, T.; Veciana, J.; Stamou, D.; Ventosa, N. Influence of the Preparation Route on the Supramolecular Organization of Lipids in a Vesicular System. *Journal of the American Chemical Society* **2012**, *134* (4), 1918–1921.

(16) Okahara, A.; Tanioka, H.; Takada, K.; Kawazu, K. Ocular Toxicity of Benzalkonium Chloride Homologs Compared with Their Mixtures. *Journal of Toxicologic Pathology* **2013**, *26* (4), 343–349.

(17) Segura, M. .; Gallego, S.; Sánchez de Toledo, J.; Sorianao, A.; Boloix, A.; Segovia, N.; Ventosa, N.; Veciana, J. Nanovesicles and Its Use for Nucleic Acid Delivery. Patent appl. EP19382372.

(18)   Boloix, A. Quatsomes as a Novel Nanocarrier for Clinical Delivery of Small RNA, Universitat Autònoma de Barcelona (UAB), **2019**.

(19)   Vallet-Regi, M.; Rámila, A.; Del Real, R. P.; Pérez-Pariente, J. A New Property of MCM-41: Drug Delivery System. *Chemistry of Materials* **2001**, *13* (2), 308–311.

(20)   Vallet-Regí, M.; Balas, F.; Arcos, D. Mesoporous Materials for Drug Delivery. *Angewandte Chemie - International Edition* **2007**, *46* (40), 7548–7558.

(21)   Li, Y.; Shi, J.; Hua, Z.; Chen, H.; Ruan, M.; Yan, D. Hollow Spheres of Mesoporous Aluminosilicate with a Three-Dimensional Pore Network and Extraordinarily High Hydrothermal Stability. *Nano Letters* **2003**, *3* (5), 609–612.

(22)   Slowing, I. I.; Trewyn, B. G.; Lin, V. S. Y. Mesoporous Silica Nanoparticles for Intracellular Delivery of Membrane-Impermeable Proteins. *Journal of the American Chemical Society* **2007**, *129* (28), 8845–8849.

(23)   He, Q.; Shi, J.; Chen, F.; Zhu, M.; Zhang, L. An Anticancer Drug Delivery System Based on Surfactant-Templated Mesoporous Silica Nanoparticles. *Biomaterials* **2010**, *31* (12), 3335–3346.

(24)   Trewyn, B. G.; Giri, S.; Slowing, I. I.; Lin, V. S. Y. Mesoporous Silica Nanoparticle Based Controlled Release, Drug Delivery, and Biosensor Systems. *Chemical Communications* **2007**, No. 31, 3236–3245.

(25)   Slowing, I. I.; Vivero-Escoto, J. L.; Wu, C. W.; Lin, V. S. Y. Mesoporous Silica Nanoparticles as Controlled Release Drug Delivery and Gene Transfection Carriers. *Advanced Drug Delivery Reviews* **2008**, *60* (11), 1278–1288.

(26)   Liong, M.; Lu, J.; Kovochich, M.; Xia, T.; Ruehm, S. G.; Nel, A. E.; Tamanoi, F.; Zink, J. I. Multifunctional Inorganic Nanoparticles for Imaging, Targeting, and Drug Delivery. *ACS Nano* **2008**, *2* (5), 889–896.

(27)   Manzano, M.; Colilla, M.; Vallet-Reg, M. Drug Delivery from Ordered Mesoporous Matrices. *Expert Opinion on Drug Delivery* **2009**, *6* (12), 1383–1400.

(28)   Vivero-Escoto, J. L.; Slowing, I. I.; Lin, V. S. Y.; Trewyn, B. G. Mesoporous Silica Nanoparticles for Intracellular Controlled Drug Delivery. *Small* **2010**, *6* (18), 1952–1967.

(29)   Asefa, T.; Tao, Z. Biocompatibility of Mesoporous Silica Nanoparticles. *Chemical Research in Toxicology* **2012**, *25* (11), 2265–2284.

(30)   Mal, N. K.; Fujiwara, M.; Tanaka, Y. Photocontrolled Reversible Release of Guest Molecules from Coumarin-Modified Mesoporous Silica. *Nature* **2003**, *421* (6921), 350–353.

(31)   Yang, Q.; Wang, S.; Fan, P.; Wang, L.; Di, Y.; Lin, K.; Xiao, F. S. PH-Responsive Carrier System Based on Carboxylic Acid Modified Mesoporous Silica and Polyelectrolyte for Drug Delivery. *Chemistry of Materials* **2005**, *17* (24), 5999–6003.

(32)   Zhu, Y.; Shi, J.; Shen, W.; Dong, X.; Feng, J.; Ruan, M.; Li, Y. Stimuli-Responsive Controlled Drug Release from a Hollow Mesoporous Silica Sphere/Polyelectrolyte Multilayer Core-Shell Structure. *Angewandte Chemie* **2005**, *117* (32), 5213–5217.

(33)   Nguyen, T. D.; Leung, K. C.-F.; Liong, M.; Pentecost, C. D.; Stoddart, J. F.; Zink, J. I. Construction of a PH-Driven Supramolecular Nanovalve. *Organic Letters* **2006**, *8* (5), 3363–3366.

(34)   You, Y. Z.; Kalebaila, K. K.; Brock, S. L.; Oupický, D. Temperature-Controlled Uptake and Release in PNIPAM-Modified Porous Silica Nanoparticles. *Chemistry of Materials* **2008**, *20* (10), 3354–3359.

(35)   He, Q.; Zhang, Z.; Gao, Y.; Shi, J.; Li, Y. Intracellular Localization and Cytotoxicity of Spherical Mesoporous Silica Nano-and Microparticles. *Small* **2009**, *5* (23), 2722–2729.

(36)   Lu, F.; Wu, S. H.; Hung, Y.; Mou, C. Y. Size Effect on Cell Uptake in Well-Suspended, Uniform Mesoporous Silica Nanoparticles. *Small* **2009**, *5* (12), 1408–1413.

(37)   Lv, X.; Zhang, L.; Xing, F.; Lin, H. Controlled Synthesis of Monodispersed Mesoporous Silica Nanoparticles: Particle Size Tuning and Formation Mechanism Investigation. *Microporous and Mesoporous Materials* **2016**, *225*, 238–244.

(38)   Vilmin, F.; Bottero, I.; Travert, A.; Malicki, N.; Gaboriaud, F.; Trivella, A.; Thibault-Starzyk,

F. Reactivity of Bis[3-(Triethoxysilyl)Propyl] Tetrasulfide (TESPT) Silane Coupling Agent over Hydrated Silica: Operando IR Spectroscopy and Chemometrics Study. *Journal of Physical Chemistry C* **2014**, *118* (8), 4056–4071.

(39)   Stober, W.; Fink, A.; Ernst Bohn, D. Controlled Growth of Monodisperse Silica Spheres in the Micron Size Range 1. *Journal of colloid and interface science* **1968**, *26* (1), 62–69.

(40)   Kim, M. H.; Na, H. K.; Kim, Y. K.; Ryoo, S. R.; Cho, H. S.; Lee, K. E.; Jeon, H.; Ryoo, R.; Min, D. H. Facile Synthesis of Monodispersed Mesoporous Silica Nanoparticles with Ultralarge Pores and Their Application in Gene Delivery. *ACS Nano* **2011**, *5* (5), 3568–3576.

(41)   Giakoumettis, D.; Kritis, A.; Foroglou, N. C6 Cell Line: The Gold Standard in Glioma Research. *Hippokratia* **2018**, *22* (3), 105–112.

(42)   Maggini, L.; Cabrera, I.; Ruiz-Carretero, A.; Prasetyanto, E. A.; Robinet, E.; De Cola, L. Breakable Mesoporous Silica Nanoparticles for Targeted Drug Delivery. *Nanoscale* **2016**, *8* (13), 7240–7247.

(43)   De Cola, L.; Maggini, L.; Adi, E. Matériau d'oxyde Organométallique Poreux Désintégrable. IP 14151167.5, **2014.**

(44)   ALOthman, Z. A. A Review: Fundamental Aspects of Silicate Mesoporous Materials. *Materials* **2012**, *5* (12), 2874–2902.

General conclusions and perspectives

As a general conclusion, in this thesis, it is explored the combination of different systems to form hybrid materials to perform their singular properties attributed to one material. The designs are thought to develop new alternatives in the field of nanomaterials for drug delivery applications. A new hybrid material synthesized by PLGA and mesoporous silica nanoparticles was developed as a multi-delivering system. It was built in order to deliver cannabinoids and chemotherapeutic drugs to produce a synergetic activity against cancer (*Chapter 2*). The system is designed in the way that the two drugs are delivering in two different parts of the cell (intra and extra membranal). The approaches carried out in these chapters opens a new barrier for the development of drug delivery systems. In this project, two different cannabinoids were synthesized and characterized by NMR, IR, HR ESI-TOF-MS as examples of an analog and active endocannabinoids. Different kinds of MSNPs were synthesized as an example of all the varieties of materials that could be included in the PLGA@vehicles. And different techniques were used to synthesize the PLGA@vehicles as the solvent evaporation method, self-organized precipitation route (SORP) and the hydrogel template method. This last methodology was the only one in which the homogeneity regarding size and morphology is preserved even with the inclusion of cannabinoids and mesoporous silica nanoparticles

A second hybrid material based on QS and silica was fabricated (*Chapter 3*). The construction is designed to condensate silica around the vesicles forming a shell around them, which gives more structural and mechanical stability to the QS. The silica shell mainly prevents the loss of cargo before the carrier arrives at the targeting point. This material contributes to the development of drug delivery applications. Moreover, responsive silica shell systems were synthesized to make

redox-organic response materials, which specifically breaks in presence of a reducing agent, inside of cancer cells, releasing the cargo and breaking in small pieces to prevent accumulation in the body. These materials could have a potential interest in biomedical applications.

Fluorescent molecules have been incorporated in the system silica-coated QS to produce *Label silica shell QS* for different objectives (*Chapter 4*). These systems could act as luminescent bio probes and their study was a proof of concept of their potentiality as a drug delivery system. Moreover, stimuli redox- label response systems were synthesized to carry out different studies. The spectroscopy characterization was carried out by FRET (Energy transfer) studies which were done for the loaded QS, revealing that the dye inside the Qs and the dye in the silica shell are approximated in a distance <10nm. Confocal and STORM analyses were done as a probe of the presence of the label silica and its characterization. The Breakability tests were carried out in presence of a reducing agent (GSH) and revealed that the breakability of the silica shell modifies the FRET signal in the system during the time. Permeability tests showed the protection of the QS when the silica shell is present. Release studies show a protection of the 62% of the drug loaded using a hydrophobic dye as a model drug under, the first 25h of release. Further investigations should be studied for the release of hydrophilic drugs under these systems.

Stimulus redox-response breakable silica shell was fabricated in a new kind of QS based on Myristalkonium chloride (MKC) and cholesterol. These materials are synthesized in proof of the formation of a more biocompatible system for further drug delivery proposes (*Chapter 5*). In this chapter also, the use of the MKC surfactant was proposed to be included in the synthesis of mesoporous silica nanoparticles as a template for their formation. Non-breakable silica nanoparticles and Breakable silica nanoparticles were prepared. Stimulus redox-response particles are synthesized using a disulfide linker as an organic group. Moreover, big pores were produced of the breakable mesoporous nanoparticles using MKC surfactant as a template. More biocompatible systems arrived from this work for better drug delivery materials for biomedical applications.

Mariel Ruiz Kubli

Home Address: 11 Presqu'île André-Malraux, 67100 Strasbourg, France.

November 17th 1987, México city. México.

Cell Phone :+33 777343851   **e-mail**: mariel.ruiz-kubli@etu.unistra.fr

mariel_kubli@hotmail.com

GOALS

Work with supramolecular nanostructures for Biomedical Applications.

PROFESSIONAL EXPERIENCES AND EDUCATION

2017-2020 | **PhD STUDIES**
LABORATORY OF SUPRAMOLECULAR BIOMATERIALS AND CHEMISTRY
ISIS - INSTITUT DE SCIENCE ET D'INGÉNIERIE SUPRAMOLÉCULAIRES
ECOLE DOCTORALE DES SCIENCES CHIMIQUES
Prof. Luisa De Cola
PhD IN CHEMICAL SCIENCES
Thesis: Design and synthesis of hybrid particles for drug delivery

2019-2020 | **PhD internship (8 months) OLIGO-NANOMED-RISE PROJECT**
NANOMOL TECHNOLOGIES SL and NANOMOL group
INSTITUT DE CIÈNCIA DE MATERIALS DE BARCELONA (ICMAB-CSIC)
CAMPUS UAB (UNIVERSITAT AUTÒNOMA DE BARCELONA)
Dr. Alba Córdoba, Dr. Nora Ventosa and Prof. Jaume Veciana

2014-2017 | **Research assistant**
DEPARTMENT OF INORGANIC CHEMISTRY
UNIVERSIDAD AUTÓNOMA DE MÉXICO (UNAM)|FACULTAD DE QUÍMICA
Prof. Anatoly Yatsimirsky.

2012-2014 | **MASTER STUDIES**
UNIVERSIDAD AUTÓNOMA DE MÉXICO (UNAM)|FACULTAD DE QUÍMICA
MASTER IN SCIENCES |Chemistry

Thesis: Catalytic rupture of Phosphodiesters models of RNA and DNA using lanthanide complexes with derivatives of picolinic acid, Tris and cyclodextrins as ligands.
Prof**.** Anatoly Yatsimirsky.

2006-2011 | **BACHELOR STUDIES**
UNIVERSIDAD AUTÓNOMA DEL ESTADO DE MORELOS (UAEM) | FACULTAD DE CIENCIAS
BACHELOR IN SCIENCE| Chemistry
Thesis: Prediction and analysis of the tertiary structure of the hemoglobin 3 and 4 of rice (*Oryza sativa*)
Dr. Raúl Arredondo Peter.

SKILLS

-Synthesize and characterization of mesoporous silica nanoparticles, PLGA vehicles and Quatsomes as carriers for drug delivery systems for medical applications.
-Synthesize and characterization of small organic molecules.
-Use and handling of the following equipment: SEM, STEM, EDX, DLS, ZP, TGA, nitrogen adsorption instruments. Fluorometry, UV-Vis-NIR, NMR, FTIR spectroscopies. CLSM, XRD, confocal microscope and optical microscope instruments.
- Analyze data through various characterization techniques, i.e. SAXS, XPS, TEM / SEM / STEM / EDX, DLS, ZP, TGA, Fluorometry, UV-Vis-NIR, NMR and FTIR spectroscopies, CLSM, BET analysis, confocal microscope, optical microscope instruments and data provided from STORM analysis.
- Loading and delivery of molecules in materials.
- Be responsible of instruments (FTIR, TGA, DLS, XRD).
- Collaborating with international scientists / groups from different fields (biologists, biochemists, physicists, engineers…).
- Oral communication skills expressed with several presentations of the research results at international meetings and congresses through oral and poster presentations.
-Capable to use different Softwares: Office, Chembiodraw, Origin and MestRenova.
-Languages: Spanish (native), English (fluent) and French (basic).

PUBLICATIONS

2020 | Patent under study: L. De Cola, **Ruiz-Kubli M**., Talamini L., Didier P., Köber M., Ventosa N. Breakable Silica Coated Qs.

2020 | **Ruiz-Kubli M.**, Talamini L., Didier P., Köber M., Ventosa N., De Cola L., "Breakable Silica Coated Qs: a new breakable hybrid material for a stimuli response drug release". *Under revision.*

2020 | **Ruiz-Kubli M.** Talamini L., De Cola L., "Myristalkonium chloride (MKC) as a template for a non-toxic Mesoporous silica Nanoparticles". *Manuscript in preparation.*

2020 | **Ruiz-Kubli M.** and De Cola L., "Design and synthesis of hybrid particles for tandem release of cannabinoids and chemotherapeutic drugs for the treatment of cancer tumors". *Manuscript in preparation.*

2016 | **Ruiz-Kubli M.**, Yatsimirsky AK. "Phosphodiester Cleavage by Trivalent Lanthanides in the Presence of Native Cyclodextrins". *Inorganica Chimica Acta*. 2016; 440: 9-15.

2011 | Lira-Ruan V., **Ruiz-Kubli M.**, Arredondo-Peter R. "Expression of non-symbiotic hemoglobin 1 and 2 genes in rice (Oryza sativa) embryonicorgans". *Communicative & Integrative Biology*. 2011; 4(4): 457-458.

2010 | **Ruiz-Kubli M.**, Arredondo-Peter R. "Un mundo polimérico" (A polymeric World). Published in the newspaper "La Unión de Morelos" on Monday May 17, 2010. http://acmor.org.mx/descargas/10_may_17_polimerico.pdf

AWARDS AND SCHOLARSHIPS

2019-2020 | RISE Nano-oligomed Project-Nanomol Technologies ICMAB- European Union's Horizon 2020 research and innovation programme under the Marie Skłodowska-Curie grant agreement No 778133.

2017-2020 | CONACyT (Consejo Nacional de Ciencia y Tecnología) fellowship. UNAM, Facultad de Química. DF México. From February 2017 to July 2020.

2012-2014 | CONACyT (Consejo Nacional de Ciencia y Tecnología) fellowship. UNAM, Facultad de Química. DF México. From August 2012 to August 2014.

CONFERENCES AND TALKS

2019 |PRESENTATION

Ruiz-Kubli M., De Cola L., Ventosa N., "SILICA COATED QUATSOMES". Presented at the Institut de Ciència de Materiales de Barcelona (ICMAB-CSIC), Campus UAB(UNIVERSITAT AUTÒNOMA DE BARCELONA)
Applications-Nano-OligoMed Rice project-Marie Curie Actions.
Barcelona, Spain. July 21th, 2020.

2019 |PRESENTATION

Ruiz-Kubli M., De Cola L., Ventosa N., "HYBRID HARD/SOFT CORE-SHELL SYSTEM FOR DRUG DELIVERY APPLICATIONS -SILICA COATED QUATSOMES". Presented at the European Commision for the Hybrid Nanostructured Oligonucletide Plataforms for Biomedical Applications-Nano-OligoMed Rice project-Marie Curie Actions. Brussels, Belgium. September 2nd, 2019.

2019|POSTER   **Ruiz-Kubli M**., De Cola L., "DESIGN AND SYNTHESIS OF HYBRID PARTICLES FOR THE TANDEM RELEASE OF CANNABINOIDS AND CHEMOTHERAPEUTIC DRUGS". Presented at the 6th International Conference on Multifunctional, Hybrid and Nanomaterials. Sitges, Spain. March 11-15, 2019.

2019 |PRESENTATION

Ruiz-Kubli M., De Cola L., "DESIGN AND SYNTHESIS OF HYBRID PARTICLES FOR THE TANDEM RELEASE OF CANNABINOIDS AND CHEMOTHERAPEUTIC DRUGS". Presented at the L'European Synchrotron Radiation Facility. Grenoble, France. January 11th, 2019.

2018 |PRESENTATION

Ruiz-Kubli M., De Cola L., "DESIGN AND SYNTHESIS OF HYBRID PARTICLES FOR THE TANDEM RELEASE OF CANNABINOIDS AND CHEMOTHERAPEUTIC DRUGS". Presented at the Journées des Doctorants in the European Doctoral College, Strasbourg, France. November 23th, 2018.

2018 |POSTER ISIS

Ruiz-Kubli M., De Cola L., "DESIGN AND SYNTHESIS OF HYBRID PARTICLES FOR THE TANDEM RELEASE OF CANNABINOIDS AND TEMOZOLOMIDE**".** Presented in ISIS - INSTITUT DE SCIENCE ET D'INGÉNIERIE SUPRAMOLÉCULAIRES, June, 2018.

2014 |POSTER   **Ruiz-Kubli M**., Yatsimirsky A. K. "PHOSPHODIESTER HYDROLYSIS BY LANTHANIDE COMPLEXES OF POLYHYDROXY LIGANDS". Presented at Dalton Discussion 14: Advancing the chemistry of the f-elements. Edinburgh, Scotland. July 28-30, 2014.

2014 |PRESENTATION

Ruiz-Kubli M., Yatsimirsky A. K. "CATALYTIC RUPTURE OF PHOSPHODIESTERS MODELS OF RNA AND DNA USING LANTHANIDE COMPLEX WITH POLYHYDROXIDE LIGANDS". Presented at "49° Congreso Mexicano de Química y 33°Congreso Nacional de Educación Química Mérida Yucatán", Mexico. September 17-21, 2014.

2013 |POSTER   **Ruiz-Kubli M**., Yatsimirsky A. K. "CATALYTIC RUPTURE OF PHOSPHODIESTERS MODELS OF RNA AND DNA USING LANTHANIDE COMPLEX WITH BIS-TRIS AS LIGAND". Presented at "Simposio Impacto de la Química de Coordinación en 100 años", UNAM, DF México. December 4, 2013.

2010 |POSTER   **Ruiz-Kubli M.,** Arredondo-Peter R**.** "PREDICTION AND ANALYSIS OF THE TERTIARY STRUCTURE OF THE HEMOGLOBIN 3 AND 4 OF RICE (ORYZA SATIVA)". Presented at "Congreso de estudiantes de la Facultad de Ciencias", UAEM, Cuernavaca Morelos, México, 2010.

2010 | Following the intrinsic reaction path of the $CH_4 + F^- \rightarrow CH_3F + H^-$ reaction. Universidad autónoma del estado de Morelos (UAEM). Centro de investigaciones Químicas. January 2011.

2008 | Informative talk to high school students to promote the Faculty of Science (Chemistry) UAEM. Prepartoria 1. Blvd. Cuauhnahuac Km 1.5 Cuernavaca, Morelos. March 7, 2008.

2008 | Un encuentro con la Química. Academia de Ciencias de Morelos. Instituto Tecnológico de Zacatepec Cuernavaca Morelos. September 11, 2008.

Mariel RUIZ KUBLI

Design and synthesis of hybrid particles for drug delivery

Université de Strasbourg
Excellence University

EDSC
École Doctorale des
Sciences Chimiques

Résumé

Cette thèse présente la combinaison de plusieurs systèmes d'administration pour former de nouveaux matériaux hybrides pour des applications biomédicales. Une nanoparticule poreuse cassable à base de silice intégrée dans un système hybride polymérique a été conçue pour la libération en tandem de cannabinoïdes et de médicaments chimiothérapeutiques pour le traitement du cancer. Un second matériau a été réalisé en combinant des quatsomes et de la silice. Des systèmes répondant à des stimuli ont été synthétisés pour fabriquer des matériaux sensibles à l'oxydoréduction afin d'empêcher leur accumulation dans l'organisme. Des molécules fluorescentes ont été marquées dans ces systèmes, créant ainsi de nouvelles biosondes luminescentes, capables de charger différentes molécules. En outre, un agent tensioactif non toxique a été utilisé comme modèle pour la formation de nanoparticules de silice mésoporeuse afin de produire des systèmes plus biocompatibles. Grâce à ces travaux, des matériaux plus biocompatibles peuvent arriver à améliorer l'étude des plateformes d'administration de médicaments dans le domaine de la nanomédecine.

Mots-clés : Nanomédecine, matériaux hybrides, administration de médicaments.

Résumé en anglais

This thesis presents the combination of several delivery systems to form new hybrid materials for biomedial applications. A porous breakable silica-based nanoparticle integrated in a polymeric hybrid system was created for the tandem release of cannabinoids and chemotherapeutic drugs for the treatment of cancer. A second material was designed combining quatsomes and silica. Redox-organic responsive materials were synthetized providing breakable properties to the system to allow.a safe excretion and therefore preventing their accumulation in the body. Fluorescent molecules were labelled in these systems creating new luminescent bioprobes, capable of loading different molecules. Furthermore, a non-toxic surfactant was used as a template for the formation of mesoporous silica nanoparticles to produce highly biocompatible systems. From this work, more biocompatible materials can arrive to improve the study of drug delivery platforms in the nanomedicine field.

Keywords: Nanomedicine, hybrid materials, drug delivery.